

12-1-17
NASA Contractor Report 189192

Flow Interaction Experiment Aerothermal Modeling Phase II Final Report—Volume I

M. Nikjooy and H.C. Mongia
*Allison Gas Turbine Division
General Motors Corporation
Indianapolis, Indiana*

and

J.P. Sullivan and S.N.B. Murthy
*Purdue University
West Lafayette, Indiana*

November 1993

Prepared for
Lewis Research Center
Under Contract NAS3-24350



TABLE OF CONTENTS

<u>Section</u>	<u>Title</u>	<u>Page</u>
----------------	--------------	-------------

VOLUME I

I	Introduction	1
II	Selection of Experimental Configuration	3
2.1	Gas Turbine Combustor Flow Field Characteristics	3
2.2	Idealized Combustor Flow Model	5
2.2.1	Jet Injection into a Cross Stream	5
2.2.2	Confined Swirling Flows	7
2.3	Integrated Modeling/Experimental Approach	9
III	Experimental Rig And Instrumentation	29
3.1	Initial Rigs - Design And Operation	29
3.1.1	Five-Swirler Air Rig	29
3.1.1.1	Inlet Conditions	32
3.1.1.2	Mean Flowfield	34
3.1.1.3	Turbulence Flowfield	37
3.1.2	Five-Swirler Water Rig	40
3.1.2.1	Primary Jets Only	40
3.1.2.2	Annular and Primary Jets	41
3.2	Flow Visualization Study	195
3.3	Rig Refinement Activities	196
3.3.1	Swirling Jet	196
3.3.1.1	Experimental Apparatus	196
3.3.1.2	Results and Discussion	196
3.3.2	Single Swirler Configuration	199
3.3.2.1	Data Acquisition	200
3.3.2.2	Calibration of Annular Pipe and Primary Jet	201
3.3.2.3	Inlet Conditions	203
3.3.2.4	Downstream Data	203
3.3.2.5	Turbulence Quantities	205
3.4	Final Rig - Instrumentation And Data Reduction	305
3.4.1	Final Experimental Apparatus	305
3.4.2	Instrumentation	305
3.4.2.1	Laser Doppler Velocimeter	305
3.4.2.2	Data Acquisition System	307
3.4.2.3	Velocity Measurements and Statistics Calculation	308
3.4.2.4	Error Analysis	311
3.4.2.5	Uncertainty Errors	312
3.4.2.6	Total Uncertainty	314
3.4.2.7	Marker Nephelometry	315
3.4.2.8	Test Case - Single Turbulent Jet	318
3.4.2.9	Errors	320

VOLUME II

IV	Data Presentation And Discussion	359
4.1	Dome Annular Jets	359
4.1.1	Dome Annular Jets Only - Concentration Measurements	359
4.1.2	Dome Annular Jets - Velocity Measurements	359

TABLE OF CONTENTS (cont)

<u>Section</u>	<u>Title</u>	<u>Page</u>
	4.1.2.1 Inlet Conditions	359
	4.1.2.2 Mean Flowfield Results	359
	4.1.2.3 Turbulent Flowfield Results	360
4.2	Primary Jets	412
4.2.1	Primary Jets - Concentration Measurements	412
4.2.2	Primary Jets - Velocity Measurements	412
4.2.2.1	Inlet Conditions	412
4.2.2.2	Mean Flowfield Results	413
4.2.2.3	Turbulent Flowfield Results	414
4.3	Dome Annular Jets And Primary Jets	481
4.3.1	Dome Annular Jets and Primary Jets - Concentration Measurements	481
4.3.1.1	Smoke in Primary Jets	481
4.3.1.2	Smoke in Annular Jet	481
4.3.2	Dome Annular Jets and Primary Jets - Velocity Measurements	482
4.3.2.1	Inlet Conditions	482
4.3.2.2	Mean Flowfield Results	483
4.3.2.3	Turbulent Flowfield Results	484
V	Physical And Mathematical Models	565
5.1	Governing Equations And Turbulence Models	565
5.2	Mathematical Formulation	569
5.2.1	Discretization	569
5.2.2	Power-Law Differencing Scheme	569
5.2.3	Flux-Spline Differencing Scheme	570
VI	Model Validation	575
6.1	Dome Annular Jets	575
6.2	Primary Jets	602
6.3	Dome Annular Jets And Primary Jets	616
VII	Summary and Conclusions	639
Appendix A	Turbulent Flow Equations for the k- ϵ Model	643
Appendix B	Turbulent Flow Equations for DSM Closure	647
Appendix C	Publications Partially Supported by this Study	653

LIST OF ILLUSTRATIONS

<u>Figure</u>	<u>Title</u>	<u>Page</u>
VOLUME I		
2.1-1	Model predictions of flow field around and within combustor	4
2.3-1	Nominal distribution of survey points within the test section	11
2.3-2	Longitudinal velocity vector plots for baseline configuration	12
2.3-3	Cross-sectional velocity vector plots for baseline configurations	13
2.3-4	Contour plots for plane through center of swirler for baseline configuration	14
2.3-5	Longitudinal velocity vector plots for configuration with primary jets at $x/H = 0.5$	15
2.3-6	Cross-sectional velocity vector plots for configuration with primary jets at $x/H = 0.5$	16
2.3-7	Contour plots for plane through center of swirler for configuration with primary jets of $x/H = 0.5$	17
2.3-8	Longitudinal velocity vector plots for configuration with doubled primary jet flow	18
2.3-9	Cross-sectional velocity vector plots for configuration with doubled primary jet flow	19
2.3-10	Contour plots for plane through center of swirler for configuration with doubled primary jet flow	20
2.3-11	Longitudinal velocity vector plots for annular configuration	21
2.3-12	Cross-sectional velocity vector plots for annular configuration	22
2.3-13	Contour plots for plane through center of swirler for annular configuration	23
2.3-14	Longitudinal velocity vector plots for configuration with swirler only	24
2.3-15	Cross-sectional velocity vector plots for configuration with swirler only	25
2.3-16	Contour plots for plane through center of swirler for configuration with swirler only	26
3.1.1-1	Three-view drawing of annular combustion chamber model	44
3.1.1-2	Photograph of annular combustor chamber model	45
3.1.1-3	Arrangement of the swirler cells	45
3.1.1-4	Actual annular combustor	47
3.1.1-5	Allison Gas Turbine 570-K annular combustor	48
3.1.1-6	Annular jet and throttle valve	49
3.1.1-7	Vane swirler from model combustor	50
3.1.1-8	Original swirler orientation and flow pattern	50
3.1.1-9	Modified swirler orientation and flow pattern	51
3.1.1-10	Primary cross jet and throttle valve	52
3.1.1-11	Plenum chamber and centrifugal fan	53
3.1.1-12	Contour and line plots of V for primary cross jet at $y=0.06$ in	55
3.1.1-13	Contour and line plots of V_{rms} for primary cross jet at $y=0.06$ in	56
3.1.1-14	Comparison of V data at $y=0.06$ in. to classical pipe flow data of Laufer	57
3.1.1-15	Comparison of V_{rms} data at $y=0.06$ in. to classical pipe flow data of Laufer	58
3.1.1-16	Contour and line plots of V for primary cross jet at $y=0.25$ in	59
3.1.1-17	Contour and line plots of V_{rms} for primary cross jet at $y=0.25$ in	60
3.1.1-18	Contour and line plots of V for primary cross jet at $y=0.50$ in	61
3.1.1-19	Contour and line plots of V_{rms} for primary cross jet at $y=0.50$ in	62
3.1.1-20	Contour and line plots of V for primary cross jet at $y=0.75$ in	63
3.1.1-21	Contour and line plots of V_{rms} for primary cross jet at $y=0.75$ in	64
3.1.1-22	Contour and line plots of V for primary cross jet at $y=1.00$ in	65
3.1.1-23	Contour and line plots of V_{rms} for primary cross jet at $y=1.00$ in	66
3.1.1-24	Contour and line plots of V for primary cross jet at $y=1.25$ in	67

LIST OF ILLUSTRATIONS (cont)

Figure	Title	Page
3.1.1-25	Contour and line plots of V_{rms} for primary cross jet at $y=1.25$ in.....	68
3.1.1-26	Contour and line plots of V for primary cross jet at $y=1.50$ in.....	69
3.1.1-27	Contour and line plots of V_{rms} for. primary cross jet at $y=1.50$ in.....	70
3.1.1-28	xy plane measurement grid for the primary cross jets	71
3.1.1-29	xz plane measurement grids for the primary cross jets for (a) $y=0.06$ in. and $y=0.25$ in. (b) $y=0.50, 0.75, 1.0, 1.2$	72
3.1.1-30	yz plane measurement grid.....	73
3.1.1-31	xy plane measurement grid	74
3.1.1-32	xy plane mean velocity vector plots (a) $z=5.80$ in. (b) $z=6.00$ in. (c) $z=6.20$ in.....	75
3.1.1-33	xy plane mean velocity vector plots (a) $z=6.40$ in. (b) $z=6.60$ in. (c) $z=6.80$ in.....	76
3.1.1-34	xy plane mean velocity vector plots (a) $z=7.00$ in. (b) $z=7.20$ in. (c) $z=7.40$ in.....	77
3.1.1-35	xy plane mean velocity vector plots (a) $z=7.60$ in. (b) $z=7.80$ in. (c) $z=8.00$ in.....	78
3.1.1-36	xy plane mean velocity vector plots (a) $z=8.20$ in. (b) $z=8.40$ in. (c) $z=8.60$ in.....	79
3.1.1-37	xy plane mean velocity vector plots (a) $z=8.80$ in. (b) $z=9.00$ in	80
3.1.1-38	Recirculation zone cross-sections (a) $x=1.00$ in. (b) $x=1.50$ in. (c) $x=2.00$ in. (d) $x=2.50$	81
3.1.1-39	yz plane mean velocity vector plots (a) $x=1.00$ in. (b) $x=1.50$ in	82
3.1.1-40	yz plane mean velocity vector plots (a) $x=2.00$ in. (b) $x=2.50$ in	83
3.1.1-41	yz plane mean velocity vector plots (a) $x=3.50$ in. (b) $x=4.00$ in	84
3.1.1-42	yz plane mean velocity vector plots (a) $x=4.50$ in. (b) $x=6.00$ in	85
3.1.1-43	yz plane mean velocity vector plot at $x=9.00$ in	86
3.1.1-44	Radial jet flow pattern (a) xy plane view (b) yz plane view	87
3.1.1-45	Line plot of U at $x=1.00, 1.50, 2.00$, and 2.50 in.....	88
3.1.1-46	Line plots of U at $x=3.00, 3.50, 4.00$, and 4.50 in	89
3.1.1-47	Line plots of U at $x=6.00$ in. and 9.00 in., and of V at $x=1.00$ in. and 1.50 in	90
3.1.1-48	Line plots of V at $x=2.00, 2.50, 3.00$, and 3.50 in	91
3.1.1-49	Line plots of V at $x=4.00, 4.50, 6.00$, and 9.00 in	92
3.1.1-50	Line plots of W at $x=1.00, 1.50, 2.00$, and 2.50 in	93
3.1.1-51	Line plots of W at $x=3.50, 4.00, 4.50$, and 6.00 in	94
3.1.1-52	Line plots of W at $x=9.00$ in	95
3.1.1-53	Contour and line plots of U_{rms} at $x=1.00$ in	96
3.1.1-54	Contour and line plots of V_{rms} at $x=1.00$ in	97
3.1.1-55	Contour and line plots of W_{rms} at $x=1.00$ in	98
3.1.1-56	Contour and line plots of turbulent kinetic energy (K) at $x=1.00$ in	99
3.1.1-57	Contour and line plots of U_{rms} at $x=1.50$ in	100
3.1.1-58	Contour and line plots of V_{rms} at $x=1.50$ in	101
3.1.1-59	Contour and line plots of W_{rms} at $x=1.50$ in	102
3.1.1-60	Contour and line plots of turbulent kinetic energy (K) at $x=1.50$ in	103
3.1.1-61	Contour and line plots of U_{rms} at $x=2.00$ in	104
3.1.1-62	Contour and line plots of V_{rms} at $x=2.00$ in	105
3.1.1-63	Contour and line plots of W_{rms} at $x=2.00$ in	106
3.1.1-64	Contour and line plots of turbulent kinetic energy (K) at $x=2.00$ in	107
3.1.1-65	Contour and line plots of U_{rms} at $x=2.50$ in	108
3.1.1-66	Contour and line plots of V_{rms} at $x=2.50$ in	109
3.1.1-67	Contour and line plots of W_{rms} at $x=2.50$ in	110
3.1.1-68	Contour and line plots of turbulent kinetic energy (K) at $x=2.50$ in	111
3.1.1-69	Contour and line plots of U_{rms} at $x=3.00$ in	112
3.1.1-70	Contour and line plots of V_{rms} at $x=3.00$ in	113
3.1.1-71	Contour and line plots of U_{rms} at $x=3.50$ in	114
3.1.1-72	Contour and line plots of V_{rms} at $x=3.50$ in	115

LIST OF ILLUSTRATIONS (cont)

Figure	Title	Page
3.1.1-73	Contour and line plots of W_{rms} at $x=3.50$ in	116
3.1.1-74	Contour and line plots of turbulent kinetic energy (K) at $x=3.50$ in	117
3.1.1-75	Contour and line plots of U_{rms} at $x=4.00$ in	118
3.1.1-76	Contour and line plots of V_{rms} at $x=4.00$ in	119
3.1.1-77	Contour and line plots of W_{rms} at $x=4.00$ in	120
3.1.1-78	Contour and line plots of turbulent kinetic energy (K) at $x=4.00$ in	121
3.1.1-79	Contour and line plots of U_{rms} at $x=4.50$ in	122
3.1.1-80	Contour and line plots of V_{rms} at $x=4.50$ in	123
3.1.1-81	Contour and line plots of turbulent kinetic energy (K) at $x=4.50$ in	124
3.1.1-82	Contour and line plots of U_{rms} at $x=6.00$ in	125
3.1.1-83	Contour and line plots of V_{rms} at $x=6.00$ in	126
3.1.1-84	Contour and line plots of W_{rms} at $x=6.00$ in	127
3.1.1-85	Contour and line plots of turbulent kinetic energy (K) at $x=6.00$ in	128
3.1.1-86	Contour and line plots of U_{rms} at $x=9.00$ in	129
3.1.1-87	Contour and line plots of V_{rms} at $x=9.00$ in	130
3.1.1-88	Contour and line plots of W_{rms} at $x=9.00$ in	131
3.1.1-89	Contour and line plots of turbulent kinetic energy (K) at $x=9.00$ in	132
3.1.1-90	Contour and line plots of $U'V'$ at $x=1.00$ in	133
3.1.1-91	Contour and line plots of $U'V'$ at $x=1.50$ in	134
3.1.1-92	Contour and line plots of $U'V'$ at $x=2.00$ in	135
3.1.1-93	Contour and line plots of $U'V'$ at $x=2.50$ in	136
3.1.1-94	Contour and line plots of $U'V'$ at $x=3.00$ in	137
3.1.1-95	Contour and line plots of $U'V'$ at $x=3.50$ in	138
3.1.1-96	Contour and line plots of $U'V'$ at $x=4.00$ in	139
3.1.1-97	Contour and line plots of $U'V'$ at $x=4.50$ in	140
3.1.1-98	Contour and line plots of $U'V'$ at $x=6.00$ in	141
3.1.1-99	Contour and line plots of $U'V'$ at $x=9.00$ in	142
3.1.2-1	Model annular combustor test rig schematic	143
3.1.2-2	Detail of model annular combustor test section	144
3.1.2-3	Section of model annular combustor test section	145
3.1.2-4	Flow calibration curves for primary jet flow	146
3.1.2-5	Venturi calibration curve for total jet flow	147
3.1.2-6	Model annular combustor coordinate system	147
3.1.2-7	Single frame primary jet concentration field visualization image without annular jet flow ($z = 7.5$ in.)	149
3.1.2-8	One hundred twenty-seven frame average primary jet concentration field visualization image without annular jet flow ($z = 7.5$ in.)	149
3.1.2-9	Single frame primary jet concentration field visualization image without annular jet flow ($z = 7.0$ in.)	151
3.1.2-10	One hundred twenty-seven frame average primary jet concentration field visualization image without annular jet flow ($z = 7.0$ in.)	151
3.1.2-11	Mean primary jet concentration without annular jet flow ($z = 7.5$ in.)	153
3.1.2-12	Mean primary jet concentration without annular jet flow ($z = 7.0$ in.)	154
3.1.2-13	Mean primary jet concentration without annular jet flow ($z = 6.5$ in.)	155
3.1.2-14	Mean primary jet concentration without annular jet flow ($z = 6.0$ in.)	156
3.1.2-15	Mean primary jet concentration without annular jet flow ($x = 3.0$ in.)	157
3.1.2-16	Root mean square primary jet concentration without annular jet flow ($z = 7.5$ in.)	158
3.1.2-17	Root mean square primary jet concentration without annular jet flow ($z = 7.0$ in.)	159

LIST OF ILLUSTRATIONS (cont)

<u>Figure</u>	<u>Title</u>	<u>Page</u>
3.1.2-18	Root mean square primary jet concentration without annular jet flow (z = 6.5 in.)	160
3.1.2-19	Root mean square primary jet concentration without annular jet flow (z = 6.0 in.)	161
3.1.2-20	Root mean square primary jet concentration without annular jet flow (c = 3.0 in.)	162
3.1.2-21	Single frame primary jet concentration field visualization image with annular jet flow (z = 7.5 in.)	163
3.1.2-22	One hundred twenty-seven frame average primary jet concentration field visualization image with annular jet flow (z = 7.5 in.)	163
3.1.2-23	Single frame primary jet concentration field visualization image with annular jet flow (z = 7.0 in.)	165
3.1.2-24	One hundred twenty-seven frame average primary jet concentration field visualization image with annular jet flow (z = 7.0 in.)	165
3.1.2-25	Mean primary jet concentration with annular jet flow (z = 7.5 in.)	167
3.1.2-26	Mean primary jet concentration with annular jet flow (z = 7.0 in.)	168
3.1.2-27	Mean primary jet concentration with annular jet flow (z = 6.5 in.)	169
3.1.2-28	Mean primary jet concentration with annular jet flow (z = 6.0 in.)	170
3.1.2-29	Mean primary jet concentration with annular jet flow (x = 3.0 in.)	171
3.1.2-30	Root mean square primary jet concentration with annular jet flow (z = 7.5 in.)	172
3.1.2-31	Root mean square primary jet concentration with annular jet flow (z = 7.0 in.)	173
3.1.2-32	Root mean square primary jet concentration with annular jet flow (z = 6.5 in.)	174
3.1.2-33	Root mean square primary jet concentration with annular jet flow (z = 6.0 in.)	175
3.1.2-34	Root mean square primary jet concentration with annular jet flow (x = 3.0 in.)	176
3.1.2-35	Root mean square primary jet concentration normalized by $\bar{C}_{CL,MAX}$ with annular jet flow (x = 3.0 in.)	177
3.1.2-36	Comparison of primary jet concentration with and without annular jet flow (z = 7.5 in.)	178
3.1.2-37	Comparison of primary jet concentration with and without annular jet flow (x = 3.0 in.)	179
3.1.2-38	Single frame annular jet concentration field visualization image (z = 7.5 in.)	181
3.1.2-39	Frame average annular jet concentration field visualization image (z = 7.5 in.)	181
3.1.2-40	Single frame annular jet concentration field visualization image (z = 7.0 in.)	183
3.1.2-41	Frame average annular jet concentration field visualization image (z = 7.0 in.)	183
3.1.2-42	Mean annular jet concentration (z = 7.5 in.)	185
3.1.2-43	Mean annular jet concentration (z = 7.0 in.)	186
3.1.2-44	Mean annular jet concentration (z = 6.5 in.)	187
3.1.2-45	Mean annular jet concentration (z = 6.0 in.)	188
3.1.2-46	Mean annular jet concentration (y = 1.5 in.)	189
3.1.2-47	Root mean square annular jet concentration (z = 7.5 in.)	190
3.1.2-48	Root mean square annular jet concentration (z = 7.0 in.)	191
3.1.2-49	Root mean square annular jet concentration (z = 6.5 in.)	192
3.1.2-50	Root mean square annular jet concentration (z = 6.0 in.)	193
3.1.2-51	Root mean square annular jet concentration (y = 1.5 in.)	194
3.3.1-1	Photograph of swirling jet apparatus	207
3.3.1-2	Concentration fields for N=0.00 (a) 1 frame (b) 127 frames	209
3.3.1-3	Concentration fields for N=0.33 (a) 1 frame (b) 127 frames	211
3.3.1-4	Concentration fields for N=0.66 (a) 1 frame (b) 127 frames	213
3.3.1-5	Concentration fields for N=1.00 (a) 1 frame (b) 127 frames	215

LIST OF ILLUSTRATIONS (cont)

Figure	Title	Page
3.3.1-6	Concentration fields for $N=1.33$ (a) 1 frame (b) 127 frames	217
3.3.1-7	Concentration fields for $N=1.66$ (a) 1 frame (b) 127 frames	219
3.3.1-8	Concentration fields for $N=2.00$ (a) 1 frame (b) 127 frames	221
3.3.1-9	Relationship between spread angle and swirl ratio	223
3.3.2-1	Diagram of vane swirler	224
3.3.2-2	Drawing of annular swirler inlet.....	225
3.3.2-3	Determination of primary jet diameters	226
3.3.2-4	Drawing of primary jet	227
3.3.2-5	Single swirler loss test rig.....	228
3.3.2-6	Single swirler rig for LDV measurements	229
3.3.2-7	Results of swirler loss tests	230
3.3.2-8	Data acquisition system for LDV measurements.....	231
3.3.2-9	Laser table and boom assembly	232
3.3.2-10	Setup for measurement of flow profile	233
3.3.2-11	Primary jet flow profile.....	234
3.3.2-12	Pressure transducer arrangement for mass flow calibration of primary jet	235
3.3.2-13	Mass flow calibration plot for primary jet	236
3.3.2-14	Pressure transducer arrangement for measurement of primary jet inlet loss	237
3.3.2-15	Pressure transducer arrangement for measurement of primary jet exit loss.....	238
3.3.2-16	Pressure transducer arrangement for measurement of primary jet pressure loss....	239
3.3.2-17	Plot of primary jet inlet pressure loss	240
3.3.2-18	Plot of primary jet exit pressure loss	241
3.3.2-19	Plot of primary jet pressure loss	242
3.3.2-20	Pressure transducer arrangement for mass flow calibration of annular pipe	243
3.3.2-21	Mass flow calibration plot for annular pipe	244
3.3.2-22	Plot of annular pipe inlet pressure loss	245
3.3.2-23	Plot of annular pipe exit pressure loss	246
3.3.2-24	Plot of annular pipe pressure loss	247
3.3.2-25	Pressure transducer arrangement for measurement of swirler inlet loss	248
3.3.2-26	Plot of swirler inlet pressure loss	249
3.3.2-27	Plot of pressure loss across swirler	250
3.3.2-28	Plot of swirler pressure loss	251
3.3.2-29	Swirler inlet data grid	252
3.3.2-30	Cascade plots of swirler inlet U velocity (scans 1 and 2).....	253
3.3.2-31	Swirler inlet plots of U velocity at specific z locations (scans 1 and 2).....	254
3.3.2-32	Cascade plots of swirler inlet V and W velocities	255
3.3.2-33	Swirler inlet plots of V and W velocities at specific z locations.....	256
3.3.2-34	Vector plot of swirler inlet V and W velocities	257
3.3.2-35	Swirler inlet laser orientation	258
3.3.2-36	Cascade plots of turbulence intensity for swirler inlet (scan 1).....	259
3.3.2-37	Swirler inlet plots of turbulence intensity at specific z locations (scan 1).....	260
3.3.2-38	Cascade plots of turbulence intensity for swirler inlet (scan 2).....	261
3.3.2-39	Swirler inlet plots of turbulence intensity at specific z locations (scan 2).....	262
3.3.2-40	Downstream data grid (scans 1 and 2)	263
3.3.2-41	Combined data grid	264
3.3.2-42	Laser orientation for downstream data	265
3.3.2-43	Cascade plots of U velocity at $x=1.5$ in. (scans 1 and 2).....	266
3.3.2-44	Plots of U velocity at $x=1.5$ in. (scans 1 and 2)	267
3.3.2-45	Cascade plots of V and W velocities at $x=1.5$ in.....	268
3.3.2-46	Plots of V and W velocities at $x=1.5$ in	269

LIST OF ILLUSTRATIONS (cont)

<u>Figure</u>	<u>Title</u>	<u>Page</u>
3.3.2-47	Vector plot of V and W velocities at x=1.5 in	270
3.3.2-48	Cascade plots of U velocity at x=3.0 in. (scans 1 and 2)	271
3.3.2-49	Plots of U velocity at x=3.0 in. (scans 1 and 2)	272
3.3.2-50	Cascade plots of V and W velocities at x=3.0 in	273
3.3.2-51	Plots of V and W velocities at x=3.0 in	274
3.3.2-52	Vector plot of V and W velocities at x=3.0 in	275
3.3.2-53	Cascade plots of U velocity at x=4.5 in. (scans 1 and 2)	276
3.3.2-54	Plots of U velocity at x=4.5 in. (scans 1 and 2)	277
3.3.2-55	Cascade plots of V and W velocities at x=4.5 in	278
3.3.2-56	Plots of V and W velocities at x=4.5 in	279
3.3.2-57	Vector plot of V and W velocities at x=4.5 in	280
3.3.2-58	Cascade plots of U velocity at x=6.0 in. (scans 1 and 2)	281
3.3.2-59	Plots of U velocity at x=6.0 in. (scans 1 and 2)	282
3.3.2-60	Cascade plots of V and W velocities at x=6.0 in	283
3.3.2-61	Plots of V and W velocities at x=6.0 in	284
3.3.2-62	Vector plot of V and W velocities at x=6.0 in	285
3.3.2-63	Contour plots of U velocity indicating regions of reverse flow	286
3.3.2-64	Vector plot at z=1.5 in	287
3.3.2-65	Sketch of swirler exit flow regimes	288
3.3.2-66	Cascade plots of turbulence intensity at x=1.5 in. (scan 1)	289
3.3.2-67	Plots of turbulence intensity at x=1.5 in. (scan 1)	290
3.3.2-68	Cascade plots of turbulence intensity at x=1.5 in. (scan 2)	291
3.3.2-69	Plots of turbulence intensity at x=1.5 in. (scan 2)	292
3.3.2-70	Cascade plots of turbulence intensity at x=3.0 in. (scan 1)	293
3.3.2-71	Plots of turbulence intensity at x=3.0 in. (scan 1)	294
3.3.2-72	Cascade plots of turbulence intensity at x=3.0 in. (scan 2)	295
3.3.2-73	Plots of turbulence intensity at x=3.0 in. (scan 2)	296
3.3.2-74	Cascade plots of turbulence intensity at x=4.5 in. (scan 1)	297
3.3.2-75	Plots of turbulence intensity at x=4.5 in. (scan 1)	298
3.3.2-76	Cascade plots of turbulence intensity at x=4.5 in. (scan 2)	299
3.3.2-77	Plots of turbulence intensity at x=4.5 in. (scan 2)	300
3.3.2-78	Cascade plots of turbulence intensity at x=6.0 in. (scan 1)	301
3.3.2-79	Plots of turbulence intensity at x=6.0 in. (scan 1)	302
3.3.2-80	Cascade plots of turbulence intensity at x=6.0 in. (scan 2)	303
3.3.2-81	Plots of turbulence intensity at x=6.0 in. (scan 2)	304
3.4.1-1	Annular jets only	321
3.4.1-2	Primary jets only	322
3.4.1-3	Annular and primary jets - three-view drawing	323
3.4.1-4	Primary and annular jet - detail drawing	324
3.4.1-5	Head assembly - detail drawing	325
3.4.2-1	Receiving optics boom support	326
3.4.2-2	LDV optics and rig setup	327
3.4.2-3	Schematic of LDV data acquisition system	328
3.4.2-4	Velocity measurement coordinate relations	329
3.4.2-5	Orientation of beams for velocity measurements	330
3.4.2-6	Actual and desired velocity component relations	331
3.4.2-7	U velocity error due to uncertainty in beam angle	331
3.4.2-8	U velocity error due to frequency resolution	332
3.4.2-9	U and Urms velocity error due to sampling uncertainty	333
3.4.2-10	V error due to rotation of optics	334

LIST OF ILLUSTRATIONS (cont)

<u>Figure</u>	<u>Title</u>	<u>Page</u>
3.4.2-11	Vrms velocity error due to rotation of optics	334
3.4.2-12	U'V' error due to rotation of optics	335
3.4.2-13	Total U velocity error	335
3.4.2-14	Total Urms velocity error	336
3.4.2-15	Total V velocity error	336
3.4.2-16	Total Vrms velocity error	337
3.4.2-17	Total U'V' error	337
3.4.2-18	Total turbulent kinetic energy error	338
3.4.2-19	Mean concentration of fluorescent dye in round jet ($x/D=0.5$)	338
3.4.2-20	Test equipment schematic design	339
3.4.2-21	Temporal and spatial image acquisition scheme	340
3.4.2-22	Instantaneous concentration profiles for consecutive image fields ($x/D=1.5$)	341
3.4.2-23	One hundred twenty-seven frame average dark response image of single jet setup	341
3.4.2-24	General diagram of experimental set-up	343
3.4.2-25	Detail of single jet test section	344
3.4.2-26	Concentration fluctuation spectrum on jet centerline ($x/D=32$)	345
3.4.2-27	Single frame concentration field visualization image	347
3.4.2-28	One hundred twenty-seven frames concentration field visualization image	347
3.4.2-29	Three-dimensional representation of mean and rms concentration profiles	349
3.4.2-30	Mean and rms concentration profiles at jet exit ($x/D=0.1$)	350
3.4.2-31	Mean concentration profile at $x/D=1.0$	350
3.4.2-32	Concentration profile for rms at $x/D=1.5$	351
3.4.2-33	Mean concentration profiles at $x/D = 2.0$ and 4.0	352
3.4.2-34	Concentration profiles for rms at $x/D=2.0$ and 4.0	353
3.4.2-35	Jet concentration half width growth	354
3.4.2-36	Uniform concentration profiles, raw data	355
3.4.2-37	Uniform concentration profiles, dark response subtracted	355
3.4.2-38	Uniform concentration profiles, two step correction applied	356

VOLUME II

4.1-1	Annular jets only - three-view drawing	362
4.1.1-1	Annular jets only single frame picture, $z=7.5$ in	363
4.1.1-2	Annular jets only 127 frame average picture, $z=7.5$ in	363
4.1.1-3	Annular jets only single frame picture, $z=7.0$ in	365
4.1.1-4	Annular jets only 127 frame average picture, $z=7.0$ in	365
4.1.1-5	Annular jets only single frame picture, $z=8.0$ in	367
4.1.1-6	Annular jets only 127 frame average picture, $z=8.0$ in	367
4.1.2-1	Annular jet scans for inlet conditions	369
4.1.2-2	Annular jets only and Urms distribution of the annular jets at $x=0.08$ in	370
4.1.2-3	Annular jets only xy plane sampling grids	371
4.1.2-4	Annular jets only mean velocity vector plot at $z=7.5$ in	372
4.1.2-5	Annular jets only mean velocity vector plots a) $z=7.4$ in. b) $z=7.6$ in	373
4.1.2-6	Annular jets only mean velocity vector plots a) $z=7.3$ in. b) $z=7.7$ in	374
4.1.2-7	Annular jets only mean velocity vector plots a) $z=7.2$ in. b) $z=7.8$ in	375
4.1.2-8	Annular jets only mean velocity vector plots a) $z=7.1$ in. b) $z=7.9$ in	376
4.1.2-9	Annular jets only mean velocity vector plots a) $z=7.0$ in. b) $z=8.0$ in	377
4.1.2-10	Annular jets only mean velocity vector plots a) $z=6.9$ in. b) $z=8.1$ in	378
4.1.2-11	Annular jets only mean velocity vector plots a) $z=6.8$ in. b) $z=8.2$ in	379

LIST OF ILLUSTRATIONS (cont)

Figure	Title	Page
4.1.2-12	Annular jets only mean velocity vector plots a) $z=6.7$ in. b) $z=8.3$ in	380
4.1.2-13	Annular jets only mean velocity vector plots a) $z=6.6$ in. b) $z=8.4$ in	381
4.1.2-14	Annular jets only mean velocity vector plots a) $z=6.5$ in. b) $z=8.5$ in	382
4.1.2-15	Annular jets only mean velocity vector plots a) $z=6.4$ in. b) $z=8.6$ in	383
4.1.2-16	Annular jets only mean velocity vector plots a) $z=6.3$ in. b) $z=8.7$ in	384
4.1.2-17	Annular jets only mean velocity vector plots a) $z=6.2$ in. b) $z=8.8$ in	385
4.1.2-18	Annular jets only mean velocity vector plots a) $z=6.1$ in. b) $z=8.9$ in	386
4.1.2-19	Annular jets only mean velocity vector plots a) $z=6.0$ in. b) $z=9.0$ in	387
4.1.2-20	Annular jets only contour plot of U_{rms} and V_{rms} at $x=0.5$ in	388
4.1.2-21	Annular jets only contour plot of U_{rms} and V_{rms} at $x=1.0$ in	389
4.1.2-22	Annular jets only contour plot of U_{rms} and V_{rms} at $x=1.5$ in	390
4.1.2-23	Annular jets only contour plot of U_{rms} and V_{rms} at $x=2.0$ in	391
4.1.2-24	Annular jets only contour plot of U_{rms} and V_{rms} at $x=2.5$ in	392
4.1.2-25	Annular jets only contour plot of U_{rms} and V_{rms} at $x=3.0$ in	393
4.1.2-26	Annular jets only contour plot of U_{rms} and V_{rms} at $x=3.5$ in	394
4.1.2-27	Annular jets only contour plot of U_{rms} and V_{rms} at $x=4.0$ in	395
4.1.2-28	Annular jets only contour plot of U_{rms} and V_{rms} at $x=6.0$ in	396
4.1.2-29	Annular jets only contour plot of U_{rms} and V_{rms} at $x=9.0$ in	397
4.1.2-30	Annular jets only U_{rms} distribution	398
4.1.2-31	Annular jets only V_{rms} distribution	399
4.1.2-32	Annular jets only contour plot of turbulent kinetic energy (K) at a) $x=0.5$ in. b) $x=1.0$ in	400
4.1.2-33	Annular jets only contour plot of turbulent kinetic energy (K) at a) $x=1.5$ in. b) $x=2.0$ in	401
4.1.2-34	Annular jets only contour plot of turbulent kinetic energy (K) at a) $x=2.5$ in. b) $x=3.0$ in	402
4.1.2-35	Annular jets only contour plot of turbulent kinetic energy (K) at a) $x=3.5$ in. b) $x=4.0$ in	403
4.1.2-36	Annular jets only contour plot of turbulent kinetic energy (K) at a) $x=6.0$ in. b) $x=9.0$ in	404
4.1.2-37	Annular jets only turbulent kinetic energy (K) distribution	405
4.1.2-38	Annular jets only contour plot of $U'V'$ at a) $x=0.5$ in. b) $x=1.0$ in	406
4.1.2-39	Annular jets only contour plot of $U'V'$ at a) $x=1.5$ in. b) $x=2.0$ in	407
4.1.2-40	Annular jets only contour plot of $U'V'$ at a) $x=2.5$ in. b) $x=3.0$ in	408
4.1.2-41	Annular jets only contour plot of $U'V'$ at a) $x=3.5$ in. b) $x=4.0$ in	409
4.1.2-42	Annular jets only contour plot of $U'V'$ at a) $x=6.0$ in. b) $x=9.0$ in	410
4.1.2-43	Annular jets only $U'V'$ distribution	411
4.2-1	Primary jets only - three-view drawing	417
4.2.1-1	Primary jets only single frame picture, $z=7.5$ in	419
4.2.1-2	Primary jets only 127 frame average picture, $z=7.5$ in	419
4.2.1-3	Primary jets only single frame picture, $z=7.0$ in	421
4.2.1-4	Primary jets only 127 frame average picture, $z=7.0$ in	421
4.2.1-5	Primary jets only single frame picture, $z=8.0$ in	423
4.2.1-6	Primary jets only 127 frame average picture, $z=8.0$ in	423
4.2.1-7	Primary jets only mean concentration distribution, $z=7.5$ in	425
4.2.1-8	Primary jets only mean concentration distribution, $z=7.0$ in	426
4.2.1-9	Primary jets only mean concentration distribution, $z=8.0$ in	427
4.2.1-10	Primary jets only mean concentration distribution, $z=6.5$ in	428
4.2.1-11	Primary jets only mean concentration distribution, $z=8.5$ in	429
4.2.1-12	Primary jets only mean concentration along primary jet axis, $x=1.5$ in	430

LIST OF ILLUSTRATIONS (cont)

<u>Figure</u>	<u>Title</u>	<u>Page</u>
4.2.2-1	Primary jets only - three-view drawing	431
4.2.2-2	xy plane primary jets sampling grid.....	432
4.2.2-3	xz plane primary jets sampling grid	432
4.2.2-4	Primary jets only and Vrms distribution of the primary jets at y=0.1 in	433
4.2.2-5	Primary jets only and Vrms distribution of the primary jets at y=0.25 in	434
4.2.2-6	Primary jets only and Vrms distribution of the primary jets at y=0.5 in	435
4.2.2-7	Primary jets only and Vrms distribution of the primary jets at y=0.75 in	436
4.2.2-8	Primary jets only and Vrms distribution of the primary jets at y=1.0 in	437
4.2.2-9	Primary jets only and Vrms distribution of the primary jets at y=1.25 in	438
4.2.2-10	Primary jets only and Vrms distribution of the primary jets at y=1.5 in	439
4.2.2-11	Primary jets only and Vrms distribution comparison of the primary jets at y=0.6 in. and y=2.4 in	440
4.2.2-12	Primary jets only xy plane sampling grid	441
4.2.2-13	Primary jets only mean velocity vector plot at z=7.5 in.....	442
4.2.2-14	Primary jets only mean velocity vector plots a) z=7.4 in. b) z=7.6 in	443
4.2.2-15	Primary jets only mean velocity vector plots a) z=7.3 in. b) z=7.7 in	444
4.2.2-16	Primary jets only mean velocity vector plots a) z=7.2 in. b) z=7.8 in	445
4.2.2-17	Primary jets only mean velocity vector plots a) z=7.1 in. b) z=7.9 in	446
4.2.2-18	Primary jets only mean velocity vector plots a) z=7.0 in. b) z=8.0 in	447
4.2.2-19	Primary jets only mean velocity vector plots a) z=6.9 in. b) z=8.1 in	448
4.2.2-20	Primary jets only mean velocity vector plots a) z=6.8 in. b) z=8.2 in	449
4.2.2-21	Primary jets only mean velocity vector plots a) z=6.7 in. b) z=8.3 in	450
4.2.2-22	Primary jets only mean velocity vector plots a) z=6.6 in. b) z=8.4 in	451
4.2.2-23	Primary jets only mean velocity vector plots a) z=6.5 in. b) z=8.5 in	452
4.2.2-24	Primary jets only mean velocity vector plots a) z=6.4 in. b) z=8.6 in	453
4.2.2-25	Primary jets only mean velocity vector plots a) z=6.3 in. b) z=8.7 in	454
4.2.2-26	Primary jets only mean velocity vector plots a) z=6.2 in. b) z=8.8 in	455
4.2.2-27	Primary jets only mean velocity vector plots a) z=6.1 in. b) z=8.9 in	456
4.2.2-28	Primary jets only mean velocity vector plots a) z=6.0 in. b) z=9.0 in	457
4.2.2-29	Primary jets only contour plot of Urms and Vrms at x=0.5 in.....	458
4.2.2-30	Primary jets only contour plot of Urms and Vrms at x=1.0 in.....	459
4.2.2-31	Primary jets only contour plot of Urms and Vrms at x=1.5 in.....	460
4.2.2-32	Primary jets only contour plot of Urms and Vrms at x=2.0 in.....	461
4.2.2-33	Primary jets only contour plot of Urms and Vrms at x=2.5 in.....	462
4.2.2-34	Primary jets only contour plot of Urms and Vrms at x=3.0 in.....	463
4.2.2-35	Primary jets only contour plot of Urms and Vrms at x=3.5 in.....	464
4.2.2-36	Primary jets only contour plot of Urms and Vrms at x=4.0 in.....	465
4.2.2-37	Primary jets only contour plot of Urms and Vrms at x=6.0 in.....	466
4.2.2-38	Primary jets only Urms distribution	467
4.2.2-39	Primary jets only Vrms distribution	468
4.2.2-40	Primary jets only contour plot of turbulent kinetic energy (K) at a) x=0.5 in. b) x=1.0 in	469
4.2.2-41	Primary jets only contour plot of turbulent kinetic energy (K) at a) x=1.5 in. b) x=2.0 in	470
4.2.2-42	Primary jets only contour plot of turbulent kinetic energy (K) at a) x=2.5 in. b) x=3.0 in	471
4.2.2-43	Primary jets only contour plot of turbulent kinetic energy (K) at a) x=3.5 in. b) x=4.0 in	472
4.2.2-44	Primary jets only contour plot of turbulent kinetic energy (K) at x=6.0 in.....	473
4.2.2-45	Primary jets only turbulent kinetic energy (K) distribution.....	474

LIST OF ILLUSTRATIONS (cont)

<u>Figure</u>	<u>Title</u>	<u>Page</u>
4.2.2-46	Primary jets only contour plot of U'V' at a) x=0.5 in. b) x=1.0 in.....	475
4.2.2-47	Primary jets only contour plot of U'V' at a) x=1.5 in. b) x=2.0 in.....	476
4.2.2-48	Primary jets only contour plot of U'V' at a) x=2.5 in. b) x=3.0 in.....	477
4.2.2-49	Primary jets only contour plot of U'V' at a) x=3.5 in. b) x=4.0 in.....	478
4.2.2-50	Primary jets only contour plot of U'V' at x=6.0 in	479
4.2.2-51	Primary jets only U'V' distribution	480
4.3-1	Annular and primary jets - three-view drawing	487
4.3.1-1	Annular and primary jets with smoke in primary jet, single frame picture, z=7.5 in	489
4.3.1-2	Annular and primary jets with smoke in primary jet, 127 frame average picture, z=7.5 in	489
4.3.1-3	Annular and primary jets with smoke in primary jet, single frame picture, z=7.0 in	491
4.3.1-4	Annular and primary jets with smoke in primary jet, 127 frame average picture, z=7.0 in	491
4.3.1-5	Annular and primary jets with smoke in primary jet, single frame picture, z=8.0 in	493
4.3.1-6	Annular and primary jets with smoke in primary jet, 127 frame average picture, z=8.0 in	493
4.3.1-7	Annular and primary jets mean concentration distribution with smoke in lower primary jet, z=7.5 in	495
4.3.1-8	Annular and primary jets mean concentration distribution with smoke in lower primary jet, z=7.0 in	496
4.3.1-9	Annular and primary jets mean concentration distribution with smoke in lower primary jet, z=8.0 in	497
4.3.1-10	Annular and primary jets mean concentration distribution with smoke in lower primary jet, z=6.5 in	498
4.3.1-11	Annular and primary jets mean concentration distribution with smoke in lower primary jet, z=8.5 in	499
4.3.1-12	Annular and primary jets mean concentration along primary jet axis with smoke in lower primary jet, x=1.5 in	500
4.3.1-13	Annular and primary jets with smoke in annular jet, single frame picture, z=7.5 in	501
4.3.1-14	Annular and primary jets with smoke in annular jet, 127 frame average picture, z=7.5 in	501
4.3.1-15	Annular and primary jets with smoke in annular jet, single frame picture, z=7.0 in	503
4.3.1-16	Annular and primary jets with smoke in annular jet, 127 frame average picture, z=7.0 in	503
4.3.1-17	Annular and primary jets with smoke in annular jet, single frame picture, z=8.0 in	505
4.3.1-18	Annular and primary jets with smoke in annular jet, 127 frame average picture, z=8.0 in	505
4.3.1-19	Annular and primary jets mean concentration distribution with smoke in annular jet, z=7.5 in	507
4.3.1-20	Annular and primary jets mean concentration distribution with smoke in annular jet, z=7.0 in	508
4.3.1-21	Annular and primary jets mean concentration distribution with smoke in annular jet, z=8.0 in	509

LIST OF ILLUSTRATIONS (cont)

Figure	Title	Page
4.3.1-22	Annular and primary jets mean concentration distribution with smoke in annular jet, $z=6.5$ in	510
4.3.1-23	Annular and primary jets mean concentration distribution with smoke in annular jet, $z=8.5$ in	511
4.3.2-1	Annular and primary jets - three-view drawing	512
4.3.2-2	Annular and primary jets and V_{rms} distribution of the primary jets at $y=0.1$ in	513
4.3.2-3	Annular and primary jets and V_{rms} distribution of the primary jets at $y=0.25$ in	514
4.3.2-4	Annular and primary jets and V_{rms} distribution of the primary jets at $y=0.5$ in	515
4.3.2-5	Annular and primary jets and V_{rms} distribution of the primary jets at $y=0.75$ in	516
4.3.2-6	Annular and primary jets and V_{rms} distribution of the primary jets at $y=1.0$ in	517
4.3.2-7	Annular and primary jets and V_{rms} distribution of the primary jets at $y=1.25$ in	518
4.3.2-8	Annular and primary jets and V_{rms} distribution of the primary jets at $y=1.5$ in	519
4.3.2-9	Annular and primary jets and V_{rms} distribution comparison of the primary jets at $y=0.6$ in. and $y=2.4$ in	520
4.3.2-10	Annular and primary jets and U_{rms} distribution of the annular jets at $x=0.08$ in	521
4.3.2-11	Annular and primary jets xy plane sampling grid	522
4.3.2-12	Annular and primary jets mean velocity vector plot at $z=7.5$ in	523
4.3.2-13	Annular and primary jets mean velocity vector plot at a) $z=7.4$ in. b) $z=7.6$ in	524
4.3.2-14	Annular and primary jets mean velocity vector plot at a) $z=7.3$ in. b) $z=7.7$ in	525
4.3.2-15	Annular and primary jets mean velocity vector plot at a) $z=7.2$ in. b) $z=7.8$ in	526
4.3.2-16	Annular and primary jets mean velocity vector plot at a) $z=7.1$ in. b) $z=7.9$ in	527
4.3.2-17	Annular and primary jets mean velocity vector plot at a) $z=7.0$ in. b) $z=8.0$ in	528
4.3.2-18	Annular and primary jets mean velocity vector plot at a) $z=6.9$ in. b) $z=8.1$ in	529
4.3.2-19	Annular and primary jets mean velocity vector plot at a) $z=6.8$ in. b) $z=8.2$ in	530
4.3.2-20	Annular and primary jets mean velocity vector plot at a) $z=6.7$ in. b) $z=8.3$ in	531
4.3.2-21	Annular and primary jets mean velocity vector plot at a) $z=6.6$ in. b) $z=8.4$ in	532
4.3.2-22	Annular and primary jets mean velocity vector plot at a) $z=6.5$ in. b) $z=8.5$ in	533
4.3.2-23	Annular and primary jets mean velocity vector plot at a) $z=6.4$ in. b) $z=8.6$ in	534
4.3.2-24	Annular and primary jets mean velocity vector plot at a) $z=6.3$ in. b) $z=8.7$ in	535
4.3.2-25	Annular and primary jets mean velocity vector plot at a) $z=6.2$ in. b) $z=8.8$ in	536
4.3.2-26	Annular and primary jets mean velocity vector plot at a) $z=6.1$ in. b) $z=8.9$ in	537
4.3.2-27	Annular and primary jets contour plot of U_{rms} and V_{rms} at $x=0.5$ in	538
4.3.2-28	Annular and primary jets contour plot of U_{rms} and V_{rms} at $x=1.0$ in	539
4.3.2-29	Annular and primary jets contour plot of U_{rms} and V_{rms} at $x=1.5$ in	540
4.3.2-30	Annular and primary jets contour plot of U_{rms} and V_{rms} at $x=2.0$ in	541
4.3.2-31	Annular and primary jets mean velocity vector plot at a) $z=6.0$ in. b) $z=9.0$ in	542
4.3.2-32	Annular and primary jets contour plot of U_{rms} and V_{rms} at $x=2.5$ in	543
4.3.2-33	Annular and primary jets contour plot of U_{rms} and V_{rms} at $x=3.0$ in	544
4.3.2-34	Annular and primary jets contour plot of U_{rms} and V_{rms} at $x=3.5$ in	545
4.3.2-35	Annular and primary jets contour plot of U_{rms} and V_{rms} at $x=4.0$ in	546
4.3.2-36	Annular and primary jets contour plots of U_{rms} and V_{rms} at $x=6.0$ in	547
4.3.2-37	Annular and primary jets contour plots of U_{rms} and V_{rms} at $x=9.0$ in	548
4.3.2-38	Annular and primary jets U_{rms} distribution	549
4.3.2-39	Annular and primary jets V_{rms} distribution	550
4.3.2-40	Annular and primary jets contour plots of turbulent kinetic energy (K) at a) $x=0.5$ in. b) $x=1.0$ in	551
4.3.2-41	Annular and primary jets contour plots of turbulent kinetic energy (K) at a) $x=1.5$ in. b) $x=2.0$ in	552
4.3.2-42	Annular and primary jets contour plots of turbulent kinetic energy (K)' at a) $x=2.5$ in. b) $x=3.0$ in	553

LIST OF ILLUSTRATIONS (cont)

<u>Figure</u>	<u>Title</u>	<u>Page</u>
4.3.2-43	Annular and primary jets contour plots of turbulent kinetic energy (K) at a) $x=3.5$ in. b) $x=4.0$ in	554
4.3.2-44	Annular and primary jets contour plots of turbulent kinetic energy (K) at a) $x=6.0$ in. b) $x=9.0$ in	555
4.3.2-45	Annular and primary jets turbulent kinetic energy (K) distribution	556
4.3.2-46	Annular and primary jets contour plot of $U'V'$ at a) $x=0.5$ in. b) $x=1.0$ in	557
4.3.2-47	Annular and primary jets contour plot of $U'V'$ at a) $x=1.5$ in. b) $x=2.0$ in	558
4.3.2-48	Annular and primary jets contour plot of $U'V'$ at a) $x=2.5$ in. b) $x=3.0$ in	559
4.3.2-49	Annular and primary jets contour plot of $U'V'$ at a) $x=3.5$ in. b) $x=4.0$ in	560
4.3.2-50	Annular and primary jets contour plot of $U'V'$ at a) $x=6.0$ in. b) $x=9.0$ in	561
4.3.2-51	Annular and primary jets $U'V'$ distribution	562
5.2.1-1	Control volume around the grid point P	572
5.2.3-1	One-dimensional condition	572
6.1-1	Geometry for an annular jet-induced flow in a duct	579
6.1-2	Inlet conditions for the medium-grid	580
6.1-3	Inlet conditions for the fine-grid	581
6.1-4	Axial velocity profiles at $z = 7.5$ in. plane, medium grid (k- ϵ model)	582
6.1-5	Variations of the centerline axial velocity, medium grid (k- ϵ model)	583
6.1-6	Axial velocity profiles at $y = 1.5$ in. plane, medium grid (k- ϵ model)	584
6.1-7	Axial velocity profiles at $z = 7.5$ in. plane (DSM)	585
6.1-8	Axial velocity profiles at $y = 1.5$ in. plane (DSM)	586
6.1-9	Centerline axial velocity profiles predicted by DSM using flux-spline and power-law schemes	587
6.1-10	Axial velocity profiles predicted by DSM	588
6.1-11	Axial velocity profiles predicted by DSM	589
6.1-12	Axial velocity profiles predicted by DSM	590
6.1-13	Axial velocity profiles predicted by DSM	591
6.1-14	Axial velocity profiles predicted by DSM	592
6.1-15	Axial velocity profiles predicted by DSM and ASM using power-law at $z = 7.5$ in. plane	593
6.1-16	Axial velocity profiles predicted by DSM and ASM using power-law at $y = 1.5$ in. plane	594
6.1-17	Centerline velocity profiles predicted by DSM and ASM using the power-law scheme	595
6.1-18	Axial turbulence intensity profiles predicted by DSM and ASM using power-law at $z = 7.5$ in. plane	596
6.1-19	Axial turbulence intensity profiles predicted by DSM using flux-spline and power-law at $z = 7.5$ in. plane	597
6.1-20	Axial velocity profiles at $z = 7.5$ in. plane, fine-grid (k- ϵ)	598
6.1-21	Variations of the centerline axial velocity, fine grid (k- ϵ model)	599
6.1-22	Turbulent kinetic energy at $z = 7.5$ in., fine-grid	600
6.1-23	Axial velocity profiles at $y = 1.5$ in. plane, fine grid (k- ϵ)	601
6.2-1	Inlet velocity profile	605
6.2-2	Opposed jets grid layout	606
6.2-3	Axial velocity profiles at $z = 7.5$ in. plane (k- ϵ model)	607
6.2-4	Centerline axial velocity profiles predicted by k- ϵ model	608
6.2-5	Turbulent kinetic energy predicted by k- ϵ model and flux-spline scheme	609
6.2-6	Axial velocity profiles predicted by k- ϵ model and power-law at $z = 7.5$ in. plane	610

LIST OF ILLUSTRATIONS (cont)

<u>Figure</u>	<u>Title</u>	<u>Page</u>
6.2-7	Centerline axial velocity profiles predicted by k- ϵ model and power-law scheme	611
6.2-8	Axial velocity profiles predicted by k- ϵ model	612
6.2-9	Axial velocity profiles predicted by DSM and ASM	613
6.2-10	Axial turbulence intensity profiles predicted by DSM and ASM	614
6.2-11	Radial turbulence intensity profiles predicted by DSM and ASM	615
6.3-1	Inlet profiles.....	619
6.3-2	Annular and primary jets grid layout	620
6.3-3	Axial velocity profiles at z = 7.5 in. plane (DSM).....	621
6.3-4	Axial turbulence intensity profiles at z = 7.5 in. plane (DSM)	622
6.3-5	Radial turbulence intensity profiles at z = 7.5 in. plane (DSM)	623
6.3-6	Turbulent shear stress profiles at z = 7.5 in. plane (DSM).....	624
6.3-7	Axial velocity profiles at x = 0.5 in. and various lateral stations (DSM)	625
6.3-8	Axial velocity profiles at x = 1.0 in. and various lateral stations (DSM)	626
6.3-9	Axial velocity profiles at x = 1.5 in. and various lateral stations (DSM)	627
6.3-10	Axial velocity profiles at x = 2.0 in. and various lateral stations (DSM)	628
6.3-11	Axial velocity profiles at x = 2.5 in. and various lateral stations (DSM)	629
6.3-12	Axial velocity profiles at x = 3.0 in. and various lateral stations (DSM)	630
6.3-13	Axial velocity profiles at x = 3.5 in. and various lateral stations (DSM)	631
6.3-14	Axial velocity profiles at x = 4.0 in. and various lateral stations (DSM)	632
6.3-15	Axial velocity profiles at x = 6.0 in. and various lateral stations (DSM)	633
6.3-16	Axial velocity profiles at x = 9.0 in. and various lateral stations (DSM)	634
6.3-17	Axial velocity profiles at z = 7.5 in. plane (k- ϵ) model.....	635
6.3-18	Turbulent kinetic energy profiles at z = 7.5 in. plane (k- ϵ) model.....	636

LIST OF TABLES

<u>Table</u>	<u>Title</u>	<u>Page</u>
VOLUME I		
3.4-I	LDV parameter settings	307
3.4-II	Sampling requirements for determination of various quantities	318
VOLUME II		
4.2-I	Primary jets only recirculation zone locations	415
4.3-I	Annular and primary jets recirculation zone locations.....	484
5.1-I	Values of constants in the k- ϵ model	566
5.1-II	Values of constants in the ASM and DSM closures.....	567

TABLE OF CONTENTS

<u>Section</u>	<u>Title</u>	<u>Page</u>
I	Introduction.....	1

I. INTRODUCTION

Combustor liner durability is one of the major challenges in high pressure ratio turbopropulsion engines. To resolve conflicting combustor performance requirements, along with enhanced structural durability in a cost-effective manner, conventional (empirical) combustor design techniques need to be complemented by multidimensional aerothermal analysis.

To improve predictive capabilities of aerothermal models, NASA Lewis Research Center sponsored Phase I aerothermal modeling activities (Srinivasan et al, 1983; Kenworthy et al, 1983; Sturgess, 1983*) to assess current state-of-the-art numerical schemes and physical models. The main objectives of aerothermal modeling Phase II are:

1. Develop advanced numerical schemes
2. Collect benchmark quality experimental data to quantify interaction between dome swirlers and primary jets
3. Collect benchmark quality data for fuel nozzles and their interaction with dome swirlers
4. Use advanced numerics and benchmark quality data to validate advanced aerothermal models

Two advanced numerical schemes were developed by Karki et al (1988) under NASA HOST (Hot-Section Technology) sponsorship. The experimental activities and model validation efforts for nozzle-swirler interaction were conducted jointly at University of California at Irvine and Allison Gas Turbine Division of General Motors Corporation (Nikjooy et al, 1993). This report summarizes a joint Allison/Purdue University effort on benchmark quality data and model validation for swirler-jet interaction for an idealized nonreacting primary zone.

This report consists of seven sections, including Section I, and three appendices.

In Section II, an overview of gas turbine combustor flowfield characteristics is presented. This is followed by a description of an idealized combustor flow model and an explanation of the integrated modeling/experimental approach.

Section III presents the details of the experimental rig and instrumentation. It begins with a discussion of initial rig design and operation, and followed by a description of rig refinement activities and final test rig. Finally, flow visualization, instrumentation, and data reduction results are presented.

In Section IV, the experimental data are presented and discussed. This includes dome annular jets only, primary jets only, and dome annular jets and primary jets.

In Section V, the problem of calculating turbulent flows is posed more precisely by introducing and discussing the averaged equations governing the mean flow quantities. The appearance of turbulent transport terms in these equations makes apparent the necessity of introducing turbulence models. The models are discussed in order of increasing complexity. The details of the solution procedure adopted for the highly coupled and nonlinear governing equations are explained next.

In Section VI, the computational results are compared with experimental data. The results are presented for the standard $k-\epsilon$ model, algebraic second-moment (ASM) closure, and differential second-moment (DSM) closure.

Finally, Section VII summarizes the main conclusions that emerged from this study and puts forward some recommendations for future work.

* References for Section I are listed at the end of the section.

REFERENCES

- Karki, K. C., Patankar, S. V., Runchal, A. K., and Mongia, H. C., 1988, "Improved Numerical Methods for Turbulent Viscous Recirculating Flows," *Aerothermal Modeling Phase II Final Report*, NASA CR-182169.
- Kenworthy, M. J., Correa, S. M., and Burrus, D. L., 1983, "Aerothermal Modeling: Phase I Final Report - Volume 1 Model Assessment," NASA CR-168296.
- Nikjooy, M., Mongia, H. C., McDonell, V. G., and Samuelsen, G., S., 1993, "Fuel Injection - Air Swirl Characterization," *Aerothermal Modeling Phase II Final Report, Volumes I and II*, NASA-CR-189193.
- Srinivasan, R., Reynolds, R., Ball, I., Berry, R., Johnson, K., and Mongia, H. C., 1983, "Aerothermal Modeling Program: Phase I Final Report," NASA CR-168243.
- Sturgess, G. J., 1983, "Aerothermal Modeling: Phase I Final Report," NASA CR-168202.

TABLE OF CONTENTS

<u>Section</u>	<u>Title</u>	<u>Page</u>
II	Selection of Experimental Configuration.....	3
2.1	Gas Turbine Combustor Flow Field Characteristics	3
2.2	Idealized Combustor Flow Model	5
	2.2.1 Jet Injection into a Cross Stream	5
	2.2.2 Confined Swirling Flows	7
2.3	Integrated Modeling/Experimental Approach	9

II. SELECTION OF EXPERIMENTAL CONFIGURATION

2.1 GAS TURBINE COMBUSTOR FLOW FIELD CHARACTERISTICS

Gas turbine combustion systems need to be designed and developed to meet many mutually conflicting design requirements, including high combustion efficiency over a wide operating envelope and low NO_x emissions, low smoke and low lean flame stability limits and good starting characteristics, low combustion system pressure loss, low pattern factor, and sufficient cooling air to maintain low wall temperature levels and gradients commensurate with structural durability. The flow field around and within the combustor liner (Figure 2.1-1^{*}) is quite complex in that it includes swirl, regions of recirculation, fuel injection, atomization, fuel evaporation, mixing, turbulent combustion, soot formation/oxidation, and convective and radiative heat transfer processes. The phenomenological understanding of these processes is not well established, and the relevant nonlinear coupled transport equations are difficult to solve.

The combustor design and development process has been empirically based with limited help from multidimensional calculations. A number of correlations have been used by combustor designers to help during the design and development activities. Many researchers (Lefebvre, 1984 and 1985; Plee and Mellor, 1978 and 1979[†]) have proposed semiempirical correlations for gaseous emissions, smoke, lean blowout, ignition, pattern factor, and combustion efficiency. Professors Lefebvre and Mellor have developed very useful correlations that can be used for scaleup, for data correlations, and for providing some insight. These correlations or their variants are being used by the gas turbine industry (Steele et al, 1987; Rizk and Mongia, 1989).

The empirical/analytical combustor design methodology introduced by Mongia and Smith (1978) has been used for designing a number of gas turbine combustors (Mongia, 1982; Mongia et al, 1986). The multidimensional calculations provide a good understanding of combustor internal flow field and therefore can be used for guiding a combustor design process. However, because of incomplete understanding of the various combustion processes and numerical diffusion, the three-dimensional calculations for practical gas turbine combustors cannot be considered quantitatively accurate (Srinivasan et al, 1983; Kenworthy et al, 1983; Sturgess, 1983). Some progress is being made in further improving the numerical methods (Karki and Mongia, 1989), however more effort is needed to achieve the capability required for accurately predicting combustor performance parameters including radial profile, combustion efficiency, smoke and gaseous emissions, and wall temperature levels and gradients.

Although encouraging qualitative comparisons between data and calculations were achieved for the practical combustors (Rizk and Mongia, 1991), it became quite clear that a significantly increased level of effort is required to achieve the model accuracy required for providing definitive guidance during design process. Moreover, each important process of combustion (e.g., turbulence, kinetics, turbulence/kinetic interaction, spray, etc) should be investigated separately and in combination so as to improve fundamental understanding. Model calculations were, therefore, performed for existing data from simple to complex flow under HOST sponsorship (Srinivasan et al, 1983) and the following main conclusions were made:

1. Improve phenomenological understanding of nonreacting flows relevant to those encountered in gas turbine combustors.
2. Make benchmark quality measurements in critical areas of interest.
3. Undertake a systematic model validation effort to identify areas of further improvement.

* Figures for Section II appear at the end of each subsection. The figure number identifies the subsection in which the figure is discussed.

† References for Section II are listed at the end of the section.

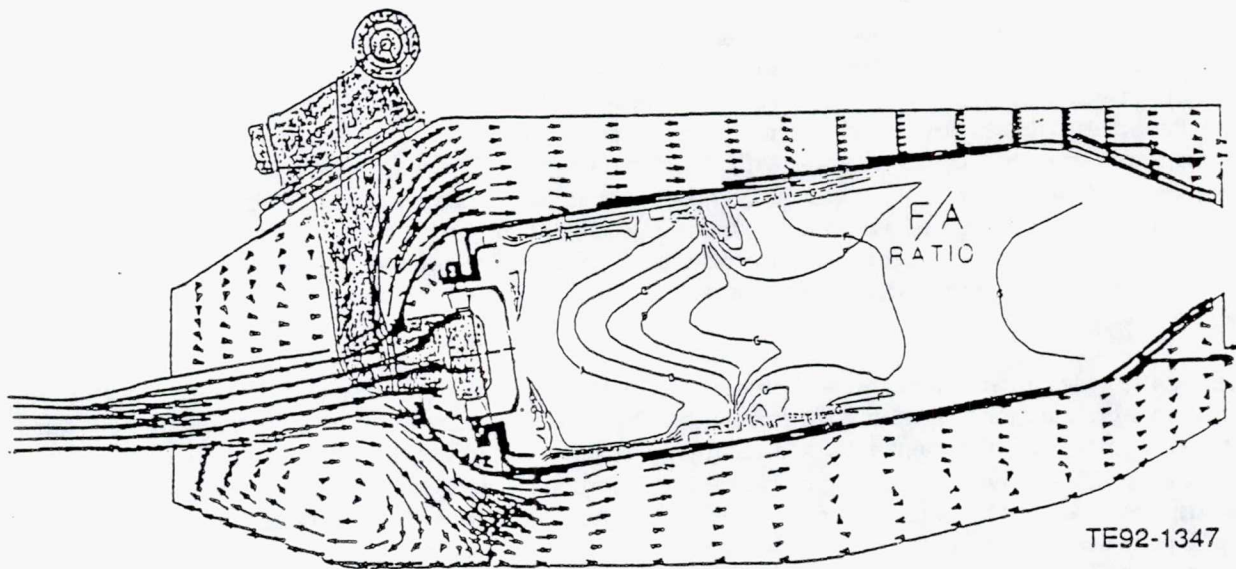


Figure 2.1-1. Model predictions of flow field around and within combustor.

2.2 IDEALIZED COMBUSTOR FLOW MODEL

The overall combustor flow field can be divided into two categories, jet flows and swirling flows. Each of these subflow categories has been extensively studied but, surprisingly, little attention has been focused on the combined problem.

2.2.1 Jet Injection into a Cross Stream

Jet injection into a cross stream has been widely studied. A paper by Crabb et al (1981) includes a list of 24 earlier experiments. Many of the early studies dealt with single jets flowing into unbounded streams, so the results were not directly relevant to primary or dilution jets in combustors. In real configurations, the jets interact with each other and the blockage causes the main stream to accelerate. Walker and Kors (1973) and Holdeman et al (1973) have reported measurements of the temperature distribution downstream of a row of cold jets injected from one side wall of a rectangular duct into a hot cross flow. This configuration was more relevant to gas turbine combustor design than previous studies, although the jet-to-mainstream density ratio was somewhat lower than what prevails in practice. Holdeman and Walker (1977) and Cox (1975) analyzed these experimental results and derived correlations that can be used for preliminary design of dilution jets in annular combustors. Although these correlations are used in practice, the failure of the original experiments to accurately simulate the flow conditions of a combustion chamber reduces the accuracy of the predictions. For example, the cross flow was essentially isothermal whereas the flow at the plane of the dilution jets in a practical combustor has both radial and circumferential temperature gradients. Second, the cross flow was not swirling, so these experiments more closely simulate the conditions that prevail for dilution jets than for primary jets. The swirl and recirculation created at the dome strongly influence the penetration and mixing of the primary jets. Finally, the fine details of the jet injection hole can influence the mixing process, and this boundary condition was not accurately simulated. Since no velocity measurements were made and the upstream boundary conditions were not determined, assumptions of numerical solutions must be considered when these results are compared with experimental results.

Similar experiments explicitly intended to model the injection and mixing of dilution jets have also been performed (Srinivasan et al, 1982). In addition to studying the effect of jet spacing and diameter and the jet-to-mainstream density and momentum-flux ratios, the experiments also included more realistic effects such as nonuniform free-stream temperature distribution and convergence of the duct.

The results for isothermal flow in a constant area duct agreed very well with the earlier data of Walker and Kors. The jet spreading characteristics in the nonisothermal cases were very similar to the isothermal case, but the temperature distribution was, not surprisingly, found to be strongly determined by the original upstream temperature distribution. For isothermal flow in a convergent duct, the jet mixing rates in both the radial and transverse directions were generally greater than in the constant area duct. However, when the free stream temperature was made nonuniform, the details of the distribution strongly influenced the mixing. When the higher temperature was toward the wall with the jets, the lateral and transverse spreading rates were not appreciably altered from the isothermal results. When the higher temperature was along the wall opposite the jets, the spreading of the jets was significantly slower.

To analyze the data, the correlations derived by Holderman and Walker (1977) were simply modified to account for nonuniform temperature distributions and area change. The new results gave good qualitative predictions, but needed refinement to be quantitatively useful. These data are useful for preliminary design of the dilution holes, but do not apply to the primary zone, largely for the same reasons discussed in connection with Walker's experiments.

Srinivasan et al (1983) did an extensive review of measurements of simple and complex turbulent flows that could be used as benchmarks for numerical simulations of the aerothermodynamic phenomena that

occur in gas turbine combustion chambers. Computations of many of these flows using advanced codes, and with several turbulent transport models, were also carried out.

Kamotani and Greber (1972) have measured velocity and temperature distributions in a heated jet injected into a semi-infinite cross stream. Mean velocity and turbulence intensity were measured with a constant current anemometer, a yaw probe was used to determine the direction of the mean velocity vector, and total temperatures were measured with a small thermocouple. The trajectory of the jet was described in terms of the loci of the points of maximum velocity and temperature. The jet momentum ratio was the major factor that controlled the trajectories, although the temperature centerline was weakly influenced by the density ratio. The path of peak velocity was always located farther from the wall than the line of peak temperature. Two counterrotating streamwise vortices were generated on either side of the jet centerline which strongly influenced the subsequent behavior of the jets.

Crabb et al (1981) reported detailed turbulence measurements in the same flow. Crabb's jet was the same temperature as the main stream, but helium was injected in the jet to act as a tracer for jet fluid. Measurements of the mean and root mean square (rms) fluctuation velocities in the streamwise and normal directions were made near the jets with a single component laser Doppler velocimeter (LVD) system. Downstream, where the turbulence intensity was less than 0.30, hot wires were used to measure all three velocity components (mean and rms) and two Reynolds shear stresses. Probability distributions were determined with both instruments. A gas sampling probe was used to determine the mean concentration of helium. The measurements showed that away from the injection plane, the locus of maximum velocity does not correspond to jet fluid, even though the initial jet velocity was larger than the free stream velocity. This explained Kamotani's results. The Reynolds stress distributions indicate that gradient diffusion models for momentum, such as the k- ϵ model, will not yield accurate results, particularly in the wake region near the wall. While this single-jet flow is only a subcomponent of the jet-swirl interaction, both of these sets of measurements could be used for some benchmark computations.

Rho et al (1988) measured the turbulent characteristics of a cross jet mixing after the geometric cross point of the centerlines of the two nozzles. The flow has been generated by two circular nozzles and the crossing angle of the jets was fixed at 45 deg with respect to each other. The flow field is strongly influenced by the cross point stagnation region, which creates an elliptical jet region. The measurements have been performed at Reynolds numbers of 5.2×10^4 and 6.5×10^4 and some influences of nonsimilarity have been studied.

Catalano et al (1989) reported measurements and computations for the flow of a turbulent jet discharging into a cross flow confined between two parallel plates. For jet-to-cross flow velocity ratios equal to 2 and 4, mean and fluctuating velocity components were measured by laser Doppler anemometry. Results show that impingement of the jet on the opposite wall occurs at a velocity ratio of 4.

Koutmos and McGuirk (1989) reported measurements of mean velocity components and the corresponding turbulence intensities in a water model of a can-type gas turbine combustion chamber. The effect of variation of the flow split between the swirler and the dilution holes on the flowfield in the primary zone was investigated. At low levels of swirler flow rate, a large toroidal recirculation with high levels of turbulence energy were generated in the case of the combustor. As the swirl level increases, the strength of this recirculation was observed to weaken. The flow pattern downstream of the secondary jets was the same for all flow splits due to the strong mixing.

Sherif and Pletcher (1989) reported measurements of the velocity and turbulence characteristics of a round turbulent isothermal jet in cross flow at velocity ratios of 2, 4, and 6. Their experiments were carried out in a water channel 8.53 m long and 0.61 m x 1.067 m in cross section. Mean velocities, Reynolds stresses, and correlation coefficients were measured using anemometry methods.

Liou et al (1989) reported studies on the three-dimensional jet-jet impingement flow in a closed-end cylindrical duct with two 60 deg side inlets. The impingement of jets provided an effective way to mix the fluids. The measurements were made using the laser-Doppler velocimeter. The Reynolds number of the air flow was 2.6×10^4 . Simple geometrical expressions were deduced and were found to effectively estimate the stagnation points and the optimal head heights.

Vranos et al (1991) conducted an experimental investigation of cross stream injection and mixing. The transverse injection from slanted slot and orifice injectors were studied. The main parameters of their study were momentum-ratio, density ratio, and injector geometry. Measurements of injectant concentration distributions were obtained. The data indicate that a density ratio greater than unity retards mixing. Furthermore, above a certain momentum-flux ratio, mixing with slanted slot injectors was better than with round hole injectors.

2.2.2 Confined Swirling Flows

Interest in confined swirling flows is very strong because of the highly intense turbulence that can be created. If the swirl is sufficiently strong, a recirculation region is created which can act as a flameholder. Most gas turbine combustion systems use swirl to establish a primary combustion zone in the dome region, where the equivalence ratio is close to one. Syred and Beer (1974) and Lilley (1977) reviewed the state of knowledge of swirling reacting flows almost a decade ago. Experimental and analytical advances have since increased the body of knowledge for both reacting and nonreacting flows. A review of experimental investigations of swirling confined flows was also done by Srinivasan et al (1983) as part of a larger assessment of the accuracy of the aerothermodynamic submodels. Both simple and complex flows were considered and computations using advanced numerical codes and several turbulence models were carried out. Published measurements by Escudier et al (1980), Altgeld et al (1983), Rhode et al (1983), Vu and Gouldin (1980), and Janjua et al (1982) were reviewed. The most important conclusions drawn were that the k - ϵ model and the corresponding gradient diffusion scalar transport model worked well in simple flows but were not satisfactory for recirculating swirling flow. Algebraic stress models yielded similar results from the mean velocity and scalar fields but better predictions of the Reynolds normal stresses. The Reynolds shear stress predictions were not satisfactory. Similar conclusions were drawn by Habib and Whitelaw (1980) in an experimental and analytical study of confined swirling coaxial jets.

Rhode et al (1983) measured mean velocity fields in a cylindrical chamber supplied from one end by an annular swirling jet. Chambers with two inlet geometries, a sudden expansion and gradual (45 deg) expansion, were studied. Attention was focused on the effects of increasing amounts of swirl on the recirculation regions and on the mean velocity profiles. Numerical predictions of the flow were presented in a companion paper (Rhode et al, 1982) and Janjua et al (1982) measured the turbulent characteristics of swirling and nonswirling flows in the same geometry. One of the interesting observations was that swirl causes a recirculation zone near the center line in which axial velocities are very low but the circumferential velocity is maintained.

As previously mentioned, these particular measurements were used by Srinivasan et al (1983) to evaluate the accuracy of current numerical codes. However, because no jets were injected into the flow, these measurements have limited direct application to gas turbine combustor design. A recent paper by Ferrell et al (1984) considers the case of injection of radial jets into a cylindrical duct. Both numerical and experimental results were presented. The k - ϵ model was used to predict a flow of six jets into the duct. Swirling and nonswirling flows were computed and it was found that radial penetration of the jets is reduced by the swirl. The swirl was sufficiently weak that no recirculation was induced. An experimental investigation of the flow of a single radial jet into a nonswirling flow was also described. Flow visualization photographs and mean velocity profiles only were presented. The experiments focused on the effect of jet velocity ratio and a downstream area reduction on the jet penetration. Experiments such as these are beginning to approach the complexity of the primary zone flow. Further continuation of this work to the measurements of the turbulent quantities will provide valuable results for the combustion designers.

Gouldin and his coworkers at Cornell University have published a series of investigations of reacting and nonreacting swirling flows. Vu and Gouldin (1980) used pitot and hot-wire probes to investigate the nonreacting flow in a cylindrical chamber fed from one end by coaxial jets. The strength and direction of the swirl in each jet could be independently controlled. In all of the cases reported, the average axial velocity of the outer jet was about 0.7 times that of the inner. Both coswirling and counterswirling flows were studied, and the strength of recirculation zone was found to increase as the swirl in the outer jet was reduced from positive (coswirling) to negative (counterswirling) values. This was associated with increased turbulent dissipation within the interjet shear layer. Emissions measurements made in a geometrically similar combustion chamber were directly correlated with these results (Oven et al, 1979). The counterswirling flow had lower combustion efficiency because the vigorous mixing in this shear layer rapidly quenched the combustion reactions.

In a recent paper, Halthore and Gouldin (1984) reported measurements of mean and fluctuating density made in the recirculating primary zone of a cylindrical combustion chamber. Methane at an equivalence ratio of 0.80 was supplied through a central swirling jet located on the axis of the chamber. More air was supplied through an outer coaxial jet that could also be made to swirl. Time-resolved measurements of total molecular number-density were made using Rayleigh scattering and the mean number-density of methane molecules was measured with Raman scattering. The results showed that the recirculation zones created by counter and corotating jets are different. Velocity measurements in both nonreacting and reacting flows in the same combustion chamber have also been reported (Gouldin et al, 1983). Together these data represent another flow that can usefully serve for verification of numerical codes, but again, because no primary zone jets were injected, the data have limited direct applicability to the design of gas turbine combustors.

Johnson and Bennett (1984) and Roback and Johnson (1983) have made very careful and complete measurements of confined coaxial jets. Their geometry was basically the same as that of Habib and Whitelaw (1980) and they too studied both swirling and nonswirling flows. The most important aspect of this work is that data on both turbulent mass and momentum transport were taken. Velocity measurements were made with one and two component LDV systems. The concentration of fluorescent dye initially injected only in the central jet was determined by measuring the intensity of the fluorescence from a small volume of fluid illuminated with a laser. Under appropriate conditions the intensity of the fluorescence is directly proportional to the number-density of fluorescent molecules. By observing the crossing volume of a dual beam LDV system with two photodetectors, one of which used a filter which passed only the laser radiation while the second used a filter which passed only the fluorescent radiation, turbulent transport of the dye, defined by the cross correlation between velocity and concentration fluctuations, was measured. The velocity concentration data pairs were analyzed to determine probability density functions for axial, radial, and circumferential velocity fluctuations, concentration fluctuations, and their various products. Moments of these distributions up to the fourth-order were calculated. In addition, detailed surveys of the velocity distributions at the exits of the swirlers were measured. This very complete data set represents an excellent example of a benchmark experiment which can be used for validating current and advanced prediction codes. Again, however, the lack of secondary jets reduces the direct applicability of the data to the understanding and design of flow in the dome region of a combustor.

Many excellent studies of various aspects of the fluid dynamic phenomena in gas turbine combustors have been performed. Most of these, however, have omitted key factors which would have greatly increased the applicability of the results throughout the combustor. Jet injection studies have omitted swirl and recirculation in the primary stream, thus restricting their usefulness to dilution jets near the combustor exit. Studies of swirling recirculating flows have typically omitted jet injection, but most gas turbine combustion systems require additional combustion air to be injected through holes in the dome to establish the correct fuel/air ratios for stable combustion.

2.3 INTEGRATED MODELING/EXPERIMENTAL APPROACH

An experimental rig of rectangular cross section was selected for this investigation (Figure 2.3-1). The rig satisfies two important requirements, it simulates many important features of advanced annular combustors and it has been designed so that all of the boundary conditions will be accurately known. The annular combustor model was designed to simulate the cold flow characteristics of current gas turbine combustors. Air enters the test section through five swirlers mounted in the head plate at one end of the rectangular duct. The swirler center-to-center spacing is equal to the duct height, and the vanes are flat plates set at an angle of 60 deg with respect to the centerline of the nozzle. Air through two separately controlled lines enters through the primary jets located in the top and bottom of the duct. The 3.0 in. x 15.0 in. (7.5 cm x 38.1 cm) cross section has the same hydraulic diameter as a typical advanced combustor.

A 3-D code was used to predict the flow field for a number of test configurations to help identify the experimental test matrix. The calculations determined areas of strong velocity gradients where measurements would be taken. Since the purpose of the flow interaction program is to obtain benchmark data with which to verify 3-D turbulence models, it is necessary to involve the 3-D model in the selection of the experimental configuration. This is important for several reasons. First, the 3-D model can help identify significant features of the configuration, and in so doing can help determine which parameters are important and which are not, thus concentrating effort on fruitful test procedures. Secondly, the 3-D model is also useful in establishing boundary conditions and the overall scope of the work.

Before the proposed experimental configuration was selected, a number of preliminary cases were computed using a 3-D code. The calculations were made for the two-equation $k-\epsilon$ model. There were several reasons for not using advanced turbulence models. First, the models are only illustrations used to help select the experimental configurations. Secondly, the results were obtained with a relatively coarse grid. Since these calculations are not grid independent, there is an excessive and unknown amount of numerical diffusion, thus obscuring the advantages offered by advanced models.

Five preliminary cases were run with a grid size of $22 \times 14 \times 14$. This was considered sufficient to describe each case adequately without requiring excessive computer time. Using a finer grid would have increased the accuracy but would not have affected the trend of the results.

The first case (designated as baseline) consisted of parallel axial swirlers side-by-side in a rectangular duct (in a manner analogous to annular combustor design) with opposing primary jets in line with the swirlers and downstream one duct height (3.0 in.). The swirler spacing was 3.0 in, and the swirlers had a tip diameter of 1.5 in. and a hub diameter of 1.0 in. The primary jet flow was set equal to 75% of the swirler flow, the flow rates were scaled for inlet velocities of 400 ft/sec.

Velocity vector plots at four longitudinal planes are shown in Figure 2.3-2. The planes are located at 0.5 in. increments, starting midway between swirlers with the last plane, in line with the center of the swirler. These plots show the flow patterns as they are affected by the swirler and the primary jets.

Similar velocity vector plots at six cross-sectional planes are shown in Figure 2.3-3. These are located at distances of 0.75, 1.5, 2.25, 3.0, 3.75, and 4.5 in. ($x/H = 0.25, 0.5, 0.75, 1, 1.25, 1.5$) from the swirler, respectively. From these plots it can be seen that the swirl quickly degenerates into two transverse streams until the streams are broken up by the primary jets. One interesting result is that the transverse flow direction is reversed by the primary jets.

Figure 2.3-4 shows contour plots of the axial velocity and the kinetic energy of turbulence in the longitudinal plane through the center of the swirler. The axial velocity contour plot shows the shape of the recirculation zone extending from the swirler hub to the primary jets. The neck in the recirculation zone

suggests that the primary jets should be located nearer to the swirler to obtain a more efficient recirculation flow. The contours of kinetic energy of turbulence also suggests the same conclusion.

In the second case, the primary jets were moved closer to the swirler to a distance of one-half test section height, i.e., 1.5 in. Analogous plots are shown in Figures 2.3-5, 2.3-6, and 2.3-7. The contour plots of Figure 2.3-7 indicate that the recirculation zones set up by the swirler and by the primary jets have coalesced and the overall recirculation is reduced. A primary jet location somewhere between 1.5 to 3.0 in. would probably be better.

The third case was similar to the baseline except that the primary jet flow was doubled. The plots for this case are presented in Figures 2.3-8, 2.3-9, and 2.3-10. Again, the axial velocity contour plots of Figures 2.3-9 and 2.3-10 indicate some coalescing of the recirculating region. For primary jets at this location the baseline flow should be increased a little less than double from the baseline.

The fourth case was an annular version of the baseline configuration. For this case the inner wall radius was 5.5 in. and the outer wall radius was 8.5 in. The analogous plots (Figures 2.3-11, 2.3-12, and 2.3-13) show a deflection of the flow toward the outer wall. While there are differences between the annular and rectangular configurations, the similarities of the trends make the rectangular case a worthwhile test of the computer model.

The last case was the same as the baseline but without the primary jets. The plots for this case (Figures 2.3-14, 2.3-15, and 2.3-16), when compared with those for the baseline case, indicate that the effect of the primary jets is quite apparent.

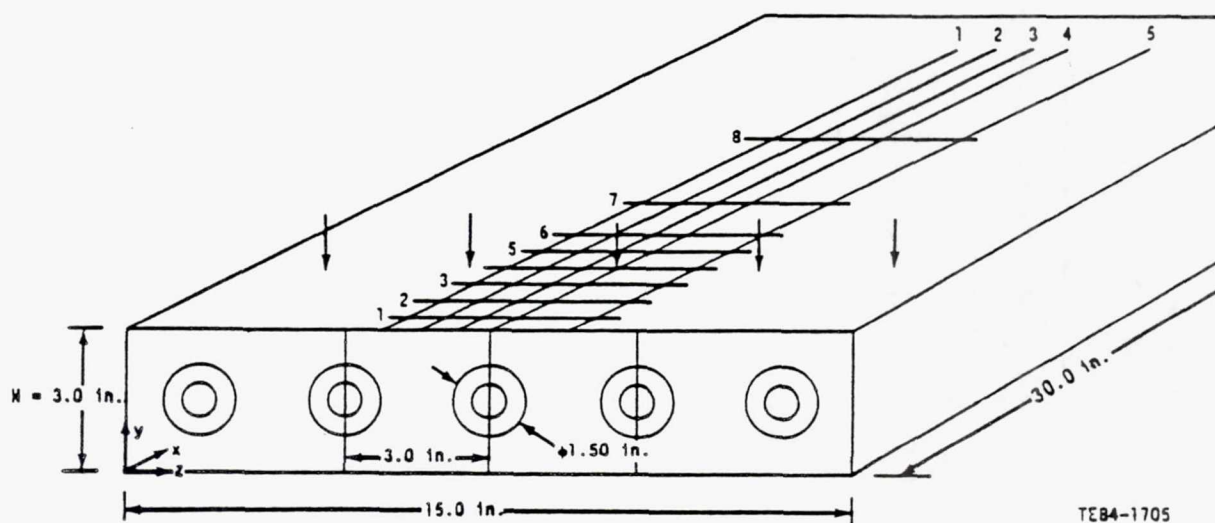


Figure 2.3-1. Nominal distribution of survey points within the test section.

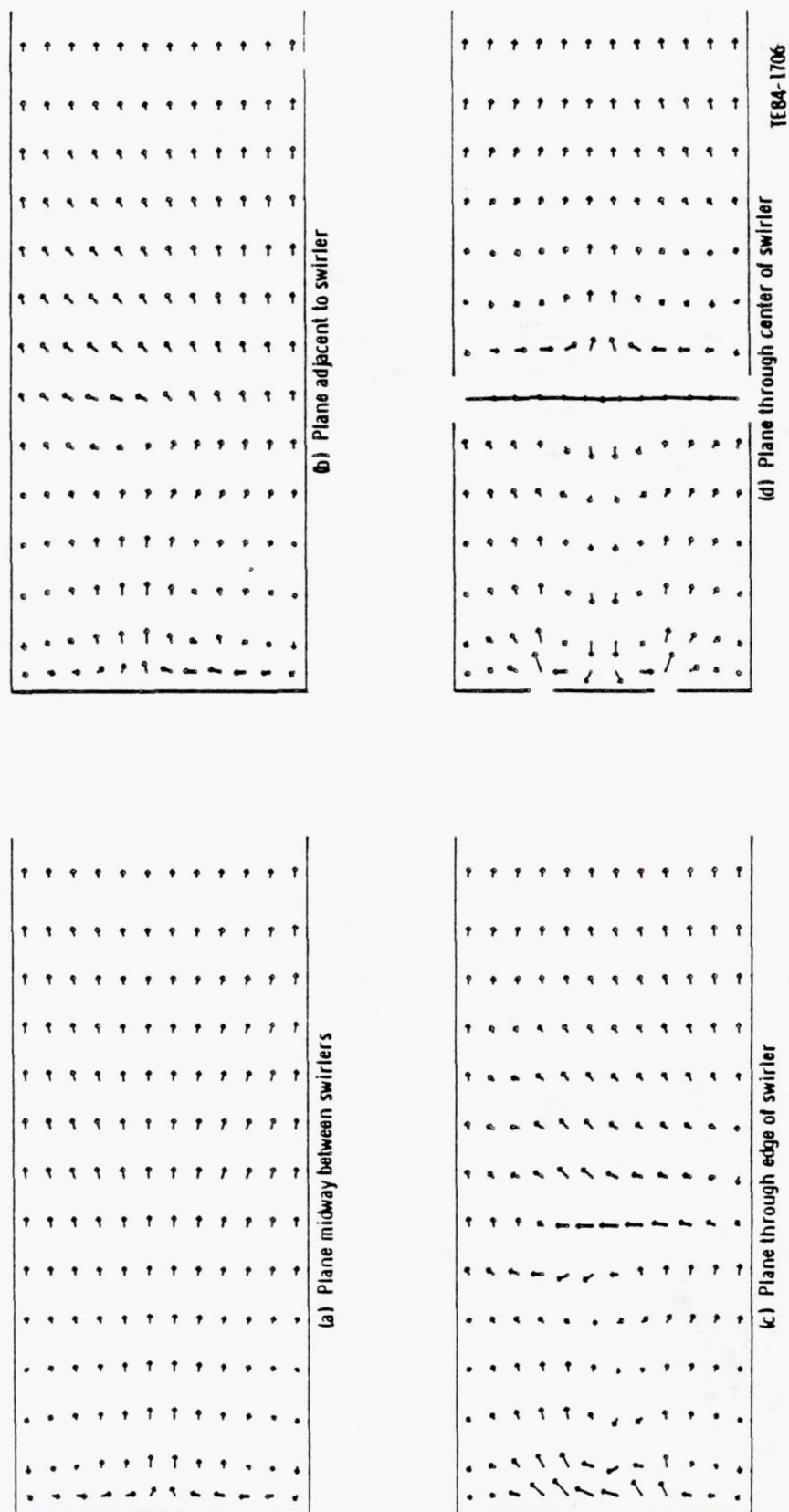
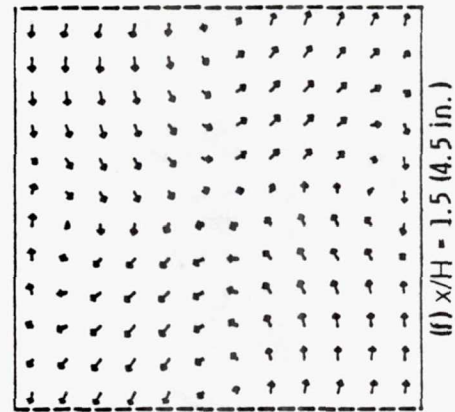
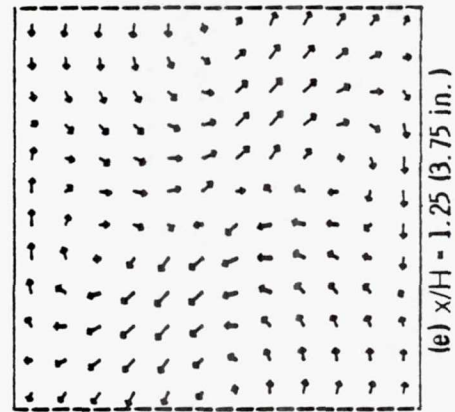
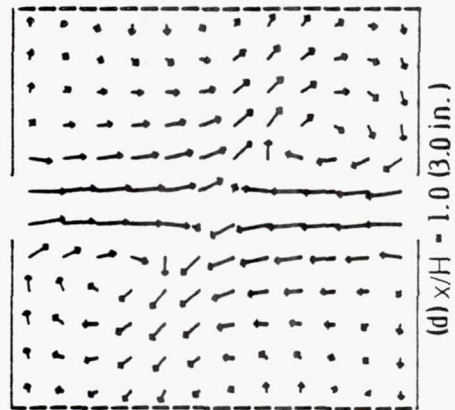
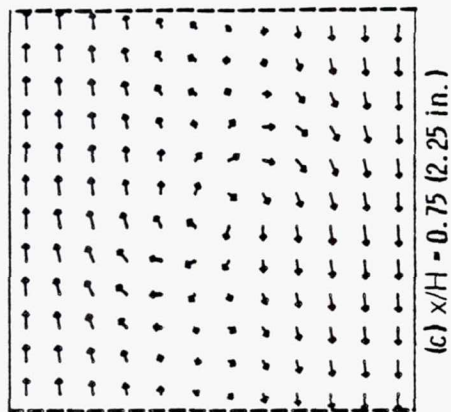
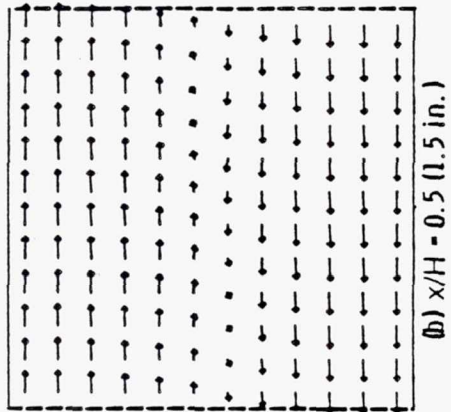
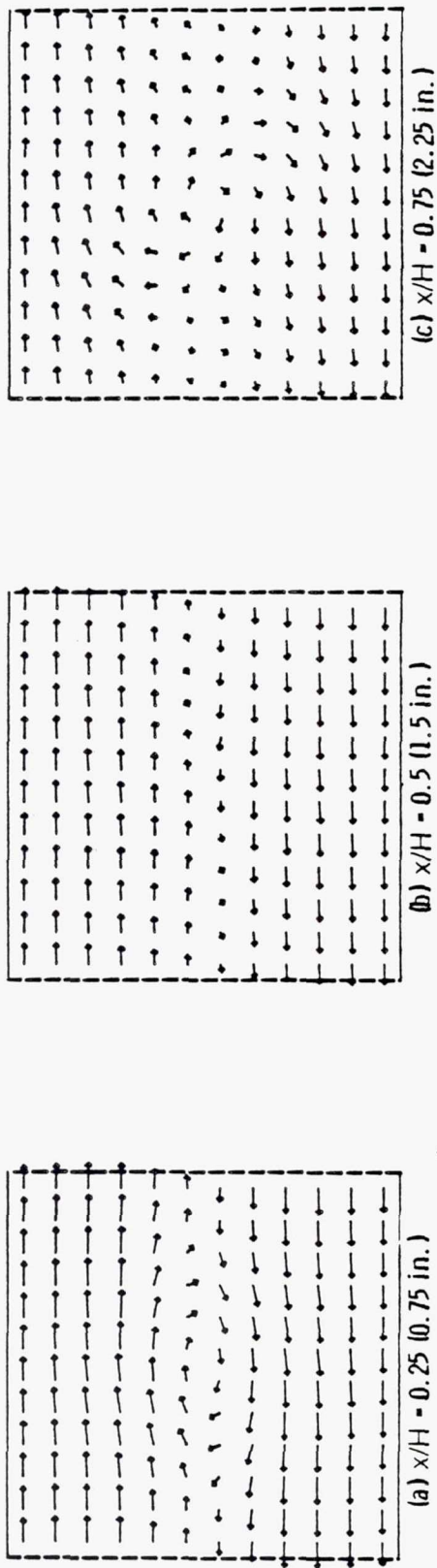
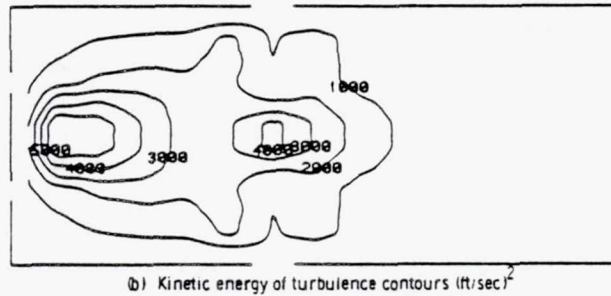
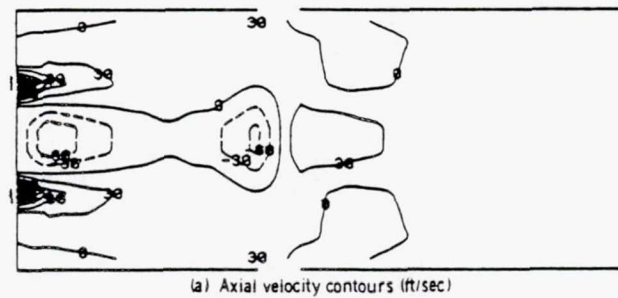


Figure 2.3-2. Longitudinal velocity vector plots for baseline configuration.



TE84-1707

Figure 2.3-3. Cross-sectional velocity vector plots for baseline configurations.



TE84-1708

Figure 2.3-4. Contour plots for plane through center of swirler for baseline configuration.

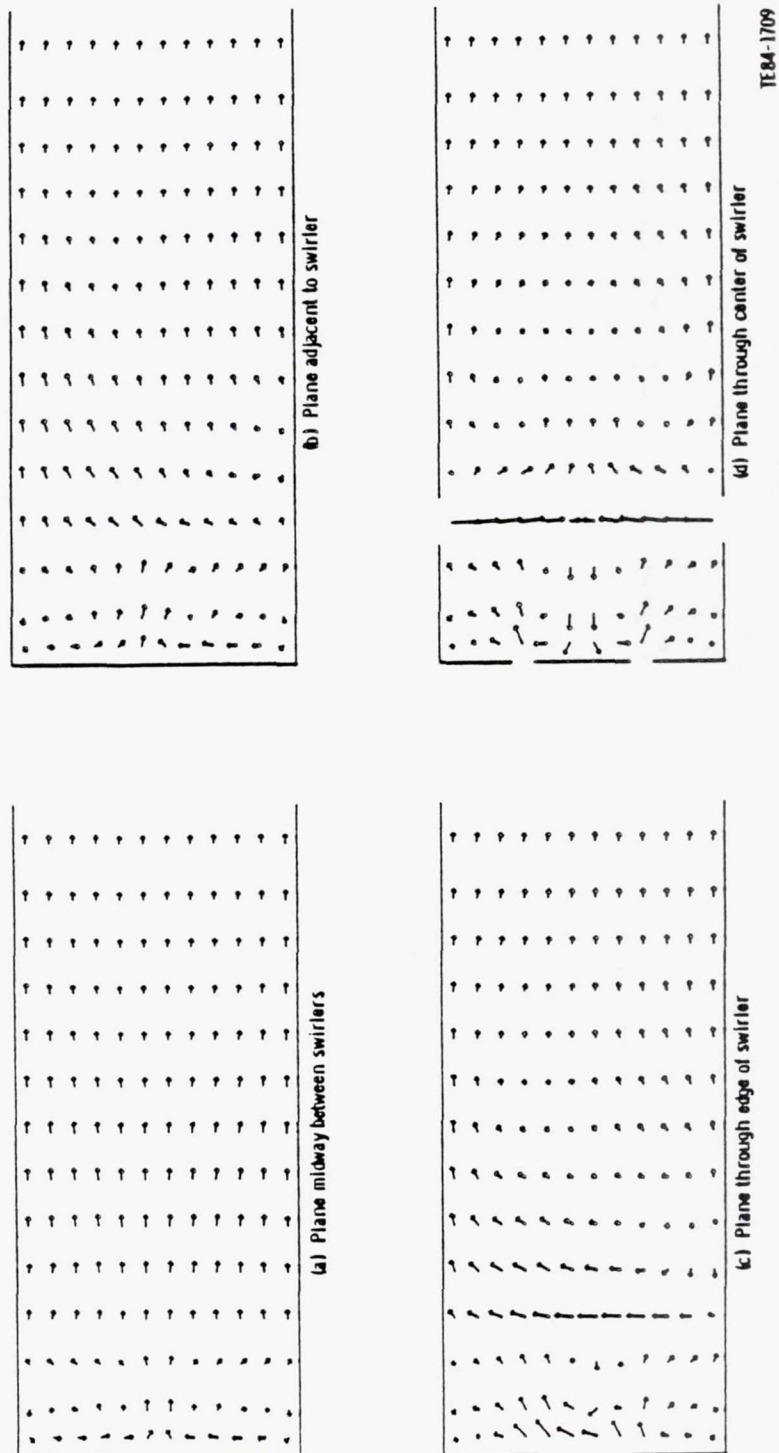
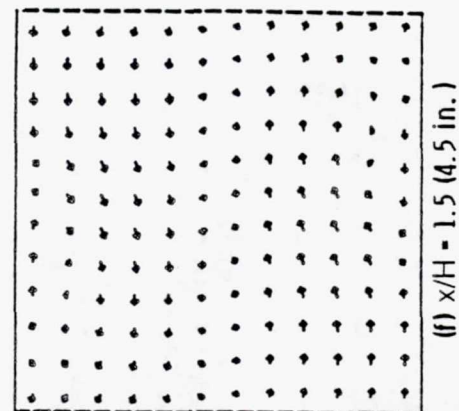
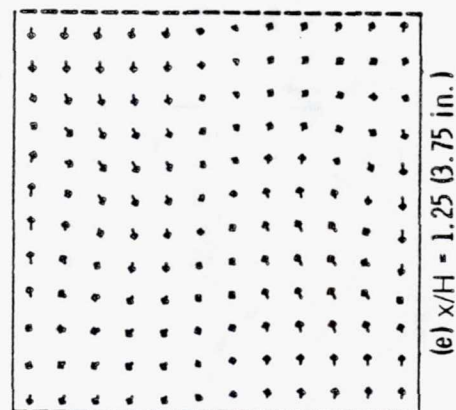
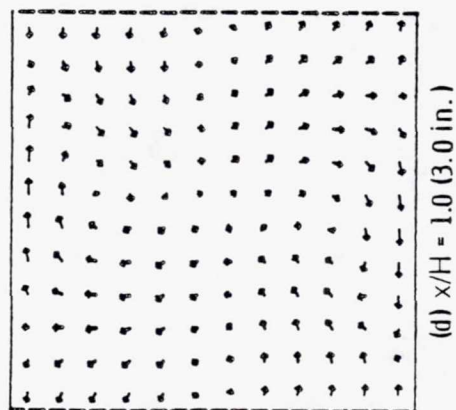
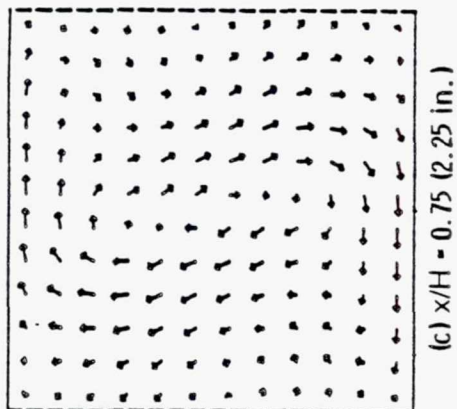
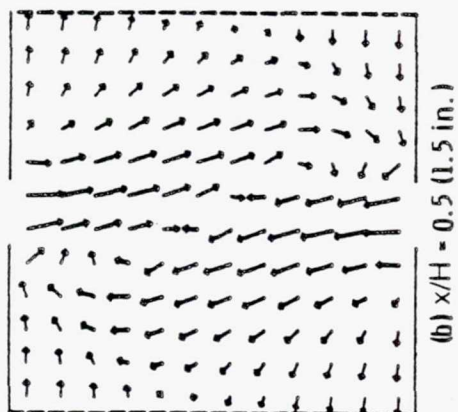
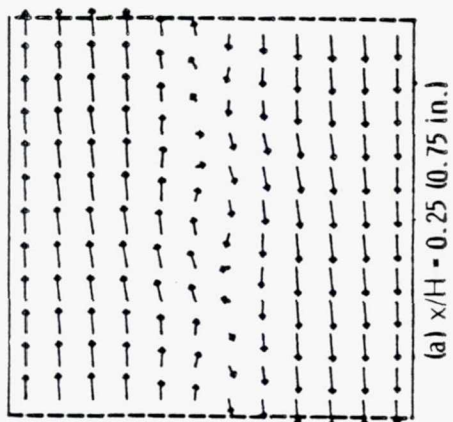


Figure 2.3-5. Longitudinal velocity vector plots for configuration with primary jets at $x/H = 0.5$.



TF84-1710

Figure 2.3-6. Cross-sectional velocity vector plots for configuration with primary jets at $x/H = 0.5$.

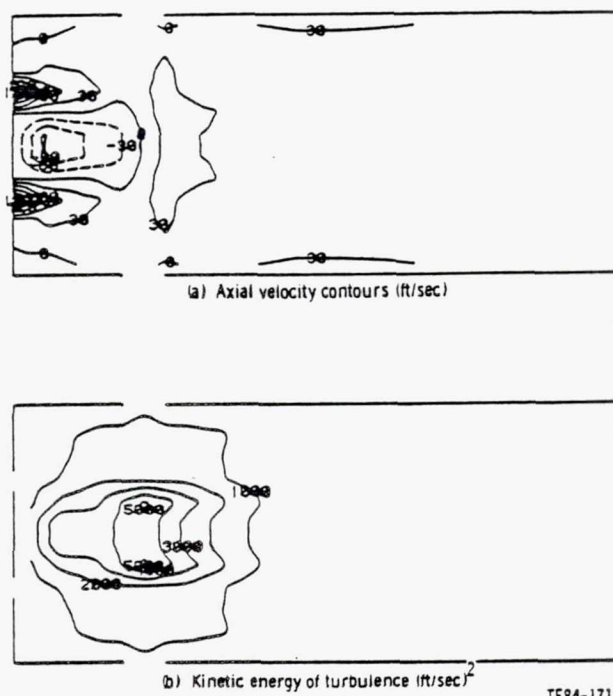


Figure 2.3-7. Contour plots for plane through center of swirler for configuration with primary jets of $x/h = 0.5$.

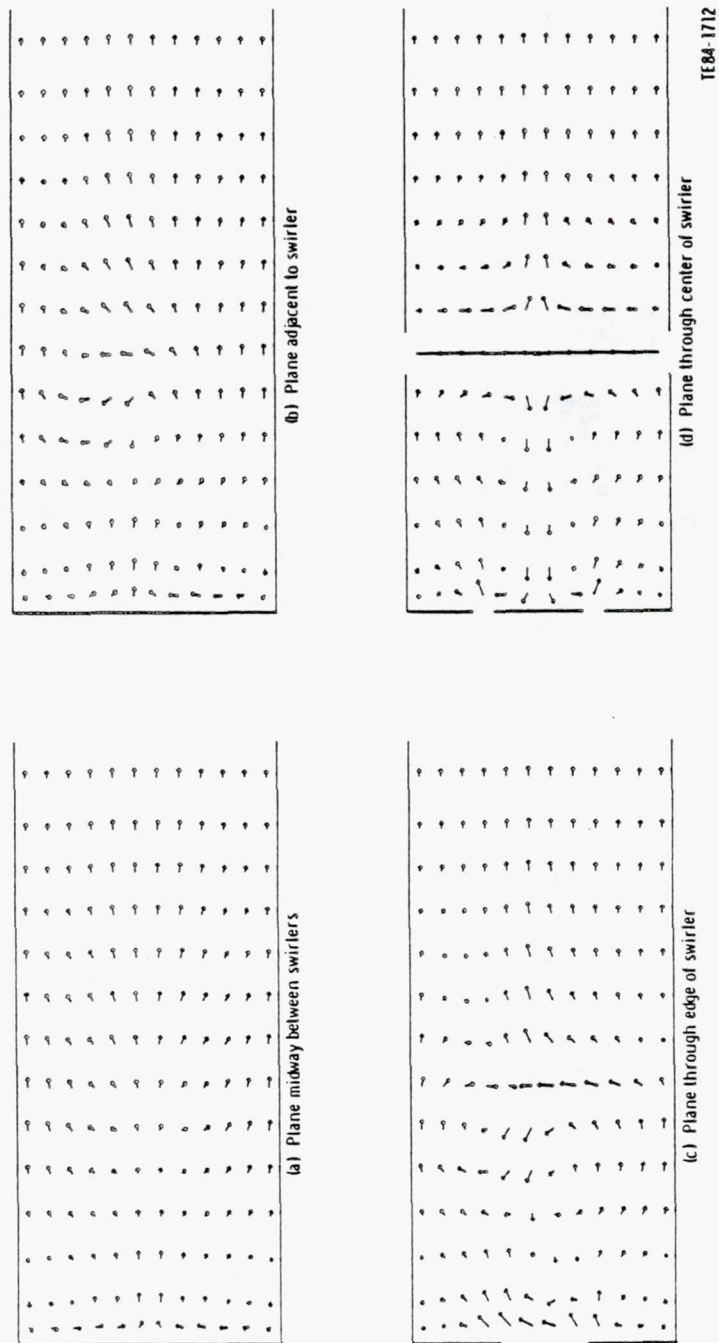
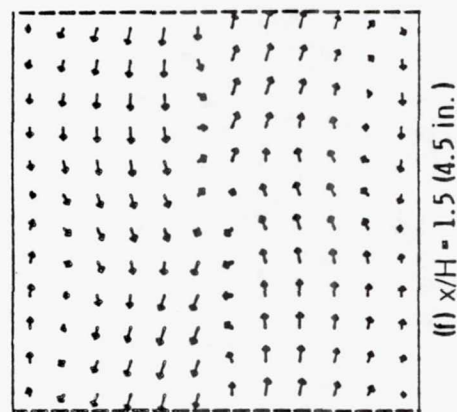
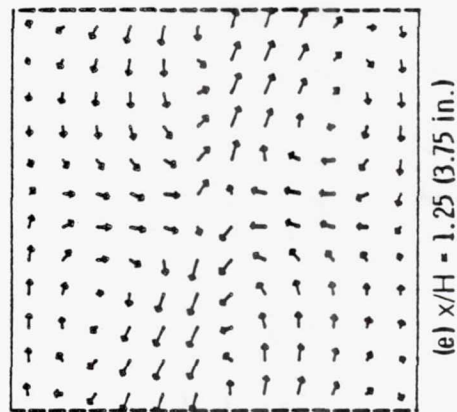
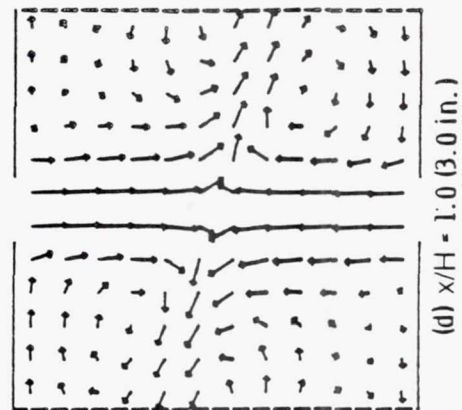
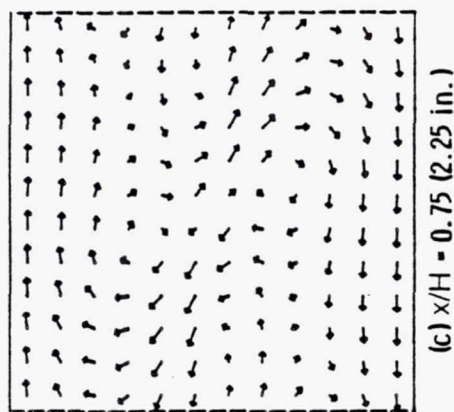
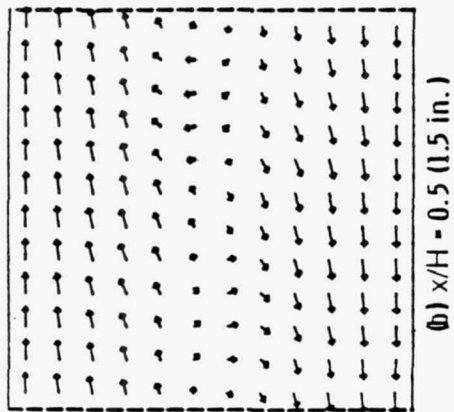
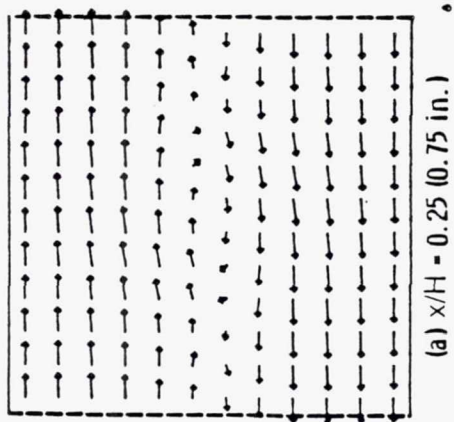
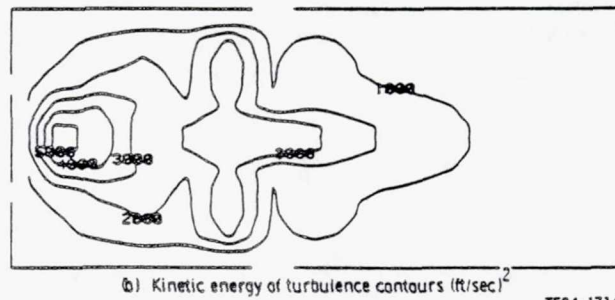
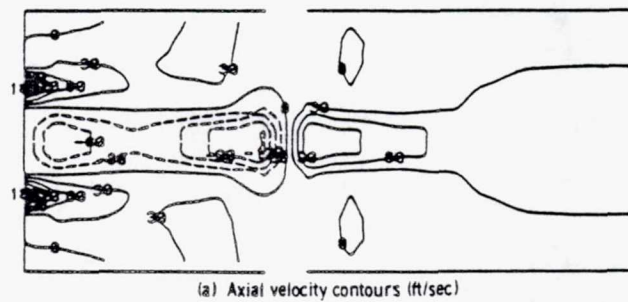


Figure 2.3-8. Longitudinal velocity vector plots for configuration with doubled primary jet flow.



TE84-1713

Figure 2.3-9. Cross-sectional velocity vector plots for configuration with doubled primary jet flow.



TE84-1714

Figure 2.3-10. Contour plots for plane through center of swirler for configuration with doubled primary jet flow.

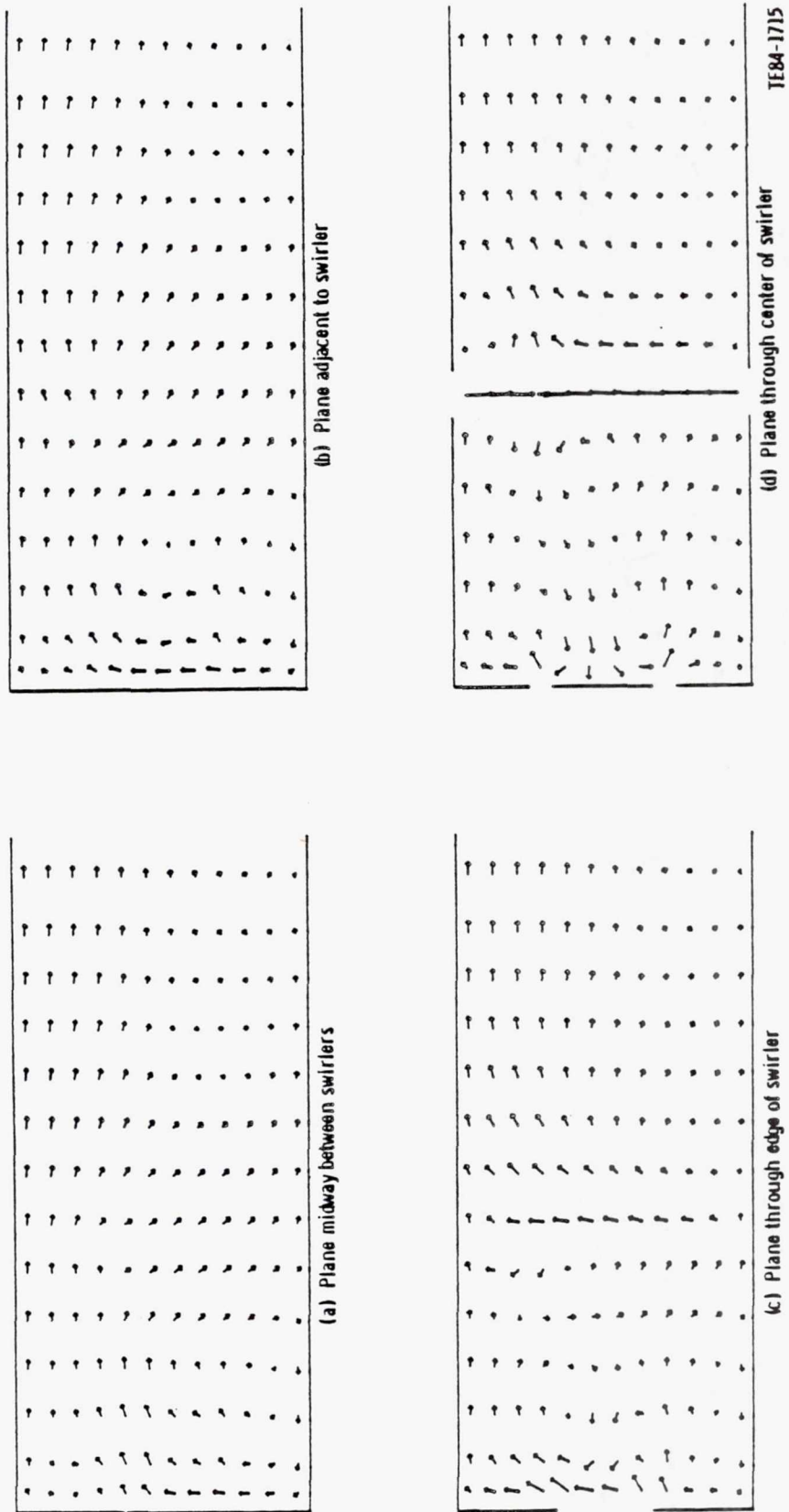


Figure 2.3-11. Longitudinal velocity vector plots for annular configuration.

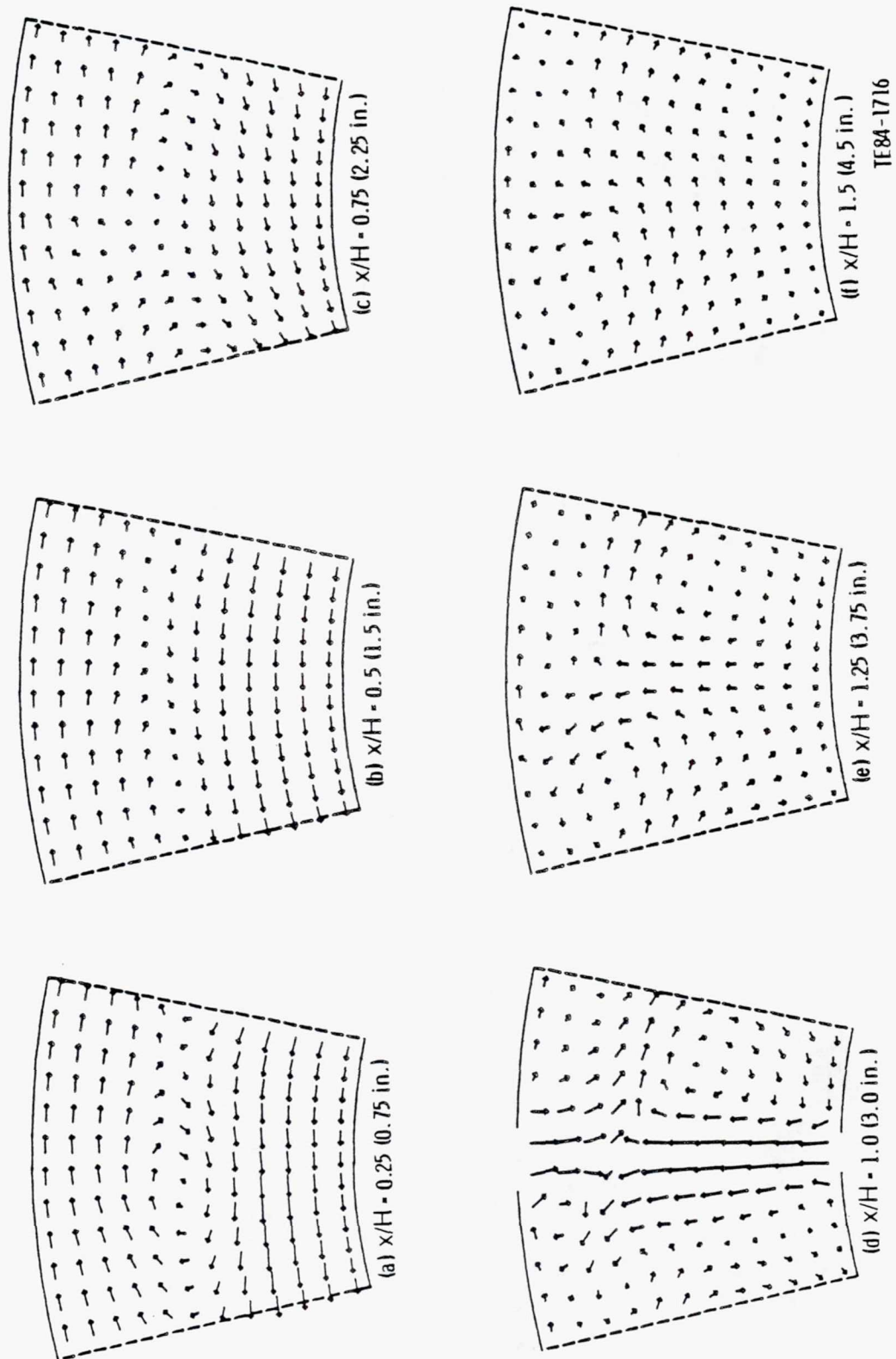


Figure 2.3-12. Cross-sectional velocity vector plots for annular configuration.

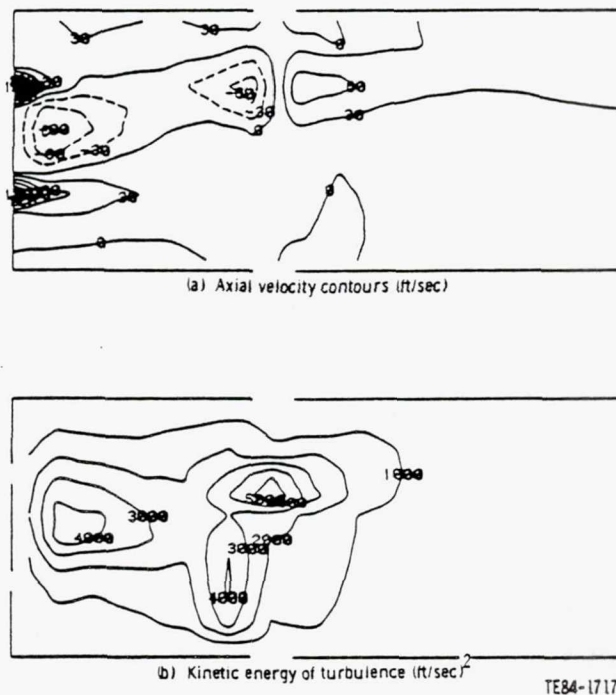


Figure 2.3-13. Contour plots for plane through center of swirler for annular configuration.

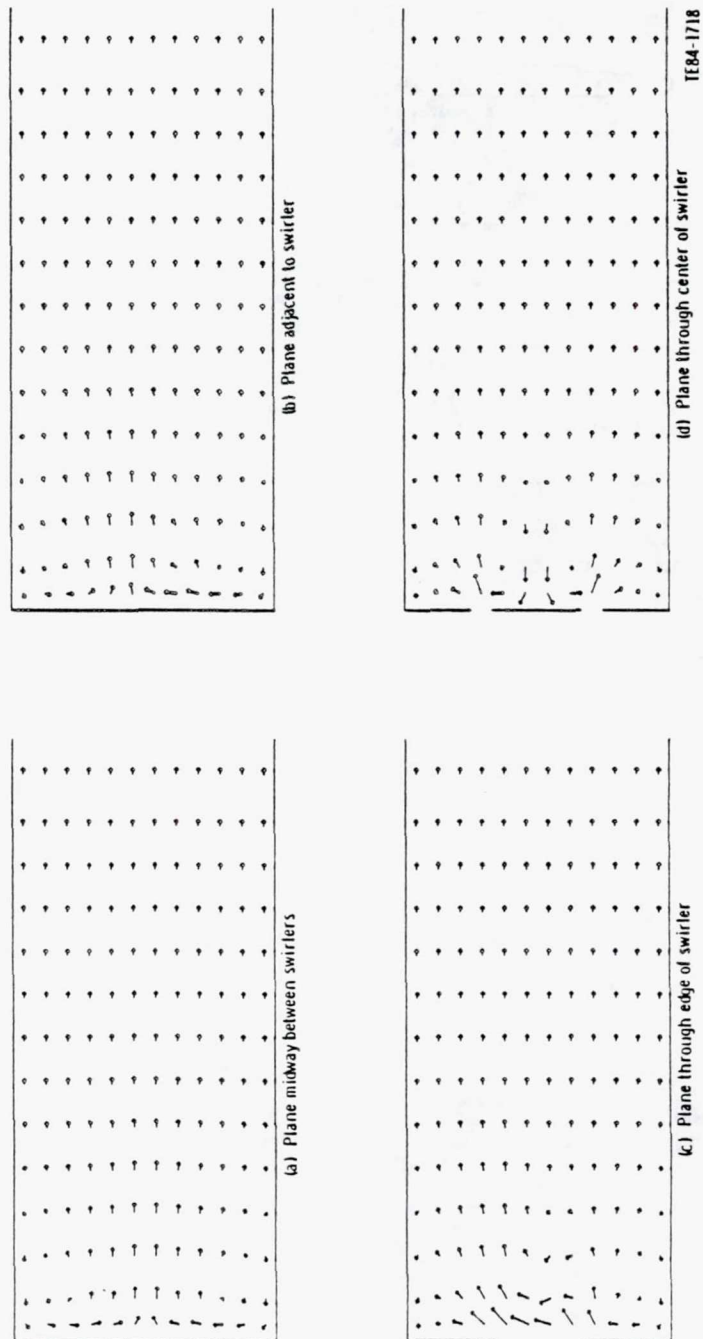


Figure 2.3-14. Longitudinal velocity vector plots for configuration with swirler only.

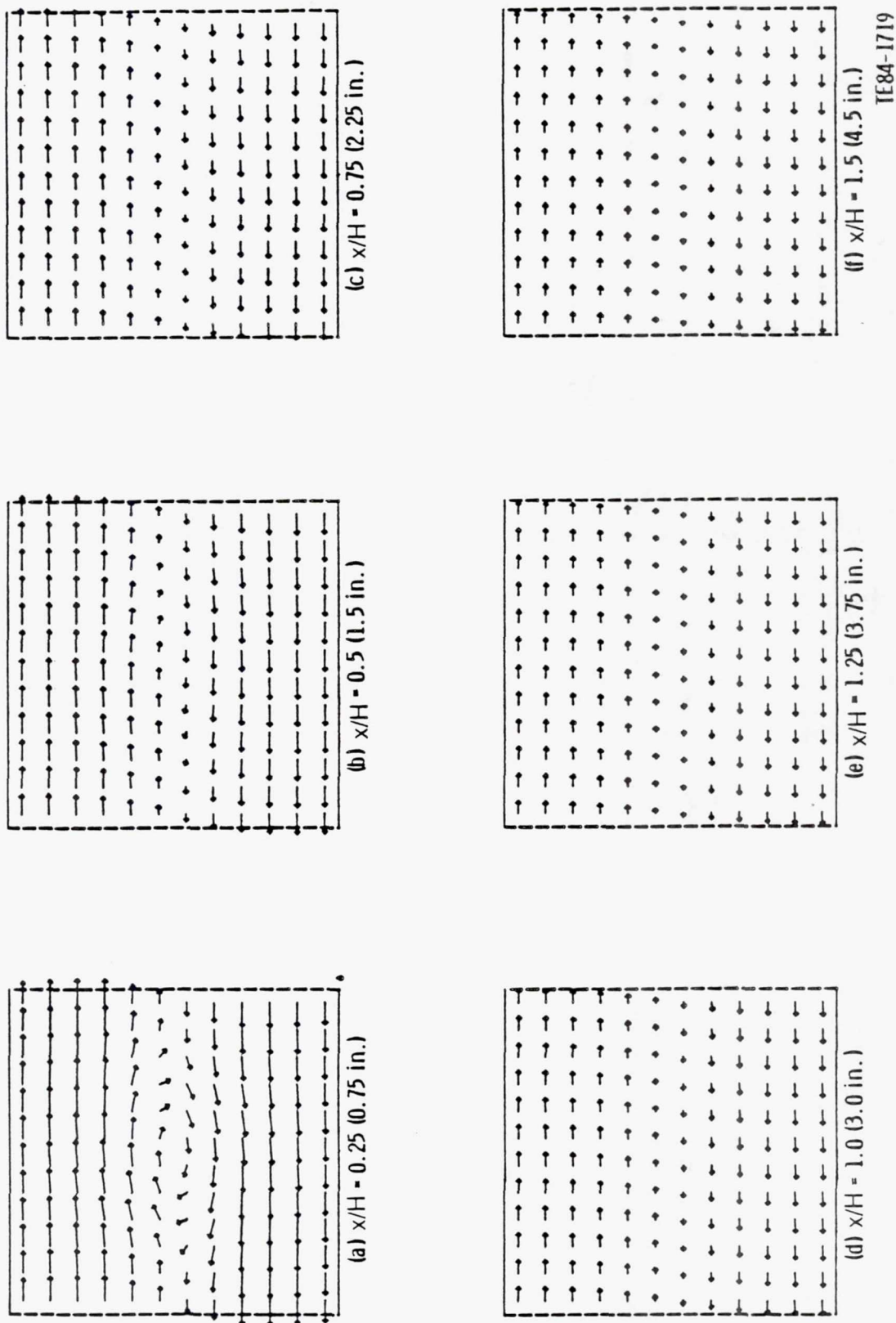


Figure 2.3-15. Cross-sectional velocity vector plots for configuration with swirler only.

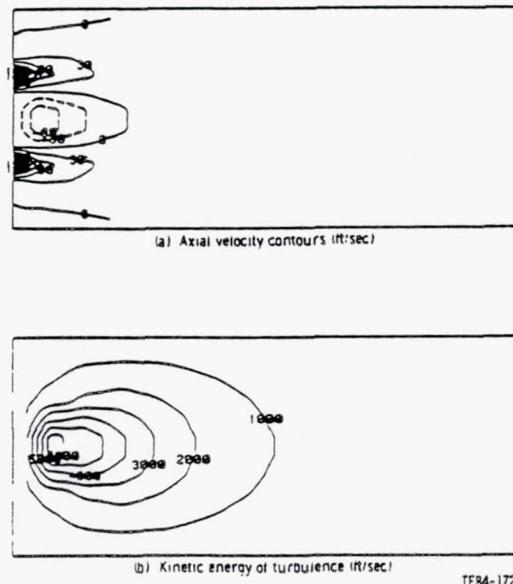


Figure 2.3-16. Contour plots for plane through center of swirler for configuration with swirler only.

REFERENCES

- Altgeld, H., Jones, W. P., and Whilhelmi, J., 1983, "Velocity Measurements in a Confined Swirl Driven Recirculating Flow," *Experiments in Fluids*, Vol 1, No. 2, pp 73-78.
- Catalano, G. D., Chang, K. S., and Mathis, J. A., 1989, "An Analytical and Experimental Investigation of Turbulent Jet Impingement in a Confined Cross flow," AIAA-89-0665.
- Cox, Jr., G. B., 1975, "Multiple Jet Correlations for Gas Turbine Engine Combustor Design," ASME Paper 75-GT-45, presented at ASME Gas Turbine Conference, Houston, TX, March 2-6.
- Crabb, D., Durao, D. F. G., and Whitelaw, J. H., 1981, "A Round Jet Normal to a Cross Flow," *Journal of Fluids Engineering*, Vol 2, No. 103, March, pp 142-153.
- Escudier, M. P., Bornstein, J., and Zehnder, N., 1980, "Observations and LDA Measurements of Confined Turbulent Vortex Flow," *Journal of Fluid Mechanics*, Vol 98, No. 1, pp 49-63.
- Ferrell, G. B., et al, 1984, "Lateral Jet Injection into Typical Combustor Flow Fields," AIAA paper 84-0374, presented at AIAA 22nd Aerospace Science Meeting, Reno, NV, January.
- Gouldin, F. C., Depsky, J. S., and Lee, S. L., 1983, "Velocity Field Characteristics of a Swirling Flow Combustor," AIAA paper 83-0314, presented at AIAA 21st Aerospace Sciences Meeting, Reno, NV, January 10-13.
- Habib, M. A., and Whitelaw, J. H., 1980, "Velocity Characteristics of Confined Coaxial Jets With and Without Swirl," *Journal of Fluids Engineering*, Vol 102, March pp 47-53.
- Halthore, R. N., and Gouldin, F. C., 1984, "Laser Scattering Measurements for Density in a Swirling Flow Combustor," AIAA Paper 84-0199, presented at AIAA 2nd Aerospace Sciences Meeting, Reno, NV, January 9-12.
- Holdeman, J. D., Walker, R. E., and Kors, D. L., 1973, "Mixing of Multiple Jets with a Hot Primary Airstream for Gas Turbine Combustors," AIAA Paper 73-1249, presented at AIAA/SAE 9th Propulsion Conference, Las Vegas, NV, November.
- Holdeman, J. D., and Walker, R. E., 1977, "Mixing of a Row of Jets with a Continued Cross Flow," *AIAA Journal*, Vol 15, No. 2, February, pp 243-249.
- Janjua, S. I., et al, 1982, "Turbulence Measurements in a Confined Jet Using a Six-Orientation Hot Wire Technique," AIAA Paper 82-1262.
- Johnson, B. V., and Bennett, J. C., 1984,, "Statistical Characteristics of Velocity, Concentration, Mass Transport, and Momentum Transport for Coaxial Jet Mixing in a Confined Duct," *Journal Engineering for Gas Turbines and Power*, Vol 106, No. 1, January, pp 121-127.
- Kamotani, Y., and Greber, I., 1972, "Experiments on a Turbulent Jet in a Cross Flow," *AIAA Journal*, Vol 10, No. 11, November, pp 1425-1429.
- Karki, K., and Mongia, H. C., 1989, "Recent Developments in Computational Combustion Dynamics," AIAA Paper 89-2808, July.
- Koutmos, P., and McGuirk, J. J., 1989, "Investigation of Swirler/Dilution Jet Flow Split on Primary Zone Flow Patterns in a Water Model Can-Type Combustor," *Journal of Engineering for Gas Turbines and Power*, Vol 111, pp. 310-317.
- Lefebvre, A. H., 1984, "Fuel Effects on Gas Turbine Combustion - Liner Temperature, Pattern Factor, and Pollutant Emissions," *Journal of Aircraft*, Vol 21, No. 11, pp 887-898.
- Lefebvre, A. H., 1985, "Fuel Effects on Gas Turbine Combustion - Ignition, Stability, and Combustion Efficiency," Transactions of the ASME, *Journal of Engineering for Gas Turbines and Power*, Vol 107, No. 1, pp 24-37.
- Lilley, D. G., 1977, "Swirl Flows in Combustion: A Review," *AIAA Journal*, Vol 15, No. 8, August, pp 1063-1078.
- Liou, T. M., Hwang, Y. H., and Wu, S. M., 1989, "The Three-Dimensional Jet-Jet Impingement Flow in a Closed-End Cylindrical Duct," *Journal of Fluid Engineering*, Vol 112, pp. 171-178.
- Mongia, H. C., and Smith, K. F., 1978, "An Empirical Analytical Design Methodology for Gas Turbine Combustor," AIAA Paper 78-998, July.
- Mongia, H. C., 1982, *Application of Multidimensional Modeling Techniques to the Design and Development of Gas Turbine Combustors*, 1982 Air Force Office of Scientific Research, Annual Contractors Meeting.

- Mongia, H. C., Reynolds, R. S., and Srinivasan, R., 1986, "Multidimensional Gas Turbine Combustion Modeling: Applications and Limitations," *AIAA Journal*, Vol 24, No. 6, June, pp 890-904.
- Nikjooy, M., Mongia, H. C., McDonell, V. G., and Samuelson, G. S., 1992, "Fuel Injection - Air Swirl Characterization," *Aerothermal Modeling Phase II Final Report*, NASA-CR-189193.
- Oven, M. J., Gouldin, F. C., and McClean, N. J., 1979, "Temperature and Species Concentration Measurements in a Swirl Stabilized Combustor," *17th Symposium (International) on Combustion*, The Combustion Institute, pp 363-374.
- Plee, S. L., and Mellor, A. M., 1978, "Flame Stabilization in Simplified Prevaporizing Partially Vaporizing and Conventional Gas Turbine Combustors," *Journal of Energy*, Vol 2, No. 6, pp 346-353.
- Plee, S. L., and Mellor, A. M., 1979, "Characteristic Time Correlation for Lean Blowoff of Bluff-Body-Stabilized Flames," *Combustion and Flame*, Vol 35, pp 61-80.
- Reynolds, R. S., Kuhn, T. E., and Mongia, H. C., 1977, "Advanced Combustor Analytical Design Procedure and its Application in the Design and Development Testing of a Premix/Prevaporized Combustion System," Spring meeting of the Central States Comb Dist.
- Rho, B. J., Kim, J. K., and Dwyer, H. A., 1989, "Experimental Study of a Turbulent Cross Jet," *AIAA Journal*, Vol 28, No. 5, pp. 784-789.
- Rhode, D. L., Lilley, D. G., and McLaughlin, D. K., 1982, "On the Prediction of Swirling Flow Fields Found in Axisymmetric Combustor Geometries," *Journal of Fluids Engineering*, Vol 104, September, pp 384-388.
- Rhode, D. L., Lilley, D. G., and McLaughlin, D. K., 1983, "Mean Flow Fields in Axisymmetric Combustor Geometries with Swirl," *AIAA Journal*, Vol 21, No. 4, April, pp 593-600.
- Rizk, N. K., and Mongia, H. C., 1989, "Correlations of High Density Fuel Effects," AIAA Paper 89-0216, January.
- Rizk, N. K., and Mongia, H. C., 1991, "Gas Turbine Combustor Performance Evaluation," AIAA Paper 91-0640, January.
- Roback, R., and Johnson, B. V., 1983, *Mass and Momentum Turbulent Transport Experiments with Confined Swirling Coaxial Jets*, NASA CR-168252, August.
- Sherif, S. A., and Pletcher, R. H., 1989, "Measurements of the Flow and Turbulence Characteristics of Round Jets in Crossflow," *Journal of Fluid Engineering*, Vol 111, pp. 165-171.
- Srinivasan, R., Berenfield, A., and Mongia, H. C., 1982, *Dilution Jet Mixing Program-Phase I*, NASA CR-168031, November.
- Srinivasan, R., Reynolds, R., Ball, I., Berry, R., Johnson, K., and Mongia, H. C., 1983, *Aerothermal Modeling Program: Phase I Final Report*, NASA CR-168243.
- Steele, L. L., Grant, J. R., Harrold, D. P., and Erhart, J. J., 1987, *Application of System Identification Techniques to Combustor Post-Stall Dynamics*, Air Force Wright Aeronautical Lab, Wright-Patterson AFB, Ohio, AFWAL-TR86-2105, February.
- Syred, N., and Beer, J. M., 1974, "Combustion in Swirling Flows: A Review," *Combustion and Flame*, Vol 23, pp 143-201.
- Vranos, A., Liscinsky, D. S., True, B., and Holdeman, J. D., 1991, "Experimental Study of Cross Stream Mixing in a Cylindrical Duct," AIAA-91-2459.
- Vu, B. T., and Gouldin, F. C., 1980, "Flow Measurements in a Model Swirl Combustor," AIAA Paper 80-0076, presented at 18th AIAA Aerospace Sciences Meeting, Pasadena, CA, 14-16 January.
- Walker, R. E., and Kors, D. L., 1973, *Multiple Jet Study*, NASA CR-121217, June.

TABLE OF CONTENTS

<u>Section</u>	<u>Title</u>	<u>Page</u>
III	Experimental Rig And Instrumentation	29
3.1	Initial Rigs - Design And Operation.....	29
3.1.1	Five-Swirler Air Rig.....	29
3.1.1.1	Inlet Conditions	32
3.1.1.2	Mean Flowfield	34
3.1.1.3	Turbulence Flowfield	37
3.1.2	Five-Swirler Water Rig.....	40
3.1.2.1	Primary Jets Only	40
3.1.2.2	Annular and Primary Jets	41
3.2	Flow Visualization Study	195
3.3	Rig Refinement Activities	196
3.3.1	Swirling Jet	196
3.3.1.1	Experimental Apparatus.....	196
3.3.1.2	Results and Discussion	196
3.3.2	Single Swirler Configuration	199
3.3.2.1	Data Acquisition	200
3.3.2.2	Calibration of Annular Pipe and Primary Jet	201
3.3.2.3	Inlet Conditions	203
3.3.2.4	Downstream Data	203
3.3.2.5	Turbulence Quantities	205
3.4	Final Rig - Instrumentation And Data Reduction	305
3.4.1	Final Experimental Apparatus.....	305
3.4.2	Instrumentation	305
3.4.2.1	Laser Doppler Velocimeter.....	305
3.4.2.2	Data Acquisition System.....	307
3.4.2.3	Velocity Measurements and Statistics Calculation	308
3.4.2.4	Error Analysis.....	311
3.4.2.5	Uncertainty Errors	312
3.4.2.6	Total Uncertainty	314
3.4.2.7	Marker Nephelometry	315
3.4.2.8	Test Case - Single Turbulent Jet	318
3.4.2.9	Errors	320

III. EXPERIMENTAL RIG AND INSTRUMENTATION

The experimental phase of the work was performed at Purdue University. An experimental rig that was considered adequate for obtaining "benchmark" quality data was designed and constructed by Allison Gas Turbine for use by Purdue University. It was anticipated from the outset that the jet-swirl interactions would be extremely complex and possibly unsteady, with many aperiodic features. Accordingly, it was decided that an experimental rig that could be operated with water as the working fluid and that would be suitable for exploration of various features of interaction through flow visualization would be a valuable adjunct facility to the air-operated facility to be utilized for obtaining quantitative data. Such a rig, identical in all respects to the air-operated rig, was designed and constructed by Allison Gas Turbine and provided to Purdue University for investigations.

Preliminary investigations with the air-operated and the water-operated rigs confirmed the existence of various dynamical features in the flowfield. It also became clear that the experimental results would be extremely sensitive to relatively small and apparently insignificant differences in the geometrical features and initial flow conditions in the two test rigs. After a substantial amount of testing, and analysis of flowfield data and observations, it was concluded that at least the following three features needed careful investigations: (i) the geometrical veracity of the test section; (ii) the symmetry of the swirler that was utilized to generate the swirling flow; and (iii) the flowfield generated by the primary jets, including both velocity distribution and unsteadiness of flow. A series of small-scale experimental studies was undertaken on each of the aforementioned flow features by building individual, dedicated experimental rigs and carrying out both quantitative and flow-visualization tests. The results obtained with such rigs are of considerable interest in themselves. They revealed both the type of complex interactions arising in the flowfield and the accuracy required in the construction of the two large air- and water-operated rigs.

Based on such data, the original rigs were modified for the conduct of experiments and the generation of the main body of flowfield data.

It should be pointed out that the preliminary studies conducted on the two test rigs also revealed the difficulties in utilizing standard intrusive and nonintrusive measurement techniques and means in such complex flowfields. Thus, it was found that the use of laser Doppler velocimetry (LDV) in the air-operated rig, and that of nephelometry in the water-operated rig, required considerable development in application. The final body of test data provided was obtained following all of the desired modifications to the basic test rigs and to the means of diagnostics and measurement.

The data presented in this section are extracted from M.S. theses written by Barron, 1986; Morgan, 1988; Seal, 1988; and Dwenger, 1990, respectively.

3.1 INITIAL RIGS - DESIGN AND OPERATION

The results of extensive experimentation in the initial air and water rigs are presented in the next two subsections.

3.1.1 Five-Swirler Air Rig

The annular combustor model was designed to allow measurements in a flowfield similar to that existing in current annular combustors. These measurements are to be used as a data base in the development and analysis of computational methods for the design of future gas turbine combustors.

The annular combustion chamber model, several views of which can be seen in Figures 3.1.1-1 and 3.1.1-2*, was designed to simulate the cold (nonreacting) flow characteristics of a current gas turbine combustor; the characteristics were swirl, recirculation, primary cross jets, and high levels of turbu-

* Figures for Section III appear at the end of each subsection. The figure number identifies the subsection in which the figure is discussed.

lence. The recirculation zone, typical of mixing zones in current combustors, is generated by the swirl imparted to the inlet annular jet flow by a set of swirl vanes. The length of this recirculation zone is determined by the location and strength of the primary cross jets. In order to allow the best possible modeling of actual combustor conditions, the annular and primary cross jets were fully developed prior to entry into the test section.

In an ideal annular combustion chamber geometric similarity exists for each swirler. This geometric similarity is in the form of a volume, or cell, of the flowfield extending downstream of the swirler inlet plane. The flow patterns and characteristics in each of these cells will be the same, along with the boundary conditions. The arrangement of these cells can be seen in Figure 3.1.1-3. Therefore, in order to understand the characteristics of the flowfield there needs only to be consideration of the region or cell corresponding to one swirler.

The same principle is utilized in the experimental apparatus. Due to the possibility of cell-to-cell mass transfer resulting from secondary flow patterns, as occurs in actual combustors, the decision was made to use multiple cells in the experimental apparatus. By allowing the adjacent cells to interact the development of these secondary flows was possible. The choice of five cells over three cells was made on the basis of the two extra cells adding more interaction between cells and, hence, more realism.

In an actual combustor a cell would be slightly curved, as can be seen in Figure 3.1.1-4. Comparing this to the combustor model cell, it can be assumed that the effect of the curvature is slight or negligible, thus allowing the duct and the swirler cell to be constructed with a simple rectangular cross section.

The duct rectangle cross section has a aspect ratio of 5, with a duct height of 3.00 in., a width of 15.00 in. and a cross section corresponding to each swirler cell of 3.00 in. by 3.00 in. The duct has a downstream extension from the swirler headplate of 10 duct heights, or 30.00 in. For this experiment the configuration consisted of two opposing primary cross jets mounted along the cell centerlines. The centerlines of the jets were located one duct height, 3.00 in., downstream of the test section inlet plane.

The duct was originally constructed with 0.500 in. thick plexiglass plates throughout. This choice of materials proved unsuitable for some of the LDV measurements due to factors such as:

- loss of beam crossover at the probe volume
- loss of pinhole alignment
- change in effective focal distance to the receiving lens

All three of these factors can be attributed to the slight variations in the thickness of the plexiglass sheets. The first factor can also be attributed to scratches in the surfaces of these sheets. Scratches are a problem with plexiglass applications such as this due to the need for continuous cleaning of the surfaces.

From a series of preliminary diagnostic studies, it was found that the measurements that were the most dramatically affected by the use of plexiglass were those made in the xy plane. These measurements were affected more than those in the xz or yz planes due to the fact that the beams passed through the duct sidewalls at a considerably larger distance from the probe volume. For the measurements in the xz or yz planes this distance ranged from 0.40 in. to 2.60 in., measured from the inner wall, while the that for the xy plane measurements ranged from 6.00 in. to 9.20 in. Since the beams must travel farther, the effective change in the beam angle due to thickness variations or scratches becomes more pronounced, resulting in an increase in the signal loss.

The solution to this problem was the replacement of the plexiglass sidewalls with 0.25 in. thick glass plates. These plates facilitated unimpeded beam traversal due to very uniform thickness as well as high resistance to scratching.

The annular jets were constructed out of stainless steel, with a length of 9.55 in. and inner and outer radii of 1.084 in. and 1.459 in., resulting in a length-to-effective diameter ratio of 25. The swirlers were actual engine hardware currently being used in the Allison 570-K turboshaft gas turbine engine (Figure 3.1.1-5). These swirlers, also constructed from stainless steel, are vane-type with 12 flat vanes at blade angles of 60 deg. The approximate swirl number is calculated to be 1.52. A diagram of the annular jet can be seen in Figure 3.1.1-6, while a separate diagram of the swirler can be seen in Figure 3.1.1-7.

In order for the experimental apparatus to be representative of an annular combustor, the five annular jets must pass the same mass flow. Since the pressure drop across a jet can be related to the mass flow, or average velocity, through the jet

$$\Delta p = \frac{k}{2} \rho U_{avg}^2 \quad (1)$$

where

U = mass averaged velocity in the jet

k = loss coefficient of the jet

Δp = pressure drop across the jet

$U_{avg} = \dot{m} / (A\rho)$

Two pressure taps were installed on each jet, the distance between the taps being as large as geometrically possible to allow the measurement of the largest pressure drop. The larger the measured pressure drop the smaller the percent uncertainty of the calculated velocities.

Control of the pressure drop, and the corresponding mass flow, is allowed by the throttle valves mounted at the inlets of the annular jets. These throttles, which also can be seen in Figure 3.1.1-6, are infinitely adjustable to allow either an increase or decrease in mass flow.

Initially, the swirlers were mounted flush, as in Figure 3.1.1-8, but preliminary flow visualization showed that upon exiting the swirler the flow attached to the headplate in the manner shown. Figure 3.1.1-9 shows the modified installation of the annular jets and swirlers to the headplate of the duct. The swirlers are recessed a small distance from being flush with the headplate.

This type of flow phenomena is not desirable in gas turbine combustors since the fluid would transfer a large amount of heat to the combustor liner with the main flow losing energy. The increased heat transfer rate, as well as increased surface shear stress due to the larger velocity gradients near the wall, would serve to reduce the life of the combustor, increasing the maintenance costs. The loss in energy from the main flow results in reduced available turbine inlet temperature and a corresponding loss in power. The desired type of swirler exit flow pattern can be seen in Figure 3.1.1-9. This pattern produces a highly stable flame and regions of high combustion intensity. From these flow visualization results, the swirlers were recessed in the annular jets a distance of 0.25 in. in order to produce the desired flow pattern at the test section inlet.

The preliminary flow visualization was performed in the single swirler apparatus which, as stated previously, operated at a smaller annular pressure drop than the model combustor. Further flow visualization in the single swirler apparatus of the test section inlet flow pattern, with the swirler installed in the recessed position, was also performed. These studies indicated that a bistable flowfield pattern existed for a small annular jet pressure drop range very near the maximum of the apparatus.

For pressure drops (ΔP) of less than 0.0178 psi, the desired flow pattern existed, while for pressure drops of greater than 0.0190 psi the attached flow pattern existed. In the range $0.0178 \text{ psi} < \Delta P < 0.0190 \text{ psi}$, the flow pattern was bistable, switching between the two established flow patterns in a seemingly random fashion. From these flow visualization results it can be assumed that the model combustor, op-

erating at a pressure drop of 0.040 psi, exhibited the attached flow pattern. Due to time constraints, further modifications of the test section inlet to produce the desired flow pattern were not possible. All the measurements were, therefore, conducted with the attached inlet flow pattern.

The primary cross flow jets were constructed from stainless steel with a length of 10.75 in. and an inside diameter of 0.43 in., also resulting in a length-to-diameter ratio of 25. As with the annular jets, the primary jet mass flow balance was maintained by balancing the pressure drops on the jets. The pressure taps were mounted to give the largest possible pressure drop and the inlets of the jets were fitted with throttle valves to allow the tailoring of the pressure drops. A diagram of a sample primary cross jet and throttle valve can be seen in Figure 3.1.1-10.

An important characteristic in the analysis of a combustor of this type is the primary jet-to-annular jet mass flow ratio. Originally, the desire was to have a primary jet mass averaged exit velocity of 300 ft/sec and an annular jet mass averaged exit velocity of 150 ft/sec. These velocities gave the desired mass flow ratio of 0.81, a total duct mass flow of 0.517 lbm/sec and a duct average velocity of 21.6 ft/sec.

Although the five annular and ten primary cross jets appeared identical to each other, some inconsistencies did exist. Differences in the maximum measured velocities were discovered during preliminary testing. Since the jets were required to have the same mass flow, the maximum pressure drop was limited to the lowest measured maximum of all the jets.

The maximum average velocity for the annular jets was 93.4 ft/sec, while for the cross jets 250.0 ft/sec was the maximum. These measurements were made with a pitot tube and the LDV. The original mass flow ratio could have been obtained by adjusting the throttles valves on the cross jets to reduce their mass flow; the decision was made to have the highest possible jet exit velocities in order to keep the turbulence levels as high as possible. The resulting mass flow ratio was 1.08, with a total duct mass flow of 0.371 lbm/sec and a duct average velocity of 15.8 ft/sec.

In order to draw the ambient laboratory air into and through the test section some type of fan or blower had to be utilized. A 30-hp Chicago Blowers centrifugal blower was selected, due to its ability to pass the large required mass flow. Connecting the test section duct to the fan was a large volume plenum chamber. The large volume was chosen to minimize the possible effects of feedback of larger scale fluctuations into the test section. Preliminary tests indicated that some large-scale feedback in the form of large-scale velocity fluctuations did exist, prompting the use of screens and straws at the end of the test section. The additions did not cause a significant loss in mass flow and did eliminate the previously observed feedback. The plenum chamber and the centrifugal fan can be seen in Figure 3.1.1-11.

3.1.1.1 Inlet Conditions

Flow profiles showing the development of the primary jet flow into the test section can be found in Figures 3.1.1-12 through 3.1.1-27 (note, $y = 1.5$ in. is the horizontal centerplane, $z = 7.5$ in. is the vertical centerplane, and $z = 6$ in. and $z = 9$ in. are the vertical midplanes). These profiles, showing only the vertical (y direction) velocity component (corresponding to the jet axial velocity), are measured at the vertical locations $y=0.06, 0.25, 0.50, 0.75, 1.00, 1.25$, and 1.50 in. These mean and root mean square (rms) velocity distributions should show profiles similar to pipe flow with substantial variations with vertical distance.

The measurement grids in both the xy (same as yz) and xz planes can be seen in Figures 3.1.1-28 and 3.1.1-29. The xy plane grid shows a change in the number of grid points in the x direction, with a corresponding change in the z direction, at the third vertical station from 11 to 13 points, which was instituted since the jet flux would spread at the larger y distances. The xz plane grids corresponding to these various y locations also show the change in the grids with Figure 3.1.1-29 (a) illustrating the grid for $y=0.06$ in. and $y=0.25$ in. and Figure 3.1.1-29 (b) illustrating the grid at $y=0.50, 0.75, 1.00, 1.25$, and 1.50 in. Both of these grids use a spacing of 0.05 in. in both the x and z directions.

At the $y=0.06$ in. station a close comparison to classic pipe flow data such as that from Laufer (1954*) would be expected. A comparison of Laufer's data for both the mean and rms quantities, at Reynolds numbers (Re) (based on maximum velocity and jet diameter) of 50,000 and 500,000, to the data from the current experiment ($Re = 75,000$) can be seen in Figures 3.1.1-14 and 3.1.1-15. The data from both Laufer and the combustor model are nondimensionalized by the centerline (maximum) velocity. From Figure 3.1.1-14 it can be seen that the experimental V profile from the combustor model shows better agreement with the $Re=500,000$ data than the $Re=50,000$ data. Slight differences are to be expected, such as the slight spread of the flow due to the dissipation of the sharp gradients near the jet wall, since the combustor model measurements were made 0.06 in. from the jet exit.

Figure 3.1.1-15 shows plots of turbulence intensity (the rms velocity divided by the centerline mean velocity) for both the combustor model data and Laufer's two cases. As can be seen, both of Laufer's cases show strong peaks near the walls of the jet with maximum values near 9%. The combustor model data show a maximum near 13%, but the peak could be larger due to the rather poor resolution of the measurement grid (compared to that of Laufer). The centerline value for the combustor model is also larger, by nearly a factor of two, than both of Laufer's data sets. This large difference between the data sets is mainly attributed to the effect of the opposing cross jet as well as the effect of the local main flow.

As discussed previously, flow visualization of the jet stagnation point region indicated that the location of the stagnation point fluctuated, in a rather random fashion, within a 0.75 in. range between the exits of the two jets. The region between the two jets is evidently highly turbulent and unsteady, resulting in high levels of turbulence intensity across the test section, even near the cross jet exits. Since the centerline of the cross jets was located at $z=7.50$ in., the jet flow issued into a region of cross flow of velocity of roughly 10% of the maximum jet velocity. Although this is a relatively small magnitude crossflow velocity, this effect also resulted in an increase of the turbulence intensity.

At the $y=0.25$ in. station (Figure 3.1.1-16) the V distribution shows a slight spread in the jet flux, with not much reduction in the maximum velocity. The V_{rms} velocity shows a large increase in the turbulence fluctuations over those found at $y=0.06$ in. The values measured at this location in the combustor model are much larger than the values that would be expected from pure jet flow, again due to the opposing cross jets creating a region with very high levels of turbulence.

At $y=0.50$ in., the V distribution can be seen to be translated in both the x and z directions, this skewness corresponds to a bending of the centerline of the jet flow due to the main flow acting as a cross flow and exerting a shear force on the jet flux. The spread of the jet flux is increased over at $y=0.25$ in., with the maximum velocity remaining near 325 ft/sec. The V_{rms} distribution shows overall increases across the grid, with the peak levels, relatively sharp at the $y=0.25$ in. location, being dissipated to give a smoother contour.

The V distributions at $y=0.75$, 1.00, and 1.25 in. indicate a decrease in the maximum vertical velocity, as well as continued spread in the vertical jet flux, with distance from the jet exit. The location of the center of the vertical jet flux can also be seen to show little translation in the xz plane. The U_{rms} distributions show the decay of the circular peak region into a concentrated peak at the $y=1.25$ in. station with an xz plane location at the center of the vertical jet flux. This peak occurs in the stagnation point location fluctuation region, resulting in a very high level of turbulence.

The $y=1.50$ in. plane is located in the middle of the stagnation point fluctuation region and, thus, shows high levels of turbulence as at $y=1.25$ in. with the rms velocity contour displaying a much smoother distribution than the previous stations. The main point of interest is the reduction in the vertical jet flux, the main fluid motion in this region is in the xz plane as seen in the xy and yz plane vector plots. Also, from these vector plots the location of the stagnation point was illustrated to be near $y=1.35$ in.; from

* References for Section III are listed at the end of the section.

these results the stagnation point is not evident even at $y=1.50$ in. Since the different data sets for the primary jet and for the main flow were measured at different times, the operating conditions could have been slightly altered. The peak vertical velocity has been reduced from 180 ft/sec, at $y=1.25$ in., to 50 ft/sec, indicating that the stagnation point is close to the $y=1.50$ in. location.

3.1.1.2 Mean Flowfield

Three-dimensional information on the main flowfield has been obtained through the use of a single-component LDV system. Distributions of U , V , W , U' , V' , W' , $U'V'$, and K are calculated from the individual data samples.

The choice of a measurement grid depends on the character of the fluid motion. More detailed measurements are needed in regions of large gradients and complex flow patterns, with less detail necessary in regions of simpler, less complex flow. Due to the three-dimensionality of the flowfield, a choice was made as to the regions of the flow in which to concentrate the measurements. The yz plane was in need of a measurement grid with greater spatial resolution than that for the xy plane, due to the smaller scale structures to be found in the yz plane. Thus, measurements were to be made in yz planes for various downstream locations, with these downstream locations chosen so as to also be more concentrated in the more complex regions.

Another consideration in measurement grid sizing involves the probe volume size, the resolution of the grid should be such that probe volume overlap from one data point to the next does not occur. Rotation of the test section was necessary to allow the measurement of the W characteristics. Due to this rotation, the length of the probe volume, on the average being 0.05 in., is the driving factor for the grid spacing in both the y and z directions which was chosen to be 0.20 in., or 4 probe volume lengths, for both directions.

The spacing in the x direction of the various planes was chosen as 0.50 in. in the region of the more complex flow, $0.0 \text{ in.} < x < 4.00 \text{ in.}$, with larger spacing thereafter. The downstream locations of the yz measurement planes were $x=1.00, 1.50, 2.00, 2.50, 3.00, 3.50, 4.00, 4.50, 6.00$, and 9.00 in. The yz plane and xy plane measurement grids can be seen in Figures 3.1.1-30 and 3.1.1-31.

Although a complete scan in the yz plane from one wall to the other was desired, limits on the vertical travel of the probe volume were imposed. The range of vertical probe volume travel was, therefore, limited to $0.40 \text{ in.} < y < 2.60 \text{ in.}$ Since data pertaining to only one cell was desired, the limits on the travel of the probe volume in the z direction were $5.80 \text{ in.} < z < 9.00 \text{ in.}$, where the $z=5.80$ in. location allows comparison to a geometrically similar station at $z=8.80$ in.

In the measurement of the W characteristics some geometrical restrictions were encountered at $x=2.50, 3.00$, and 3.50 in., necessitating the removal of the cross jet throttles and mounting plate, very little resulting flowfield alteration occurred. The measurements at the $x=2.50$ in. and $x=3.50$ in. locations were then able to be made while those at $x=3.00$ in. were not, due to the necessary removal of the cross jet supporting structure.

The mean flowfield found in the model combustor is best represented by vector plots in the xy and yz planes. These vector plots allow the relative values of the velocities at points in the flowfield to be seen thus illustrating the general mean flow characteristics. The xy plane vector plots can be found in Figures 3.1.1-32 through 3.1.1-37 while the yz plane vector plots can be found in Figures 3.1.1-38 through 3.1.1-43.

From the xy plane vector plots two main characteristics can be seen, the formation of a general toroidal recirculation zone and the influence of the primary cross jets. A great amount of interaction exists between the recirculation zone and the cross jets. As a consequence of this interaction, the recirculation zone and the cross jet interaction must be discussed together, not separately.

The recirculation zone is generated by the application of swirl to the inlet annular jet flow and the step change in area at the inlet to the test section. This zone is created in order to enhance the combustion process. The general character of this zone can be seen in the xy plane vector plots. This region of backflow exists over a large portion of the cell cross section, showing asymmetric behavior.

The purpose of the primary jets is to shorten the recirculation zone in order to decrease the overall length of the combustor. This goal has been achieved as no backflow exists past the $x=3.00$ in. station, but while the length of the recirculation region is shortened by the addition of the jets, the strength of recirculation has been enhanced by the radial jet effect from the cross jet stagnation point. The location of the stagnation point is controlled by the relative strength of the two opposing jets, if the jets had equal mass flows (pressure drops), the stagnation point would be located in the vertical center of the duct. From Figures 3.1.1-34 (a) and 3.1.1-35 (a), it can be seen that this location is not in the vertical center of the duct, but at roughly $y=1.35$ in. Preliminary flow visualization had illustrated large-scale fluctuations of the location of the cross jet stagnation point in the range $1.00 \text{ in.} < y < 2.00 \text{ in.}$, indicating the unsteadiness present in the flowfield.

The influence of the cross jet stagnation point on the recirculation zone, and the downstream flow, is easily seen in Figures 3.1.1-34 and 3.1.1-35. The flow can be imagined to flow out of the jets, reach the stagnation point, and be forced to move in a radial-type motion in the xz plane. The recirculating backflow thus receives a driving force which generates stronger recirculation.

Previous studies on similar experimental apparatuses (Brondum and Bennett, 1986; Rosenweig et al, 1961; McLaughlin and Tiederman, 1973) show a recirculation region which is symmetric about the duct centerline in the xy plane. These studies, though, used axisymmetric (cylindrical) test section geometries, whereas the geometry used in this study was of rectangular cross section, with a square cell cross section. As movement is made equal distances away from the centerline location, $z=7.50$ in., with a square cross section expectations would be for the vector profiles to be the inverse of one another. Since all of the cells are assumed geometrically similar, a necessary condition is that the flow conditions at the plane boundaries separating the cells be the same. At the $z=6.00$ in. and $z=9.00$ in. boundaries, the flow conditions should be the same.

Figure 3.1.1-38 illustrates the regions of recirculating flow in the yz plane at $x=1.00$, 1.50 , 2.00 , and 2.50 in. The recirculation zone at $x=1.00$ in. appears to be located off-center in the positive z direction, with strong recirculation existing into the upper right corner and a smaller amount of recirculating mass flow exists in the upper left corner. This backflow existing in the upper left corner could be part of the recirculation zone from the adjacent cell. From the vector plots for $7.40 \text{ in.} < z < 8.00 \text{ in.}$ the effect of the attached inlet flow pattern is evident, the recirculation is strong across the duct height with positive axial flux occurring only near the walls. Strong positive axial flux can be found to exist in the lower left and lower right corners. The profiles at the z boundaries are roughly similar in form, with larger magnitudes existing at $z=9.00$ in.

The vector plots indicate the structure of the flow patterns at $x=1.50$ in. to be very similar to that at $x=1.00$ in. The recirculation can be seen to extend the entire width of the cell cross section with a larger portion of this backflow existing in the upper y range. Nearer the $z=6.00$ in. and $z=9.00$ in. boundaries, the lower y range is dominated by strong positive axial flux. The profiles at the z boundaries, like those at $x=1.00$ in., are similar in form but with much larger magnitudes existing at $z=9.00$ in.

Except in the range $7.00 \text{ in.} < z < 8.40 \text{ in.}$ the vector profiles at $x=2.00$ in. and $x=2.50$ in. are very similar. Near the center of the cell, the strong influence of the cross jets on the recirculated mass flow is illustrated. The extent of the backflow in the cell cross section can be seen to be reduced for the $x=2.50$ in. location than for the $x=2.00$ in. location, the backflow is more concentrated near the center of the cell cross section. This can be attributed to the flow from the cross jet stagnation point region. The strongest influence of the stagnation point on the recirculated mass flow is in the center of the cell cross section. For

both the $x=2.00$ in. and $x=2.50$ in. stations, the vector plots on the z boundaries are very different in shape and magnitude.

The behavior of the mean flowfield for stations downstream of the cross jet injection plane is relatively simple compared to that of the upstream stations. The main characteristic is the influence on the local flowfield from the radial jet flow pattern formed at the cross jet stagnation point. This effect is best seen in Figures 3.1.1-34 and 3.1.1-35. As one moves in the z direction, either positive or negative, the vertical spread of the radial jet can be seen. This spread is an effect of viscous dissipation and is strong enough that, for the $x=3.50$ in. plane, no influence of the cross jets can be seen at either the $z=6.00$ in. or the $z=9.00$ in. boundary. The dissipation of this effect occurs in the axial direction, as well, since no vertical variation of any consequence in the axial velocity profile can be seen at $x=6.00$ in. or $x=9.00$ in.

The yz plane vector plots (Figures 3.1.1-38 through 3.1.1-43) allow the illustration of the flow developing in the various cross-stream planes. At all of these stations some type of smaller scale swirling motion exists, with the largest concentrated near the cross jet injection location. Unexpected, however, was the absence of overall swirl. Some amount of overall swirl was expected in the first duct height of the test section due to the large amount of swirl (swirl number: $S=1.52$) applied to the inlet flow.

As with the vector plots in the xy plane, the vector plots in the yz plane show the effect of the cross jets on the flowfield. The far downstream locations, $x=6.00$ in. and $x=9.00$ in., show very little motion in the cross-stream plane, illustrating the large amount of dissipation present.

The vector plots of most interest are those of the $x=2.50$ in. and $x=3.50$ in. downstream locations. At both of these stations, the strong effect of the cross jets on the combustor model flowfield can be seen. The flow pattern in the yz plane can be seen to be dominated by four cells of vortex-type motion. For both of these locations, the left side of the plane (looking downstream, $z < 7.50$ in.) shows a much more symmetric (with the $y=1.50$ in. centerline) pattern than the right side.

The driving force behind this type of motion is, as in the case of the xy plane, the flow resulting from the cross jet stagnation point region. The flow can be seen exiting the cross jets, reaching the stagnation region, and flowing in a radial type motion in the xz plane. This radial motion exhibits itself in the yz plane as fluid motion in the positive and negative z directions. Thus, with generally no cross flow between the adjacent swirler cells, this jet effect drives this vortex-type cell motion.

Farther upstream of the $x=2.50$ in. station one can still see the swirling motion, although not nearly as structured as the $x=2.50$ in. or $x=3.50$ in. cases. The $x=2.00$ in. location shows two regions of vortex-type motion, with a more structured flow pattern possibly altered by the existence of the large amount of cross-flow at the $z=9.00$ in. boundary. This type of cross-flow is not seen at the $z=6.00$ in. boundary, and thus is a probable cause of the asymmetry in the flowfield. This cross-flow is unexpected since all the swirler cells were assumed to be geometrically similar, resulting in similar flowfields for the different cells. This cross-flow is partially responsible for the asymmetries found in the right half of the grid at the $x=2.50$ in. and $x=3.50$ in. locations.

Cross-flow can be seen to exist at the $x=1.50$ in. plane and, to a lesser extent, at the $x=1.00$ in. plane. These two locations share similarities in flow patterns other than aforementioned cross-flow from the adjacent cell. In each of the vector plots of these two locations, two regions of vortex-type motion can be observed, one in the upper right corner, and a second, much weaker, vortex motion located near the mid z and lower y ranges. The behavior in the lower z range for the full y range at both the $x=1.00$ in. and $x=1.50$ in. stations is rather undefined. At $x=1.00$ in., scattered or bad data seem to obscure flow details, while at the $x=1.50$ in. station, no prevalent type of motion exists.

As stated earlier, no overall swirling motion is found in the first duct height of the test section, as would be expected from the large amount of swirl applied to the inlet flow. The combination of the primary cross jets, attached flow pattern, and large step change in area at the test section inlet (area

ratio=12.02), serve to reduce the swirl velocities to negligible levels in this region. The effect of the cross jets on the swirl is the same as that of flow straighteners, the radial jet issuing from the cross jet stagnation point serves as a boundary (porous in this case, solid in the case of flow straighteners) across which mass flow is inhibited.

The effect of the attached flow pattern and large step change in area can be explained by angular momentum concepts. As the fluid issues from the swirler it possesses a certain amount of swirl, or angular, momentum. Since the flow is a wall jet, the fluid moves towards the cell boundaries upon exit from the swirler. When the fluid turns in the downstream direction, the large change in area will cause a large reduction in the particle velocities due to the law of conservation of angular momentum. These velocities may be further reduced due to viscous effects from the cell boundaries, but this would be a small effect. This absence of swirl, and the corresponding absence of the decay of swirl, indicates that the recirculation is formed and driven by the step change in area.

Further downstream of the $z=3.50$ in. location, at $x=4.00$ in., the well-defined 4 cell flow pattern is seen to deteriorate. Four vortex-type motions are still evident, but the cores of the vortices have translated while their strengths have been reduced. The 4.50 in. location shows almost complete breakdown of the four cells, with only one very weak region of vortex motion still existing.

The $x=6.00$ in. plane illustrates the decay of nearly all motion in the cross-stream plane, the only motion being a small amount of flow in the negative z and positive y directions in the lower z range. The $x=9.00$ in. plane shows no detectable motion of any type, this demonstrates the large amount of dissipation present in the flowfield as only 6.00 in. upstream existed a very complicated, high speed flow pattern. Additional line plots of the three mean velocity components are seen in Figures 3.1.1-45 through 3.1.1-52.

3.1.1.3 Turbulence Flowfield

The turbulence flowfield of the combustor model is best represented by contour plots of the characteristics in the yz planes for the various downstream locations. The turbulence quantities calculated from the individual data samples are the three rms velocities, U_{rms} , V_{rms} , and W_{rms} , and the corresponding turbulence kinetic energy, K , as well as the xy component of the Reynolds shear stresses, $U'V'$.

The rms velocity and turbulence kinetic energy distributions for the various downstream stations can be found in Figures 3.1.1-53 through 3.1.1-99. The data for the $x=3.00$ in. case consist of only the U_{rms} and V_{rms} , since W_{rms} was not measurable due to geometric restrictions.

The profiles for $x=1.00$ in. can be seen in Figures 3.1.1-53, 3.1.1-54, 3.1.1-55, and 3.1.1-56. The three rms velocities seem to exhibit similar behavior with flat contours near the center of the duct. U_{rms} and V_{rms} show a large amount of data scatter for most of the plane, especially the lower z range, while the W_{rms} contour is relatively flat for most of the plane, with scatter only found in the $5.80 \text{ in.} < z < 6.40 \text{ in.}$ range. The K distribution, as well, shows a well-defined central region of reduced magnitude extending into both corners on the $z=9.00$ in. boundary. The intensity of the turbulence peaks-up near the walls and near the mid y range at the $z=9.00$ in. boundary. This flat (nearly constant magnitude) central region corresponds to the strong region of backflow found at the $x=1.00$ in. plane, as seen from the mean flowfield data, while the peaking near the walls corresponds to the shear layer produced by the strong axial flow along the walls. This pattern of reduced levels of turbulence inside the backflow region as compared to the shear layer was also seen in the work of Brum and Samuelson (1987) and Vu and Gouldin (1982).

Another characteristic of the K distribution at the x location is the formation of a circular shape, high gradient region found in the lower z range. This appears to be the result of the high shear zones from

the annular jet flow. This ridge of high K extends around the central zone only for the lower z range and does not exist in the upper z range.

At $x=1.50$ in. (Figures 3.1.1-57, 3.1.1-58, 3.1.1-59, and 3.1.1-60) the U_{rms} , V_{rms} , and W_{rms} contours all display relatively flat distributions, resulting in a flat K contour. The circular, high gradient region found at $x=1.00$ in. is barely visible in the lower z range, while a peak is evident near $y=2.0$ in. on the $z=9.00$ in. boundary. This peak results from both U_{rms} and V_{rms} showing general peaks in that region. One characteristic of V_{rms} illustrated in the contour is the magnitude deficit in the lower right corner.

Moving to the $x=2.00$ in. station, some interesting flow characteristics (Figures 3.1.1-61, 3.1.1-62, 3.1.1-63, and 3.1.1-64) can be observed. Regarding the line plots, it can be seen that all three rms terms (except for V_{rms} in the upper z range) and K show very similar behavior across the cell width with nearly equal magnitudes (peaking near the mid- y region) and a trailing off of the magnitudes near the walls. The velocity gradients are larger in the y direction than in the z direction. This behavior seems to be a combination of isotropy, all three rms terms being equal, and homogeneity in the z direction, rms terms at a constant value).

The contours of the turbulence characteristics at $x=2.50$ in. (Figures 3.1.1-65, 3.1.1-66, 3.1.1-67, and 3.1.1-68), show general similarity to those at $x=2.00$ in., with general peaking in the central region of the cell cross section and larger gradients in the y direction than the z direction. The larger gradients result from the close proximity of the measurement plane to the stagnation point; the radial jet fluid is concentrated in a thin layer in the y direction while spreading in all direction in the xz plane.

The behavior of U_{rms} at $x=3.00$ in. (Figure 3.1.1-69) does not show much effect from the cross jet injection, as most of the contour displays a flat profile with a small peak in the lower right corner. The effect of the jets is clearly evident, though, in the V_{rms} distribution, with a clear and sharp peak occurring near the center of the cell cross section. Figure 3.1.1-70 presents the contour and line plots of V_{rms} at $x=3.00$ in.

Unlike that at the $x=3.00$ in. location, the U_{rms} contour for $x=3.50$ in. (Figure 3.1.1-71) shows a large central peak with the magnitude dropping off at the cell boundaries. The V_{rms} distribution given in Figure 3.1.1-72 shows magnitudes nearly equal to those at $x=3.00$ in., with a central peak trailing off at the boundaries and walls. The W_{rms} contour, given in Figure 3.1.1-73, however, shows a very asymmetric behavior, with a general peaking located off center in the negative z direction. Due to this behavior in W_{rms} , the K distribution also shows an asymmetric peaking in the same general location. Other than this abnormality, the distribution shows the turbulence kinetic energy (Figure 3.1.1-74) to be highly concentrated in the central region of the duct.

The behavior of the U_{rms} , V_{rms} , W_{rms} , and K at the $x=4.00$ in. station, seen in Figures 3.1.1-75, 3.1.1-76, and 3.1.1-77, follows that of the data at $x=3.50$ in., although with reduced magnitudes due to dissipation and decay. The asymmetric W_{rms} behavior exists in the same general form as at $x=3.50$ in., thus reducing the probability of measurement error. The contour of the turbulence kinetic energy again shows the high concentration near the center of the duct, trailing off to nearly constant values at the upper and lower walls and showing smooth profiles, peaking at mid y , on the two z boundaries. The characteristics at $x=4.50$ in. (Figures 3.1.1-78, 3.1.1-79, 3.1.1-80, and 3.1.1-81) display the same general behavior as the data at both the $x=3.50$ in. and the $x=4.00$ in. planes, only with reduced magnitudes.

The contours of data at $x=6.00$ in. (Figures 3.1.1-82, 3.1.1-83, 3.1.1-84, and 3.1.1-85) indicate near isotropy and homogeneity, although some scatter of the data is evident and the W_{rms} contour does show a slight gradient in the negative z direction. The same behavior is seen at $x=9.00$ in. (Figures 3.1.1-86, 3.1.1-87, 3.1.1-88, and 3.1.1-89), with the magnitudes of all three rms terms reduced from those at $x=6.00$ in. Regarding the K contours at both the $x=6.00$ in. and $x=9.00$ in. planes, it can be seen that

the distributions at $x=9.00$ in. seem to indicate greater isotropy and homogeneity than at $x=6.00$ in. Since the magnitudes at these stations are so much less than at $x=3.50$ in., then isotropy and homogeneity can be assumed to be valid assumptions. Although the values of the rms velocities and K at these two downstream stations are much lower than the values at the upstream stations, the values are still very high when compared to fluid flows such as channel or pipe flow.

The contour plots of the Reynolds stress component, $U'V'$, can be found in Figures 3.1.1-90 through 3.1.1-99. Higher levels, either positive or negative, of $U'V'$ are found in regions of high shear or momentum transfer in the xy plane. This component of the Reynolds shear stresses was the only one measured.

From the $U'V'$ contour at $x=1.00$ in. (Figure 3.1.1-90), the circular ridge of increased $U'V'$ in the left half of the plane (looking downstream) can immediately be seen. This ridge was also seen in the K contour at $x=1.00$ in., and corresponds to the high speed flow issuing from the swirlers creating a region of high shear and momentum transfer. This ridge appears to indicate that the flow exiting the swirler is not of the wall jet variety and appears to possess some type of swirling motion. Near the center of the duct one also sees a region of near zero magnitude, also shifted in the positive z direction, signaling a region of low or zero shear. This region corresponds to the strong backflow found at this location.

The $x=1.50$ in. station exhibits behavior similar to $x=1.00$ in. only in the sense that a slight ridge is visible for the lower z range. In general, the contour is rather flat but asymmetric with a peaking on the $z=9.00$ in. boundary. Also peaking at this same location were U_{rms} and V_{rms} (and also K), indicating the occurrence of some strong turbulence interaction.

Some interesting behavior appears at $x=2.00$ in. From Figure 3.1.1-92 regions of large, positive $U'V'$ in most of the right half plane and in the lower left corner can be seen, while between these two peaks a region of large, negative $U'V'$ can be found. Regarding the xy and yz plane vector plots, the largest gradients of U and V can be seen to occur at these locations. At $x=2.50$ in. the behavior of $U'V'$ is very asymmetric, showing a strong positive peak towards the $z=9.00$ in. boundary. The rest of the $U'V'$ contour shows small local peaking but, in general, a flat profile.

The effect of the cross jets on the turbulent shear can be clearly seen at the $x=3.00$ in. location. The central portion of the cell cross section can be seen to display large negative values of $U'V'$, while the lower y region shows a trend towards near zero values. The line plot in Figure 3.1.1-94 shows a general leveling off near the y boundaries at the $y=7.20$ in. location, with large slopes occurring near the center of the duct. These slopes, and their changes in sign, indicate the strong effect of the cross jet stagnation point on the local flowfield. The magnitude of the turbulence stress can be seen to decrease near the cell walls and boundaries, where the influence of the cross jets is much reduced.

The $U'V'$ contour at $x=3.50$ in. shows two very sharp, positive peaks near the center of the cell cross section, the two sharp positive peaks being separated by a region of much reduced turbulence stress. At the $x=3.00$ in. plane, the positive peak was found in the lower y range, with the much larger negative peak occurring near the center of the duct. For the $x=3.50$ in. case, the positive peaks are found near the middle of the duct with the negative peaks occupying the lower y range. Again the values are seen to trail off near the cell walls and boundaries.

The behavior of the turbulence stress contours at the $x=4.00$ in. and $x=4.50$ in. planes is much the same. The twin positive peaks occurring at $x=3.50$ in. are no longer evident as one large peak of nearly the same magnitude has developed at $x=4.00$ in. The location of this peak has translated to the $y=1.80$ in. location, while the negative peak, of much reduced magnitude, remains at the same vertical location. The $x=4.50$ in. location shows a much dissipated peak near $y=2.00$ in., with the negative peak remaining at the same location and strength as at $x=4.00$ in. As with the other cases, the turbulence stress drops off near the walls and boundaries.

Dissipation and mixing have a large effect on the downstream flowfield, as the $x=6.00$ in. station shows a general spread of the peaks resulting in a flatter U'V' profile. The negative peak is no longer evident and, as before, the turbulence stress goes to zero at the walls and boundaries. By $x=9.00$ in., the turbulence stress can be seen to be almost completely dissipated.

3.1.2 Five-Swirler Water Rig

The experimental apparatus is shown in Figures 3.1.2-1, 3.1.2-2, and 3.1.2-3. The test section for this test is a model of a gas turbine annular combustor. The effects of curvature have been assumed to be negligible and the annular flow channel was modeled as a rectangular channel (3 in. x 15 in.) constructed of clear plexiglass. At the top of the channel are five annular jets which would provide the fuel/secondary air mixture in the real combustor. Located 1 channel width, 3 in., downstream of the annular jets are a pair of opposing round jets for each annular jet, aligned with the annular jet. These round jets would provide the primary air in the actual combustor. The primary jets had dimensions with a diameter equaling 0.43 in. and a length/diameter equal to 25. The annular jet had an inner diameter of 1.084 in. and an outer diameter of 1.459 in. The annular jets were located 3 in. apart, center to center. The model consists of five annular jet/primary jet cells to reduce endwall effects. All measurements were made in the center cell.

The total water flow rate for all jets was determined from the venturi downstream of the test section. The primary jets' flow rate was determined from the pressure drop in the supply lines to each bank of jets. The Venturi and each jet supply line were connected to manometers for flowrate determination. Figures 3.1.2-4 and 3.1.2-5 present the calibration curves for each flow measurement. The calibration data points are shown along with the equations which were used to determine the flow rates from the manometer readings. The total flow Venturi output was determined from the difference between the manometer readings at the Venturi's large and small diameters. The primary jet flow pressure drops were referenced to the constant head tank level. Readings were taken from the scale mounted next to the manometer tubes with divisions that were used as units.

The concentration field in the model combustor was first measured with the annular jet flow turned off. This configuration demonstrated the interactions between two opposing impinging round turbulent jets. The total flow rate was 1.7 lb/sec, giving a Reynolds number based on jet diameter of 8000 for each jet. The flow control valves were adjusted to position the interface between the jets at approximately the center of the channel. Figure 3.1.2-6 presents the coordinate system used for defining locations within the test section. Measurements were made with the laser sheet at z locations of 6.0, 6.5, 7.0, and 7.5 in. These locations span the area from the center jets axes to the midway point between adjacent jet pairs. Symmetry was assumed and measurements were made on only one side of the jet axes.

The annular jets were turned on for the second configuration. This allowed visualization of the mixing between the primary jets and the annular jet. The total annular jet flow (five jets) was 1.57 lb/sec and the primary jet flow was 1.10 lb/sec, giving Reynolds numbers based on a hydraulic diameter of 2500 and 5200 for each annular jet and primary jet, respectively. A higher annular jet Reynolds number could not be attained without washing the primary jet flows downstream and eliminating the interaction between the three jets. The ratio of total primary jet momentum to annular jet momentum was 1.26. The primary jet flow rate to annular jet flow rate ratio was 0.7. Concentration measurements were made with the dye being injected first through one primary jet and then through the annular jet. As with the no annular jet flow case, the laser sheet was positioned at z locations of 6.0, 6.5, 7.0, and 7.5 in. for concentration measurements.

3.1.2.1 Primary Jets Only

The results from the measurements made with no annular jet flow are presented in Figures 3.1.2-7 through 3.1.2-20. At each z location, the data were reduced along lines of constant y , for y values of 0.5, 1.0, 1.5, and 2.0 in. This provided radial distributions across the jet entering at $y = 0.0$ in. In addition to

these radial profiles, data were reduced along a line of constant x , at $x = 3.0$ in., corresponding to the jets axes and lines parallel to the axes.

Mean and rms concentration profiles were calculated along each of the lines mentioned above. The mean concentration values are presented as a ratio to the maximum mean value on the jet centerline, $C_{cl,max}$. The rms quantities are divided by the local mean value to provide a fluctuation intensity quantity, c'/C .

Figures 3.1.2-7 through 3.1.2-10 are visualization images of the primary jet concentration field. Figures 3.1.2-7 and 3.1.2-8 are a single frame and a 127 frame average, respectively, with both figures being taken through the jet axis. The single frame image is much different from the average image, indicating the highly turbulent nature of this flow field. The spread of the jet at the impingement point is barely observable in the average image because it switches from top to bottom and in the average is greatly reduced. Figures 3.1.2-9 and 3.1.2-10 are 0.5 in. from the jet axis. The spread from the jet impingement can be clearly seen in the single frame image (Figure 3.1.2-9). Due to the very turbulent nature of this interface, the mean image (Figure 3.1.2-10) shows that the concentration is spread over a relatively large area.

Figures 3.1.2-11 through 3.1.2-15 present the mean concentration profiles at the four z locations of the laser sheet. In each figure the profiles are presented as line plots and as a 3-D graph. Also included on each figure is a diagram indicating where the profiles are located in the test section. The concentration profiles in Figure 3.1.2-11 are calculated across the jet axis and are similar to those expected for a single jet at $y = 0.5$ and 1.0 in. At higher values of y , the decrease at the location of the jet axis ($x = 3.0$ in.) is caused by the opposing jet which does not contain dye. With decreasing z , the profiles flatten as the dye mixes out toward a constant value. Figure 3.1.2-15 shows the axial mean profile along the jet axis and lines parallel to the axis. The jet spreads in the xz plane when it impacts the opposing jet. The presence of this spread can be seen in the $z = 7.0$ in. profile. The mean appears to increase initially from the exit value. This effect was also observed by Borleteau (1983) and Long, Chu, and Chang (Tennekes and Lumley, 1973). This is probably due to the camera response which is expected to be attenuated at the image edge. Long, Chu, and Chang noticed that even after correction of original digital images, the response of the camera was still attenuated at the edges. The laser sheet reflected off of the plexiglass walls, resulting in a higher laser intensity near the wall. This introduced a nonlinearity near the walls which caused the signal to be attenuated. The combination of the camera response and the reflection from the plexiglass walls results in the signal attenuation near the walls.

Figures 3.1.2-16 through 3.1.2-20 present the fluctuation intensity profiles for the case with no annular jet flow. Figure 3.1.2-16 is taken through the jet axis and shows a profile similar to that expected for a single jet at $y = 0.5$ and 1.0 in. The interface between the two jets is apparently between $y = 1.0$ and 1.5 in. The large peak which would occur at the interface is not observable. The mixing region can be seen at $y = 1.5$ in. for the decreasing values of z . Figure 3.1.2-16 is measured along the jet axis and lines parallel to the axis. The peak, at $y = 1.25$ in. for the $z = 7.5$ in. profile, indicates that the jet/jet interface is in fact between $y = 1.0$ and 1.5 in. The increase for higher values of y is due to the near zero mean value which is the denominator of the plotted quantity.

3.1.2.2 Annular and Primary Jets

The results for the configuration with annular jet flow and primary jet flow are presented in Figures 3.1.2-21 through 3.1.2-51. For the test with dye injection through a primary jet, data reductions were performed along radial and axial lines as described for the no annular jet flow case. The test with dye in the annular jet flow was analyzed by reducing data along lines of constant x , for x values of 1.0 , 2.0 , 3.0 , and 4.0 in. This provided radial distributions across the annular jet. An axial profile was also calculated along the annular jet's axis ($y = 1.5$ in.) and lines parallel to the axis. Mean values were normalized by the maximum annular jet centerline mean value, $C_{cl,max}$.

Figures 3.1.2-21 through 3.1.2-35 present the results from the test with the dye being injected into a primary jet. Figures 3.1.2-21 through 3.1.2-24 are visualization images of the primary jet concentration field. As with the previous case, the average images are greatly different from the single images indicating a highly unsteady flowfield. The effect of the annular jet is clearly evident in these images. The primary jet flow is driven downstream by the annular jet. The figures at $z = 7.0$ in. show much less primary jet flow at this location than in the case without annular jet flow. This indicates that the primary jet is more thoroughly mixed at $z = 7.0$ in., due to the annular jet flow.

Figures 3.1.2-25 through 3.1.2-29 present the mean concentration profiles. Figure 3.1.2-25 shows the profiles through the jet axis. These are similar to the case without annular jet flow, except that above the primary jets the mean value is nearly zero due to the annular jet flow. The mean values drop off with decreasing z as before. This case results in a faster decrease due to the mixing with the annular jet. Figure 3.1.2-29 shows profiles along the jet axis and lines parallel to the axis. The value at the edge is attenuated as discussed previously.

Figures 3.1.2-30 through 3.1.2-35 present the fluctuation intensity profiles. Figure 3.1.2-30 shows profiles similar to the expected curves for a single jet at $y = 0.5$ and 1.0 in. The peak on the lower x side of the jet is higher due to the increased mixing with the annular jet. This can be still be seen at $z = 7.0$ in. (Figure 3.1.2-31). At $z = 6.5$ in., the fluctuation intensity profiles are nearly zero, indicating that the mixing is nearly zero. Figures 3.1.2-34 and 3.1.2-35 are both fluctuation intensity profiles along the plane of the jet axis. Figure 3.1.2-34 only goes to $y = 1.7$ in. because the quantity c'/C was very high and erratic beyond that point, due to the nearly zero mean value. Figure 3.1.2-35 shows the rms normalized by $C_{cl,max}$ instead of C to give a better indication of the shape of the rms profile.

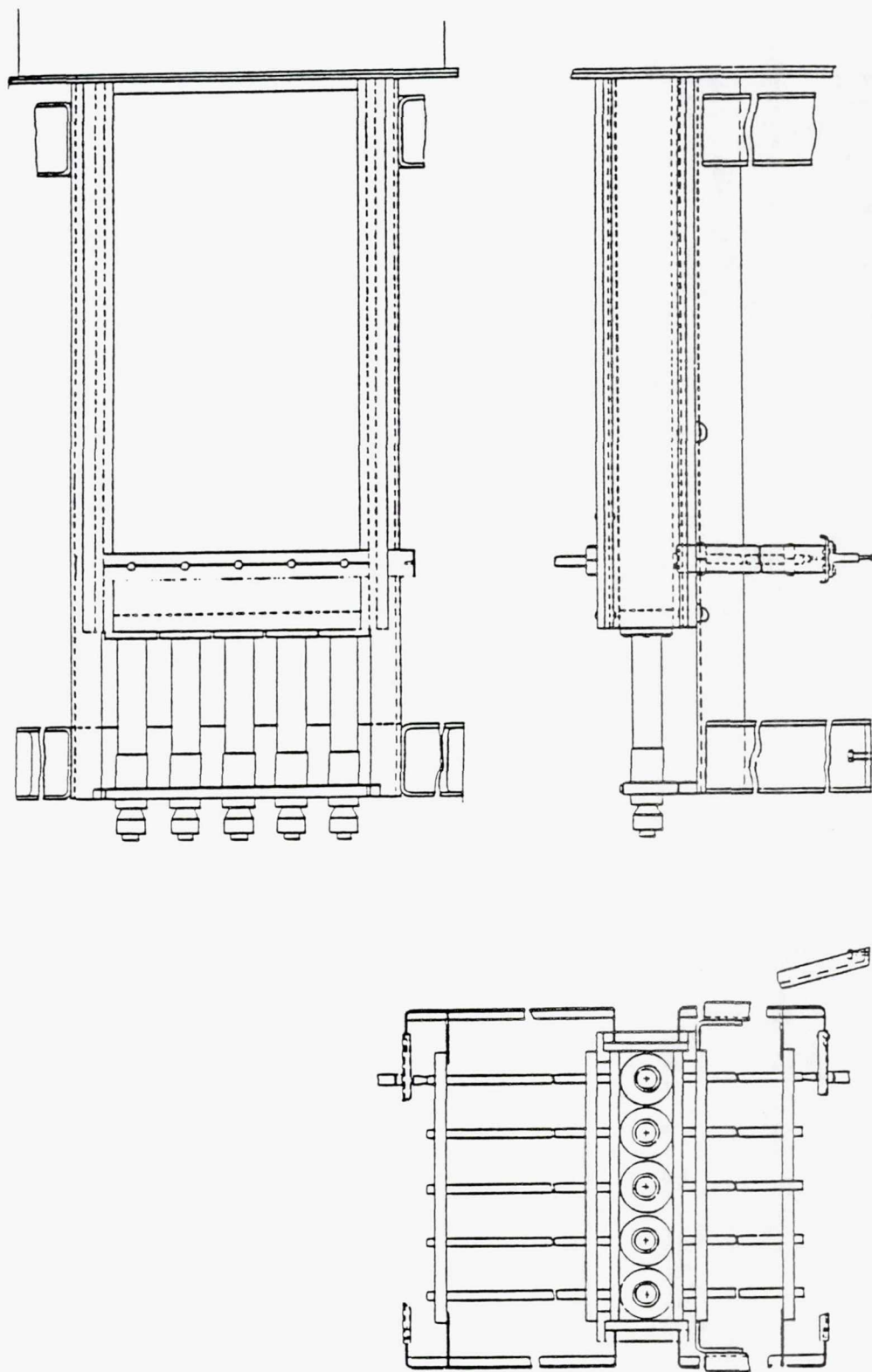
Figures 3.1.2-36 and 3.1.2-37 compare the primary jet concentration results from the test cases with, and without, annular jet flow. Figure 3.1.2-36 compares mean and fluctuation intensity profiles across the primary jet axis ($z = 7.5$ in.). The effect of the annular jet flow is seen in the mean as a decrease on the low x value side of the jet. The fluctuation intensity peak on this side of the jet is higher, with the annular jet flow, due to the increased mixing. Figure 3.1.2-37 presents mean and fluctuation intensity profiles along the primary jet axis and lines parallel to the axis. The mean profiles at $z = 7.5$ in. show that the annular jet flow does not have a very large effect at this location. That is because the annular jet momentum, although greater, is spread over a larger area than that of the primary jet. The fluctuation intensity peak at the intersection of the three jets is higher due to a more turbulent flow with the annular jet flow. At the lower z values, the profiles for the case with annular jet flow lower mean values and higher fluctuation intensity values. Both of these trends indicate more mixing with the annular jet flow, as expected.

The results for the case with dye in the annular jet flow are presented in Figures 3.1.2-38 through 3.1.2-51. Figures 3.1.2-38 through 3.1.2-41 are concentration field visualization images of the annular jet. The unsteady nature of this field can be deduced from the large differences between the single frame image and the average image. This flow does not appear as turbulent as the primary jet flow and indeed the Reynolds number is significantly lower for the annular jet flow. The images appear asymmetric with more dye on the right side of the flow. This is apparently due to an uneven flow distribution at the annular jet exit. This could be owing to the annular jet being nearly completely closed. If the jet control valve had been opened wider, the higher annular jet flow would have washed the primary jet flows downstream and eliminated any interaction between the jets in the field of observation.

The mean concentration profiles are presented in Figures 3.1.2-42 through 3.1.2-146. Figure 3.1.2-42 shows the mean profiles through the annular jet axis. The double peaked curve at $x = 1.0$ in. is slightly asymmetric, indicating the uneven flow distribution discussed above. The profile flattens and spreads downstream until, downstream of the primary jets at $x = 4.0$ in., the profile is essentially flat. At $z = 7.0$ in., there is only a single peak because the laser sheet intersects the annulus of the annular jet in just one area. This peak is off center due to the uneven flow distribution from the annular jet. Again, the

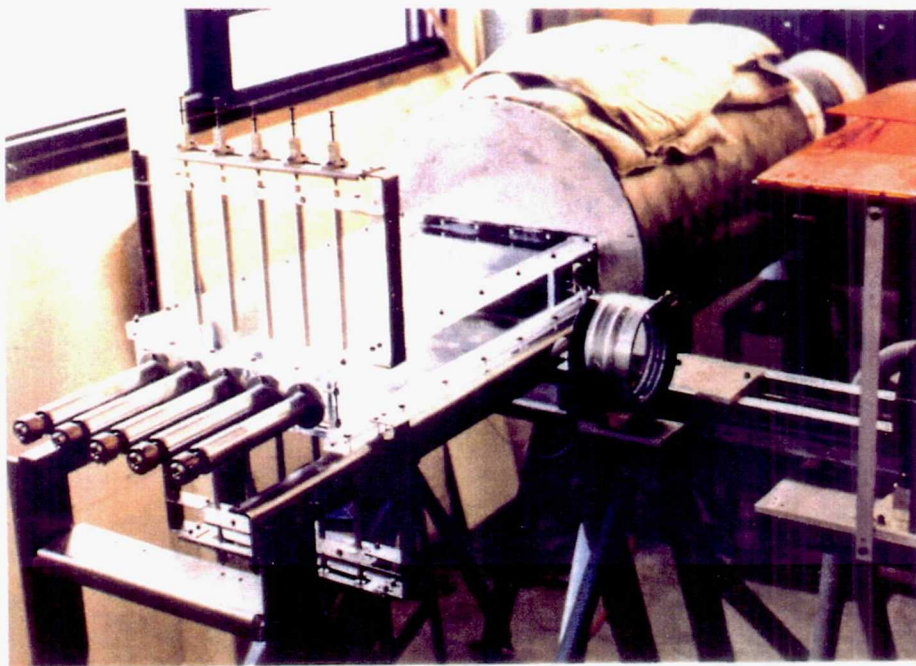
profile spreads and flattens downstream. At $z = 6.5$ in., the profile increases at $x = 3.0$ in. due to the primary jets carrying the annular jet flow across the channel to this location (Figure 3.1.2-44). The increase is not as significant at $z = 6.0$ in. due to the increased distance from the primary jet pair and the effect of the adjacent primary jet pair; this location is midway between two jet pairs. Figure 3.1.2-46 shows mean profiles along the annular jet axis and lines parallel to the axis. The effect of the primary jet pair can be seen in the profiles at $z = 7.0$ and 6.5 in. as an increased concentration level extending across the channel at $x = 3.0$ in.

Fluctuation intensity profiles are presented in Figures 3.1.2-47 through 3.1.2-51. Figure 3.1.2-47 presents measurements made with the laser sheet aligned with the annular jet axis. The edges of the jet can be seen as peaks. The overall level increases at $x = 3.0$ in., due to the mixing with the primary jets at this location. The level drops again at $x = 4.0$ in., downstream of the primary jets. The fluctuation intensity levels decrease with decreasing z as the concentration reaches a steady value and the mixing drops off. At $z = 6.0$ in., the curves are low in the middle and increase towards the sides due to the low mean value in these areas. Figure 3.1.2-51 presents fluctuation intensity profiles along the annular jet axis and lines parallel to the axis. The profiles at $z = 7.5$ in., the annular jet axis, have the expected shape, nearly zero until the primary jet location at $x = 3.0$ in. The peak at this location indicates the highly turbulent mixing occurred where all these jets interacted.



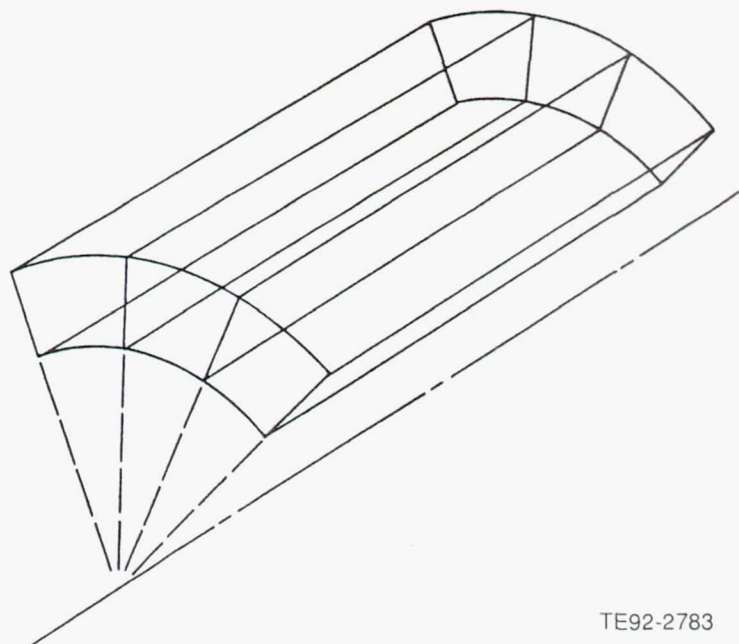
TE92-2254

Figure 3.1.1-1. Three-view drawing of annular combustion chamber model.



TE92-2255

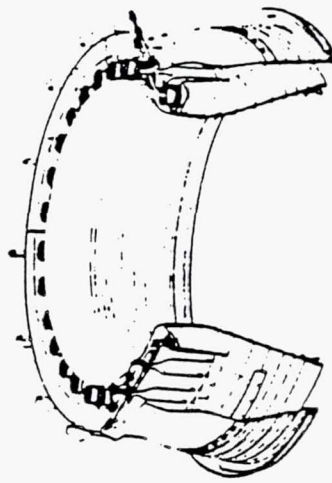
Figure 3.1.1-2. Photograph of annular combustor chamber model.



TE92-2783

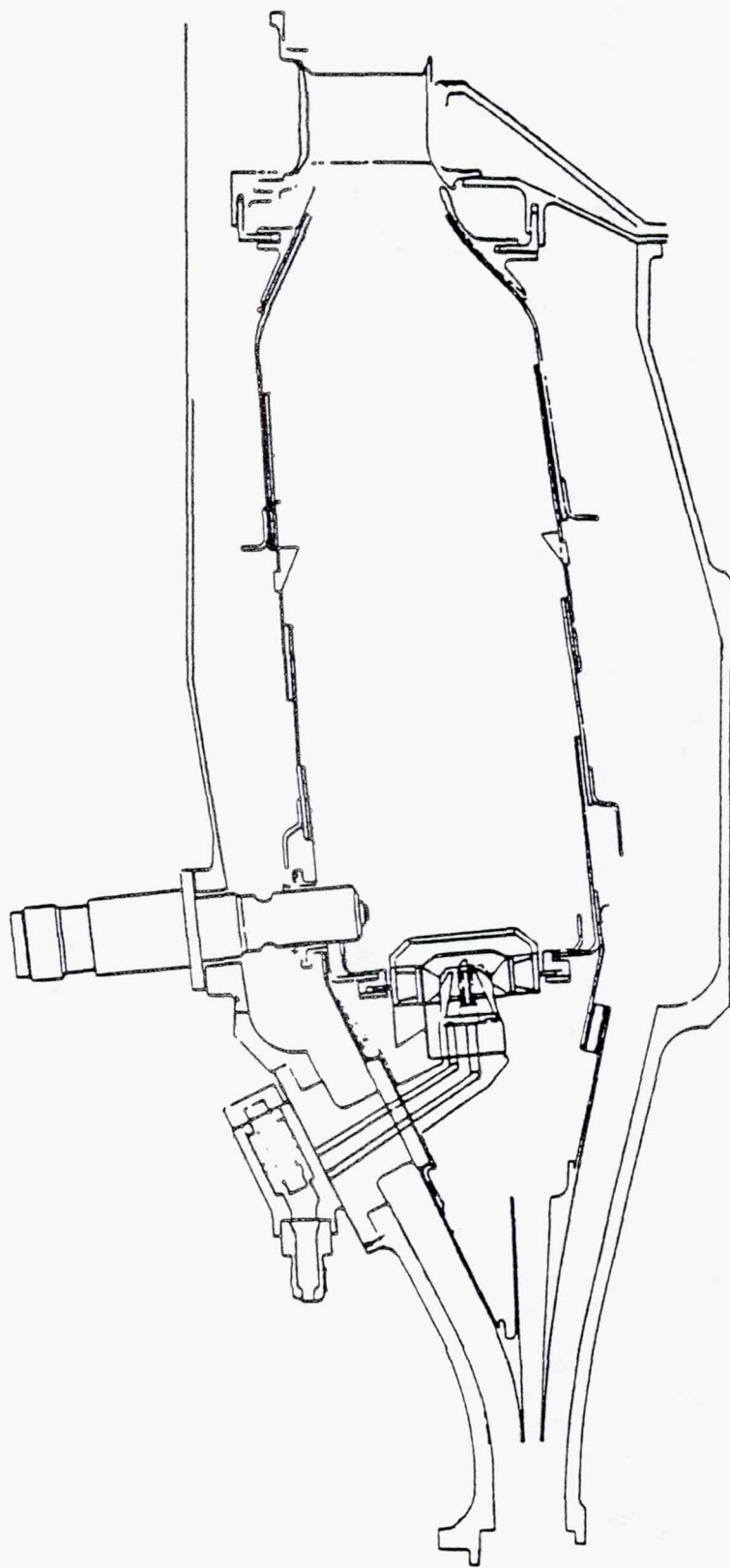
Figure 3.1.1-3. Arrangement of the swirler cells.

Page intentionally left blank



TE92-2256

Figure 3.1.1-4. Actual annular combustor.



TE92-2257

Figure 3.1.1-5. Allison Gas Turbine 570-K annular combustor.

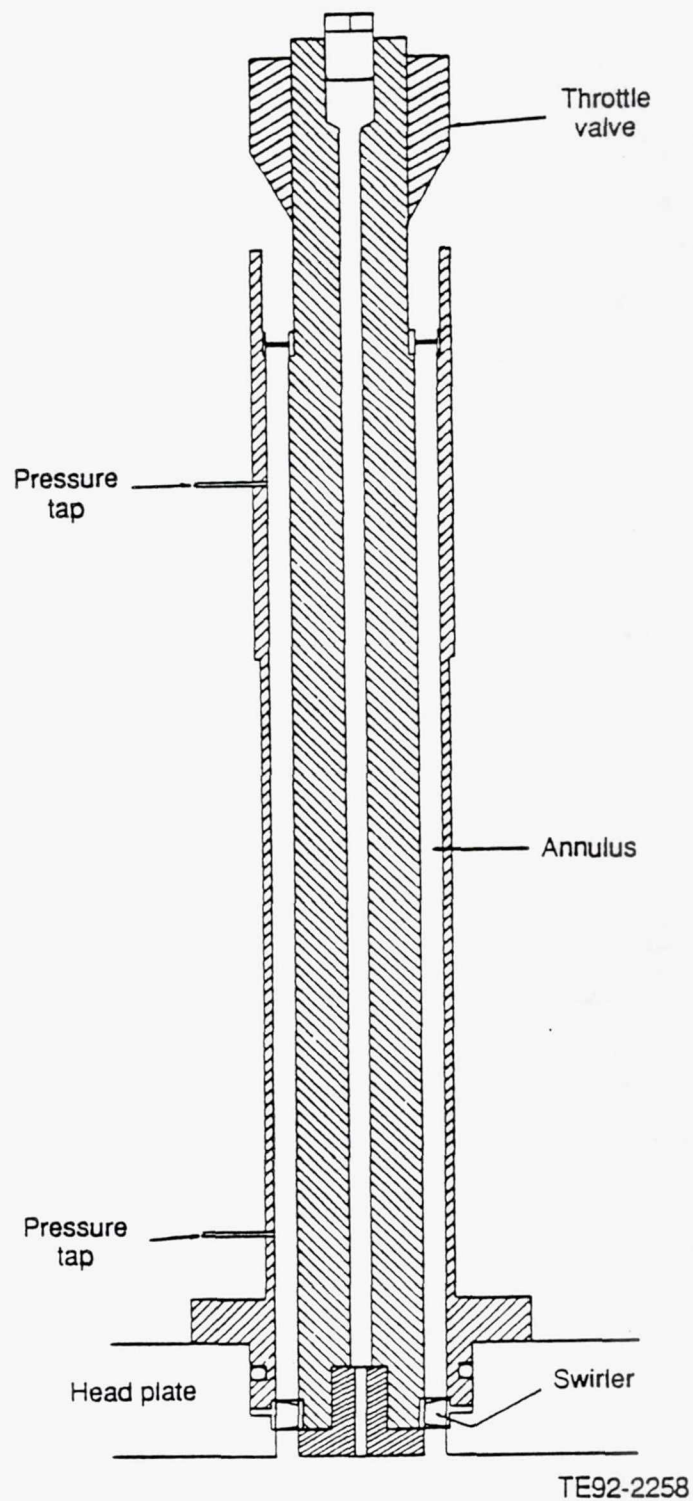


Figure 3.1.1-6. Annular jet and throttle valve.

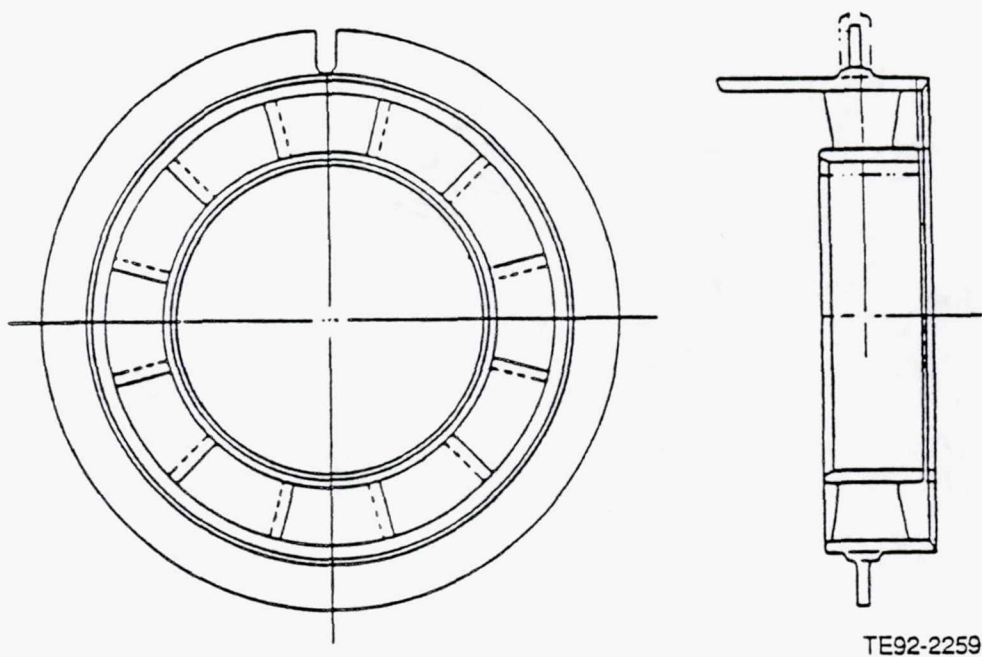


Figure 3.1.1-7. Vane swirler from model combustor.

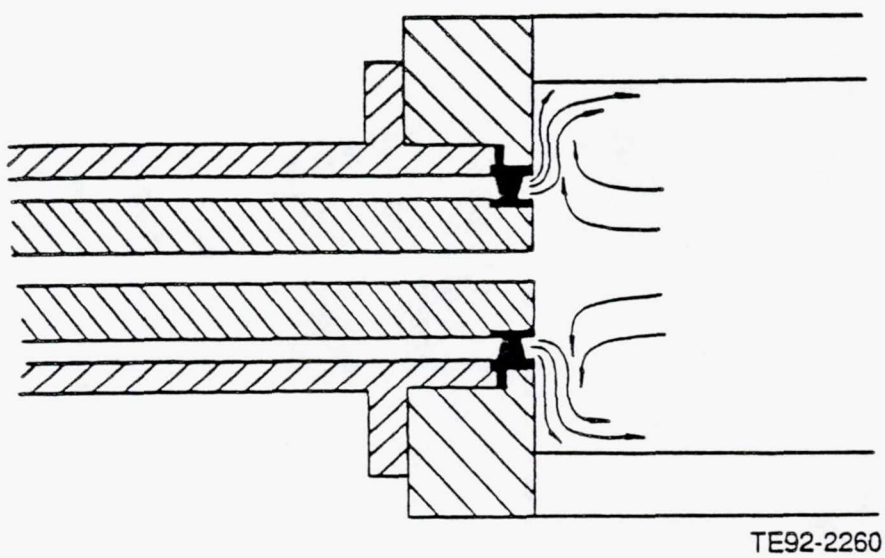


Figure 3.1.1-8. Original swirler orientation and flow pattern.

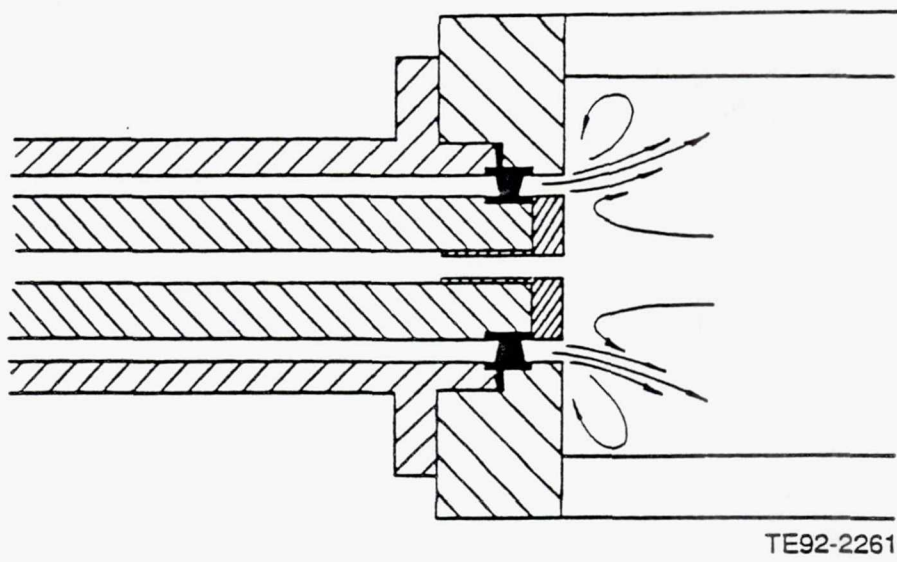


Figure 3.1.1-9. Modified swirler orientation and flow pattern.

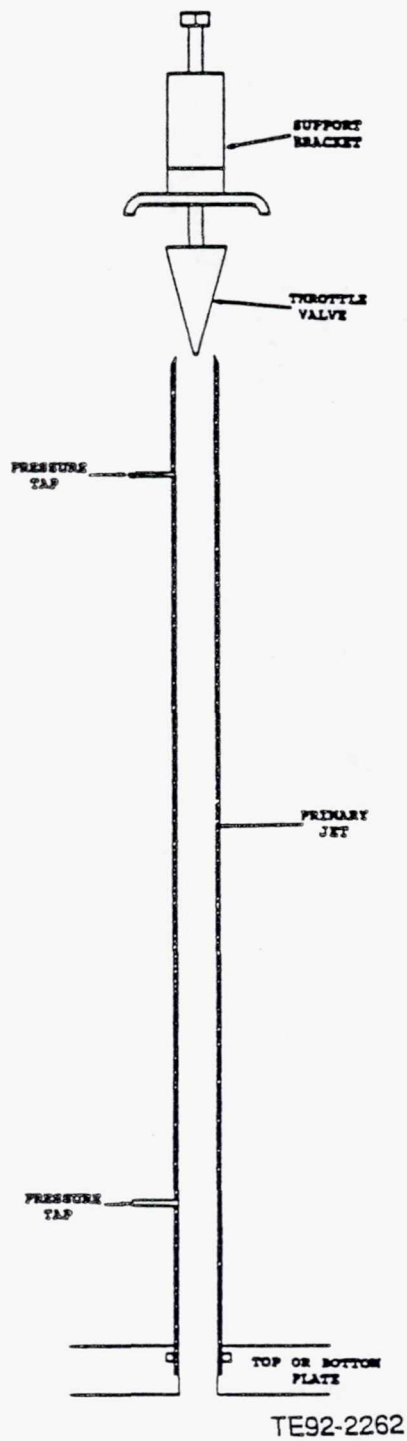
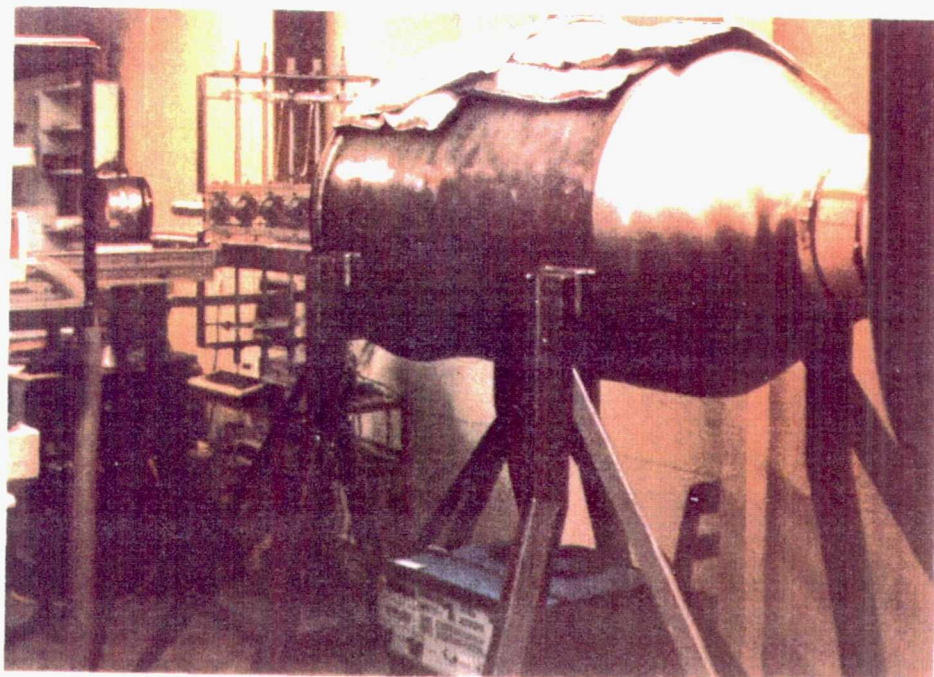


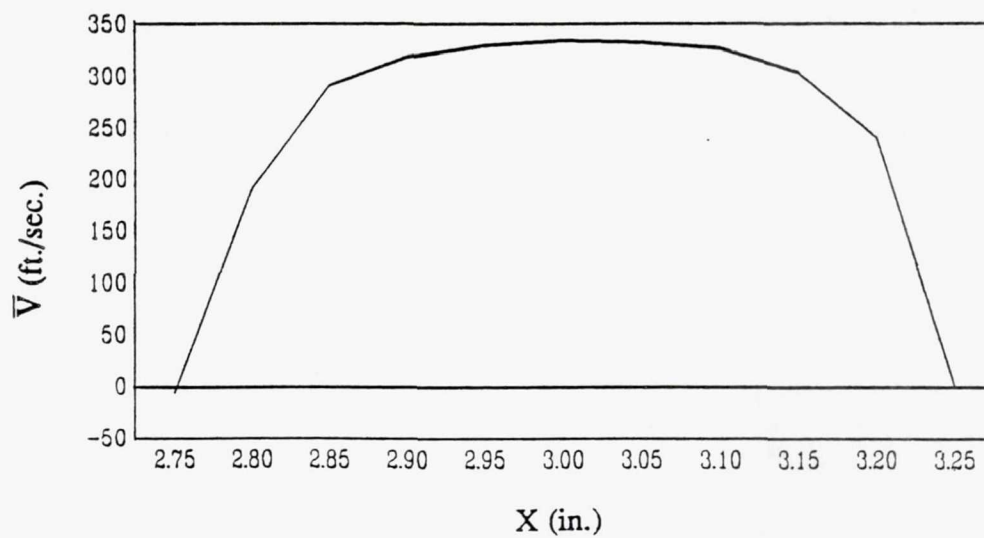
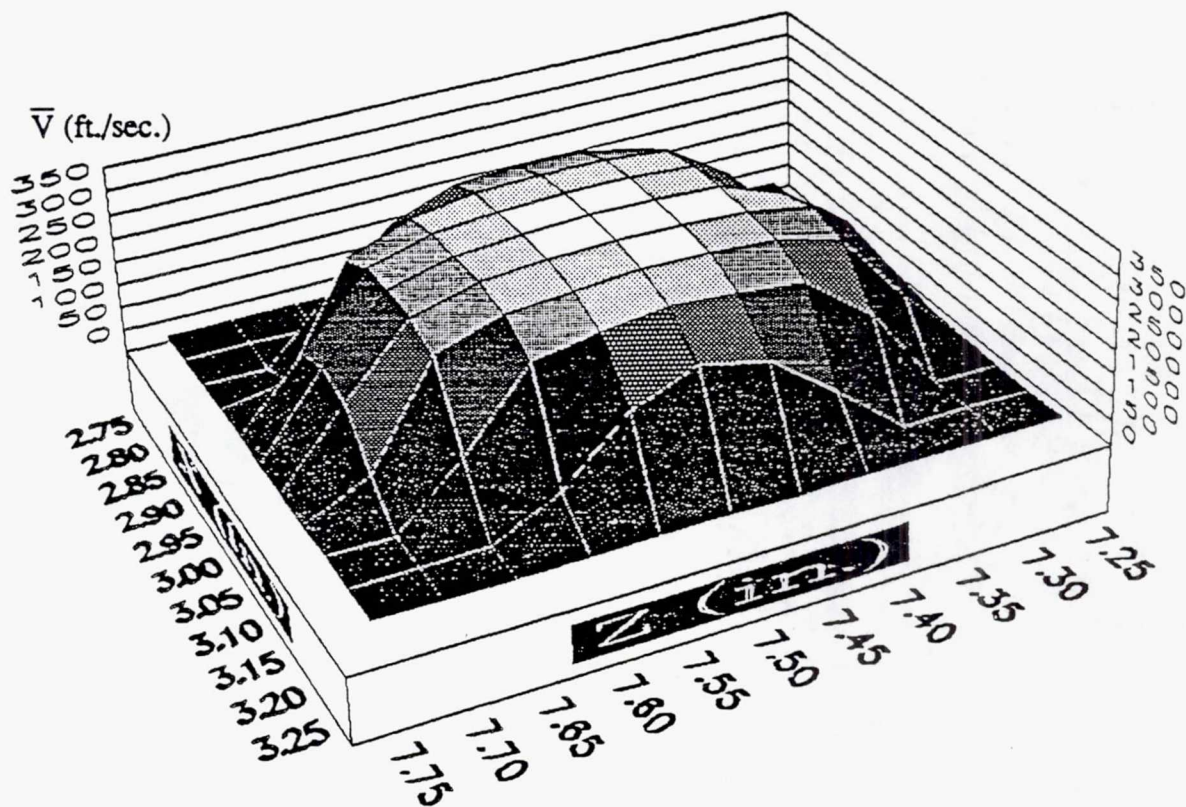
Figure 3.1.1-10. Primary cross jet and throttle valve.



TE92-2263

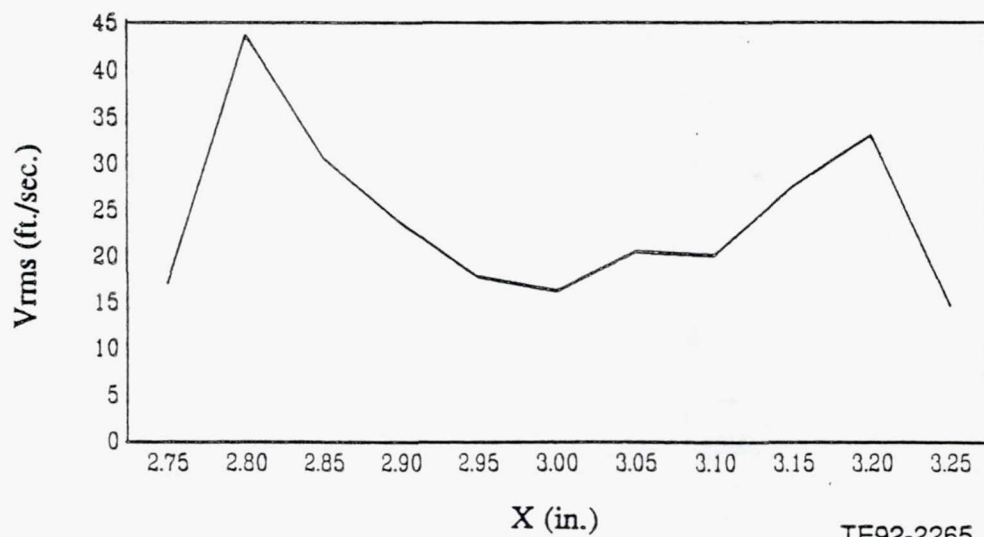
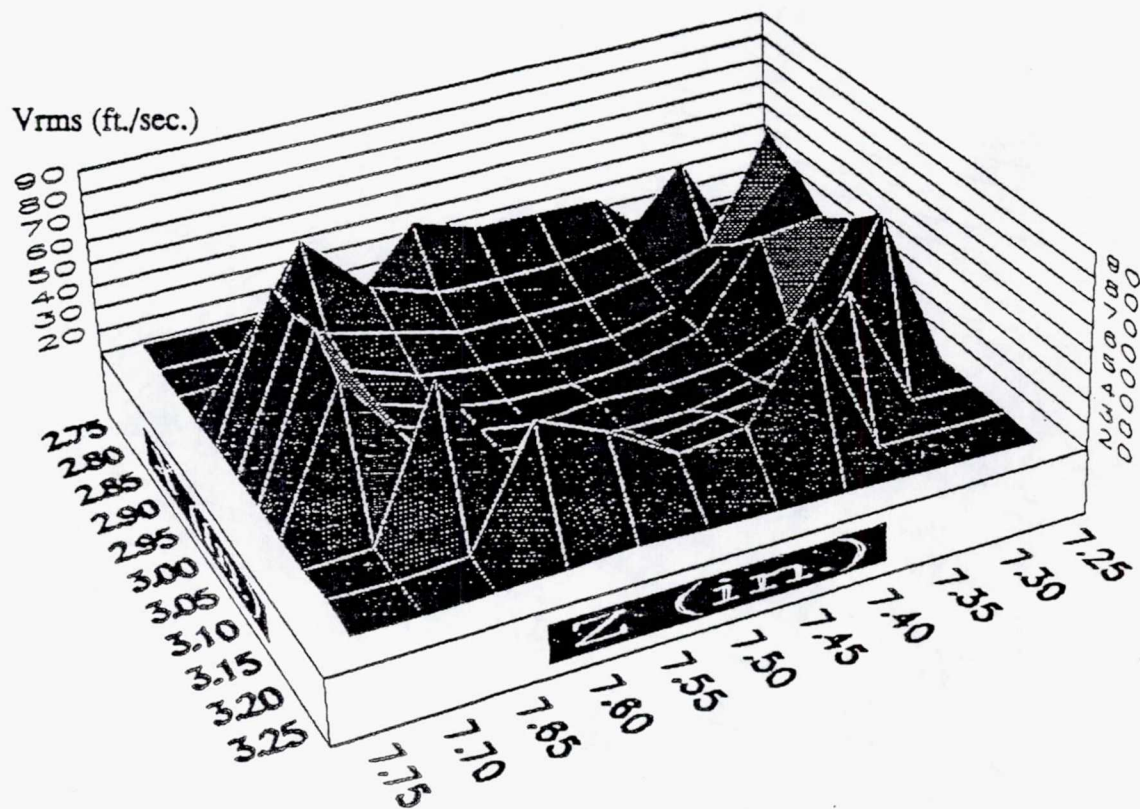
Figure 3.1.1-11. Plenum chamber and centrifugal fan.

Page intentionally left blank



TE92-2264

Figure 3.1.1-12. Contour and line plots of V for primary cross jet at $y=0.06$ in.



TE92-2265

Figure 3.1.1-13. Contour and line plots of V_{rms} for primary cross jet at $y=0.06$ in.

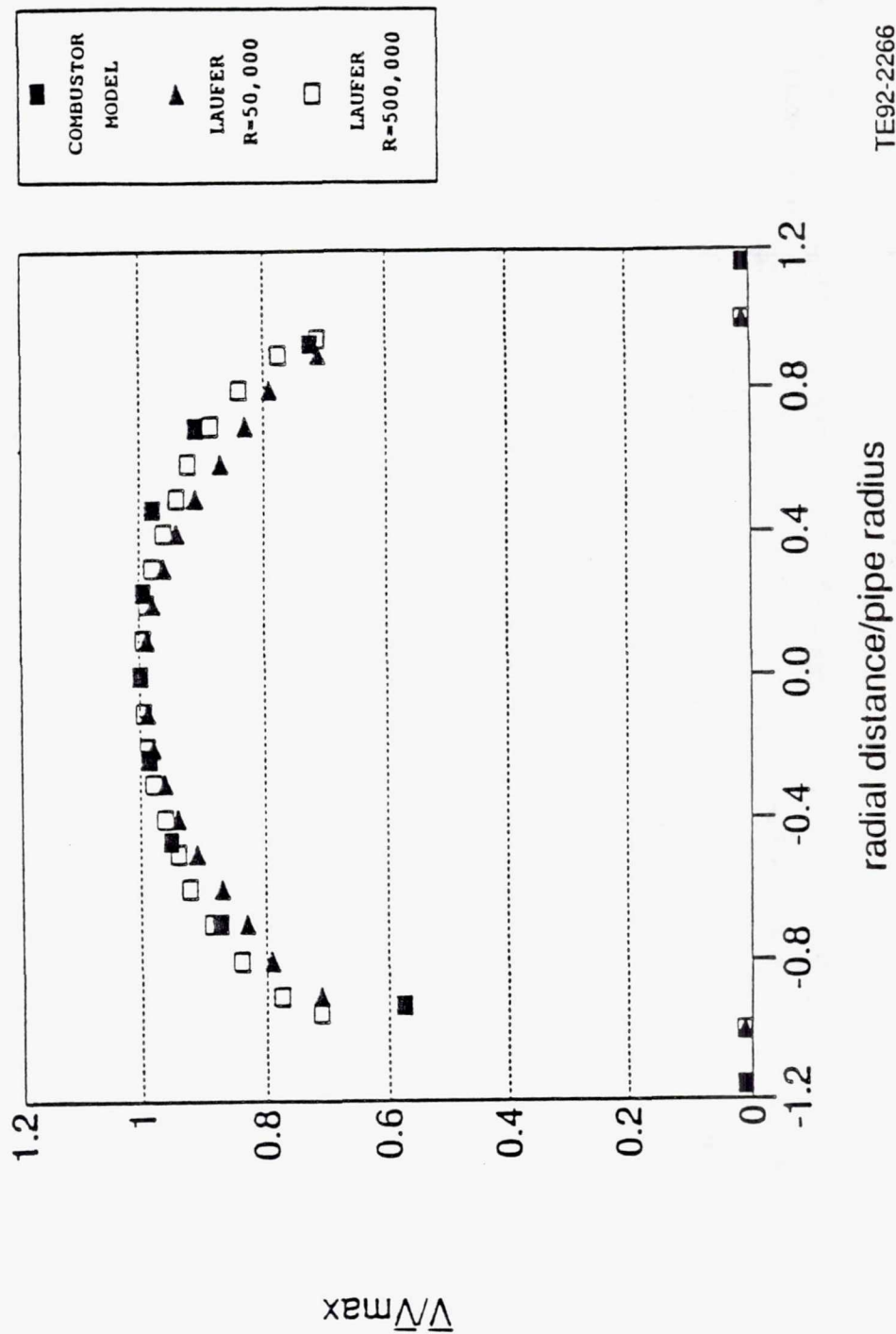
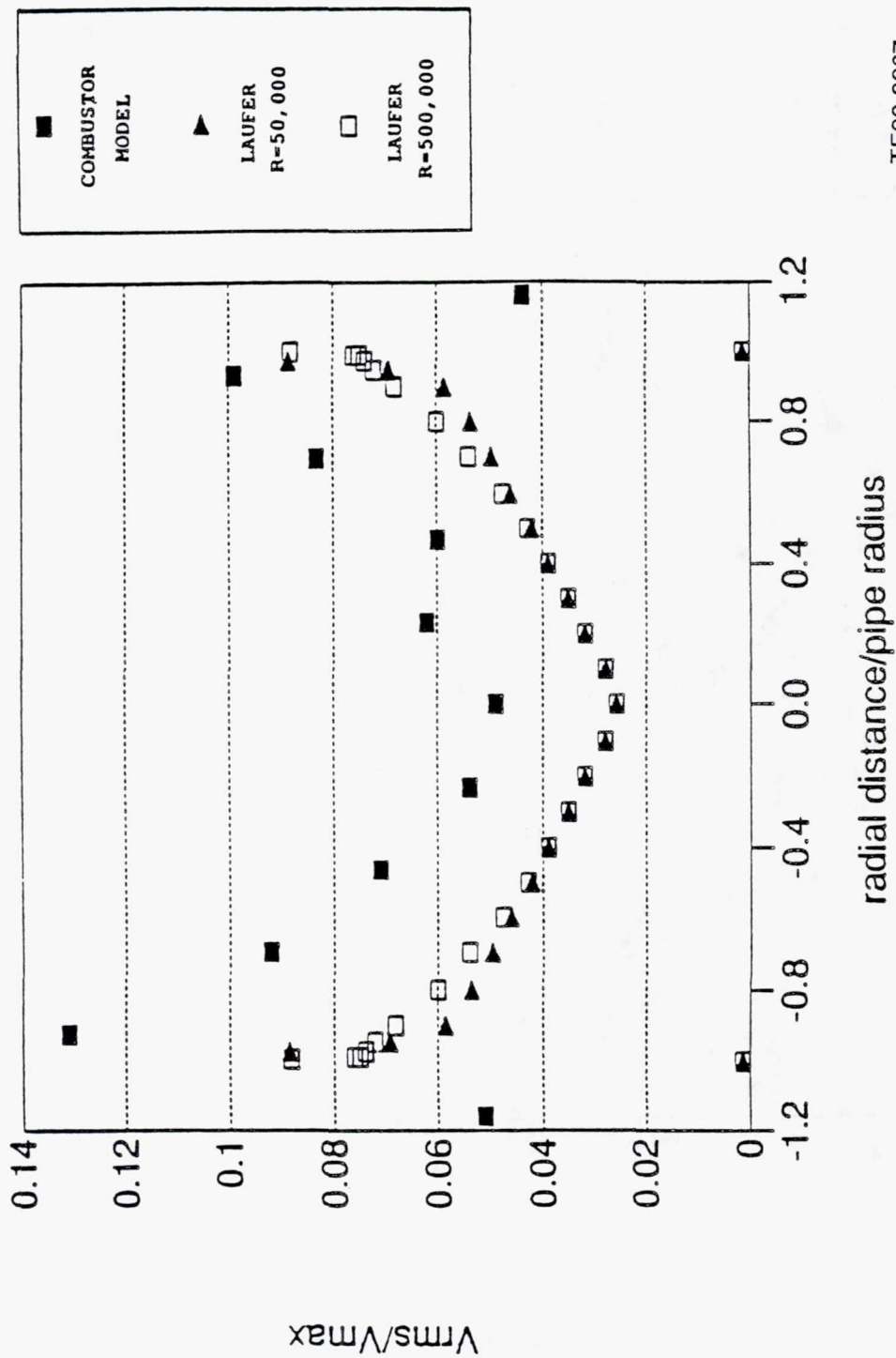
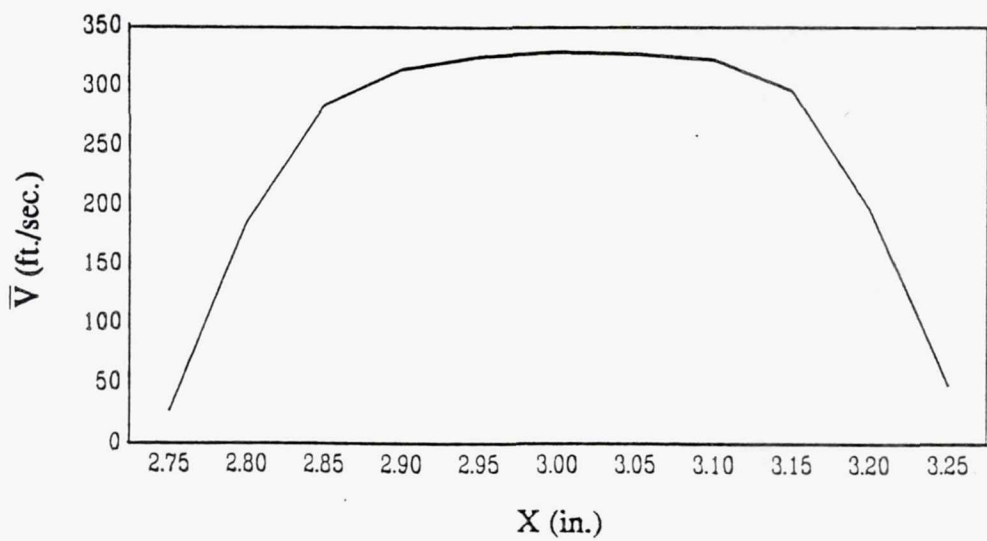
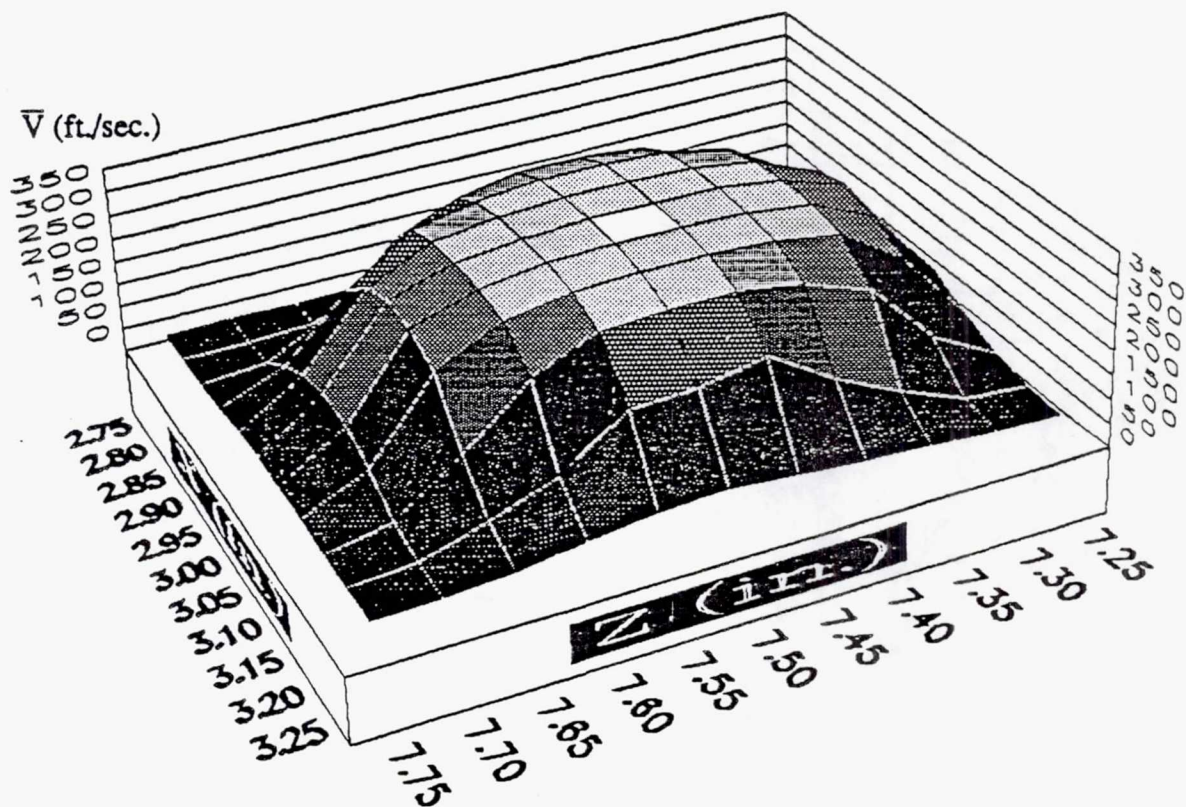


Figure 3.1.1-14. Comparison of V data at $y=0.06$ in. to classical pipe flow data of Laufer.



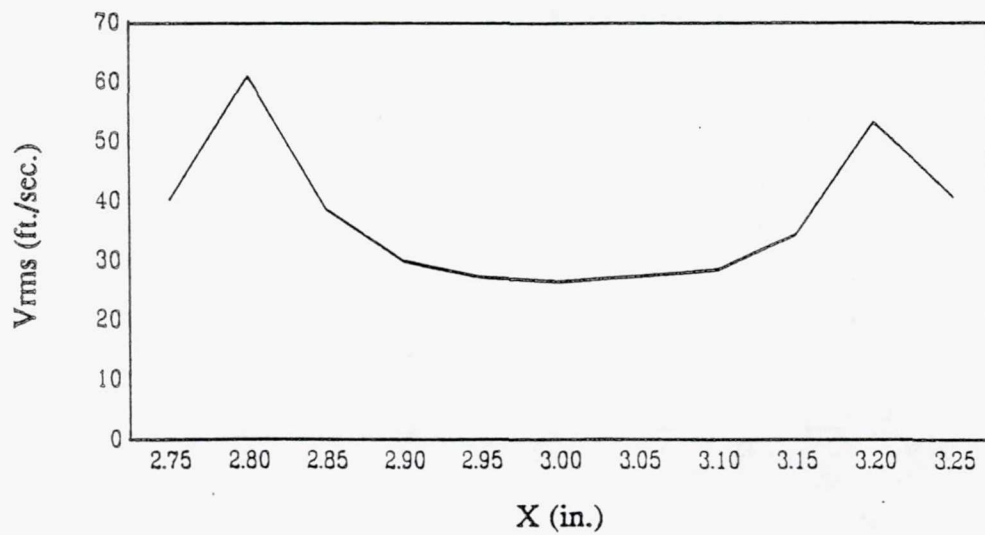
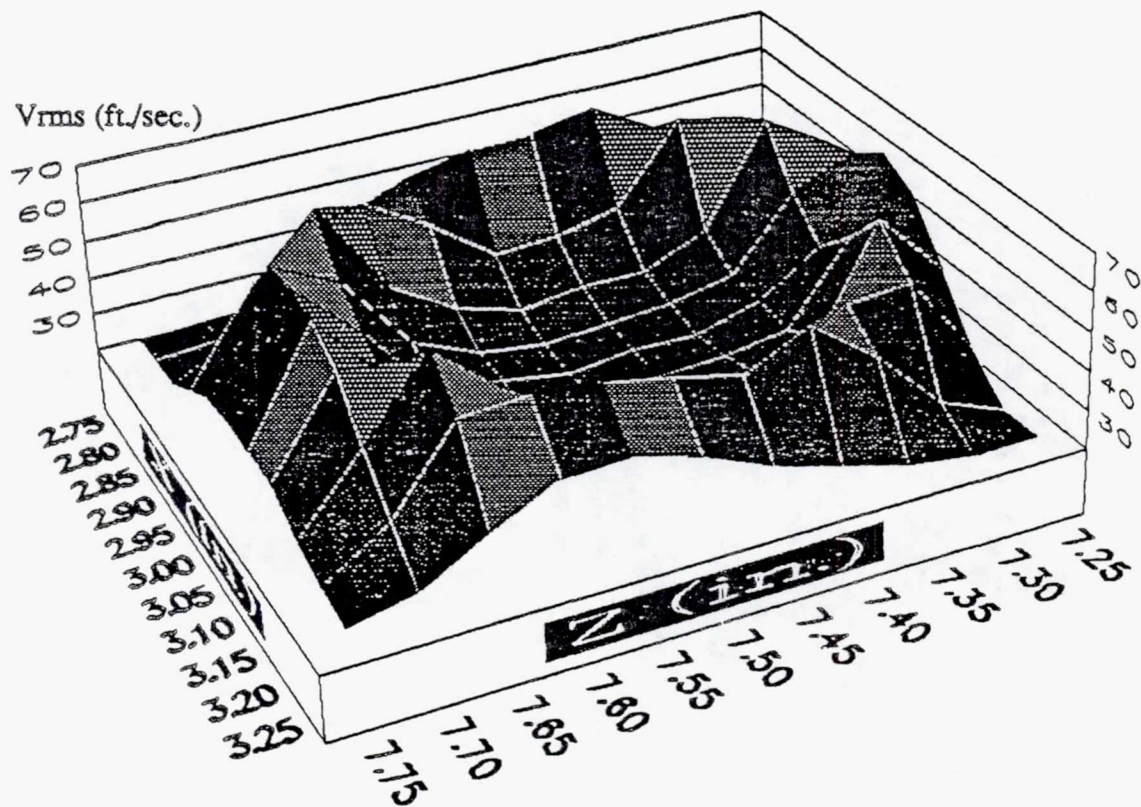
TE92-2267

Figure 3.1.1-15. Comparison of V_{rms} data at $y=0.06$ in. to classical pipe flow data of Laufer.



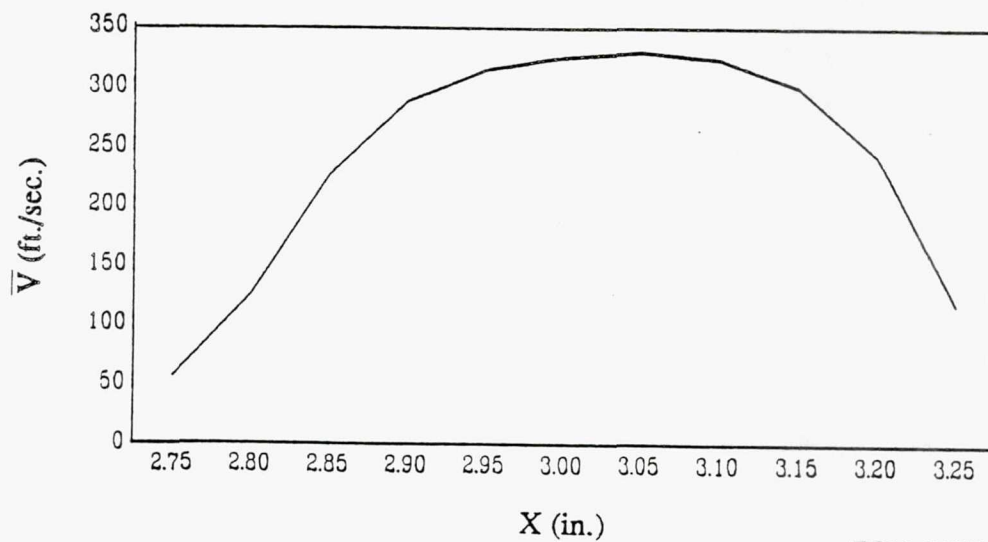
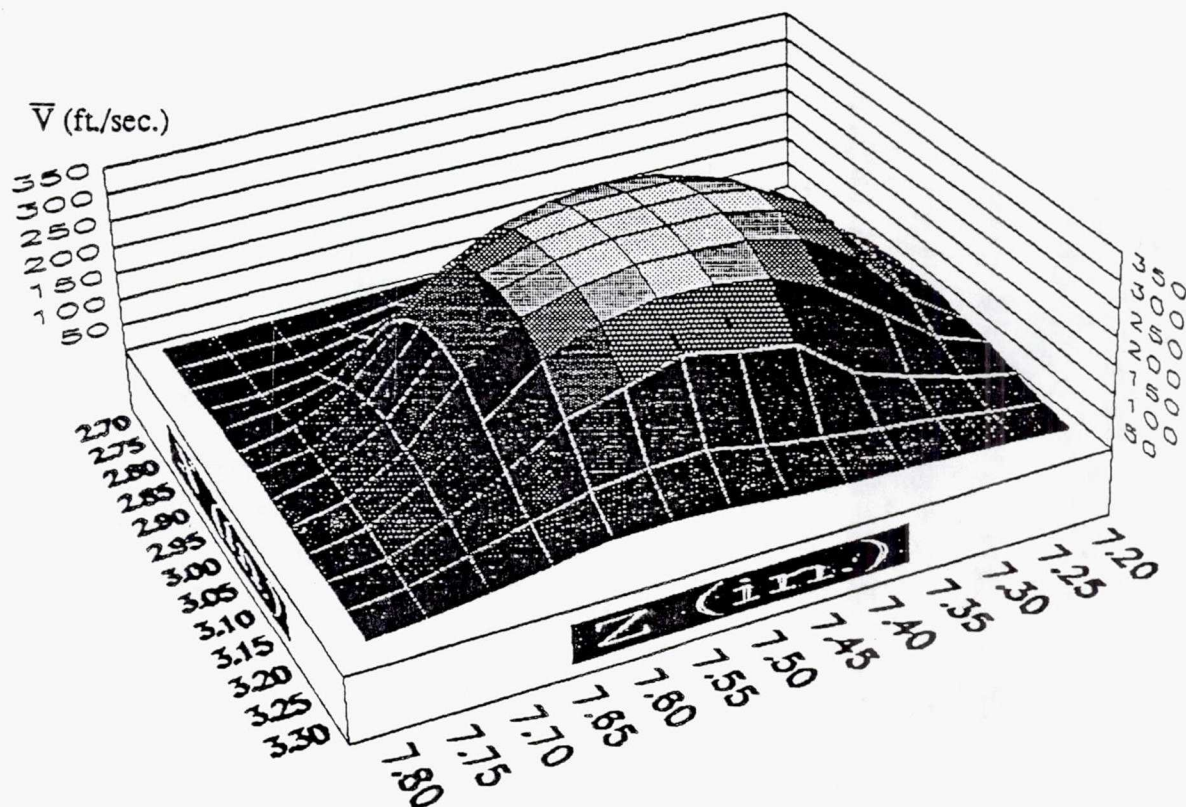
TE92-2268

Figure 3.1.1-16. Contour and line plots of V for primary cross jet at $y=0.25$ in.



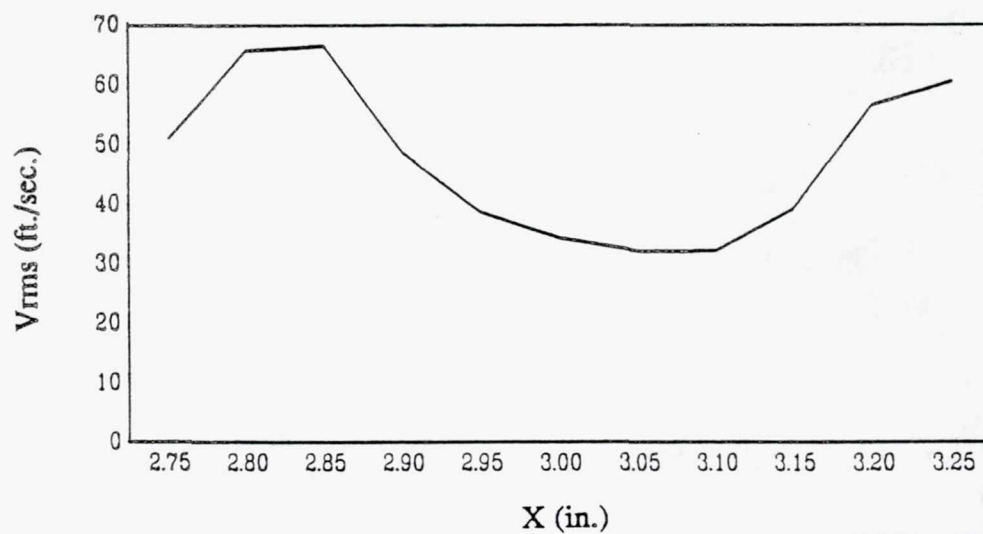
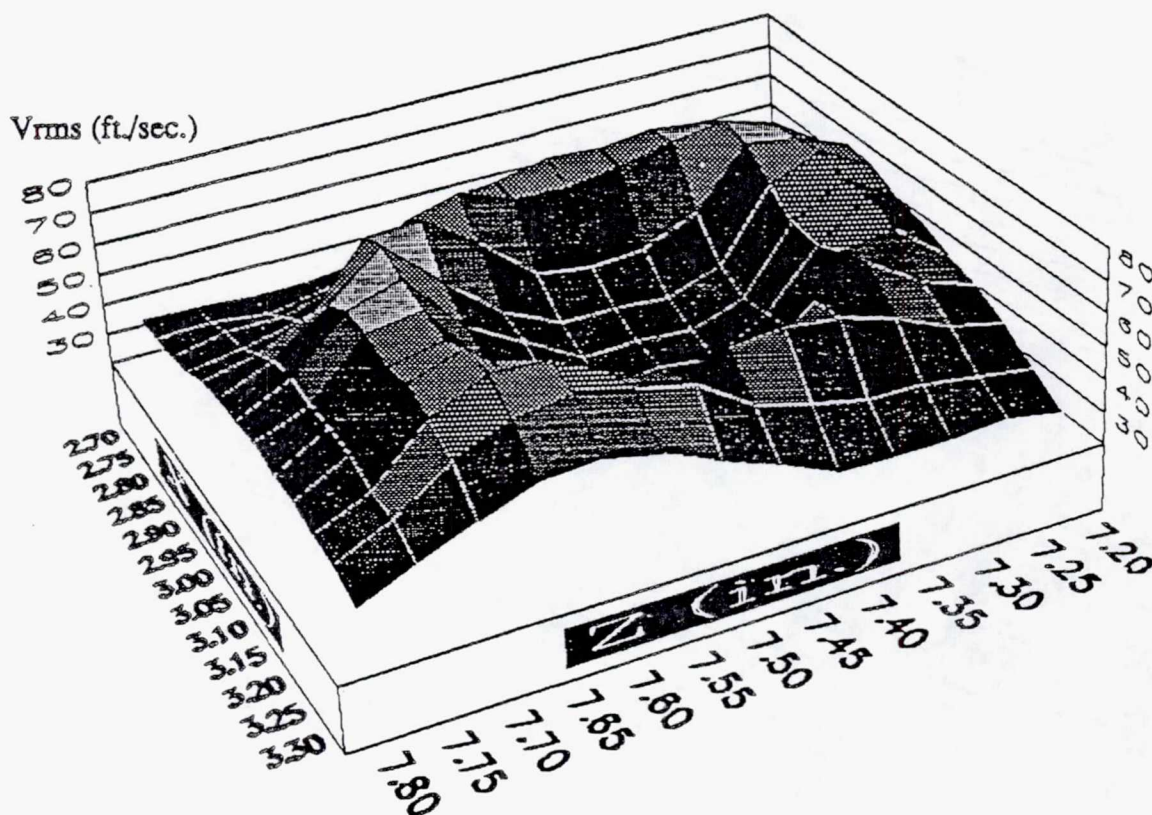
TE92-2269

Figure 3.1.1-17. Contour and line plots of V_{rms} for primary cross jet at $y=0.25$ in.



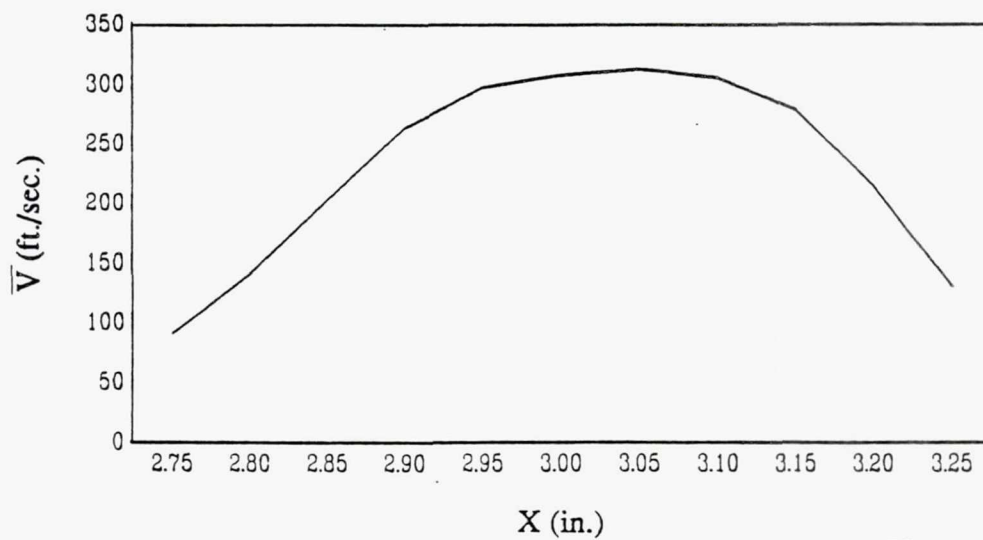
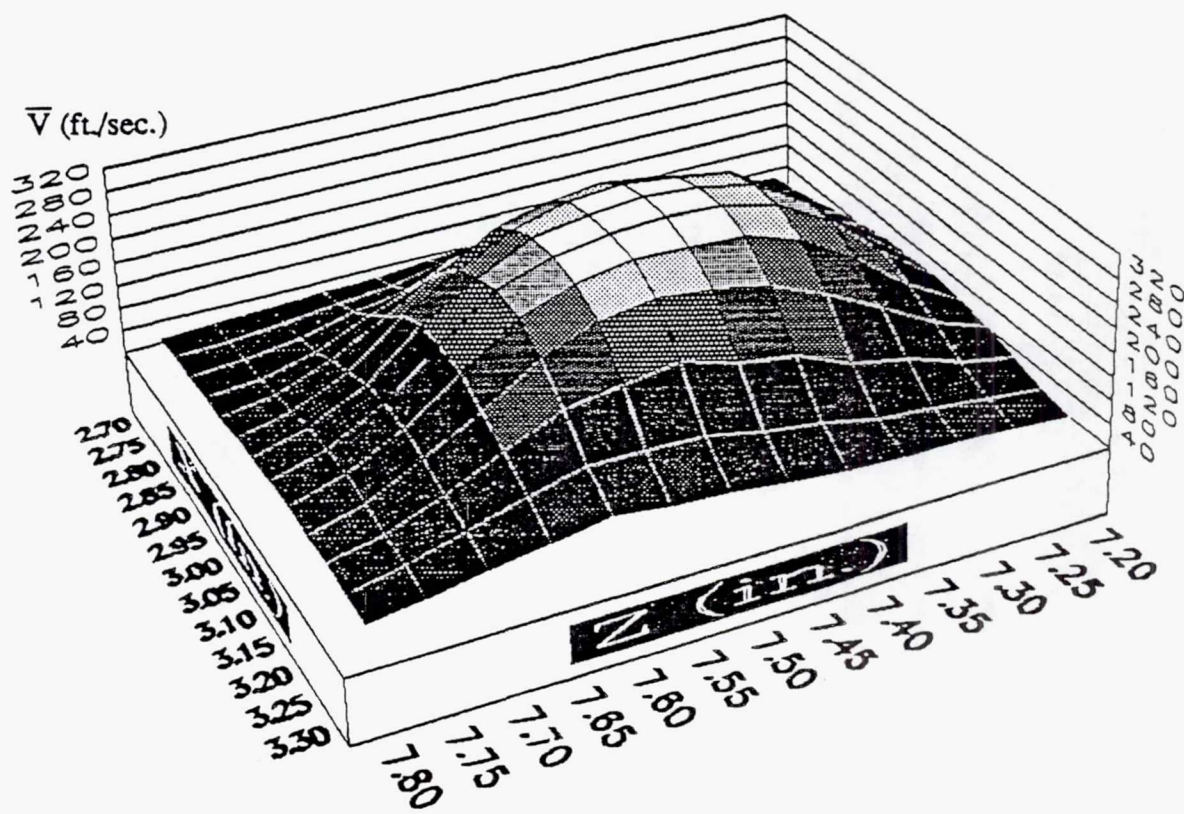
TE92-2270

Figure 3.1.1-18. Contour and line plots of V for primary cross jet at $y=0.50$ in.



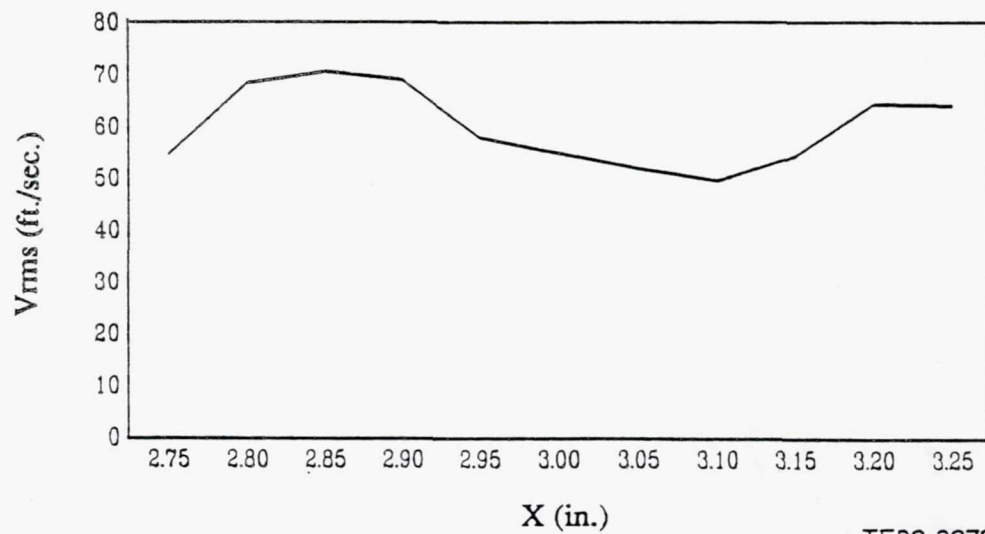
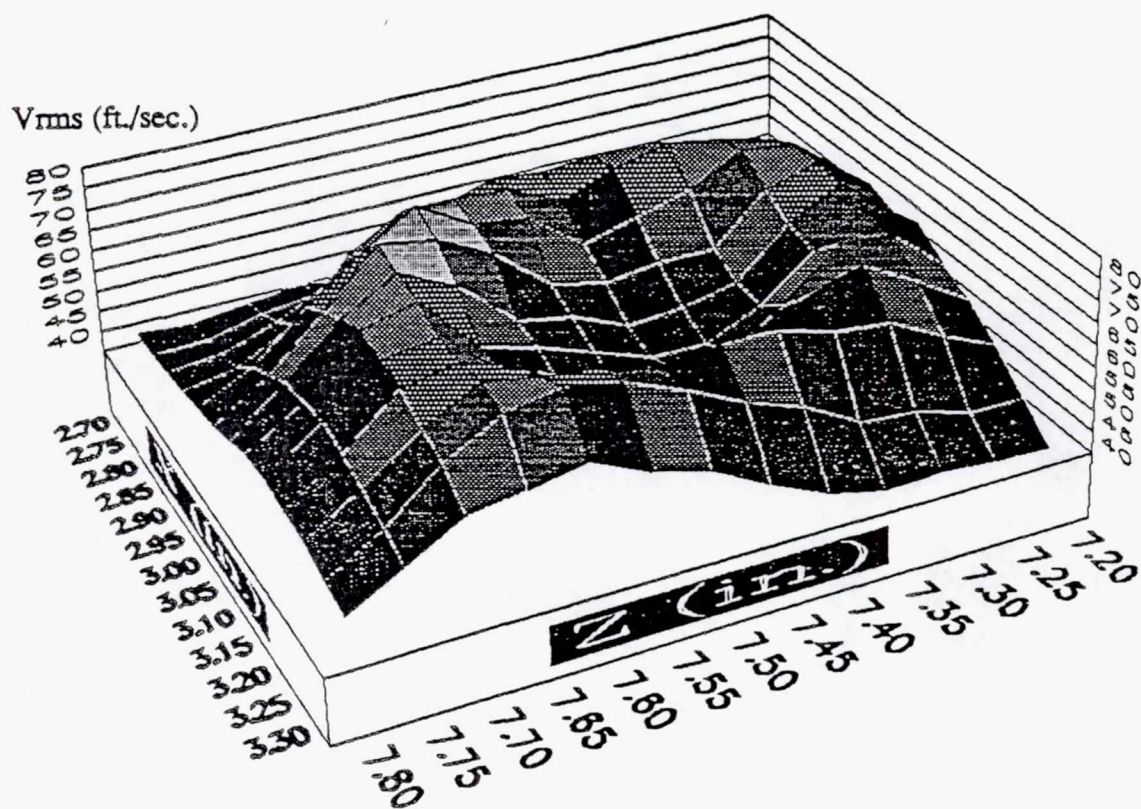
TE92-2271

Figure 3.1.1-19. Contour and line plots of V_{rms} for primary cross jet at $y=0.50$ in.



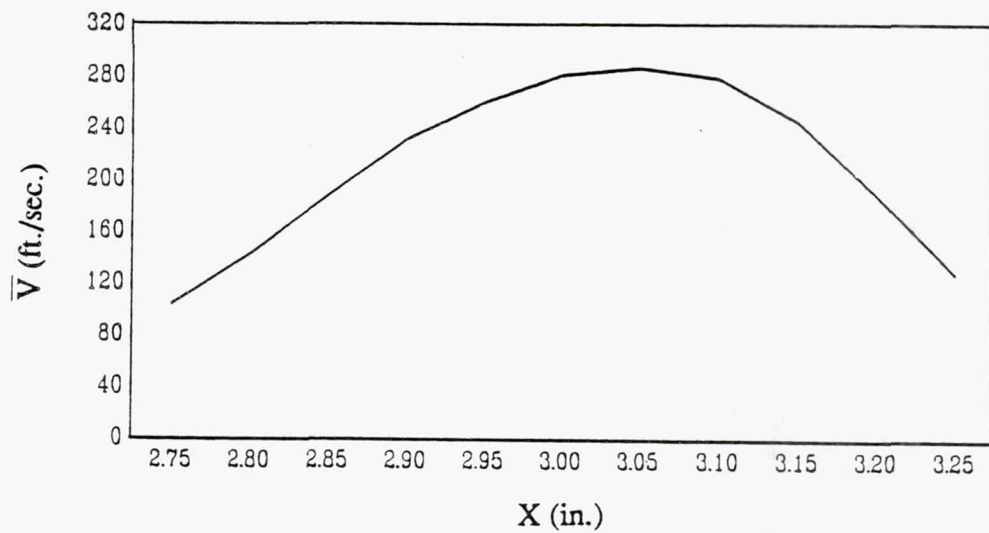
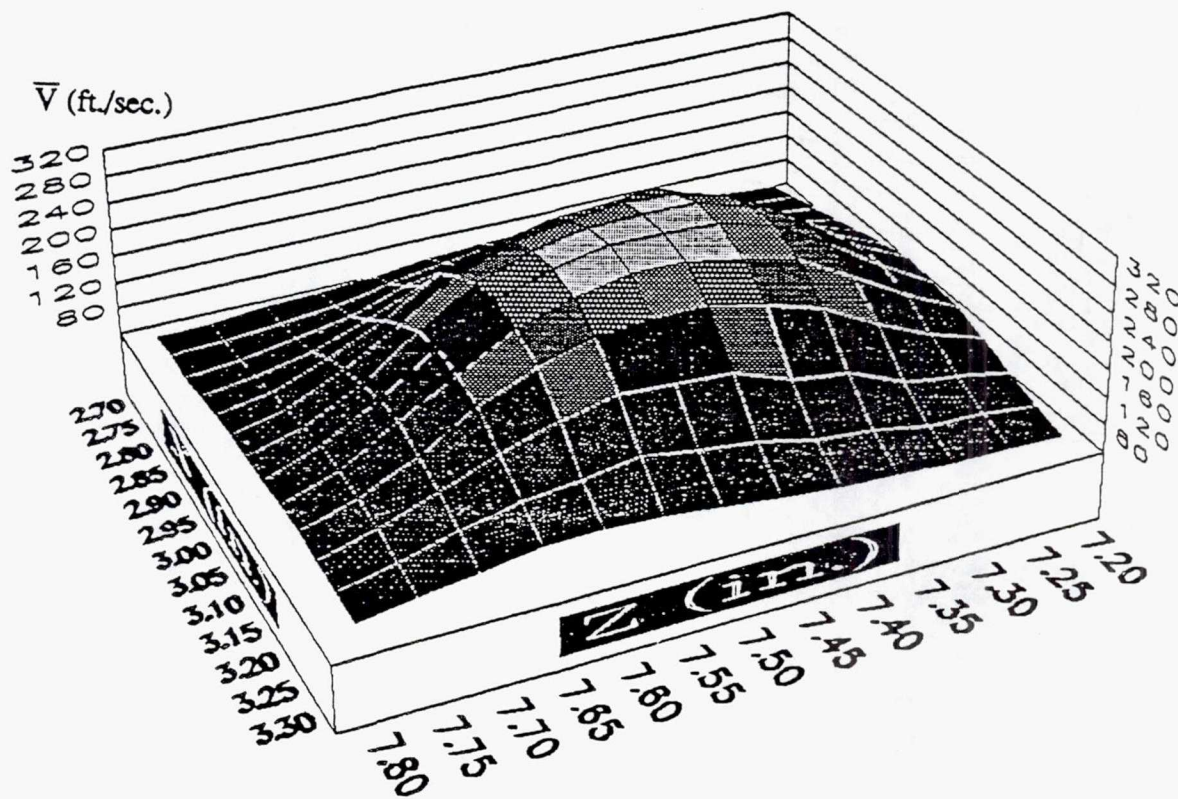
TE92-2272

Figure 3.1.1-20. Contour and line plots of V for primary cross jet at $y=0.75$ in.



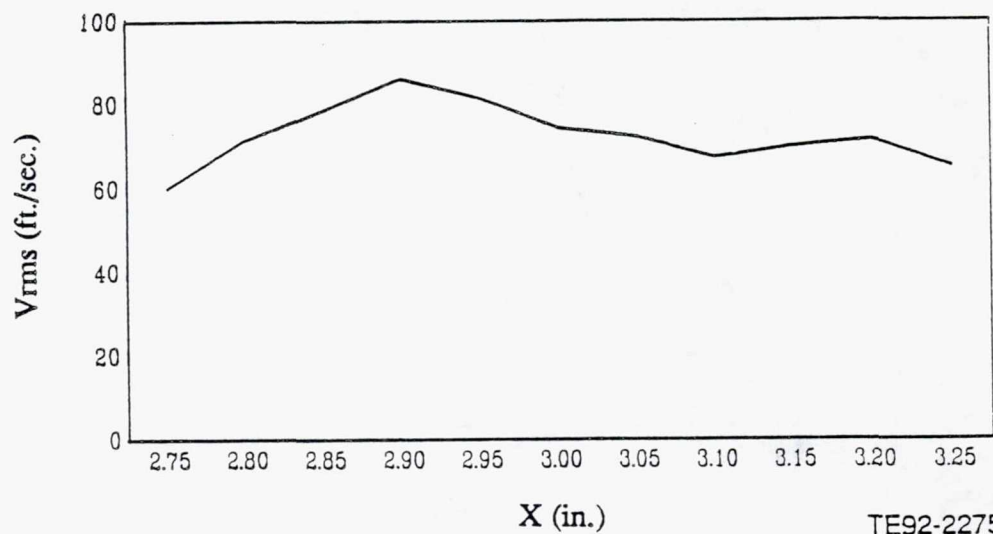
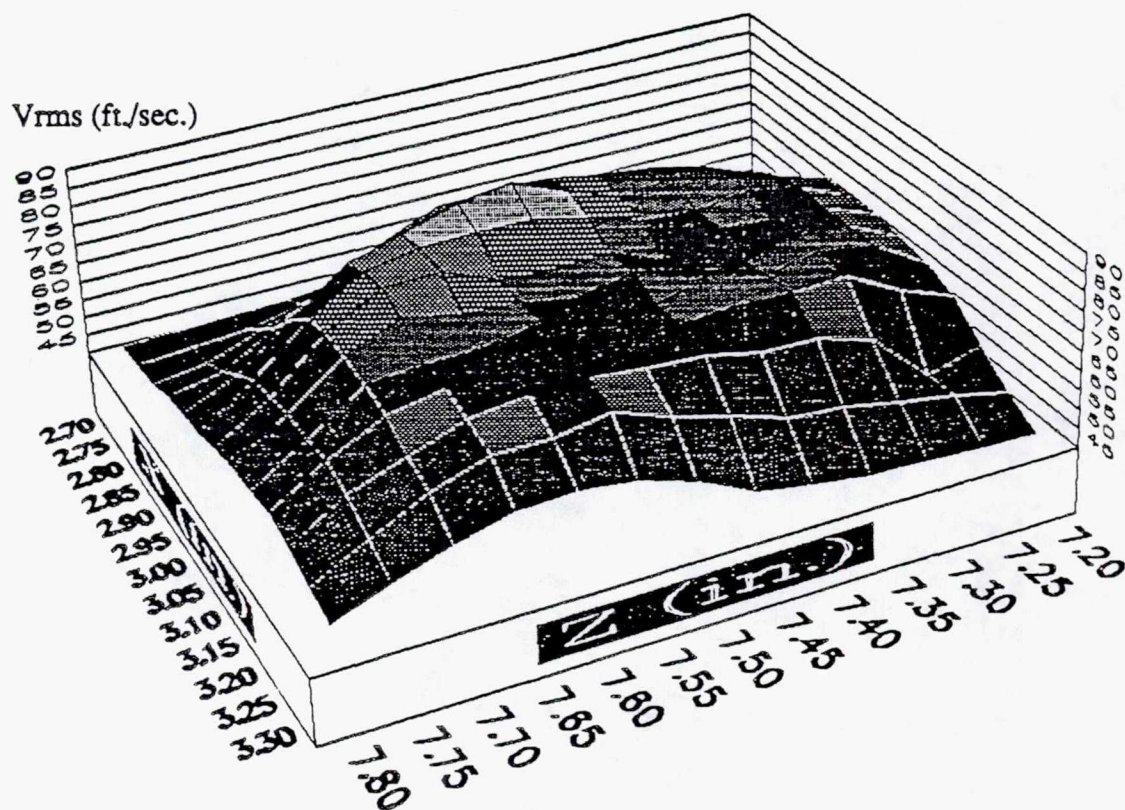
TE92-2273

Figure 3.1.1-21. Contour and line plots of V_{rms} for primary cross jet at $y=0.75$ in.



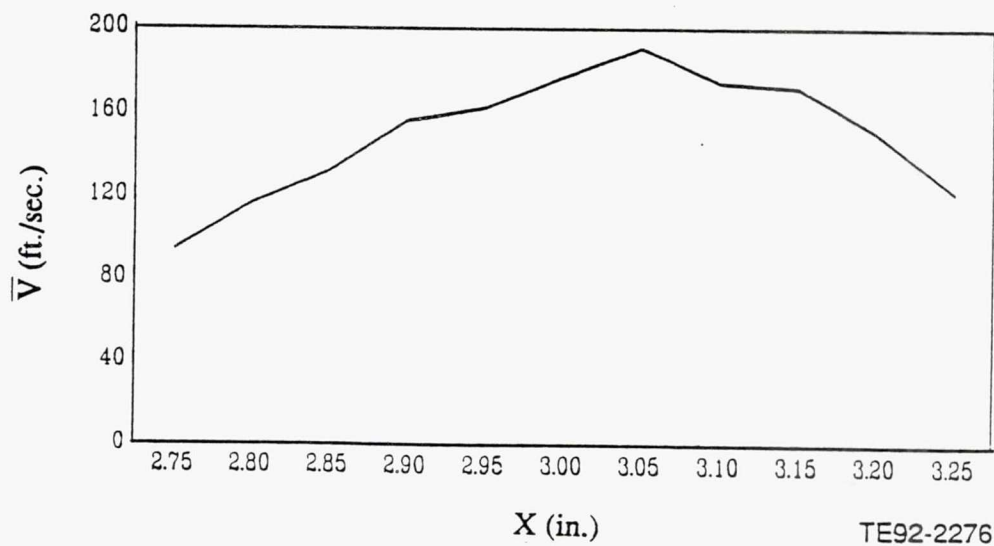
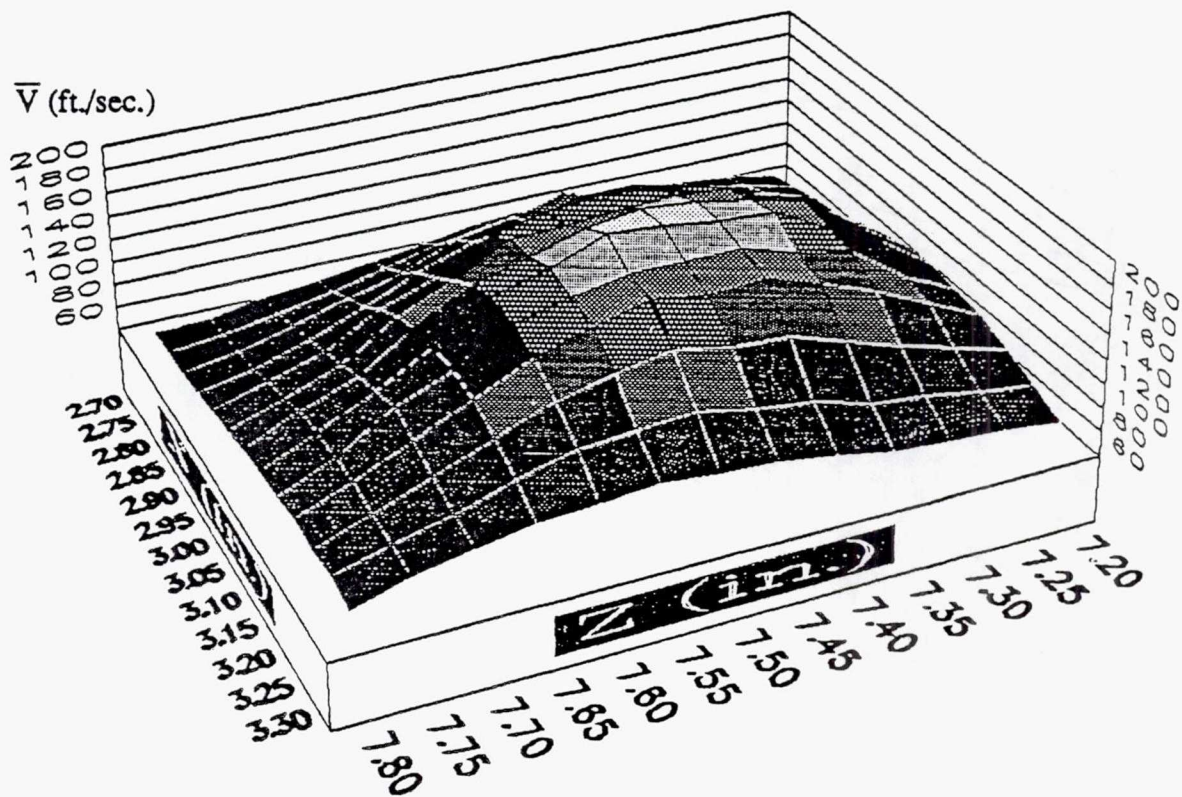
TE92-2274

Figure 3.1.1-22. Contour and line plots of V for primary cross jet at $y=1.00$ in.



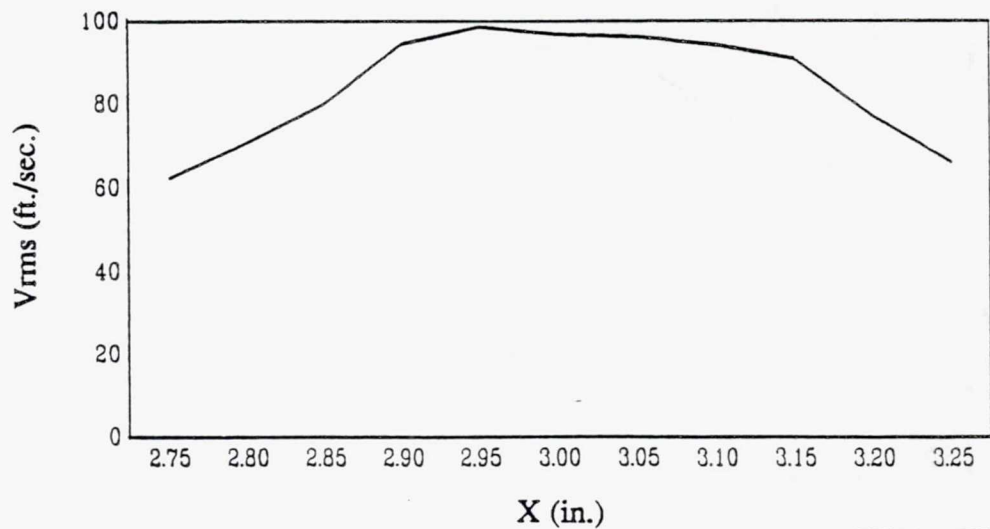
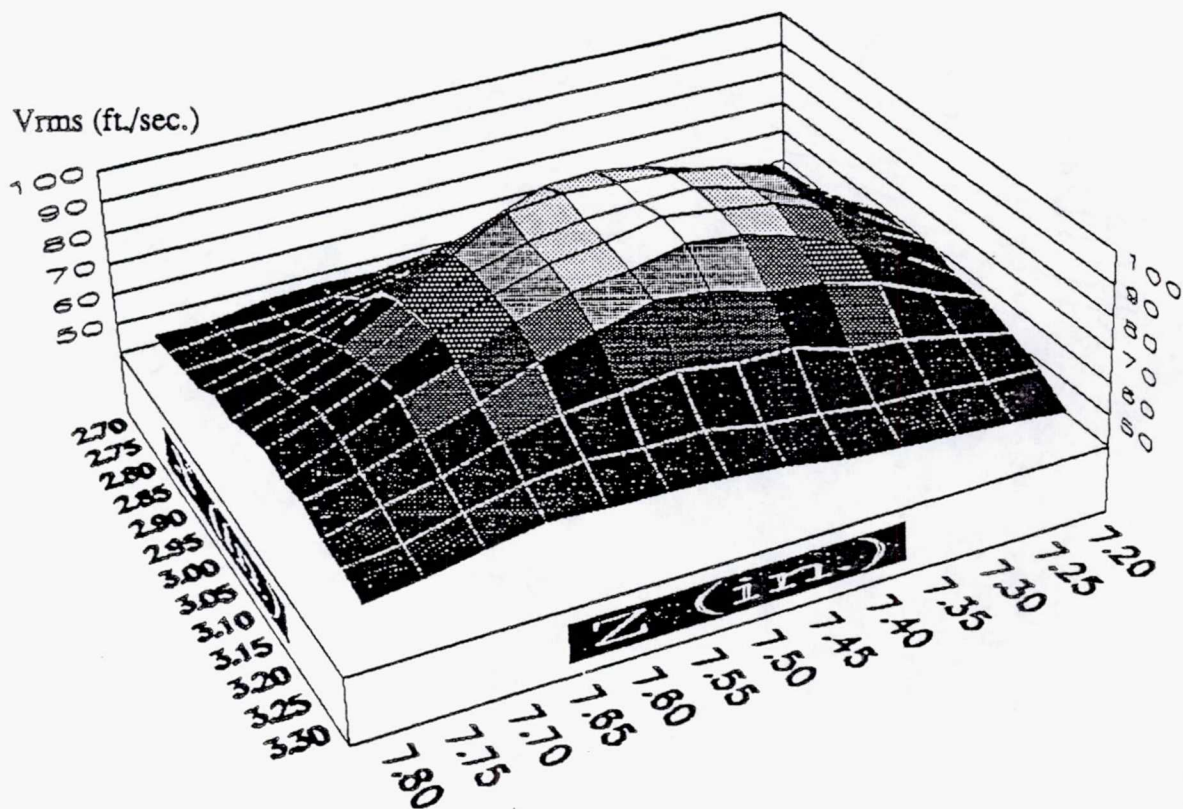
TE92-2275

Figure 3.1.1-23. Contour and line plots of V_{rms} for primary cross jet at $y=1.00$ in.



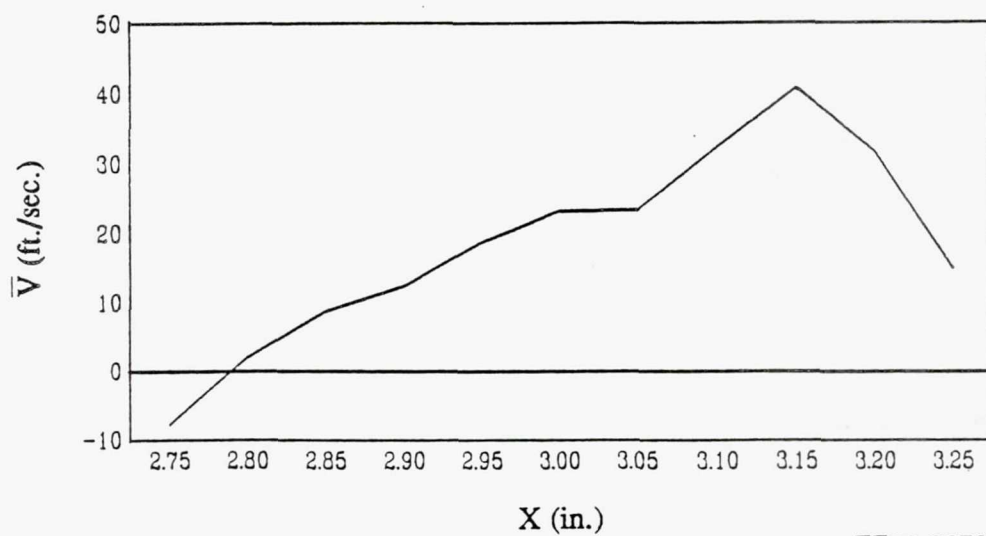
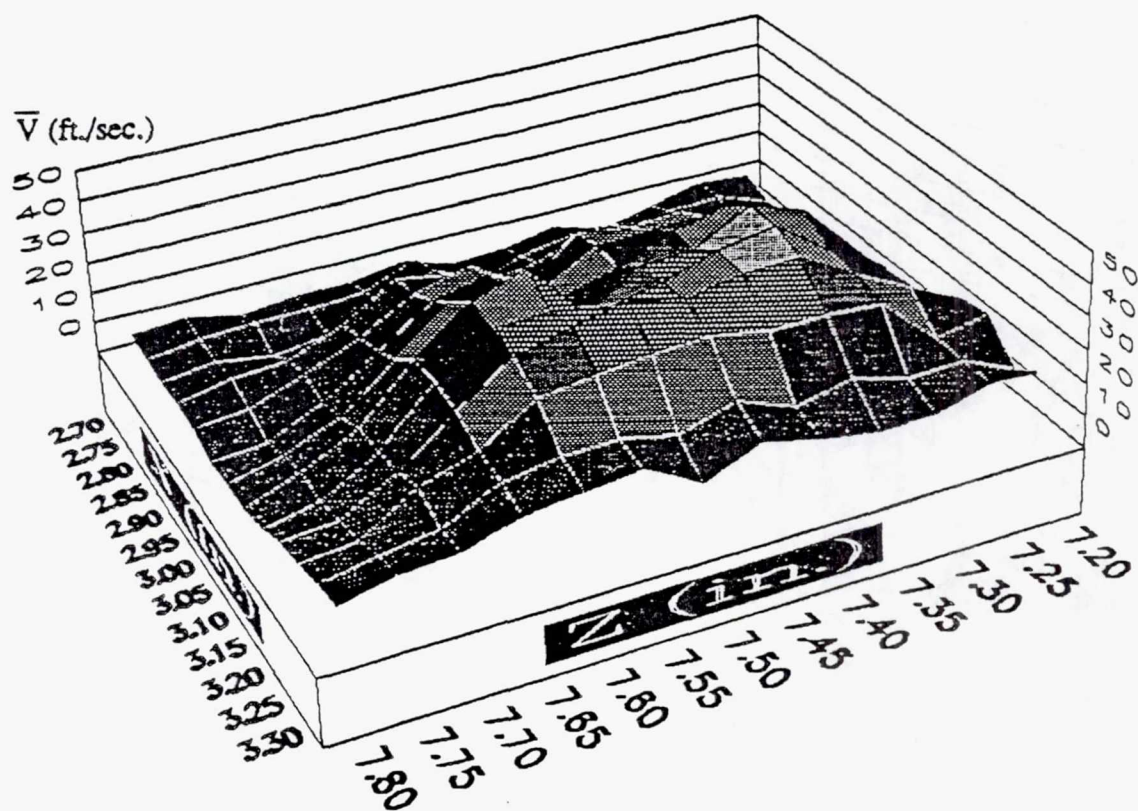
TE92-2276

Figure 3.1.1-24. Contour and line plots of V for primary cross jet at $y=1.25$ in.



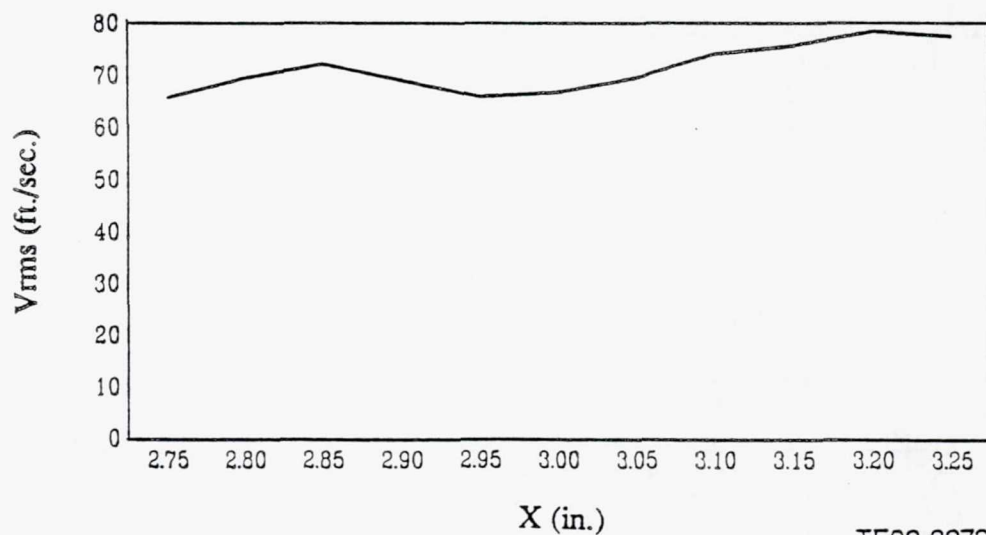
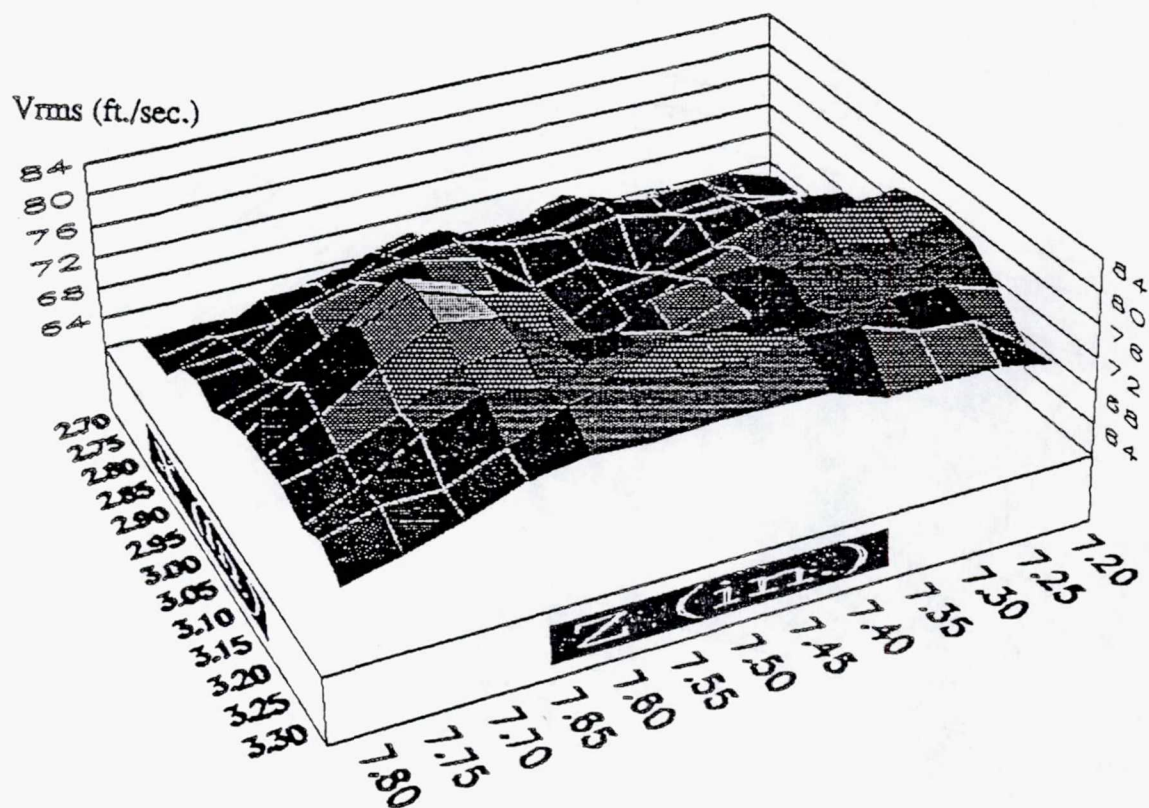
TE92-2277

Figure 3.1.1-25. Contour and line plots of V_{rms} for primary cross jet at $y=1.25$ in.



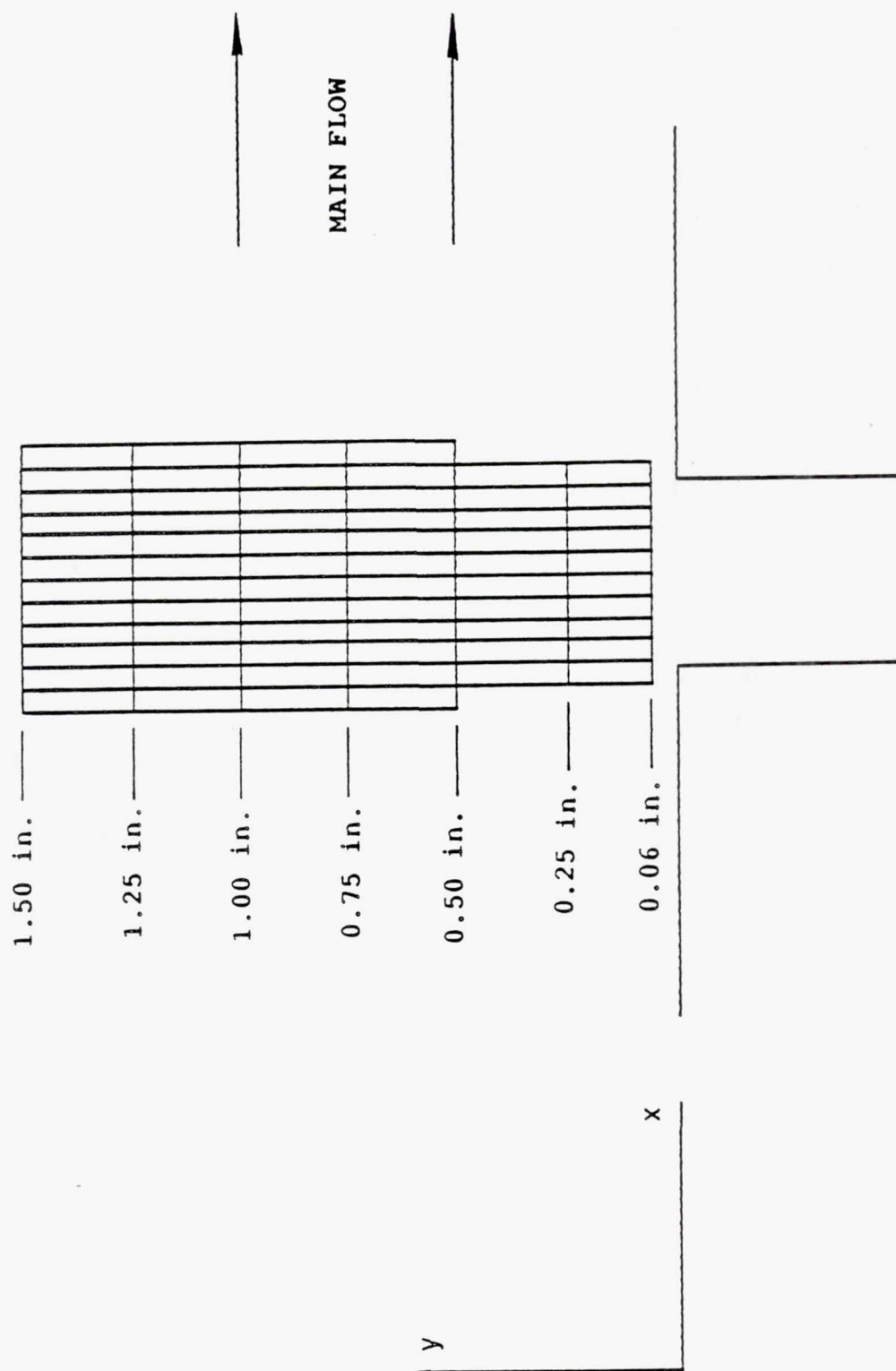
TE92-2278

Figure 3.1.1-26. Contour and line plots of V for primary cross jet at $y=1.50$ in.



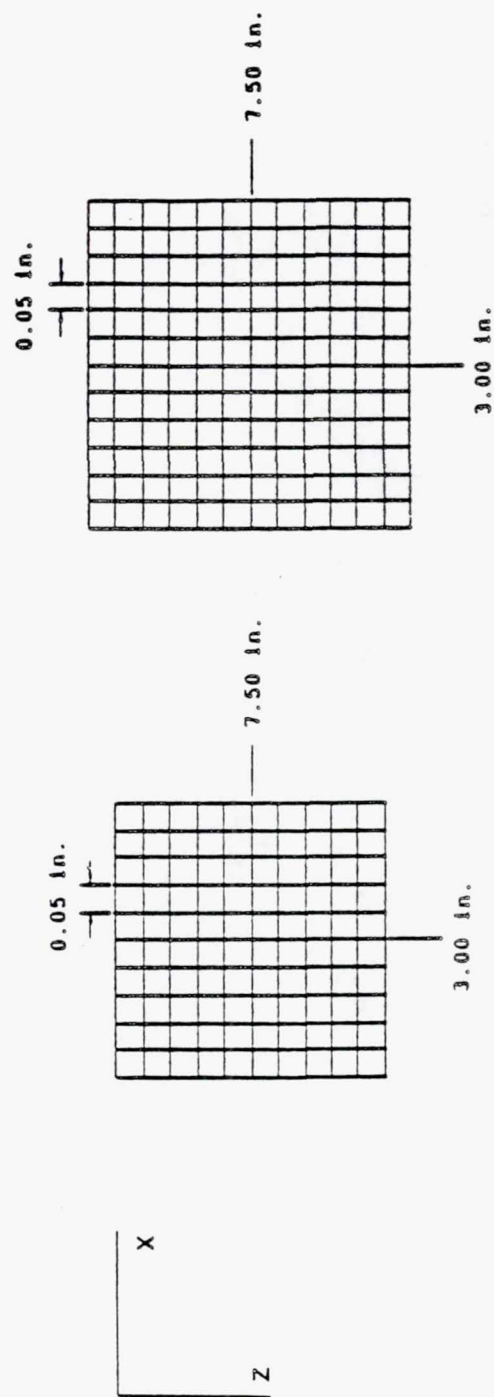
TE92-2279

Figure 3.1.1-27. Contour and line plots of V_{rms} for. primary cross jet at $y=1.50$ in.



TE92-2280

Figure 3.1.1-28. xy plane measurement grid for the primary cross jets.

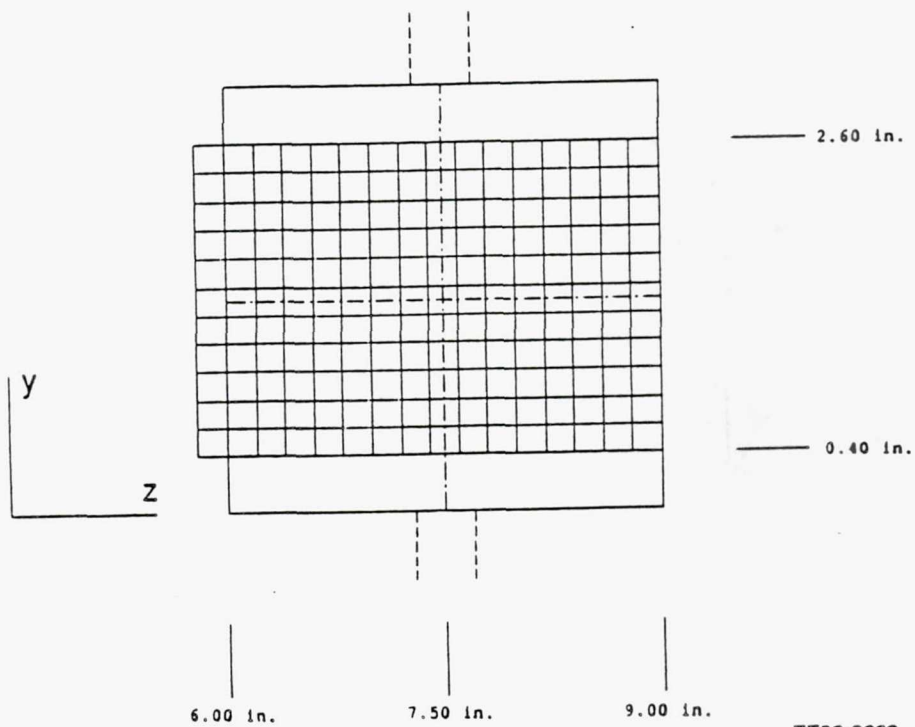


(a)

(b)

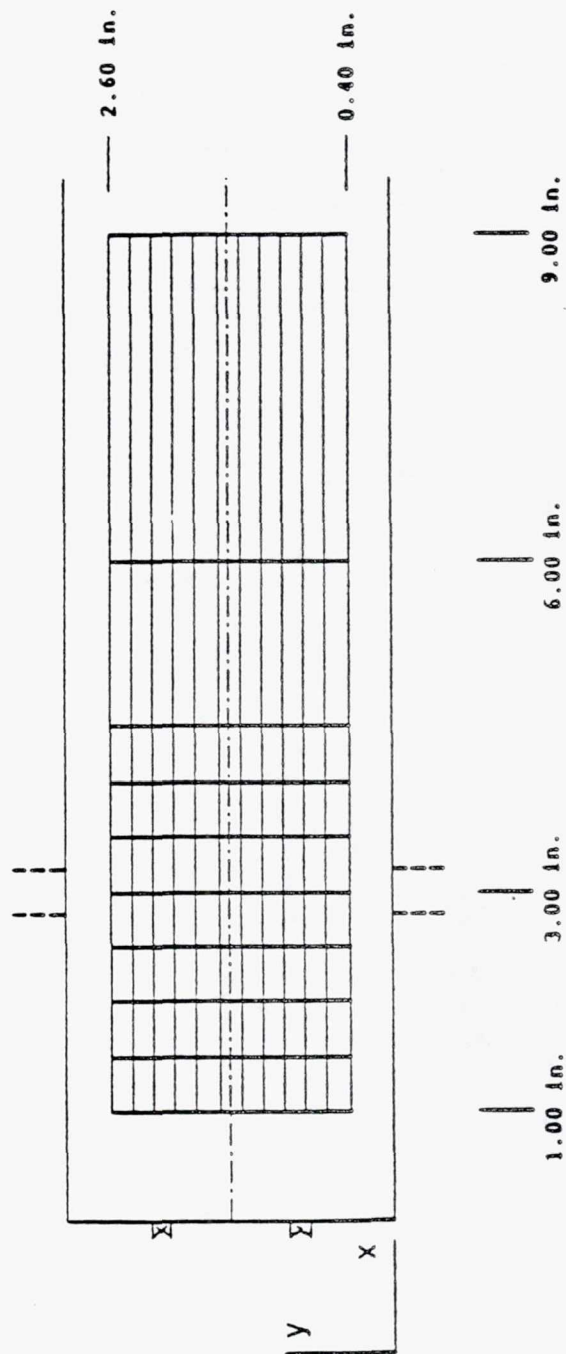
TE92-2281

Figure 3.1.1-29. xz plane measurement grids for the primary cross jets for: (a) $y=0.06$ in. and $y=0.25$ in.
(b) $y=0.50, 0.75, 1.0, 1.2$.



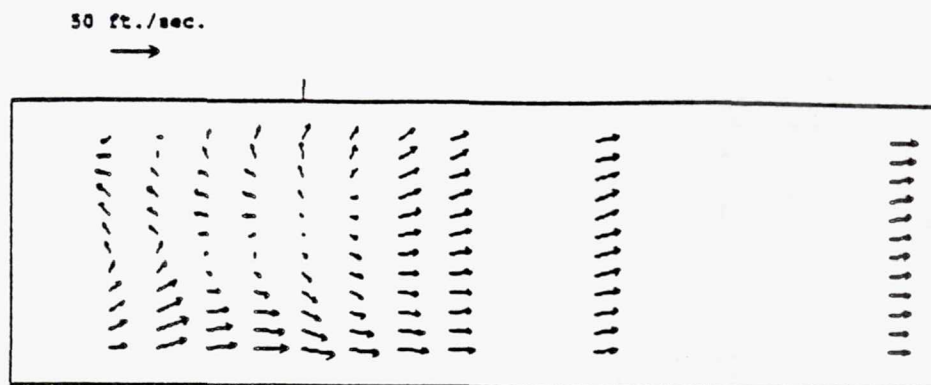
TE92-2282

Figure 3.1.1-30. yz plane measurement grid.

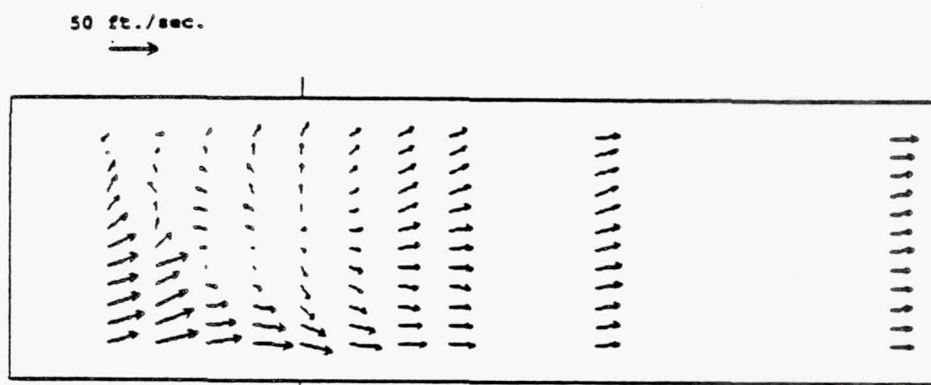


TE92-2283

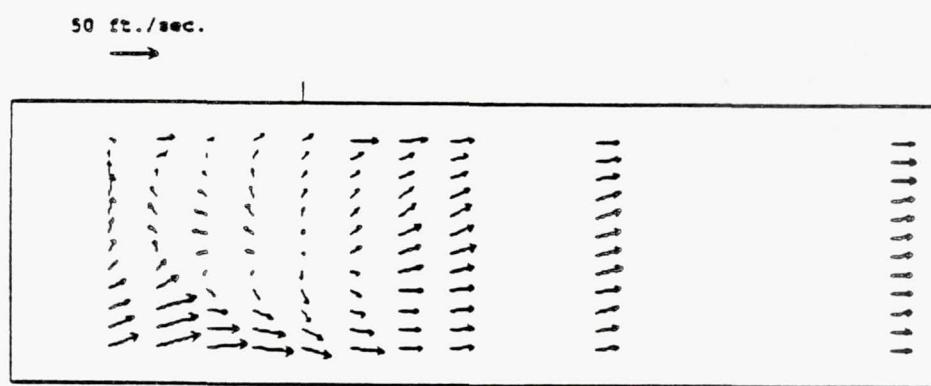
Figure 3.1.1-31. xy plane measurement grid.



(a)



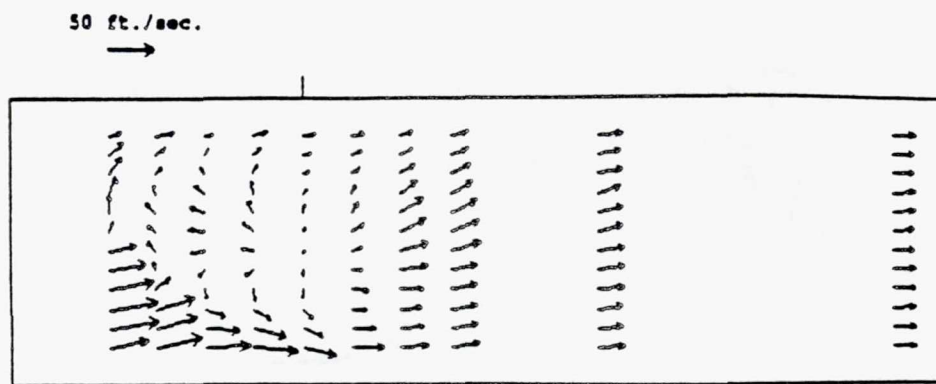
(b)



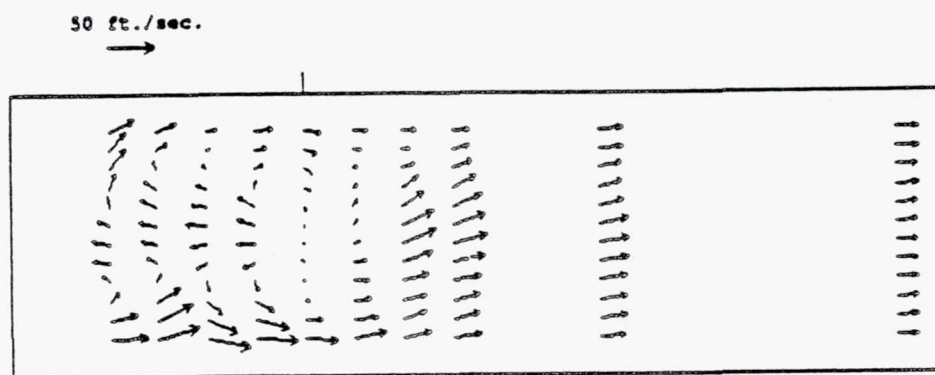
(c)

TE92-2284

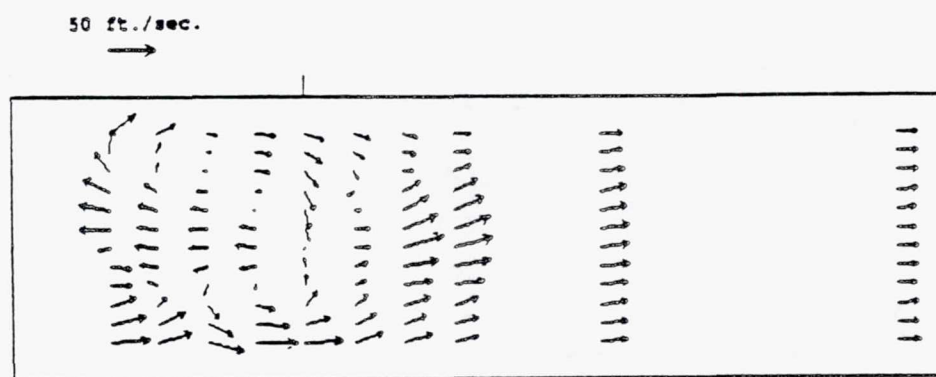
Figure 3.1.1-32. xy plane mean velocity vector plots: (a) $z=5.80$ in. (b) $z=6.00$ in. (c) $z=6.20$ in. ($z = 6.0$ in. is the midplane between two swirlers).



(a)



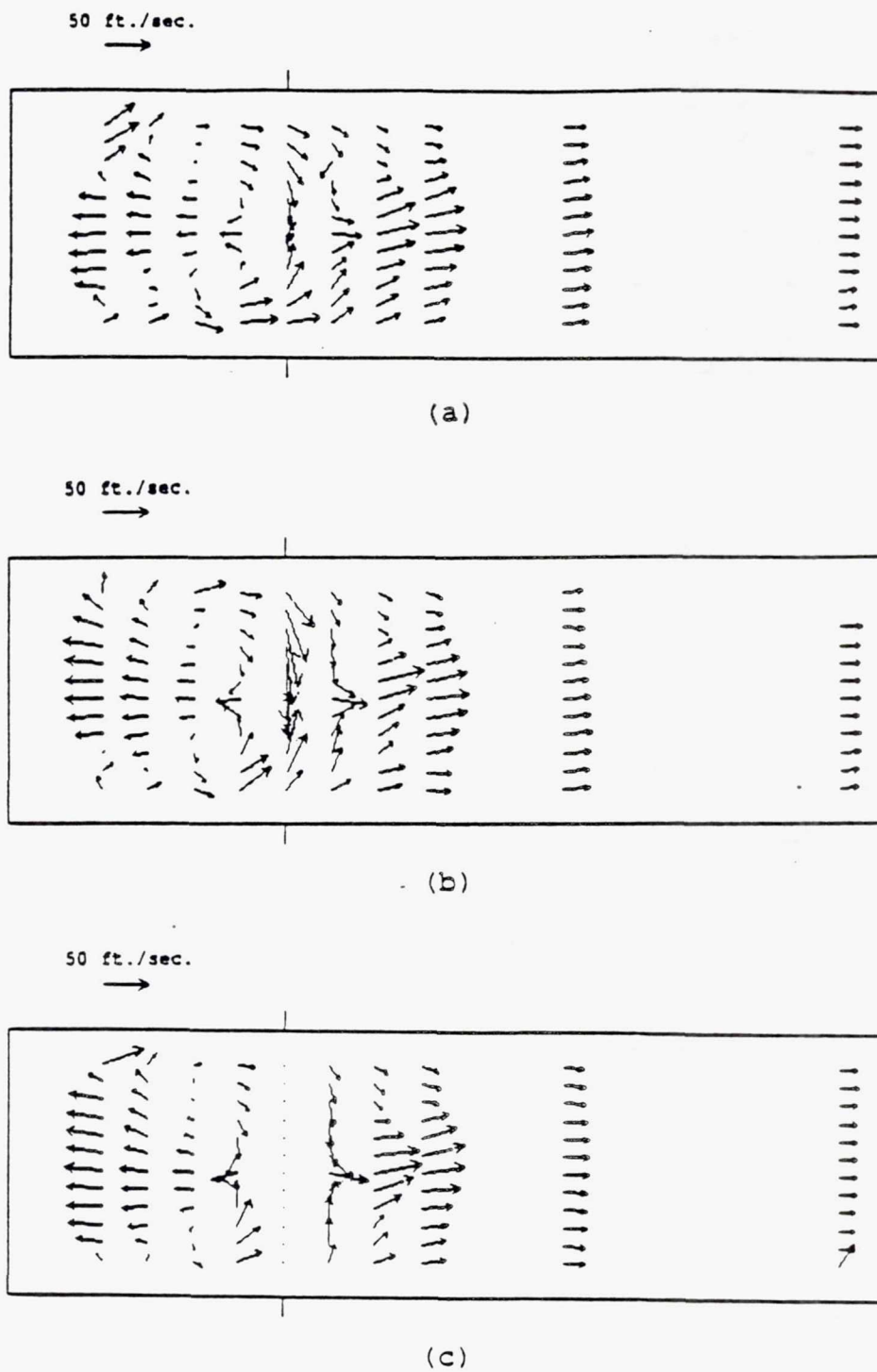
(b)



(c)

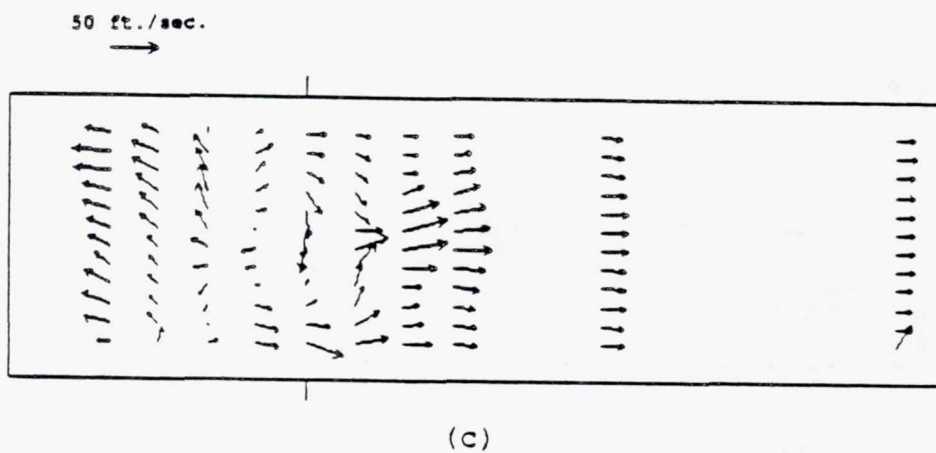
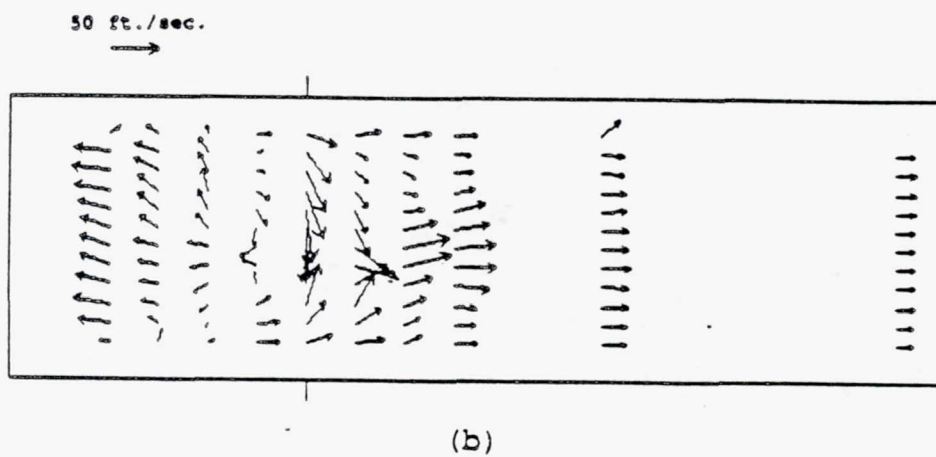
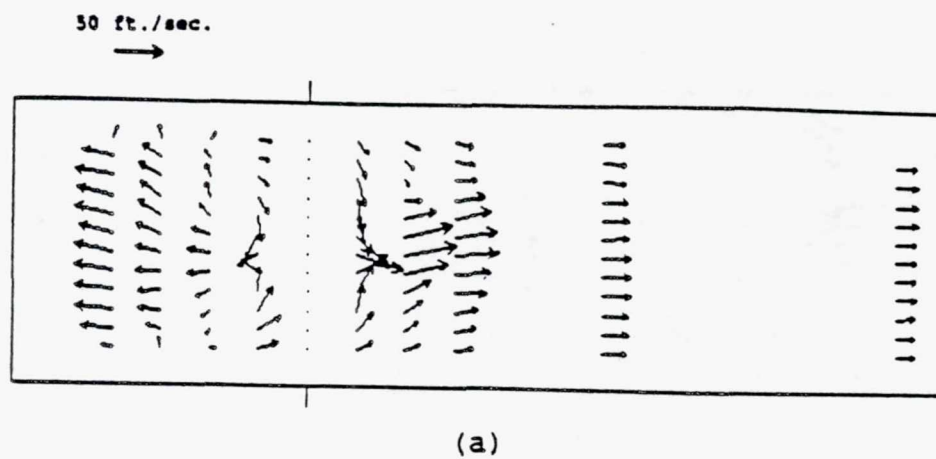
TE92-2285

Figure 3.1.1-33. xy plane mean velocity vector plots: (a) $z=6.40$ in. (b) $z=6.60$ in. (c) $z=6.80$ in.



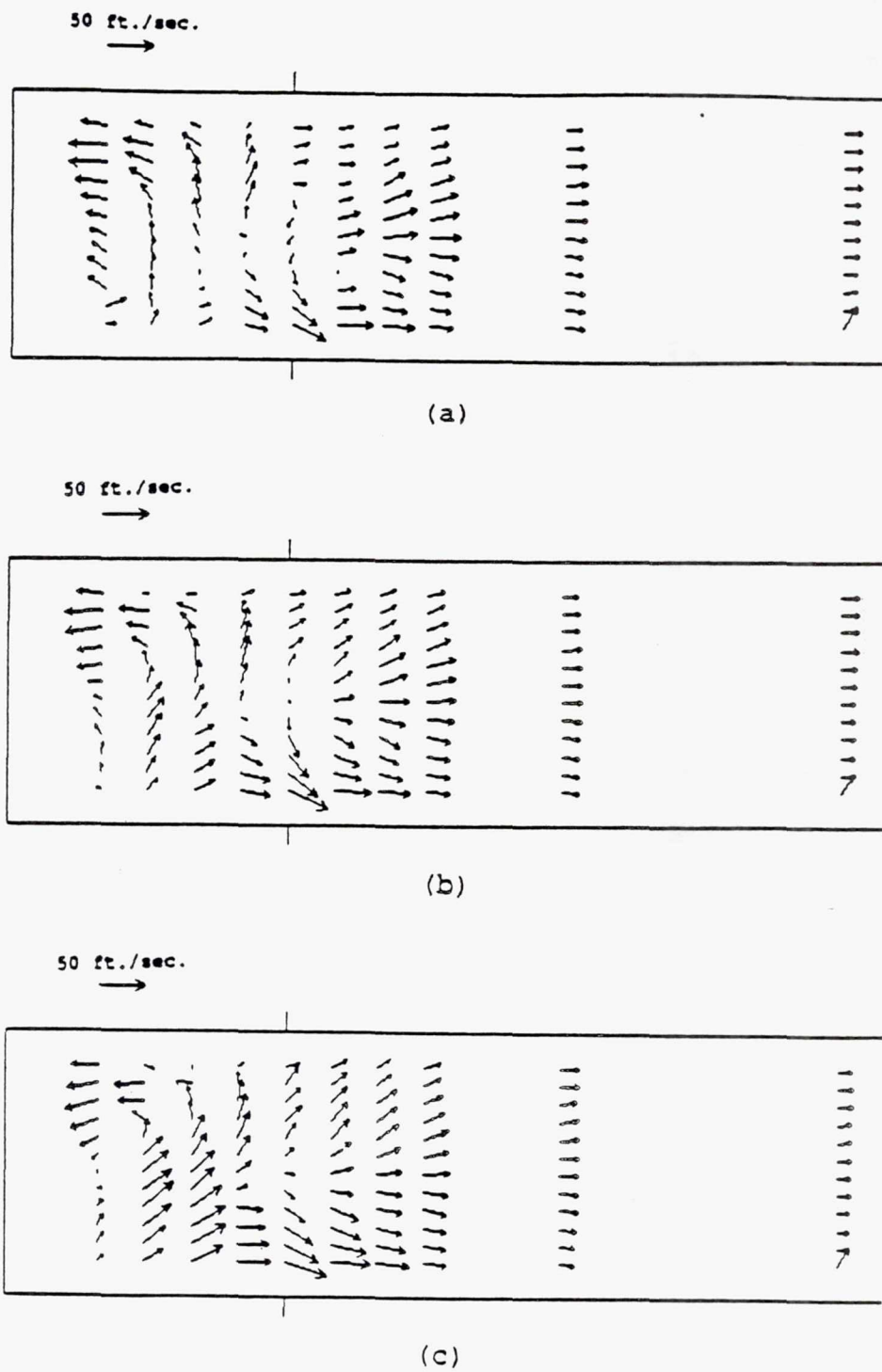
TE92-2286

Figure 3.1.1-34. x y plane mean velocity vector plots: (a) $z=7.00$ in. (b) $z=7.20$ in. (c) $z=7.40$ in.



TE92-2287

Figure 3.1.1-35. xy plane mean velocity vector plots: (a) $z=7.60$ in. (b) $z=7.80$ in. (c) $z=8.00$ in.



TE92-2288

Figure 3.1.1-36. x y plane mean velocity vector plots: (a) $z=8.20$ in. (b) $z=8.40$ in. (c) $z=8.60$ in.

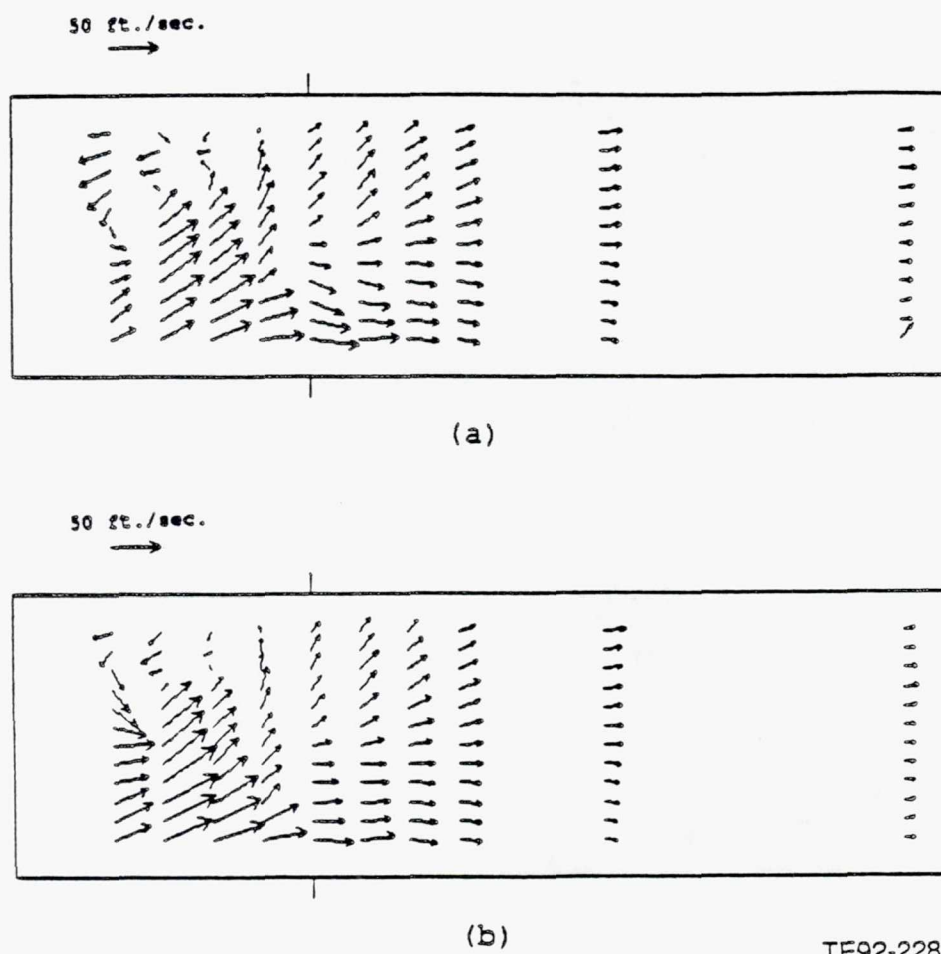
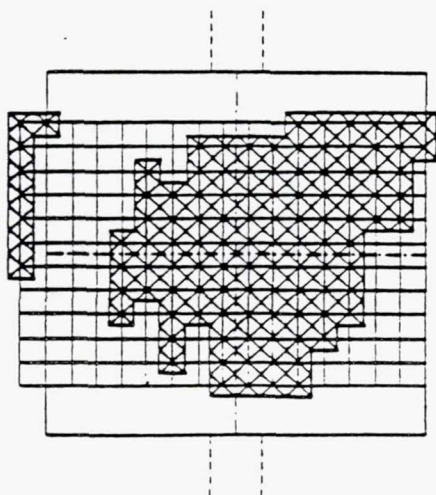
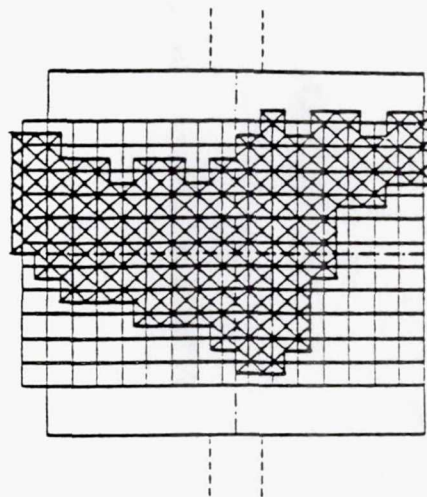


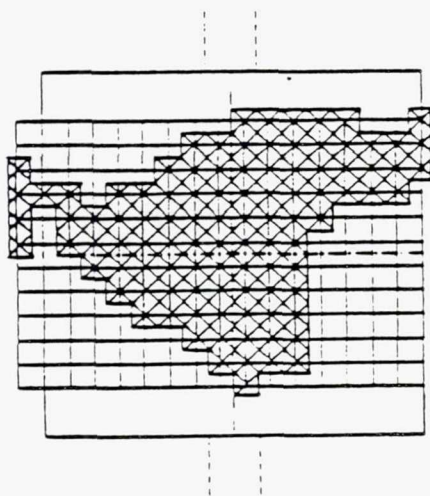
Figure 3.1.1-37. xy plane mean velocity vector plots: (a) $z = 8.80$ in. (b) $z = 9.00$ in.



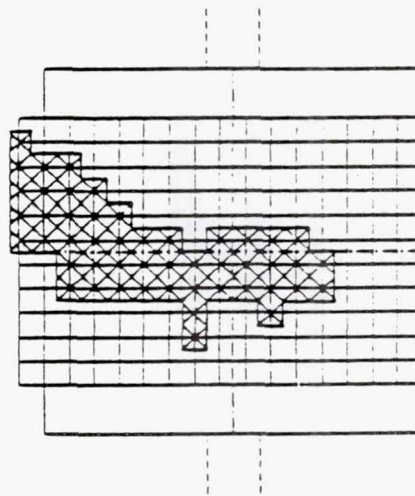
(a)



(c)



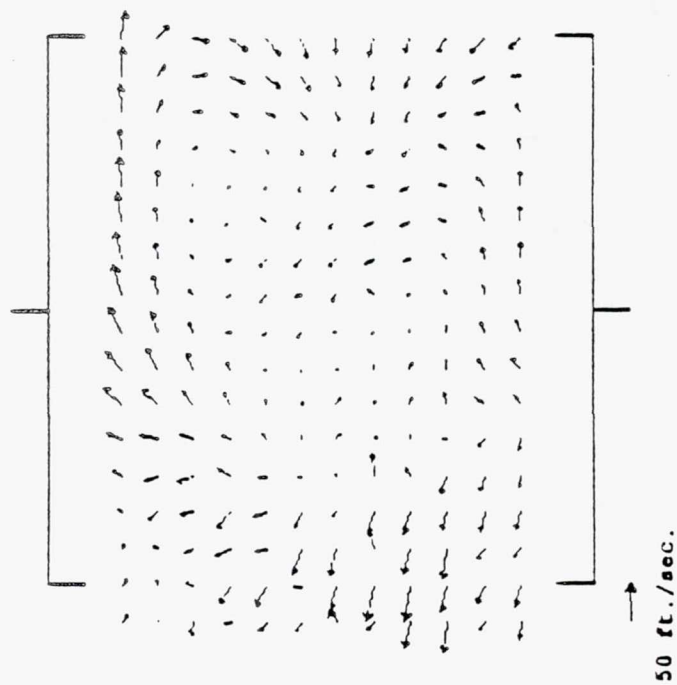
(b)



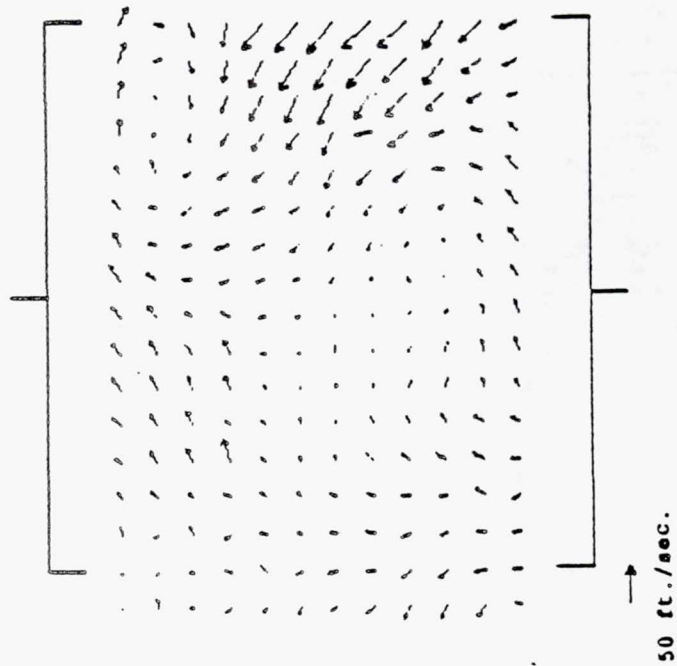
(d)

TE92-2290

Figure 3.1.1-38. Recirculation zone cross-sections: (a) $x=1.00$ in. (b) $x=1.50$ in. (c) $x=2.00$ in. (d) $x=2.50$ in.



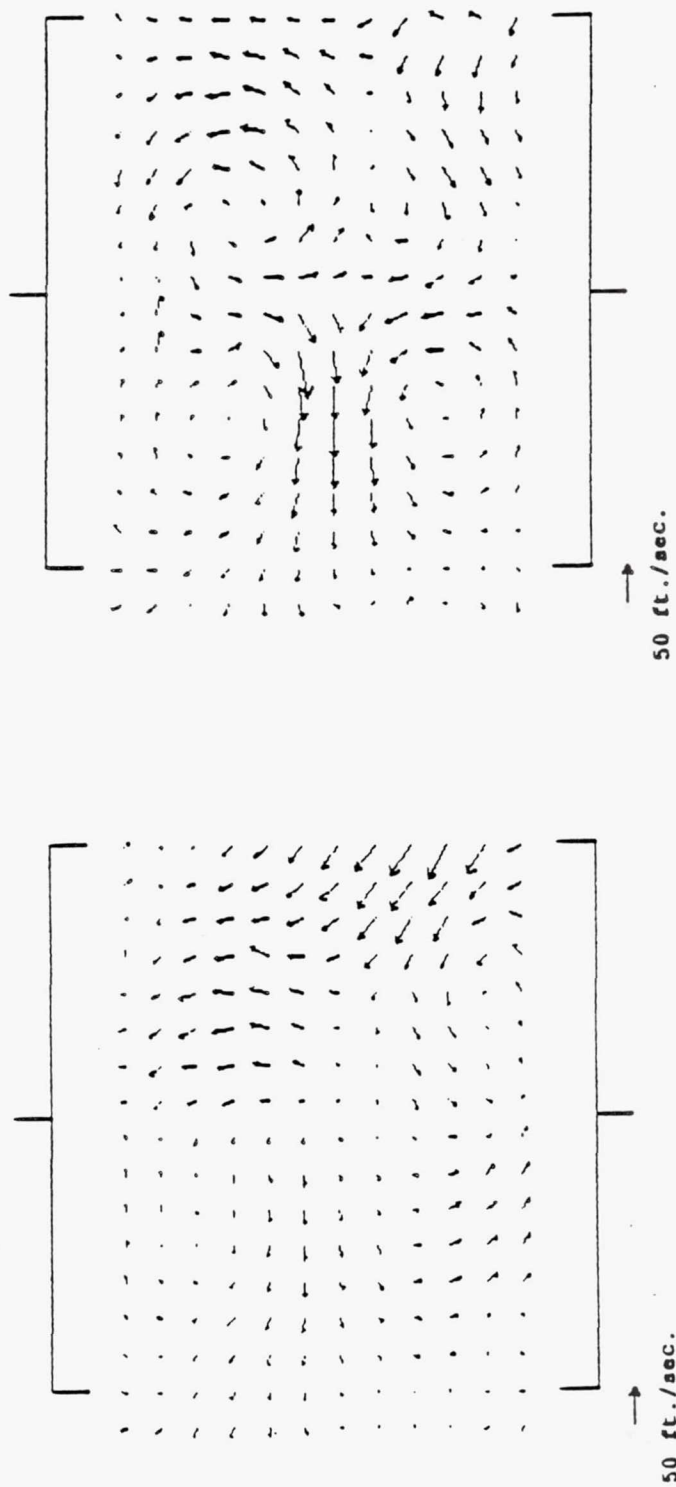
(a)



(b)

TE92-2291

Figure 3.1.1-39. yz plane mean velocity vector plots: (a) $x=1.00$ in. (b) $x=1.50$ in.

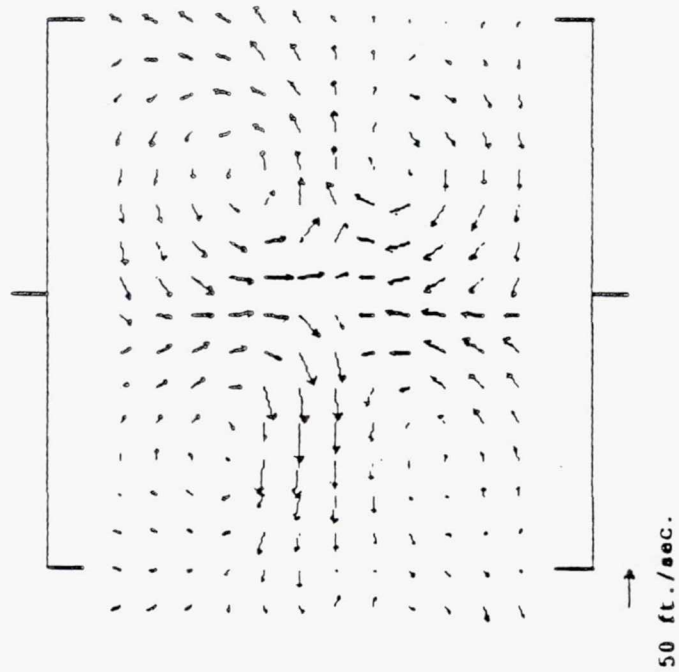


(a)

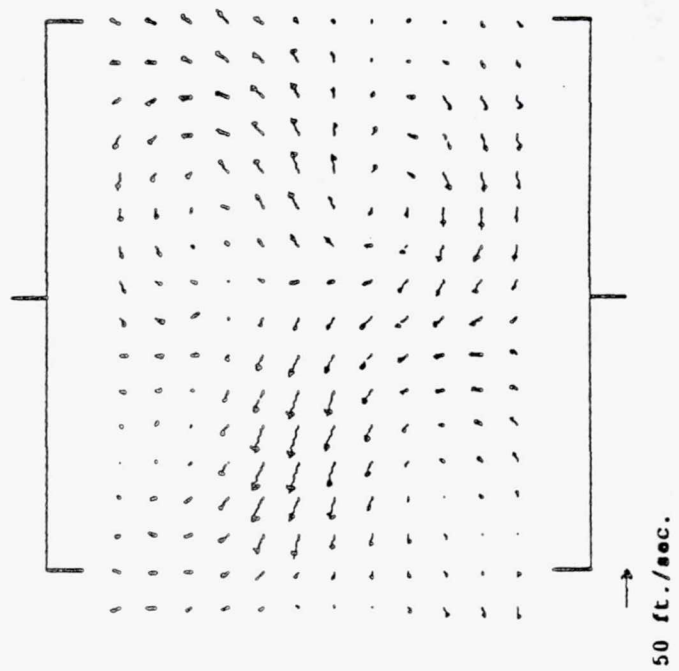
(b)

TE92-2292

Figure 3.1.1-40. y-z plane mean velocity vector plots: (a) $x=2.00$ in. (b) $x=2.50$ in.



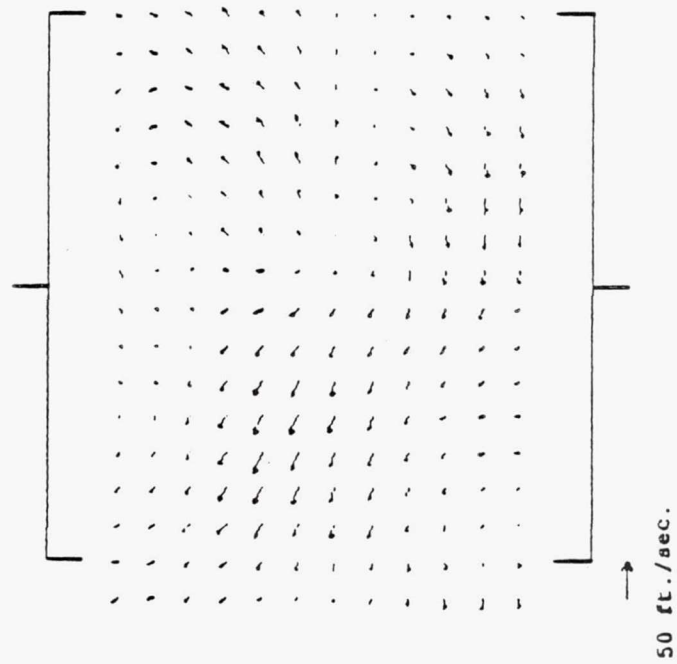
(a)



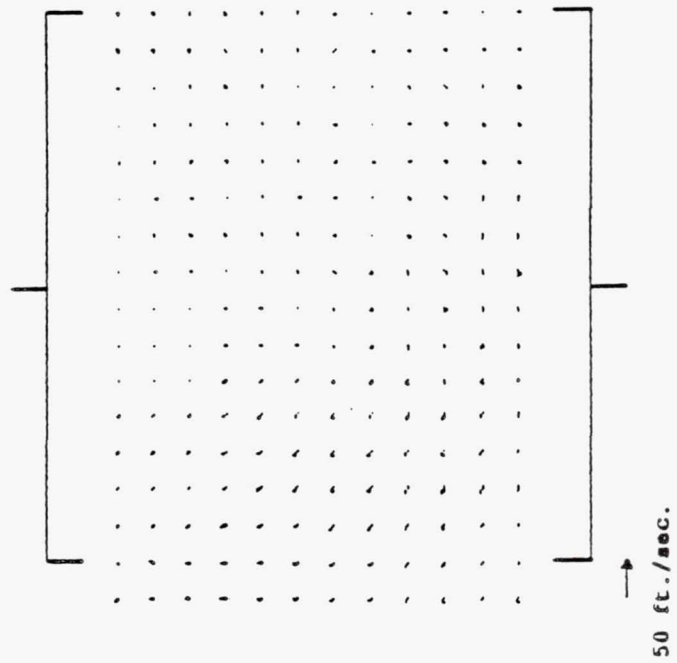
(b)

TE92-2293

Figure 3.1.1-41. YZ plane mean velocity vector plots: (a) $x=3.50$ in. (b) $x=4.00$ in.



(a)



(b)

TE92-2294

Figure 3.1.1-42. yz plane mean velocity vector plots: (a) $x=4.50$ in. (b) $x=6.00$ in.

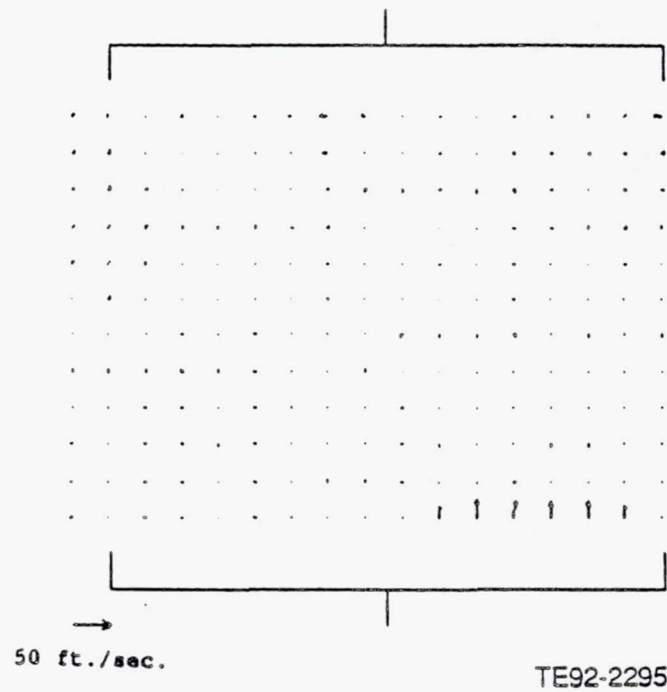
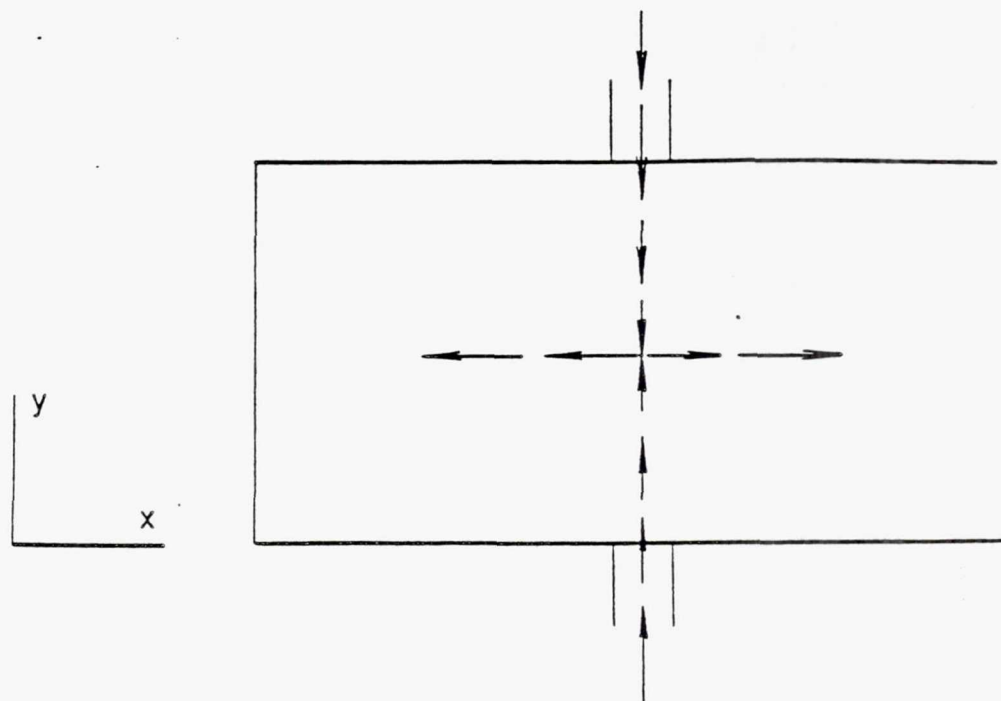
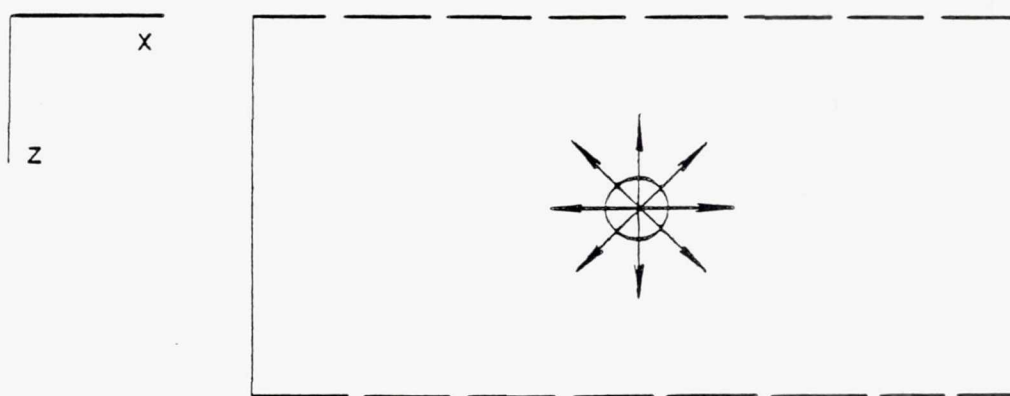


Figure 3.1.1-43. yz plane mean velocity vector plot at $x=9.00$ in.



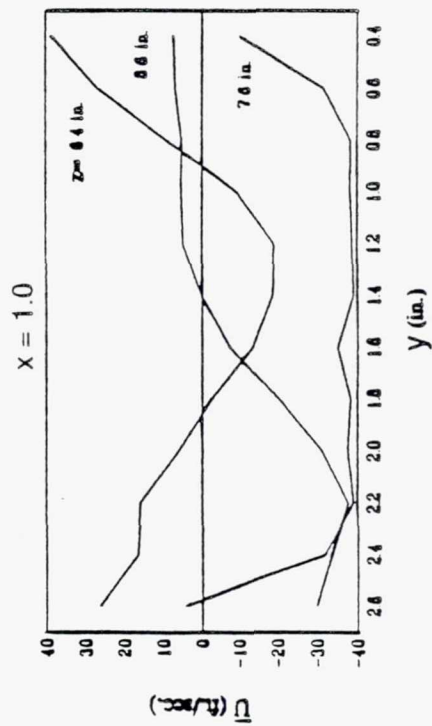
(a)



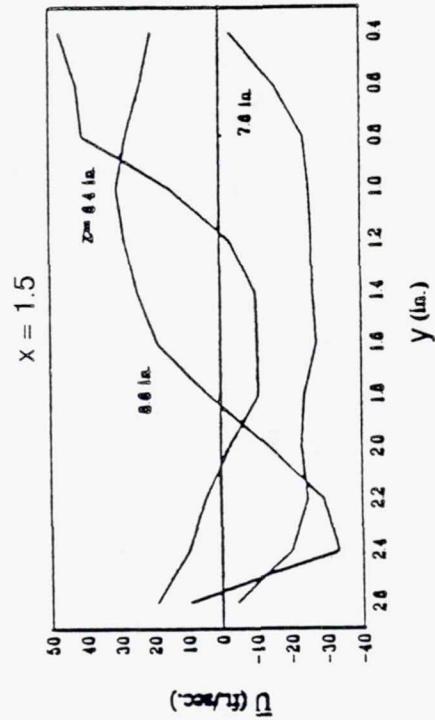
(b)

TE92-2296

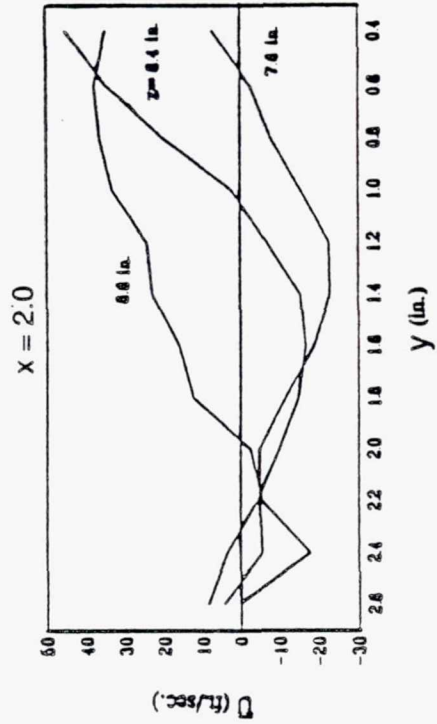
Figure 3.1.1-44. Radial jet flow pattern: (a) xy plane view (b) yz plane view.



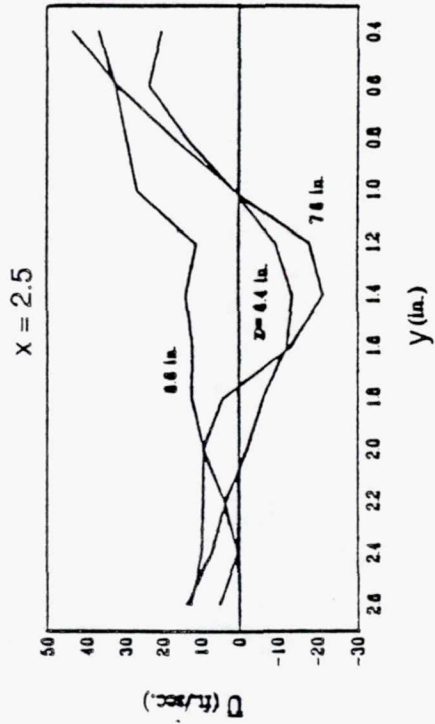
(a)



(b)



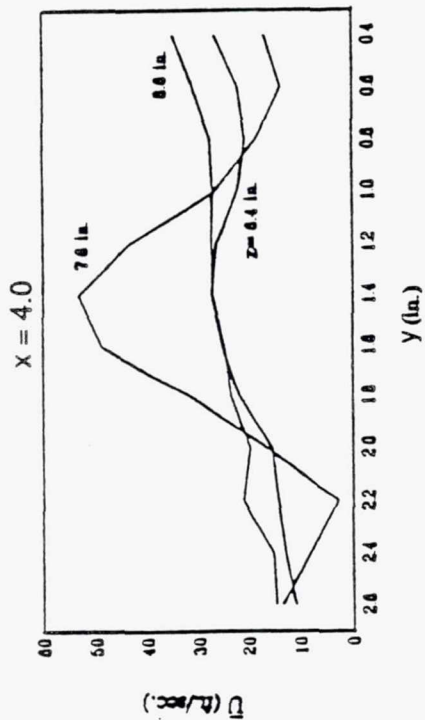
(c)



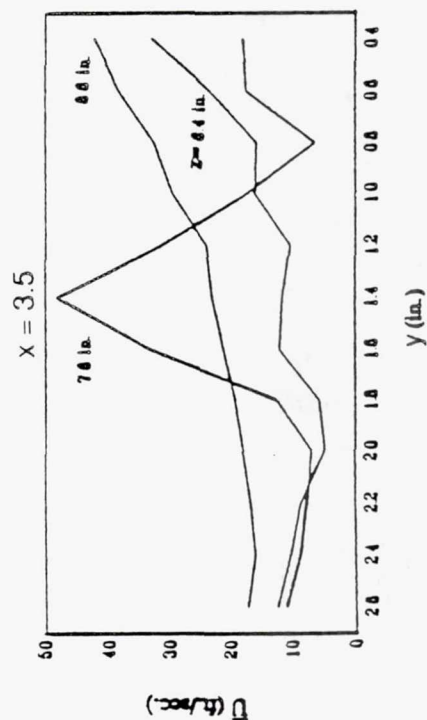
(d)

TE92-2297

Figure 3.1.1-45. Line plot of U at $x = 1.00, 1.50, 2.00$, and 2.50 in.



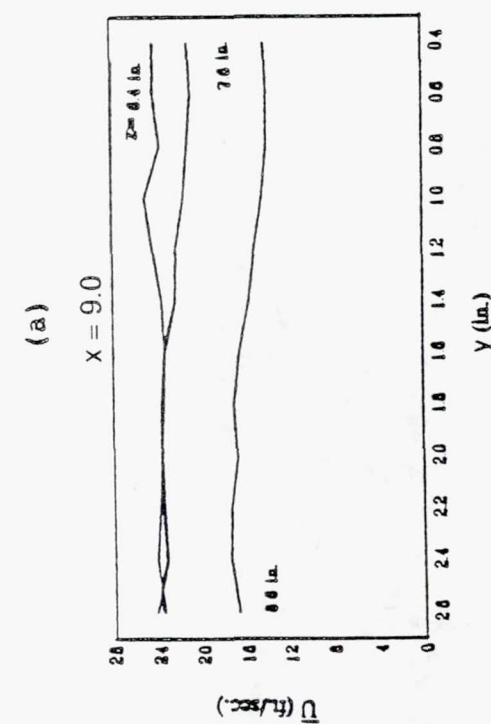
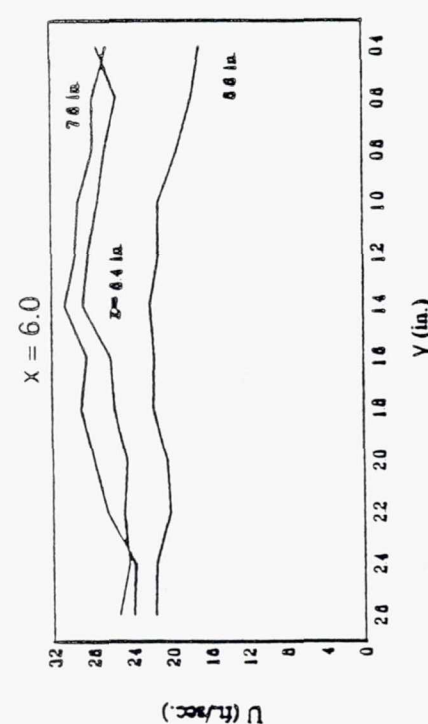
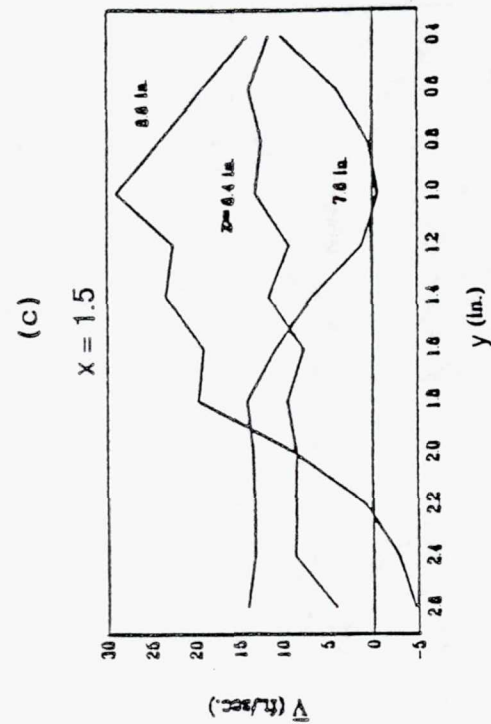
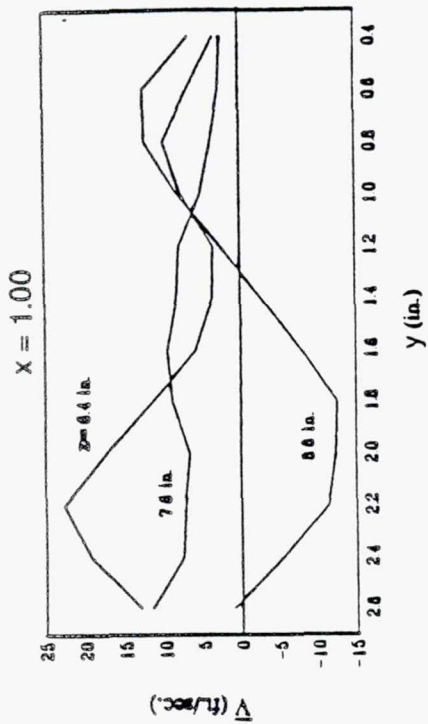
(b)



(d)

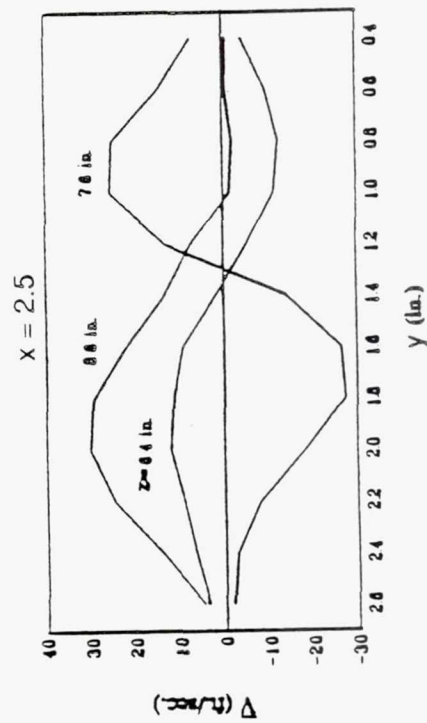
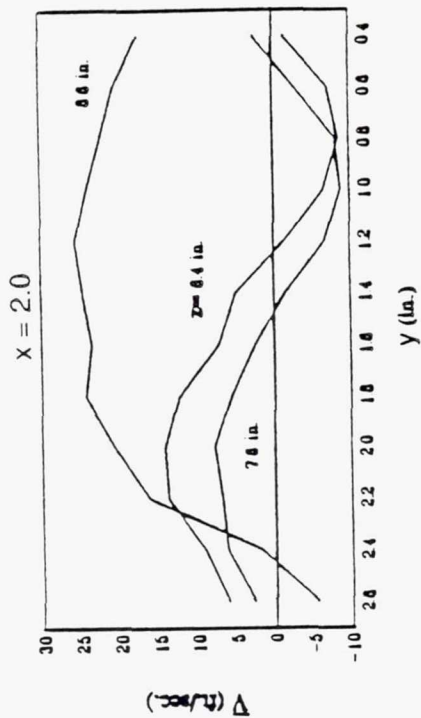
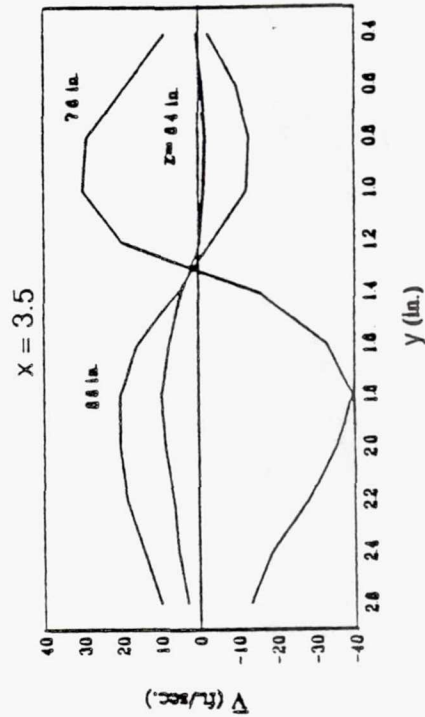
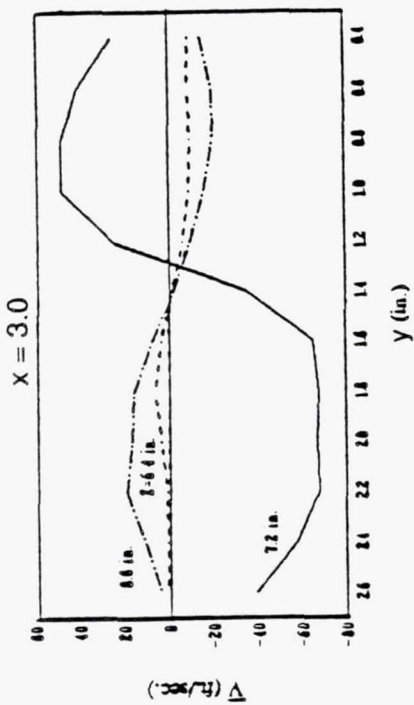
TE92-2298

Figure 3.1.1-46. Line plots of U at $x = 3.00, 3.50, 4.00$, and 4.50 in.



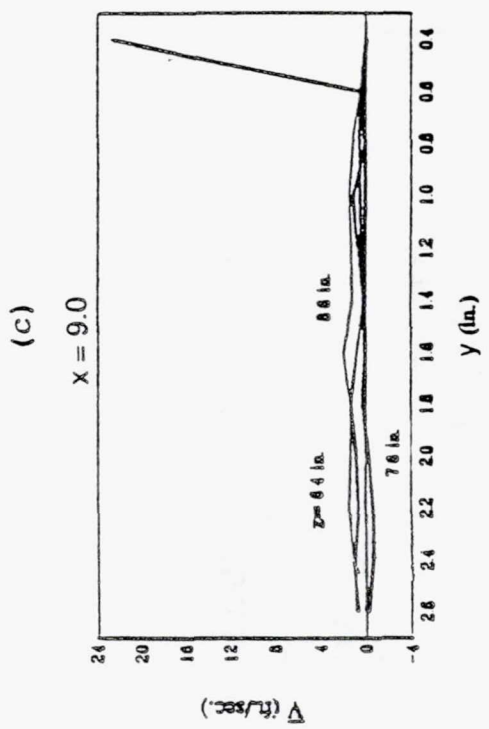
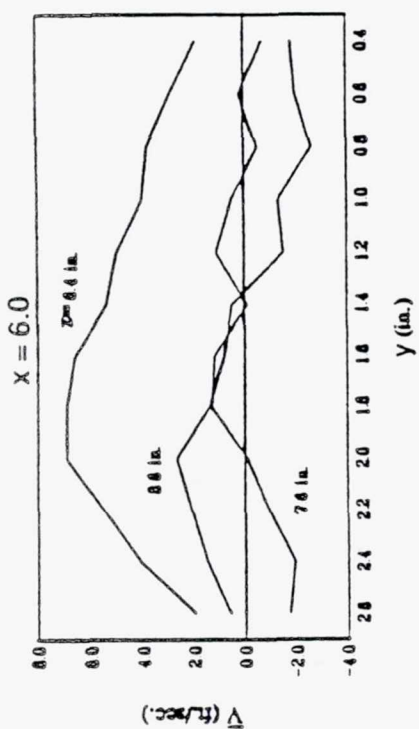
TE92-2299

Figure 3.1.1-47. Line plots of U at x=6.00 in. and 9.00 in., and of V at x=1.00 in. and 1.50 in.

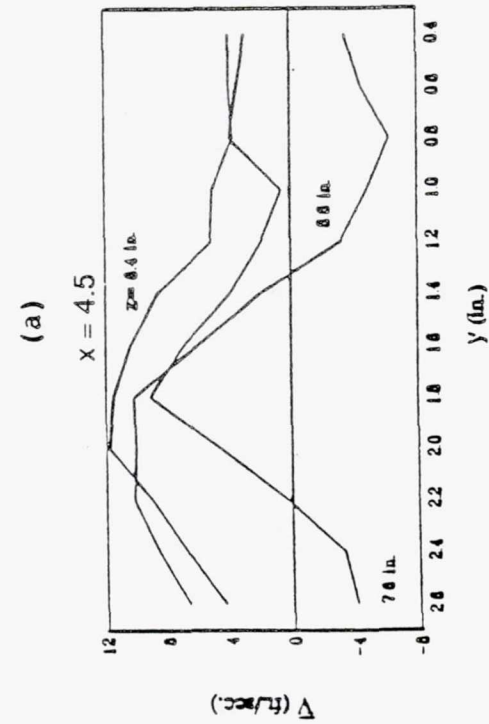
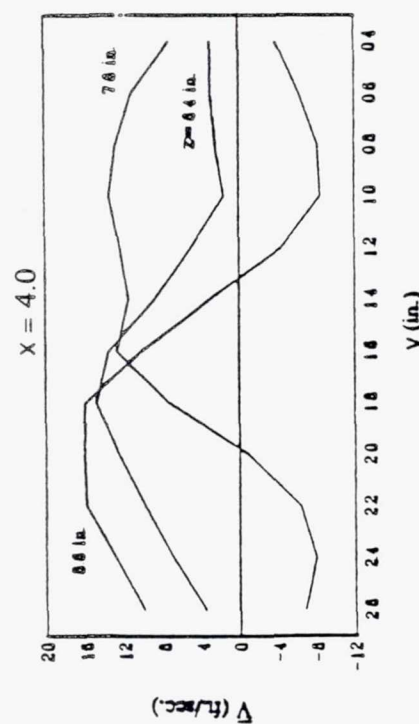


TE92-2300

Figure 3.1.1-48. Line plots of V at $x=2.00$, 2.50 , 3.00 , and 3.50 in.

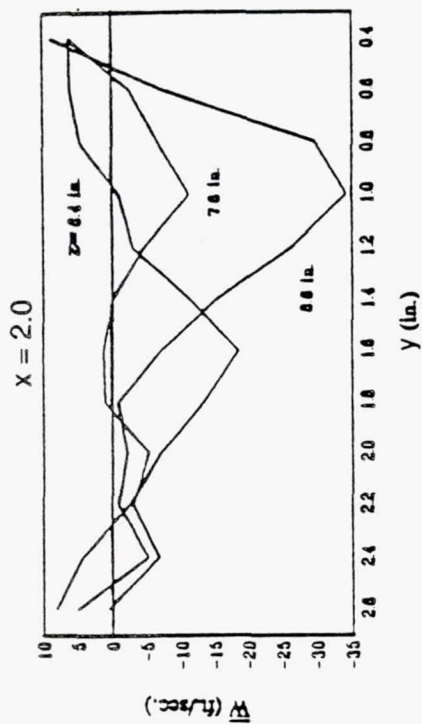


(c)

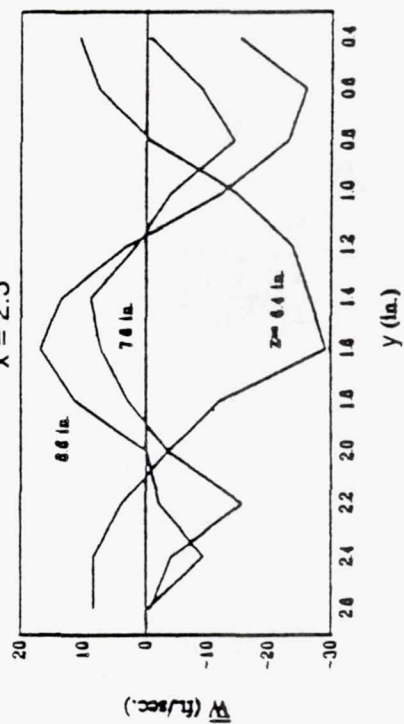


(f)

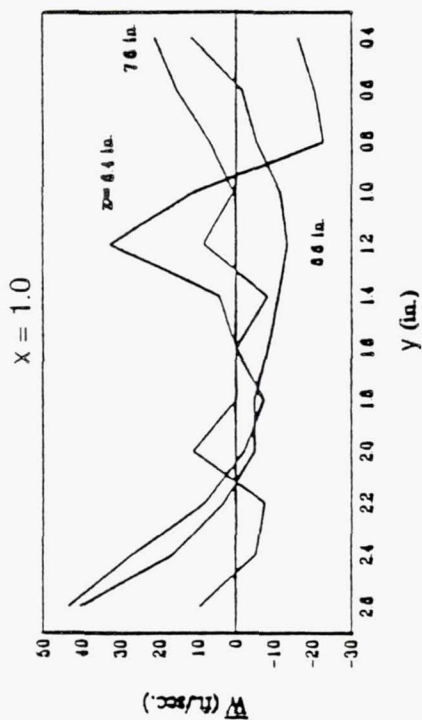
Figure 3.1.1-49. Line plots of V at $x = 4.00, 4.50, 6.00$, and 9.00 in.



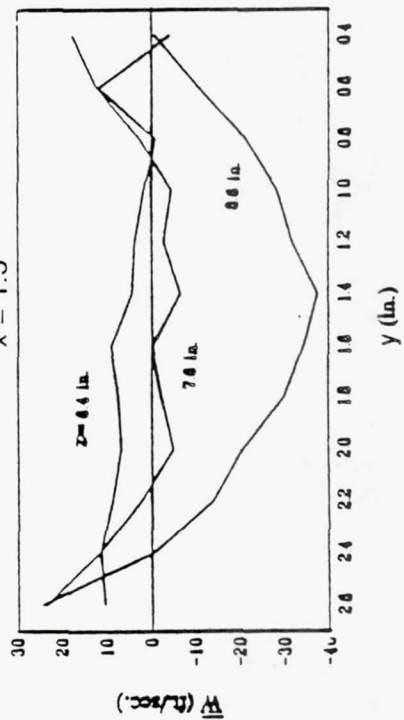
(c)



(d)



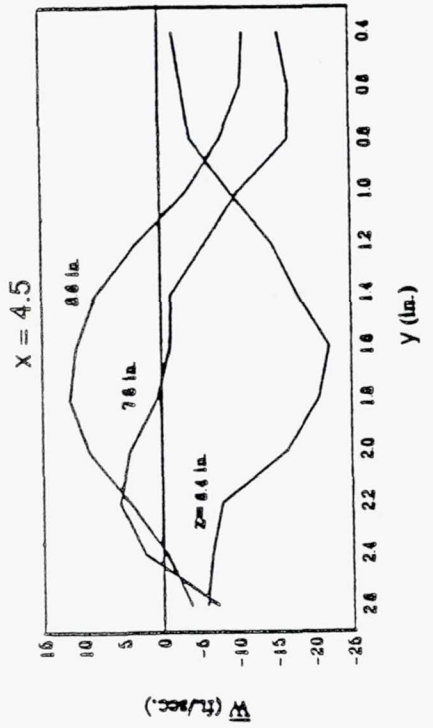
(a)



(b)

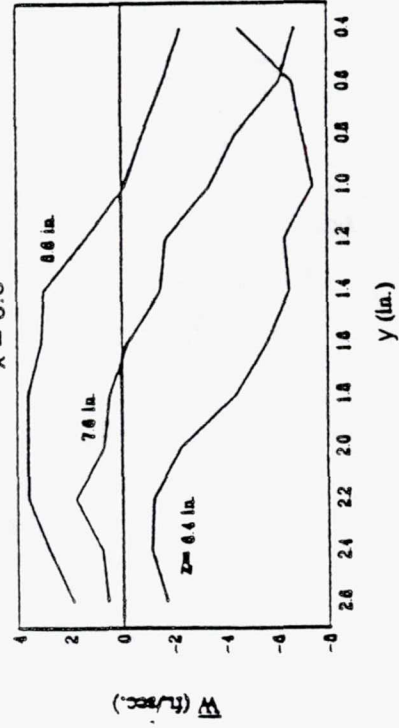
TE92-2302

Figure 3.1.1-50. Line plots of W at $x = 1.00, 1.50, 2.00,$ and 2.50 in.



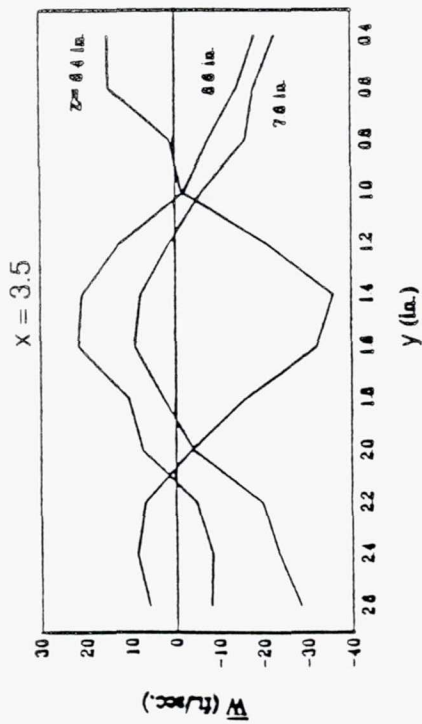
(c)

$x = 6.0$



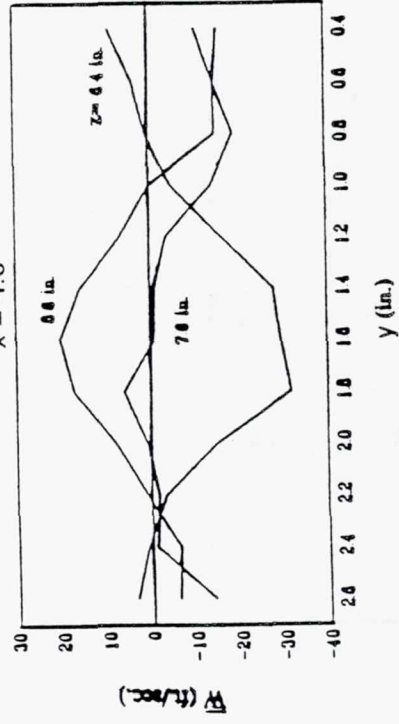
(d)

TE92-2303



(a)

$x = 4.0$



(b)

Figure 3.1.1-51. Line plots of W at $x = 3.50, 4.00, 4.50$, and 6.00 in.

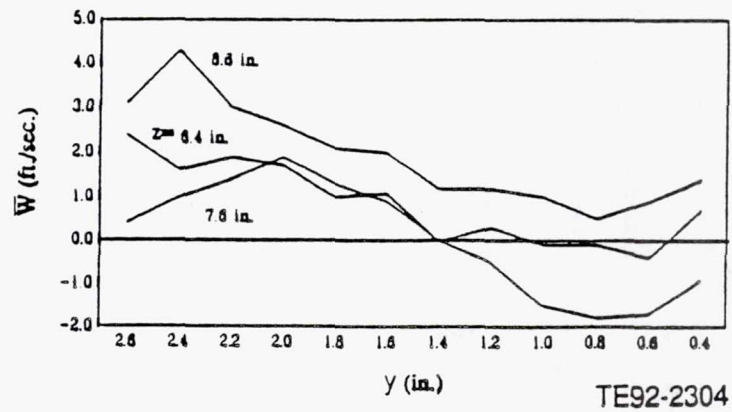
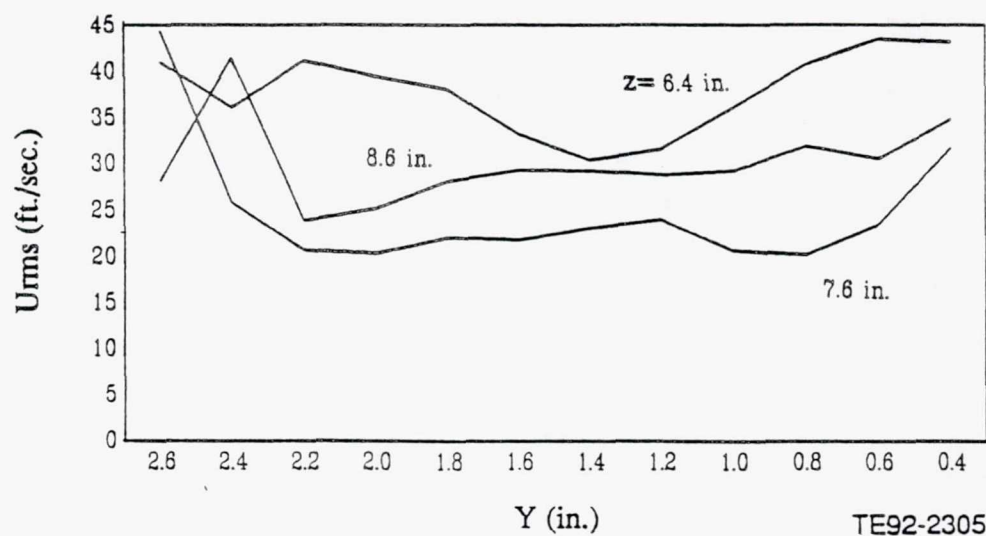
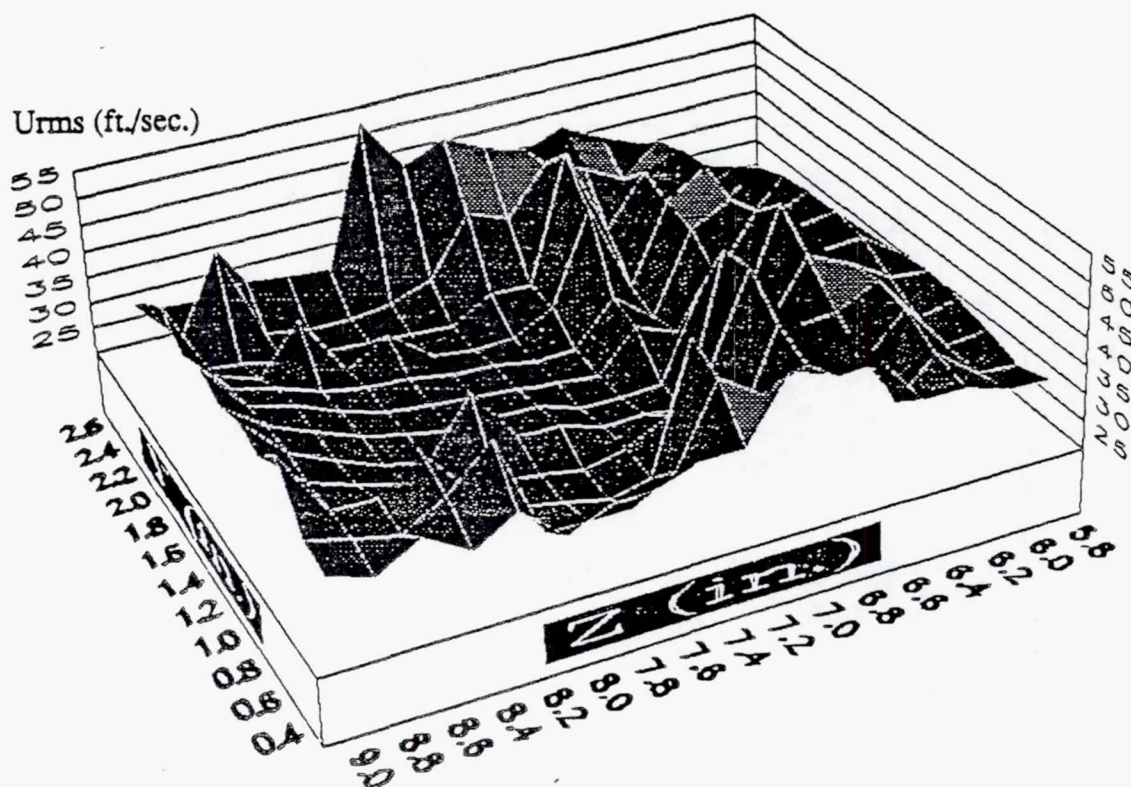
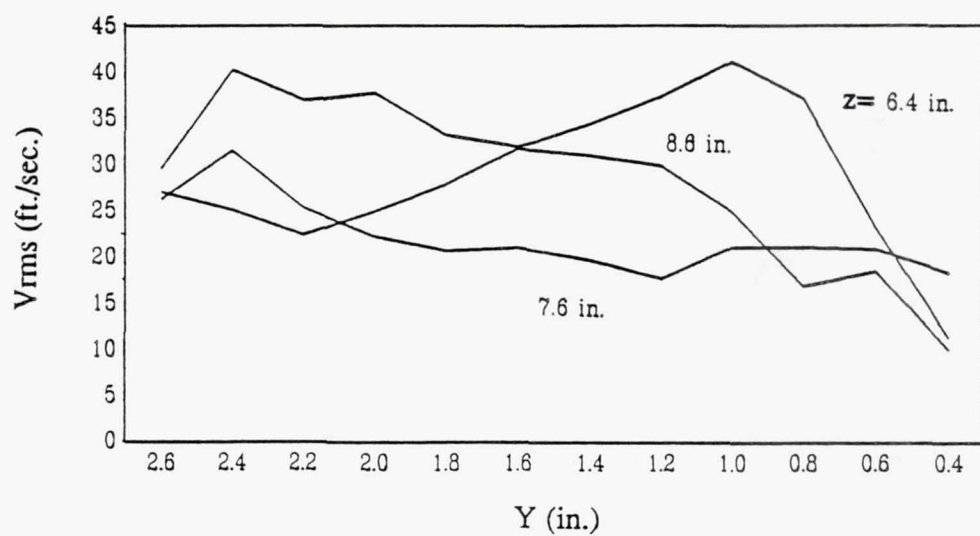
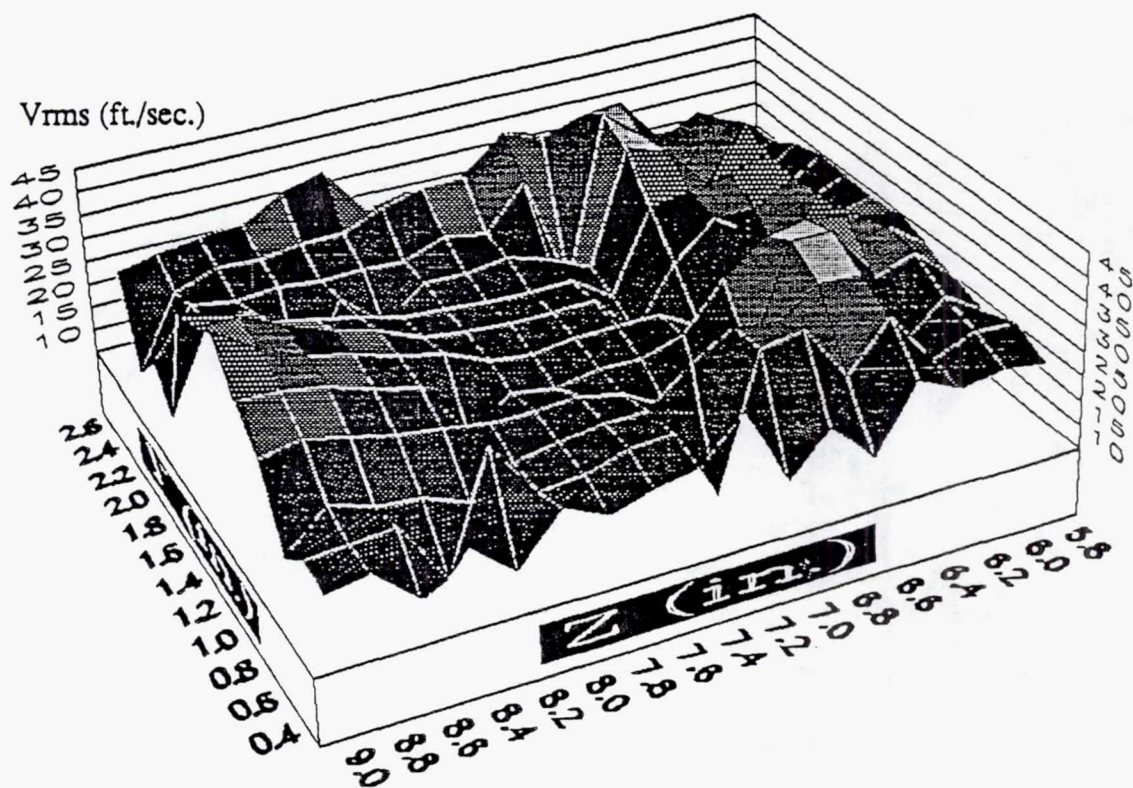


Figure 3.1.1-52. Line plots of \bar{W} at $x=9.00$ in.



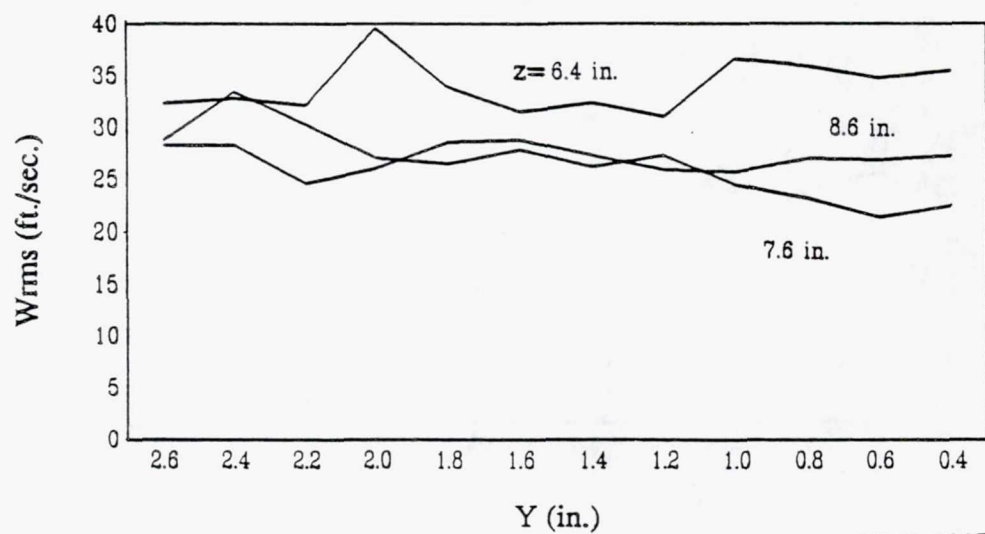
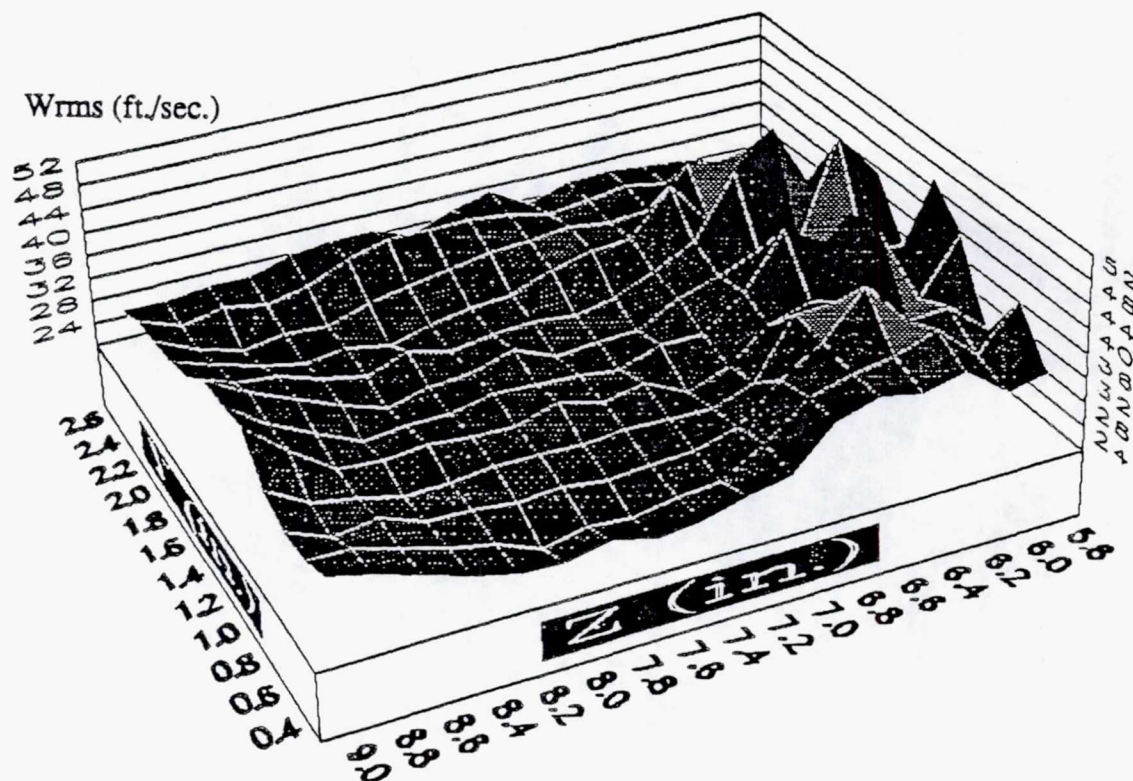
TE92-2305

Figure 3.1.1-53. Contour and line plots of U_{rms} at $x=1.00$ in.



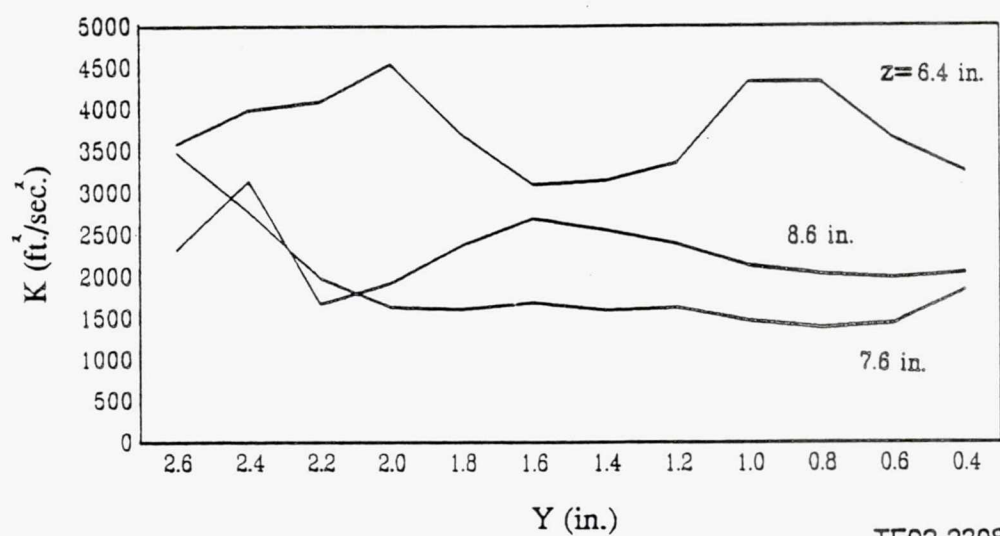
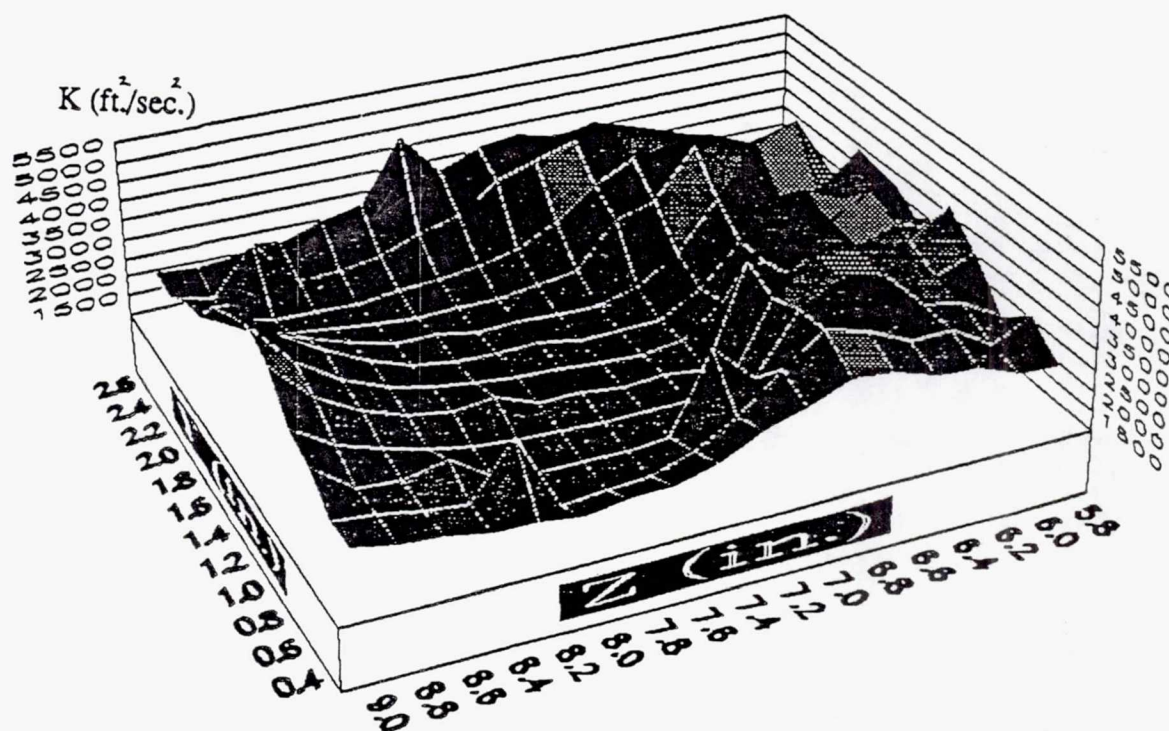
TE92-2306

Figure 3.1.1-54. Contour and line plots of V_{rms} at $x=1.00$ in.



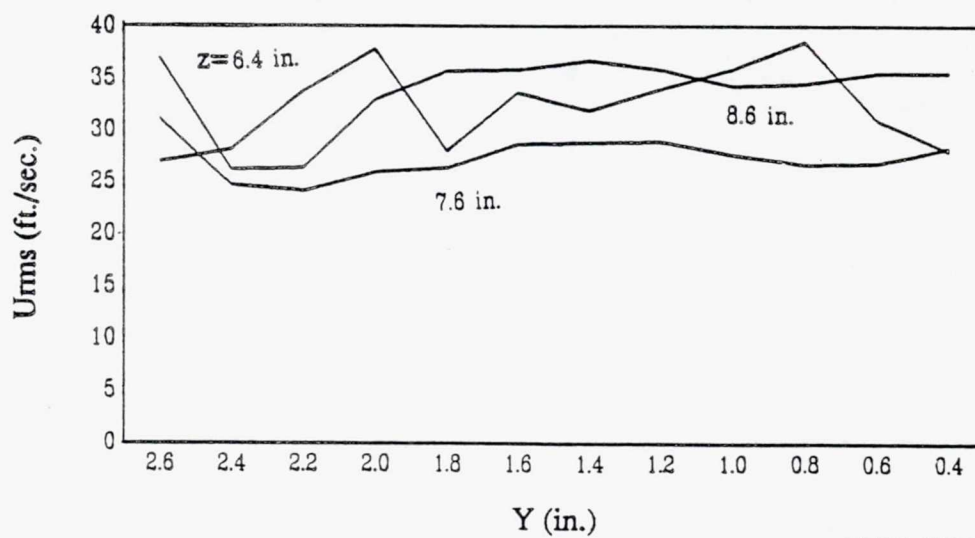
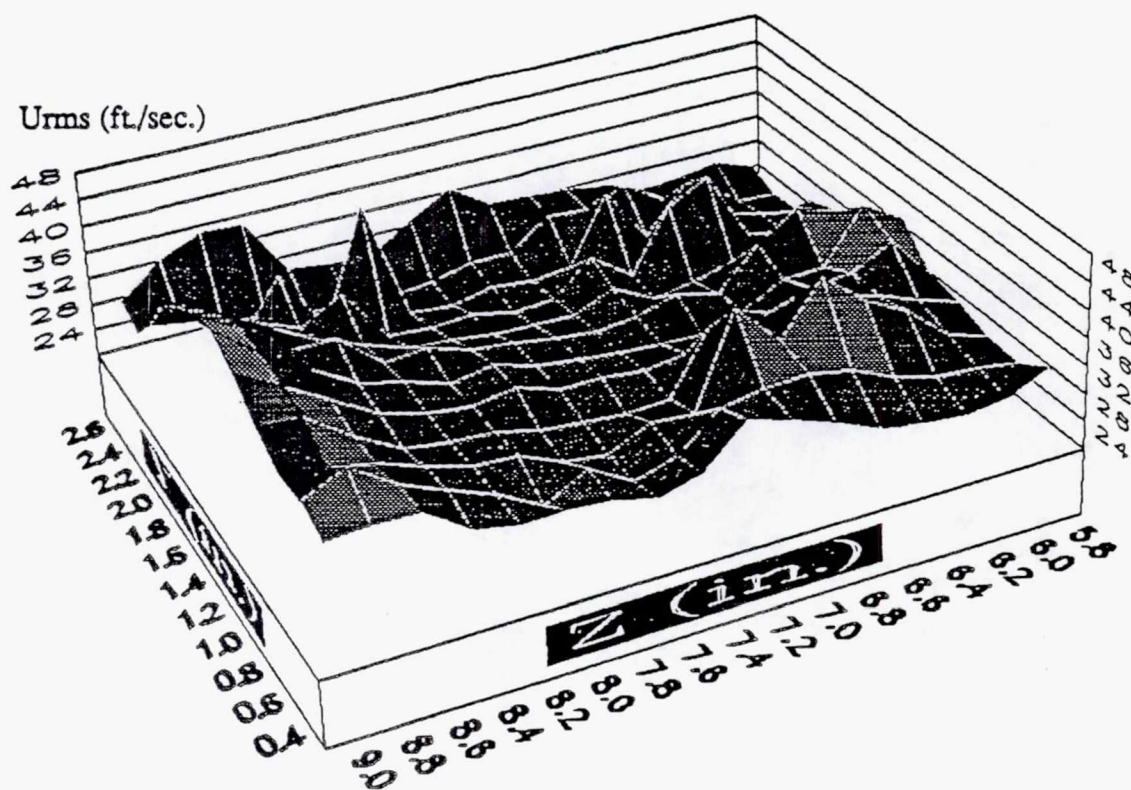
TE92-2307

Figure 3.1.1-55. Contour and line plots of W_{rms} at $x=1.00$ in.



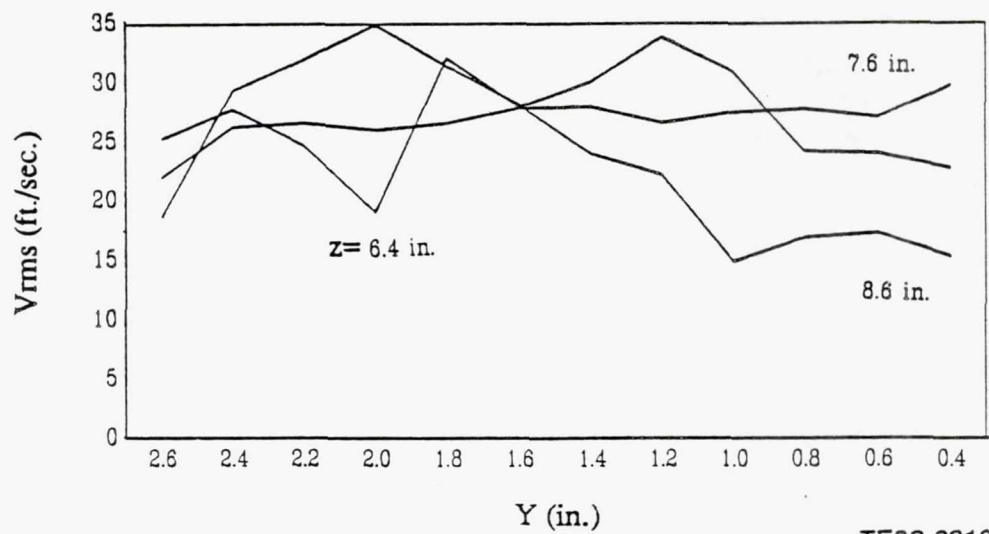
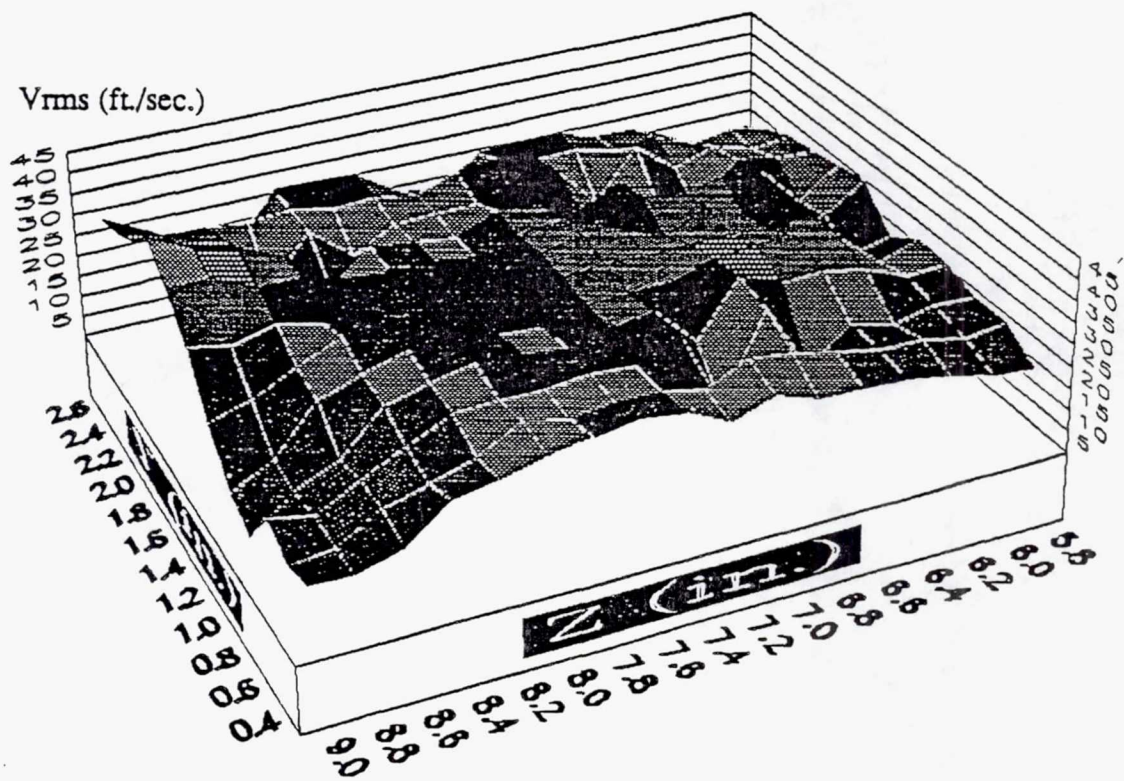
TE92-2308

Figure 3.1.1-56. Contour and line plots of K at $x=1.00$ in.



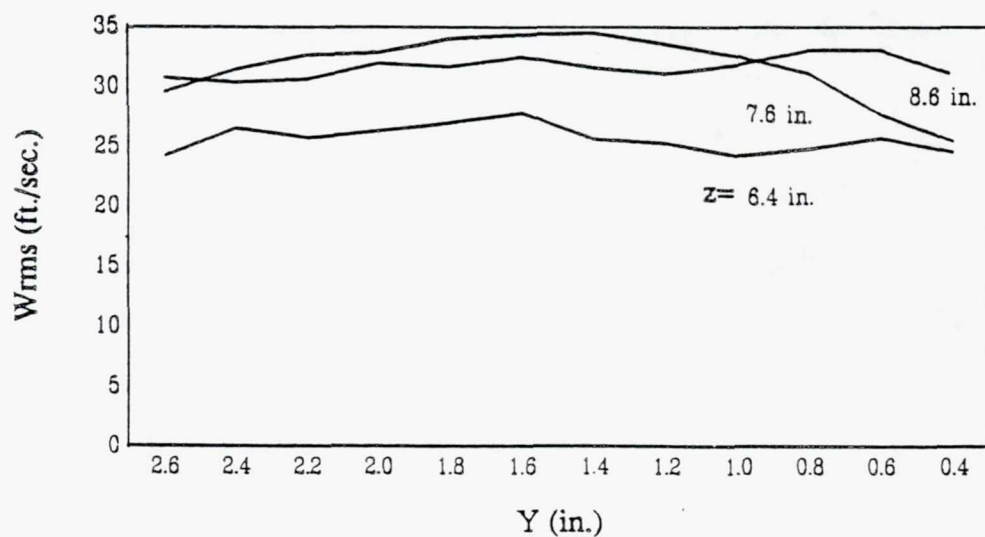
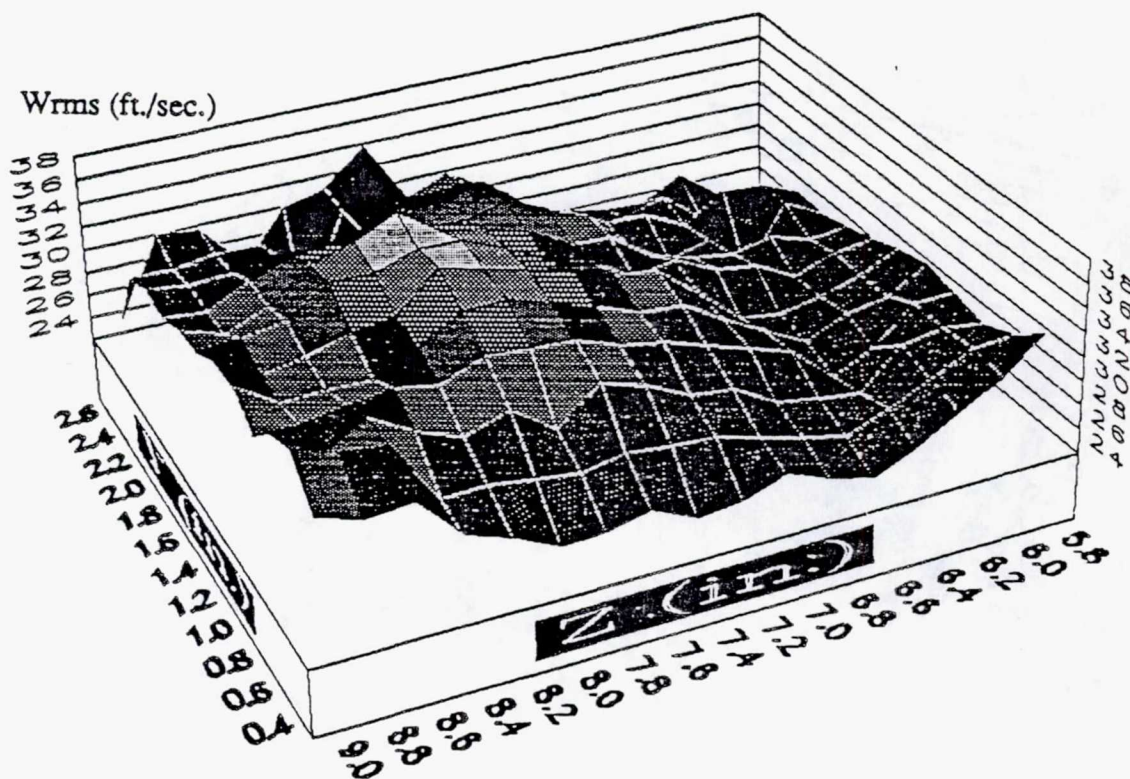
TE92-2309

Figure 3.1.1-57. Contour and line plots of U_{rms} at $x=1.50$ in.



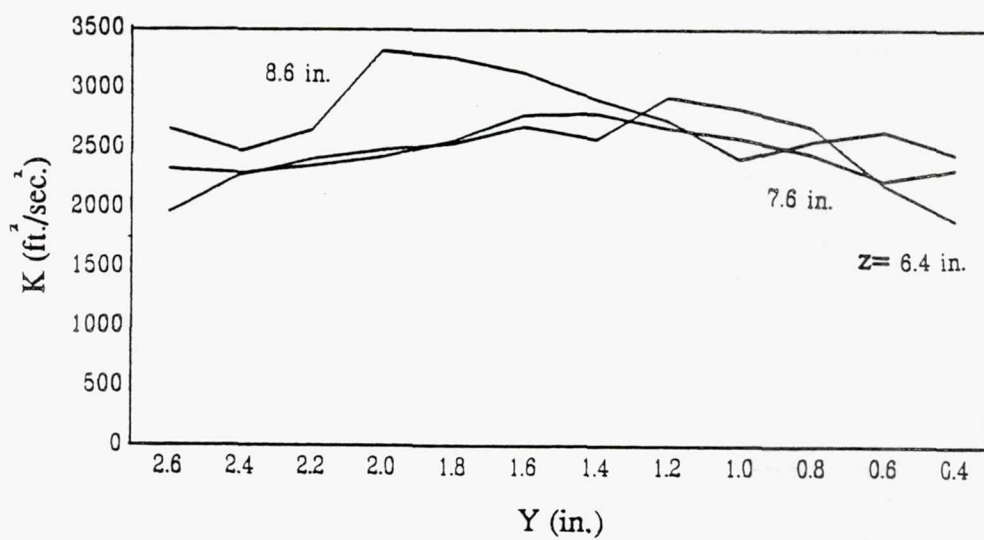
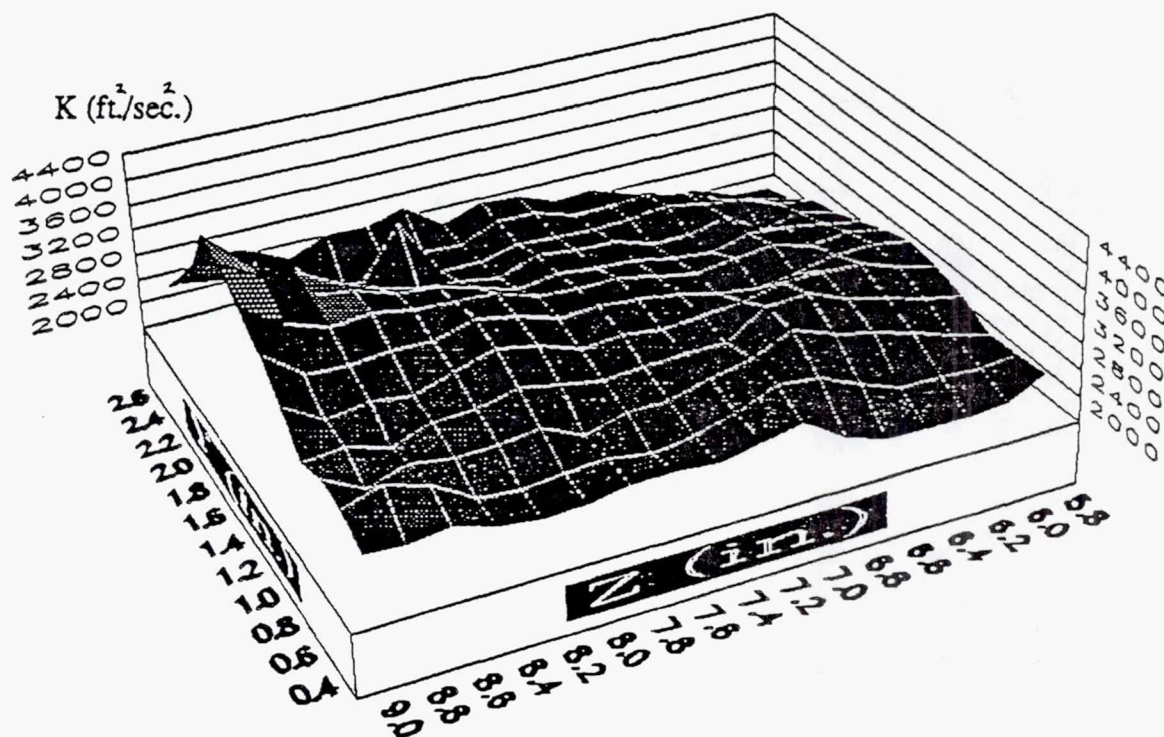
TE92-2310

Figure 3.1.1-58. Contour and line plots of V_{rms} at $x=1.50$ in.



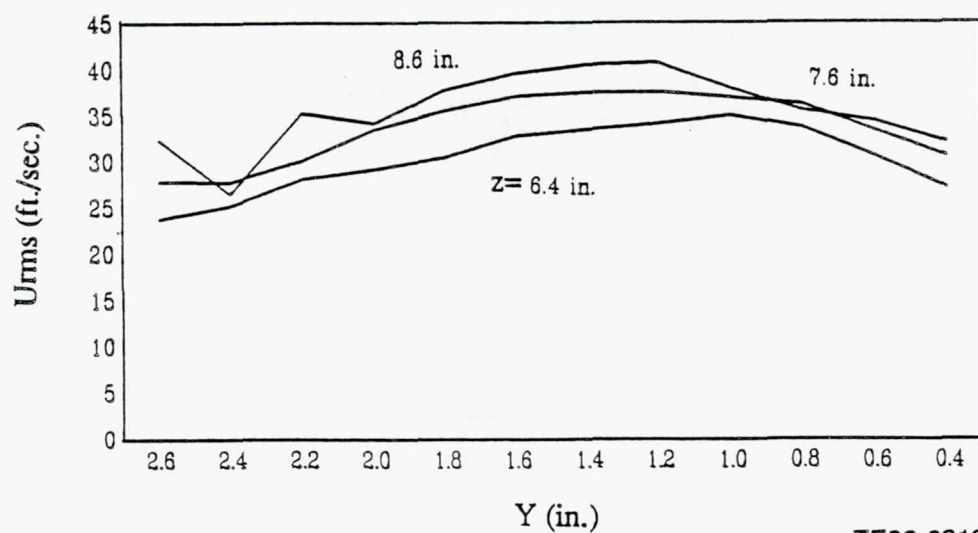
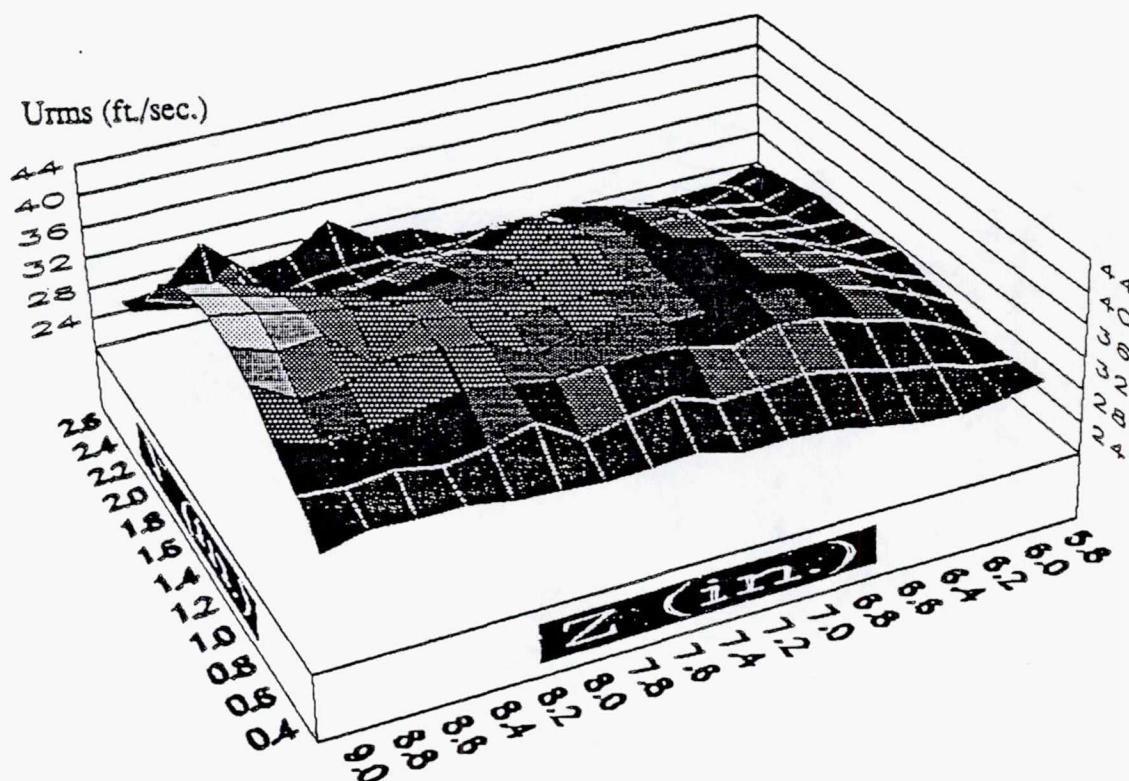
TE92-2311

Figure 3.1.1-59. Contour and line plots of W_{rms} at $x=1.50$ in.



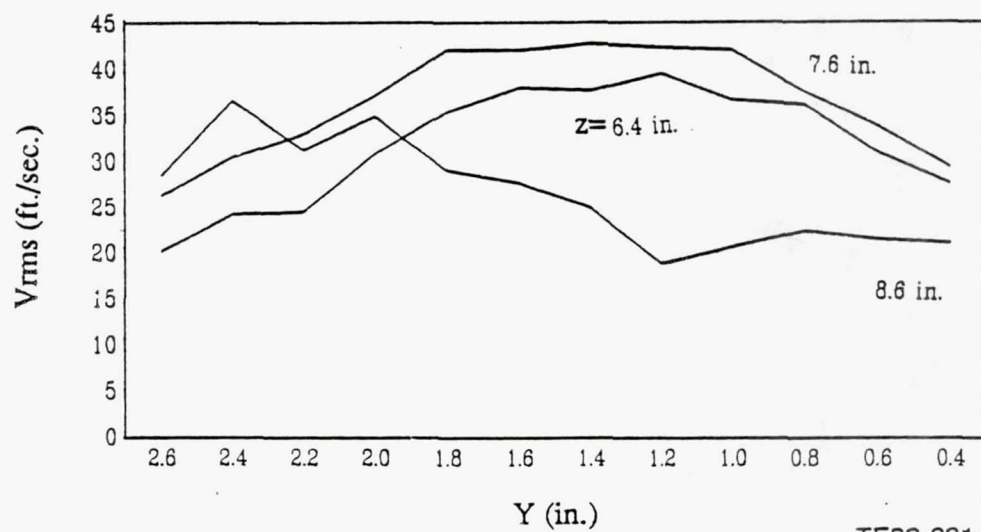
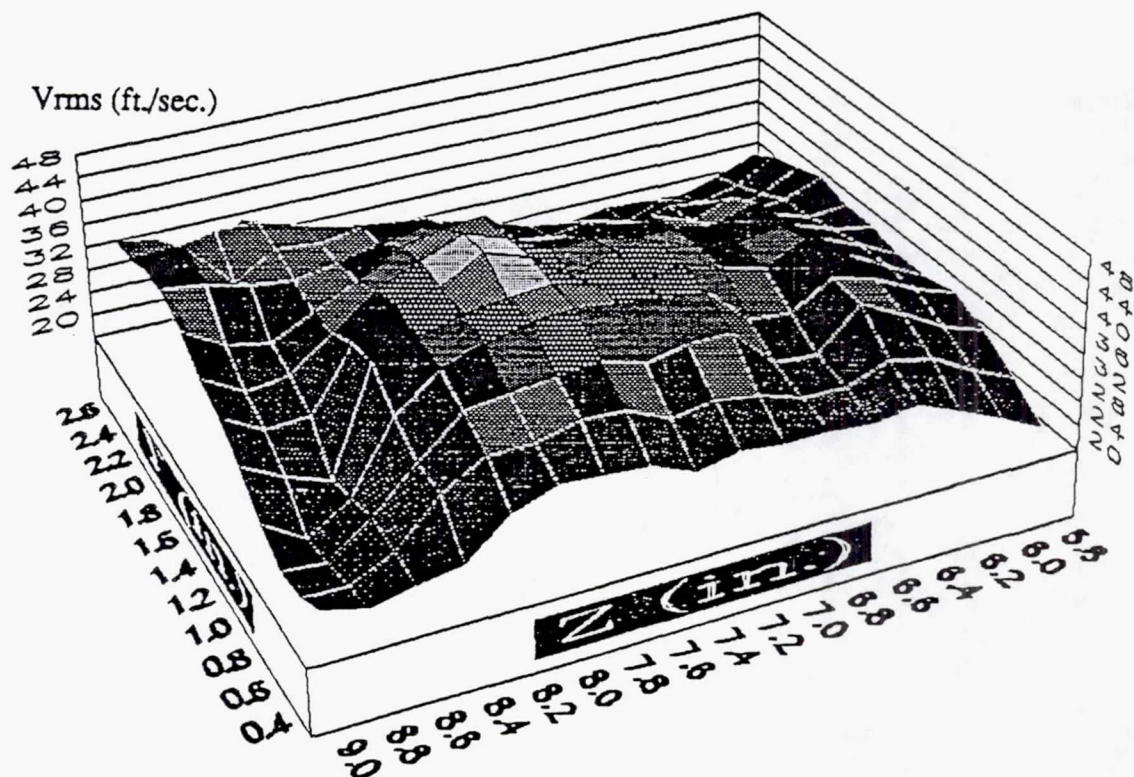
TE92-2312

Figure 3.1.1-60. Contour and line plots of K at $x=1.50$ in.



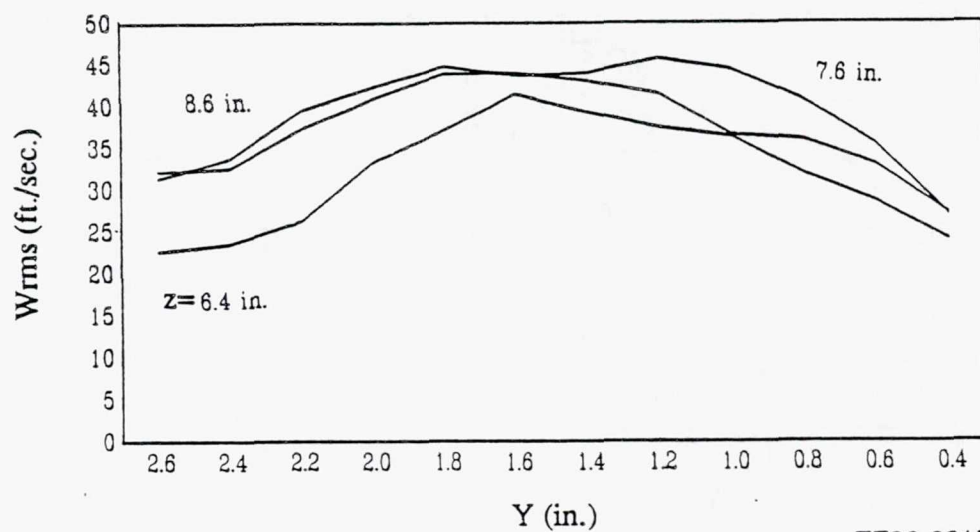
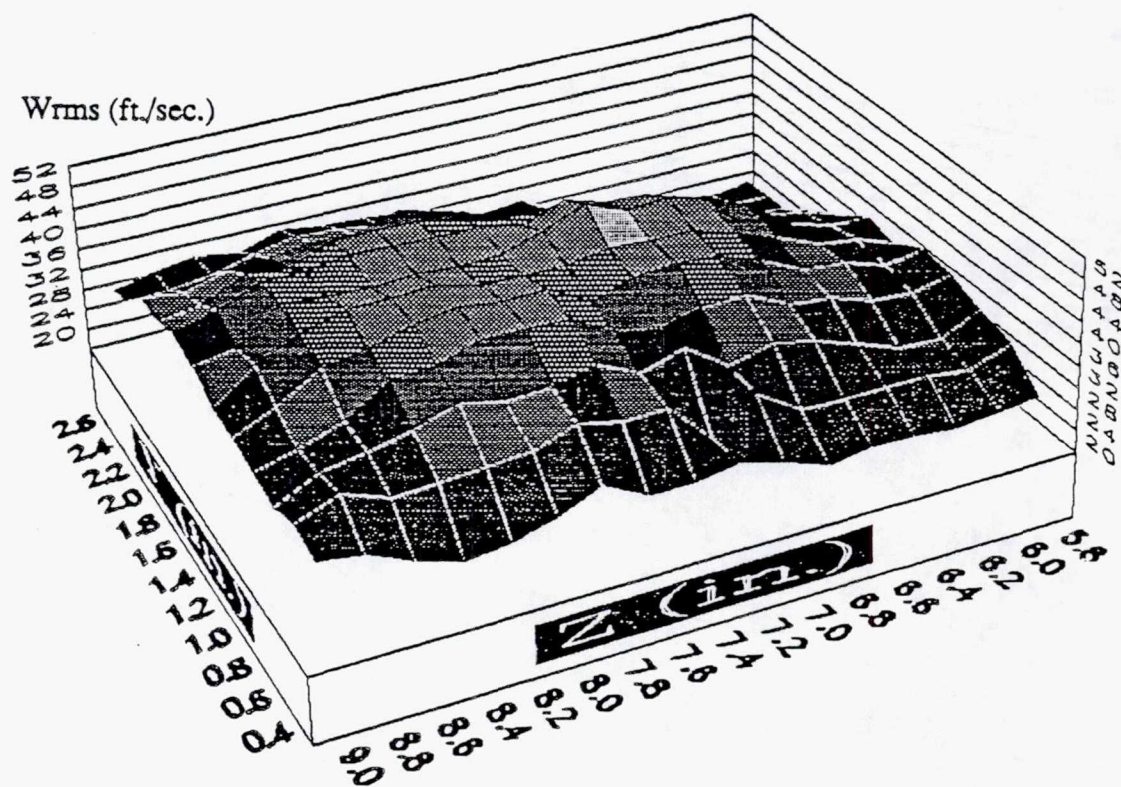
TE92-2313

Figure 3.1.1-61. Contour and line plots of U_{rms} at $x=2.00$ in.



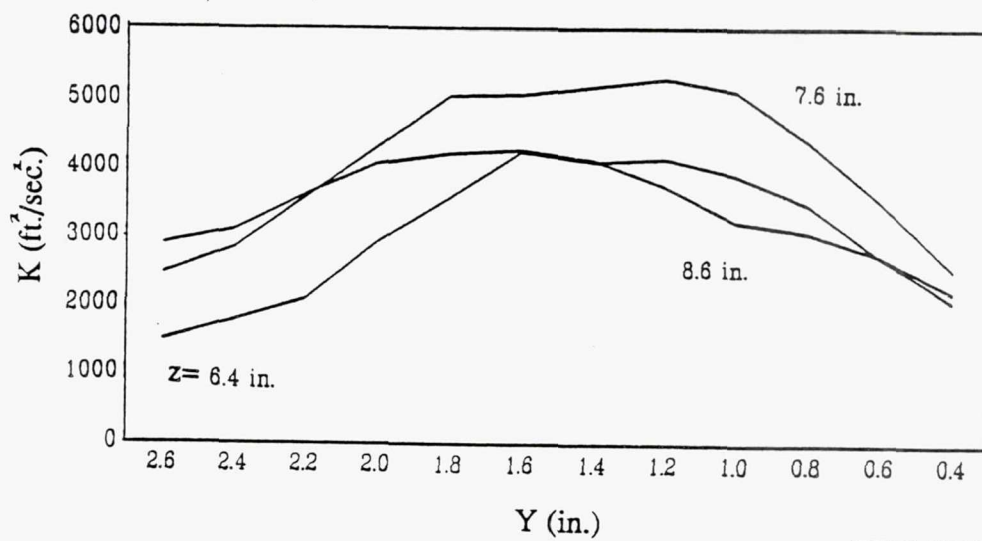
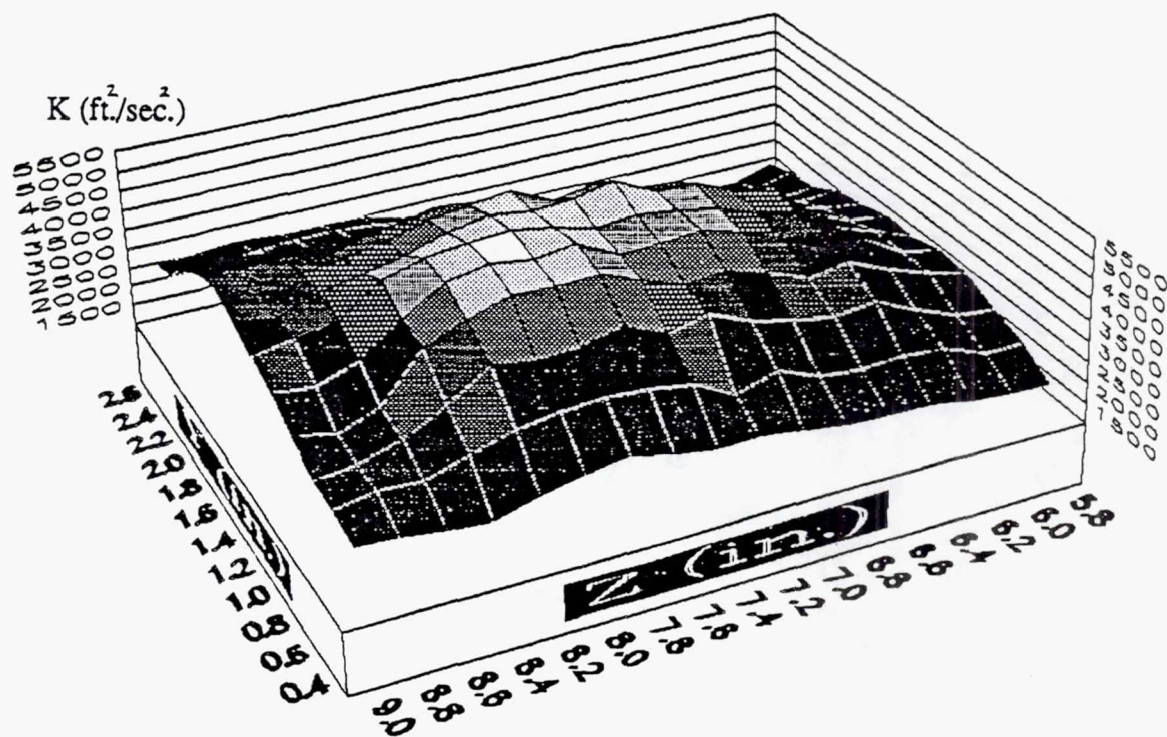
TE92-2314

Figure 3.1.1-62. Contour and line plots of V_{rms} at $x=2.00$ in.



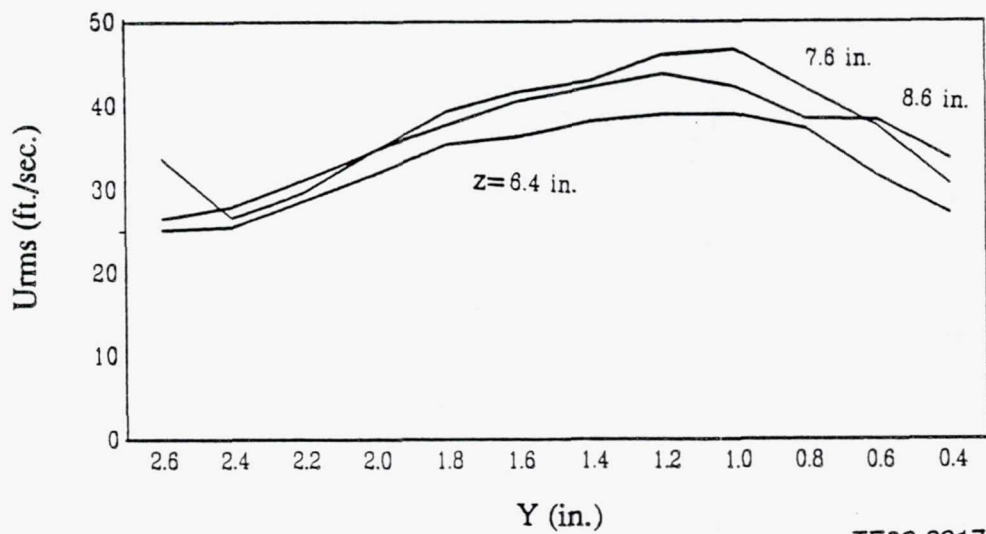
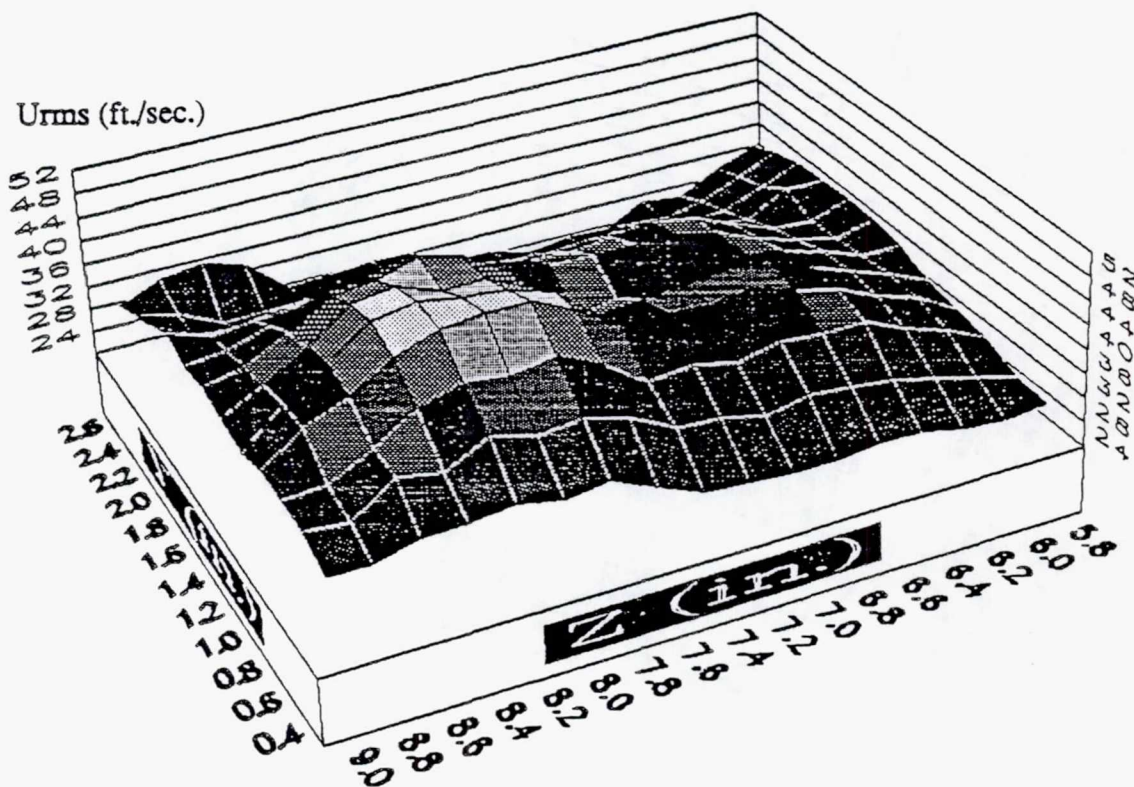
TE92-2315

Figure 3.1.1-63. Contour and line plots of W_{rms} at $x=2.00$ in.



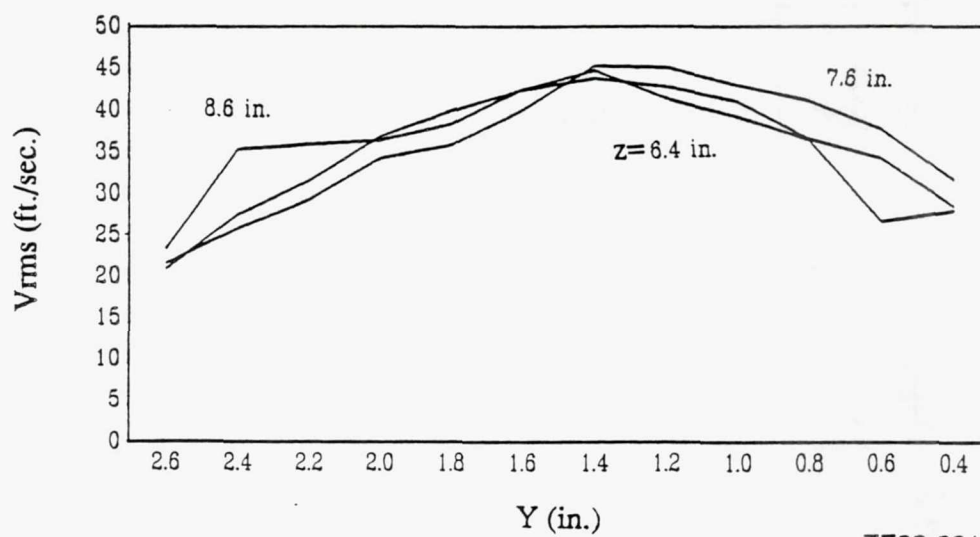
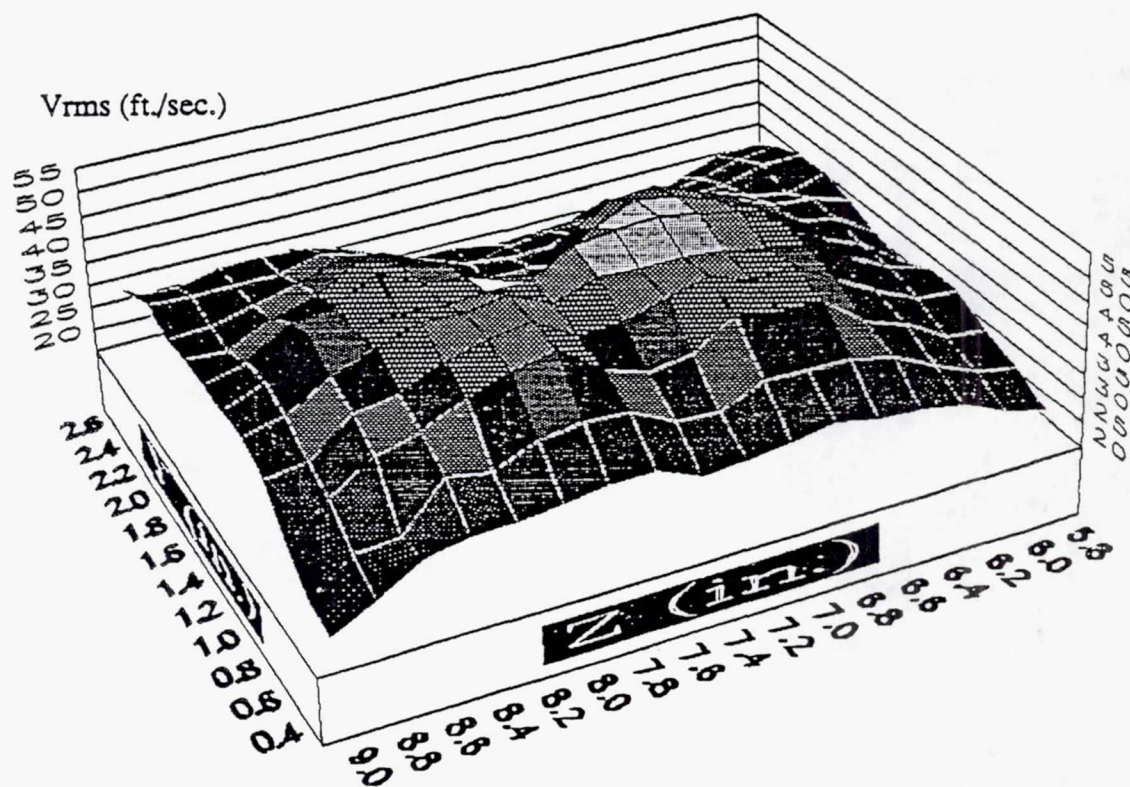
TE92-2316

Figure 3.1.1-64. Contour and line plots of K at $x=2.00$ in.



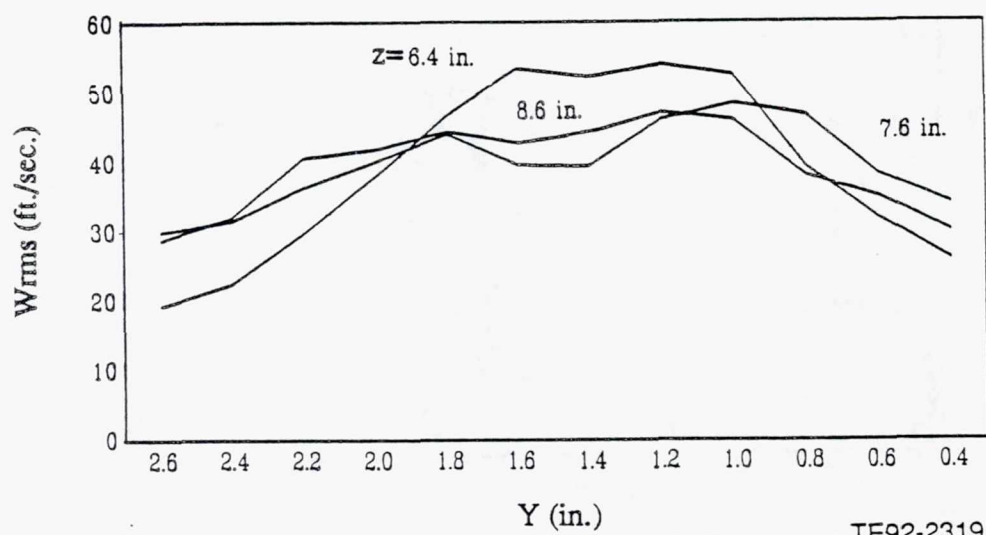
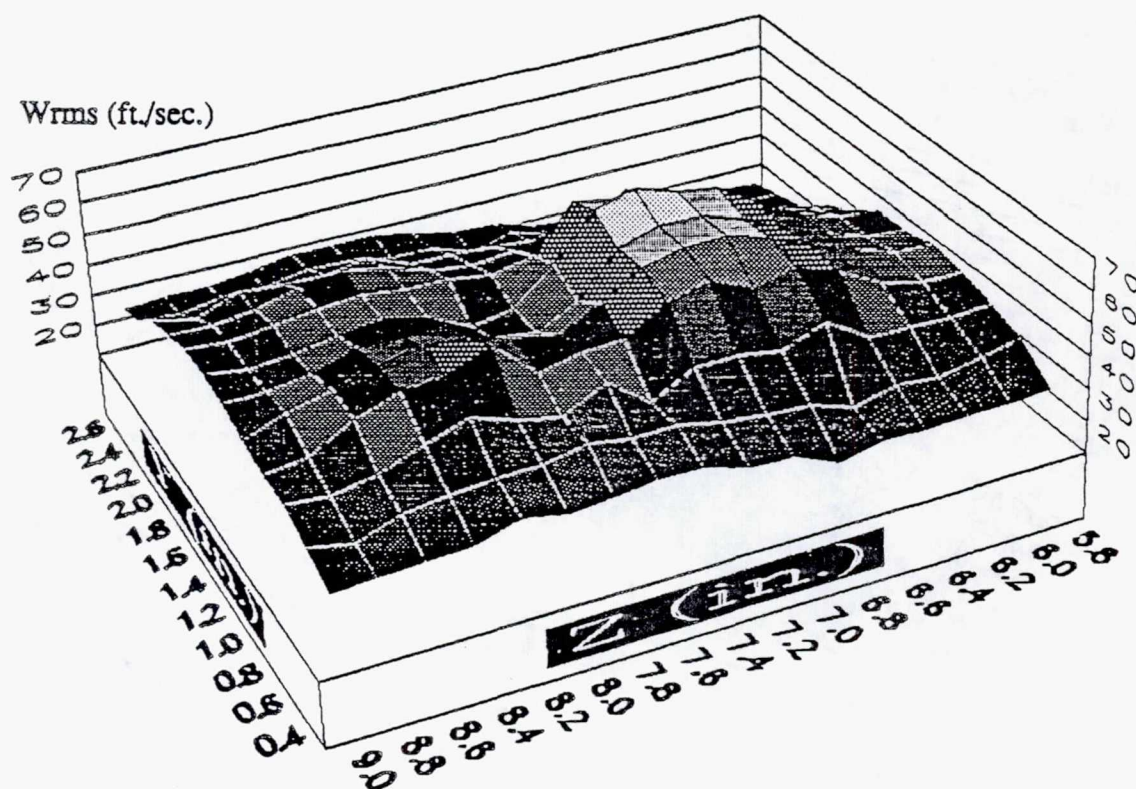
TE92-2317

Figure 3.1.1-65. Contour and line plots of U_{rms} at $x=2.50$ in.



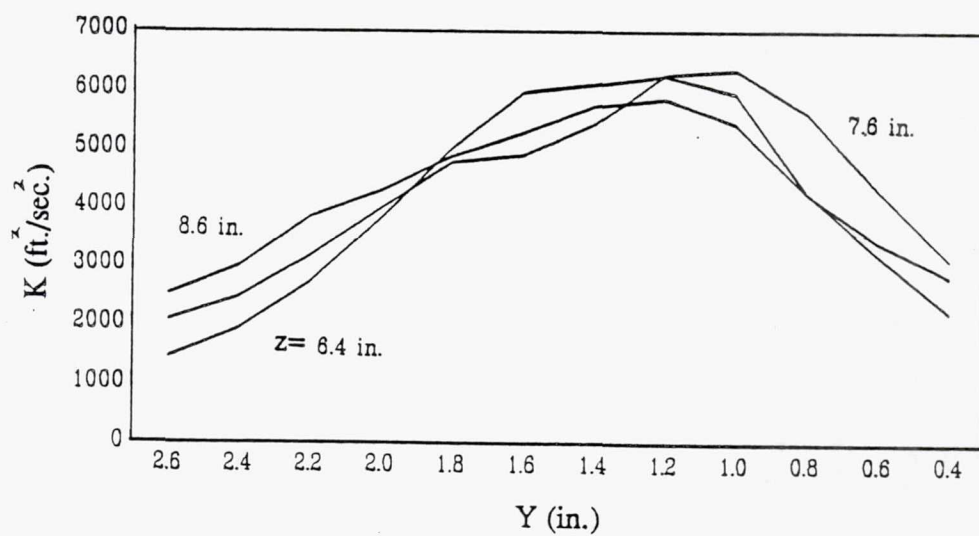
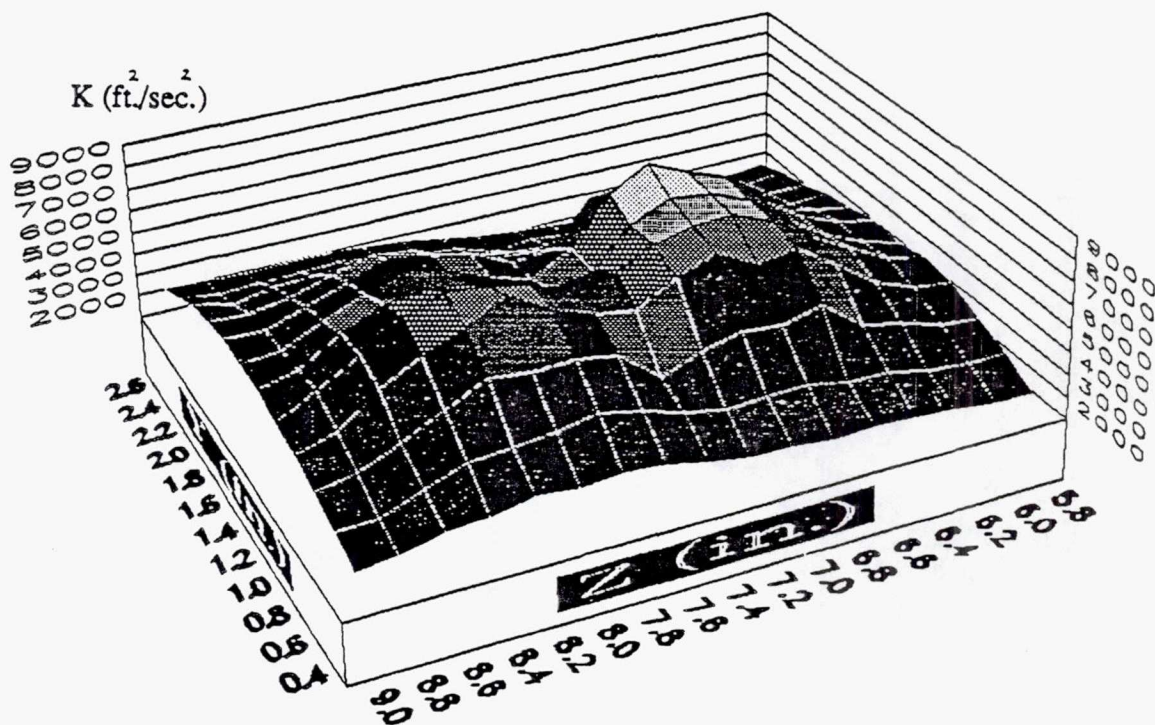
TE92-2318

Figure 3.1.1-66. Contour and line plots of V_{rms} at $x=2.50$ in.



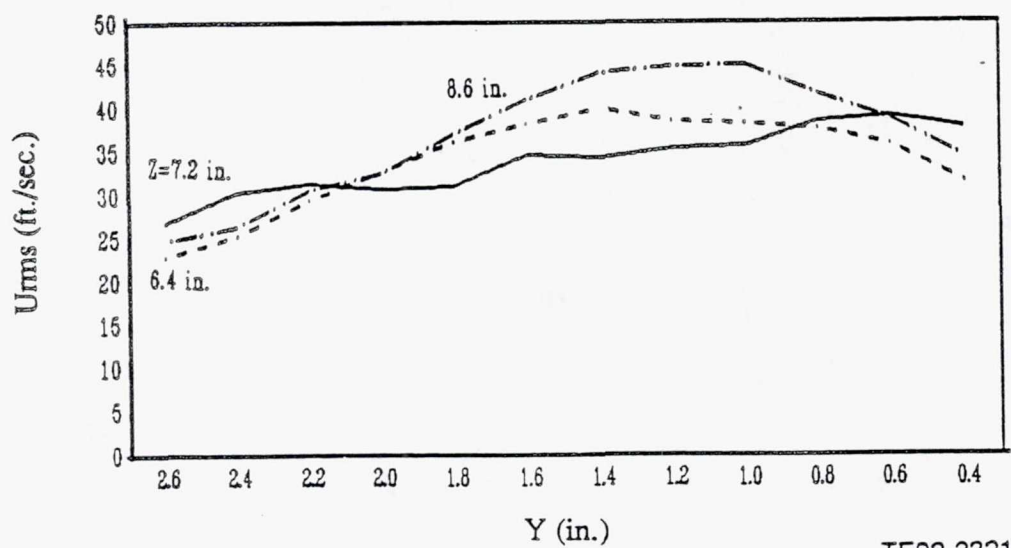
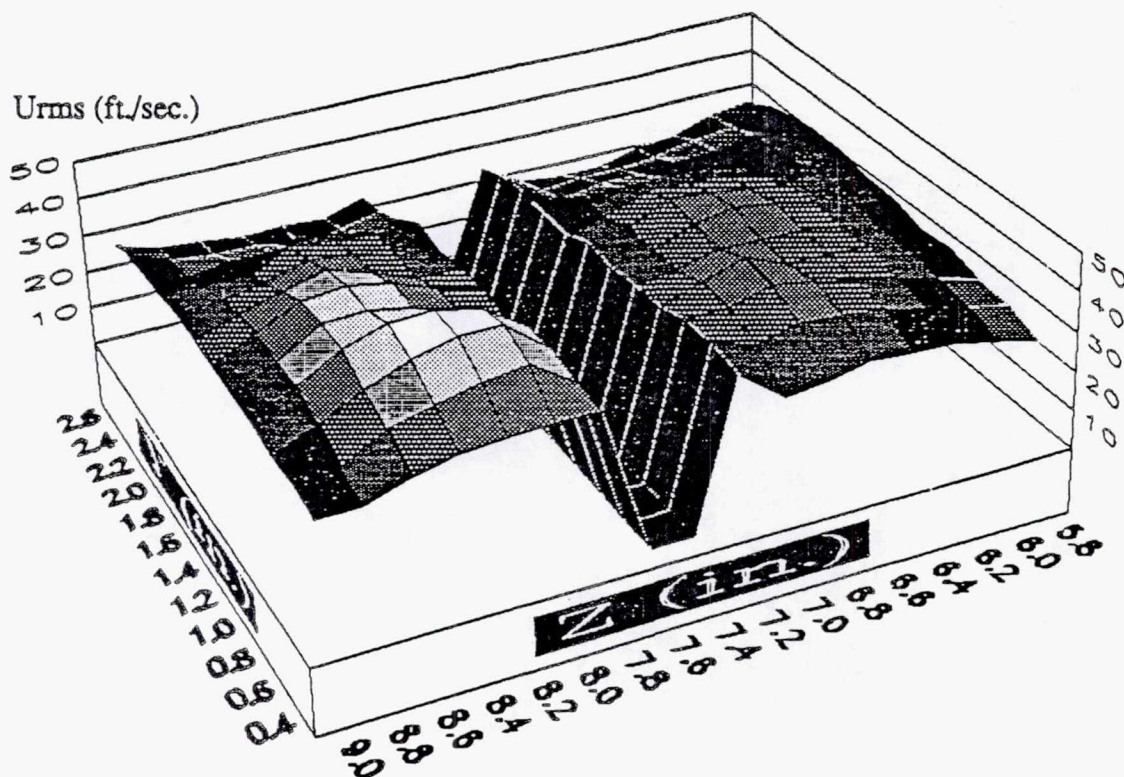
TE92-2319

Figure 3.1.1-67. Contour and line plots of W_{rms} at $x=2.50$ in.



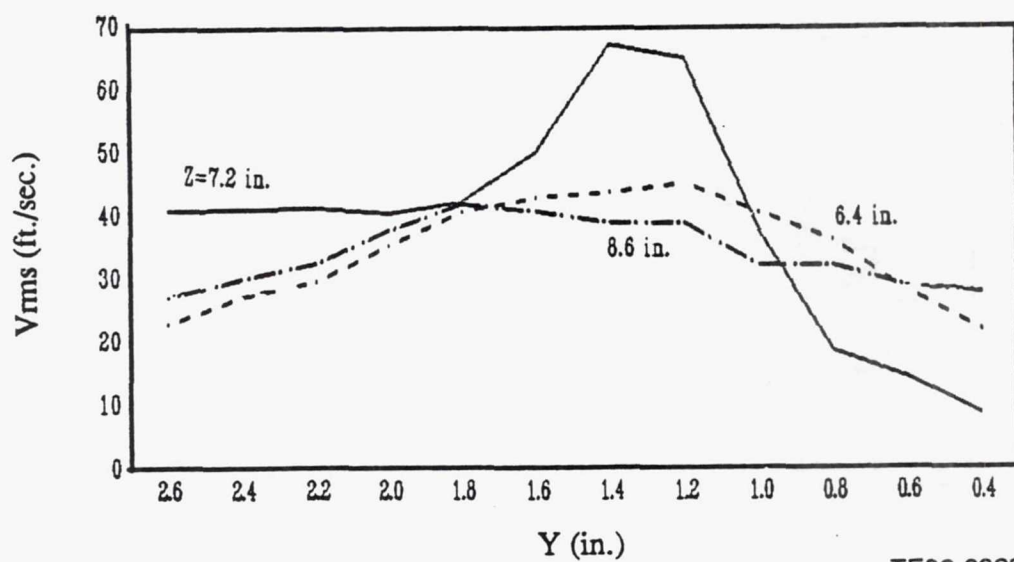
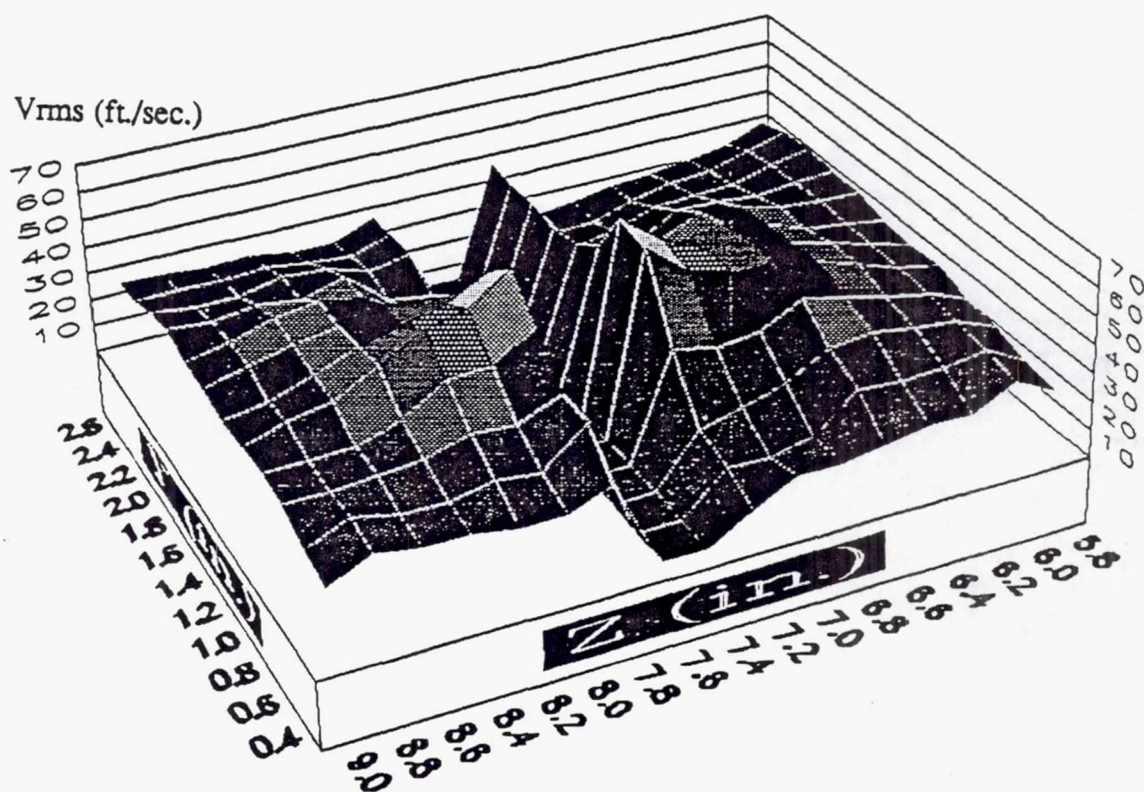
TE92-2320

Figure 3.1.1-68. Contour and line plots of K at $x=2.50$ in.



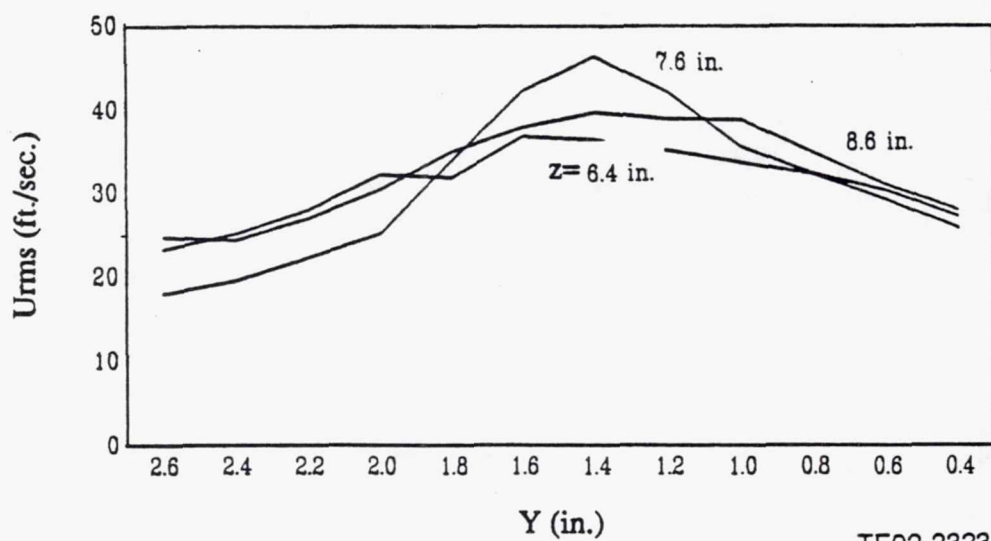
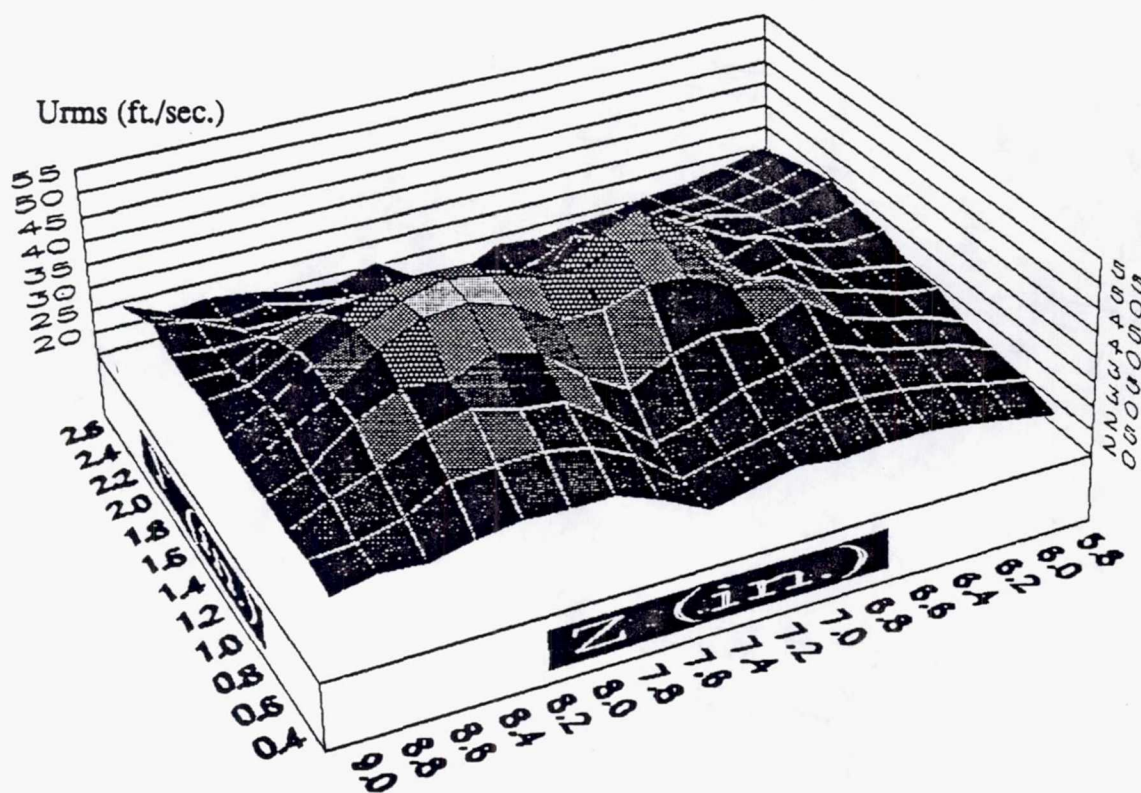
TE92-2321

Figure 3.1.1-69. Contour and line plots of U_{rms} at $x=3.00$ in.



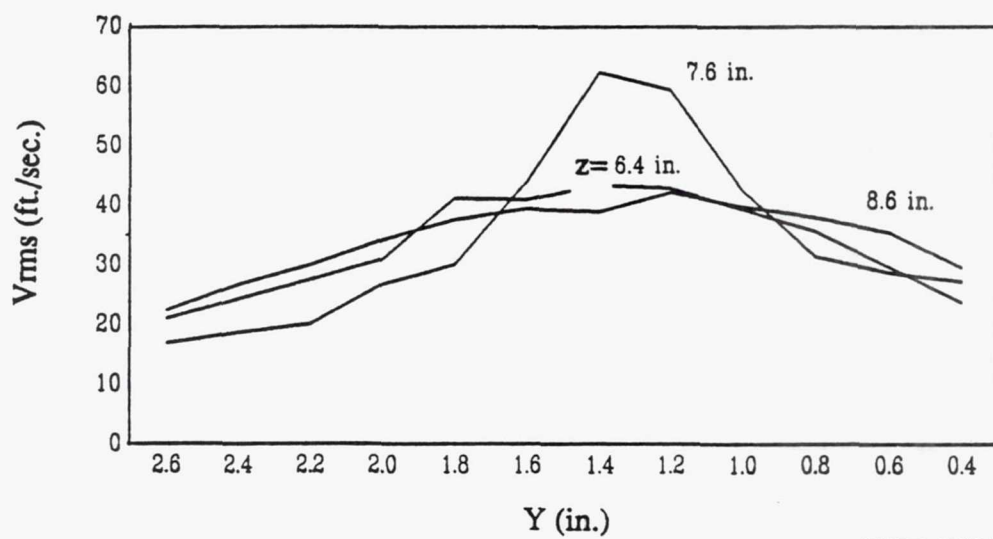
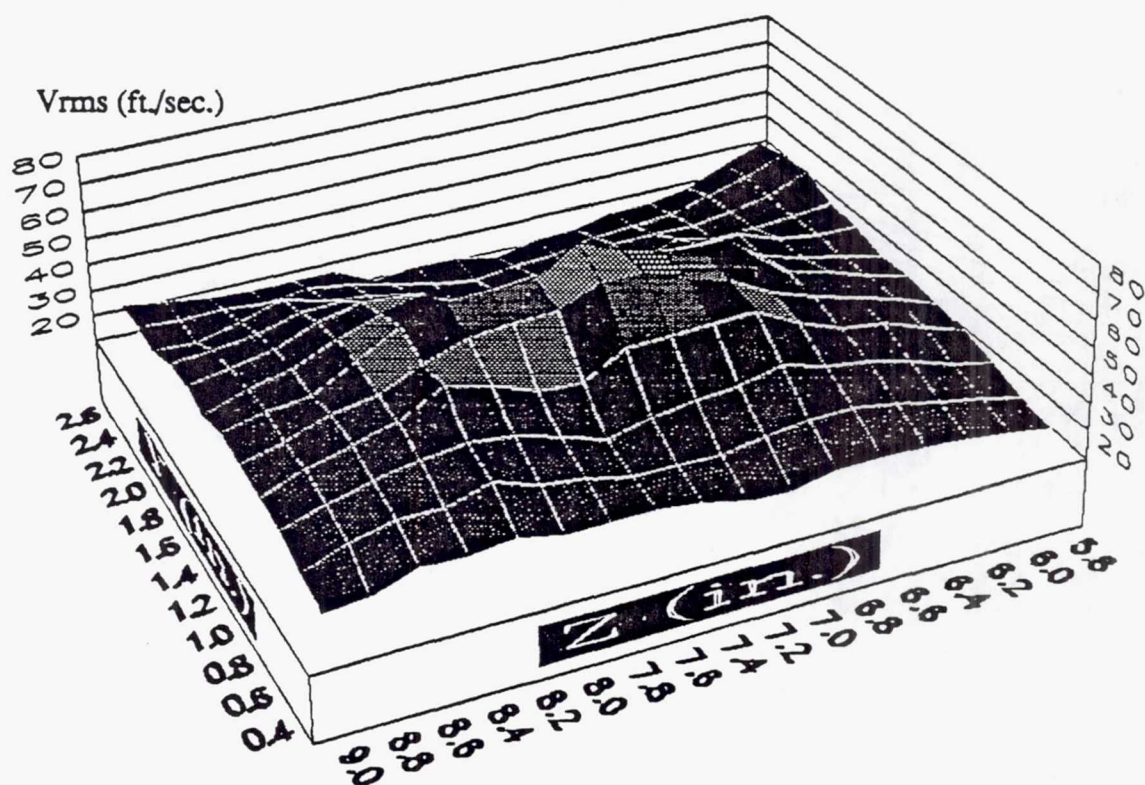
TE92-2322

Figure 3.1.1-70. Contour and line plots of V_{rms} at $x=3.00$ in.



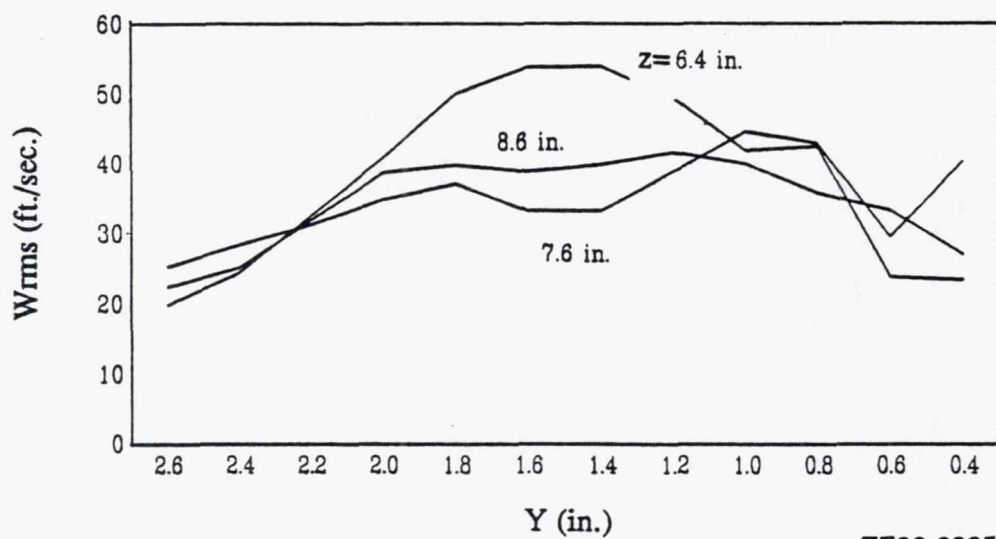
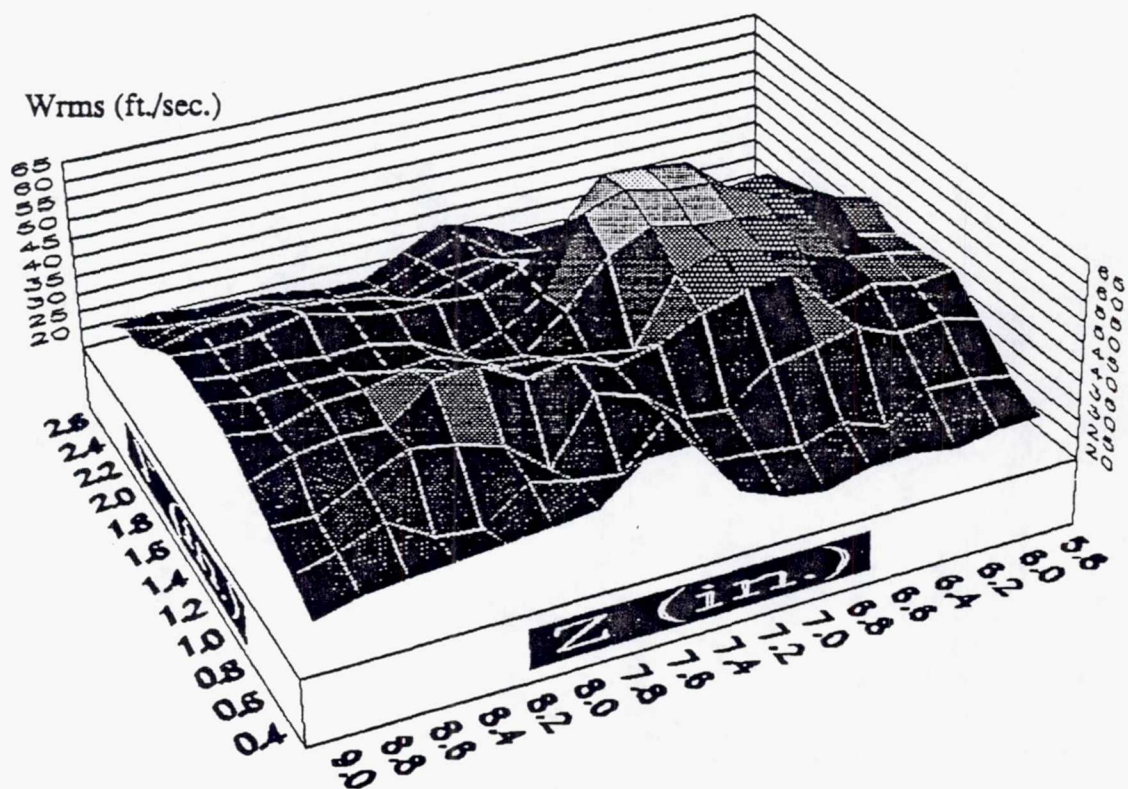
TE92-2323

Figure 3.1.1-71. Contour and line plots of U_{rms} at $x=3.50$ in.



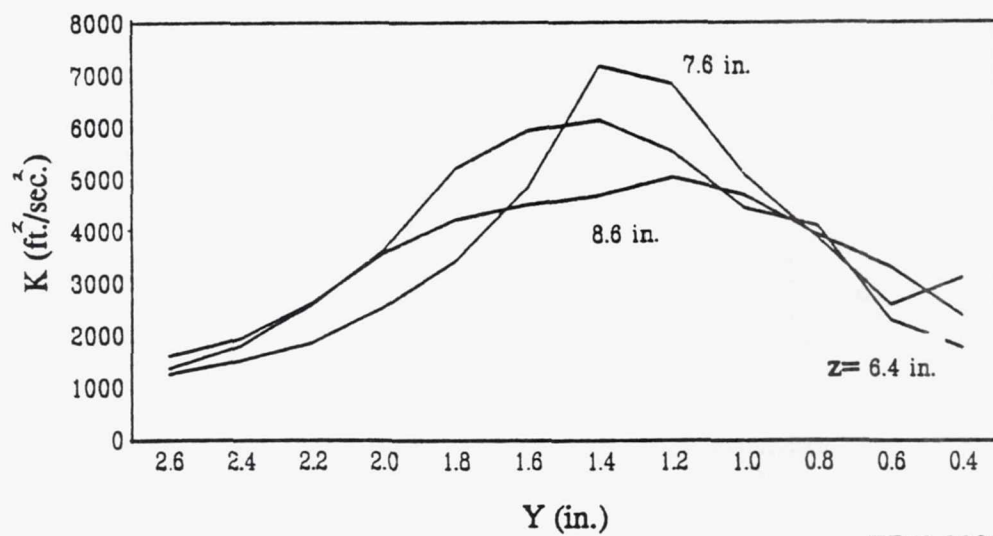
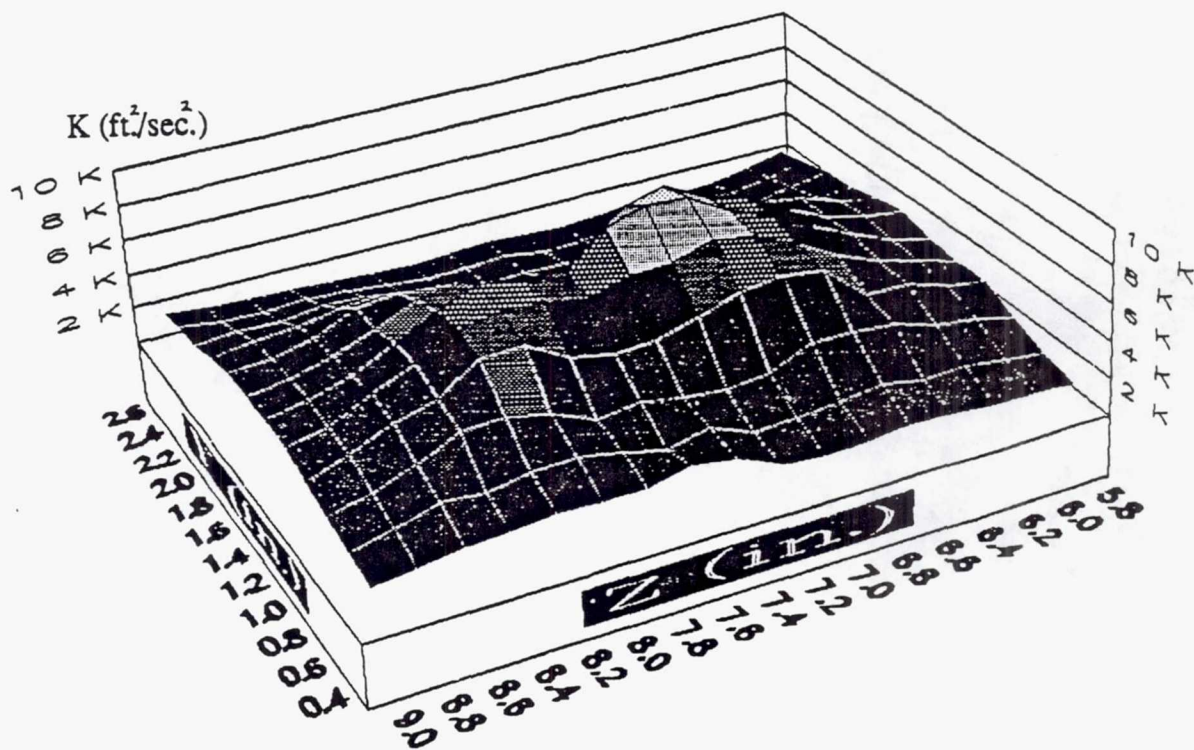
TE92-2324

Figure 3.1.1-72. Contour and line plots of V_{rms} at $x=3.50$ in.



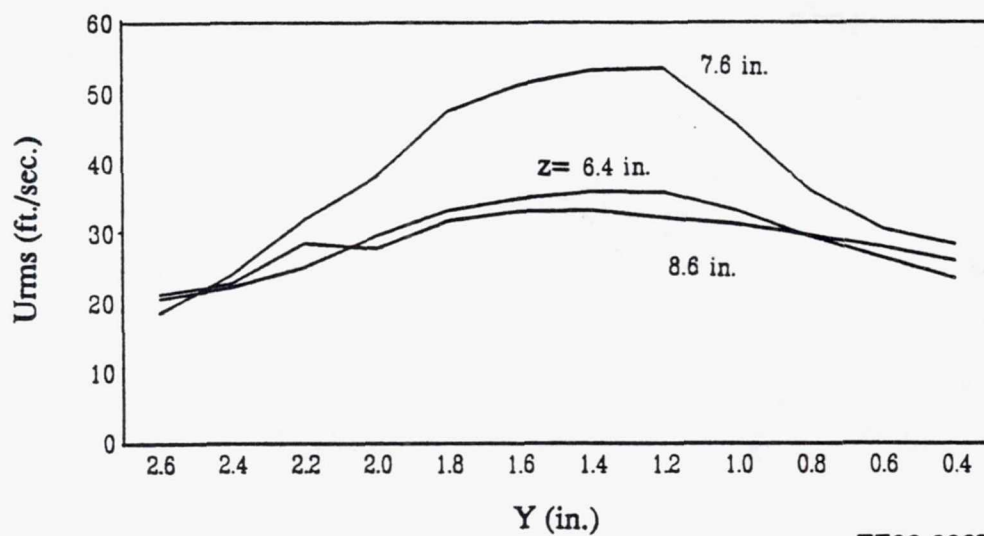
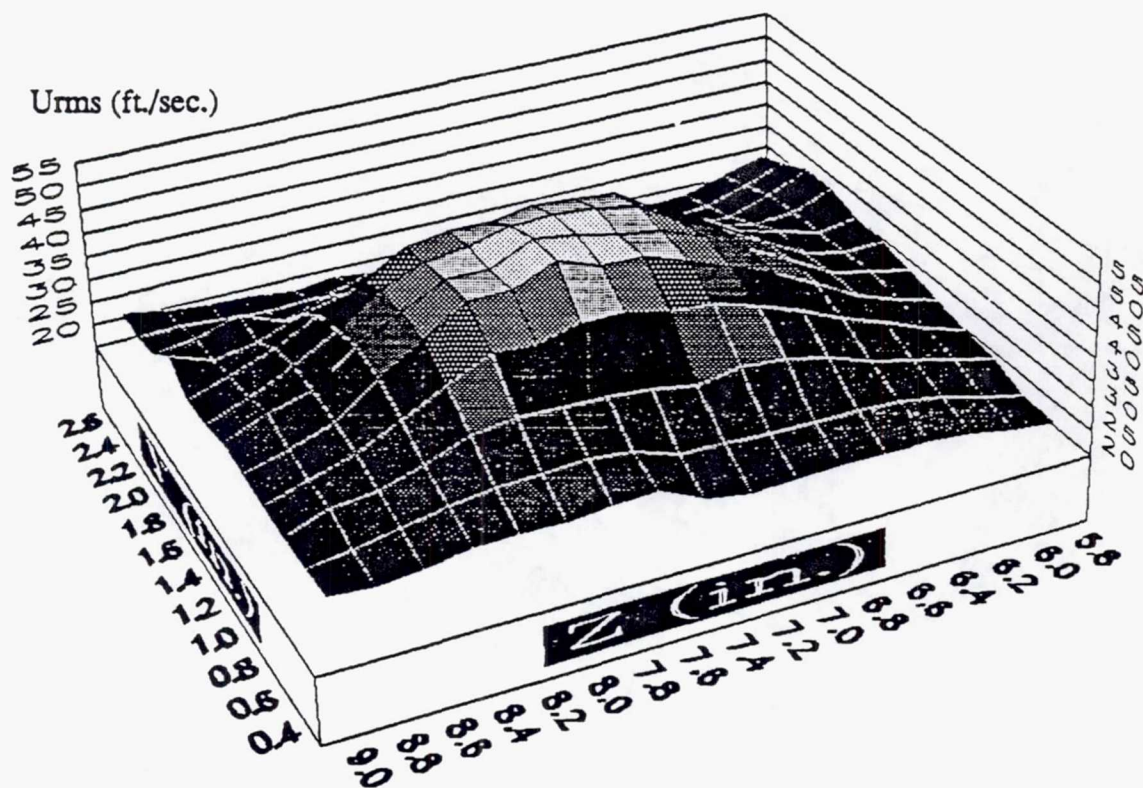
TE92-2325

Figure 3.1.1-73. Contour and line plots of W_{rms} at $x=3.50$ in.



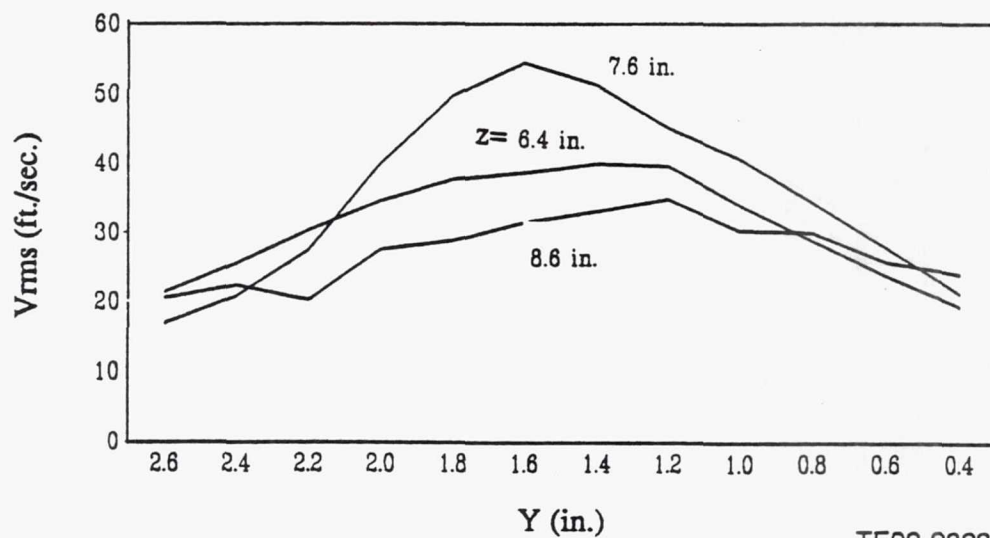
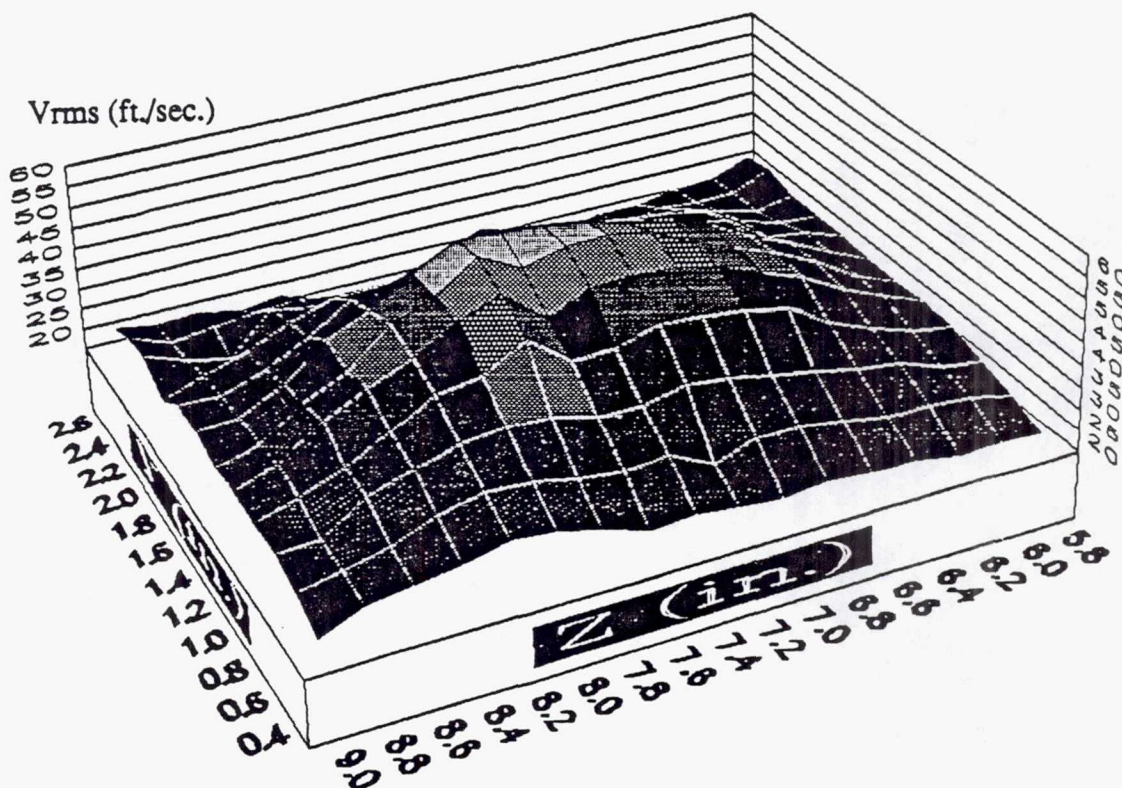
TE92-2326

Figure 3.1.1-74. Contour and line plots of K at $x=3.50$ in.



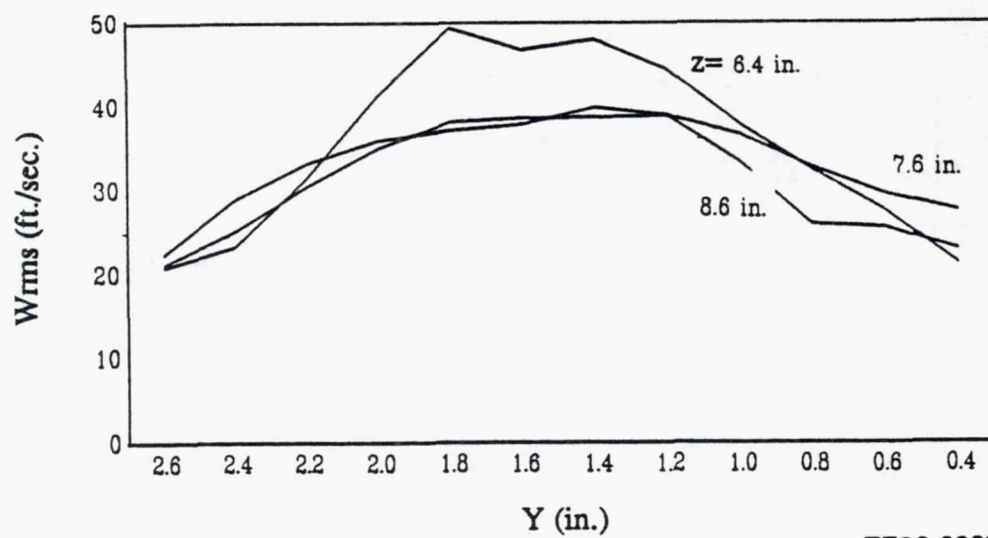
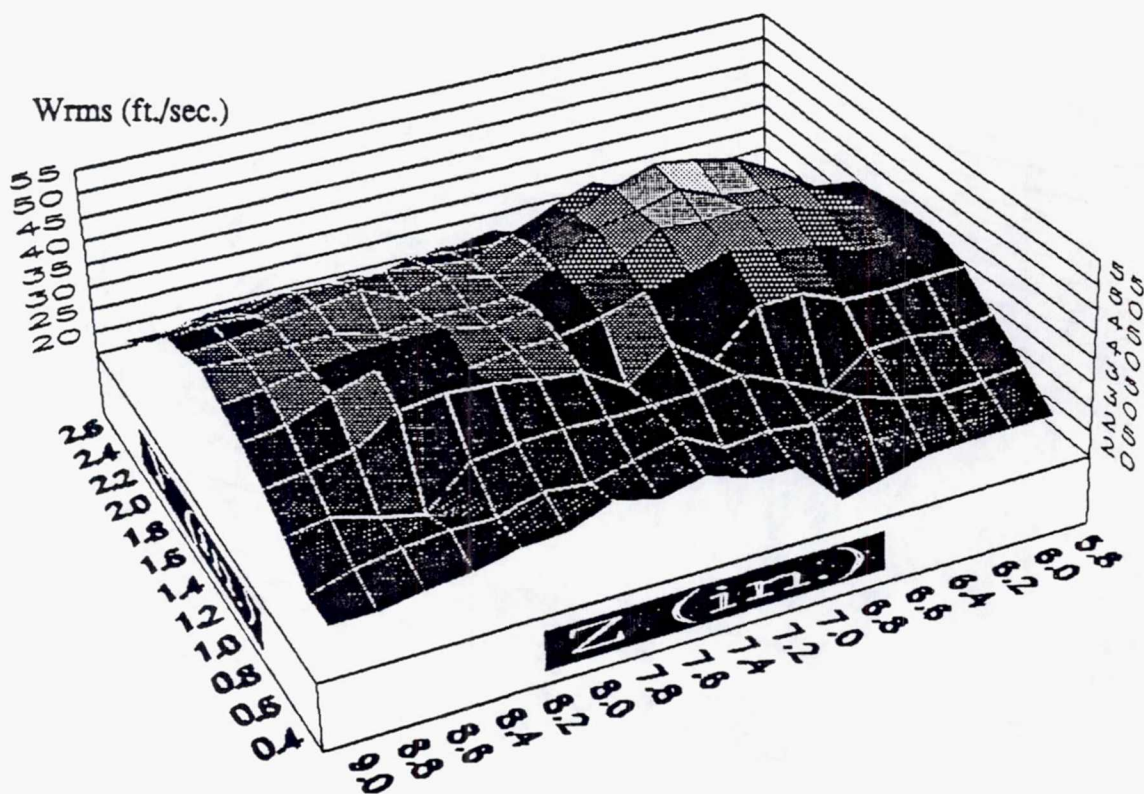
TE92-2327

Figure 3.1.1-75. Contour and line plots of U_{rms} at $x=4.00$ in.



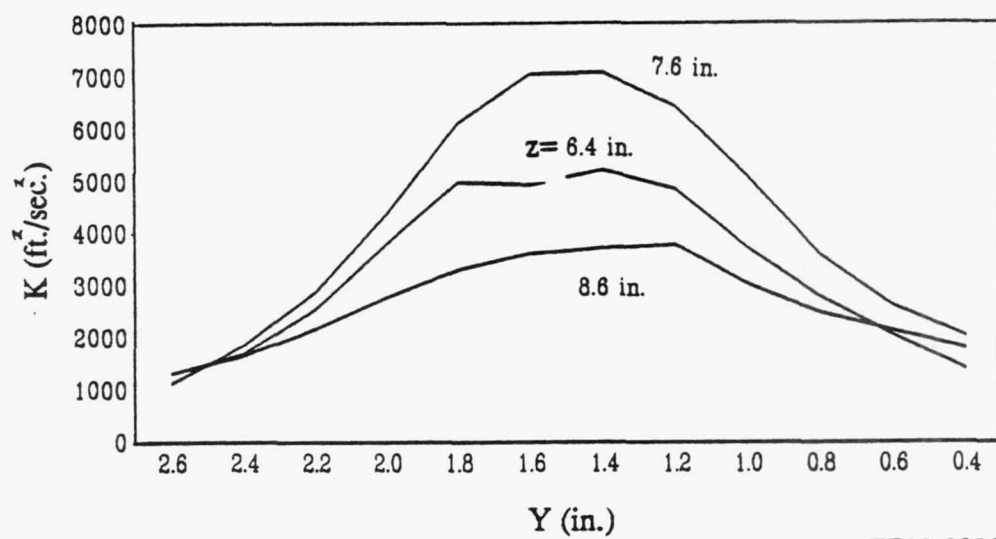
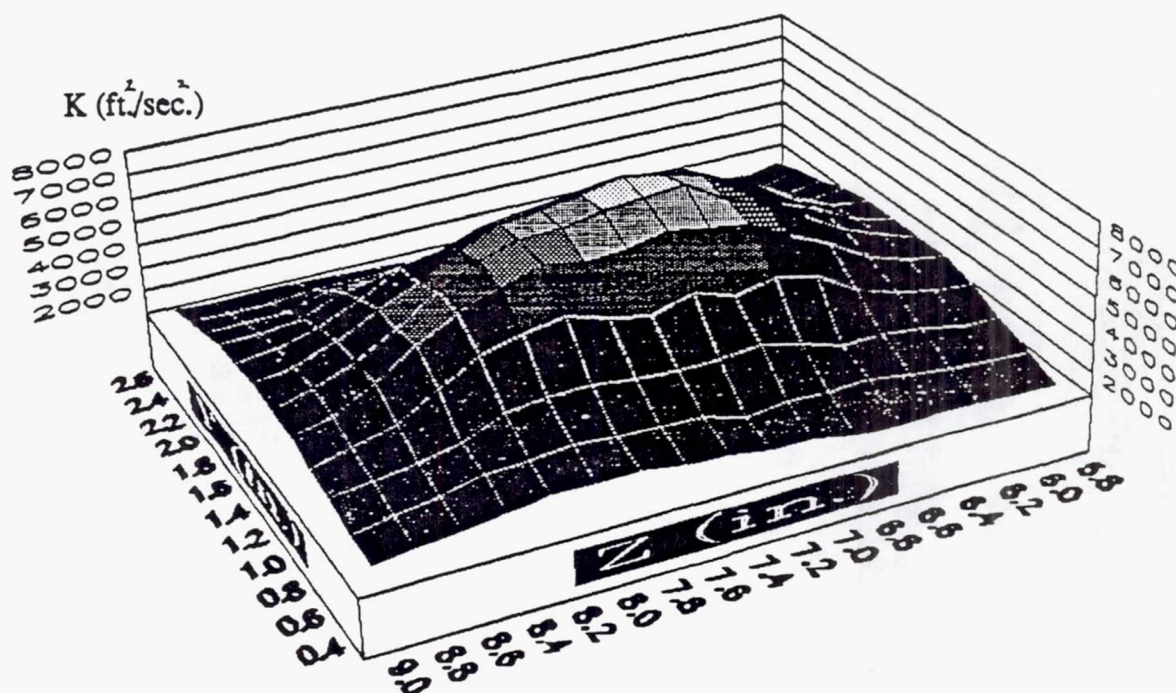
TE92-2328

Figure 3.1.1-76. Contour and line plots of V_{rms} at $x=4.00$ in.



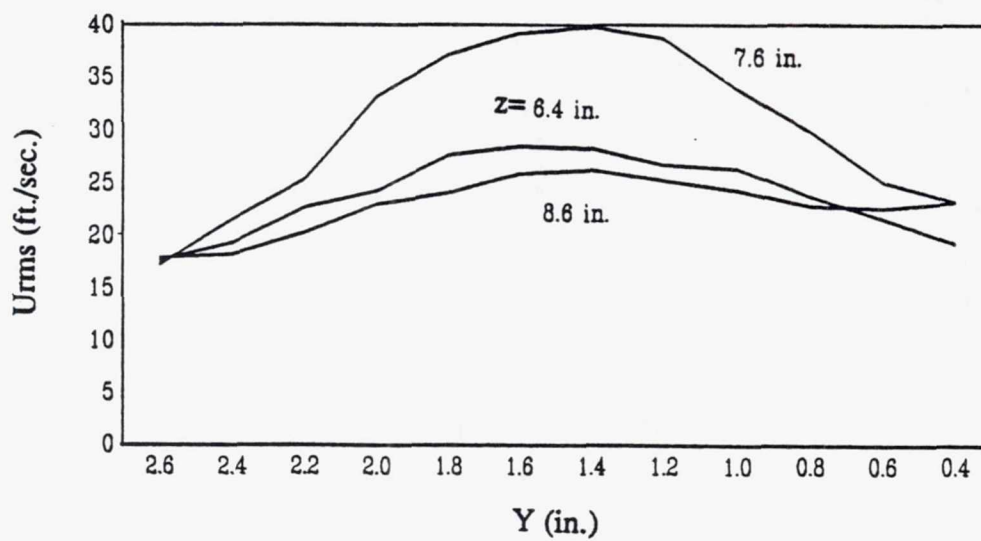
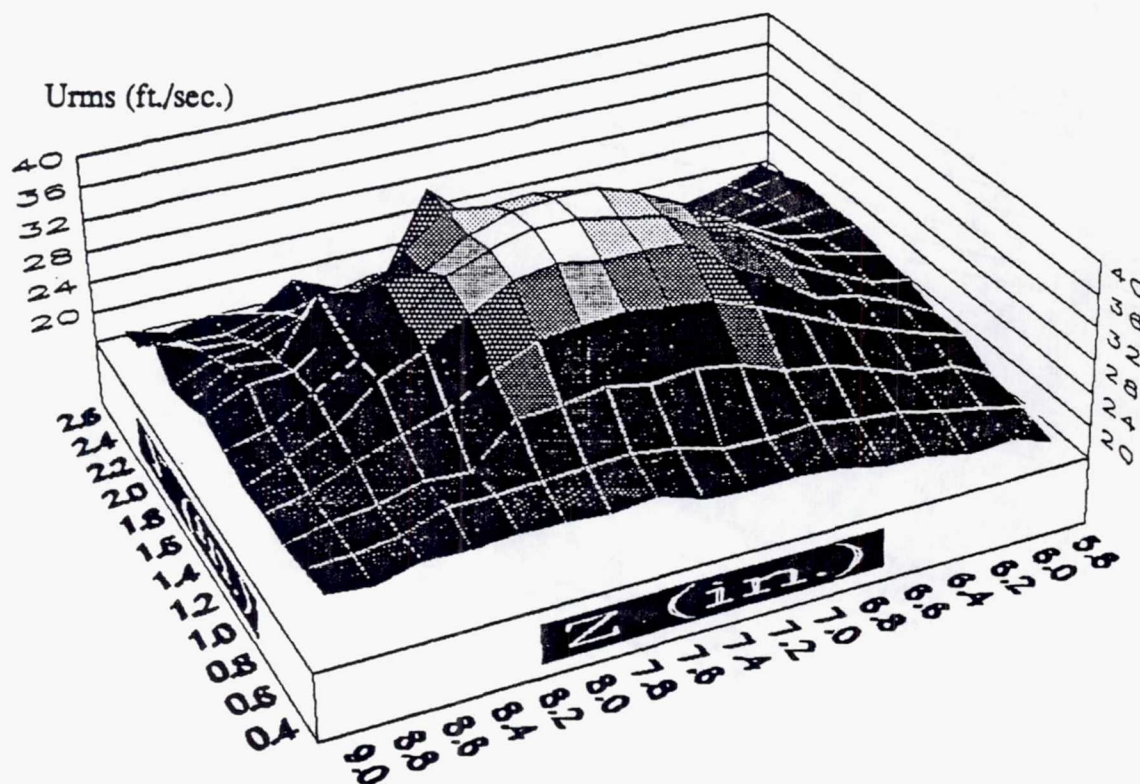
TE92-2329

Figure 3.1.1-77. Contour and line plots of W_{rms} at $x=4.00$ in.



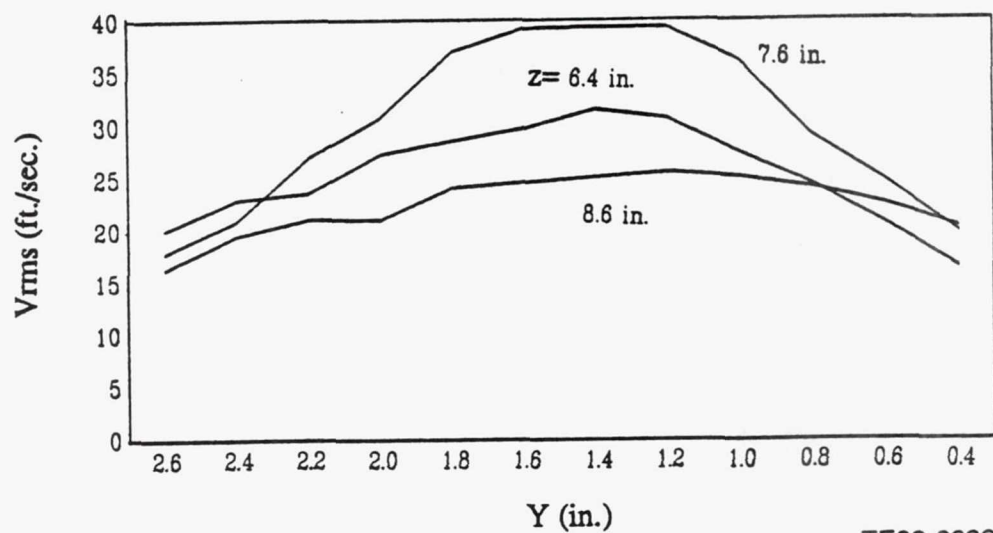
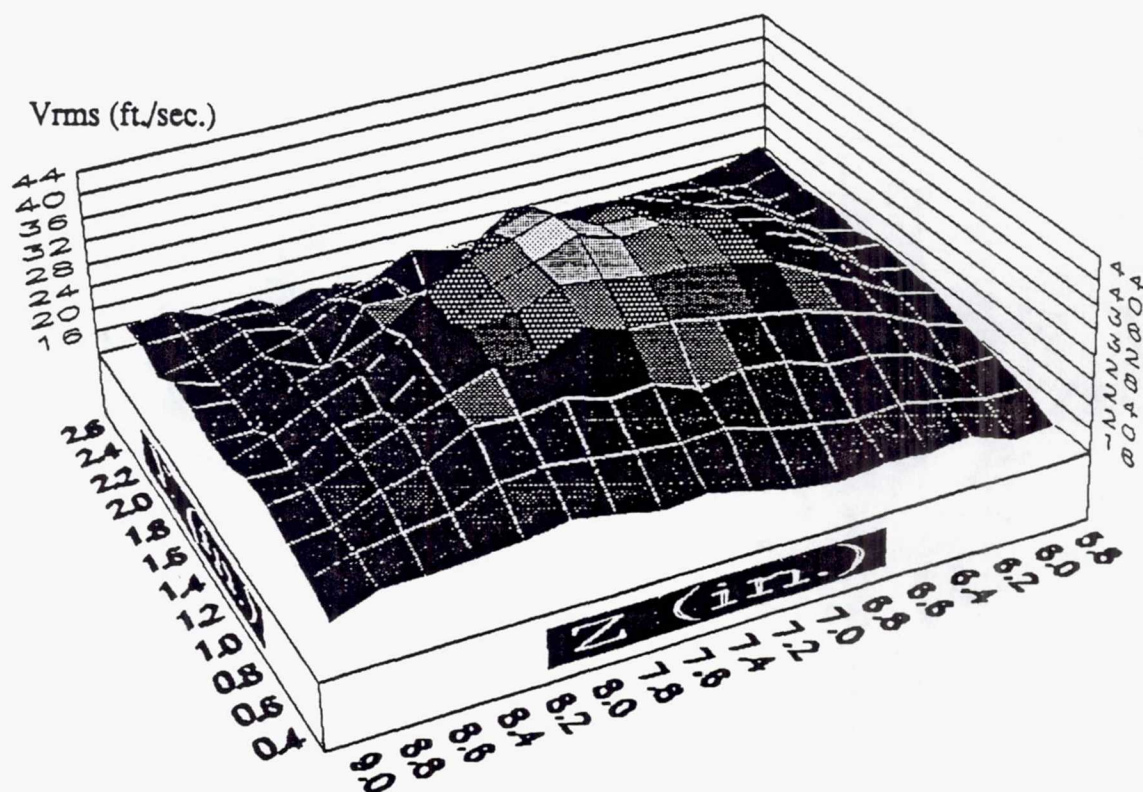
TE92-2330

Figure 3.1.1-78. Contour and line plots of K at $x=4.00$ in.



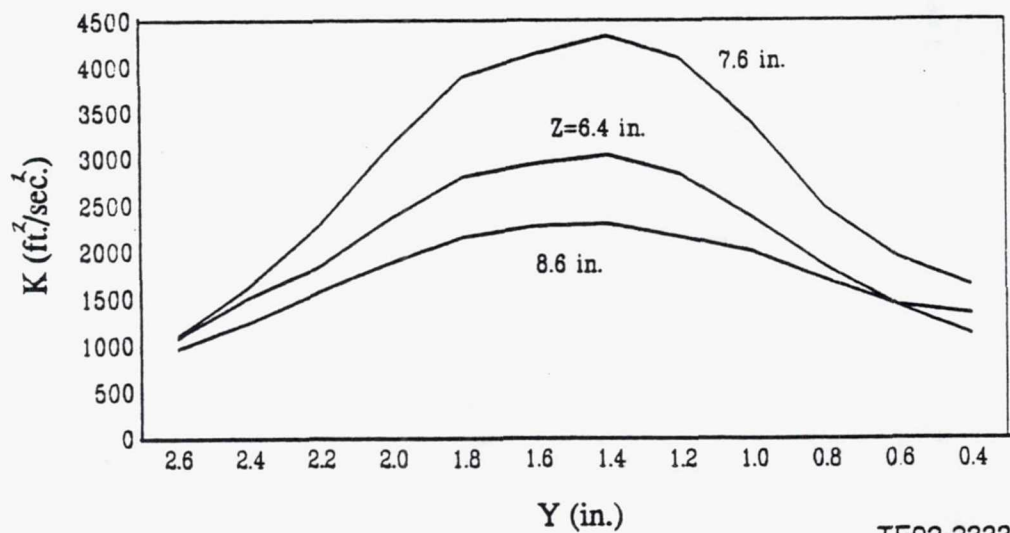
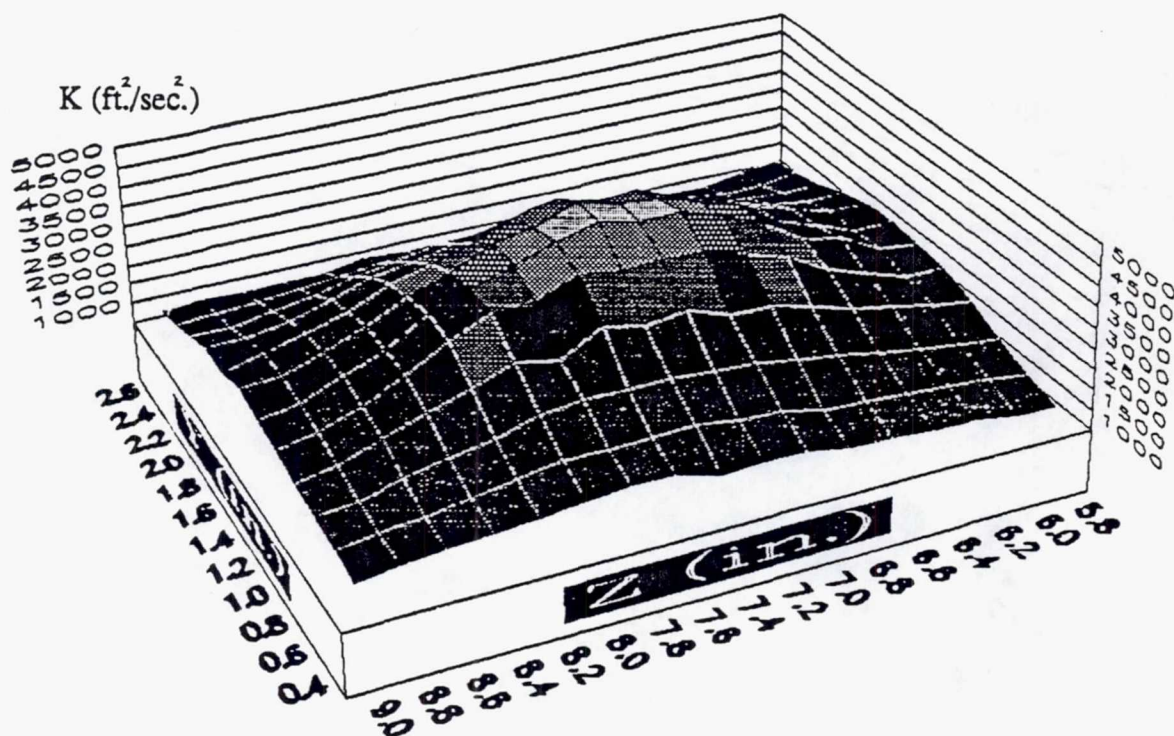
TE92-2331

Figure 3.1.1-79. Contour and line plots of U_{rms} at $x=4.50$ in.



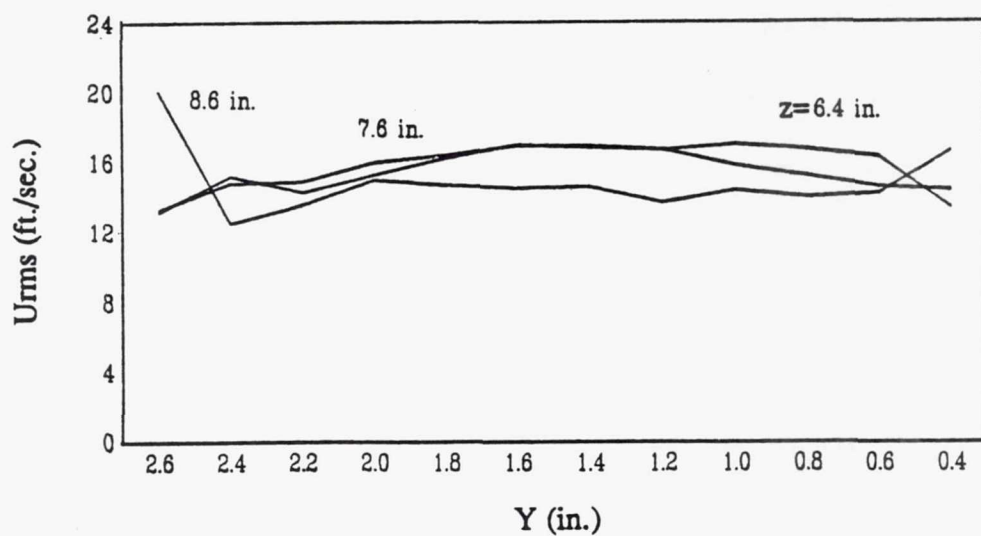
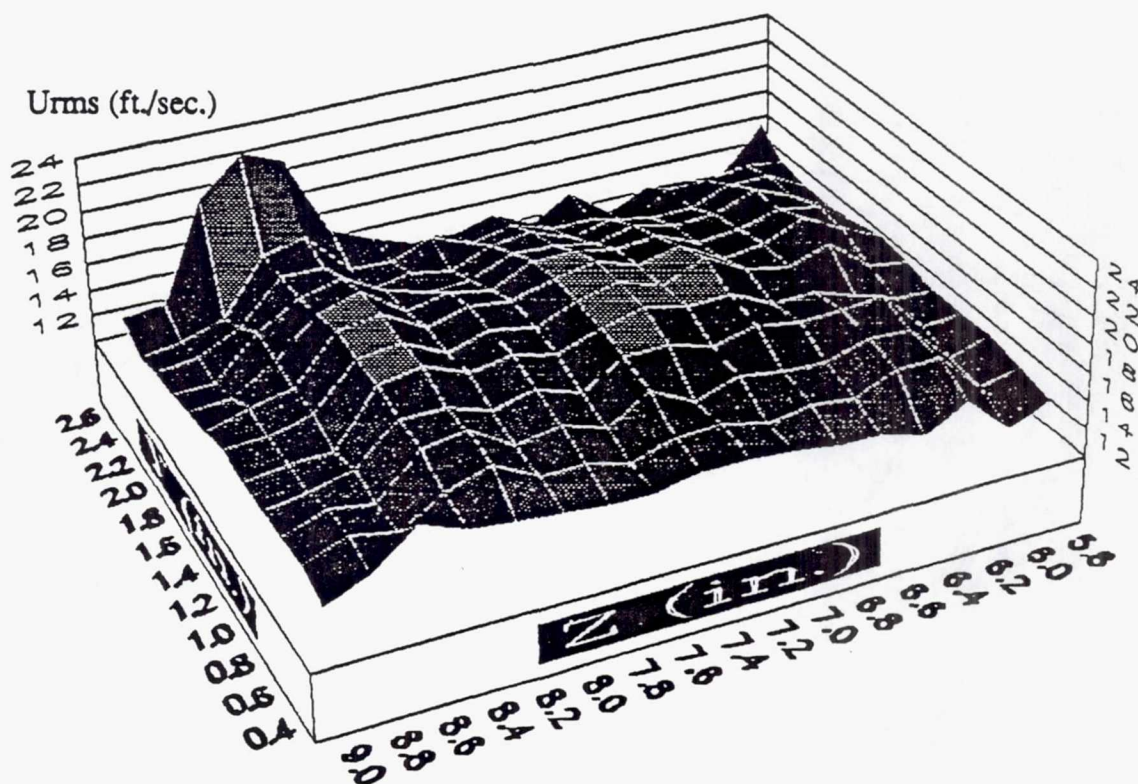
TE92-2332

Figure 3.1.1-80. Contour and line plots of V_{rms} at $x=4.50$ in.



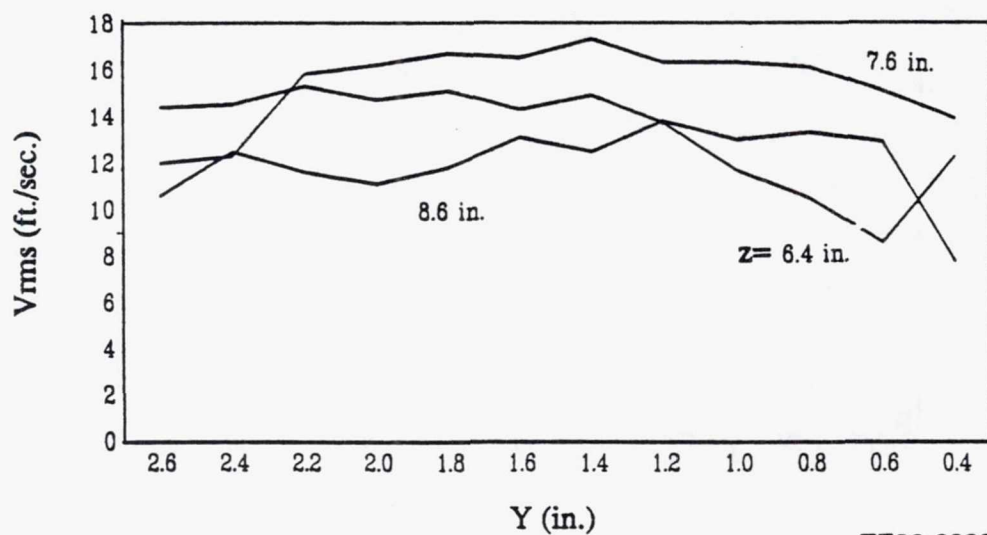
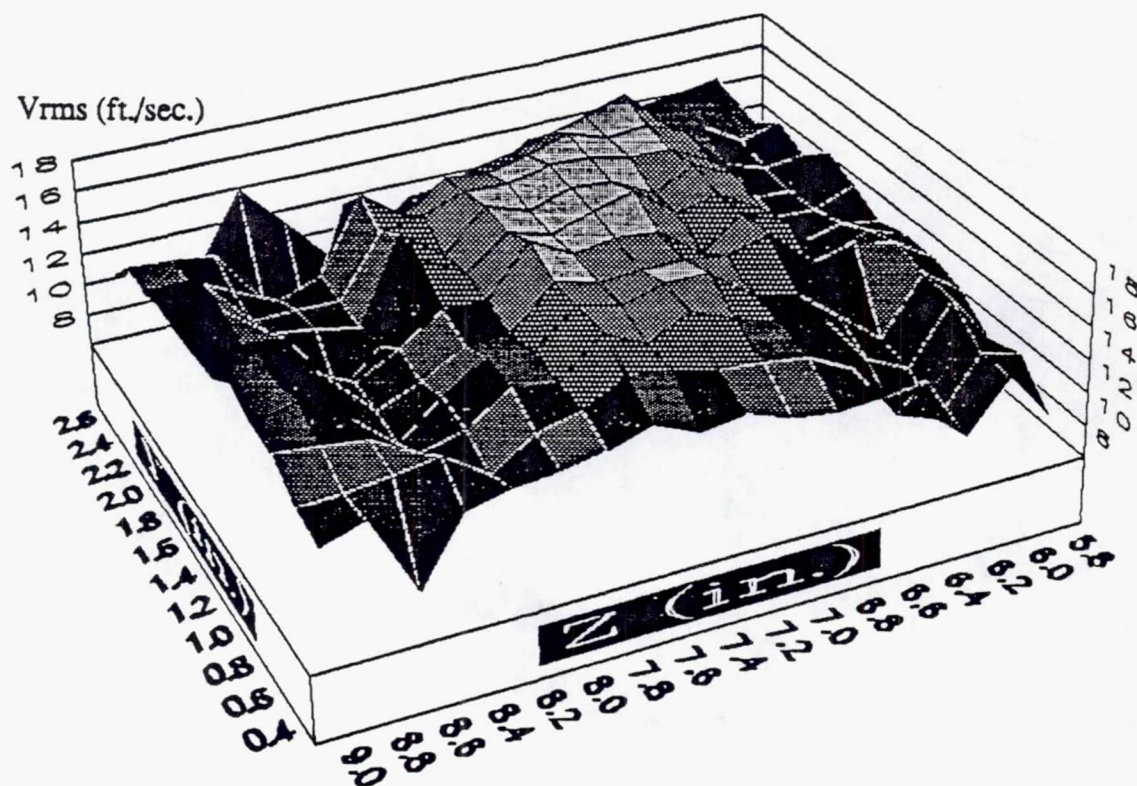
TE92-2333

Figure 3.1.1-81. Contour and line plots of K at $x=4.50$ in.



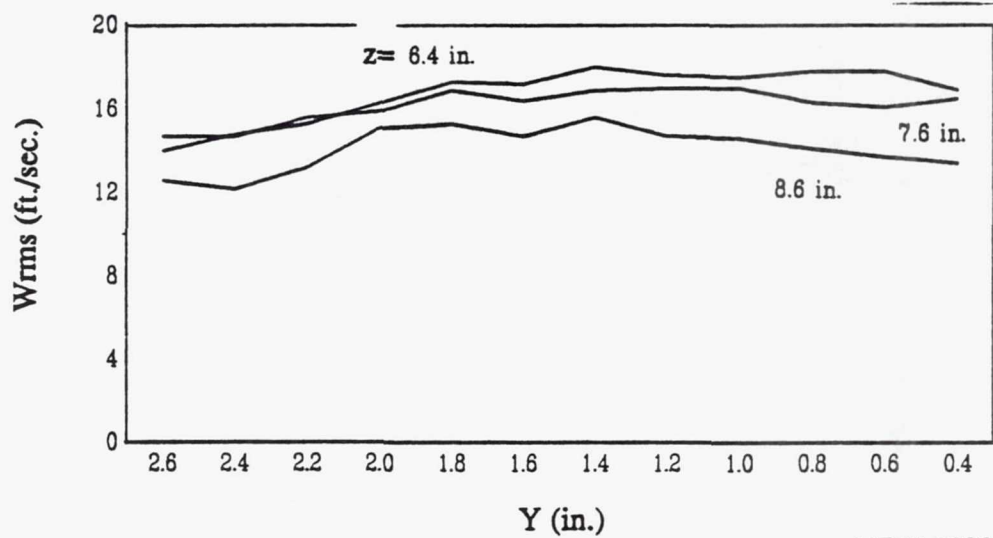
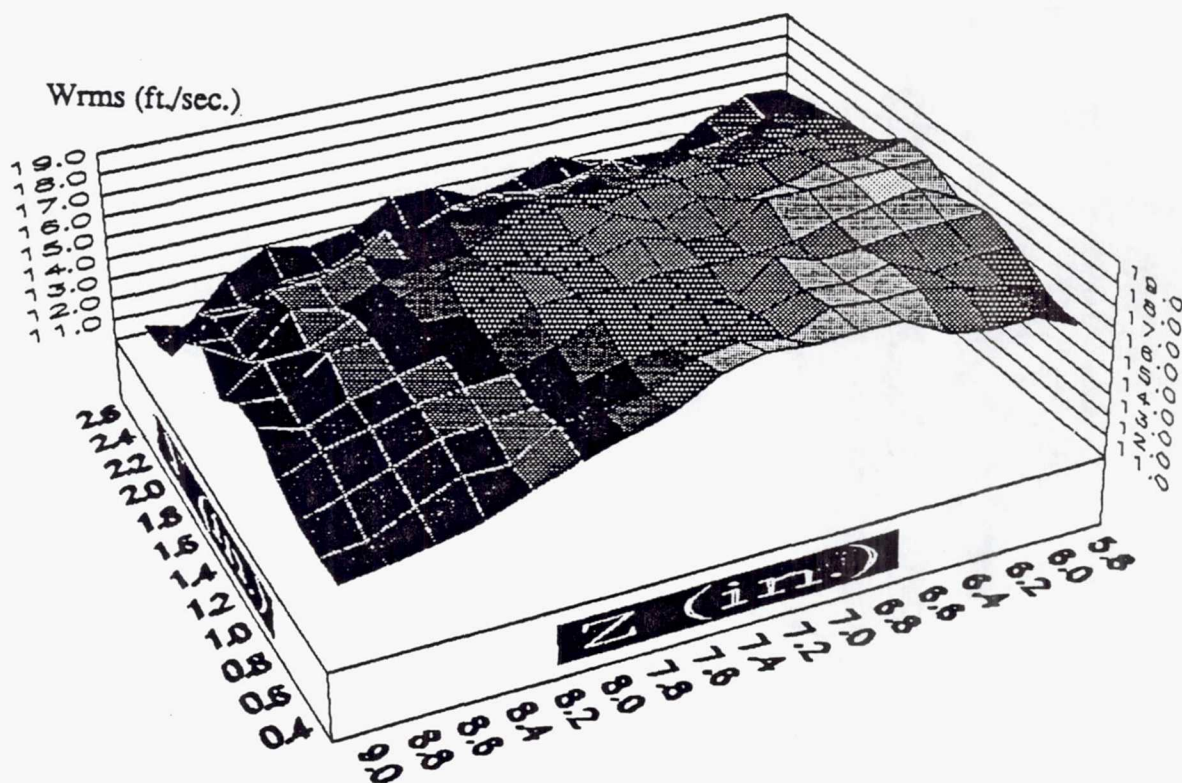
TE92-2334

Figure 3.1.1-82. Contour and line plots of U_{rms} at $x=6.00$ in.



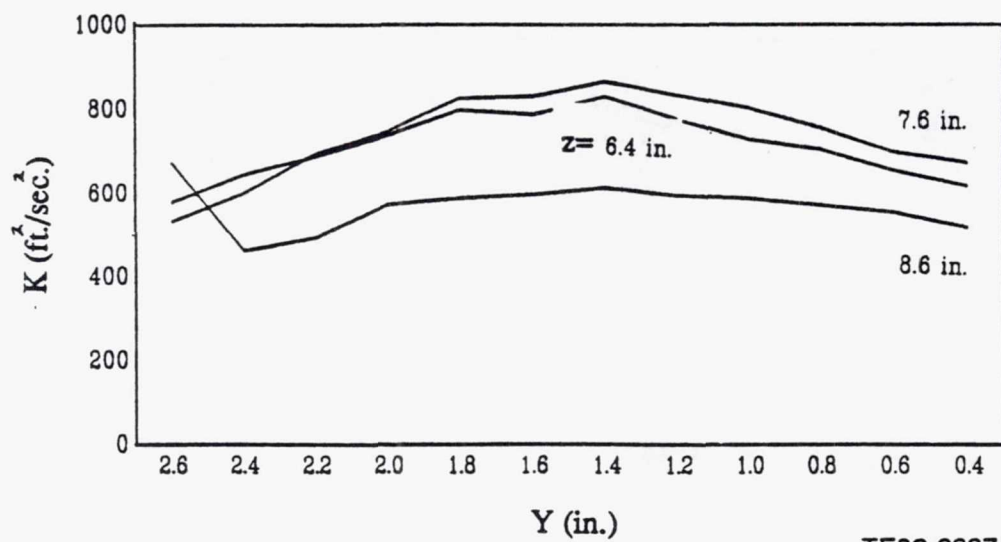
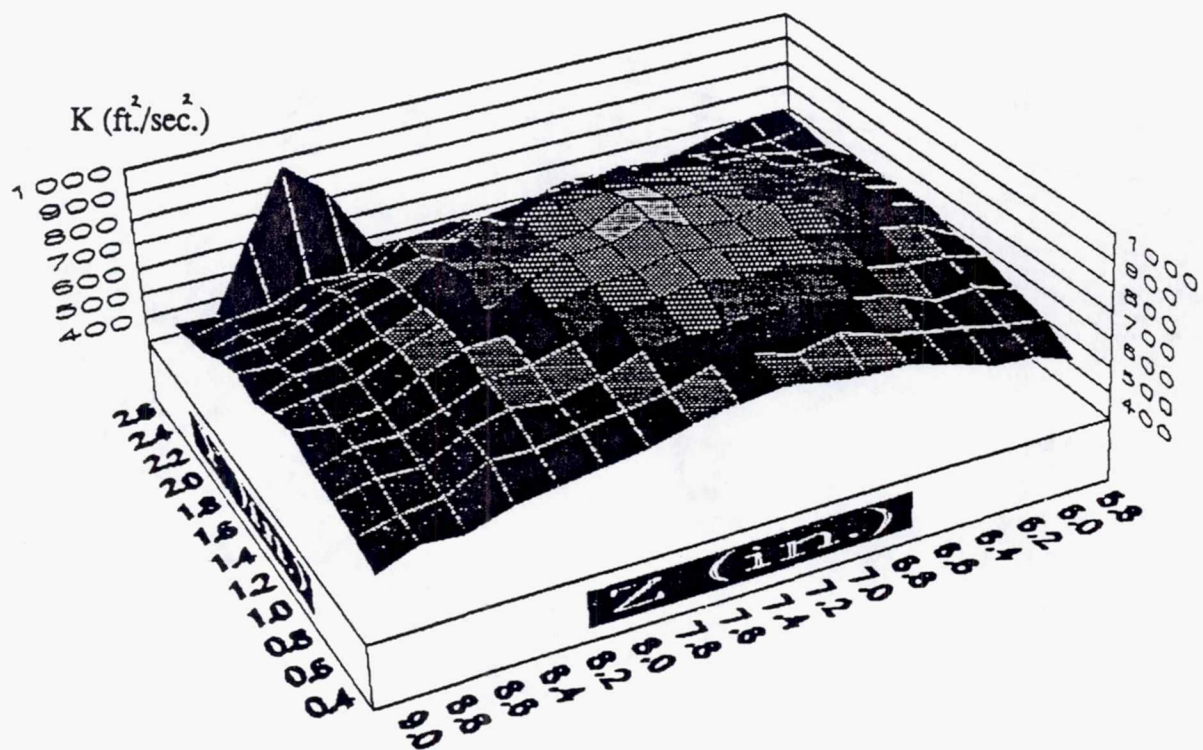
TE92-2335

Figure 3.1.1-83. Contour and line plots of V_{rms} at $x=6.00$ in.



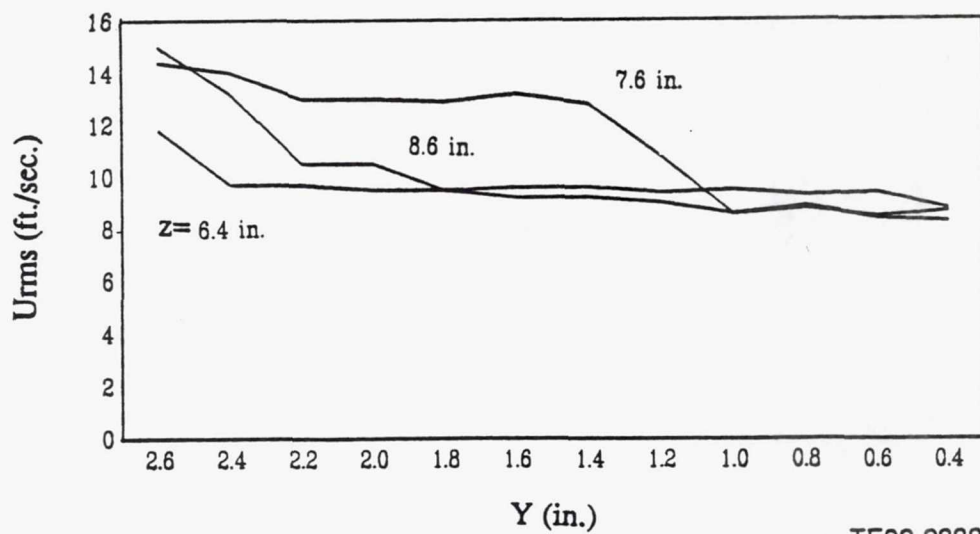
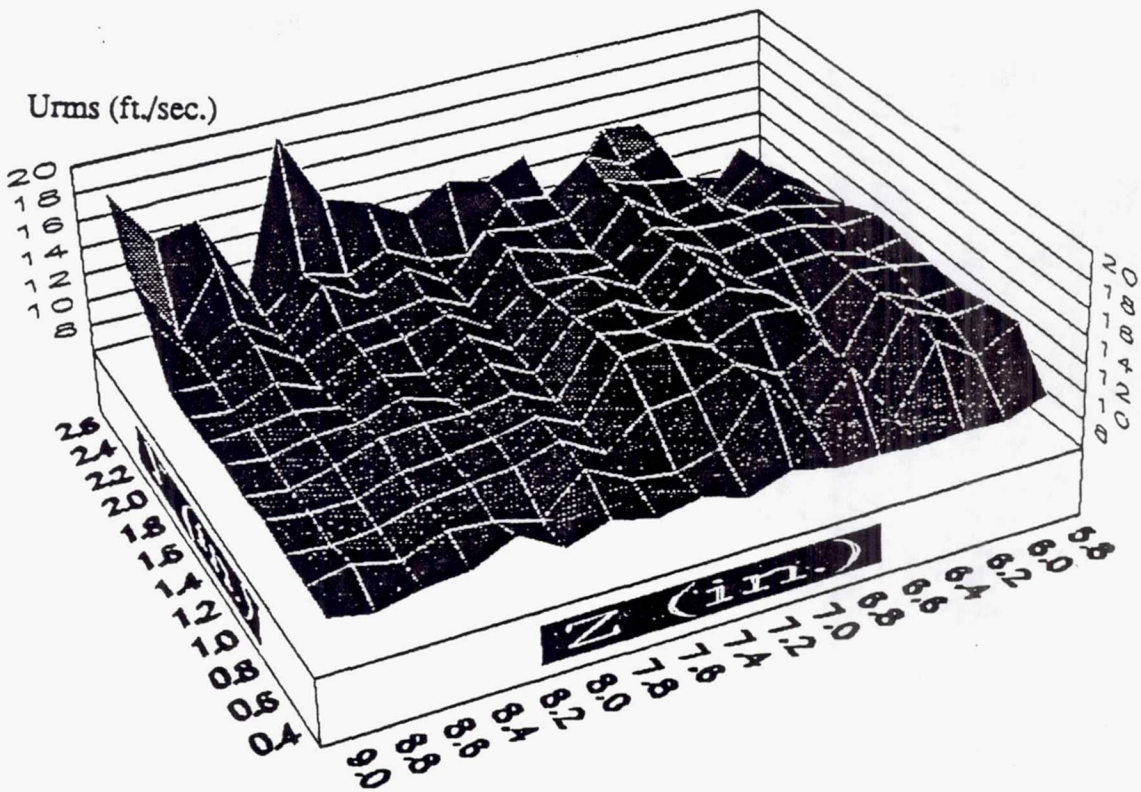
TE92-2336

Figure 3.1.1-84. Contour and line plots of W_{rms} at $x=6.00$ in.



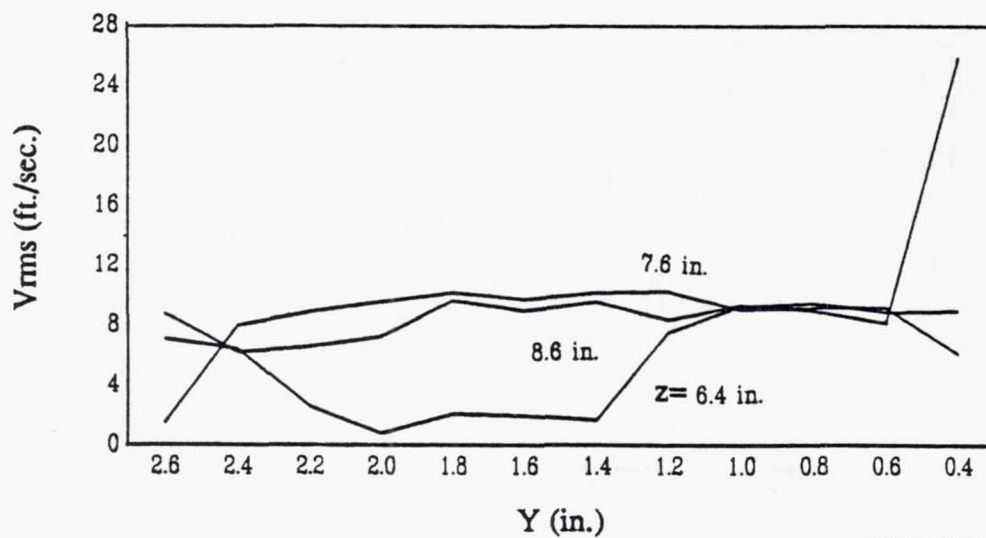
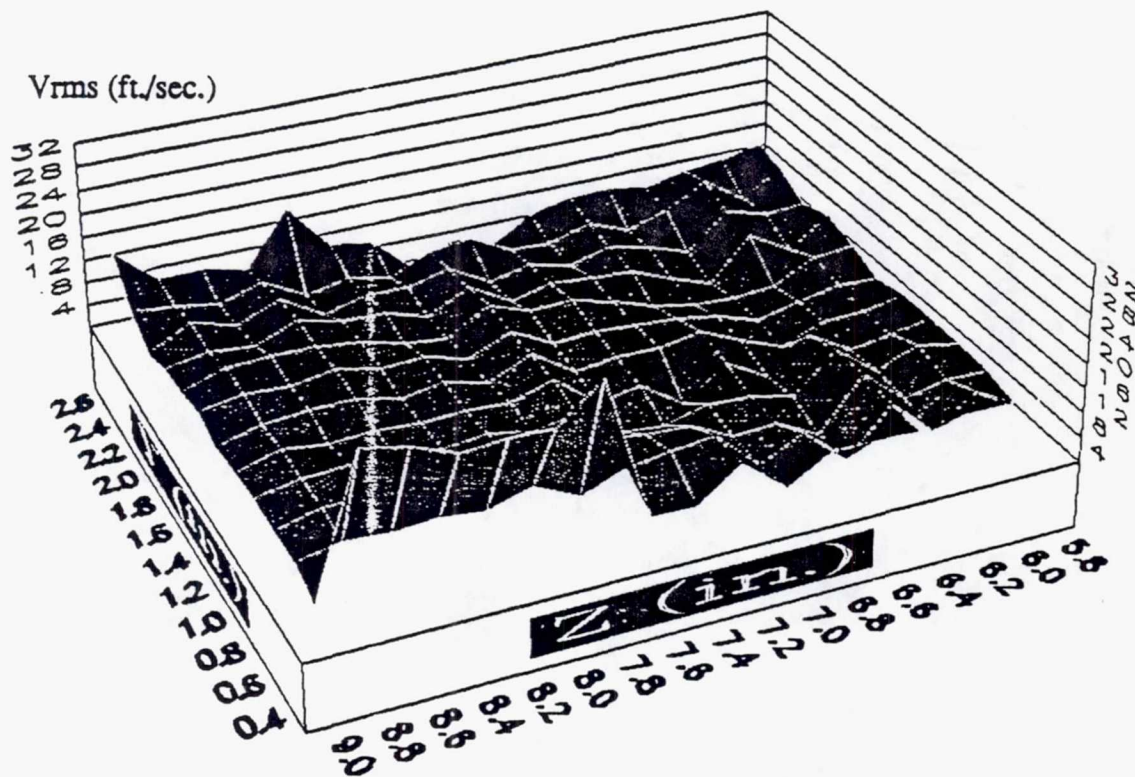
TE92-2337

Figure 3.1.1-85. Contour and line plots of K at $x=6.00$ in.



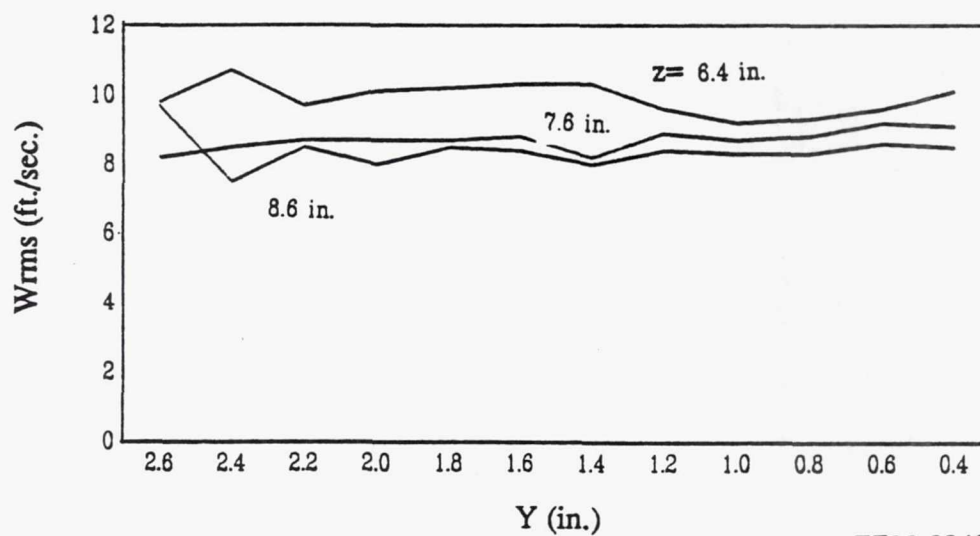
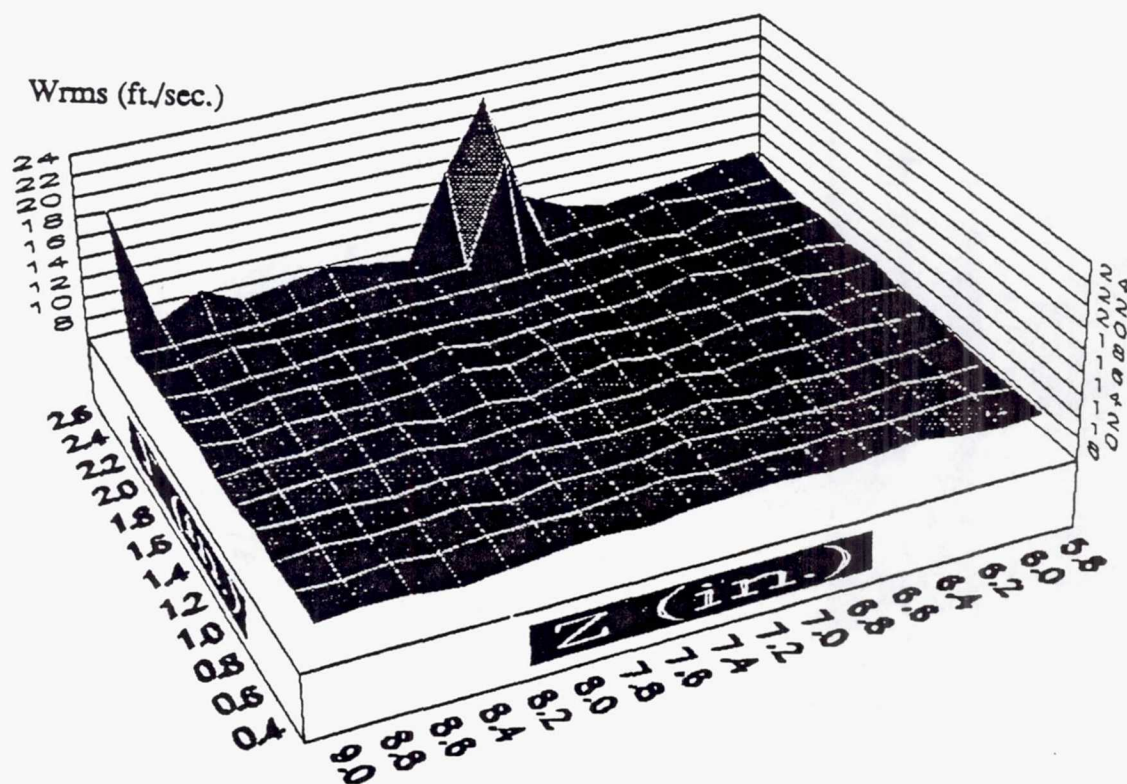
TE92-2338

Figure 3.1.1-86. Contour and line plots of U_{rms} at $x = 9.00$ in.



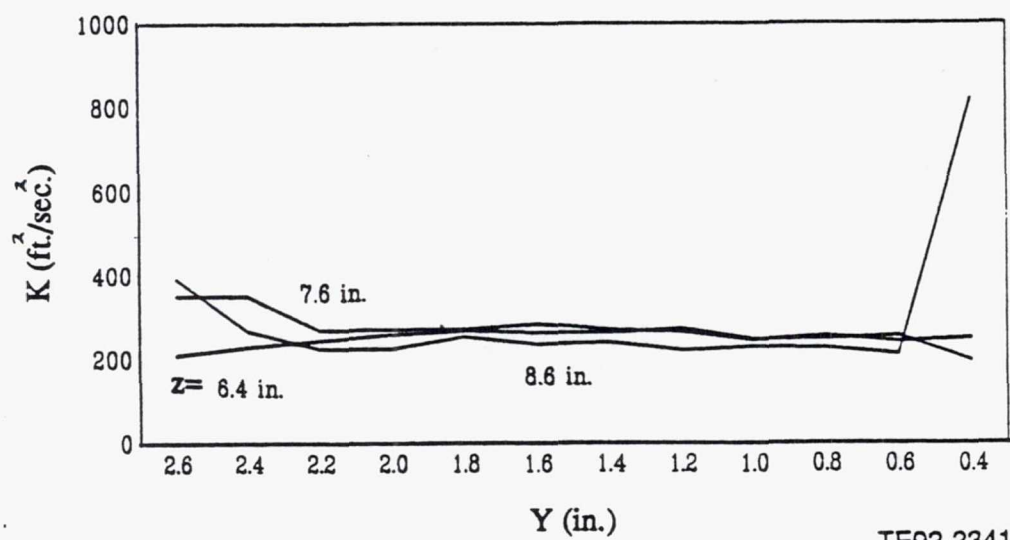
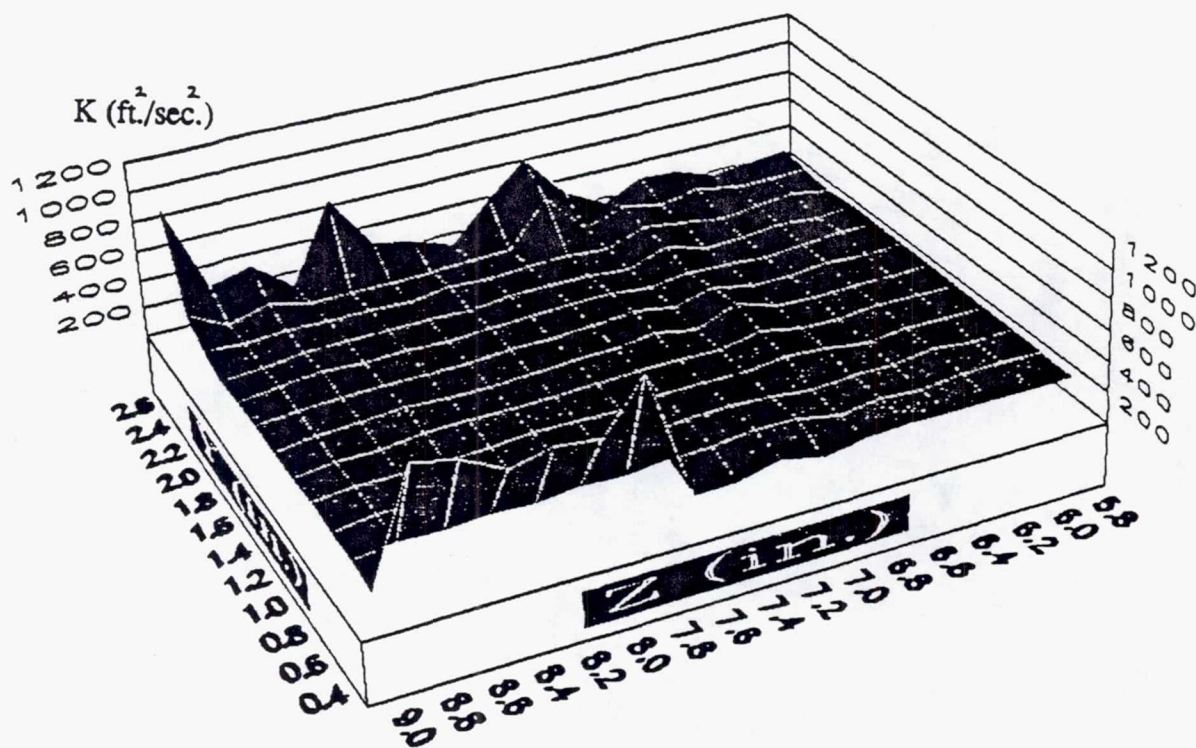
TE92-2339

Figure 3.1.1-87. Contour and line plots of V_{rms} at $x=9.00$ in.



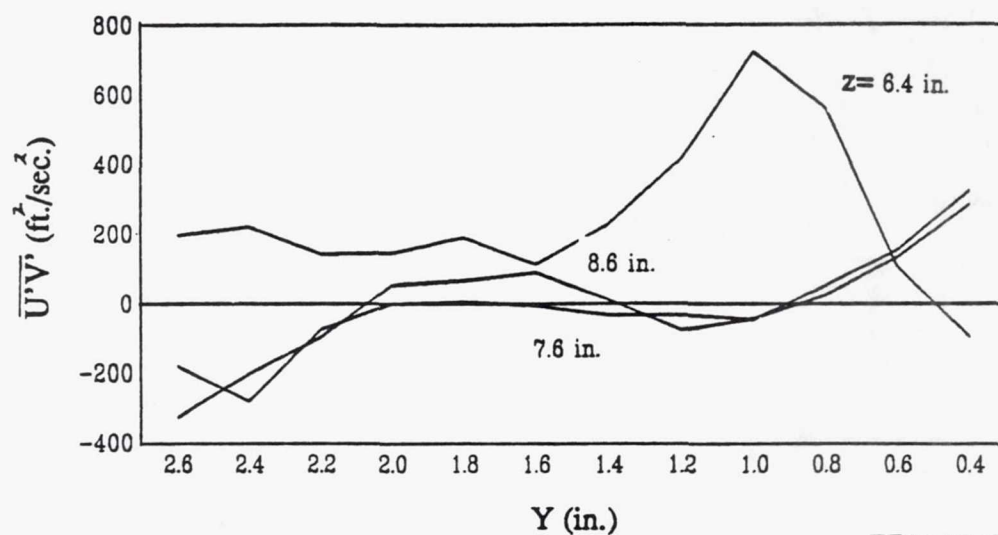
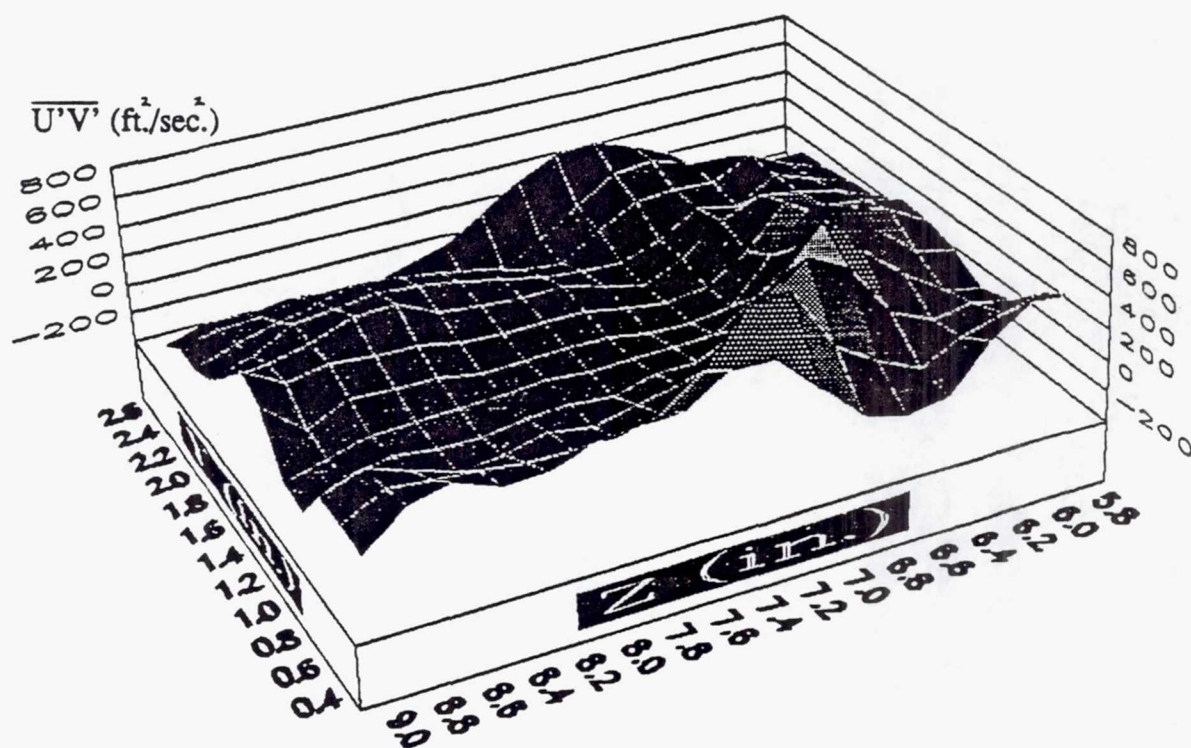
TE92-2340

Figure 3.1.1-88. Contour and line plots of W_{rms} at $x = 9.00$ in.



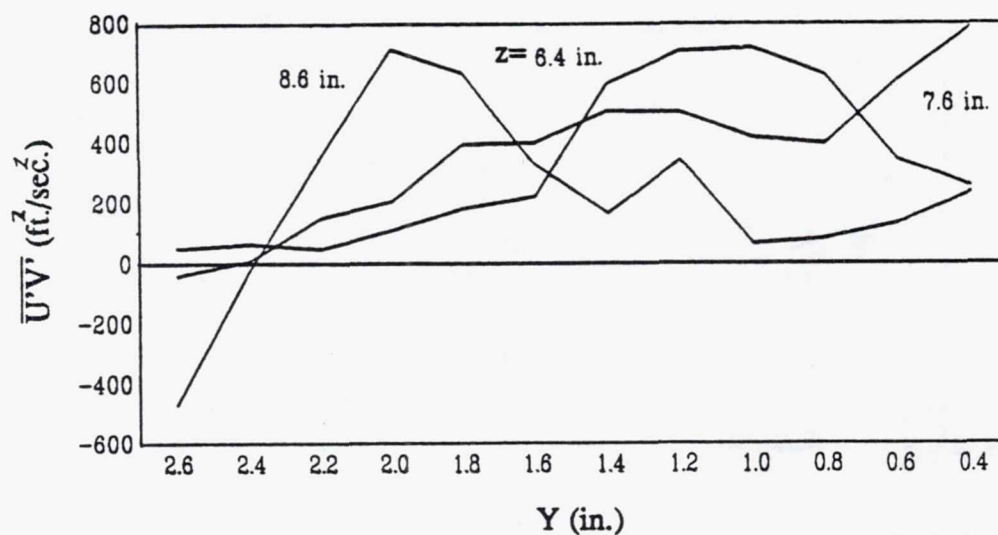
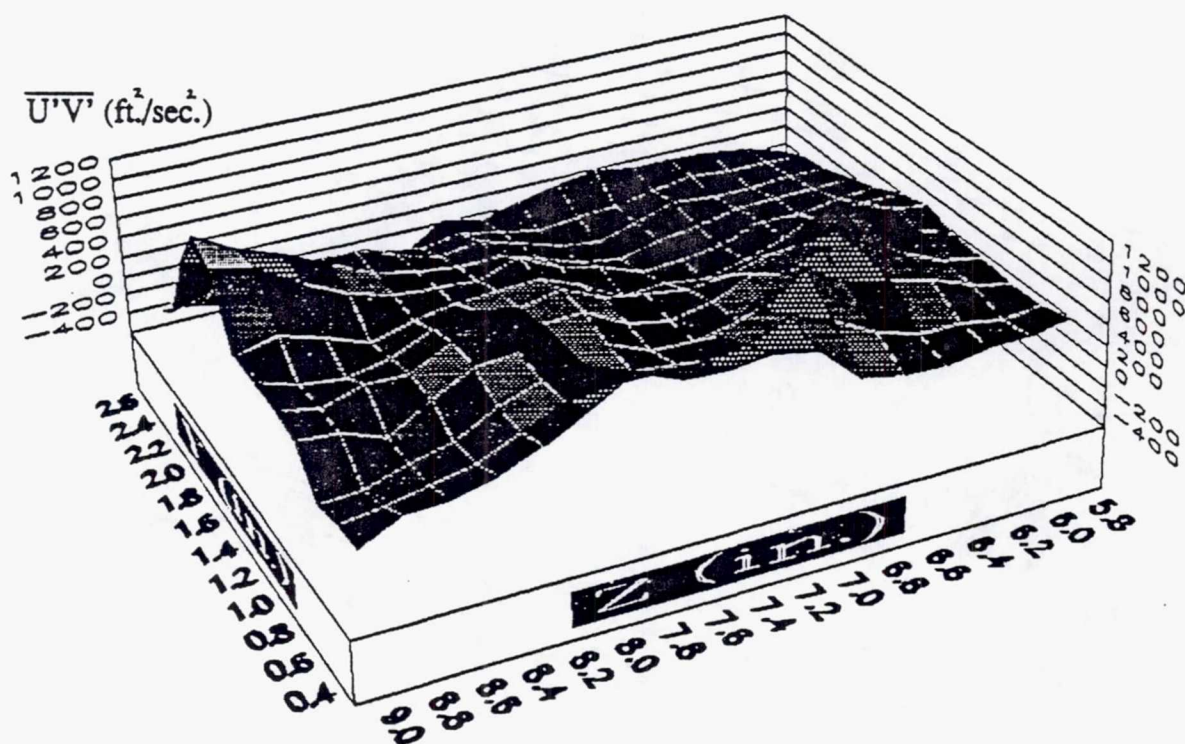
TE92-2341

Figure 3.1.1-89. Contour and line plots of K at $x=9.00$ in.



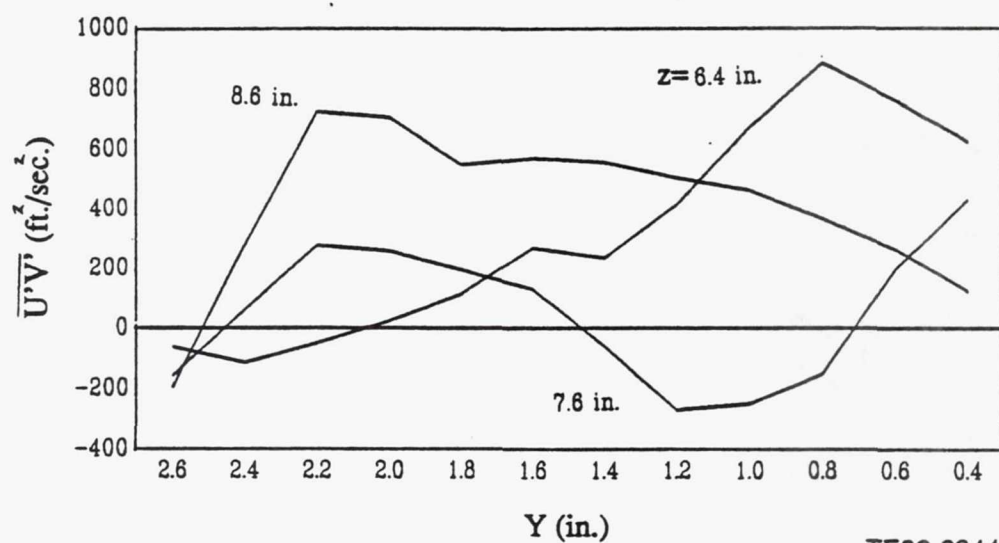
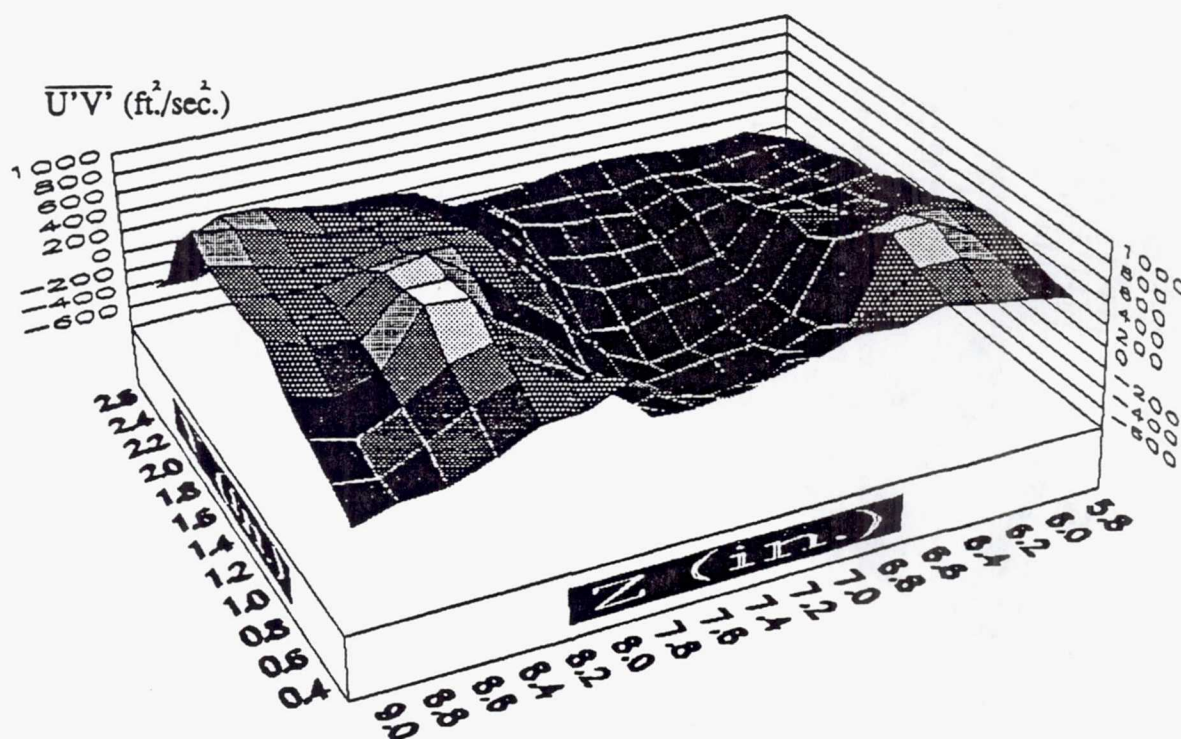
TE92-2342

Figure 3.1.1-90. Contour and line plots of $\overline{U'V'}$ at $x=1.00$ in.



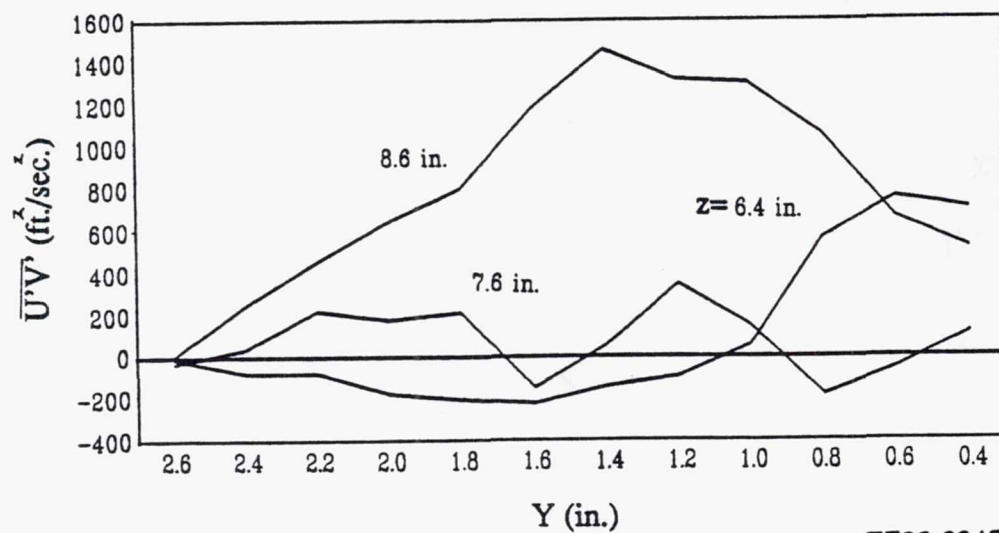
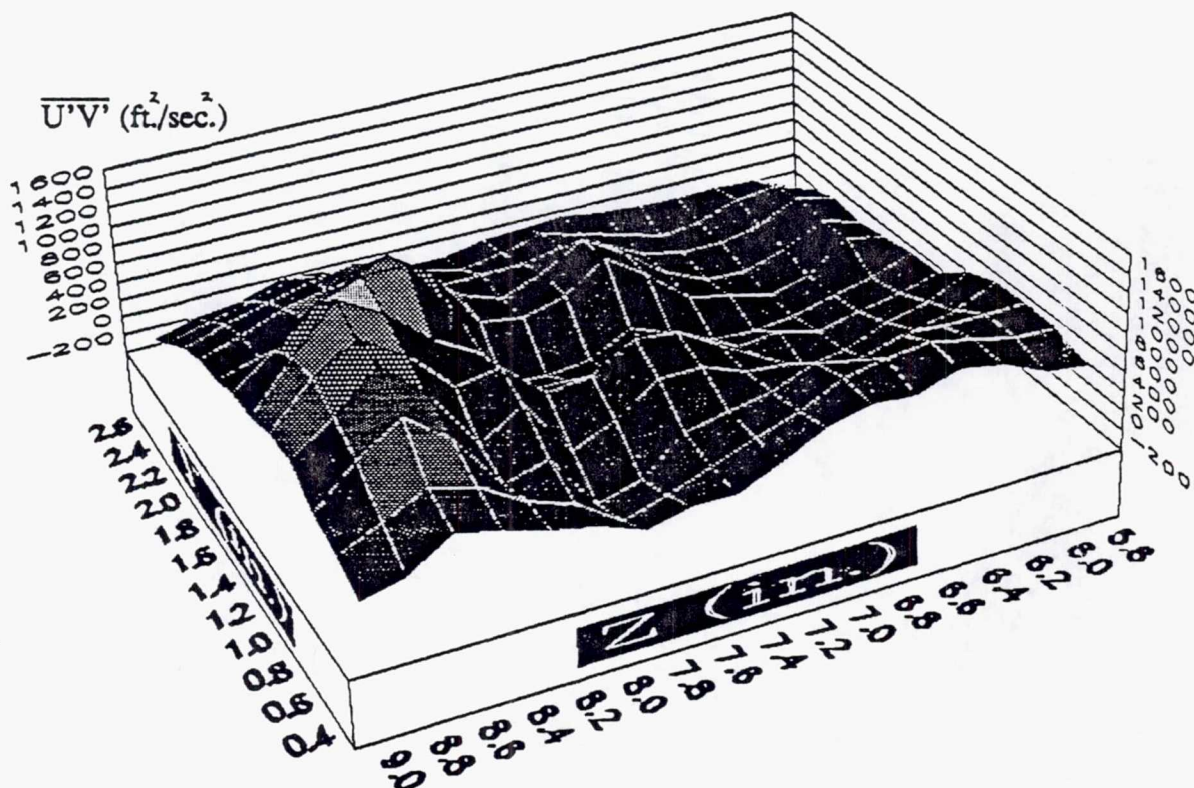
TE92-2343

Figure 3.1.1-91. Contour and line plots of $\overline{U'V'}$ at $x=1.50$ in.



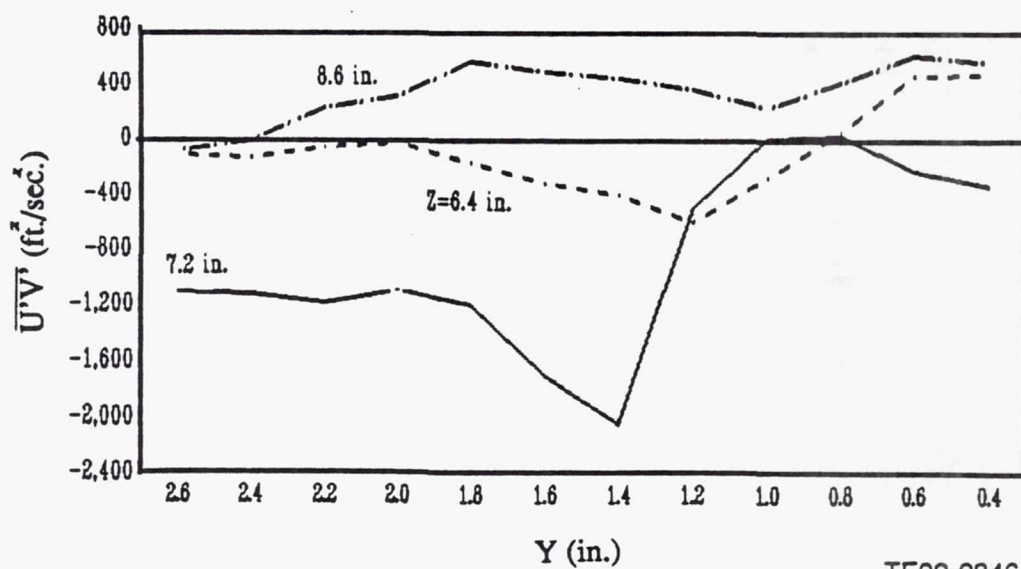
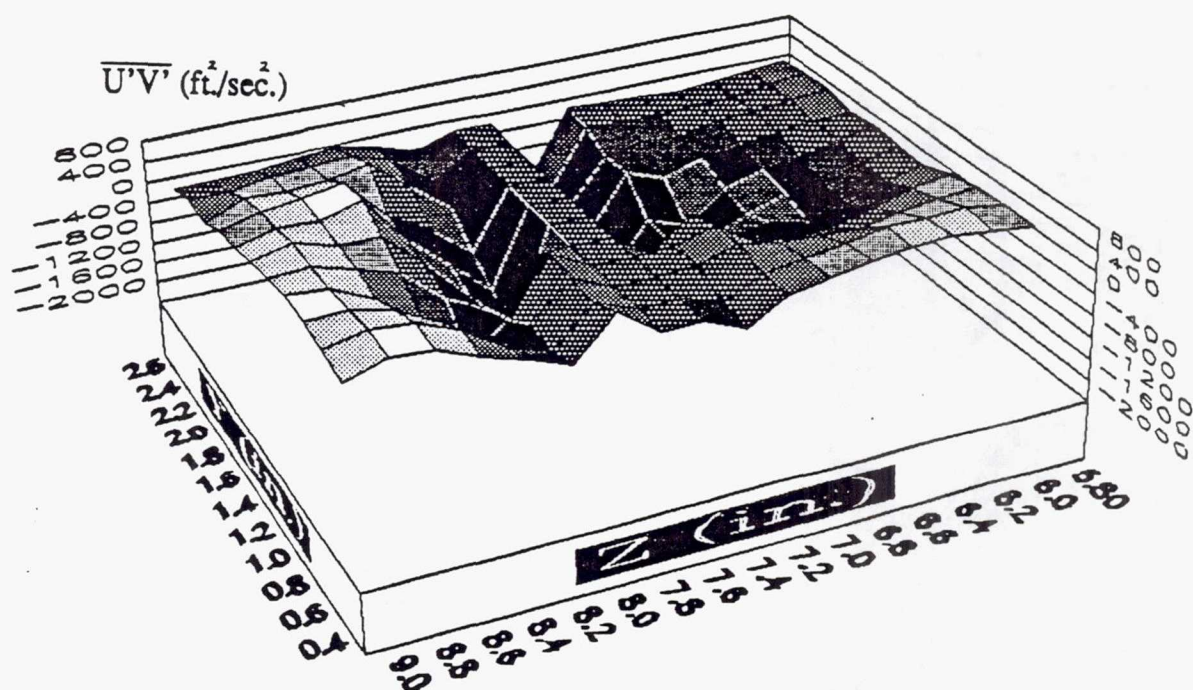
TE92-2344

Figure 3.1.1-92. Contour and line plots of $\overline{U'V'}$ at $x=2.00$ in.



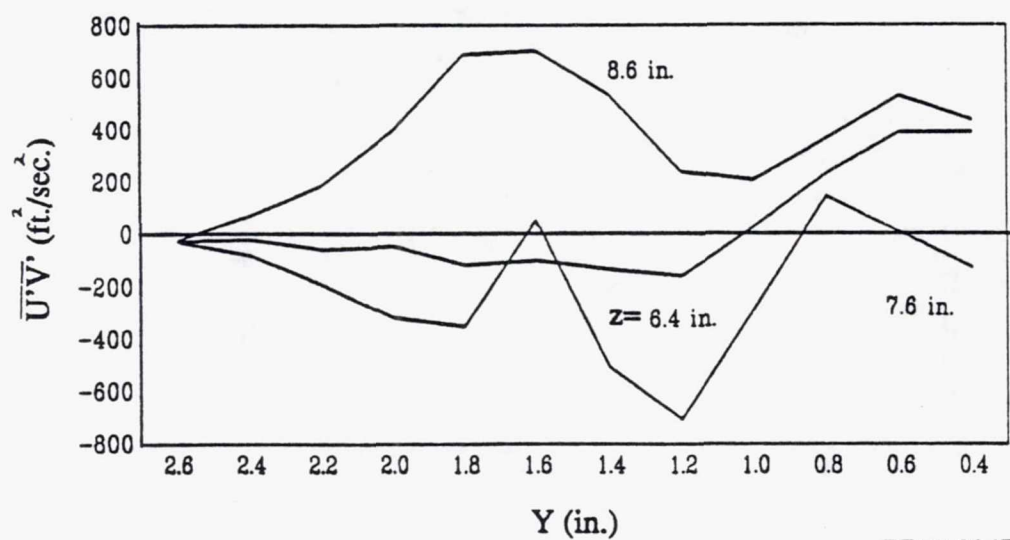
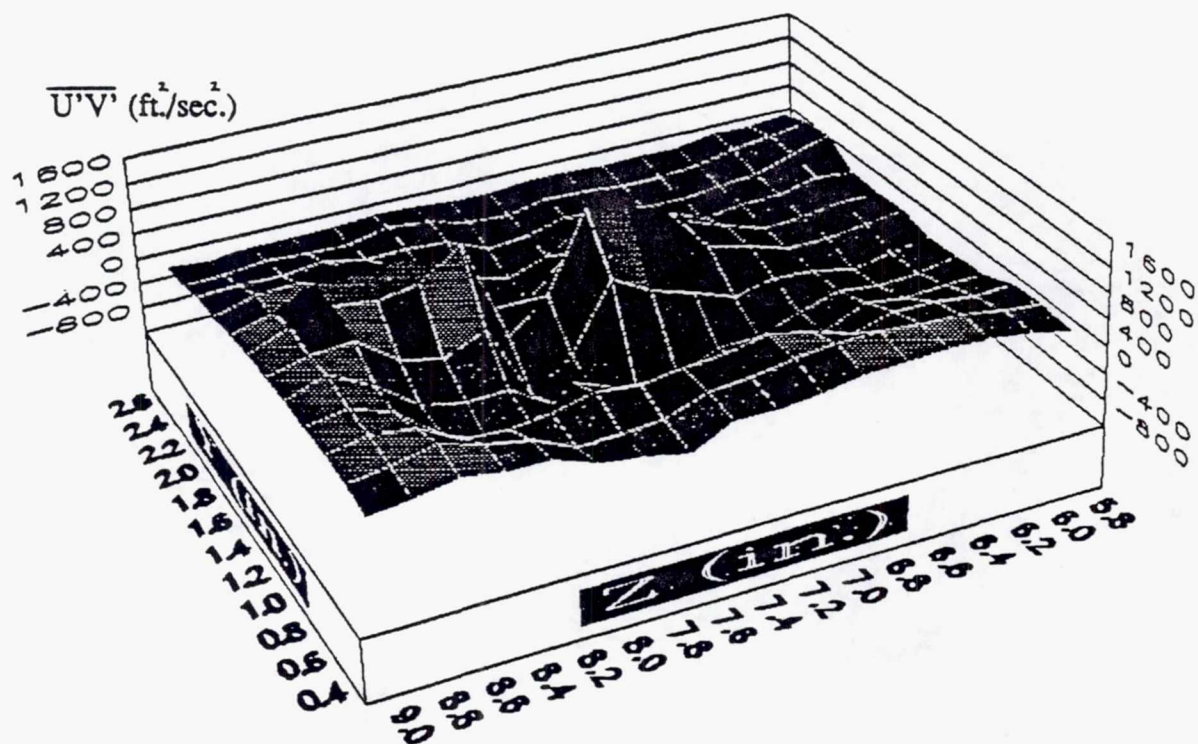
TE92-2345

Figure 3.1.1-93. Contour and line plots of $\overline{U'V'}$ at $x=2.50$ in.



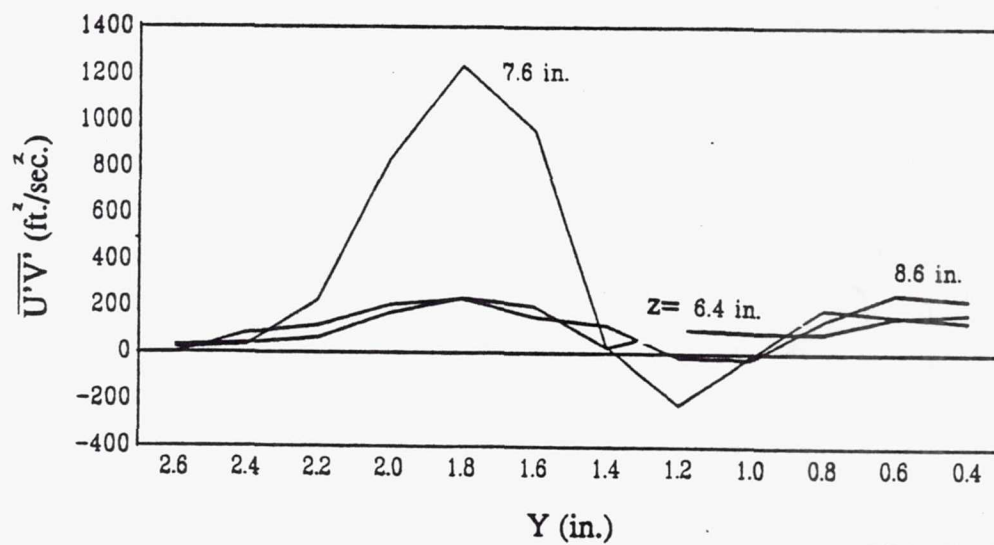
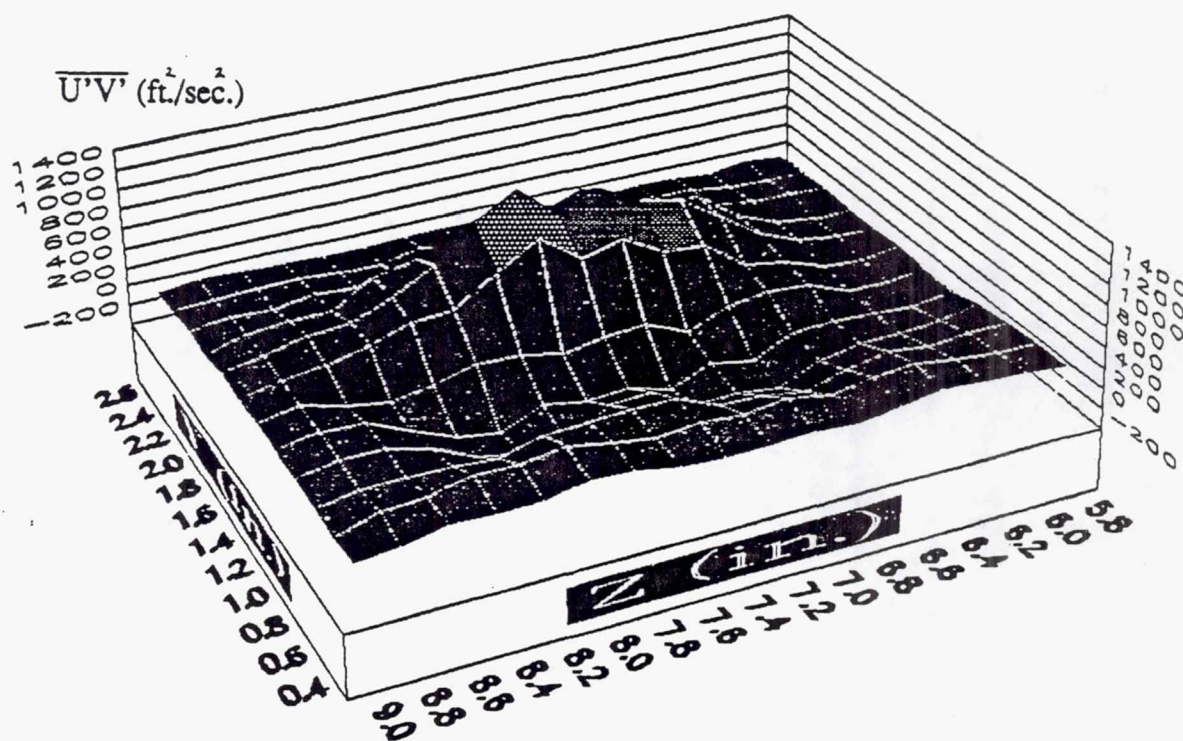
TE92-2346

Figure 3.1.1-94. Contour and line plots of $\overline{U'V'}$ at $x=3.00$ in.



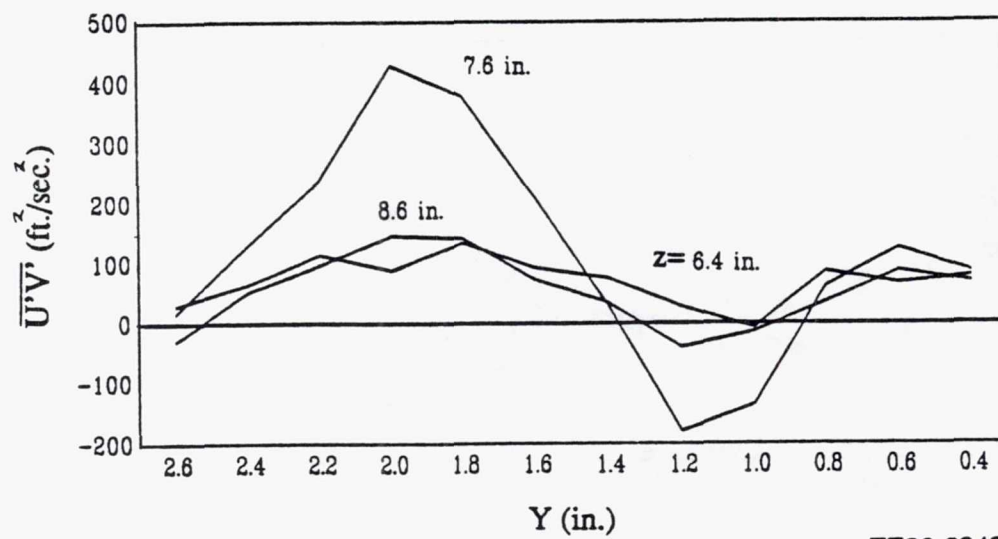
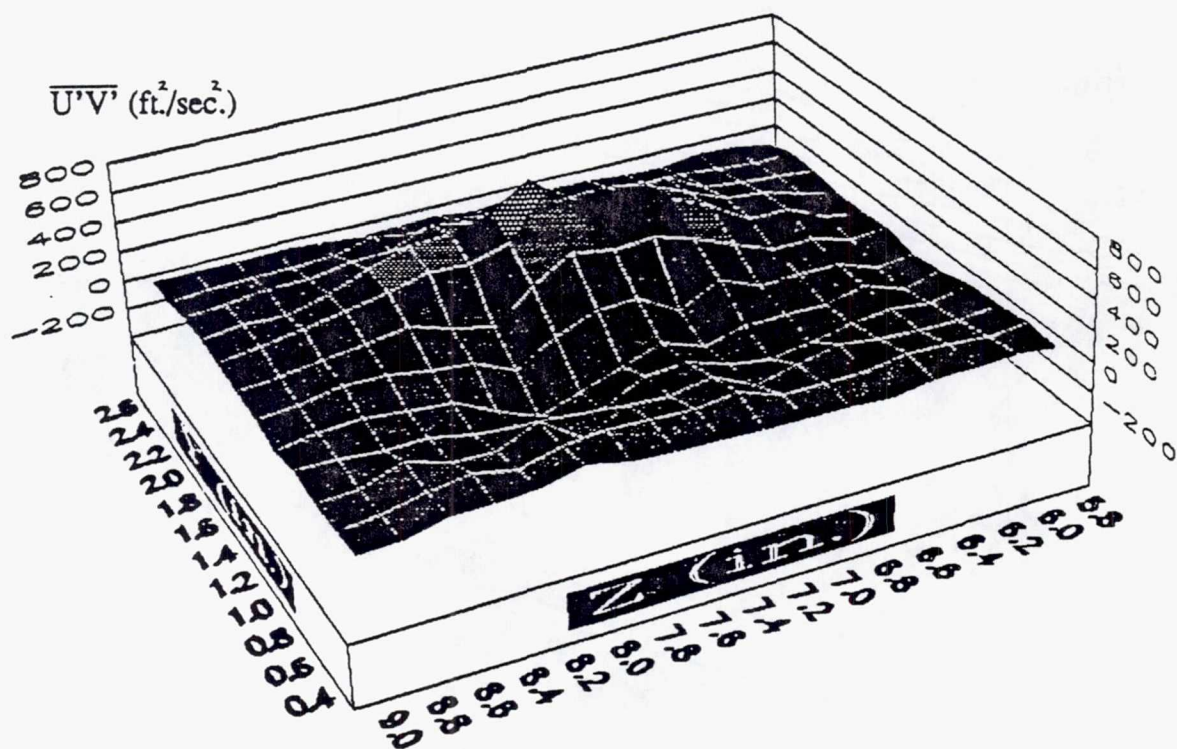
TE92-2347

Figure 3.1.1-95. Contour and line plots of $\overline{U'V'}$ at $x=3.50$ in.



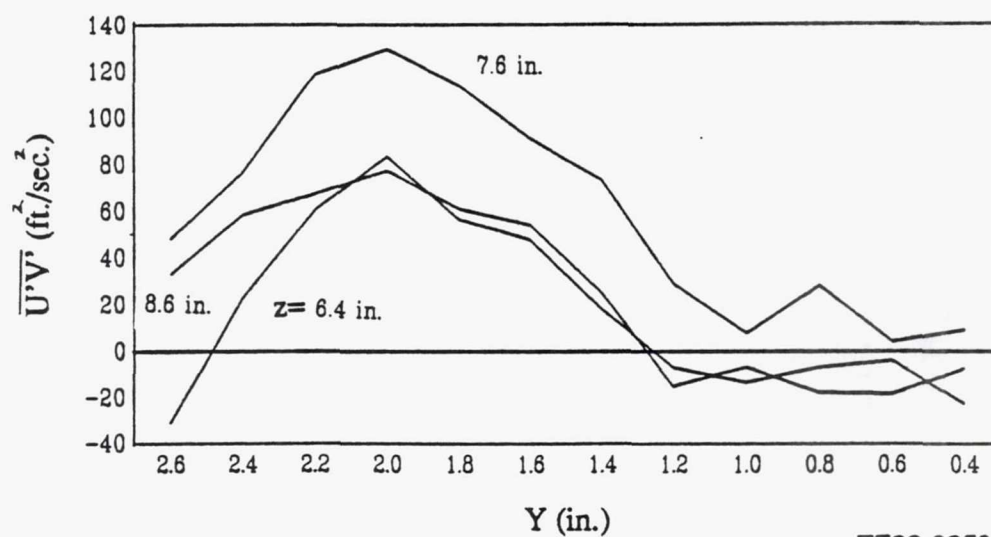
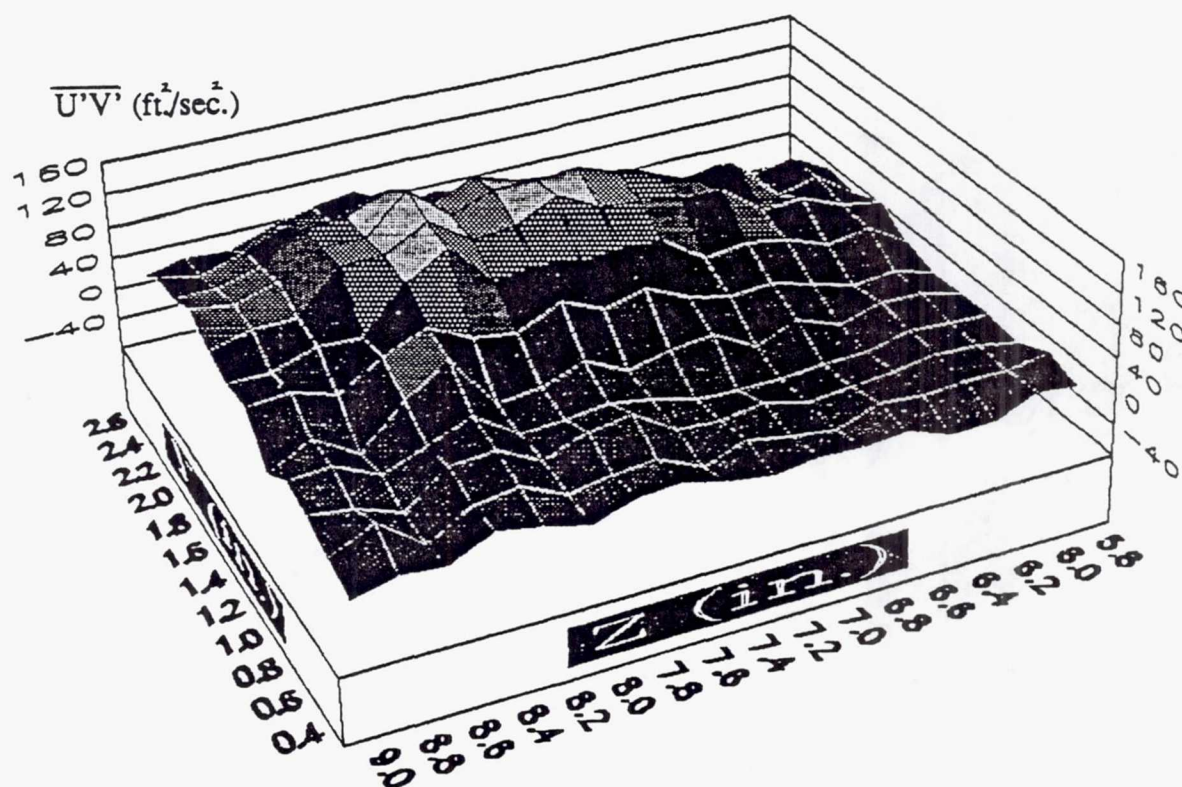
TE92-2348

Figure 3.1.1-96. Contour and line plots of $\overline{U'V'}$ at $x=4.00$ in.



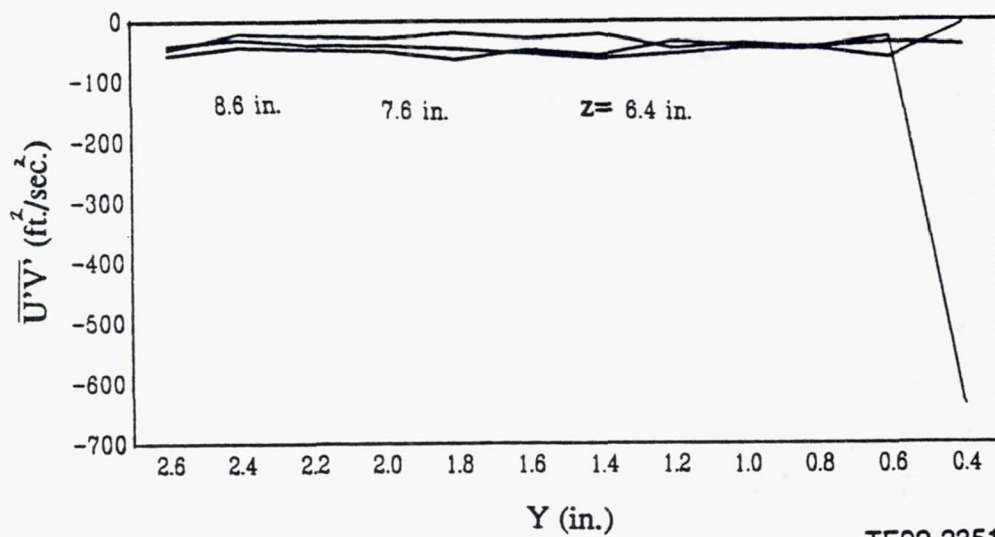
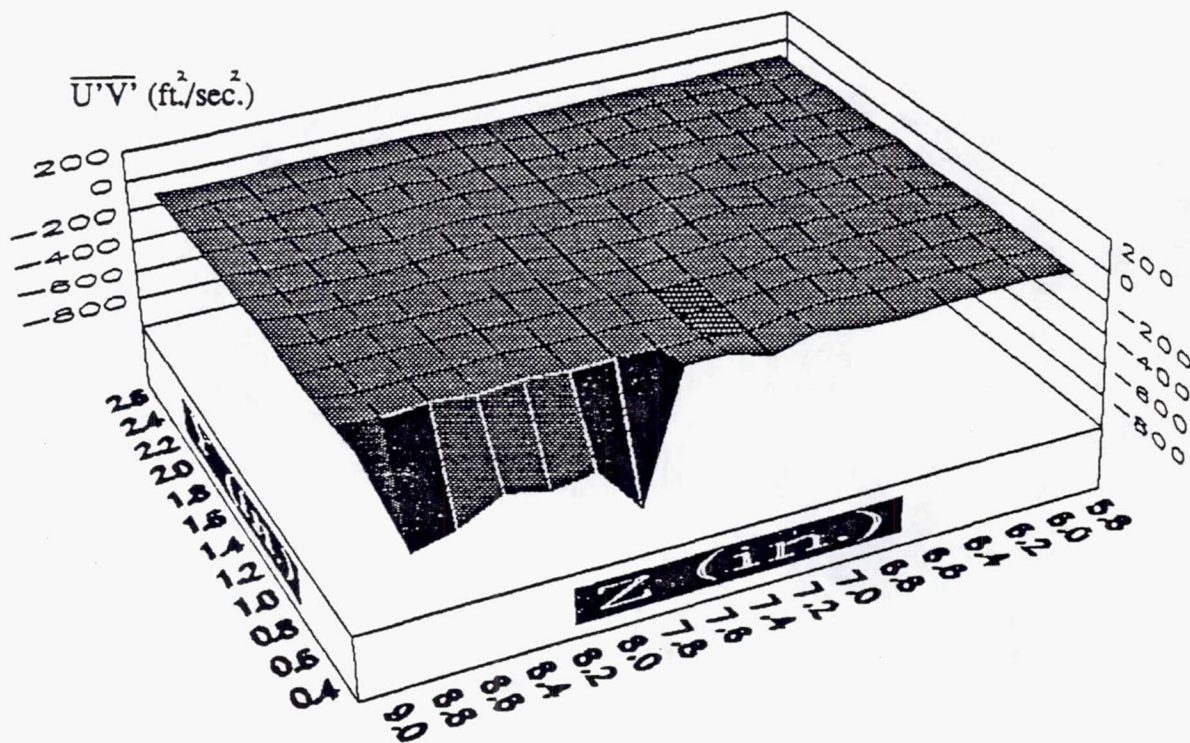
TE92-2349

Figure 3.1.1-97. Contour and line plots of $\overline{U'V'}$ at $x=4.50$ in.



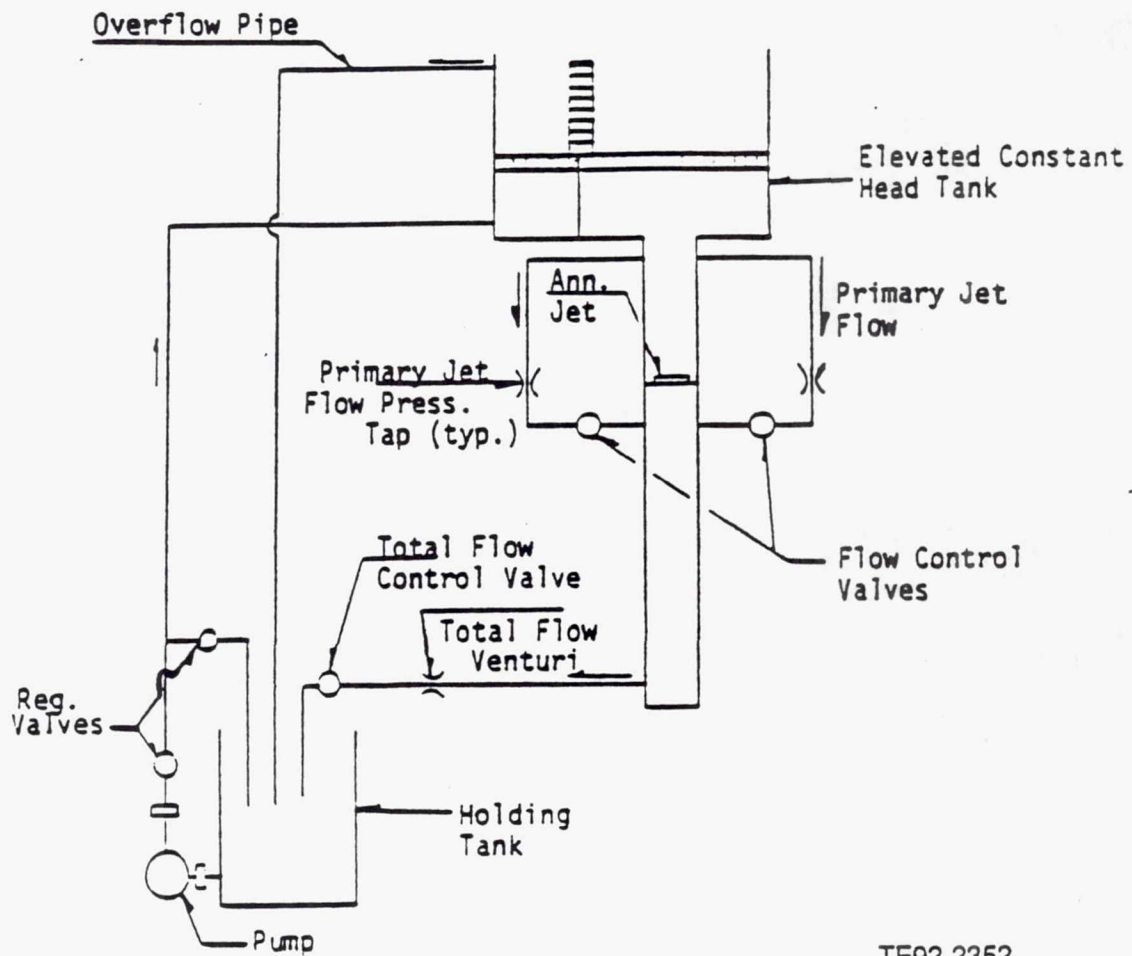
TE92-2350

Figure 3.1.1-98. Contour and line plots of $\overline{U'V'}$ at $x=6.00$ in.



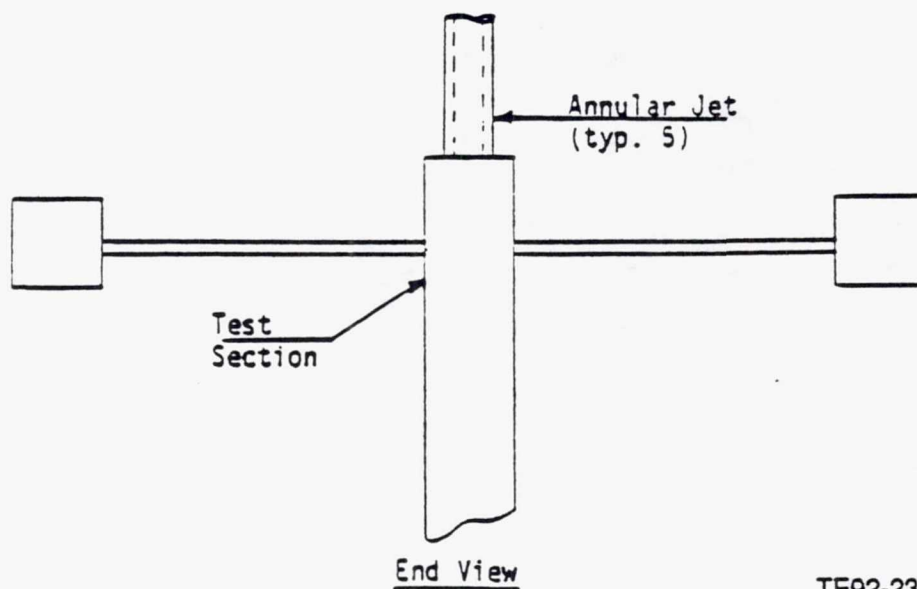
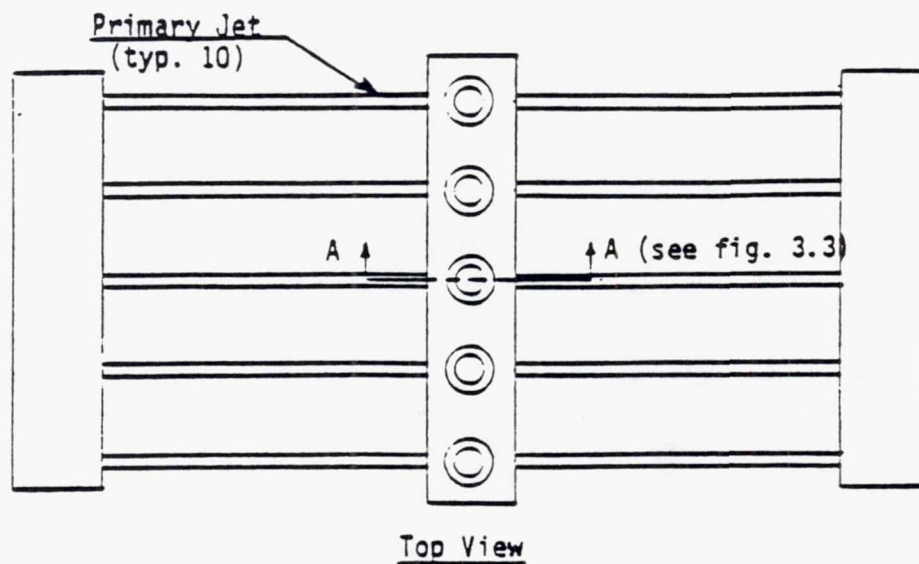
TE92-2351

Figure 3.1.1-99. Contour and line plots of $\overline{U'V'}$ at $x=9.00$ in.



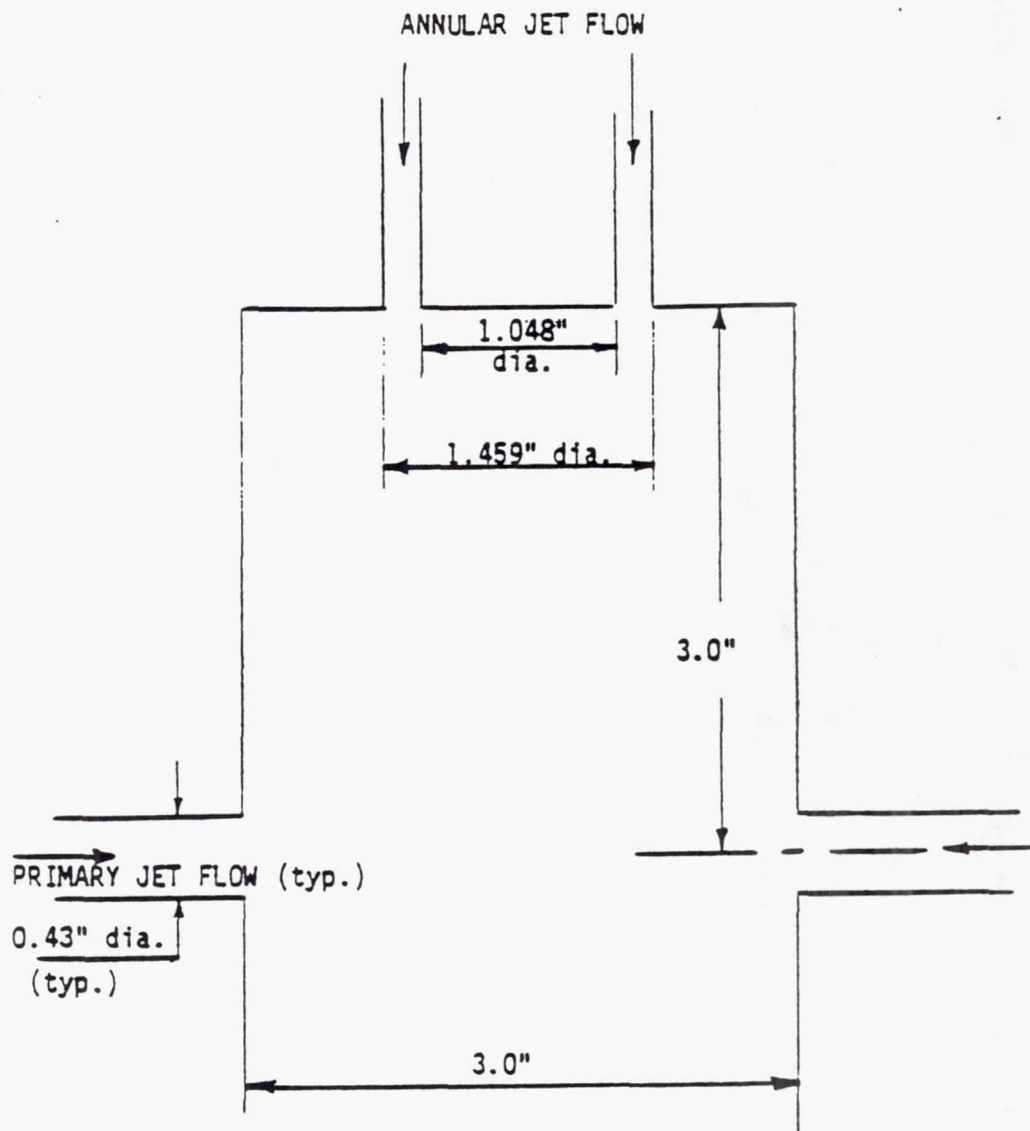
TE92-2352

Figure 3.1.2-1. Model annular combustor test rig schematic.



TE92-2353

Figure 3.1.2-2. Detail of model annular combustor test section.

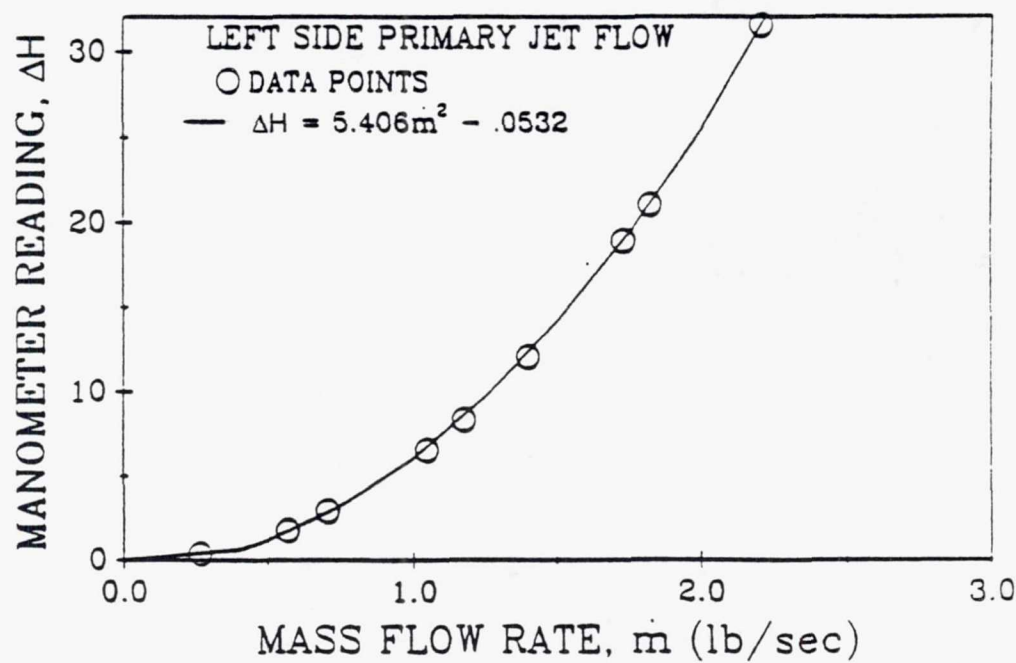
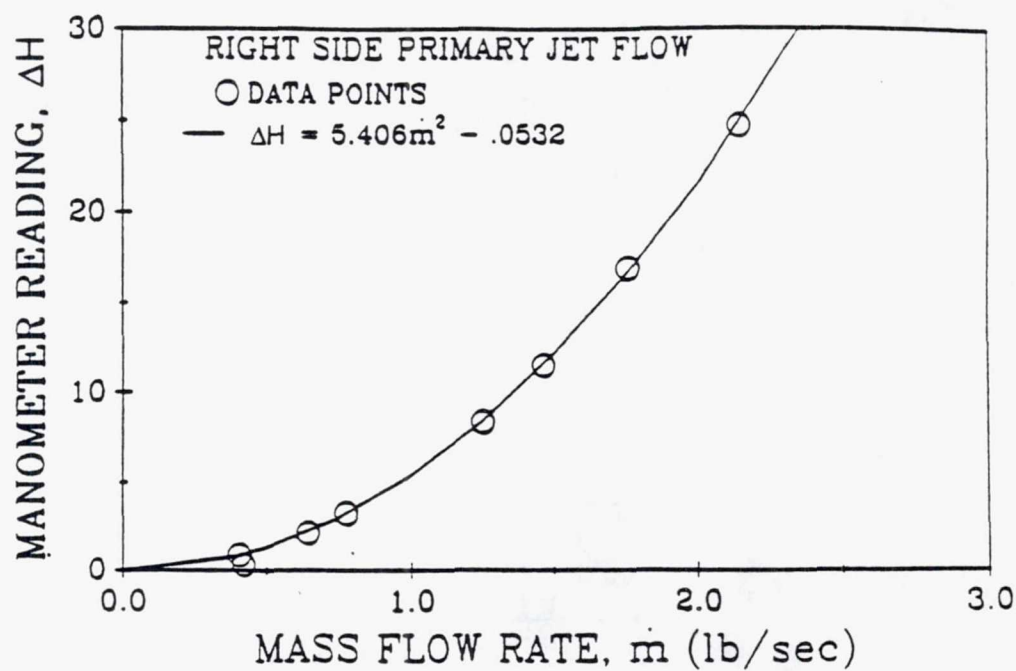


SECTION A-A (ref. figure 3.2)

NOTE: All dimensions are internal dimensions

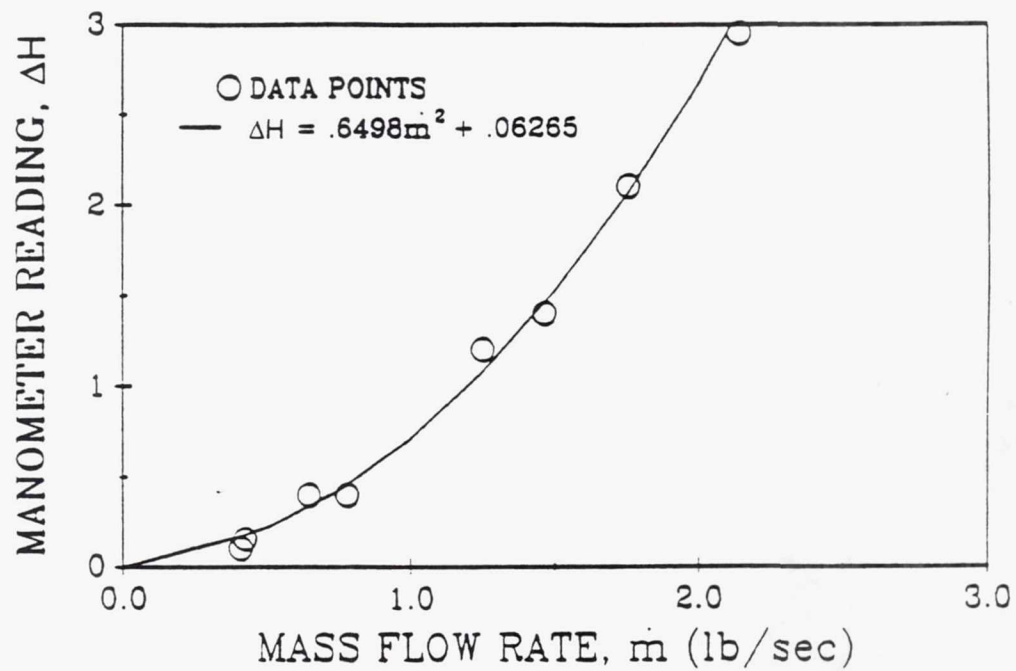
TE92-2354

Figure 3.1.2.-3. Section of model annular combustor test section.



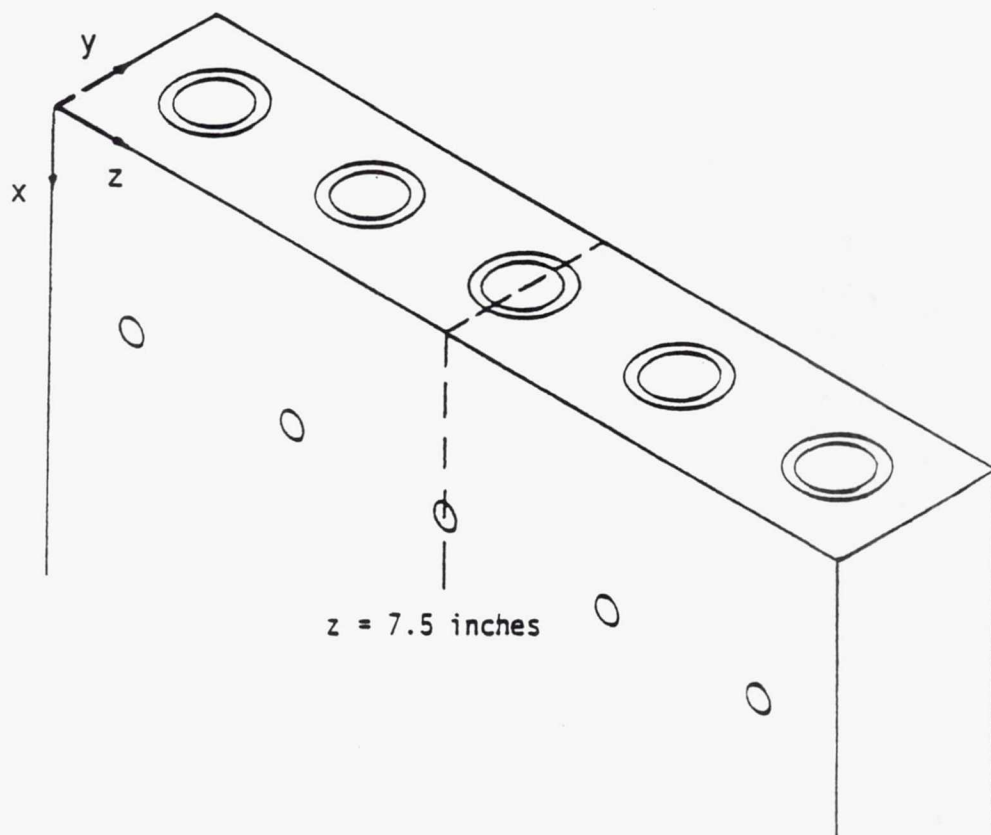
TE92-2356

Figure 3.1.2-4. Flow calibration curves for primary jet flow.



TE92-2357

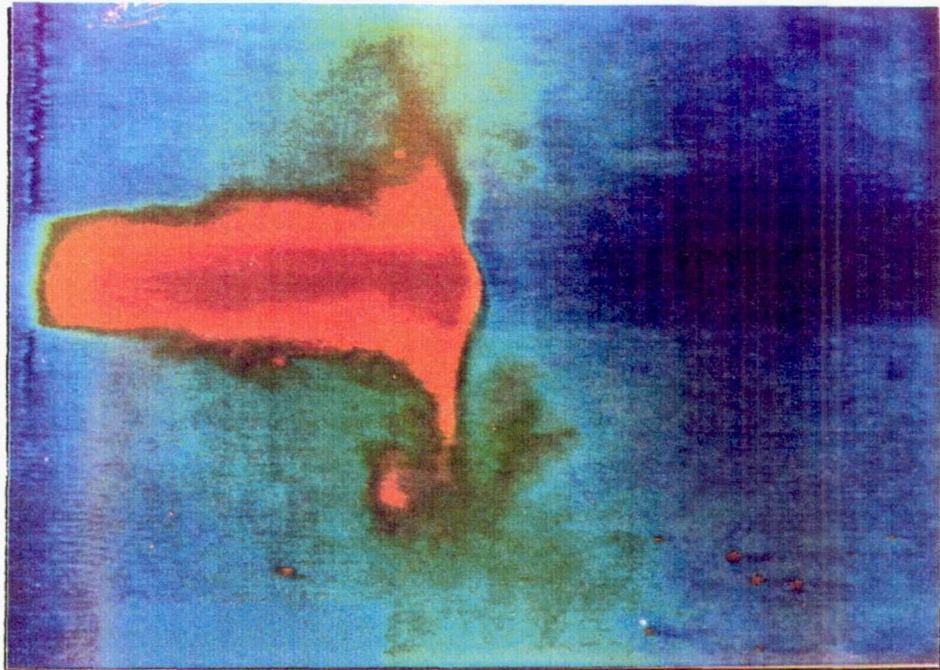
Figure 3.1.2-5. Venturi calibration curve for total jet flow.



TE92-2358

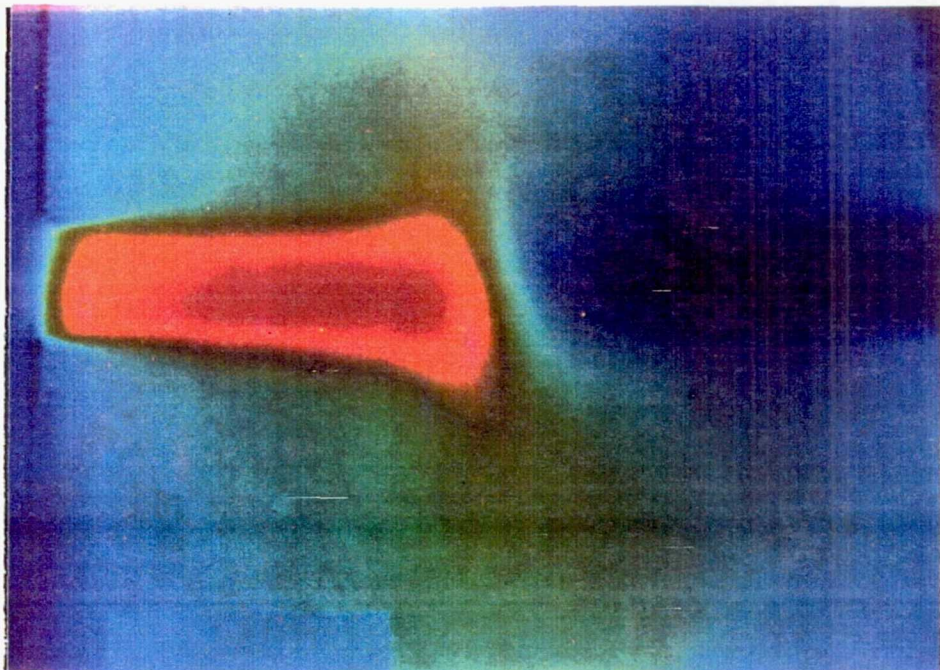
Figure 3.1.2-6. Model annular combustor coordinate system.

Page intentionally left blank



TE92-2359

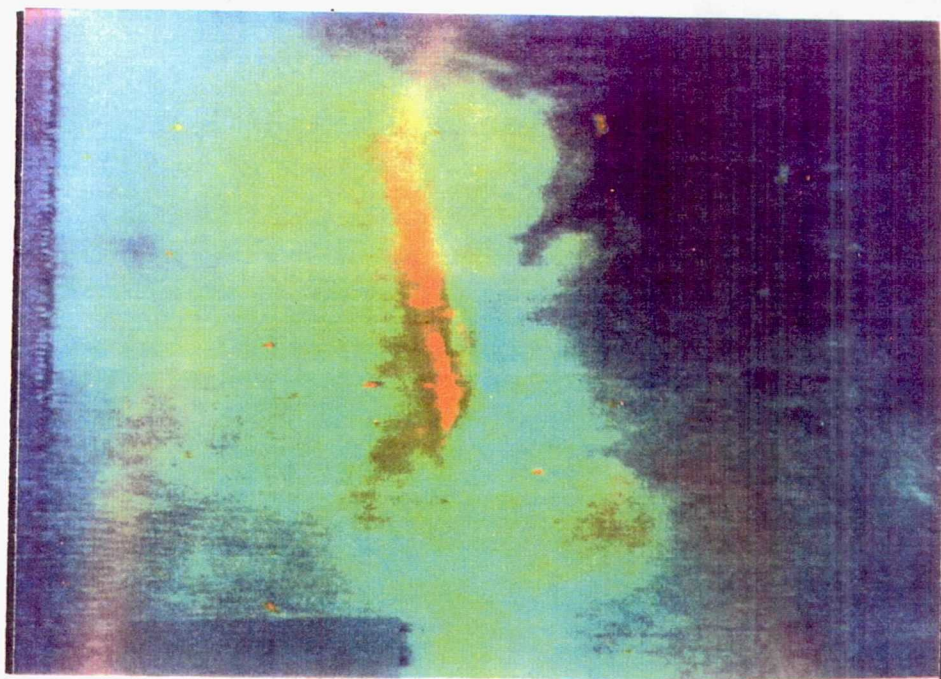
Figure 3.1.2-7. Single frame primary jet concentration field visualization image without annular jet flow ($z = 7.5$ in.).



TE92-2360

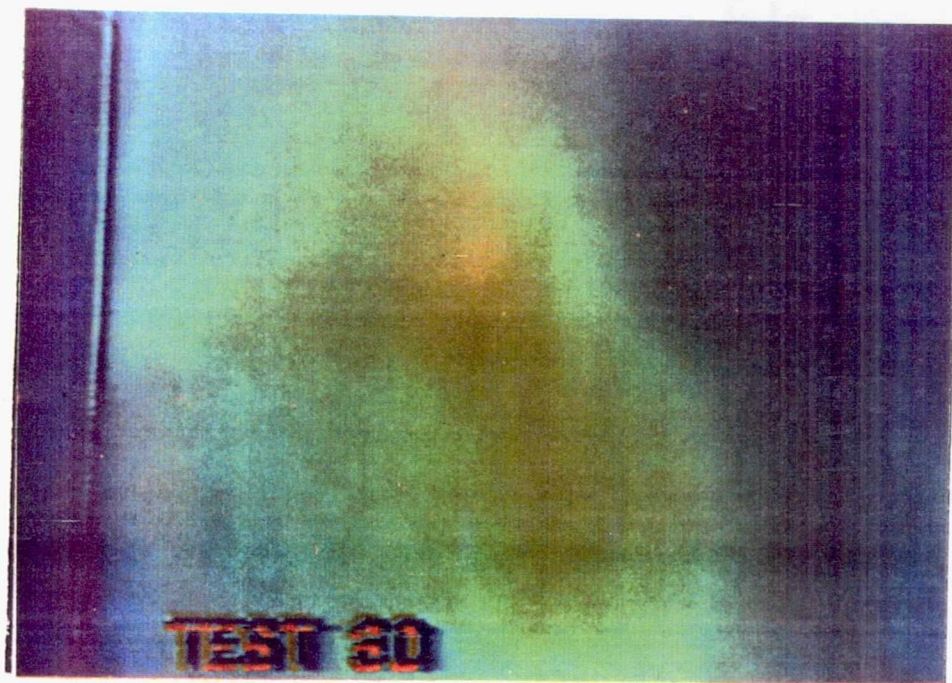
Figure 3.1.2-8. One hundred twenty-seven frame average primary jet concentration field visualization image without annular jet flow ($z = 7.5$ in.).

Page intentionally left blank



TE92-2361

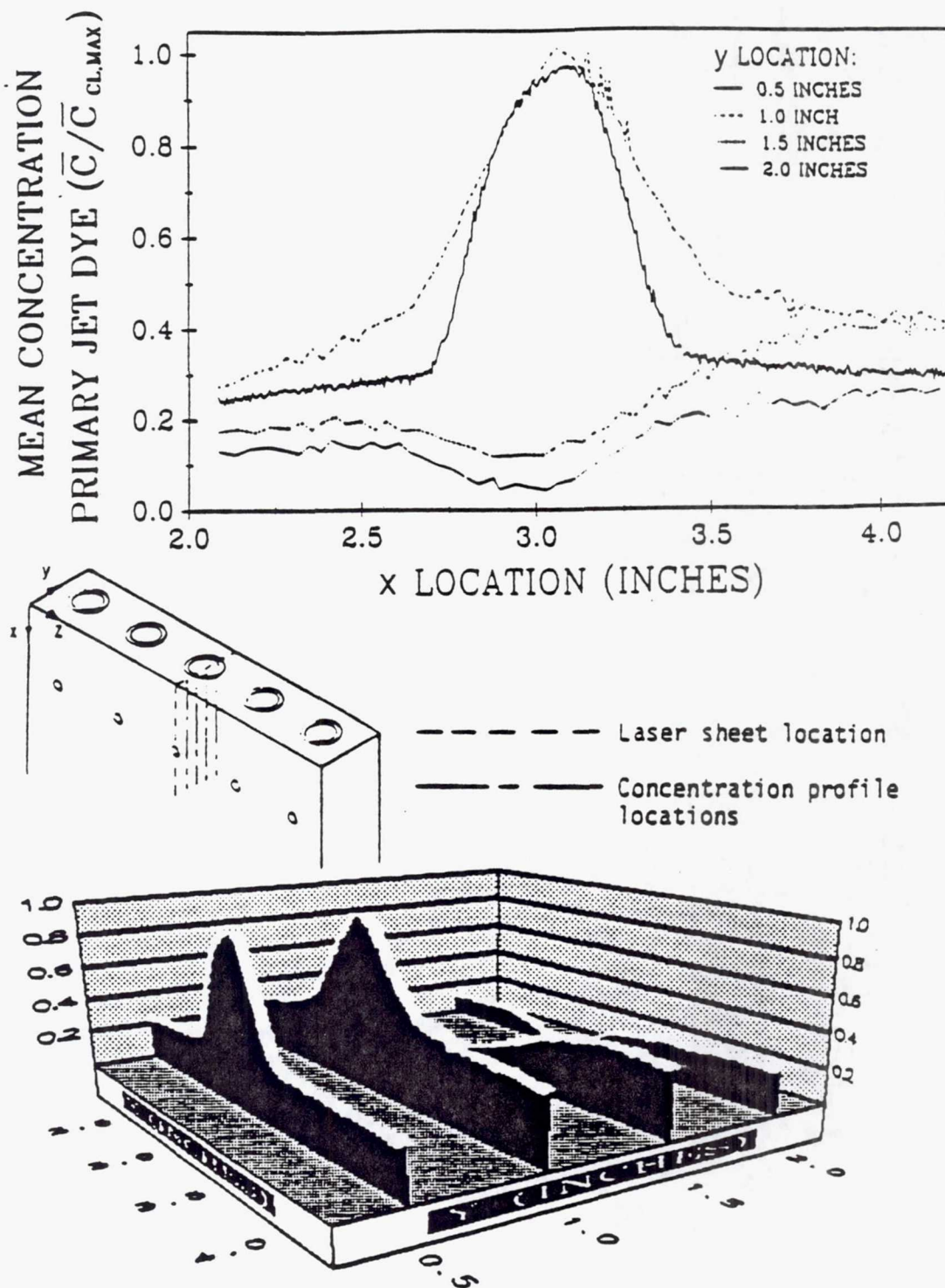
Figure 3.1.2-9. Single frame primary jet concentration field visualization image without annular jet flow ($z = 7.0$ in.).



TE92-2362

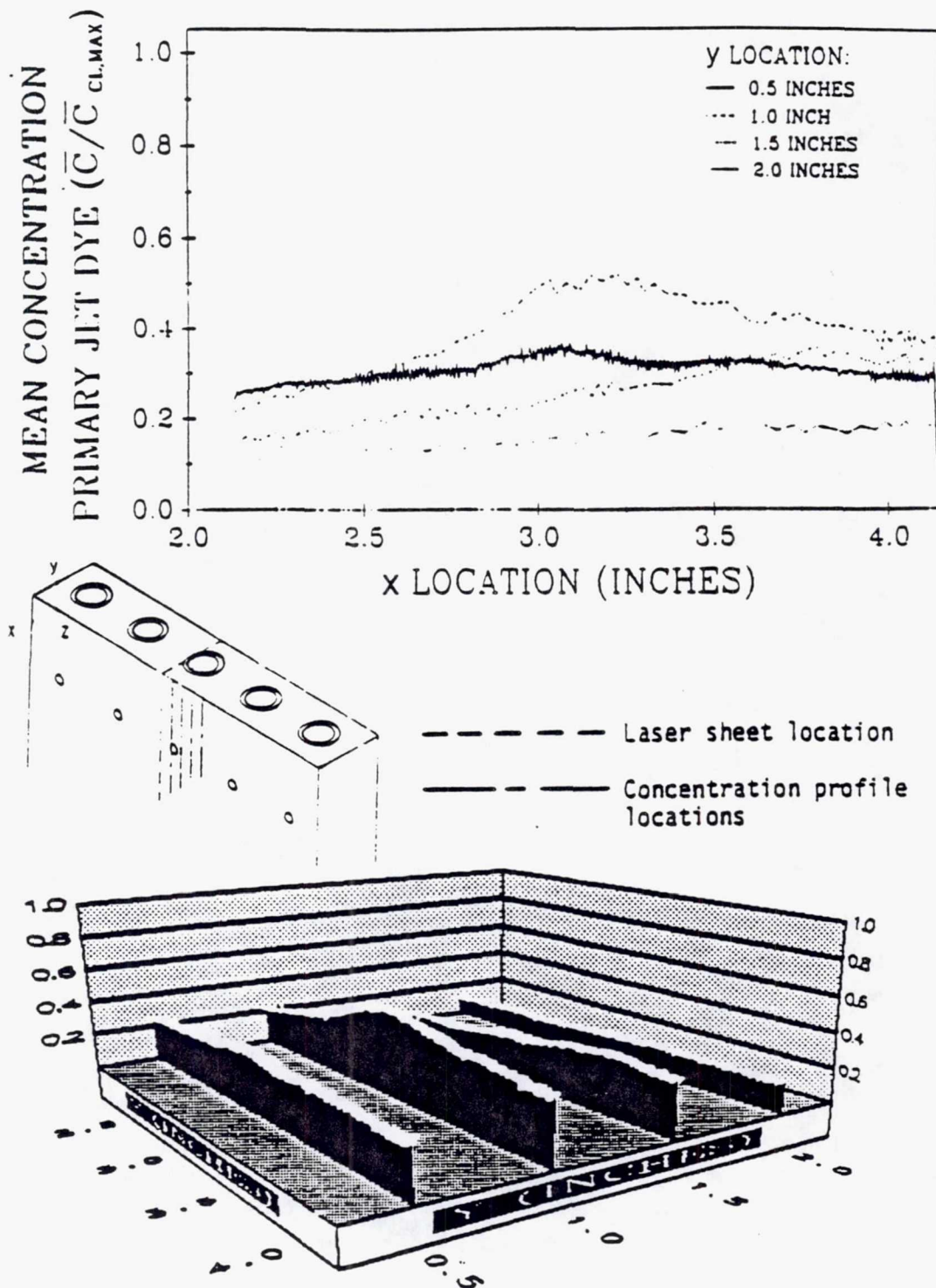
Figure 3.1.2-10. One hundred twenty-seven frame average primary jet concentration field visualization image without annular jet flow ($z = 7.0$ in.).

Page intentionally left blank



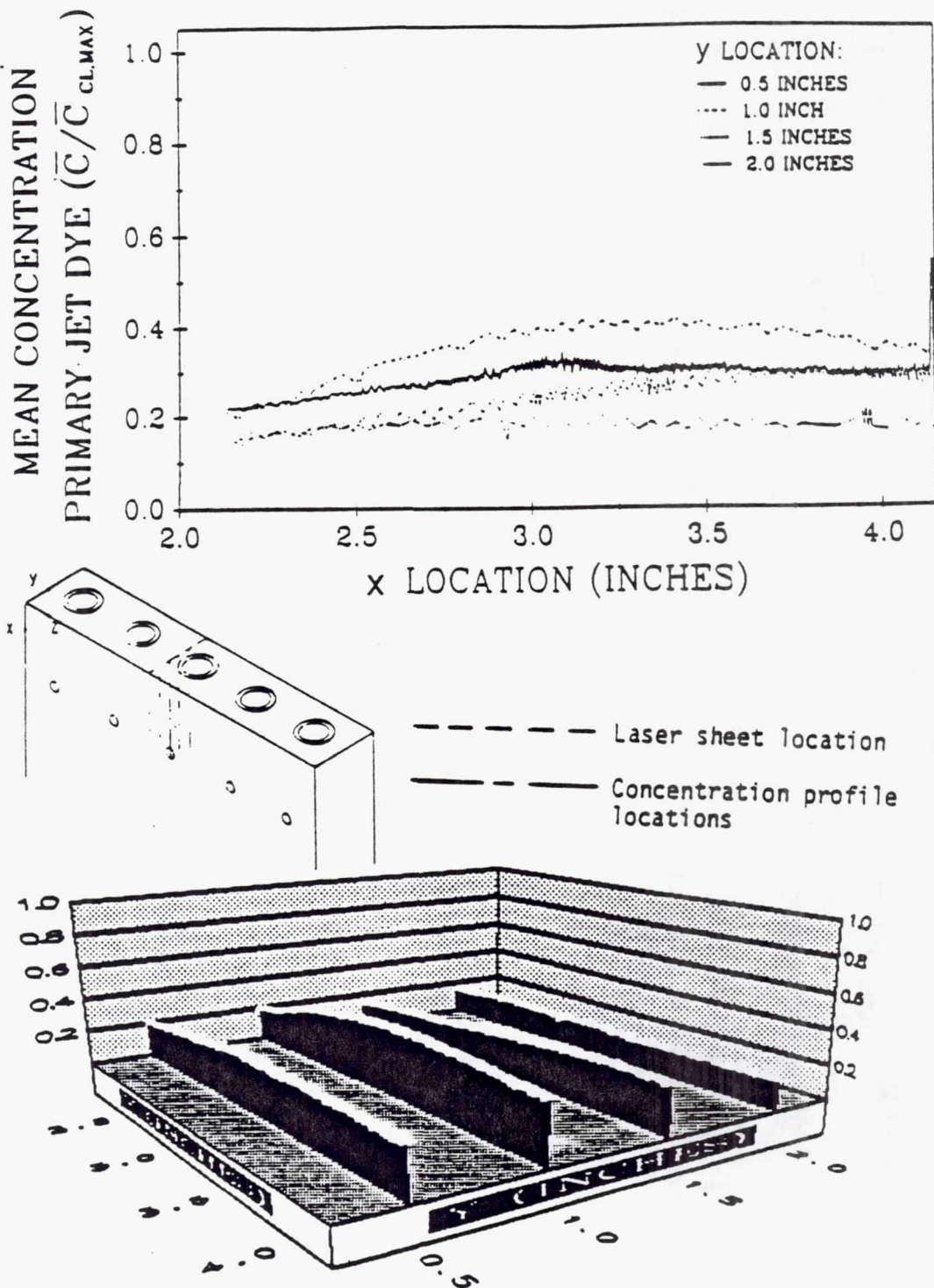
TE92-2363

Figure 3.1.2-11. Mean primary jet concentration without annular jet flow ($z = 7.5$ in.).



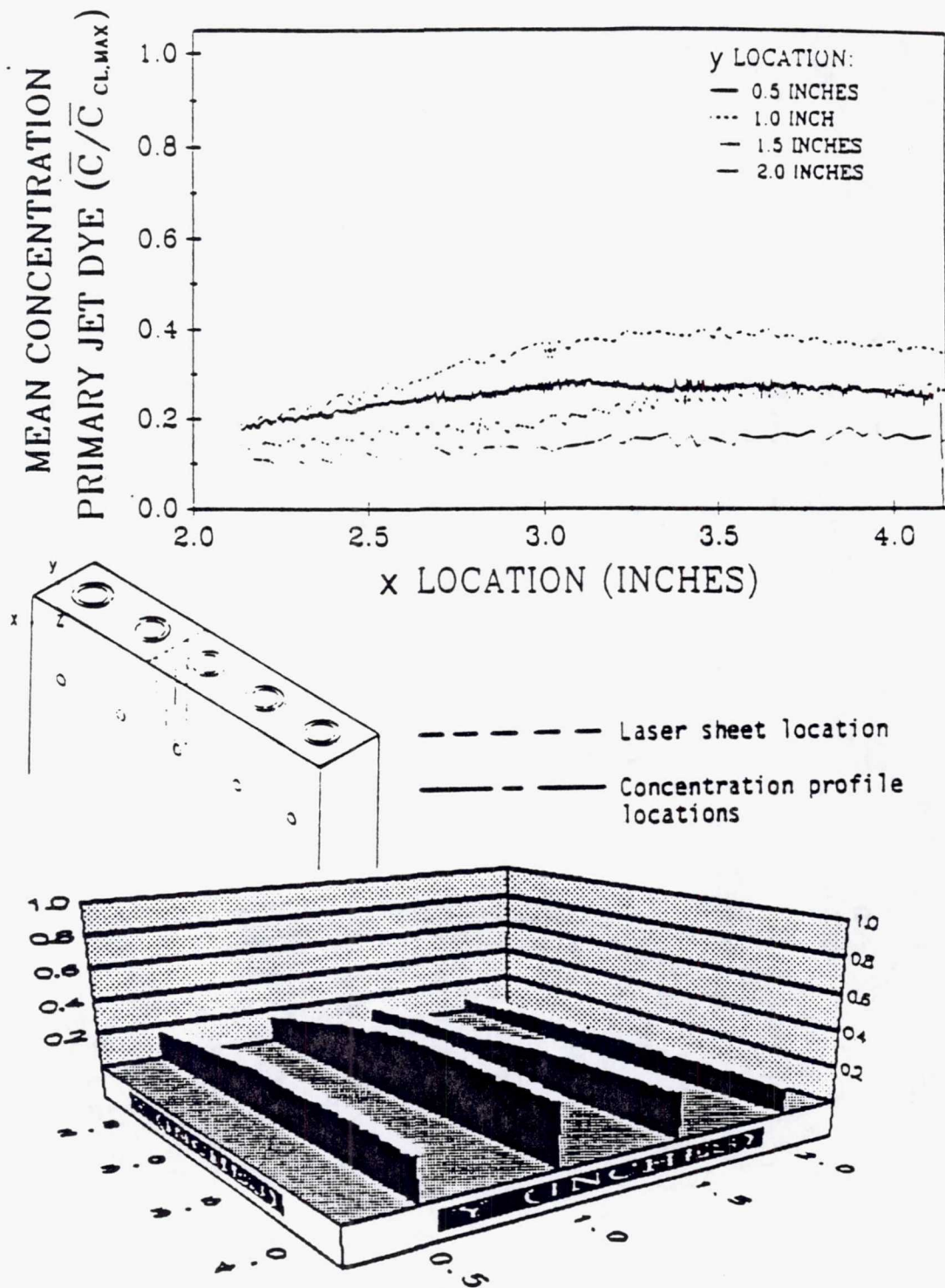
TE92-2364

Figure 3.1.2-12. Mean primary jet concentration without annular jet flow ($z = 7.0$ in.).



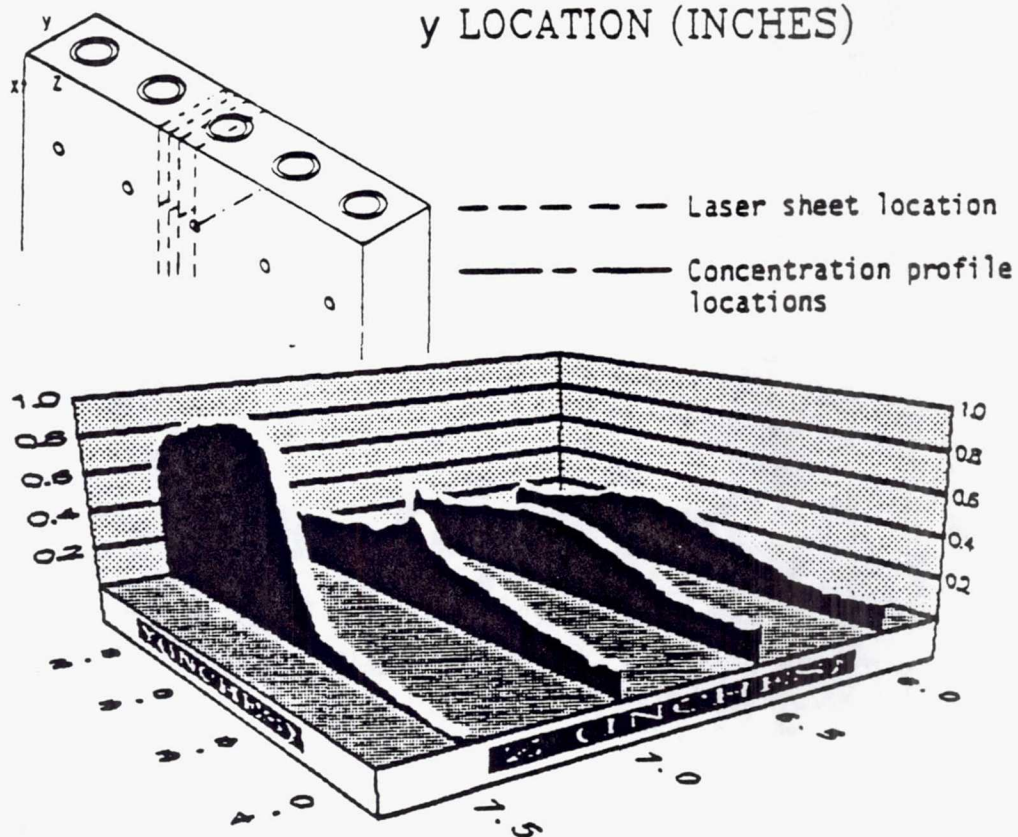
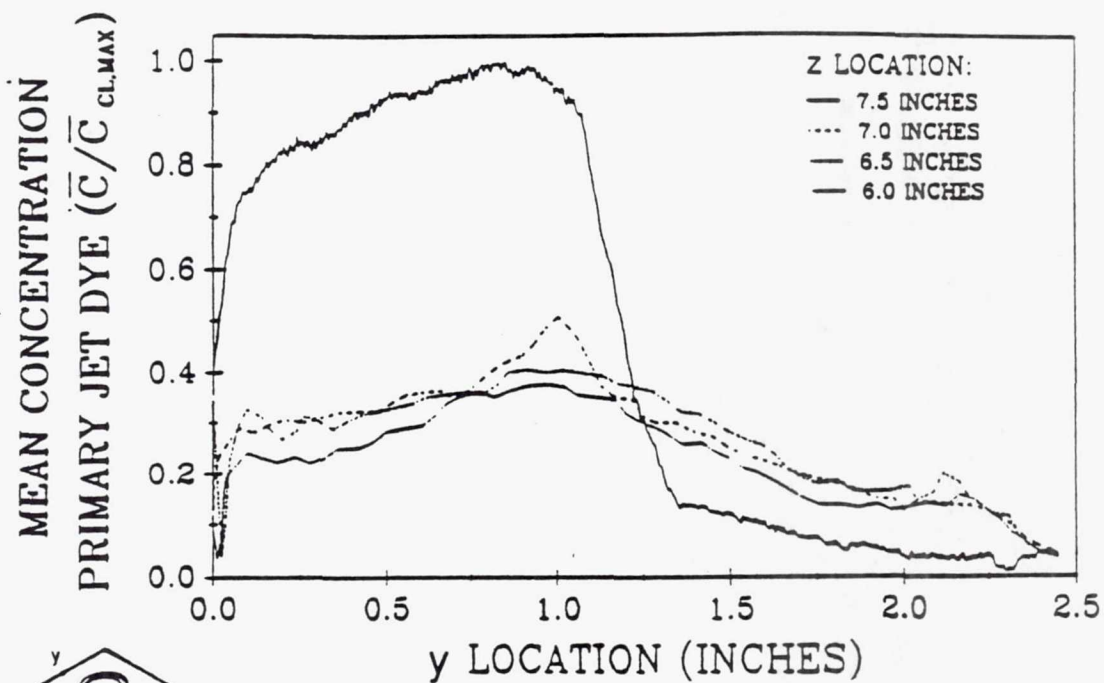
TE92-2365

Figure 3.1.2-13. Mean primary jet concentration without annular jet flow ($z = 6.5$ in.).



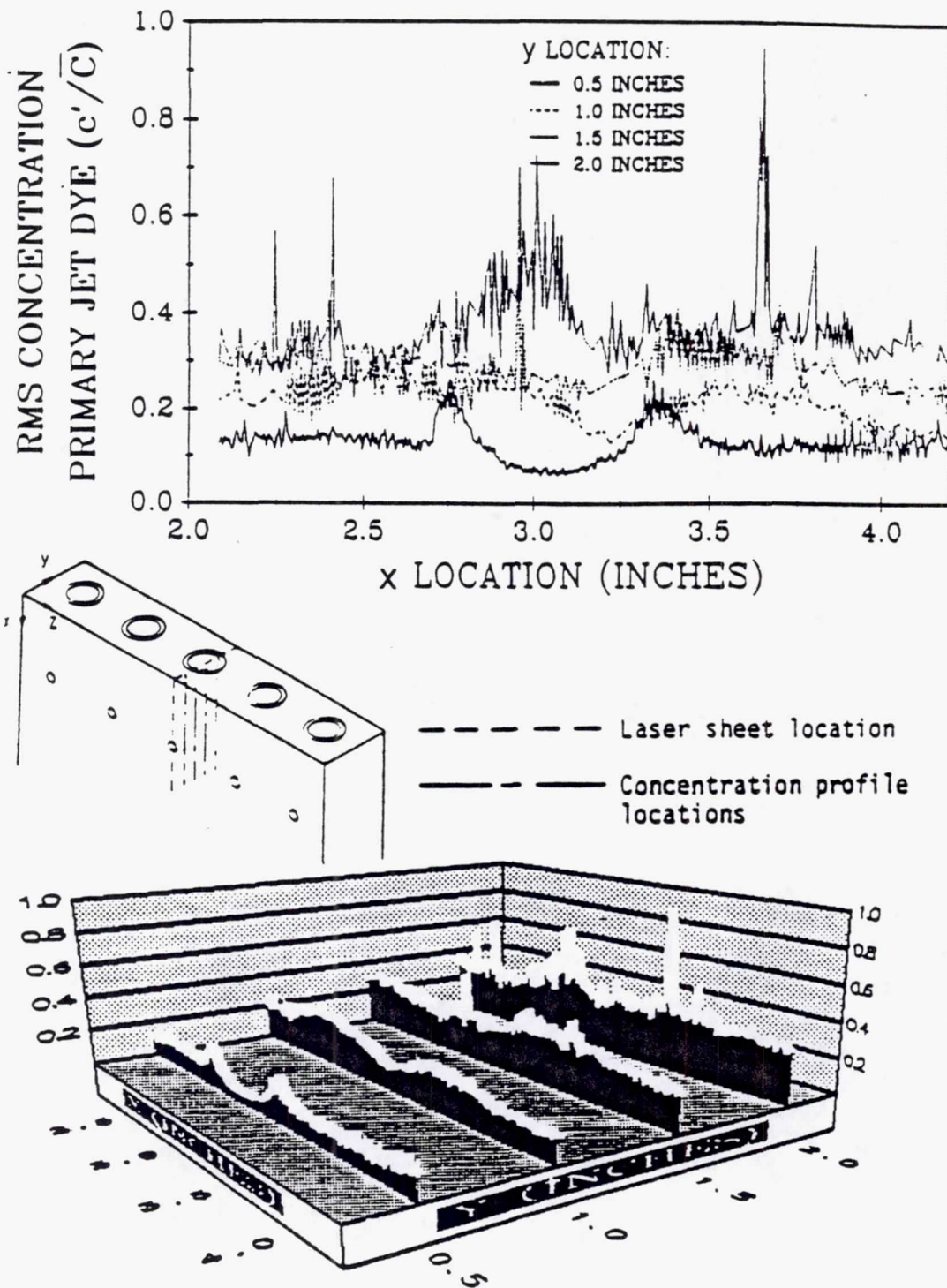
TE92-2366

Figure 3.1.2-14. Mean primary jet concentration without annular jet flow ($z = 6.0$ in.).



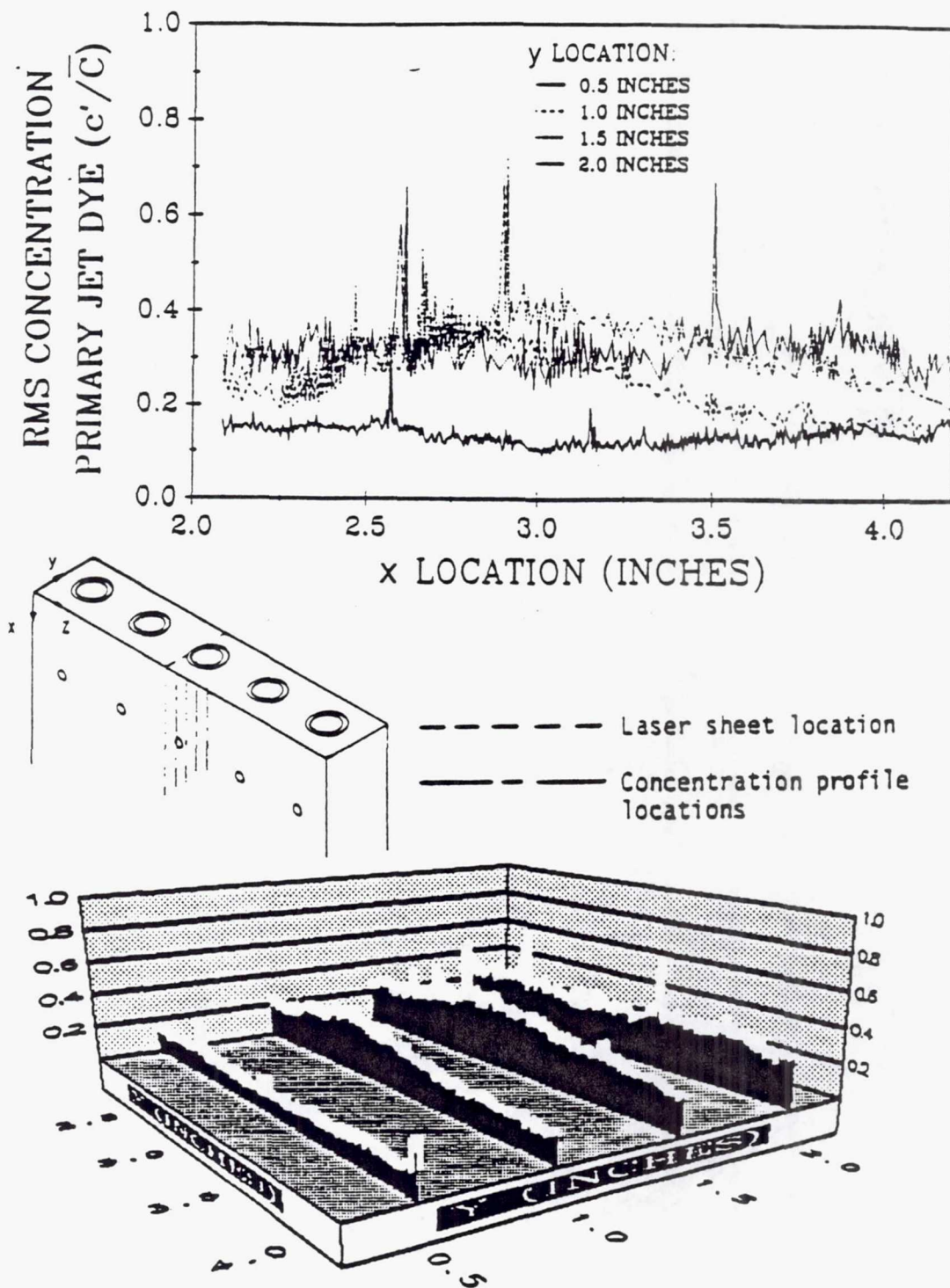
TE92-2367

Figure 3.1.2-15. Mean primary jet concentration without annular jet flow ($x = 3.0$ in.).



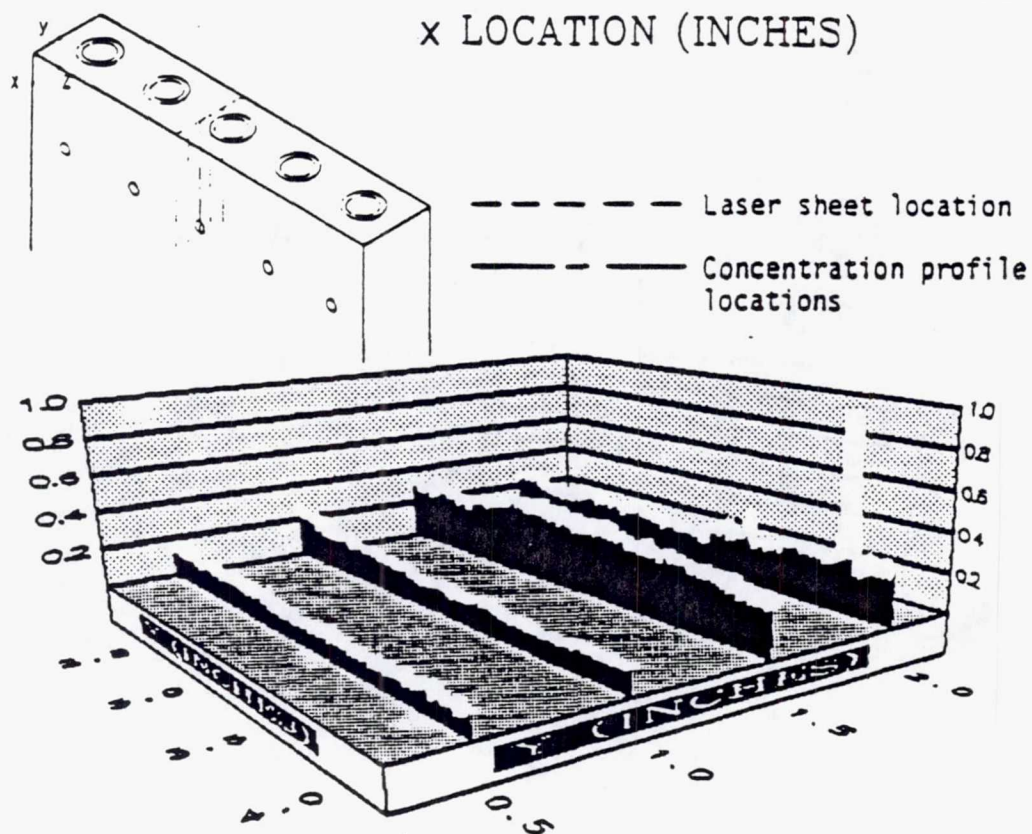
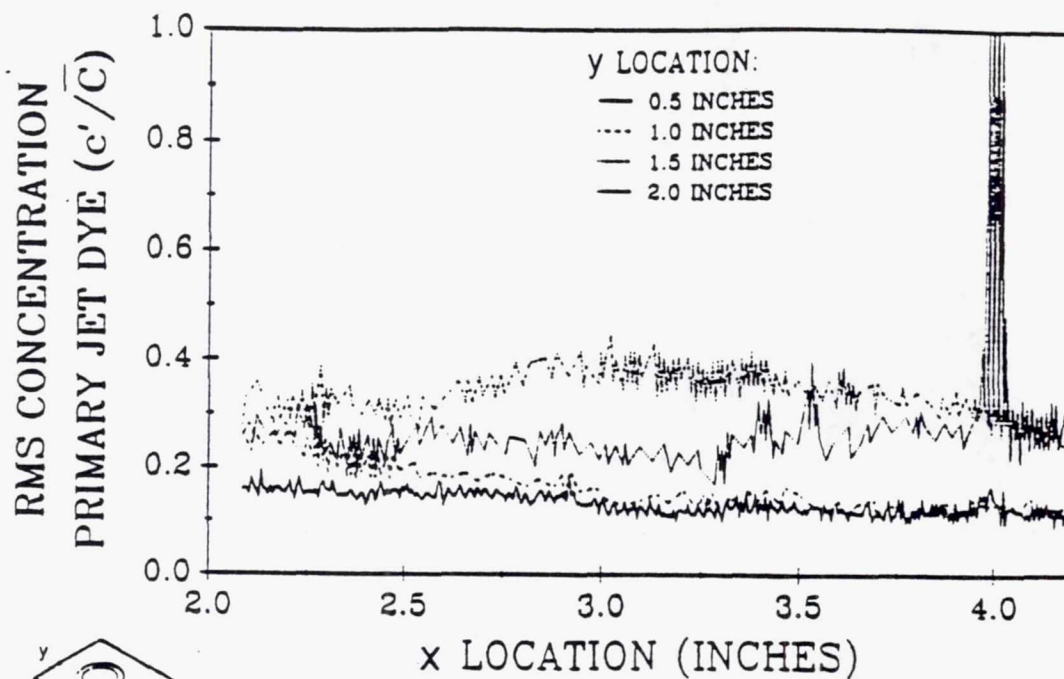
TE92-2368

Figure 3.1.2-16. Root mean square primary jet concentration without annular jet flow ($z = 7.5$ in.).



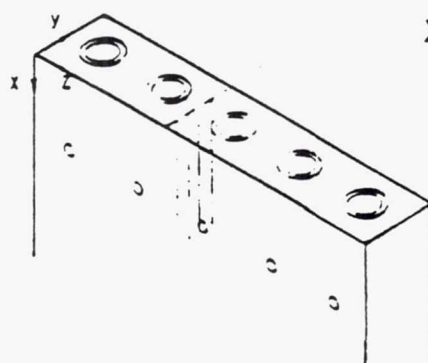
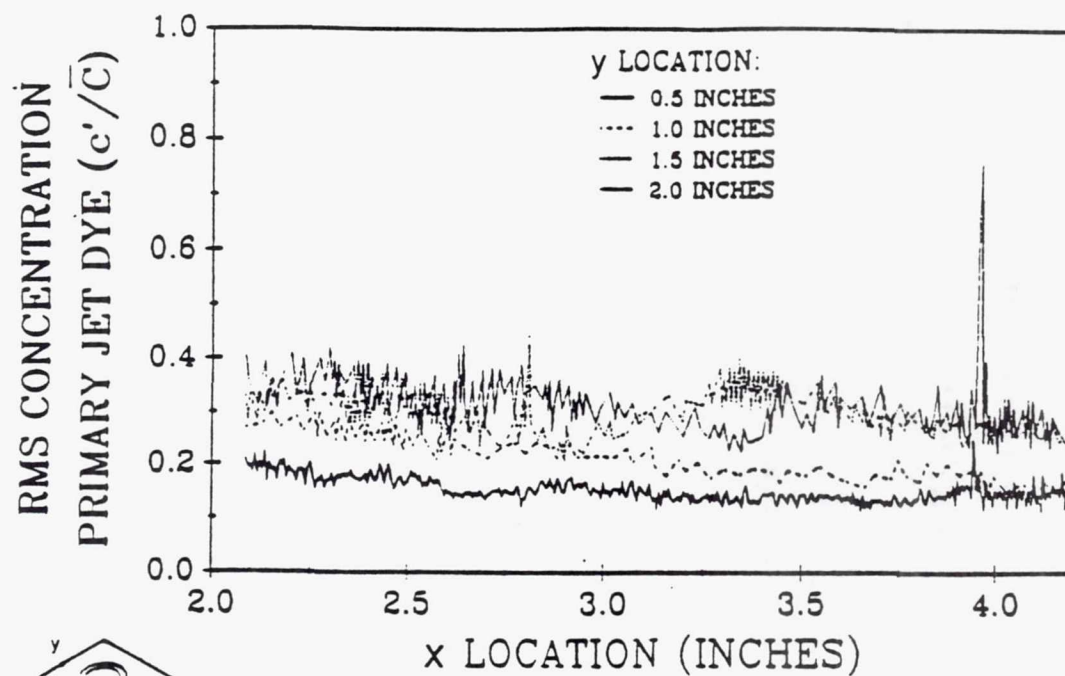
TE92-2369

Figure 3.1.2-17. Root mean square primary jet concentration without annular jet flow ($z = 7.0$ in.).

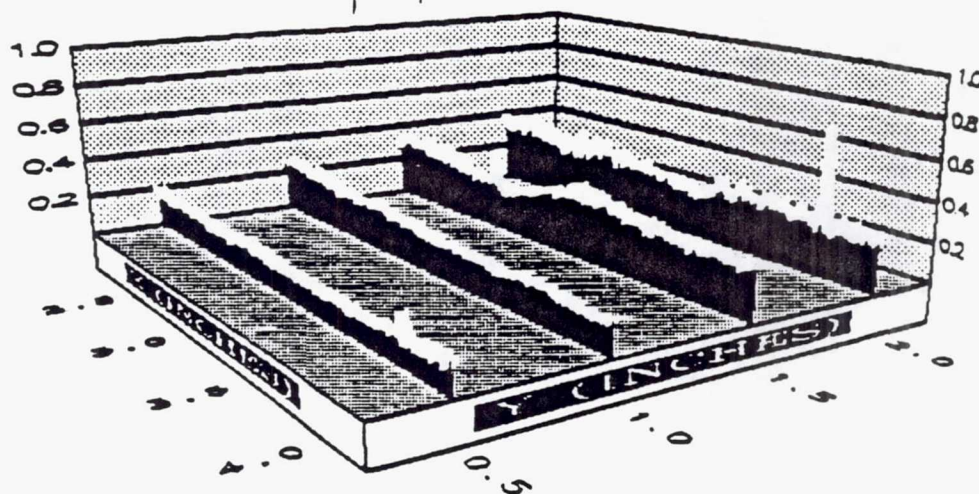


TE92-2370

Figure 3.1.2-18. Root mean square primary jet concentration without annular jet flow ($z = 6.5$ in.).

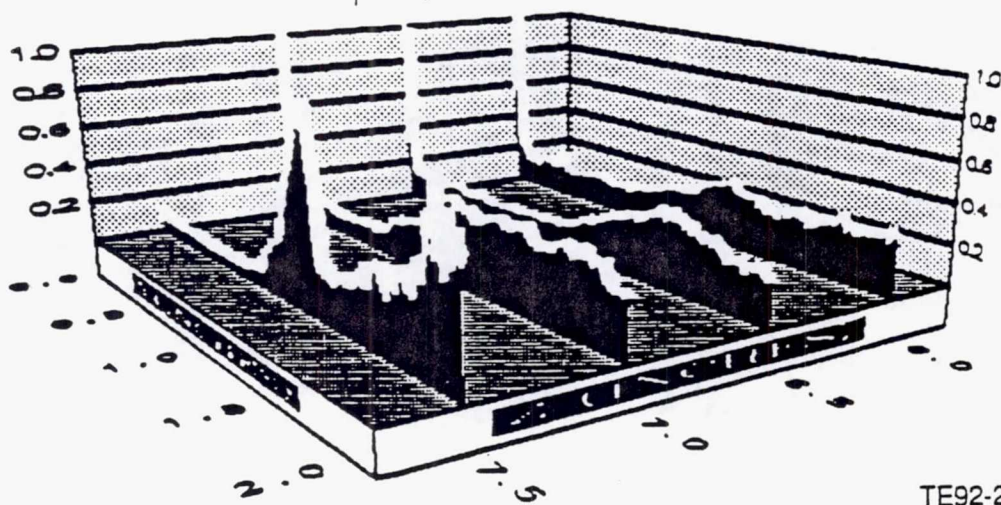
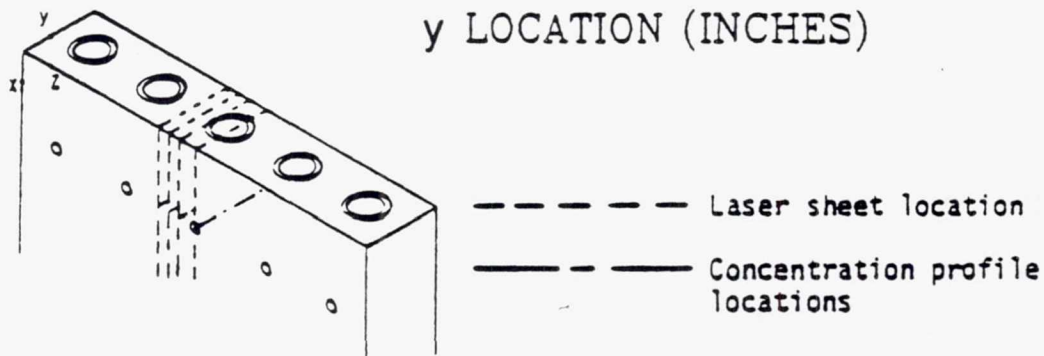
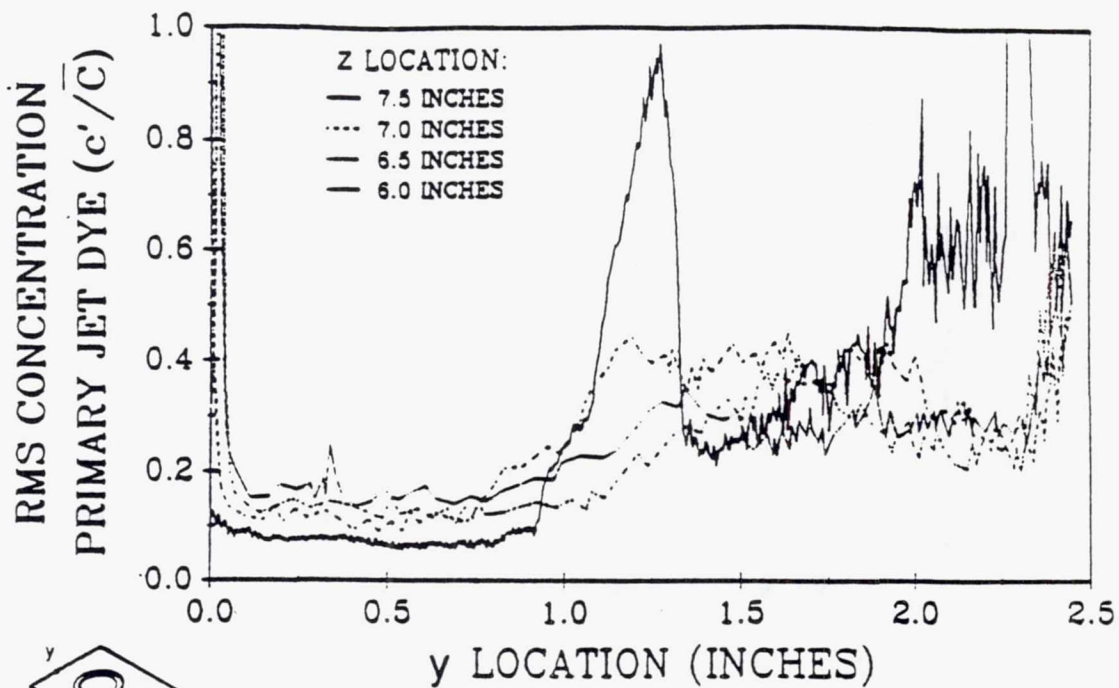


--- Laser sheet location
 --- Concentration profile locations



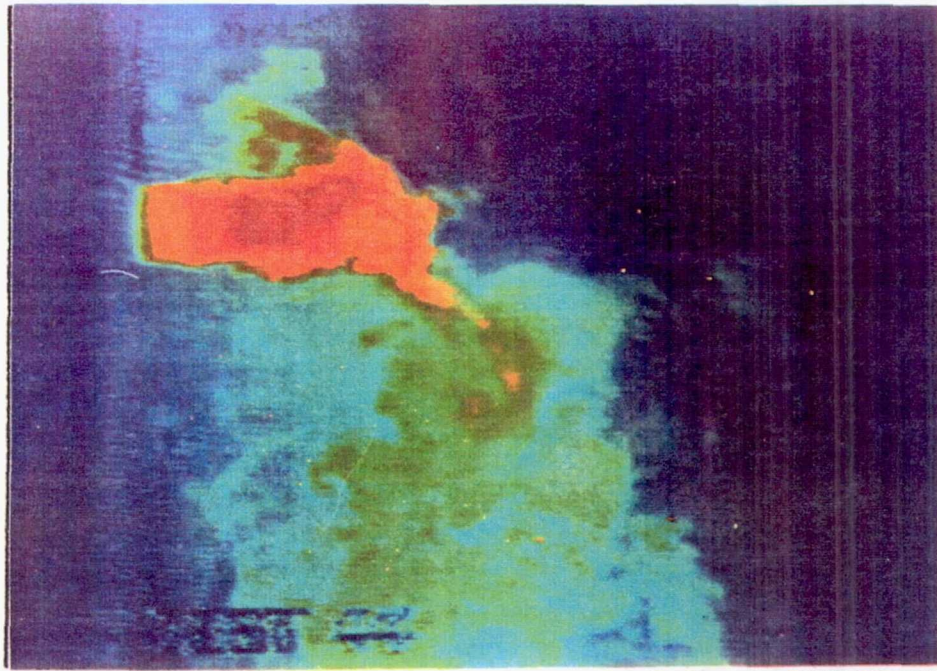
TE92-2371

Figure 3.1.2-19. Root mean square primary jet concentration without annular jet flow ($z = 6.0$ in.).



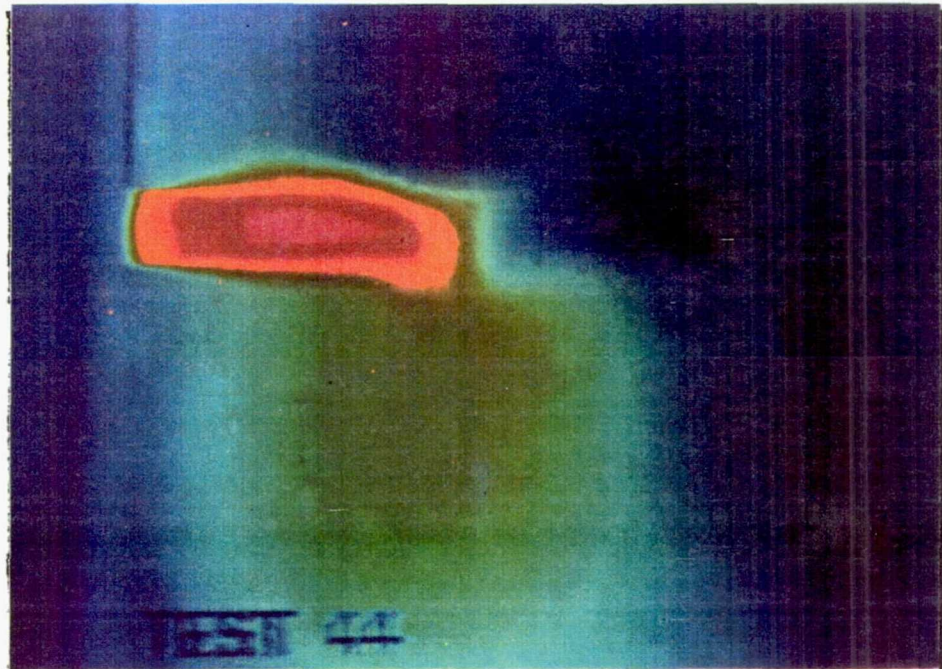
TE92-2372

Figure 3.1.2-20. Root mean square primary jet concentration without annular jet flow ($x = 3.0$ in.).



TE92-2373

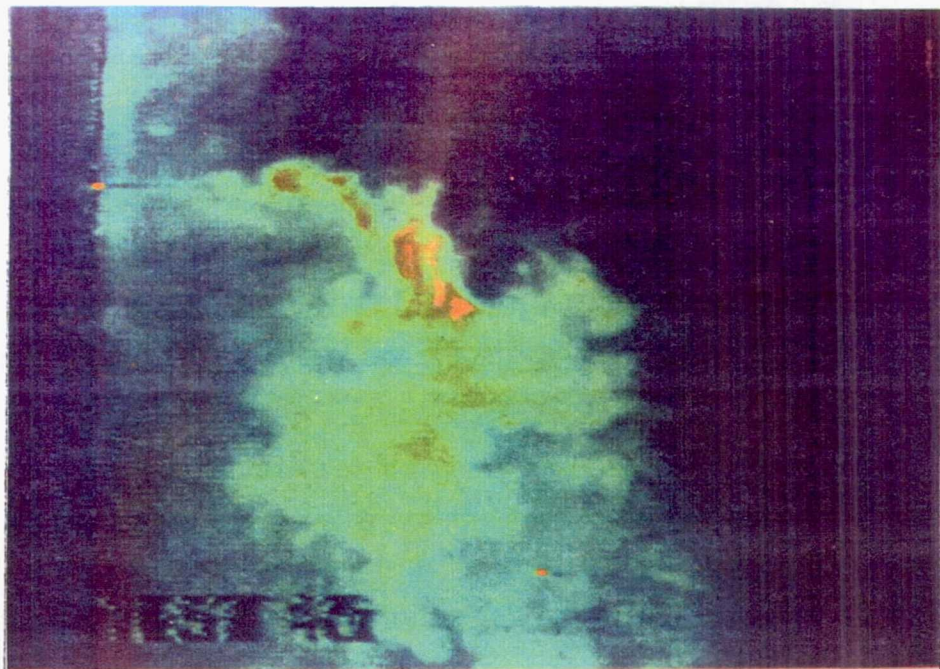
Figure 3.1.2-21. Single frame primary jet concentration field visualization image with annular jet flow ($Z = 7.5$ in.).



TE92-2374

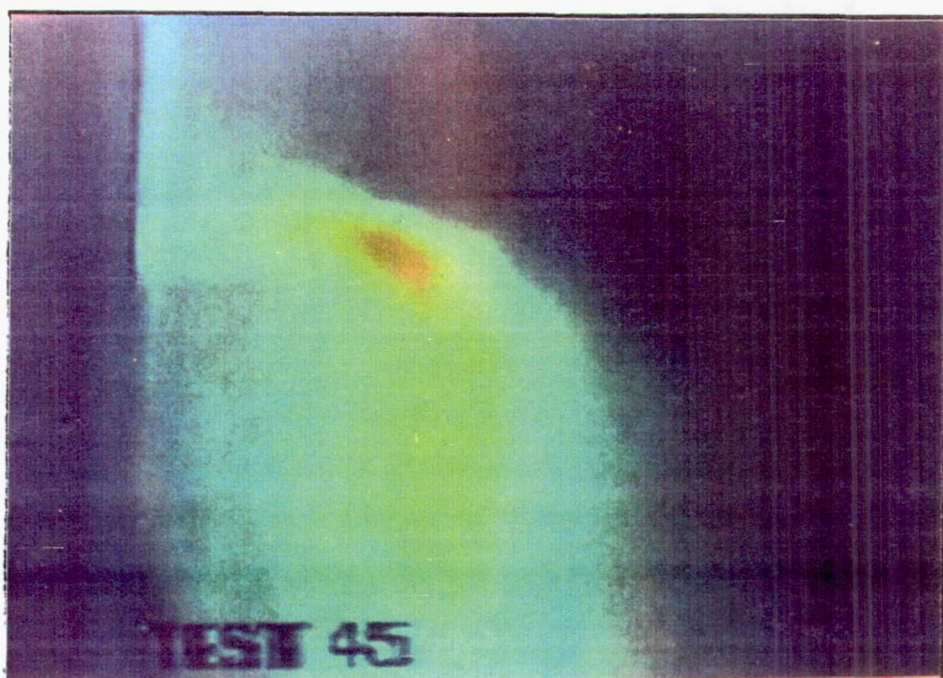
Figure 3.1.2-22. One hundred twenty-seven frame average primary jet concentration field visualization image with annular jet flow ($z \approx 7.5$ in.).

Page intentionally left blank



TE92-2375

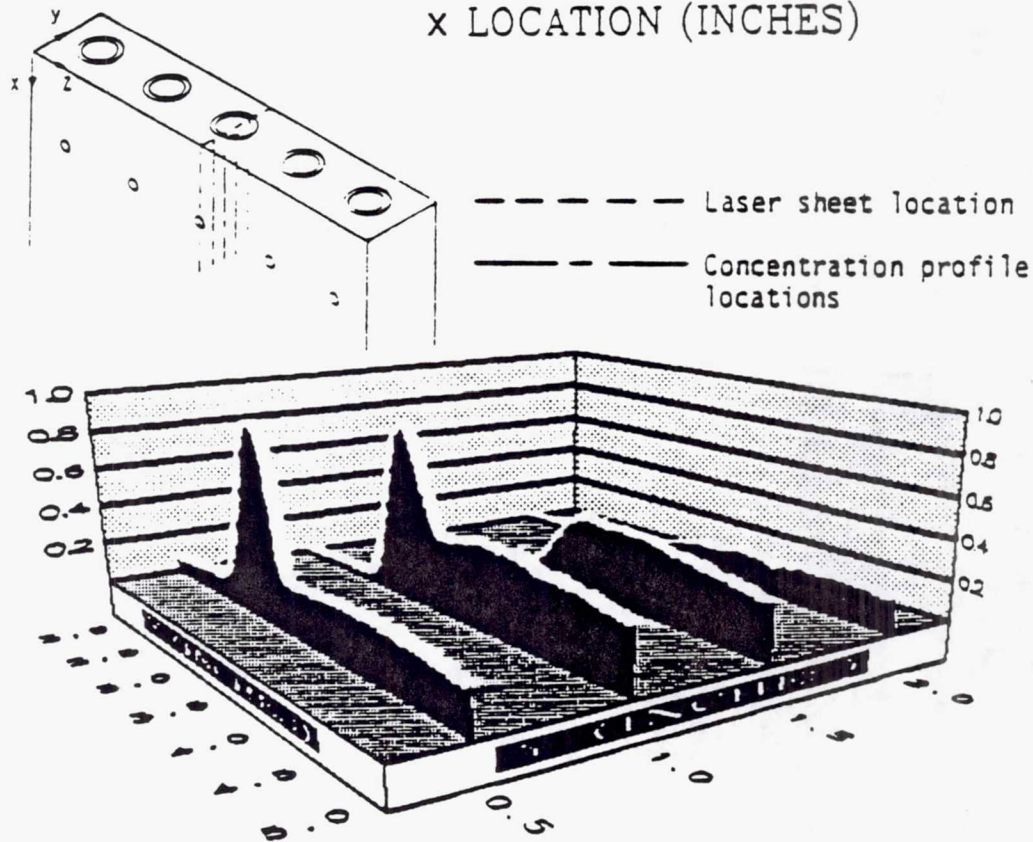
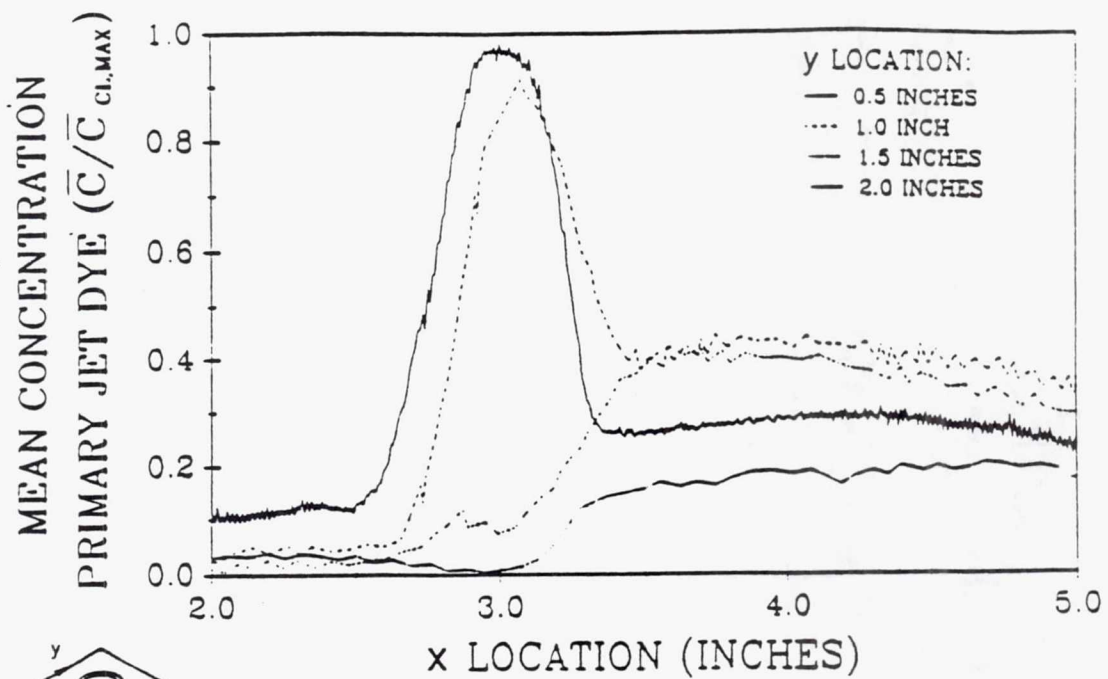
Figure 3.1.2-23. Single frame primary jet concentration field visualization image with annular jet flow ($z = 7.0$ in.).



TE92-2376

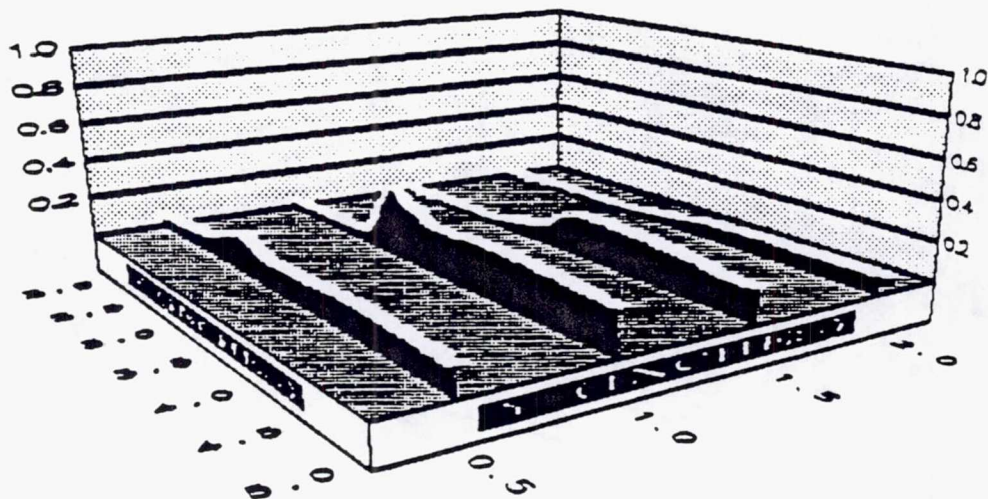
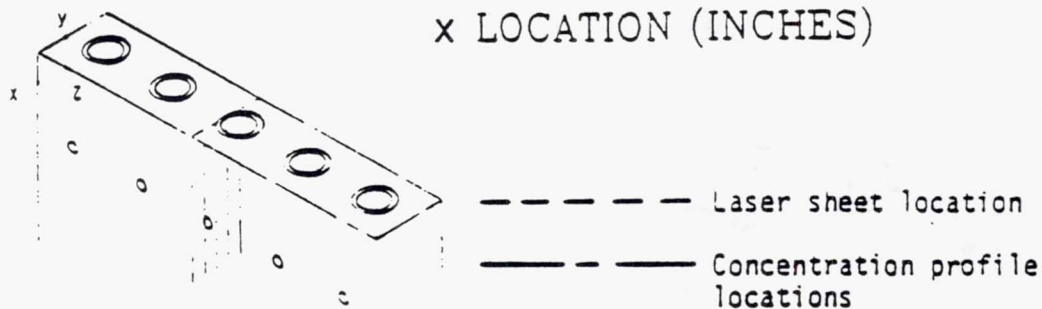
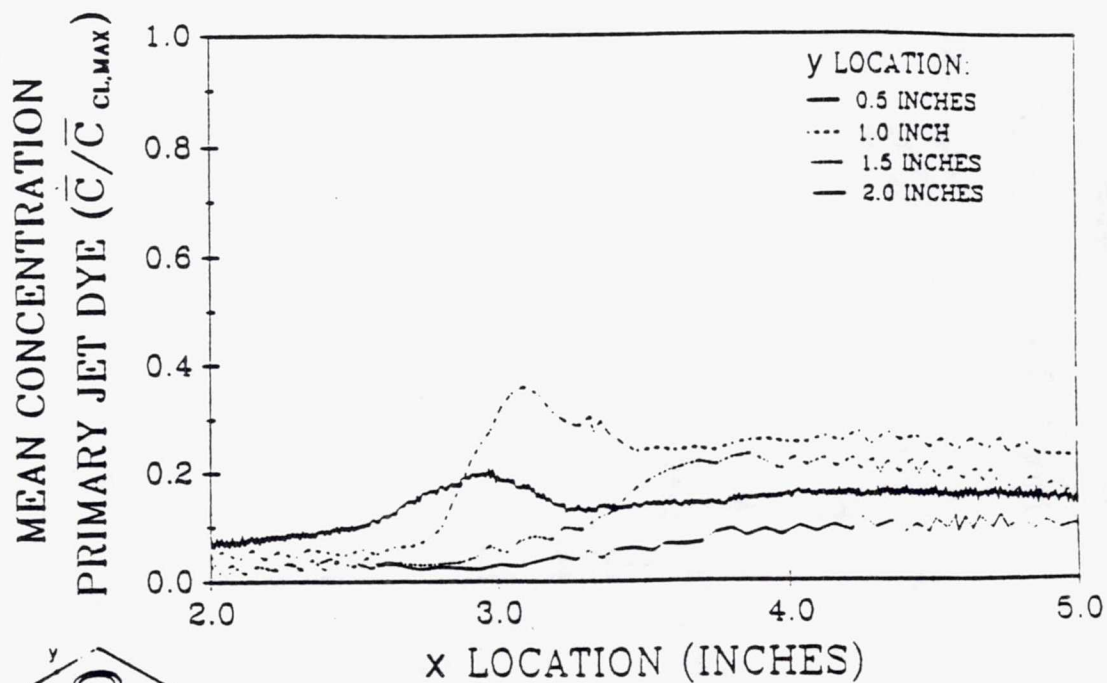
Figure 3.1.2-24. One hundred twenty-seven frame average primary jet concentration field visualization image with annular jet flow ($z = 7.0$ in.).

Page intentionally left blank



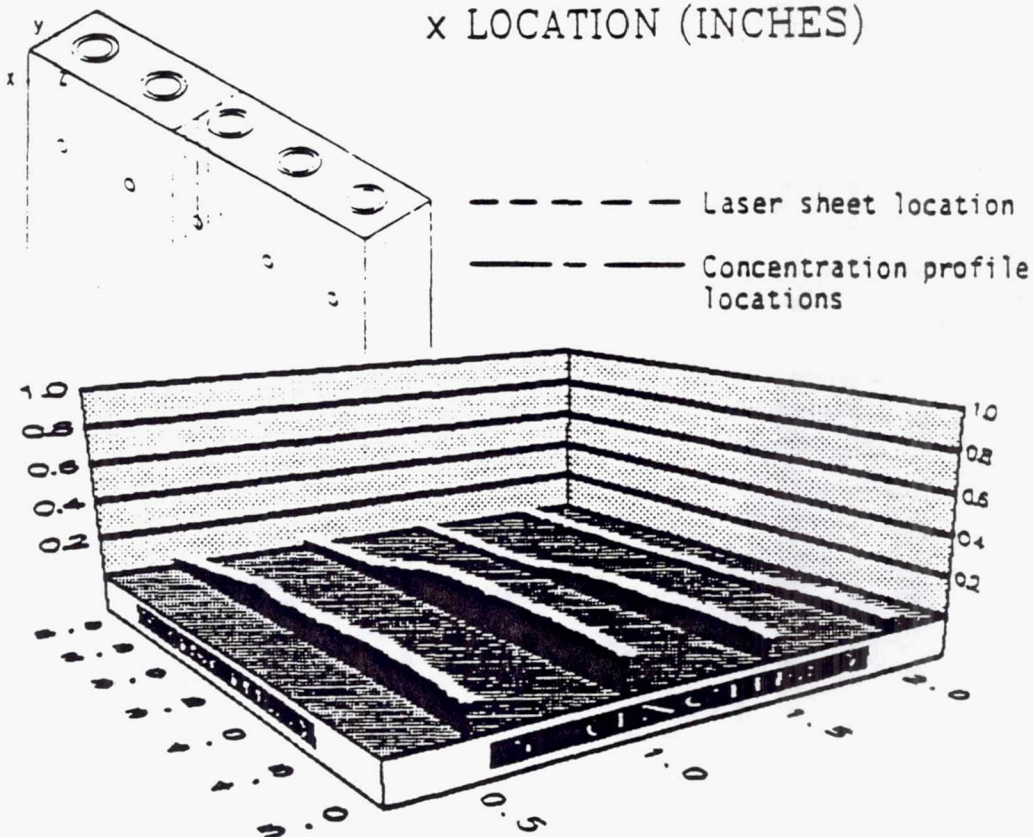
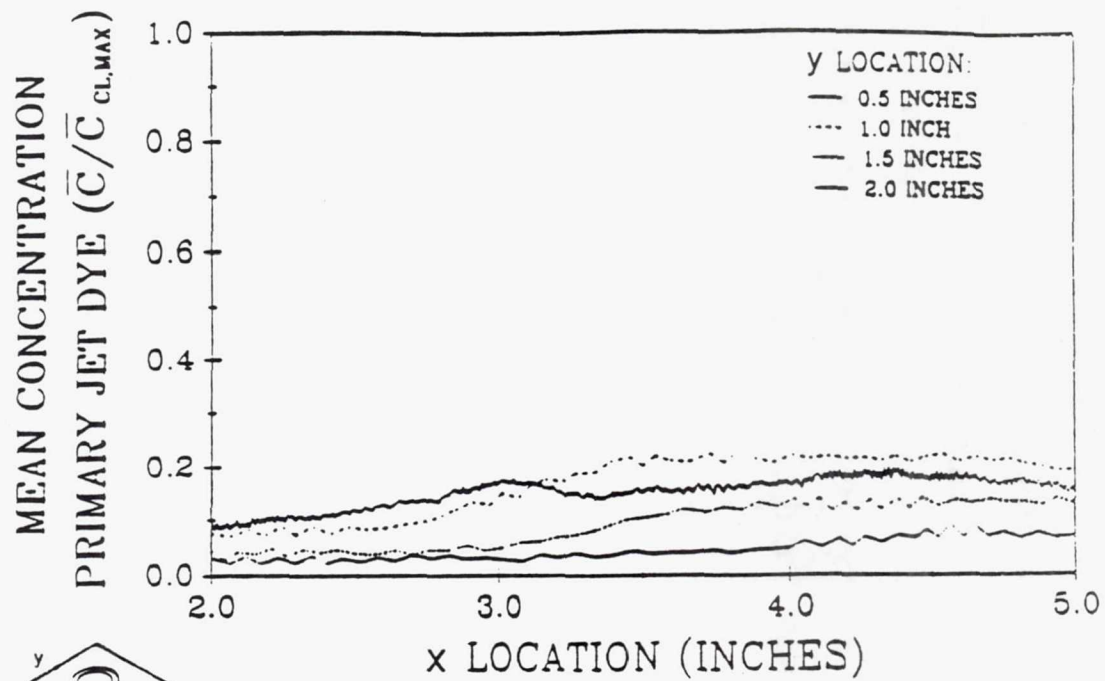
TE92-2377

Figure 3.1.2-25. Mean primary jet concentration with annular jet flow ($z = 7.5$ in.).



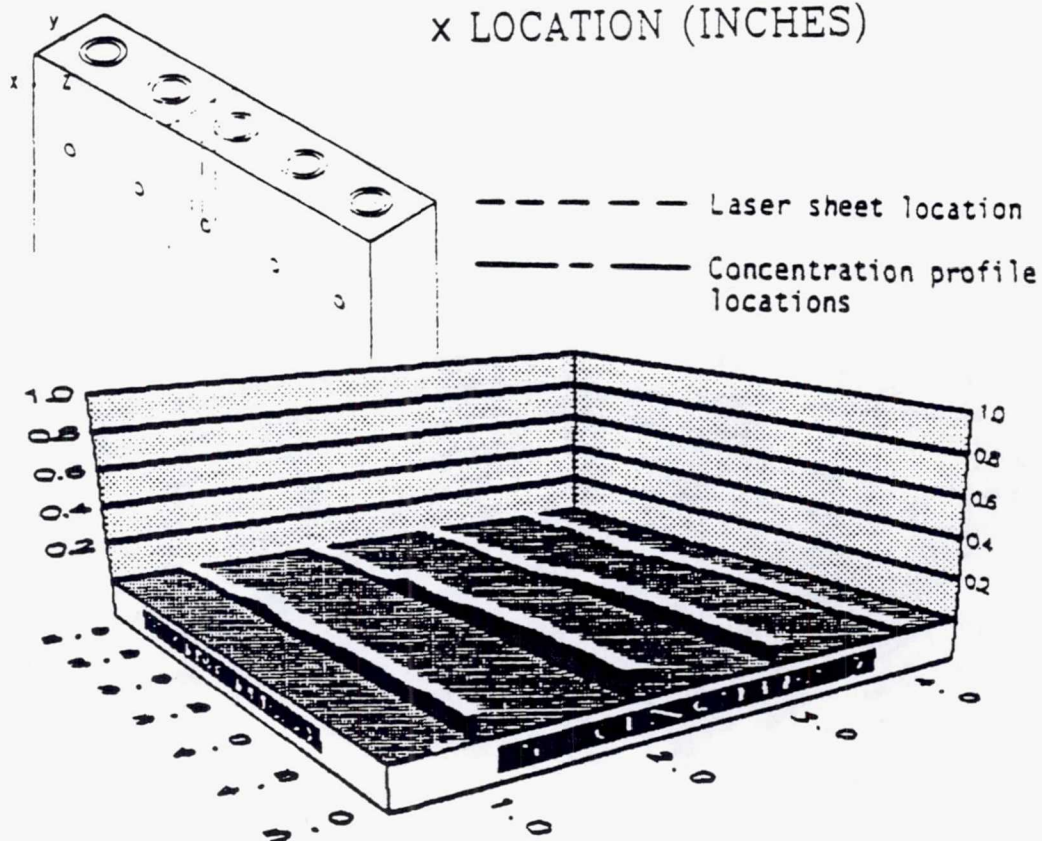
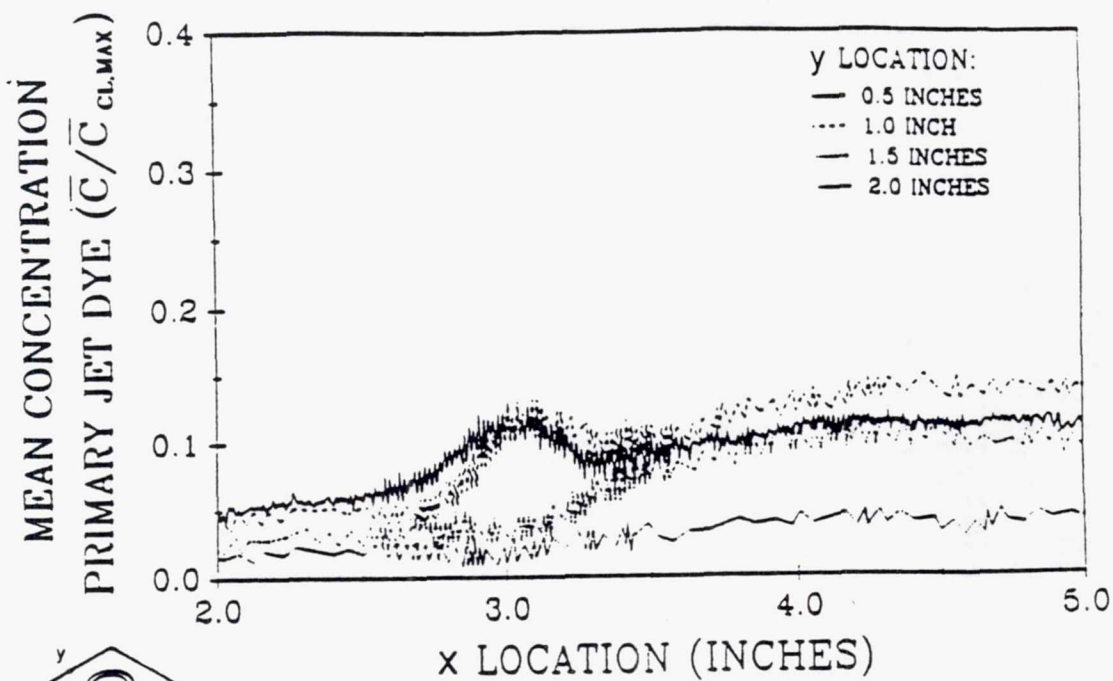
TE92-2378

Figure 3.1.2-26. Mean primary jet concentration with annular jet flow ($z = 7.0$ in.).



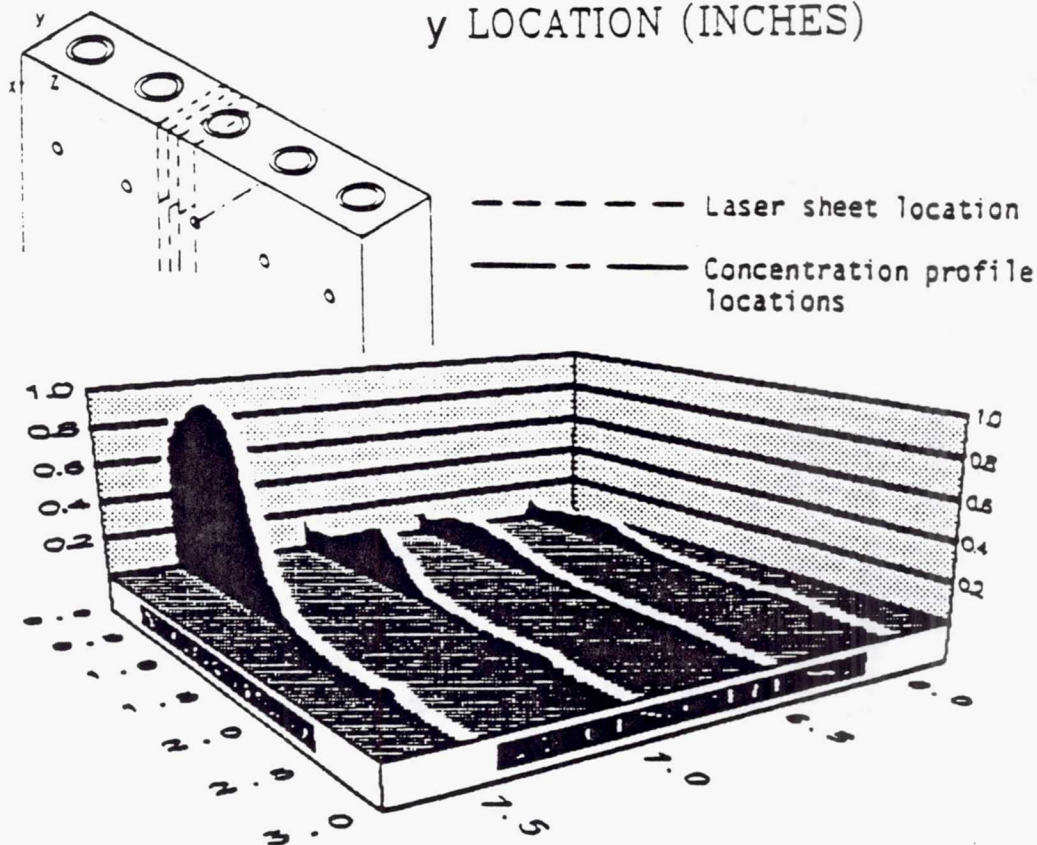
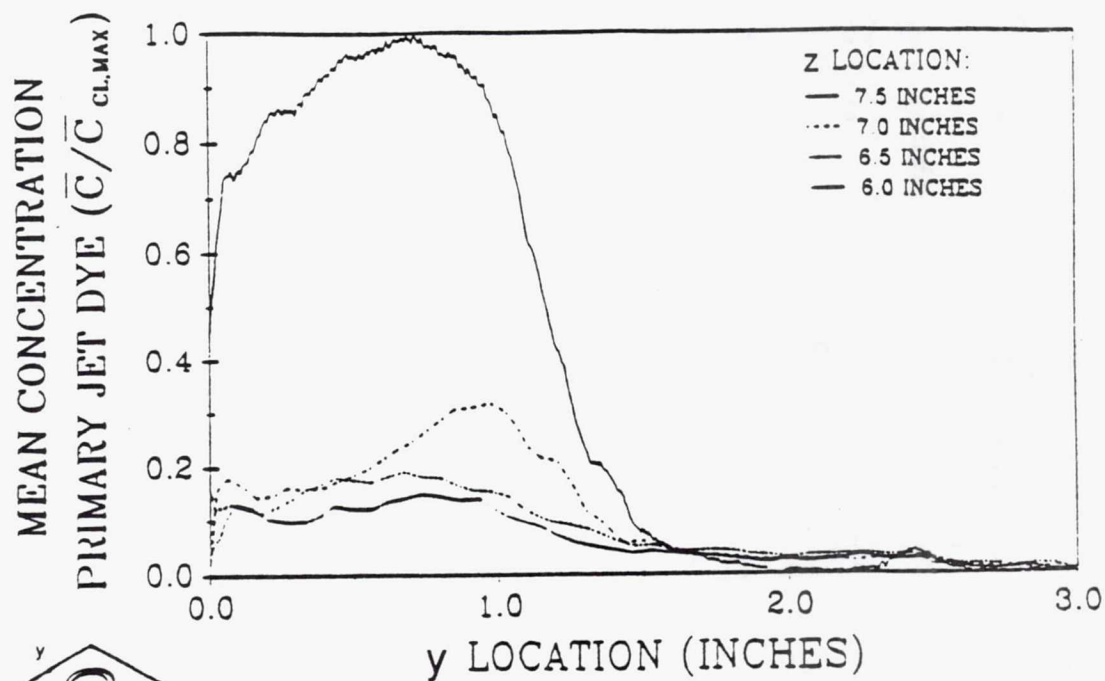
TE92-2379

Figure 3.1.2-27. Mean primary jet concentration with annular jet flow ($z = 6.5$ in.).



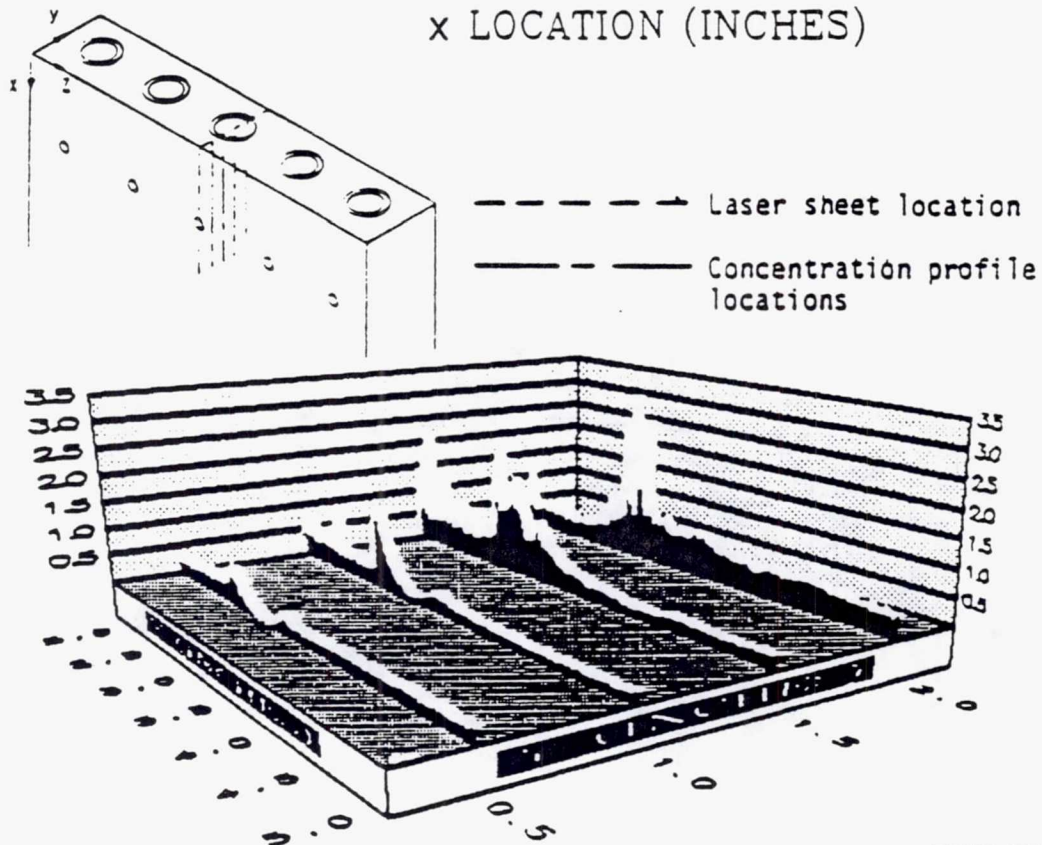
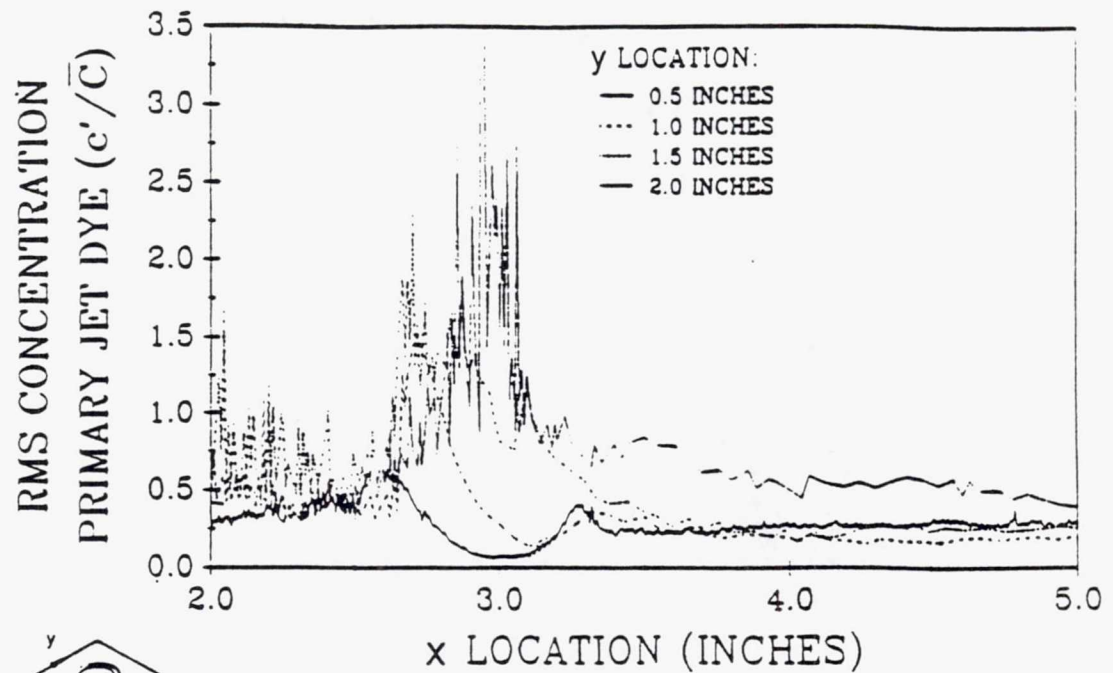
TE92-2380

Figure 3.1.2-28. Mean primary jet concentration with annular jet flow ($z = 6.0$ in.).



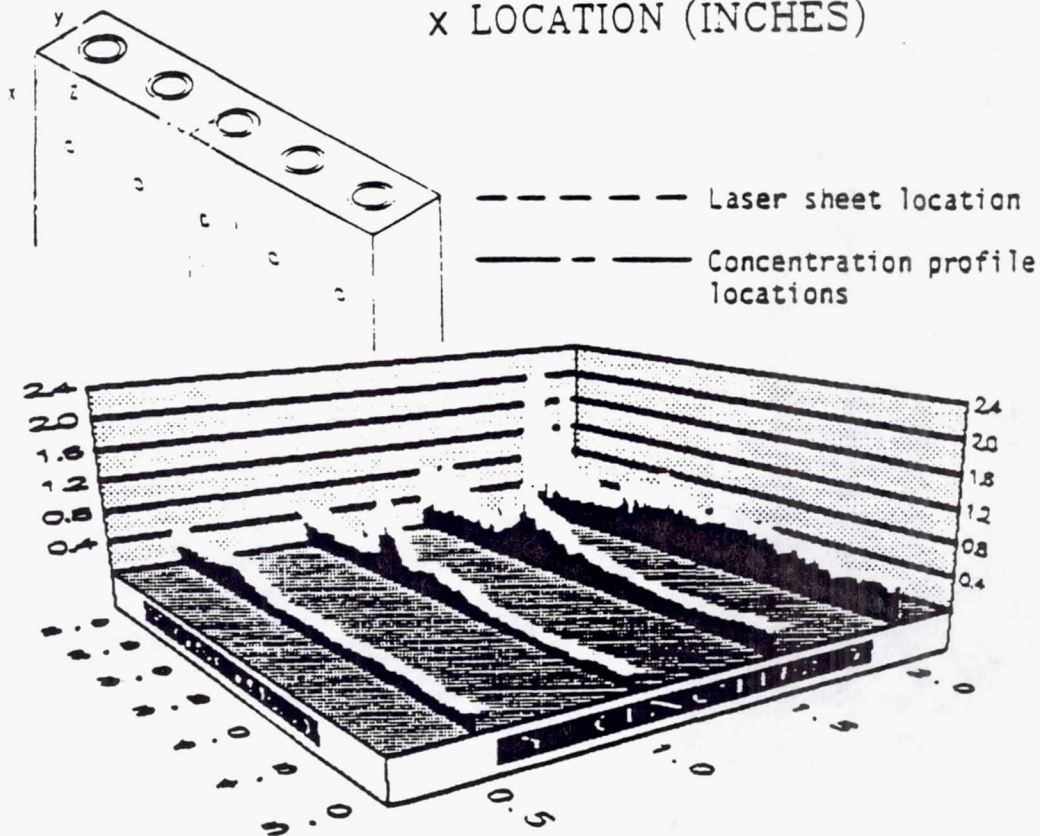
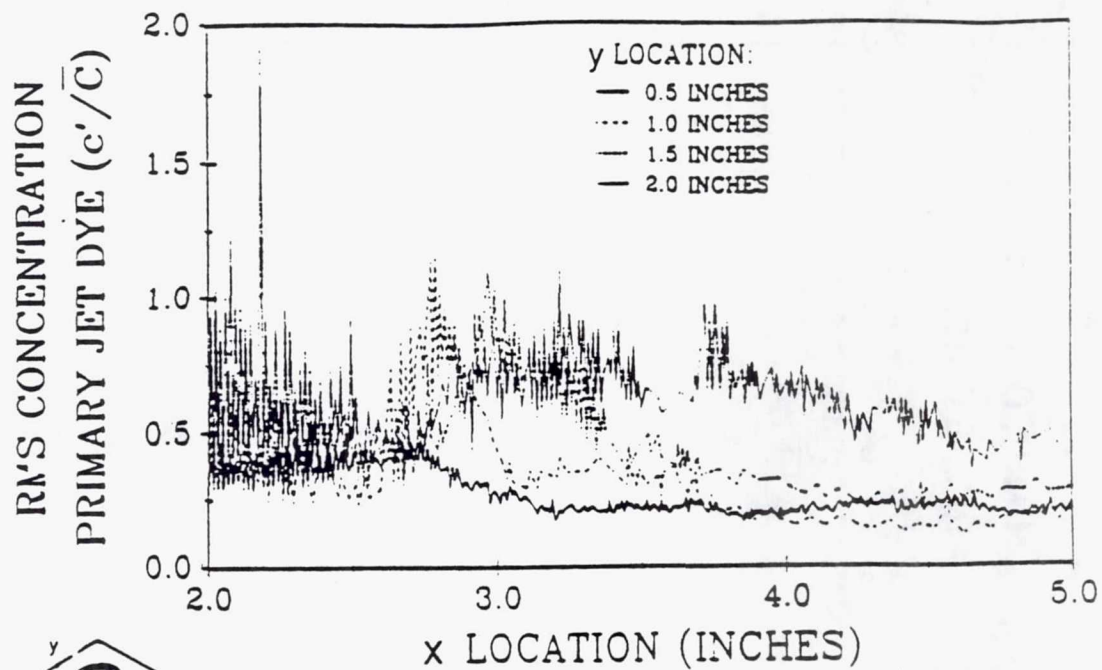
TE92-2381

Figure 3.1.2-29. Mean primary jet concentration with annular jet flow ($x = 3.0$ in.).



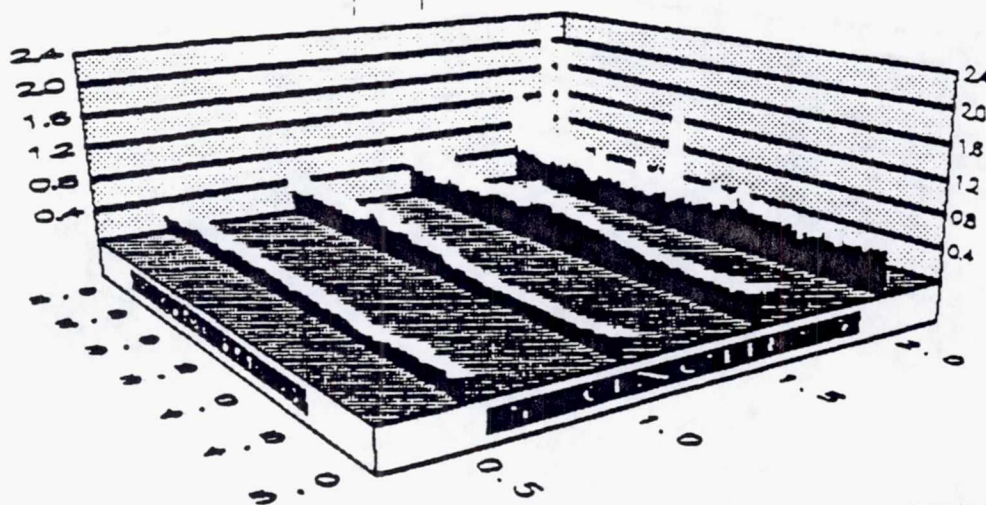
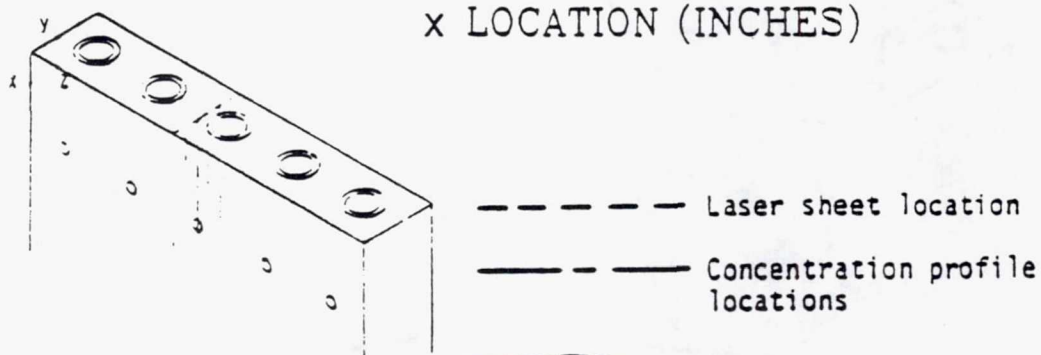
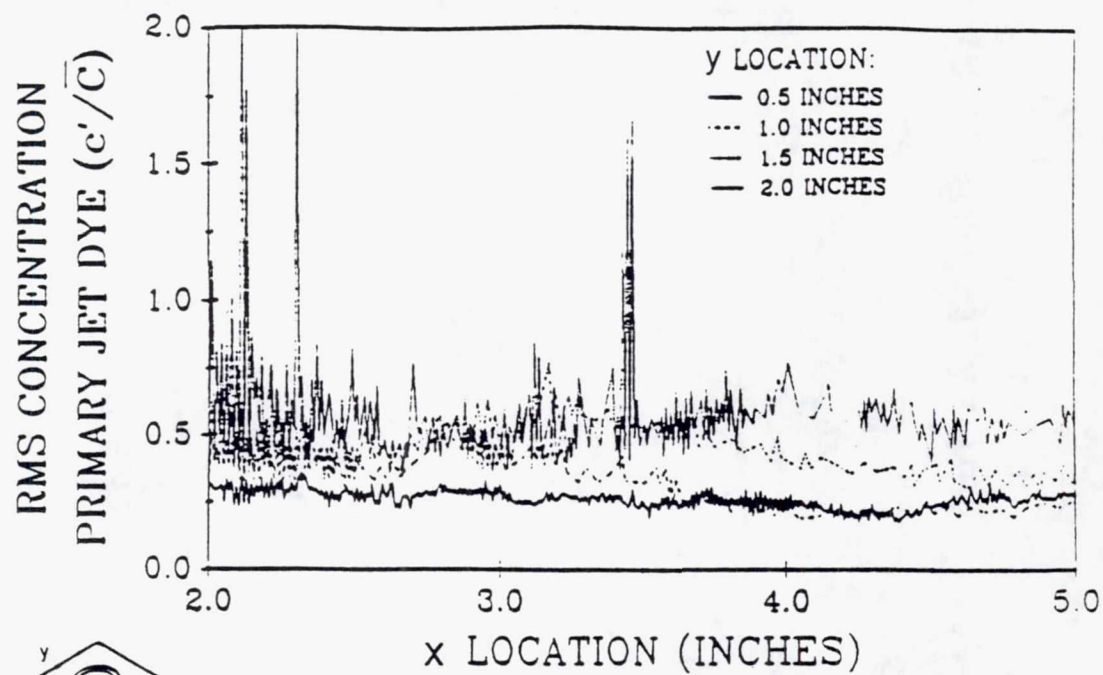
TE92-2382

Figure 3.1.2-30. Root mean square primary jet concentration with annular jet flow ($z = 7.5$ in.).



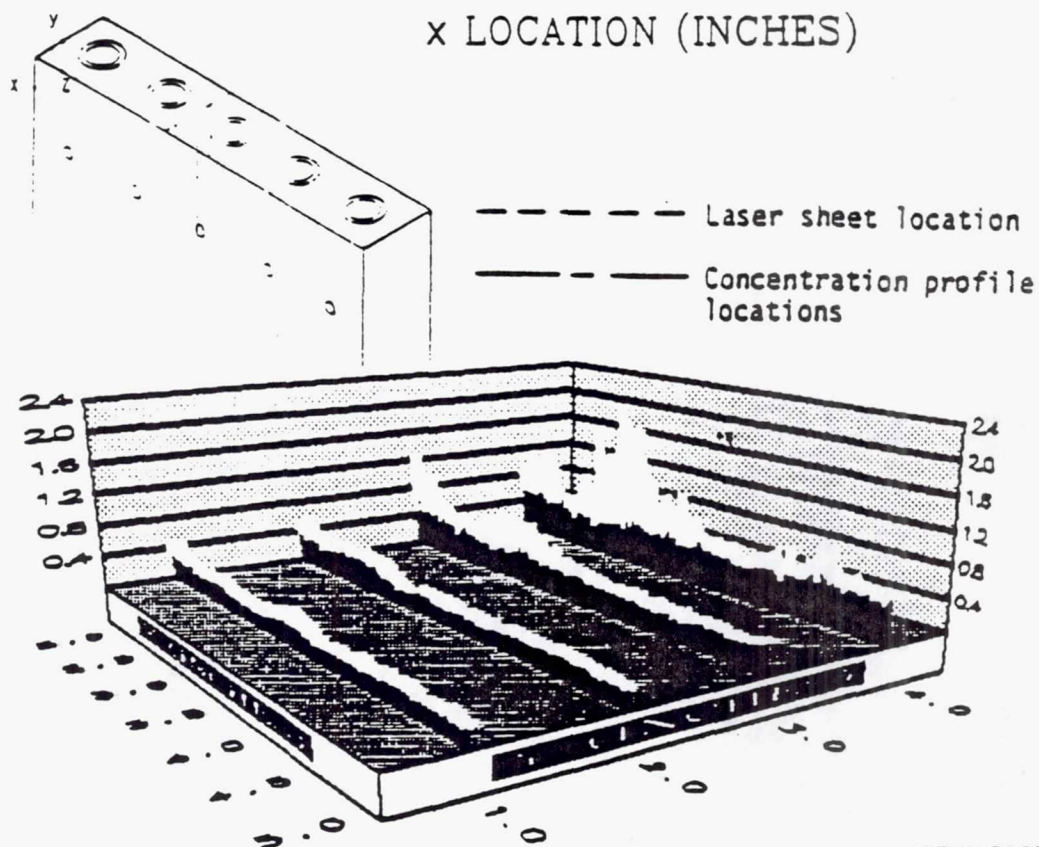
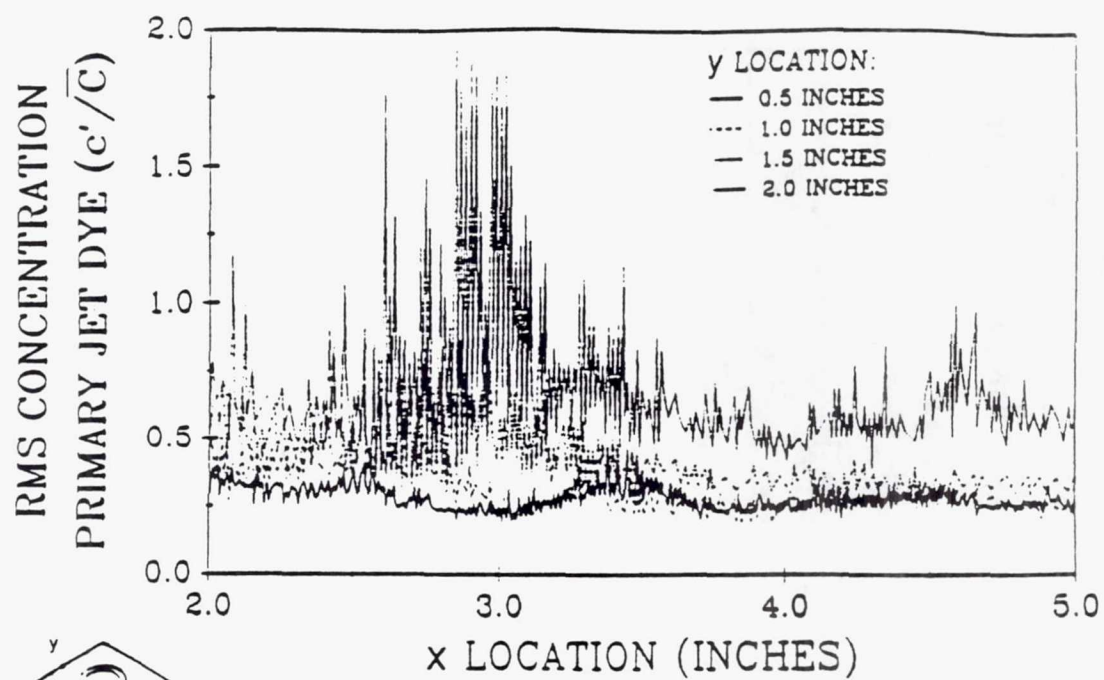
TE92-2383

Figure 3.1.2-31. Root mean square primary jet concentration with annular jet flow ($z = 7.0$ in.).



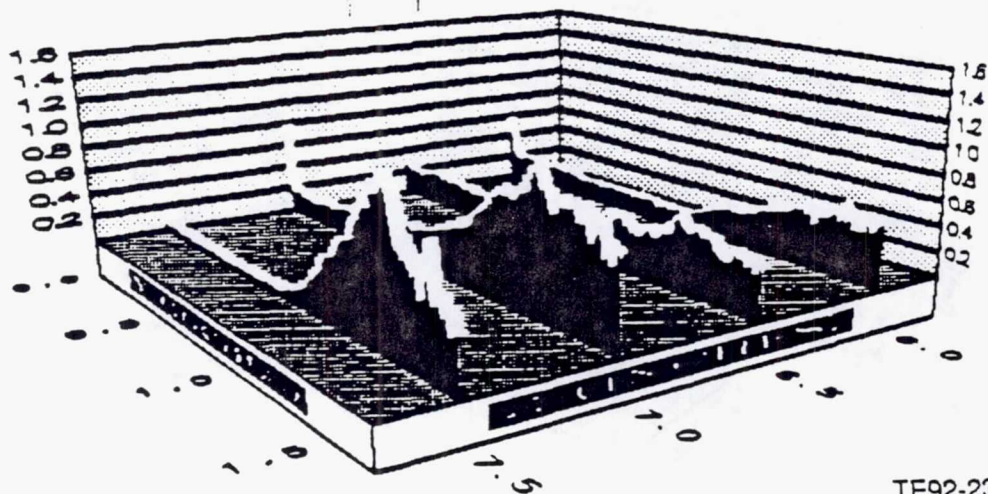
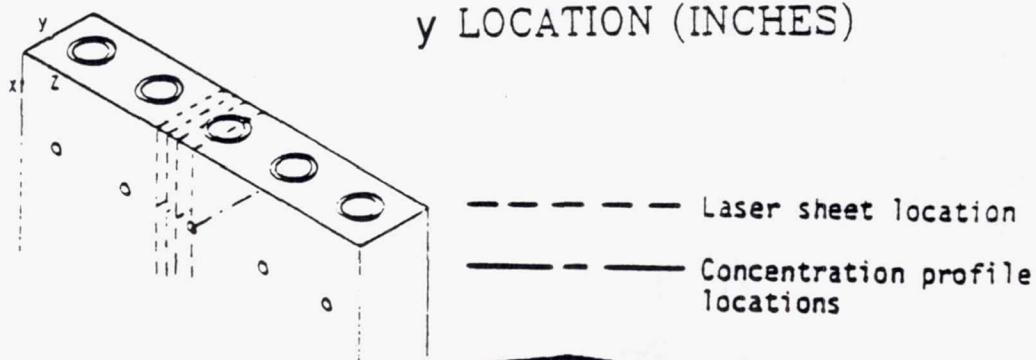
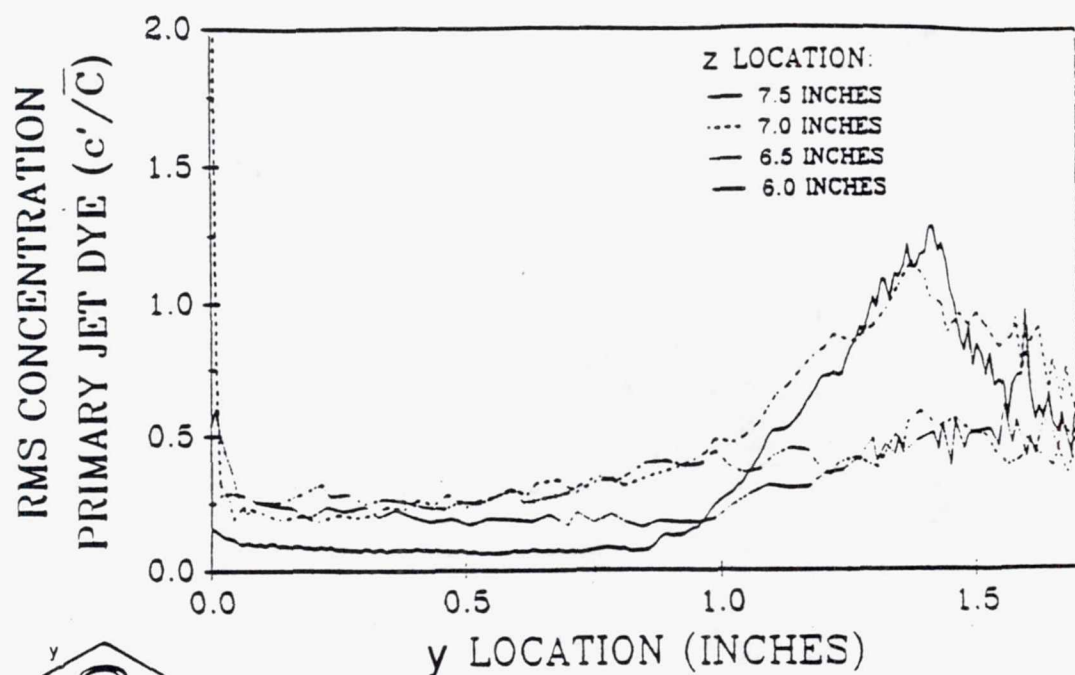
TE92-2384

Figure 3.1.2-32. Root mean square primary jet concentration with annular jet flow ($z = 6.5$ in.).



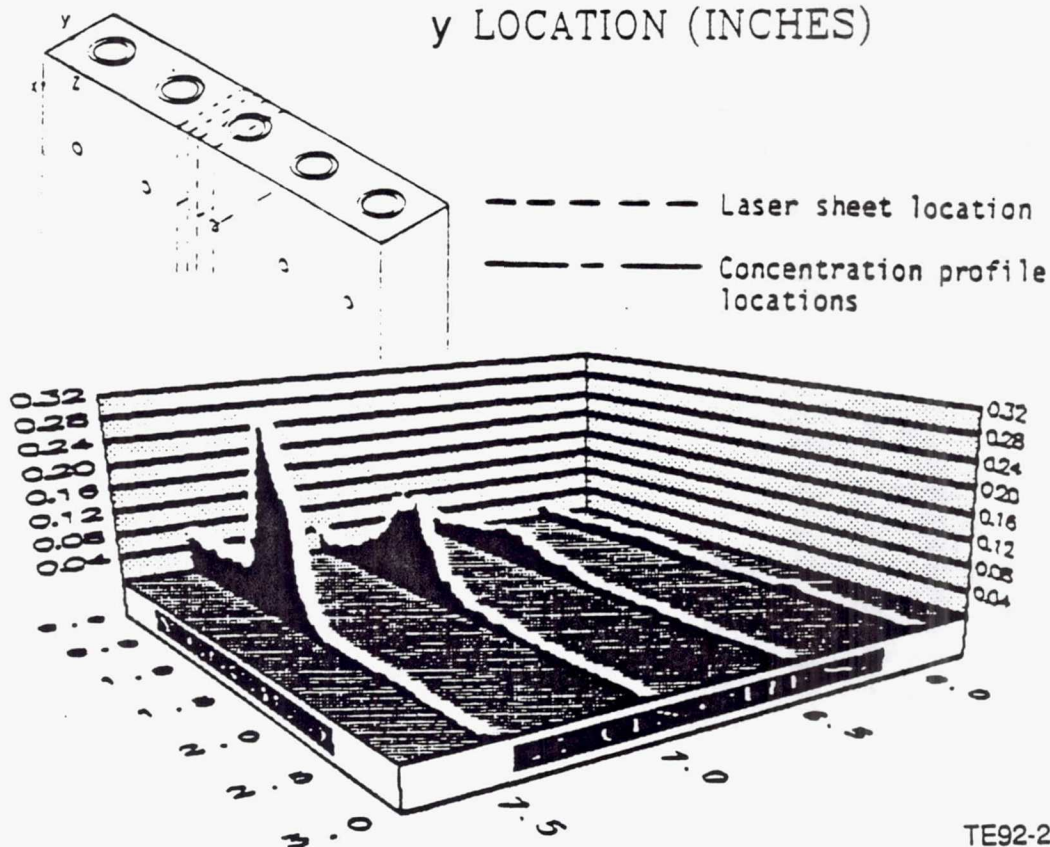
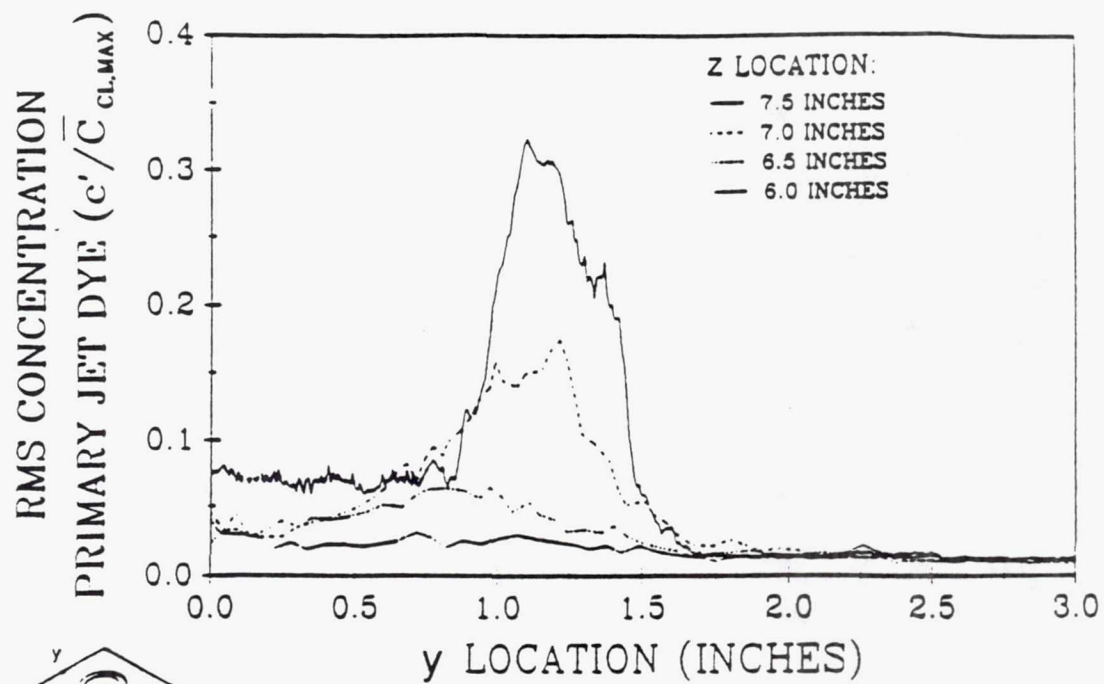
TE92-2385

Figure 3.1.2-33. Root mean square primary jet concentration with annular jet flow ($z = 6.0$ in.).



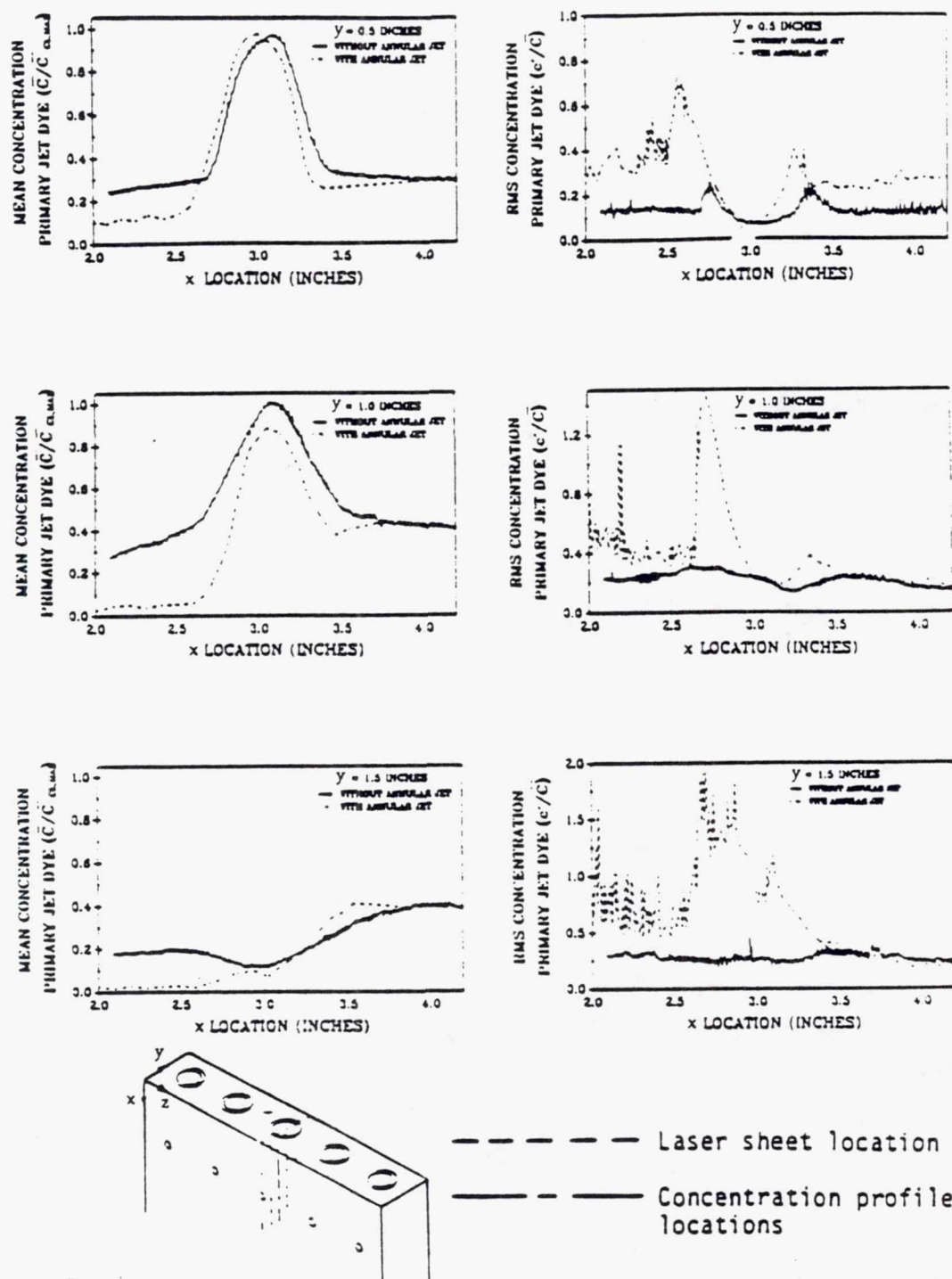
TE92-2386

Figure 3.1.2-34. Root mean square primary jet concentration with annular jet flow ($x = 3.0$ in.).



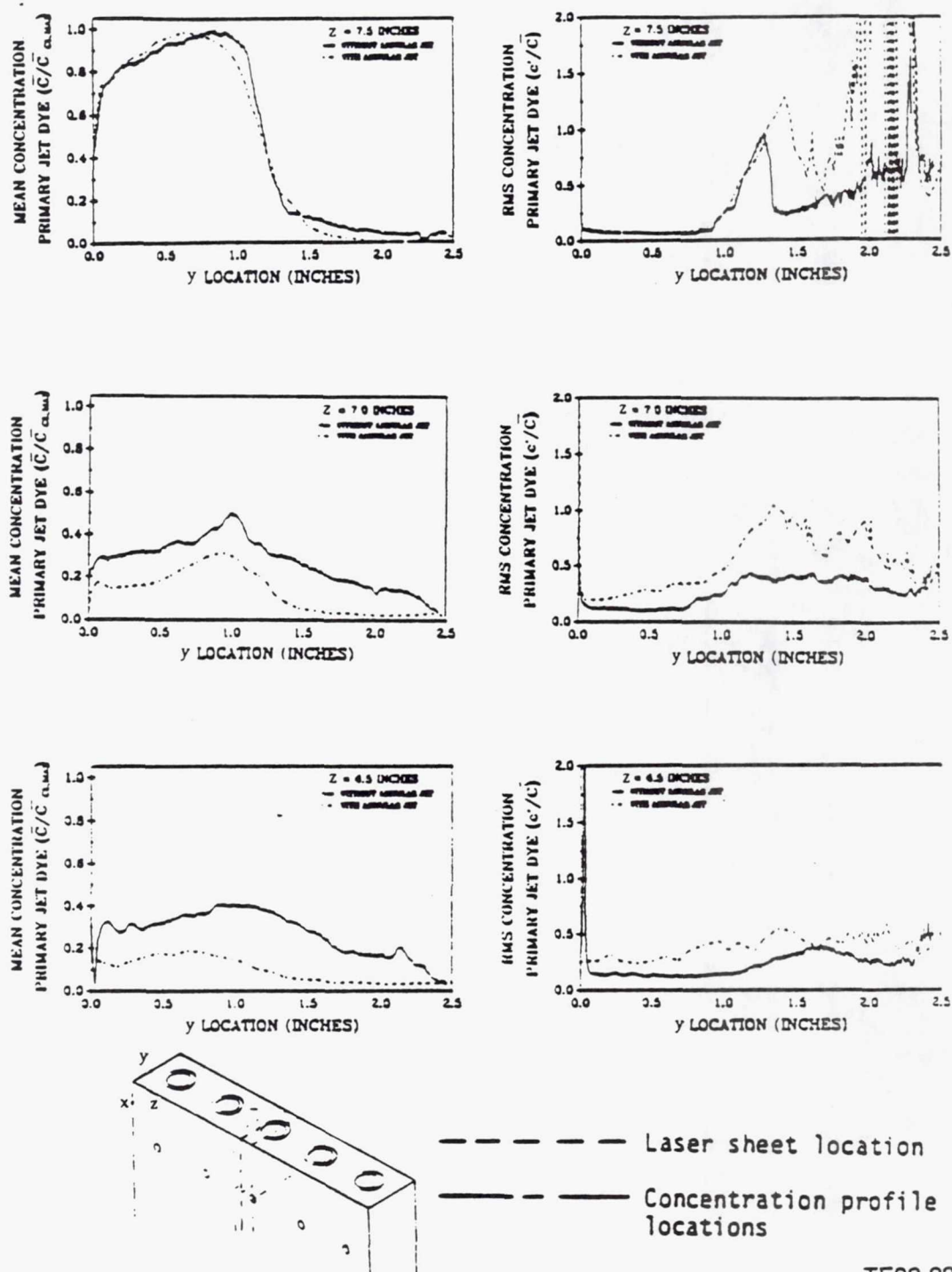
TE92-2387

Figure 3.1.2-35. Root mean square primary jet concentration normalized by $\bar{C}_{CL,MAX}$ with annular jet flow ($x = 3.0$ in.).



TE92-2388

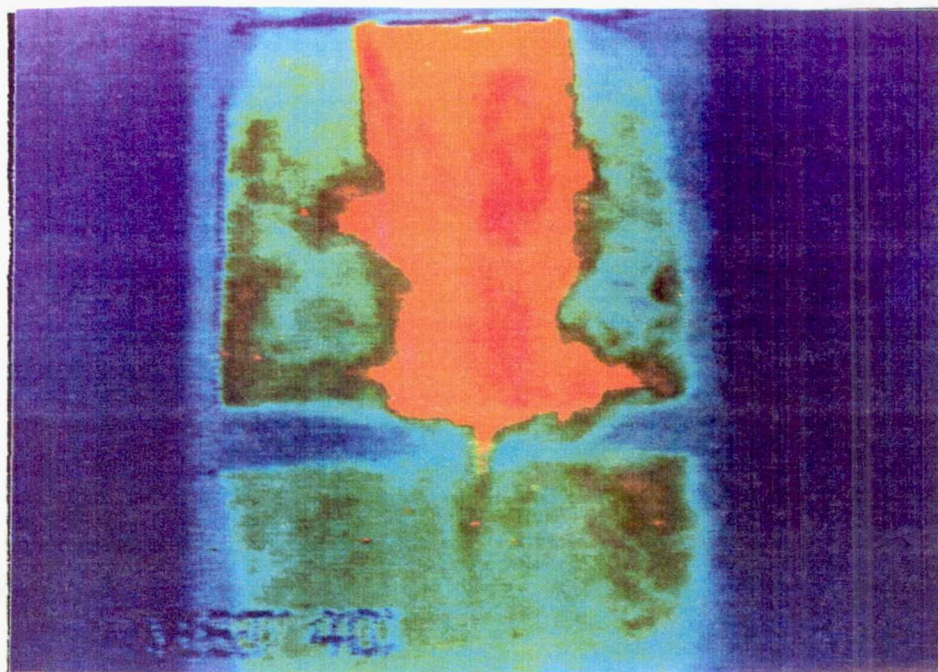
Figure 3.1.2-36. Comparison of primary jet concentration with and without annular jet flow ($z = 7.5$ in.).



TE92-2389

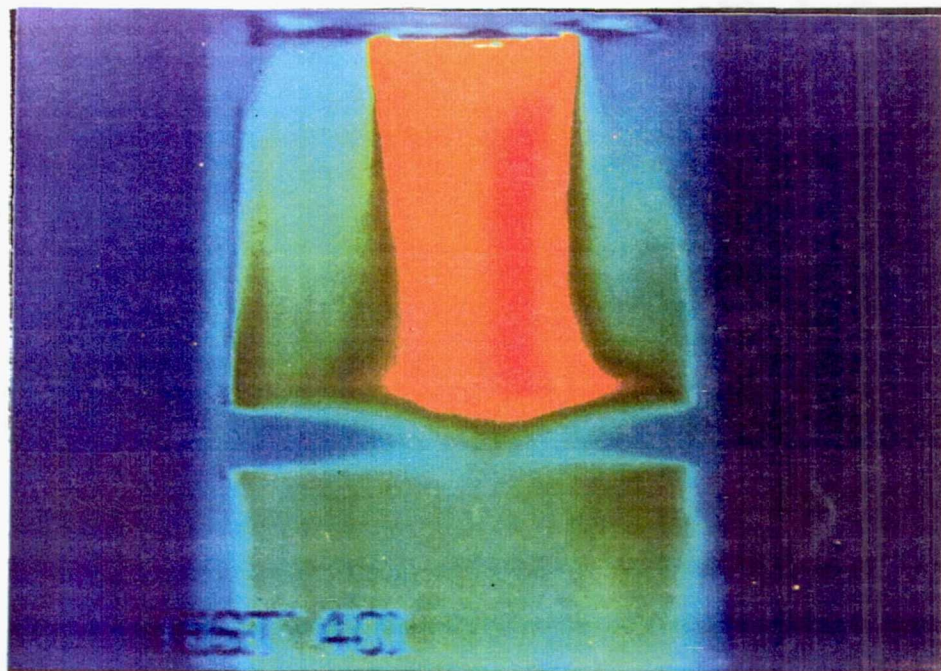
Figure 3.1.2-37. Comparison of primary jet concentration with and without annular jet flow ($x = 3.0$ in.).

Page intentionally left blank



TE92-2390

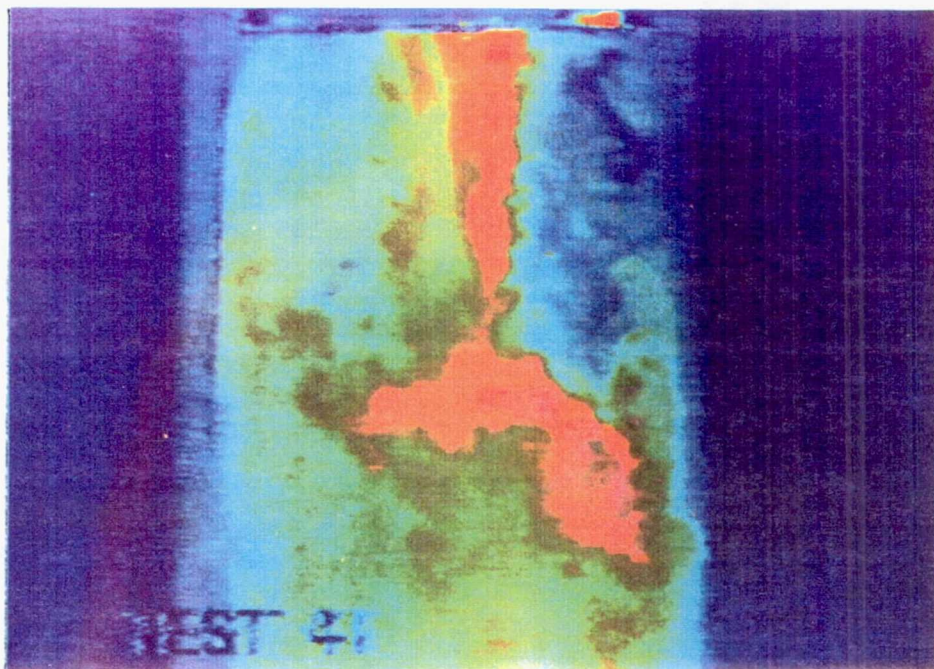
Figure 3.1.2-38. Single frame annular jet concentration field visualization image ($z = 7.5$ in.).



TE92-2391

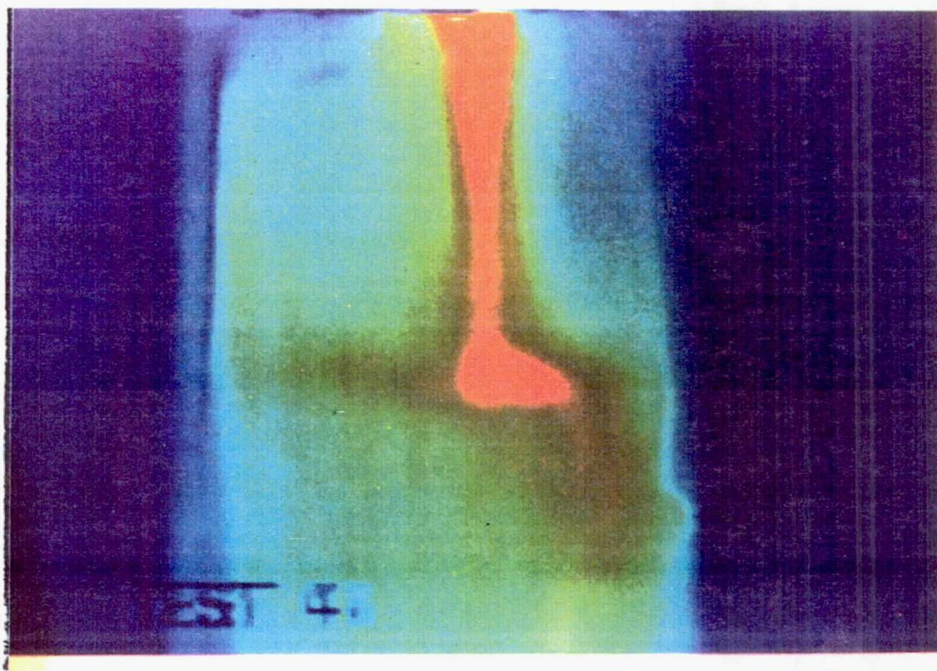
Figure 3.1.2-39. Frame average annular jet concentration field visualization image ($z = 7.5$ in.).

Page intentionally left blank



TE92-2392

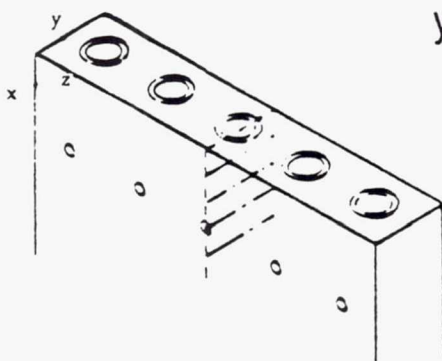
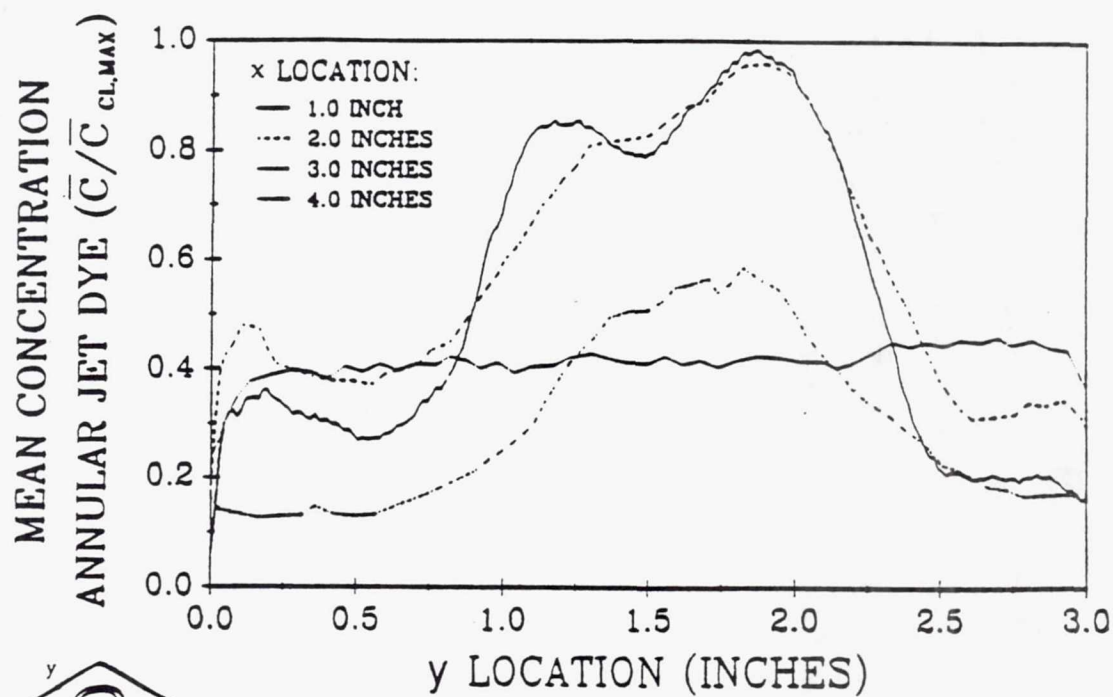
Figure 3.1.2-40. Single frame annular jet concentration field visualization image ($z = 7.0$ in.).



TE92-2393

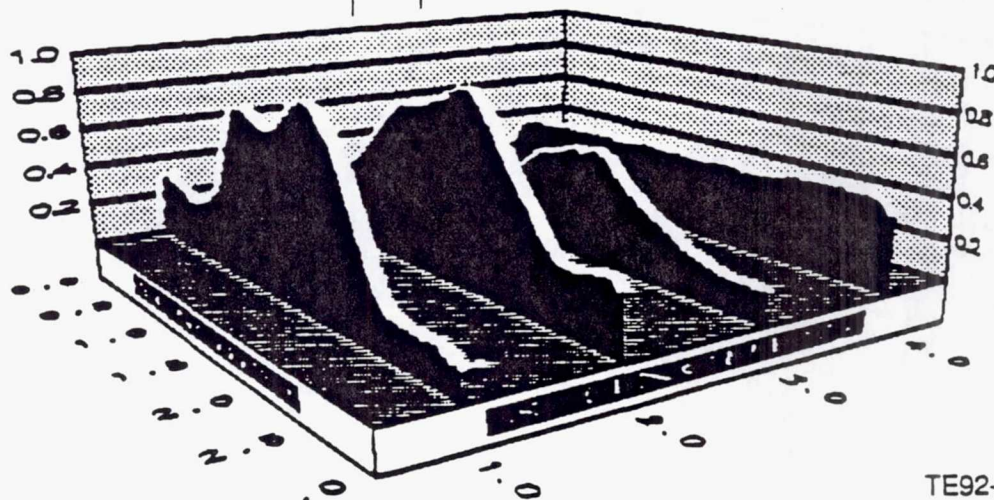
Figure 3.1.2-41. Frame average annular jet concentration field visualization image ($z = 7.0$ in.).

Page intentionally left blank



- - - Laser sheet location

- - - Concentration profile locations



TE92-2394

Figure 3.1.2-42. Mean annular jet concentration ($z = 7.5$ in.).

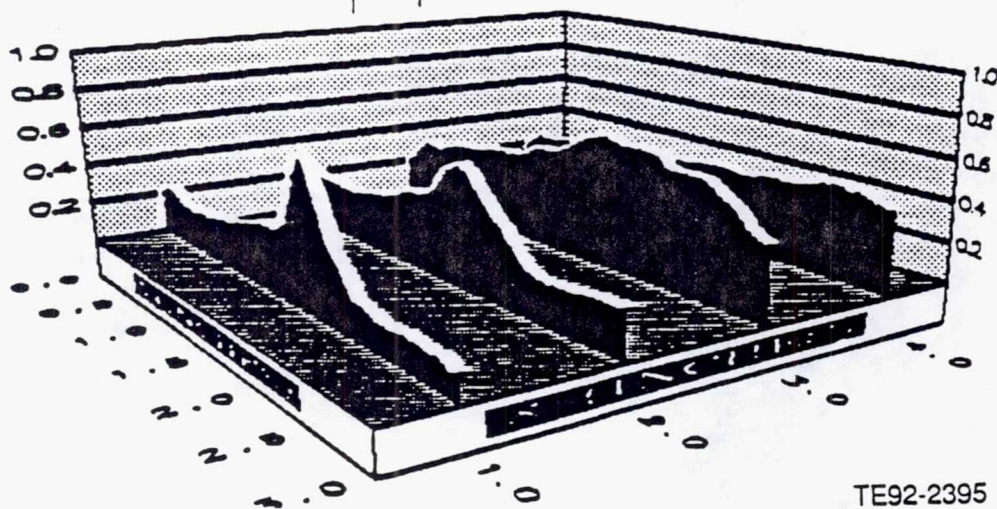
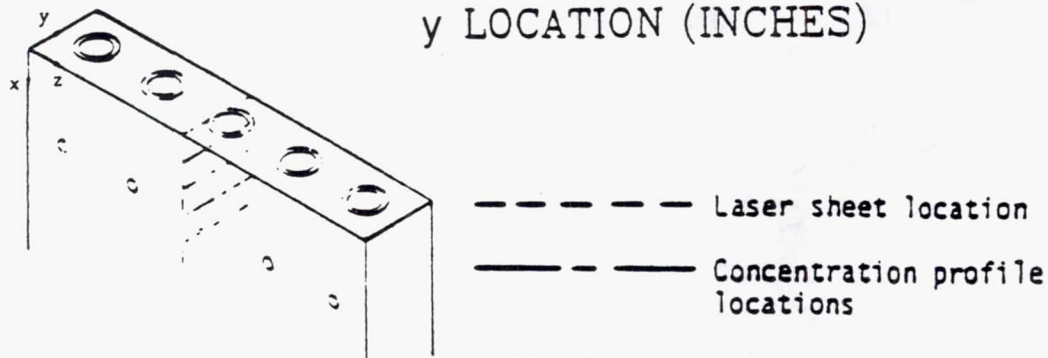
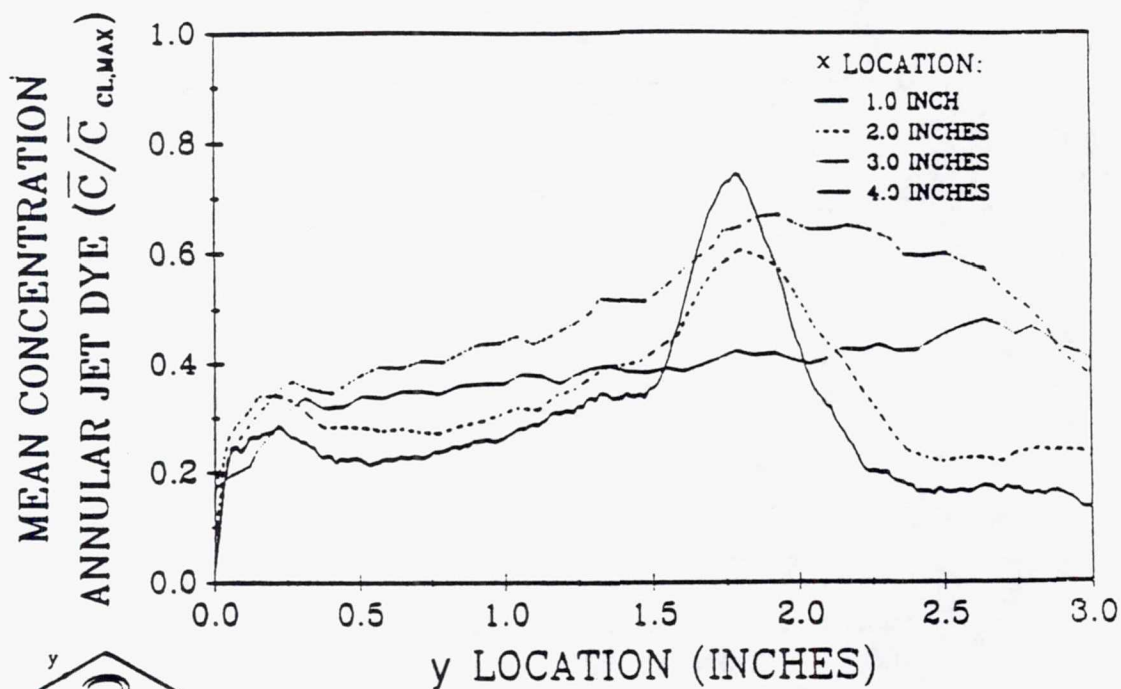
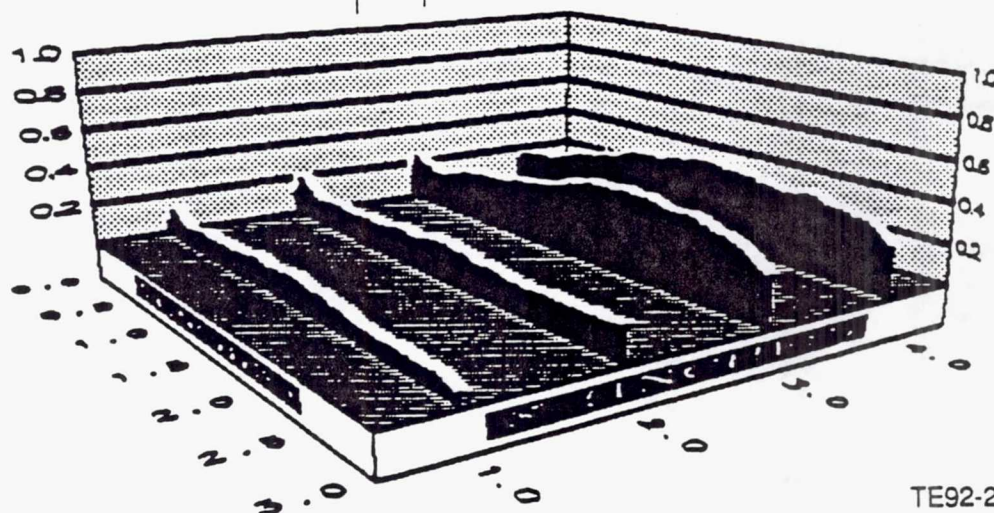
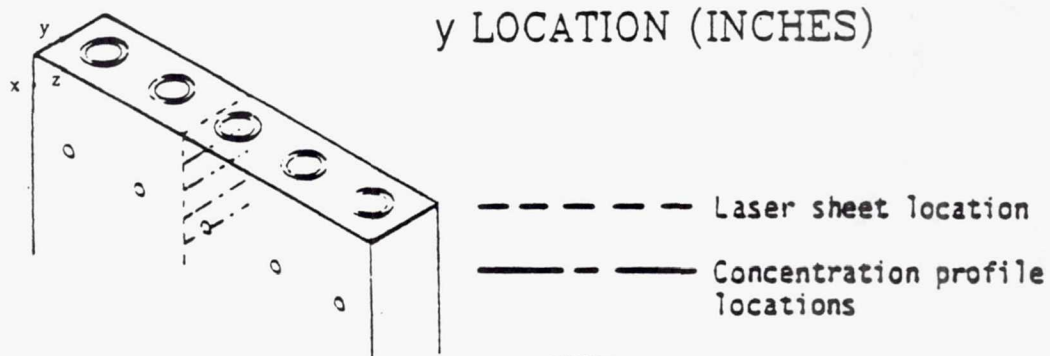
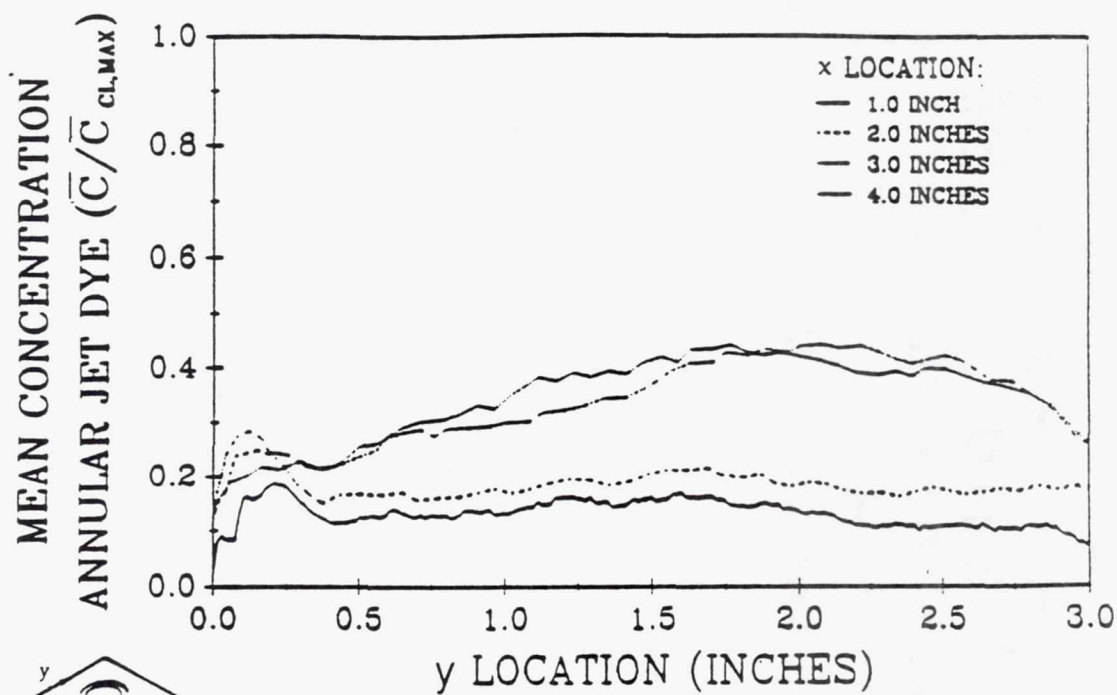
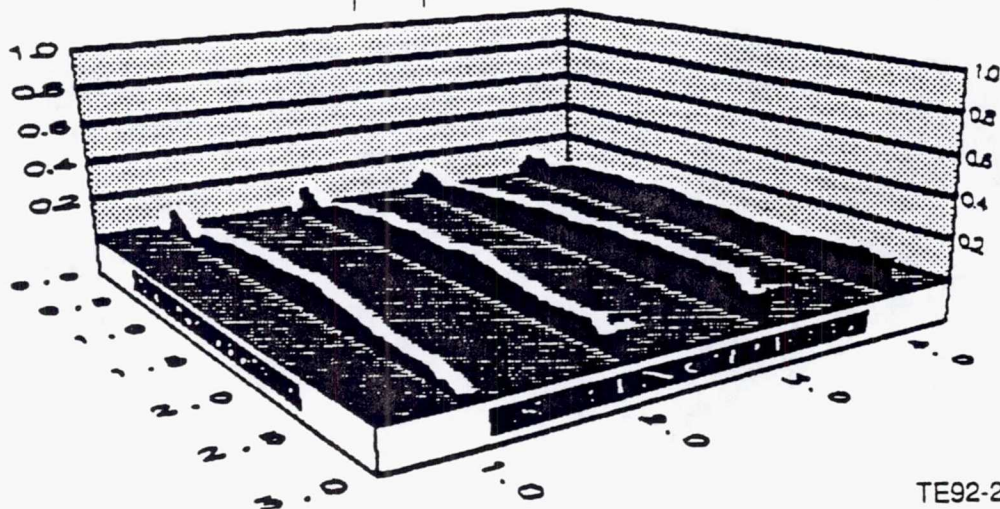
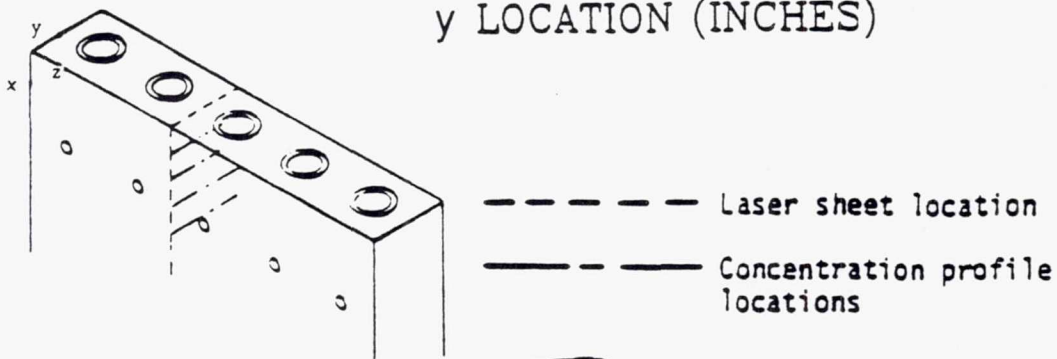
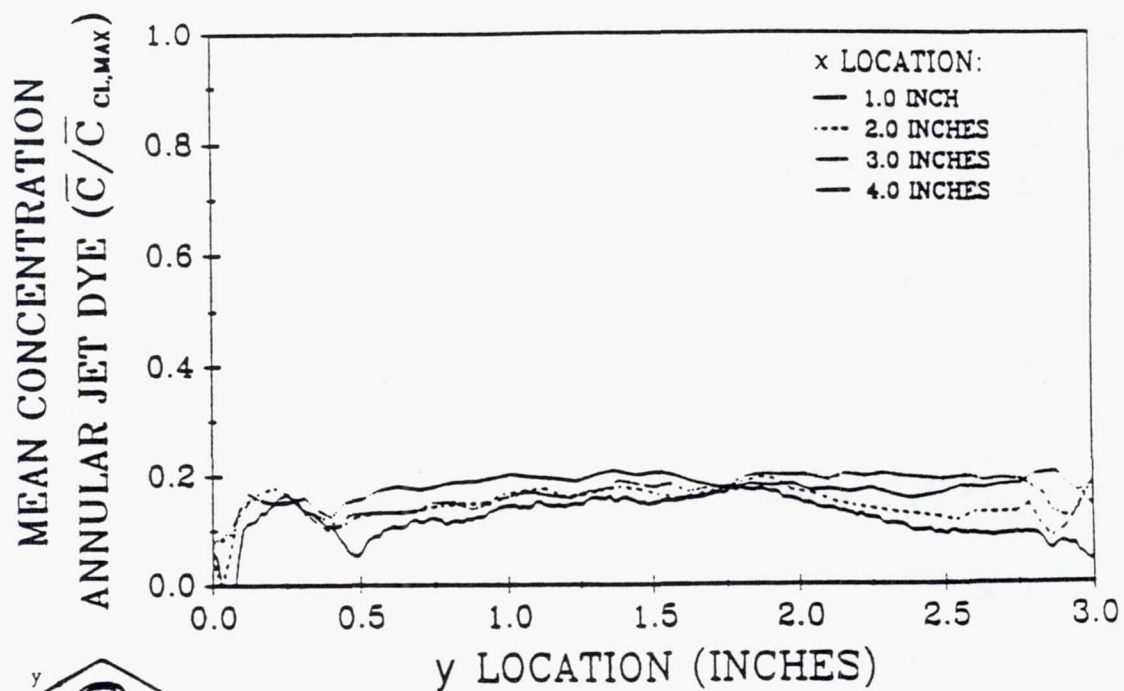


Figure 3.1.2-43. Mean annular jet concentration ($z = 7.0$ in.).



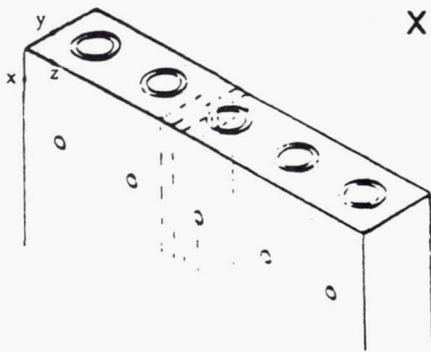
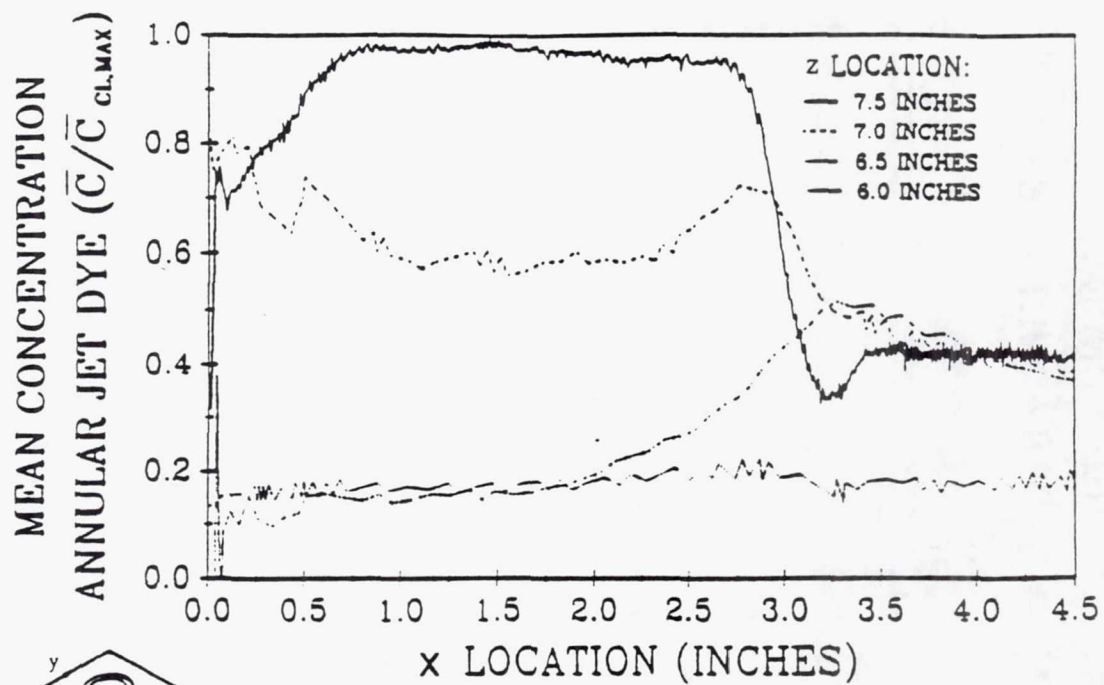
TE92-2396

Figure 3.1.2-44. Mean annular jet concentration ($z = 6.5$ in.).

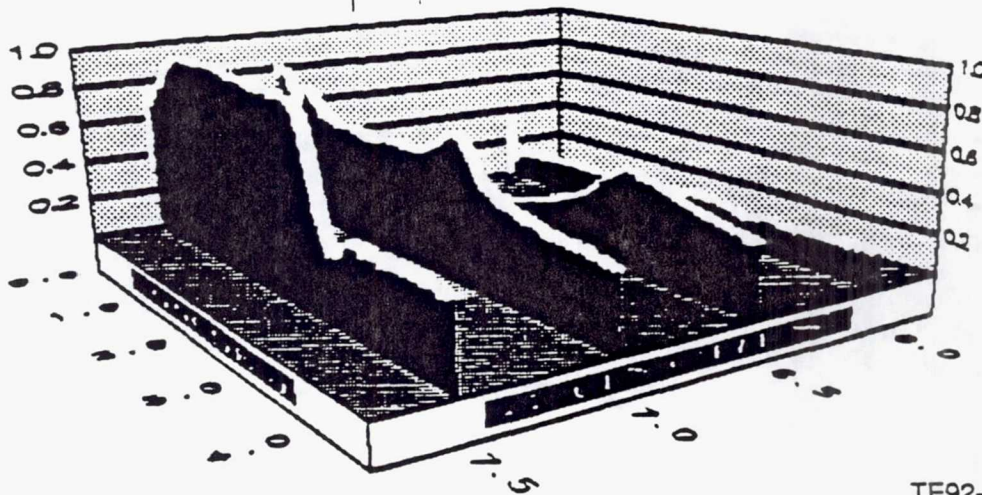


TE92-2397

Figure 3.1.2-45. Mean annular jet concentration ($z = 6.0$ in.).

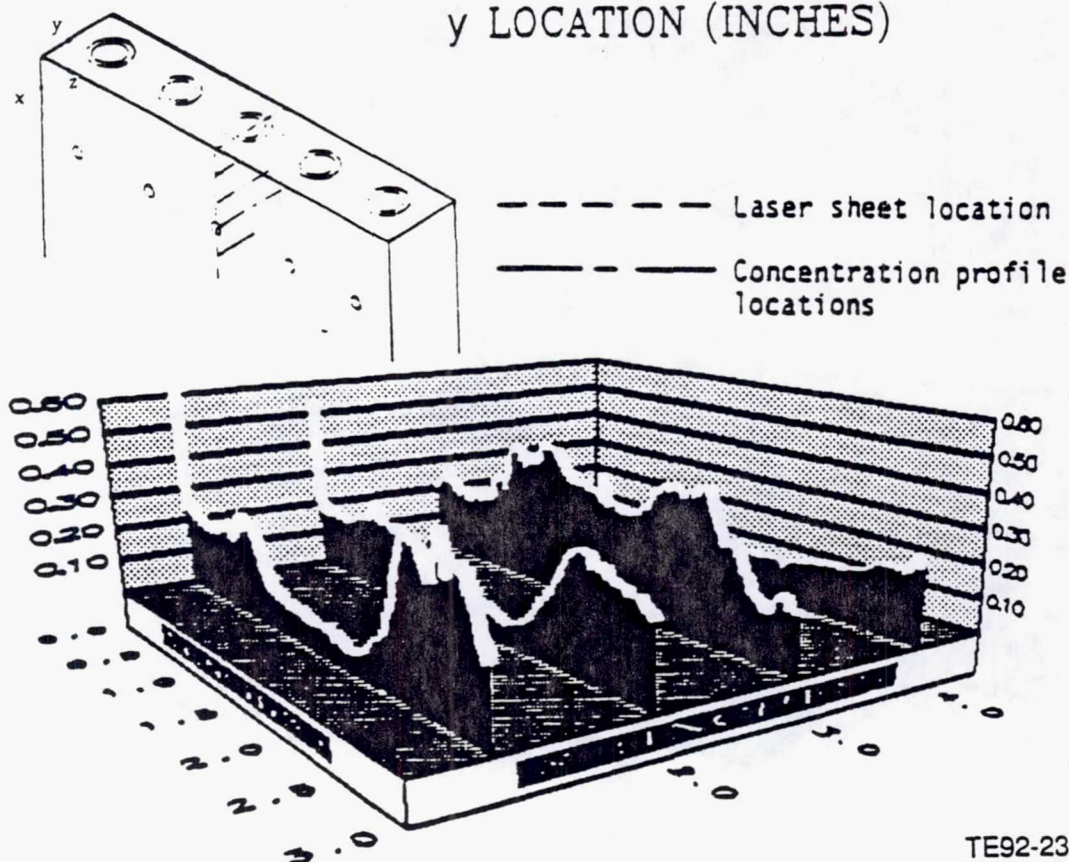
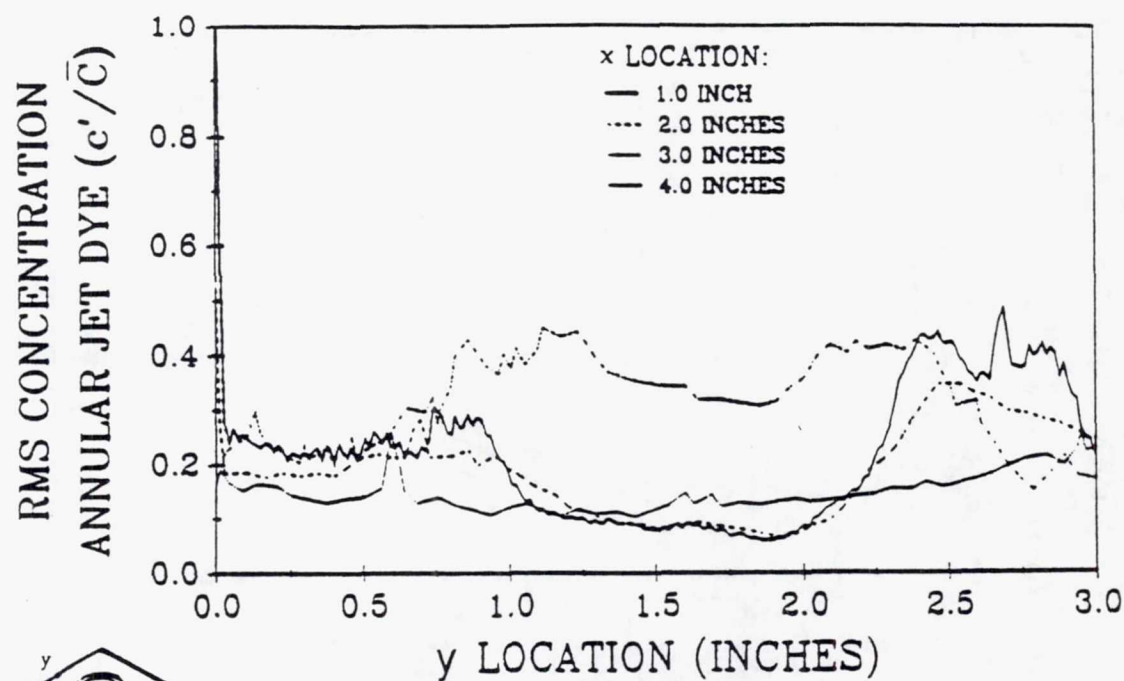


--- Laser sheet location
— Concentration profile locations



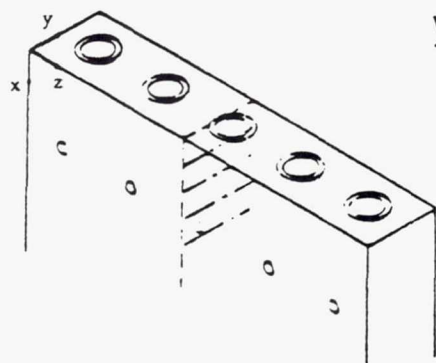
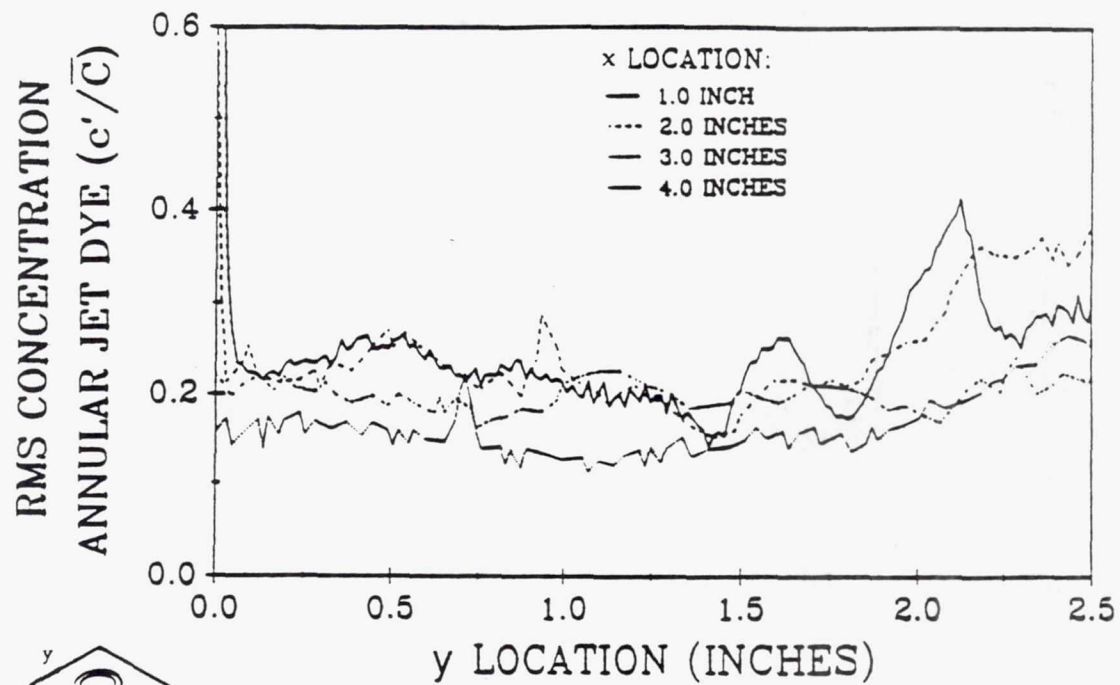
TE92-2398

Figure 3.1.2-46. Mean annular jet concentration ($y = 1.5$ in.).

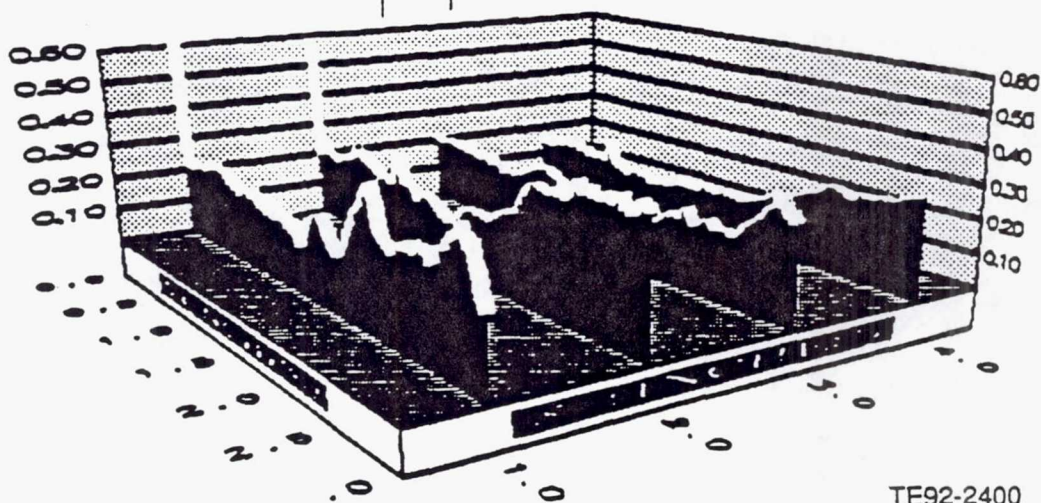


TE92-2399

Figure 3.1.2-47. Root mean square annular jet concentration ($z = 7.5$ in.).

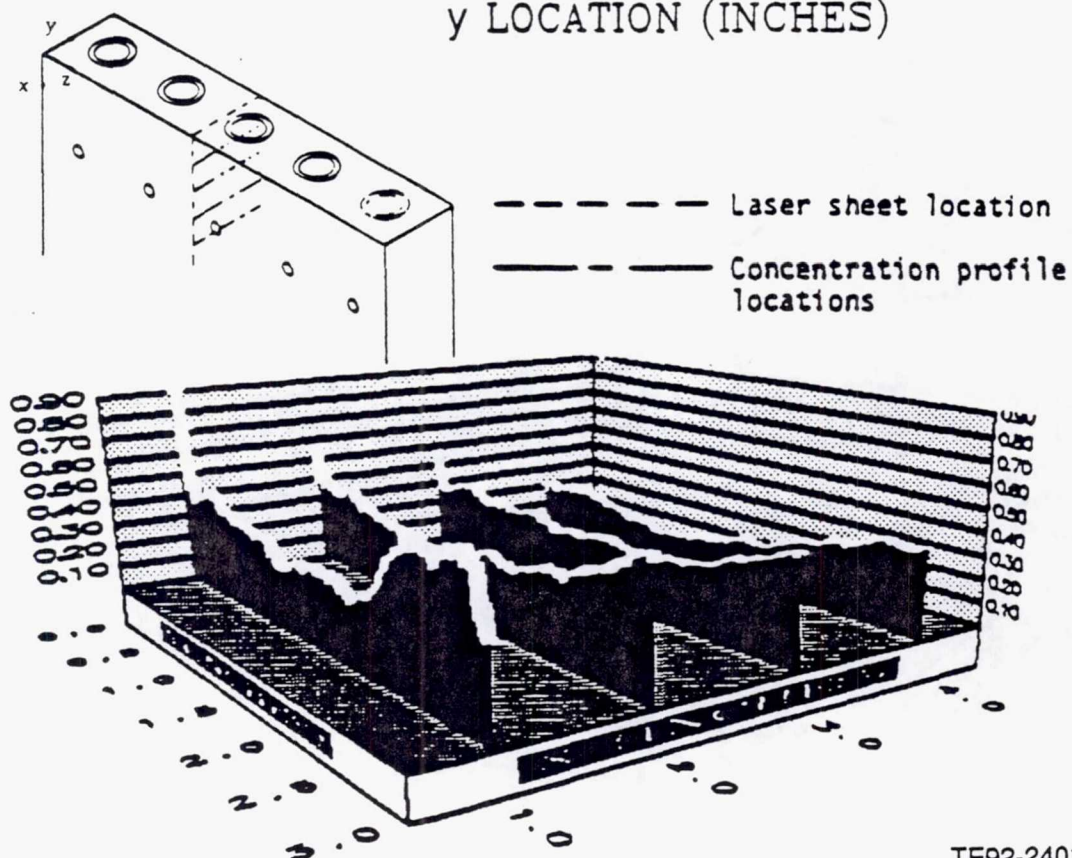
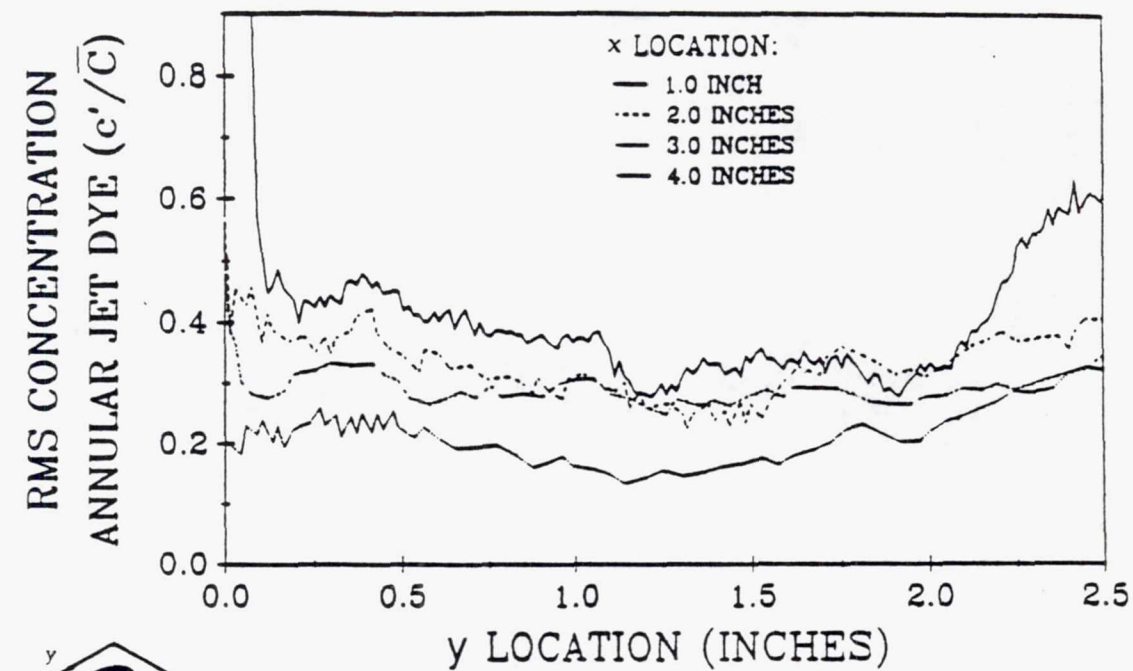


--- Laser sheet location
 --- Concentration profile locations



TE92-2400

Figure 3.1.2-48. Root mean square annular jet concentration ($z = 7.0$ in.).



TE92-2401

Figure 3.1.2-49. Root mean square annular jet concentration ($z = 6.5$ in.).

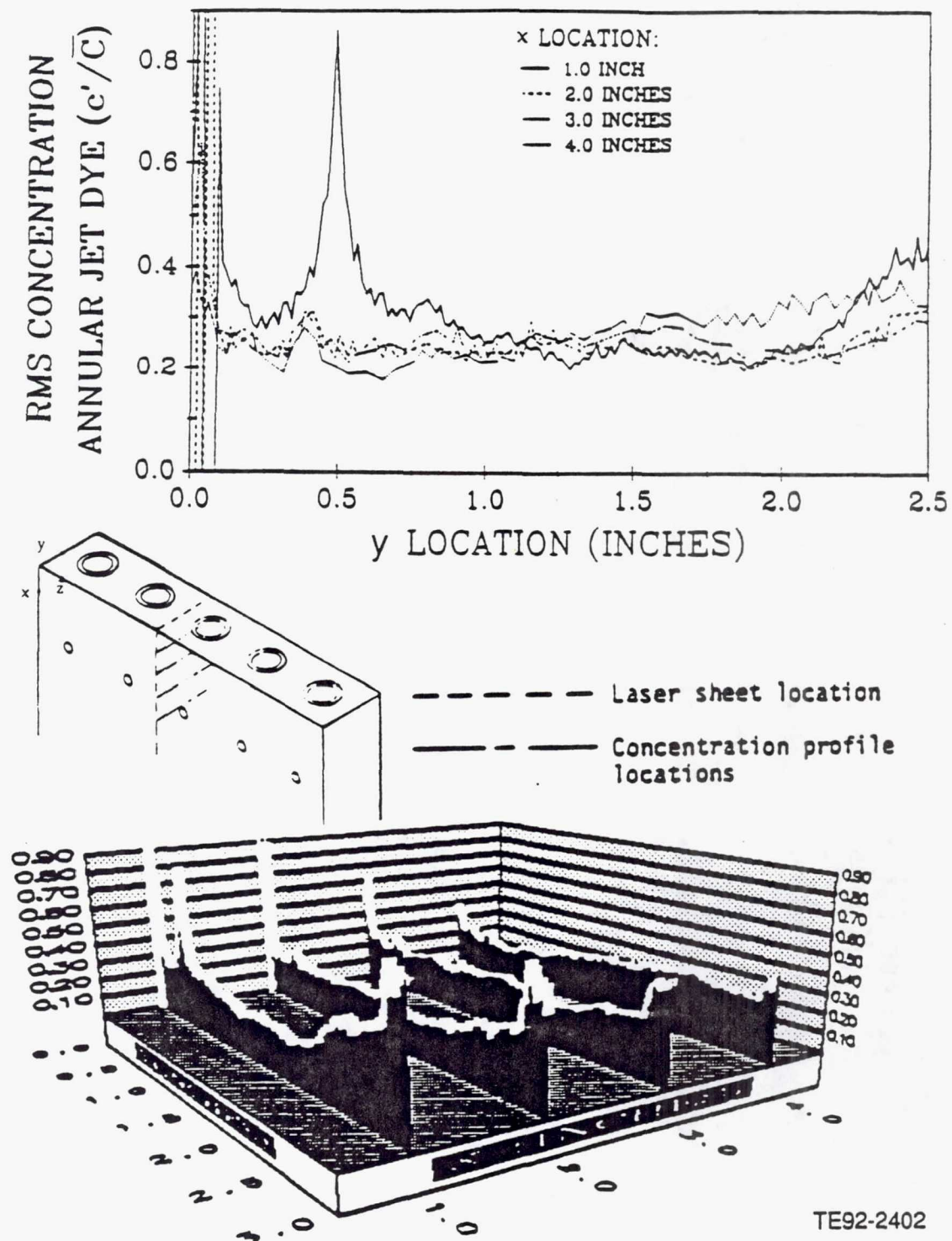


Figure 3.1.2-50. Root mean square annular jet concentration ($z = 6.0$ in.).

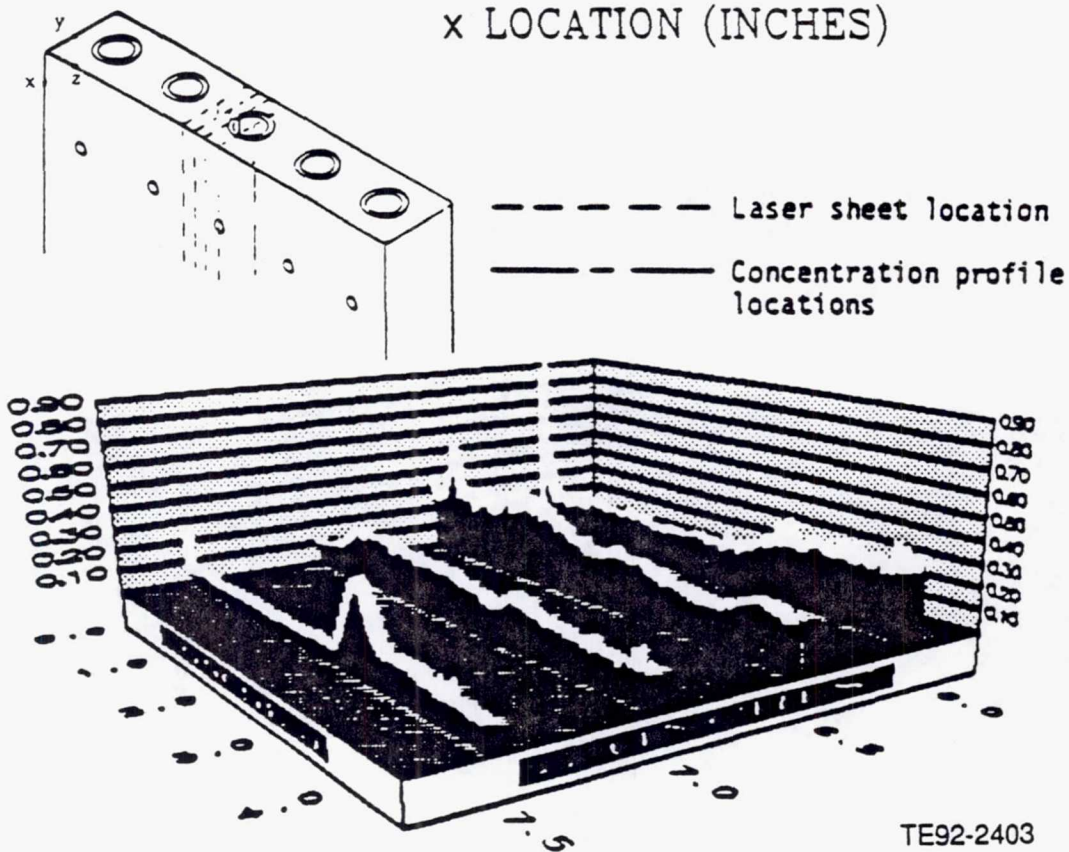
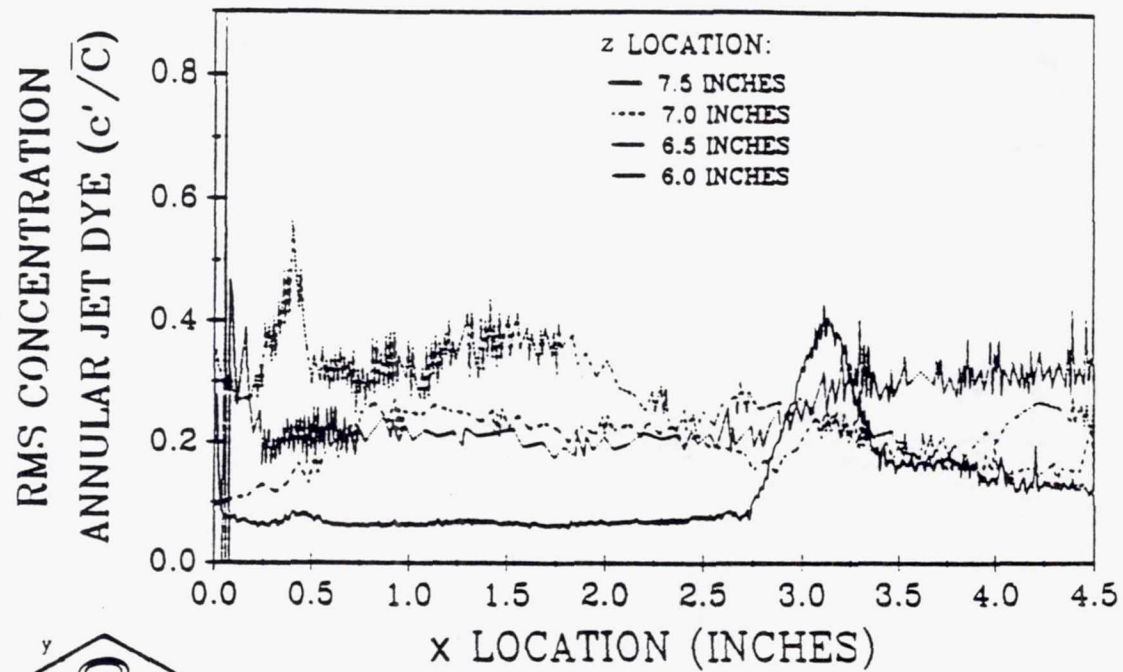


Figure 3.1.2-51. Root mean square annular jet concentration ($y = 1.5$ in.).

3.2 FLOW VISUALIZATION STUDY

An extensive flow visualization study was conducted on both water and airflow rigs to delineate the turbulent flow structure of the flowfield established by the dome swirler, primary jets, and their interaction. This effort included a systematic investigation of the dynamic flow structure on the five-swirler water rig, swirling jet established by a rotating pipe, single swirler, dome annular jets without swirl, primary jets, and interaction of primary jets with dome annular jets.

The turbulent flow structure was quite complex and exhibited considerable time unsteadiness generally stipulated for gas turbine combustor flowfield. In addition to the video tape records, a number of still flow visualization photographs were taken. The salient features of the flowfield are discussed in appropriate subsections of Sections III and IV.

3.3 RIG REFINEMENT ACTIVITIES

Based on the results from the air and water rigs, two additional experiments on a swirling jet and a single swirler apparatus were performed.

3.3.1 Swirling Jet

Of all the characteristics of swirling flows the recirculation zone is of the most interest. The recirculation zone is critical in the stability of the combustion process and, hence, must be fully understood in order to allow the improved design of combustion chambers. Although the size, shape, and strength of the recirculation zone depend on the method of swirl application or generation, the general characteristics remain the same.

This segment of the research involved the study of seed particle concentration fields of a swirling, turbulent jet. Using a light scattering concentration measurement technique known as marker nephelometry, color enhanced video images of these fields were produced. These images allowed the analysis of the formation of the recirculation zone and associated characteristics of the swirling jet. Discussions of the experimental apparatus along with the presentation and discussion of the results are included in this subsection.

3.3.1.1 Experimental Apparatus

The experimental jet apparatus for the swirling jet concentration studies is shown in Figure 3.3.1-1. Ambient laboratory air was drawn into the mixing section by an electric fan, with the injection of the seed particles occurring immediately downstream. The seed particles were created by atomization of a combination of ethyl alcohol and fog juice (Deod. Apco 467) with a TSI Atomizer and entered the mixing section of the jet apparatus with an approximate particle diameter of 1 μm . This type of seed particle was favored over other possible seed particles due to very good light scattering properties as well as the ability of the particles to follow the actual fluid motion. The mixing section contained several banks of screen and straws in order to reduce the level of turbulence, the straws and screens reduced the turbulence scales and thus increased dissipation. A contraction section (contraction ratio= 36.0) was mounted to the exit of the mixing section to increase the axial velocity and further decrease the turbulence.

Upon exit from the contraction section the flow entered the rotating section, a 3-D view of which can be seen in Figure 3.3.1-2. The rotating section consisted of a straight tube with an inside diameter of 2.00 in., the entire length of which was filled with straws. These straws, 3.00 mm in diameter, drove the solid body rotation of the flow. The rotation in this section was produced by a hydraulic motor via gear and chain drive, allowing infinite adjustability of the rotational speed. The axial average could also be controlled, allowing nearly any combination of axial speed, rotational speed, and swirl ratio. The mass-averaged speed through the jet chosen for this experiment was 8.40 ft/sec, giving a Reynolds number based on jet diameter of 8900.

3.3.1.2 Results And Discussion

Two-dimensional concentration fields/flow visualization images of the initial region ($x/D < 7$) of a swirling turbulent jet are given for seven different swirl ratios: 0.00, 0.33, 0.66, 1.00, 1.33, 1.66, and 2.00. For each of these swirl ratios color enhanced video images corresponding to single frames and 127 averaged frames are shown. These images can be seen in Figures 3.3.1-2 through 3.3.1-8.

The imaged region of the flowfield extended roughly 7 jet diameters in both the downstream direction and direction perpendicular to the jet axis. With a jet diameter of 2.0 in., the imaged area was 252 in. For this set of images the laser sheet thickness was 0.04 in., resulting in a measurement volume size of 0.03 in. x 0.03 in. x 0.04 in., small enough to resolve all but the smallest scales found in the flowfield,

such as those corresponding to the Kolmogoroff universal length scale. Using an estimate of the turbulent dissipation from Tennekes and Lumley (1973), the Kolmogoroff universal length and time scales

$$\eta = \left(\frac{v^3}{\varepsilon} \right)^{\frac{1}{4}} \quad (2)$$

$$\tau = \left(\frac{v}{\varepsilon} \right)^{\frac{1}{2}} \quad (3)$$

are found to be on the order of 0.01 in. and 0.005 sec. Since the camera operated at a 60 Hz rate, resulting in a time resolution of 0.0167 sec., the single frame images are not instantaneous but averaged over a small time interval.

When these images were acquired great care was taken to ensure that the laser intensity was the same for all the cases, thereby allowing indirect comparison between images. Before a new case was to be imaged, the test facility was flushed with fresh ambient air to ensure a near-zero background marker particle concentration level. This was required since during the operation of the swirling jet apparatus, the room became rather quickly saturated with the marker particles. The saturation occurred very slowly, though, compared with the time required for a complete sequence of images at one swirl ratio, allowing characteristics such as the time-averaged spread angle to remain constant in time.

The variations in the flowfield as the swirl ratio is increased as well as the differences between the single frames and multiple frame averages can immediately be seen. In general, several phenomena occur with an increase in swirl:

- an increase in the spread angle of the jet
- the formation of a recirculation zone when a critical swirl ratio is reached
- the growth of this recirculation region with an increase in swirl

The zero swirl case can be seen in Figure 3.3.1-2. Jet flows with zero swirl are characterized by a very small jet spread angle which, for the 127 frame average image, is measured to be 24 deg. From Figure 3.3.1-2 (b) some apparently wavy behavior of the jet boundary can be seen. This behavior can be attributed to the use of straws in the rotating section. Some of the straws were not exactly aligned parallel to the jet axis and interacted with neighboring straws to develop undesirable secondary flows and jet growth. This effect does cause some small errors in the spread angle measurement for the swirl number, $N=0.00$ and $N=0.33$, cases (swirl number is the ratio of angular momentum to axial momentum), but not for the larger levels of swirl.

The spread angles given for these images represent the spread of the visible radial extent of marker particles with downstream distance. Most jet studies, usually involving the measurement of velocity profiles, define the spread angle as the spread of the velocity half radius with downstream distance. A comparison of the single and multiple frame averaged images reveals the dissimilar nature of the single frame and averaged profiles. The single frame image can be seen to show very large-scale fluctuations for $x/D > 2$, with a correspondingly large amount of intermittency near the jet boundary, while the averaged image shows very smooth contours. Dahm and Dimotakis (1985) discovered the same behavior in their jet studies.

In Figure 3.3.1-2 a discrepancy can be seen in the background intensity level, above and below the jet, and an apparent distortion of the corners of the images is also visible. The distortion effect is due to nonlinear camera response, while the variation in the background intensity level is due to some type of reflection causing undesired illumination. These two effects are present in all the processed images but do not hinder the study of the flow structure.

Figure 3.3.1-3 shows single and averaged images corresponding to the first case of applied swirl, $N=0.33$. The measured spread angle, 22 deg, is smaller than that reported for the zero swirl case but, as stated before, the results of these two cases are in slight error. As with the zero swirl case, very large-scale fluctuations can be seen from the single frame image, resulting in profiles that do not resemble the mean.

The images for the $N=0.66$ case can be found in Figure 3.3.1-4. Immediately visible in the averaged image is the reduced downstream extension of the various intensity levels compared to the $N=0.33$ and $N=0.00$ cases. This is due to the reduction in the rate of the downstream convection which, in turn, is due to the development of a small, axial pressure gradient with increase in swirl. This pressure gradient also existed at the $N=0.33$ case, but was so small as to be almost negligible. Unlike the $N=0.00$ and $N=0.33$ cases, which show a nearly constant rate of jet spread with downstream distance, the spread for $N=0.66$ displays two distinct spread angles or 30 deg for $x/D < 2.5$ and 12 deg for $x/D > 2.5$.

The first sign of recirculating flow can be seen in the single frame image for $N=1.00$ (Figure 3.3.1-5), where large-scale fluctuations can be seen to occur much closer to the jet exit than for the previous cases. The regions of higher concentration appear to diverge at a downstream distance of $x/D=1.5$, indicating a backflow of fluid with lower marker particle concentration. This fluid must recirculate from stations located farther downstream. The averaged image shows no direct signs of recirculation, only a further reduction in the downstream extension of the various concentration levels. The averaged image also shows the change in the spread angle at the downstream location $x/D=2$, similar to that at $N=0.66$. The spread angle measured in the initial region of the flowfield is 45 deg.

The next level of swirl, $N=1.33$, shows signs of the recirculation zone in both the single frame and the multiple frame average images (Figure 3.3.1-6). The fluid exiting the jet, with very high levels of marker particle concentration, can be seen to move radially around a region of marker particle deficit, which is due to backflow from downstream stations. The formation of the forward stagnation point can be clearly seen, but is not distinctly visible for the rear (downstream) stagnation point. As with the previous cases, large-scale fluctuations are prevalent in most of the flowfield. An increase in the size of the region of intermittency also occurs as small volumes of ambient fluid are transported across most of the radial extent of the flowfield. Similar to the previous cases, the spread angle can be seen to have an increased value, 80 deg, in the initial portion of the flowfield ($x/D < 1$), with the subsequent motion of the highly concentrated fluid around the recirculation zone.

The single frame and multiple frame averaged images for the $N=1.66$ case can be seen in Figure 3.3.1-7. The recirculation zone formed at this level of swirl is larger than for the $N=1.33$ case, with a corresponding increase in the spread angle (to 140 deg) in the initial mixing region. The single frame image shows fluid of very low concentration fluid recirculating. Small regions of unmixed, ambient fluid can be seen to exist in the recirculation zone, but at a very low rate of occurrence. As with the $N=1.33$ case, the location of the forward stagnation point can be clearly seen while the rear (downstream) stagnation point cannot be discerned.

Figure 3.3.1-8 illustrates the concentration field for the $N=2.00$ case. From this figure the fluid motion appears to be completely upstream, as the highly concentrated fluid can be seen to issue from the jet exit and flow around the lip of the jet. In actuality, the recirculation zone is so large that the imaged area is only a small portion of the total recirculation zone size. This same type of behavior was observed by Gore and Ranz (1964), who applied enough swirl to a jet flow to cause it to diverge at right angles to the jet axis at the jet exit. The figure shows that most of the fluid existing in the recirculation zone is ambient, or of very low concentration levels. This indicates the large amount of diffusion that has occurred during the fluid motion around the recirculation zone, another sign of the large scale of the recirculation zone.

Finally, Figure 3.3.1-9 shows the variation in the spread angle as a function of the swirl ratio. The very smooth resulting curve, which increases past 180 deg for the higher swirl ratios, is visible. This set of data can be curve fit to be represented by the relation:

$$\theta = 12.49e^{1.41N} \quad (4)$$

3.3.2 Single Swirler Configuration

In the combustor it is desirable that the annular swirler produce a strong recirculation zone. This area of reverse flow holds the hot gases in the center of the chamber away from the liner. It also produces large amounts of fuel/air mixing near the swirler exit and shortens the needed combustor length.

Each swirler consists of an actual swirler from the production of the Allison 570-K turboshaft gas turbine engine (Figure 3.3.2-1). These are 60 deg angle flat vane swirlers with 12 vanes. They have an outer flow diameter of 1.459 in. and inner flow diameter of 1.084 in. For nonswirling flow ($S = 0$), the normal swirler is replaced with a dummy swirler having no vanes.

A measure of the strength of the swirling flow produced is the swirl number. The most commonly accepted definition:

$$\text{Swirl Number} = \frac{G_{\theta}}{G_x R_2} \quad (5)$$

where:

- G_{θ} angular momentum flux
- G_x axial momentum flux
- R_2 outer radius of swirl generator

For vane swirlers, the swirl number can be approximated by (Beer and Chigier, 1983; Mathur and McCallum, 1967):

$$S = \frac{2}{3} \left[\frac{1 - \left(\frac{R_1}{R_2}\right)^3}{1 - \left(\frac{R_1}{R_2}\right)^2} \right] \tan \theta \quad (6)$$

where:

- R_1 = inner flow radius
- R_2 = outer flow radius
- θ = swirler/vane angle

From the geometry of the swirlers, and using Equation 6, the swirl number is calculated to be 1.52. Swirl generators producing swirl numbers greater than 0.6 produce recirculation regions along the swirling axis near the exit (Beer and Chigier, 1983; Gupta et al, 1984). It is expected that the swirlers used will produce a very strong recirculation region. The annular swirler inlet tubes are made of stainless steel and have diameters equivalent to the flow diameters of the swirlers. Each inlet tube is 25 effective diameters, 9.547 in. long. Where the effective diameter is defined by:

$$D_E = \text{outer diameter} - \text{inner diameter} \quad (7)$$

Initially the swirlers were mounted at the end of the inlet annulus flush with the headplate. However, in doing some preliminary smoke flow visualization an unexpected flow phenomenon occurred. The flow would leave the swirler and make a sharp 90 deg bend and hug the headplate all the way out to the side walls. At the side walls, the flow would then proceed downstream. This phenomenon has also been observed by Gore and Ranz (1964) when high degrees of swirl are generated flush with the orifice exit.

It was not believed that this type of flow profile accurately modeled the intended combustor flow. Therefore, the swirlers were recessed 0.25 in. back from the headplate. The annulus with the recessed swirler is shown in Figure 3.3.2-2.

The primary jets provide cool additional air for mixing and combustion with the swirling air. Each primary jet is made of stainless steel and is 25 diameters long, with the diameters varying for the different configurations. The necessary jet diameters were determined using the required mass flow ratios and number of jets. Referring to Figure 3.3.2-3, the mass flow ratio is given by:

$$\frac{M_j}{M_s} = \frac{N_j \bar{V}_j \left(\frac{\pi}{4}\right) d_j^2}{N_s \bar{V}_s (A_t N_b) / N_b} \quad (8)$$

Imposing the condition that V_j is equal to V_s and solving 3.8 for d_j yields:

$$d_j = \sqrt{\frac{4 M_j N_s A_t}{\pi M_s N_j}} \quad (9)$$

From the geometry of the swirler A_t is 0.366 in^2 . Thereby, the needed diameter for the swirling flow case is 0.418 in. The actual jet being used has an inner diameter of 0.43 in. with an outer diameter of 0.5 in. For Configuration 10 the calculated diameter is 0.591 in., with actual inner and outer diameters of 0.591 in. and 0.75 in., respectively. The primary jet is shown in Figure 3.3.2-4.

To determine the losses through the rig, a single swirler rig was built. This rig is shown in Figures 3.3.2-5 and 3.3.2-6. The test section was 3.0 in. square and extended 10 duct lengths downstream. Pressure taps were installed on the swirler annular pipe, primary jet, and main duct downstream of the mixing region. Velocity measurements were taken with a hot wire downstream of the mixing region before entrance into the plenum. From these measurements, the loss coefficients were calculated for the primary jets, annular pipe, and swirler. A summary of the measured losses is shown in Figure 3.3.2-7. In this figure K is the loss coefficient in reference to the mean annular or primary jet velocity. Also, the measured values of static pressure and test section velocity are indicated.

3.3.2.1 Data Acquisition

The data acquisition system is shown in Figure 3.3.2-8. A signal from the PM tubes contains the 40 Mhz signal from the Bragg cell plus or minus the Doppler signal. PM signal is greater than 40 Mhz if the flow is into the direction of fringe movement and less than 40 Mhz if the flow is with the fringe movement.

Since the signal frequency is higher than that allowable for the processors, it is sent through a frequency mixer. The mixer heterodynes this signal with a selected mix frequency ranging from 31 to 49 Mhz.

Output from the mixer is sent to the TSI counter processors, one for each color line. The processor initially provides gain and high and low pass filtering to eliminate noise from being processed. Each par-

ticle generates a burst as it passes through the probe volume, and at the onset of a burst a timer is started. If the burst contains a set minimum number of cycles, the clock is stopped. If the burst contains less than the required number of cycles, the burst is considered invalid and the processor resets to accept another burst. This step eliminates particles that pass along the edge of the probe volume which provide a signal burst with a small number of cycles. For this experiment the cycles/bursts were set at 1/2. Finally, the time for the passage of the cycles/bursts is compared to that for 1/2 cycles/bursts. If the two values do not compare within a certain percentage the sample is discarded. A 7% comparison was used for the data acquisition. This step eliminates signals that would be generated when two particles cross through the probe volume at the same time.

The data are then sent to the DEC 11/23 minicomputer. Besides taking the data, the computer also controls the probe volume movement. The laser table is movable in two directions via computer controlled stepping motors. The third direction of movement is accomplished by movement of the field lens, and is also done with a stepping motor. This provides full 3-D movement of the probe volume in the flow field. The axis movement sensitivities are listed below.

- horizontal table movement: 1/1000 in. per pulse
- vertical table movement: 1/22574 in. per pulse
- field lens movement: 1/1000 in. per pulse

To accommodate the use of forward scatter, as mentioned previously, a sliding boom was used between the transmitting and receiving optics. The boom was bolted to the bottom of the laser table and extended under the rig to the opposite side (Figure 3.3.2-9). Bolted to the top of the boom was a sliding beam with one end attached to the filed lens and the other to the receiving optics. This provided full 3-D movement of the receiving optics with the probe volume.

3.3.2.2 Calibration of Annular Pipe and Primary Jet

To calibrate the primary jet and swirler several setups were used. The first was a setup to determine the flow profile (Figure 3.3.2-10). A high pressure air supply and plenum were used to blow air through one of the primary jets. At the exit, a total pressure probe was scanned across. A stepper motor driven traverse was used to move the probe, and a dial gage was used to measure position. From this, the pipe flow profile was determined.

The measured profile is shown in Figure 3.3.2-11. This profile fits well the one-sixth turbulent profile presented by Schlichting (1979). Thus for the rest of the measurements a one-sixth turbulent profile is assumed.

The setup used for the mass flow calibration of the primary jet is shown in Figure 3.3.2-12. This is the same rig used for the LDV measurements. The only difference is that the headplate for the swirler is replaced with one to hold the primary jet. Also, a total pressure probe is mounted on the jet centerline over the second pressure tap. Thus, the jet centerline pitot pressure is measured. Figure 3.3.2-13 is the plot of centerline pitot pressure against the pressure drop across the primary jet pressure taps. From Bernoulli's equation:

$$\Delta P_{\text{Pitot}} = \frac{1}{2} \rho V^2 \quad (10)$$

solving for V

$$V = \sqrt{\frac{2\Delta P_{\text{Pitot}}}{\rho}} \quad (11)$$

Assuming a one-sixth profile the mean jet velocity is 0.791% of the jet centerline velocity (Schlichting, 1979).

$$\bar{V} = 0.791 \sqrt{\frac{2\Delta P_{\text{Pitot}}}{\rho}} \quad (12)$$

rearranging Equation 12

$$(0.791)^2 \Delta P_{\text{Pitot}} = \frac{1}{2} \rho \bar{V}^2 \quad (13)$$

The relationship between the mean jet velocity and the static pressure drop across taps 1 and 2 is given by:

$$\Delta P_{12} = K \frac{1}{2} \rho \bar{V}^2 \quad (14)$$

Where K is the loss coefficient between the pressure taps. Using Equations 13 and 14:

$$(0.791)^2 \Delta P_{\text{Pitot}} = \frac{1}{2} \rho \bar{V}^2 = \frac{\Delta P_{12}}{K} \quad (15)$$

solving for K

$$K = \frac{\Delta P_{12}}{(0.791)^2 \Delta P_{\text{Pitot}}} \quad (16)$$

$\Delta P_{12}/\Delta P_{\text{Pitot}}$ is the inverse slope of the plot in Figure 3.3.2-13. A least squares routine was used to calculate the slope. For this plot, the slope was calculated to be 3.113 and a loss coefficient of 0.513.

With this setup it is easy to measure the losses in the other portions of the primary jet by switching pressure tap hook ups. Figures 3.3.2-14, 3.3.2-15, and 3.3.2-16 are sketches of the other pressure transducer configurations. The corresponding data plots are provided in Figures 3.3.2-17, 3.3.2-18, and 3.3.2-19.

A similar procedure was also adopted for the annular pipe. Figure 3.3.2-20 is a diagram of the setup used for the annular pipe mass flow calibration. Figure 3.3.2-21 is a plot of the measured data. The remaining data plots for the annulus are provided in Figures 3.3.2-22, 3.3.2-23, and 3.3.2-24. These plots are for the same setups as Figures 3.3.2-17, 3.3.2-18, and 3.3.2-19, except that these are for the annular pipe instead of the primary jet.

Finally, the same tests were run on the annular pipe with the swirler installed. However, since the pitot probe could not be inserted through the swirler vanes, the required pressure drops were measured against annular pipe pressure drop. That is, the pressure difference between taps 1 and 2 were measured. This is easily referenced to centerline pitot pressure through Figure 3.3.2-21, which is a plot of centerline pitot pressure versus annular pipe pressure drop. The pressure transducer arrangement for the measurement of swirler loss is shown in Figure 3.3.2-25. This data is shown in Figures 3.3.2-26, 3.3.2-27, and 3.3.2-28.

3.3.2.3 Inlet Conditions

To establish the swirler inlet flow, a finely detailed scan was taken in front of the swirler at 0.050 in. downstream of the exit. The spatial grid used is shown in Figure 3.3.2-29. A 39 x 20 point grid was taken with 0.015 in. in between each nodal point, for a total of 780 spatial points. For each spatial point, the mean and rms were computed from the 3000 samples taken. In all, a total of 9.36 million data samples were taken of the swirler inlet.

Referring to Figure 3.3.2-29, at each spatial point the laser was able to measure two components of velocity. The two components are the x component (into the plane of the paper) and y component (towards the top of the page). In order to get all three components, two scans were taken and the use of symmetry imposed. Scan 1 was able to measure u and v velocity and scan 2 was able to measure u and w components. Thus all three components were measured, with the u velocity being measured twice.

Figure 3.3.2-30 contains cascade plots of the x component of velocity for scans 1 and 2. In general, the axial velocity is lower at the hub and has maximum values at the outer flow radius. However, there is considerable discrepancy in the u velocity measured by the two scans. Referring to Figure 3.3.2-31, the maximum axial velocity varies by 40 ft/sec between scans 1 and 2.

It is expected that there would be some spatial averaging between scans 1 and 2. The probe volume has a certain length and width, and for each spatial point the measured velocity is an average over the probe volume. In scan 1 the probe volume dimension is only 0.001 in. along the y axis, where for scan 2 the probe volume dimension is 0.015 in. along the y direction. Thus, the spatial resolution in the y direction is considerably finer for scan 1 than scan 2. This would account for a slight variation between the two scans, but not a 40 ft/sec difference.

Plots of v and w velocities are provided in Figures 3.3.2-32 and 3.3.2-33. The v component converges to a relatively constant value near, or in front of, the hub. This is a strong indication of the back flow being drawn into the swirling exit flow. Also, the w component converges to near-zero in front of the hub, indicating low swirl in this region. As expected, at the left side of the plane (low z position) the v velocity is high, while the w velocity is low, with the values changing as z increases. The combination of v and w velocities are plotted in vector form in Figure 3.3.2-34. Here, the effect of the swirl is clearly evident.

As mentioned earlier, rms values were also measured. Figure 3.3.2-35 is a diagram of the laser orientation. The green and blue beams are orthogonal to each other at approximately 45 deg angles to the faceplate. The rms values have been nondimensionalized with the local mean velocity for that particular beam. Thus, Figures 3.3.2-36 through 3.3.2-39 are plots of the turbulence intensity ratio or $\text{rms}/|\text{mean}|$ velocities.

Figures 3.3.2-36 and 3.3.2-37 are plots of intensities for scan 1. The turbulence intensity is lowest in front of the annular hub or the outer flow radius. At the edge of the inner flow radius, the intensities get very large or, for the green beam, tend to infinity. Here the flow is very near zero and even slight fluctuations make the turbulence intensity very large.

For scan 2 the results are similar (Figures 3.3.2-38 and 3.3.2-39). The turbulence intensities are lowest at the outer flow radius and tend to infinity at the inner flow radius. However, even at its lowest the turbulence intensity is still upward of 20 percent.

3.3.2.4 Downstream Data

Mean and rms velocities were also taken at four downstream locations. These locations were at 0.5, 1.0, 1.5, and 2.0 duct heights downstream of the swirler exit. For each downstream location a 26 x 31 point grid was used for a total of 806 spatial points, with a spatial resolution of 0.050 in. As with the inlet

conditions two scans were taken and symmetry invoked. The grid and scans taken are shown in Figures 3.3.2-40 and 3.3.2-41. In all, a total of over 38 million data samples were taken downstream of the swirler exit. The laser orientation for each scan is shown in Figure 3.3.2-42.

Figures 3.3.2-43 through 3.3.2-46 are plots of the velocity components for the first downstream location ($x = 1.5$ in.). Referring to Figure 3.3.2-43, the u velocity is greatest along the walls and in the corners. That is, in the center of the flow there is a strong back flow, with the bulk downstream flow along the walls and in the corners. Referring to Figure 3.3.2-44 there is very good agreement between the two different values of u velocity obtained from the different scans. Looking at the centerline scan for $z = 1.5$ in., the extent of the back flow region can easily be seen. Only the half-inch nearest the wall has a positive u velocity. The rest of the channel is in back flow.

The extent of the swirling flow can be seen quite clearly in Figures 3.3.2-45 and 3.3.2-46, and also in Figure 3.3.2-47. For the centerline scan of w velocity at $y = 2.75$ (Figure 3.3.2-46) the w component is twice as strong as the u component for the same position. Figure 3.3.2-47 is a vector plot of the v and w components. Here, the strong swirling flow is clearly evident. Also, there is a slight asymmetry in the flow. That is, the apparent center of the swirl is not at the geometric center of the channel. The recirculation region takes the shape of the square duct at the 1.5 in. location.

Figures 3.3.2-48 through 3.3.2-52 are plots for the second downstream location at $x = 3.0$ in. Referring to Figure 3.3.2-48, the u velocity for scan 2 shows a strong velocity deficit in the corner. This could possibly be due to a corner vortex. However, it is uncertain if this is actually the case. It is only possible to measure two components of velocity at these positions. Thus, a full velocity profile for these positions is unavailable.

Comparing Figure 3.3.2-39 to Figure 3.3.2-44 for the centerline scan, the point of zero crossing has moved in towards the center of the duct. Thus, the size of the area of back flow has decreased considerably. Also, the magnitude of the peak velocities has decayed. For the centerline position, the maximum velocity near the wall has dropped from 40 ft/sec to 15 ft/sec. Although the strength of the flow along the walls has decreased dramatically, the strength of the recirculation flow has only decreased slightly from -25 ft/sec to -20 ft/sec.

Comparing Figure 3.3.2-46 to Figure 3.3.2-51, the W component for the centerline scan has decreased only slightly. Thus, the swirl component has only decreased slightly.

Figures 3.3.2-53 through 3.3.2-57 are plots of velocity intensity for $x = 4.5$ in. or 1.5 duct heights downstream from the swirler exit. Referring to Figures 3.3.2-53 and 3.3.2-55, again there is a sudden change in velocity at the corners.

Figures 3.3.2-58 through 3.3.2-62 are plots for $x = 6.0$. The plots at $x = 4.5$ and 6.0 are very similar to those for $x = 3.0$. The only difference is that there is a slight decay in the magnitude of the velocities but the flow profiles remain rather constant.

Thus, the flow goes through some radical changes in the first duct height (3.0 in.). After this, the flow profiles remain rather constant, with only slight decay of the magnitude of the velocities. Referring to Figure 3.3.2-63, these are contour plots of u velocity with areas of negative or back flow showing up as dotted areas. From these plots the size of the recirculation region is clearly visible. At $x = 1.5$, the effect of the square duct can easily be seen in the squared-off back flow region. By $x = 3.0$ or 1.0 duct height, the area of recirculation has diminished considerably and has become circular in shape. For $x = 4.5$ in. and 6.0 in., the size of the recirculation region diminishes very little, if at all. This is also seen in Figure 3.3.2-64, which is a vector plot at the centerline or $z = 1.5$ in. position.

In doing some flow visualization, it was later discovered that there are two exit flow regimes. These are shown schematically in Figure 3.3.2-65. At low mass flow rates, the exit flow expands outward at

an angle of considerably less than 90 deg, and is not attached to the headplate. At high mass flow rates the exit flow remains attached to the headplate all the way out to the side wall. With moderate flow rates a bistable flow situation is setup. That is, the flow will oscillate between the two regimes.

It is believed that this is the cause of the velocity discrepancy indicated in Figure 3.3.2-31. Also, evidence of this phenomenon can be seen in Figure 3.3.2-56. For the v velocity at $z = 0.3$ in. there is a very definite jump in the velocity profile when the exit flow switches from one regime to the other and back again.

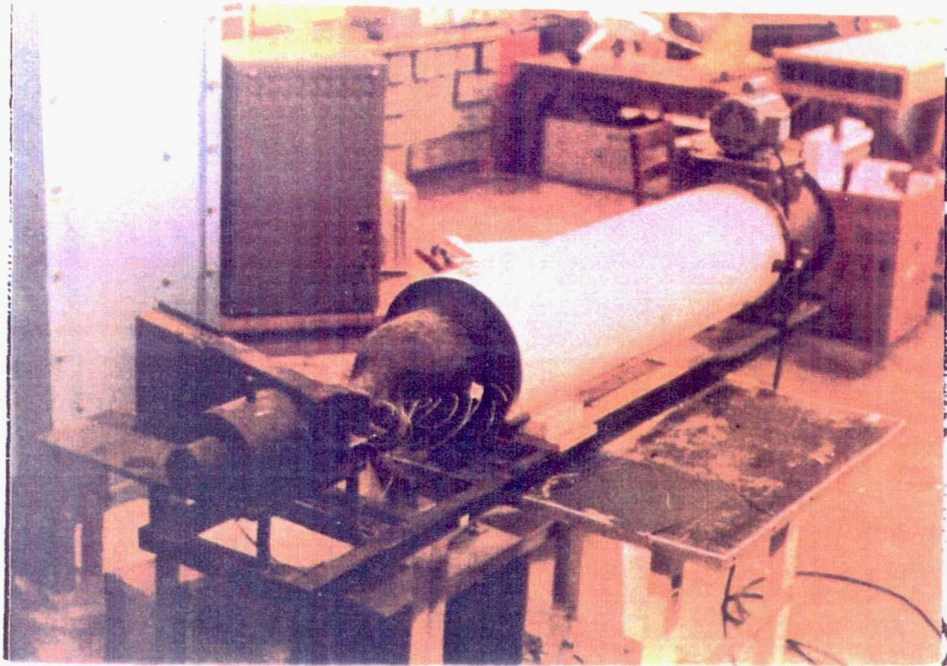
3.3.2.5 Turbulence Quantities

Figures 3.3.2-66 through 3.3.2-69 are plots of turbulence intensity for the first downstream location. As with the inlet condition data, when the mean velocity goes towards zero the turbulence intensity goes to infinity. In areas where this is not the situation, the turbulence intensity varies from 35 to 100%.

Figures 3.3.2-70 through 3.3.2-73 are plots for the second downstream location at $x=3.0$ in. Referring to Figure 3.3.2-70, the U velocity for scan 2 shows a strong velocity deficit in the corner. This could possibly be due to a corner vortex, however it is uncertain if this is actually the case. It is only possible to measure two components of velocity at these positions, thus a full velocity profile for these positions is unavailable.

Figures 3.3.2-74 through 3.3.2-81 are plots of turbulence intensity for $x = 4.5$ in. and $x = 6.0$ in. The plots at $x = 4.5$ and 6.0 in. are very similar to those at $x = 3.0$ in, the only difference is that there is a slight decay in magnitude but the flow profiles are similar.

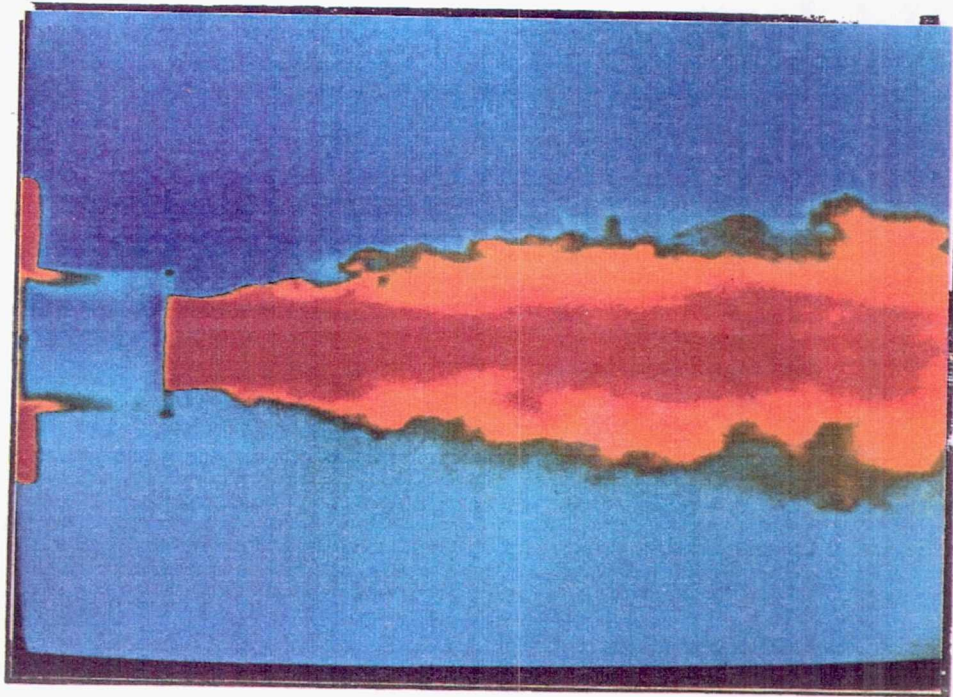
Page intentionally left blank



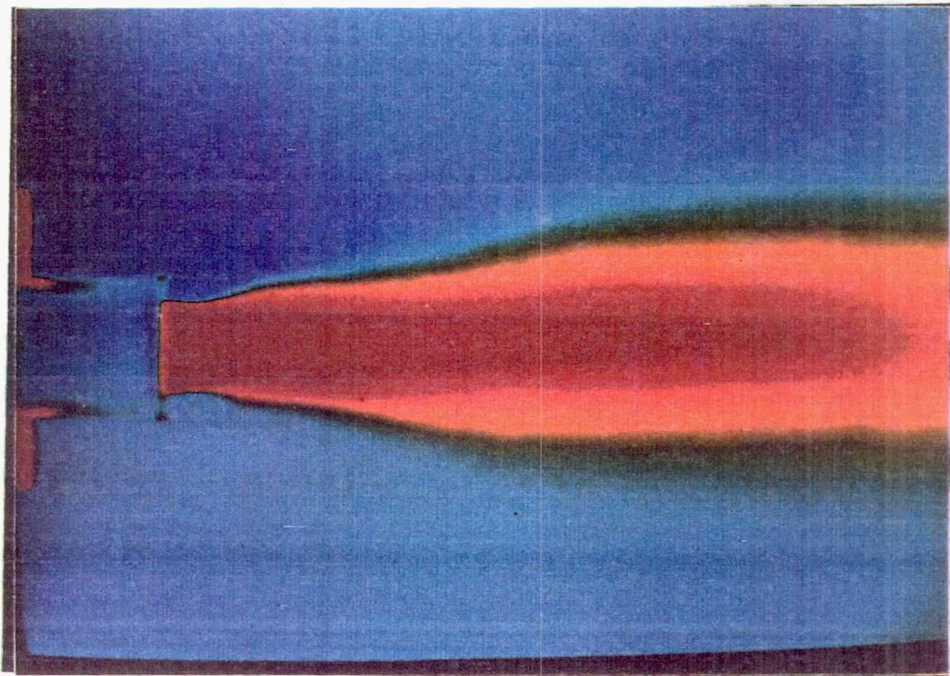
TE92-2404

Figure 3.3.1-1. Photograph of swirling jet apparatus.

Page intentionally left blank



(a)

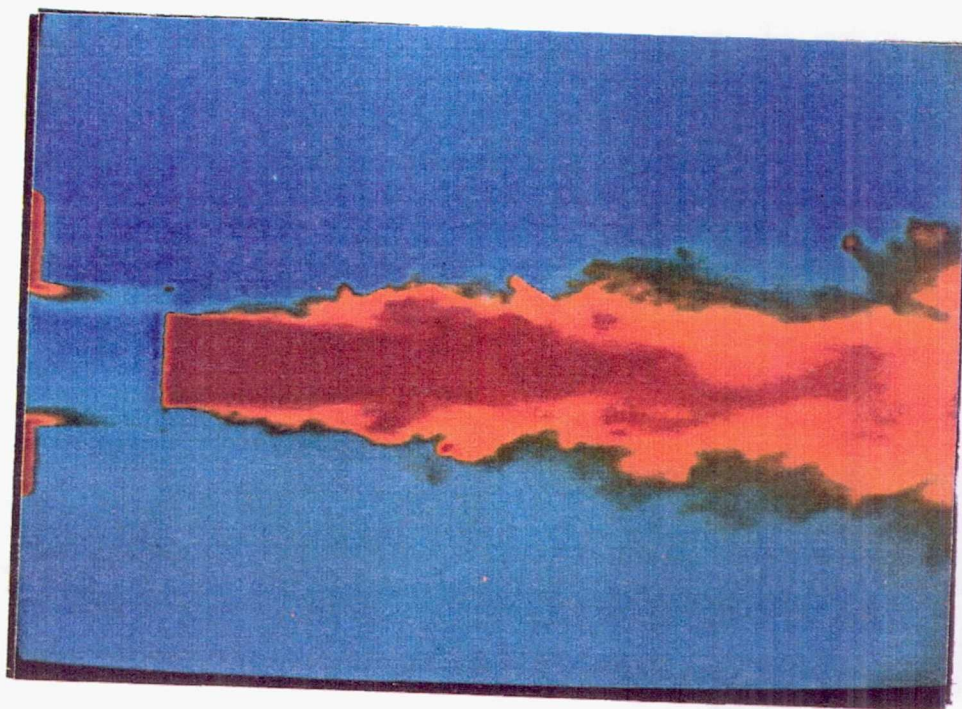


(b)

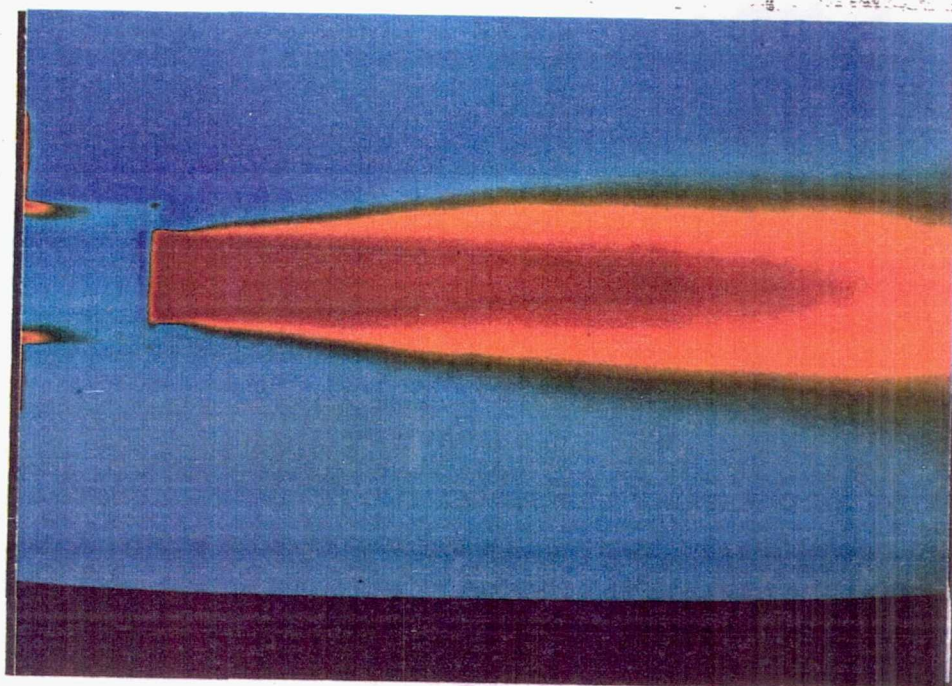
TE92-2405

Figure 3.3.1-2. Concentration fields for $N=0.00$: (a) 1 frame (b) 127 frames.

Page intentionally left blank



(a)

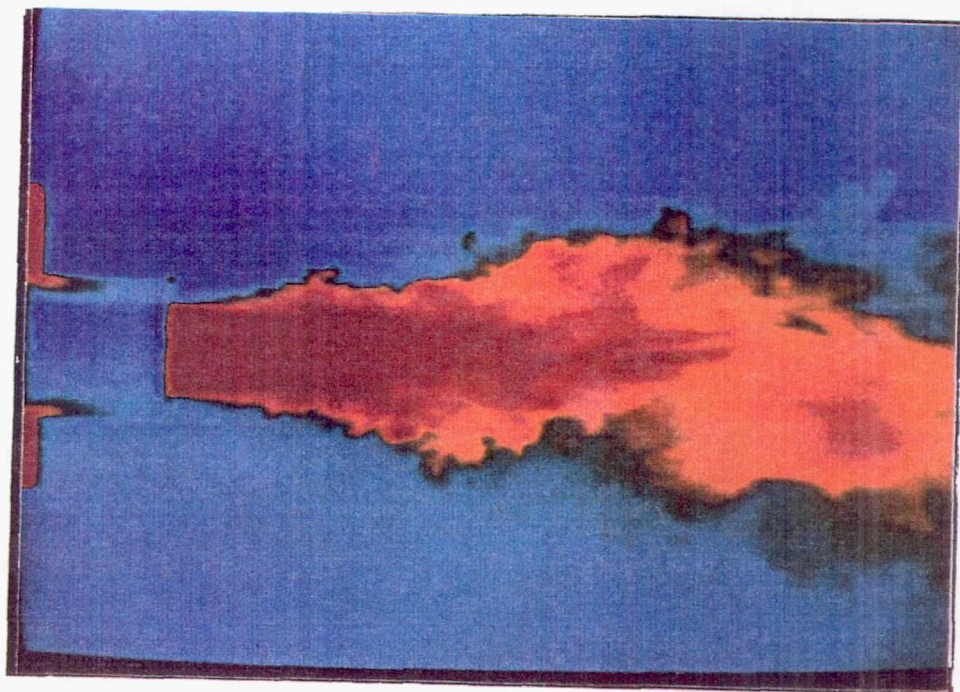


(b)

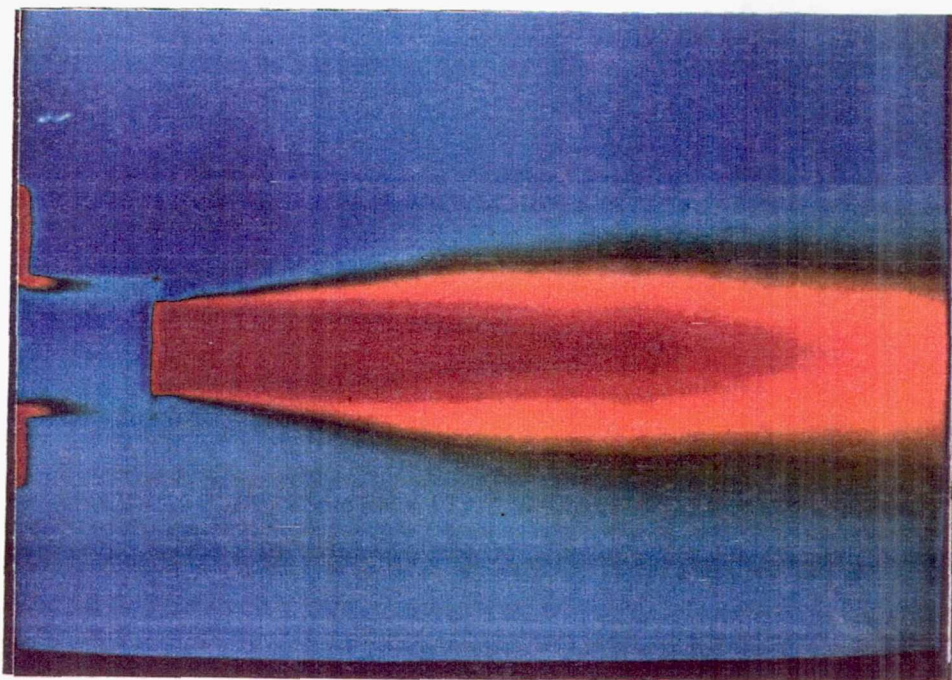
TE92-2406

Figure 3.3.1-3. Concentration fields for $N=0.33$: (a) 1 frame (b) 127 frames.

Page intentionally left blank



(a)

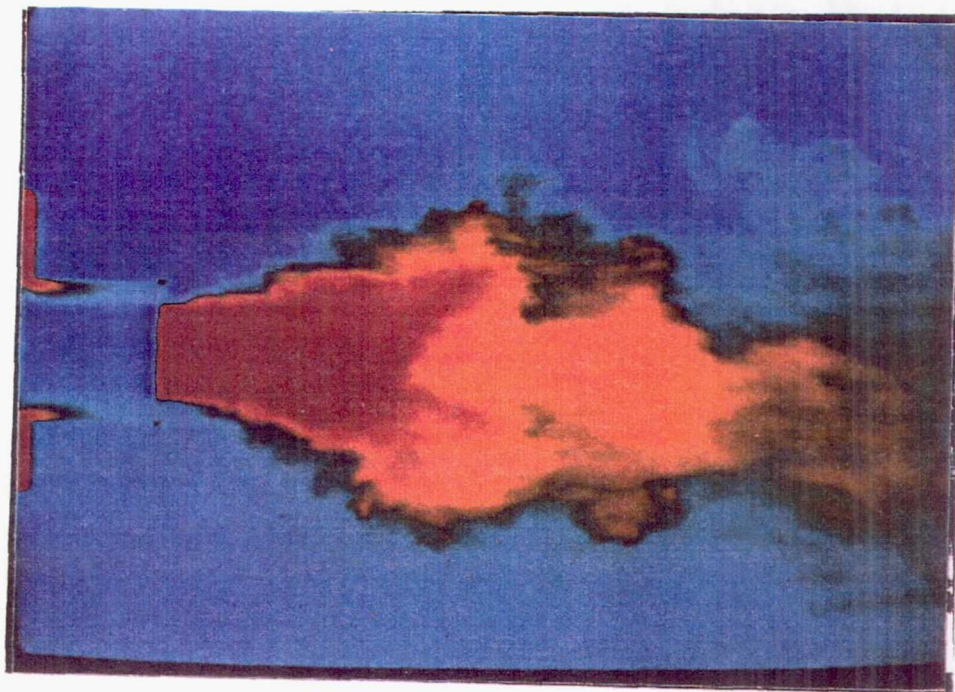


(b)

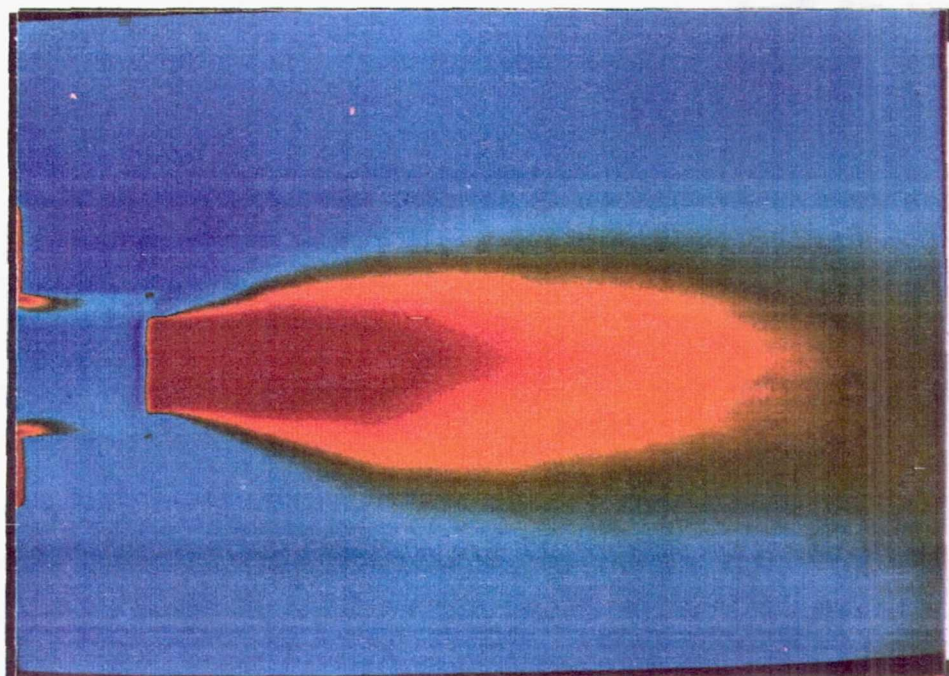
TE92-2407

Figure 3.3.1-4. Concentration fields for $N=0.66$: (a) 1 frame (b) 127 frames.

Page intentionally left blank



(a)

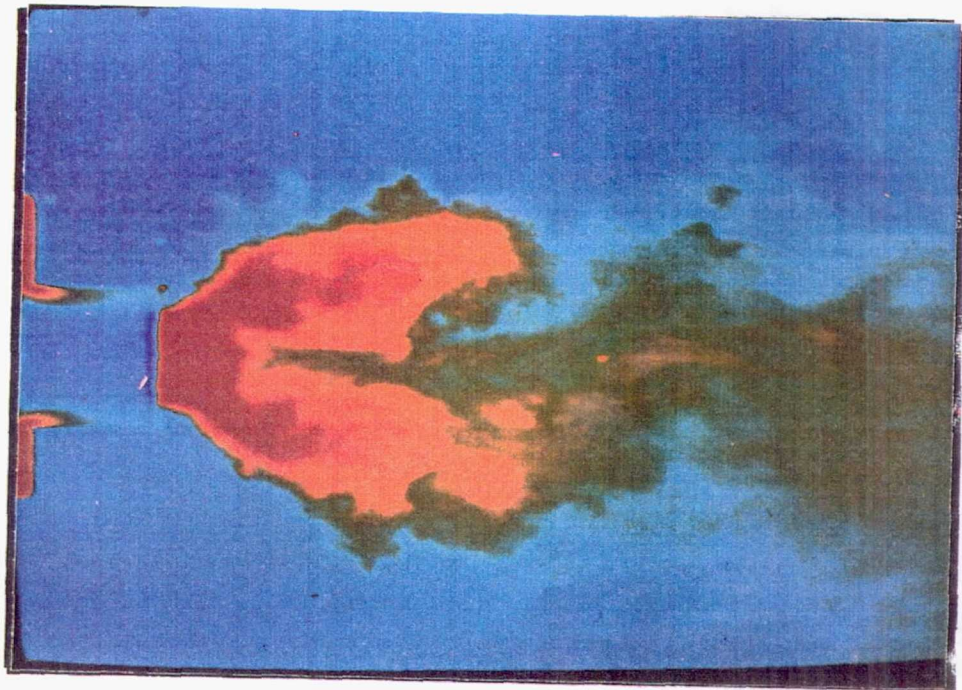


(b)

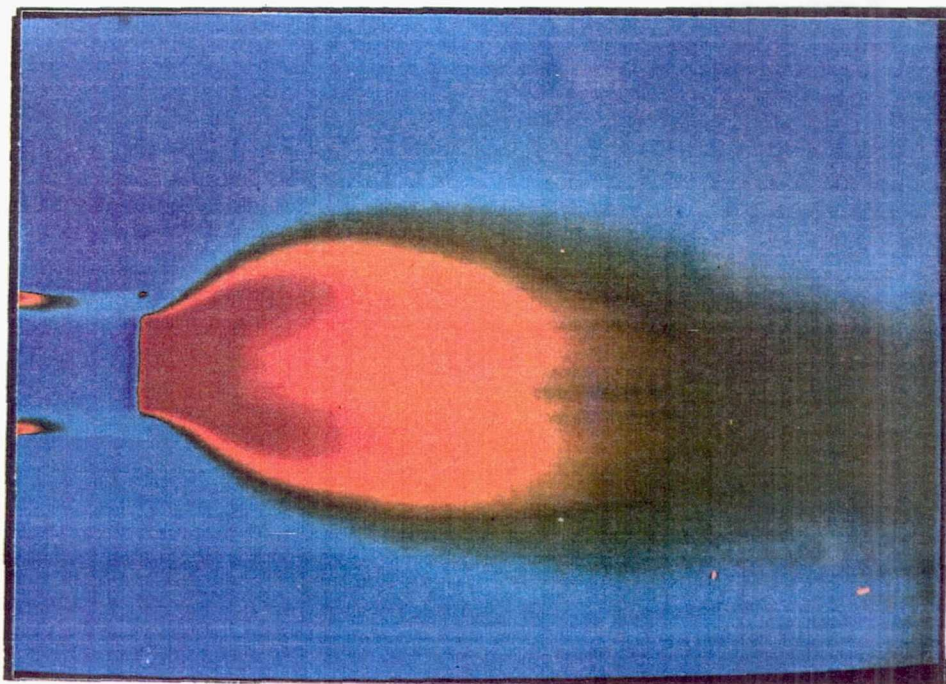
TE92-2408

Figure 3.3.1-5. Concentration fields for $N=1.00$: (a) 1 frame (b) 127 frames.

Page intentionally left blank



(a)

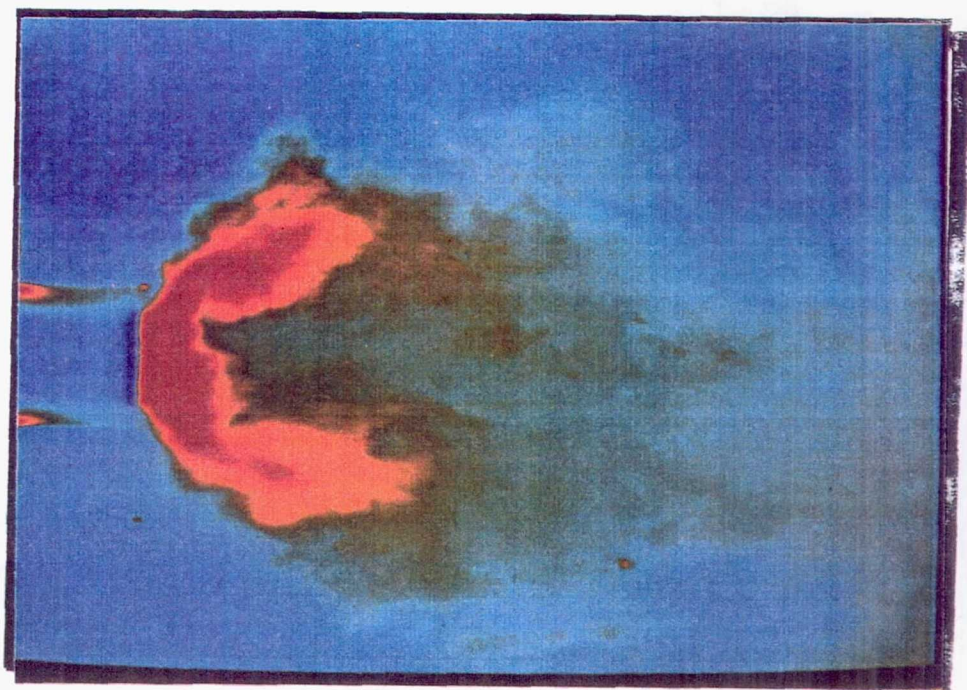


(b)

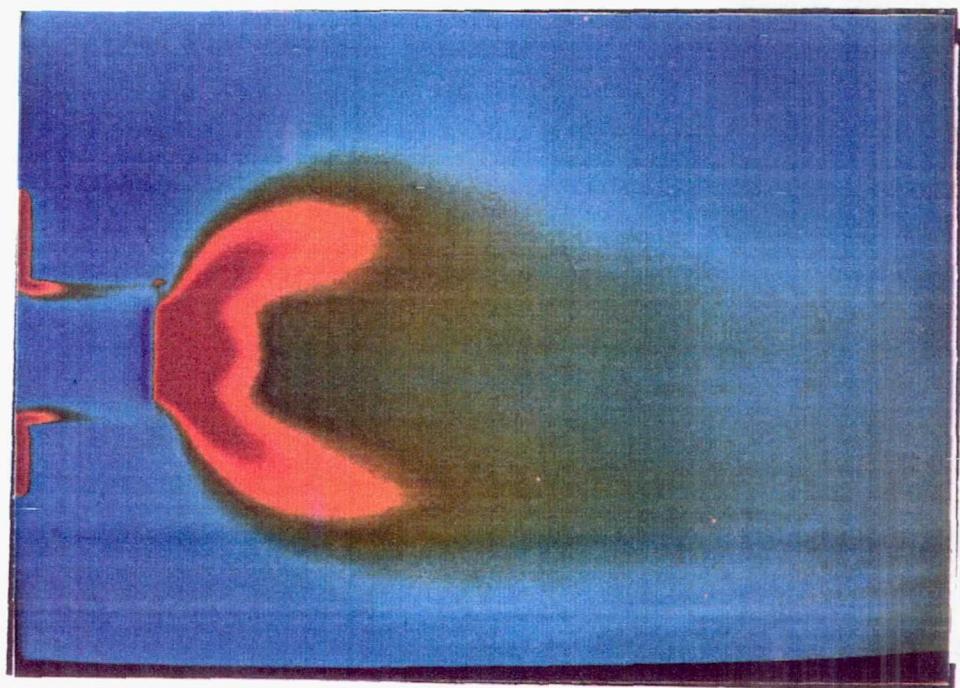
TE92-2409

Figure 3.3.1-6. Concentration fields for $N=1.33$: (a) 1 frame (b) 127 frames.

Page intentionally left blank



(a)

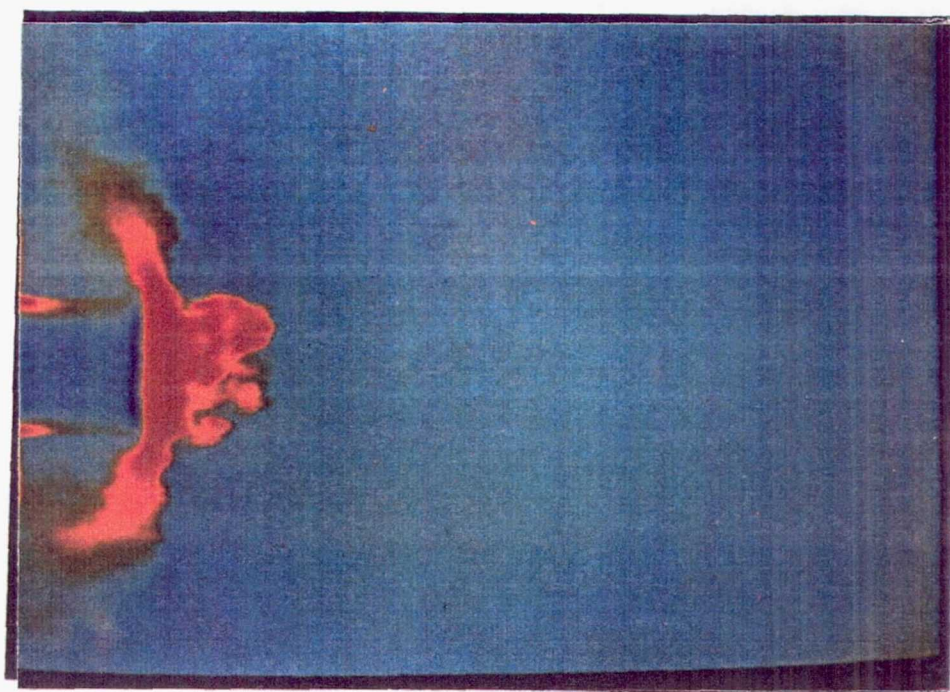


(b)

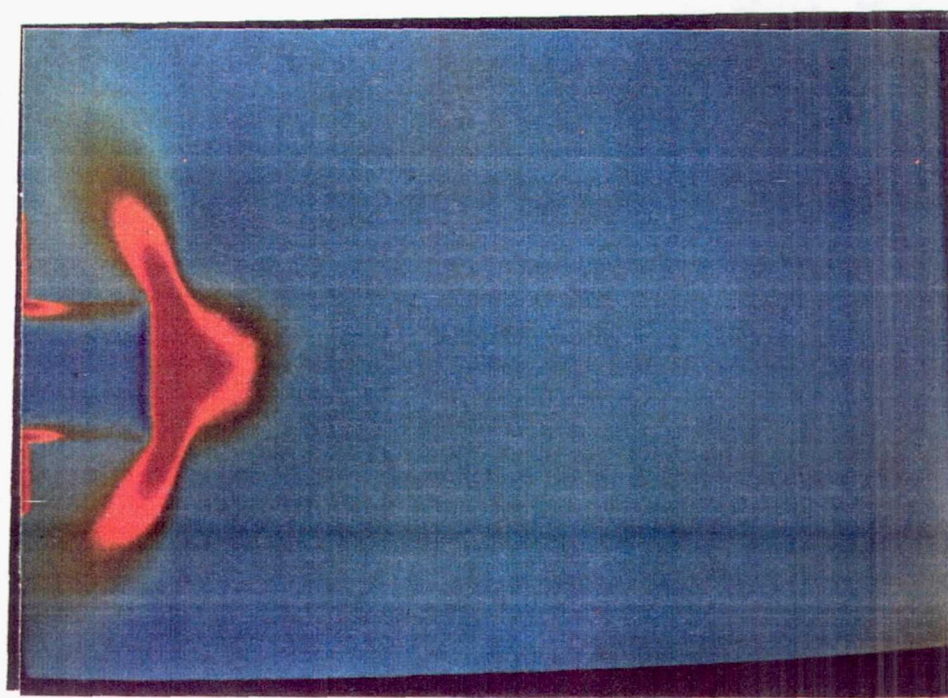
TE92-2410

Figure 3.3.1-7. Concentration fields for $N=1.66$: (a) 1 frame (b) 127 frames.

Page intentionally left blank



(a)

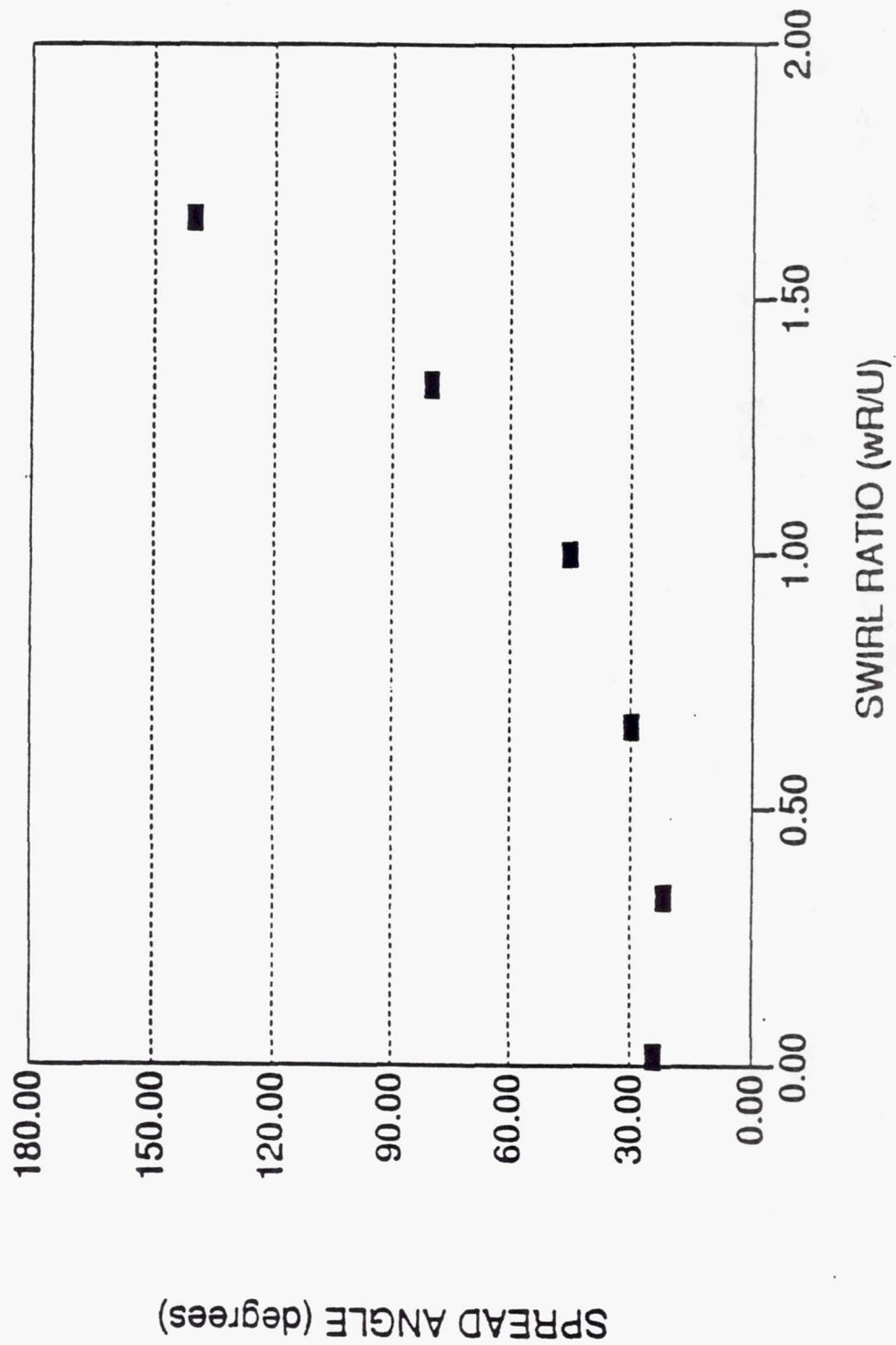


(b)

TE92-2411

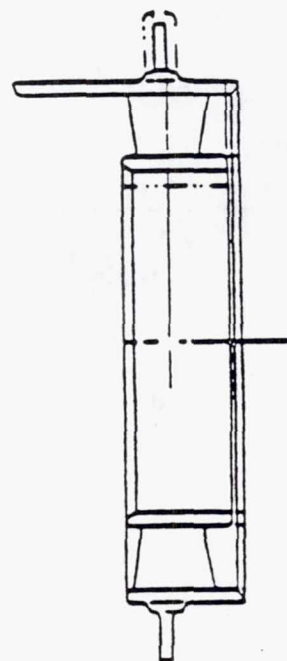
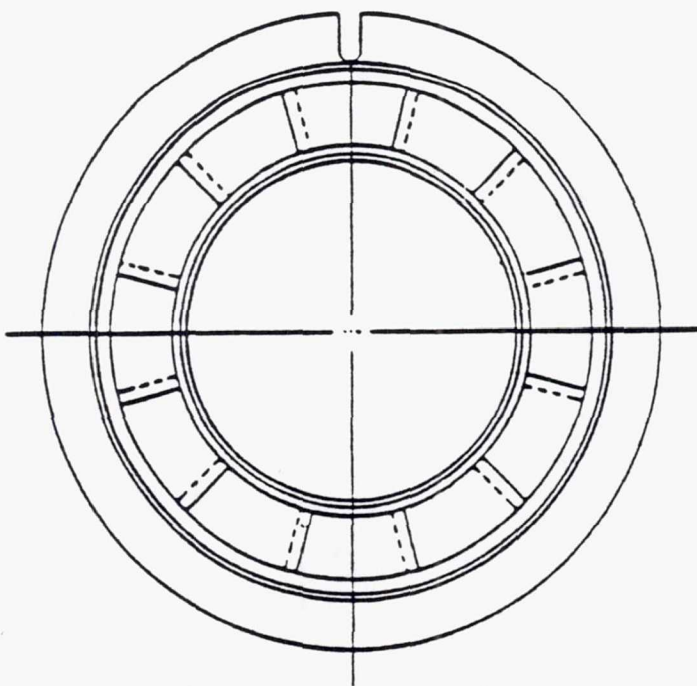
Figure 3.3.1-8. Concentration fields for $N=2.00$: (a) 1 frame (b) 127 frames.

Page intentionally left blank



TE92-2412

Figure 3.3.1-9. Relationship between spread angle and swirl ratio.



TE92-2413

Figure 3.3.2-1. Diagram of vane swirler.

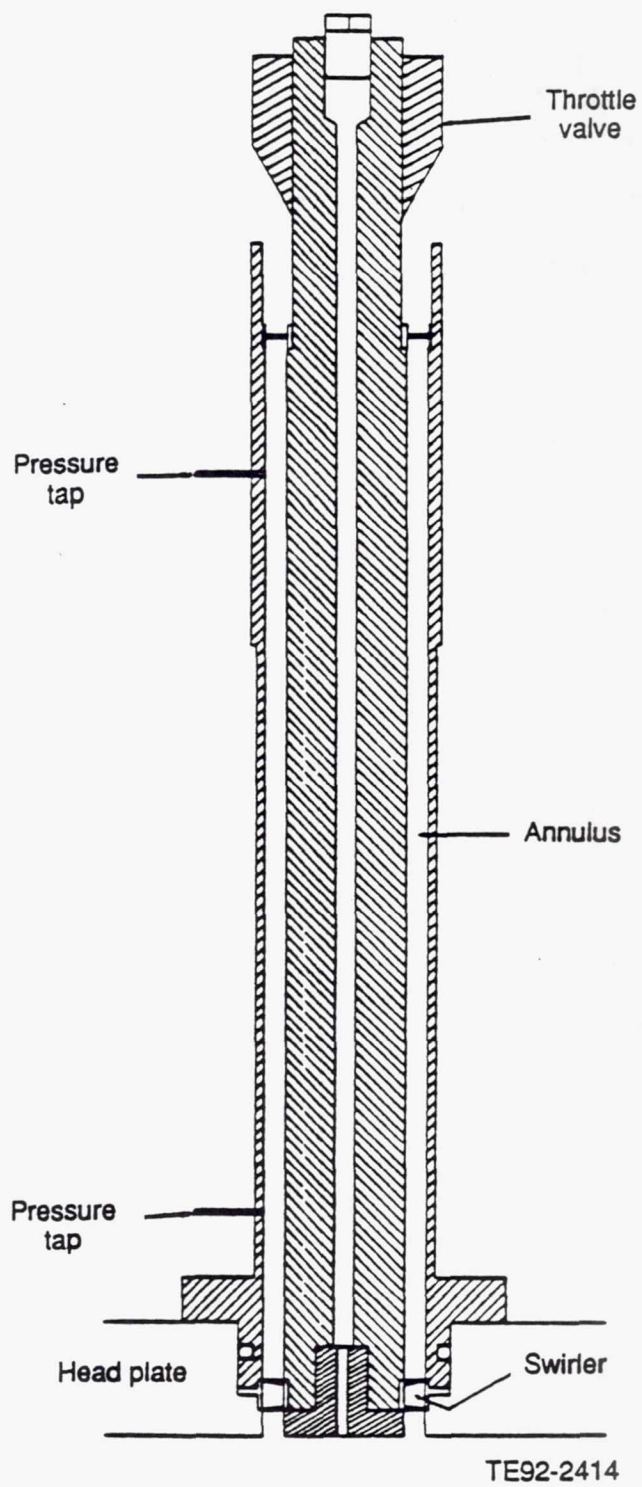
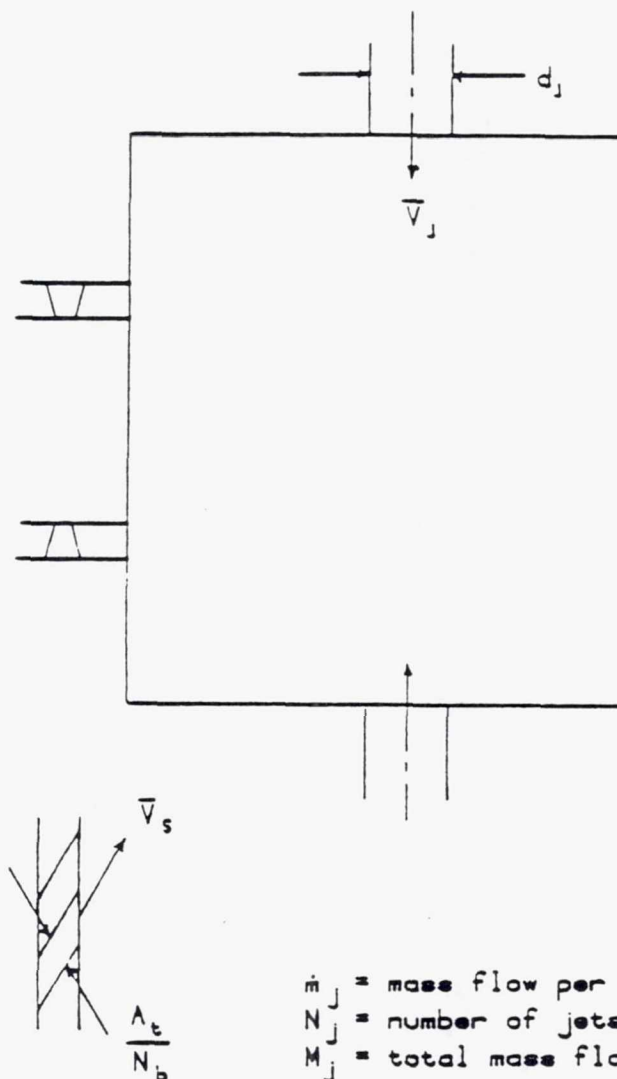


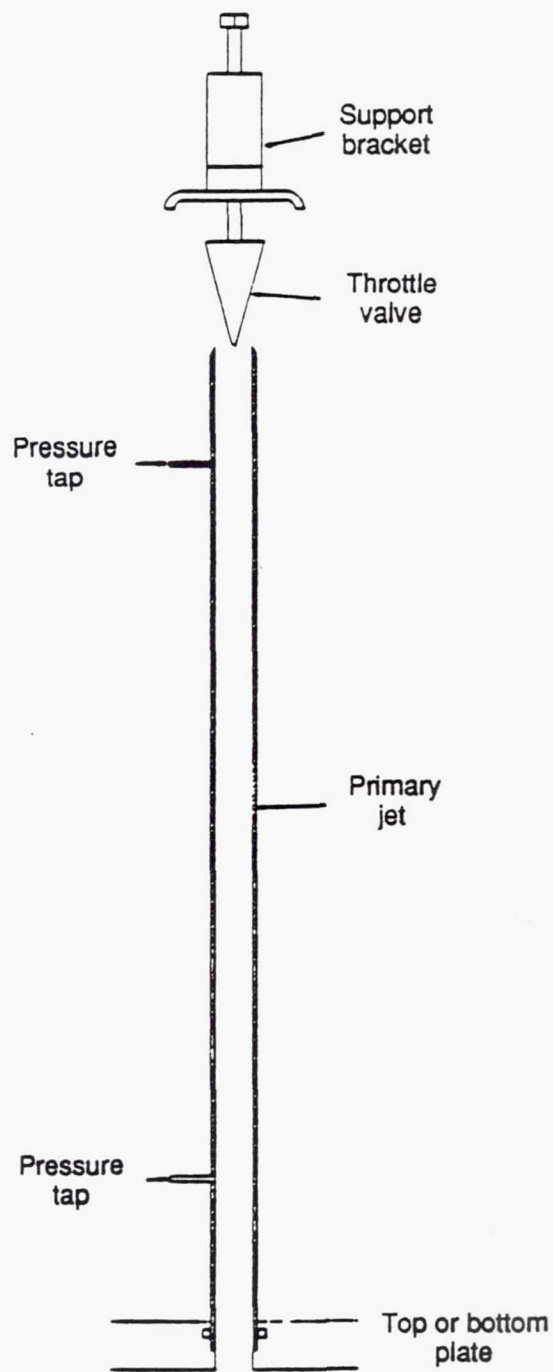
Figure 3.3.2-2. Drawing of annular swirler inlet.



- \dot{m}_j = mass flow per jet
- N_j = number of jets
- M_j = total mass flow through jets
- \dot{m}_s = mass flow per swirler
- N_s = number of swirlers
- M_s = total mass flow through swirlers
- N_b = number of blades per swirler
- A_t = total area between blades

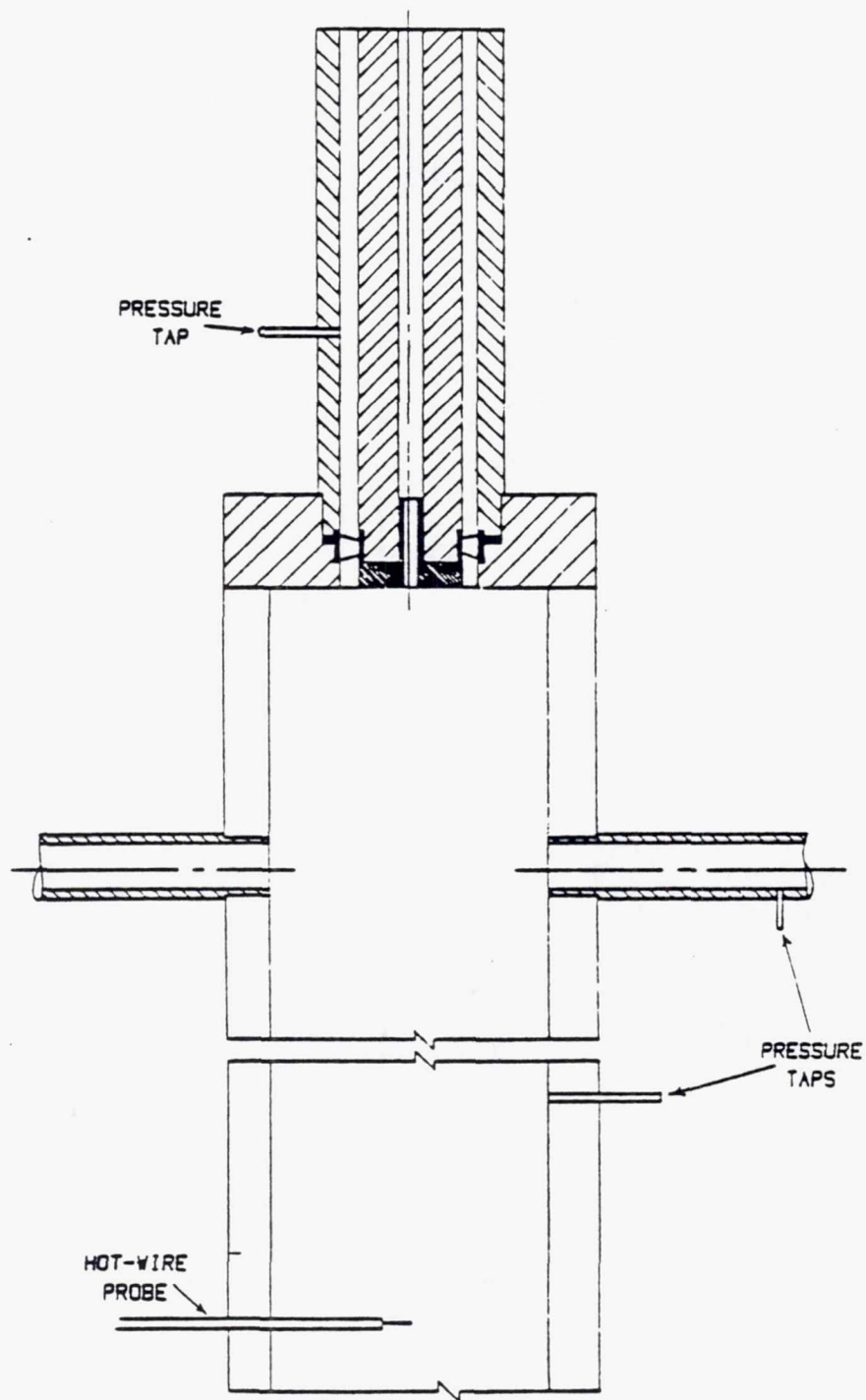
TE92-2415

Figure 3.3.2-3. Determination of primary jet diameters.



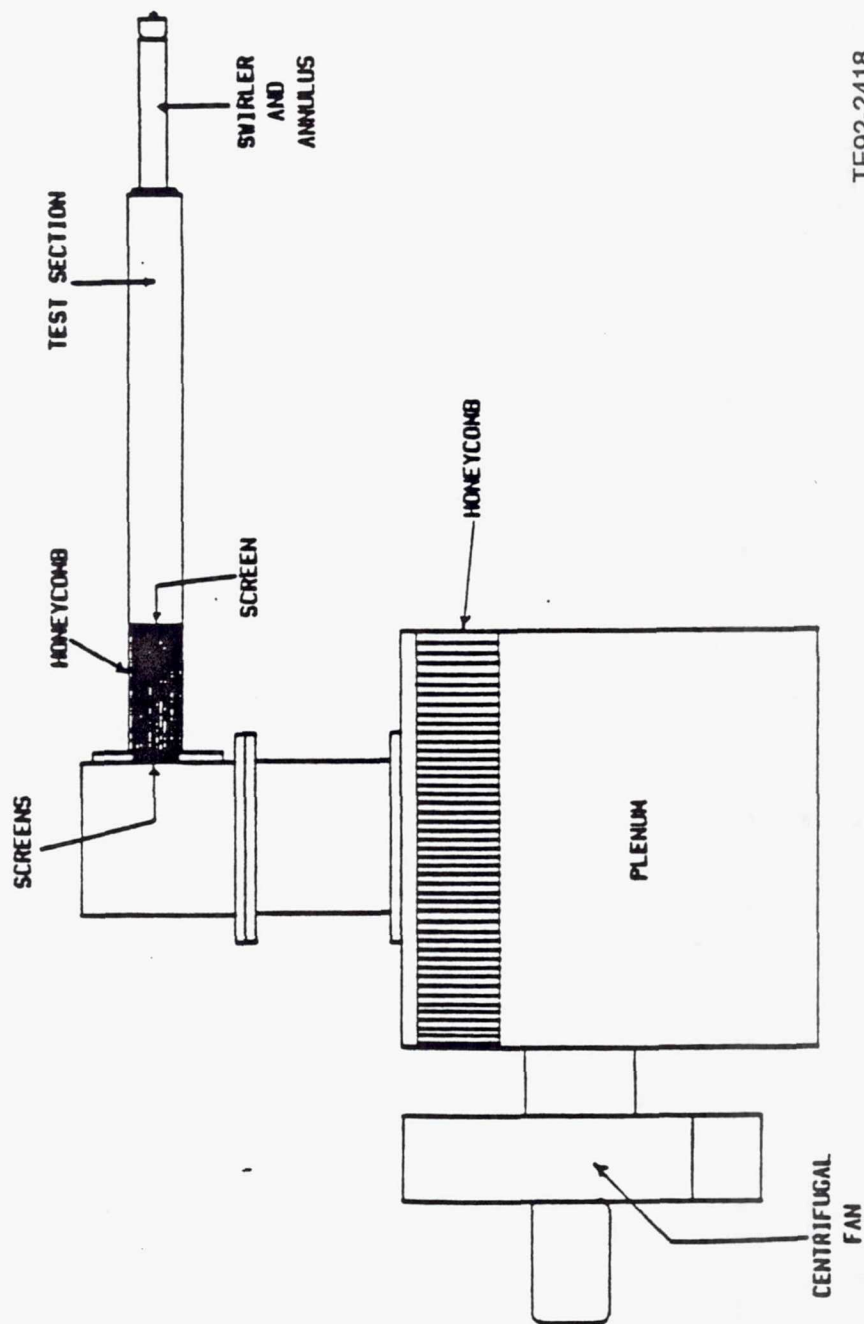
TE92-2416

Figure 3.3.2-4. Drawing of primary jet.



TE92-2417

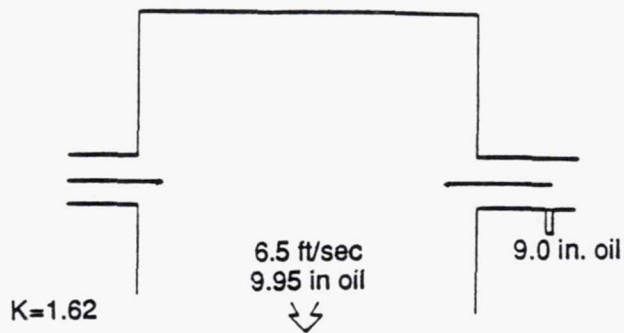
Figure 3.3.2-5. Single swirler loss test rig.



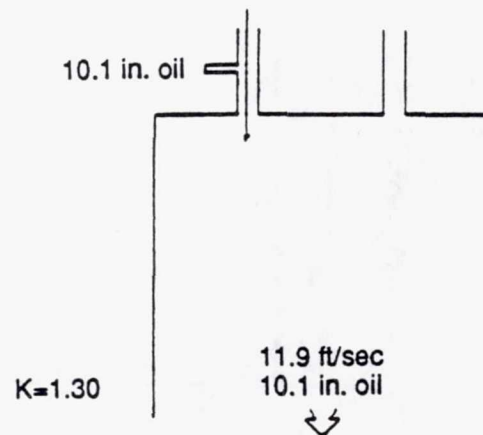
TE92-2418

Figure 3.3.2-6. Single swirler rig for LDV measurements.

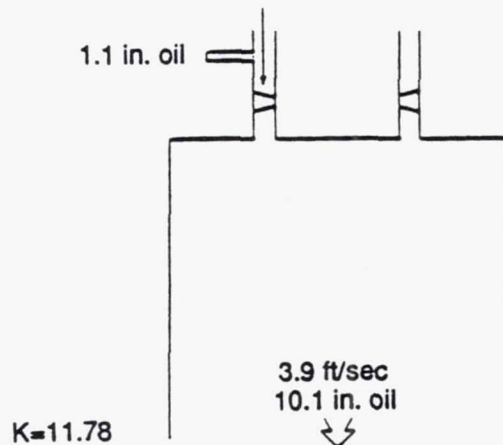
Primary jet only



Annular pipe only

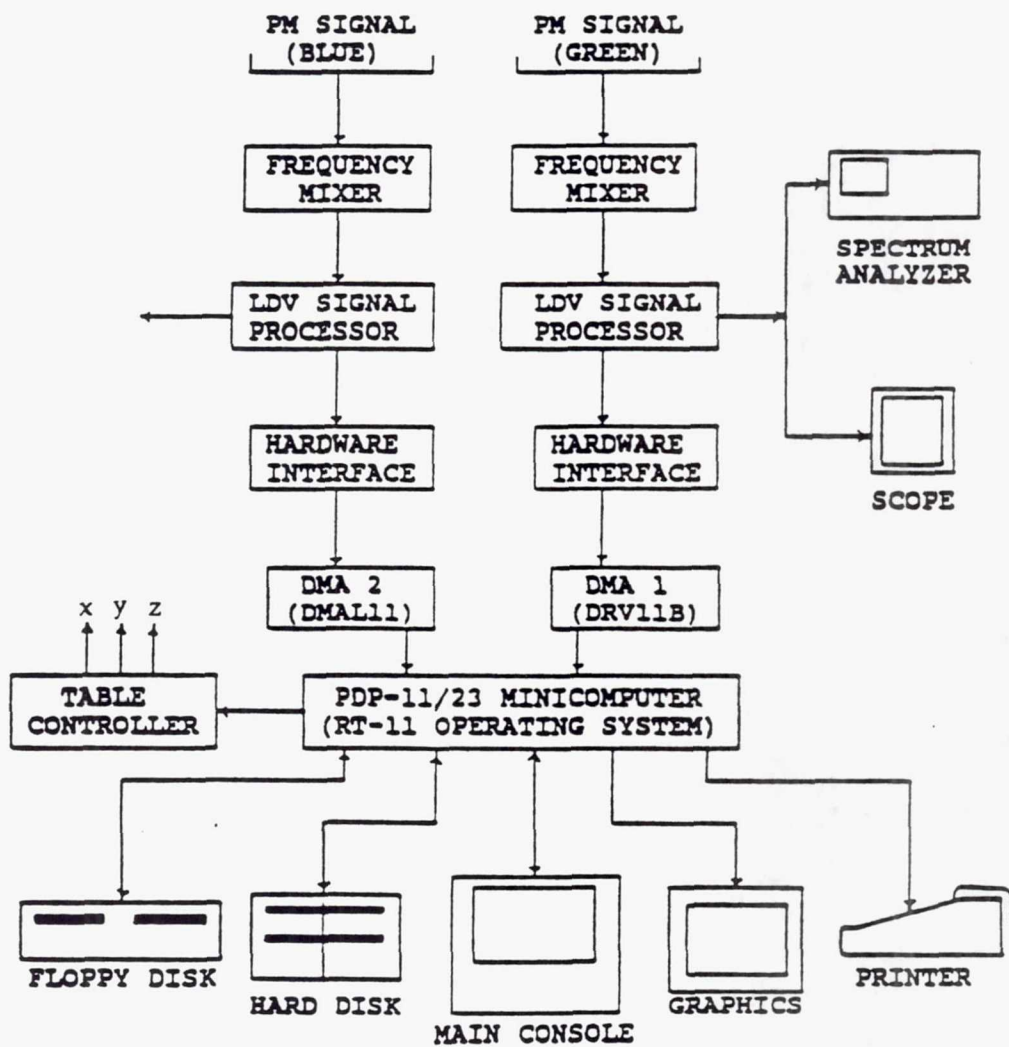


Swirler and annular pipe



TE92-2419

Figure 3.3.2-7. Results of swirler loss tests.



TE92-2420

Figure 3.3.2-8. Data acquisition system for LDV measurements.

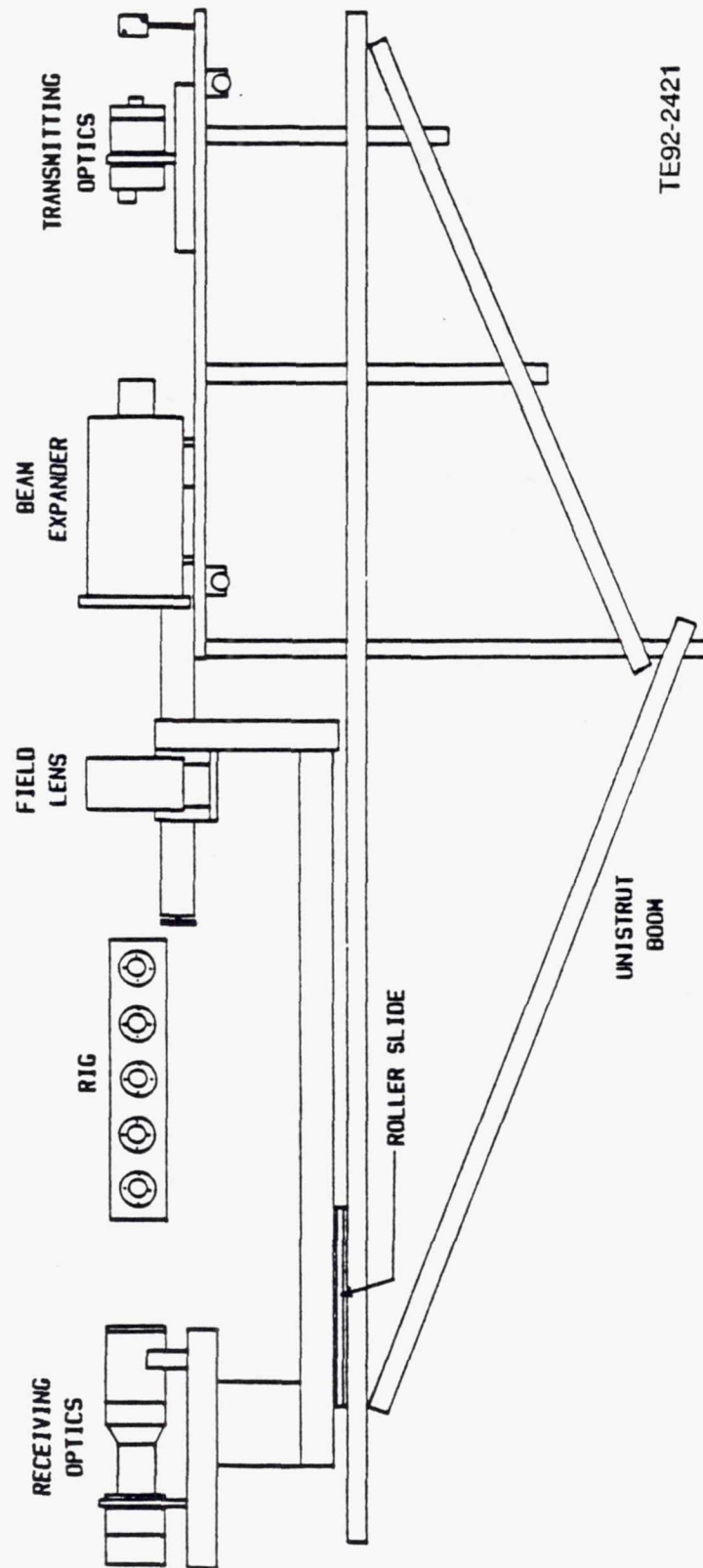


Figure 3.3.2-9. Laser table and boom assembly.

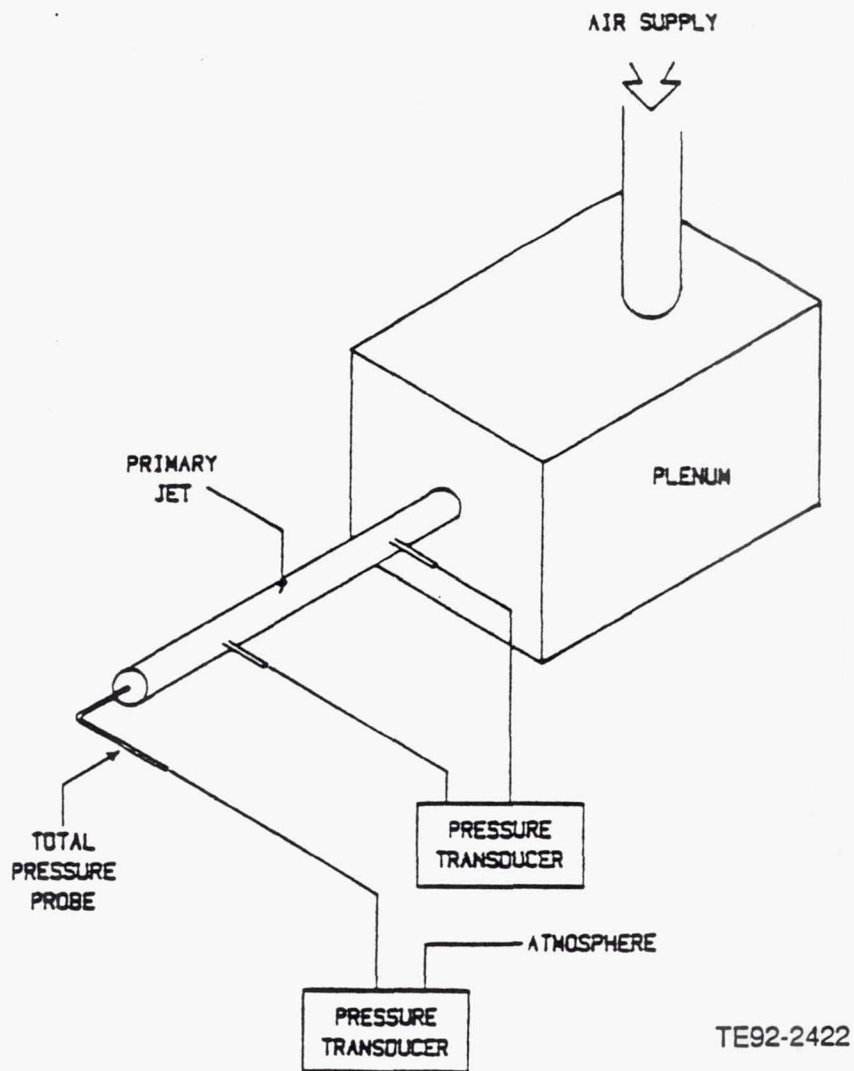
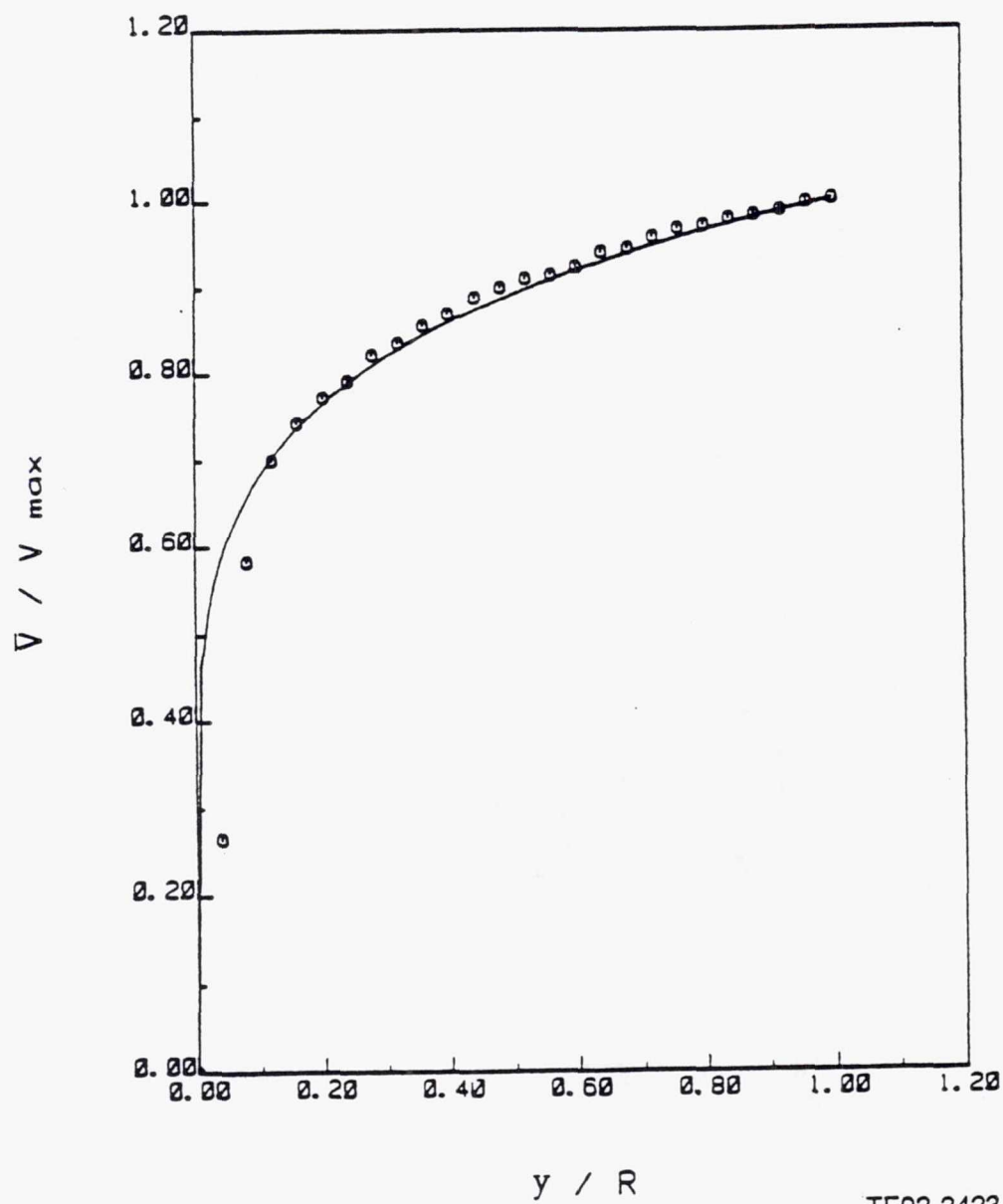
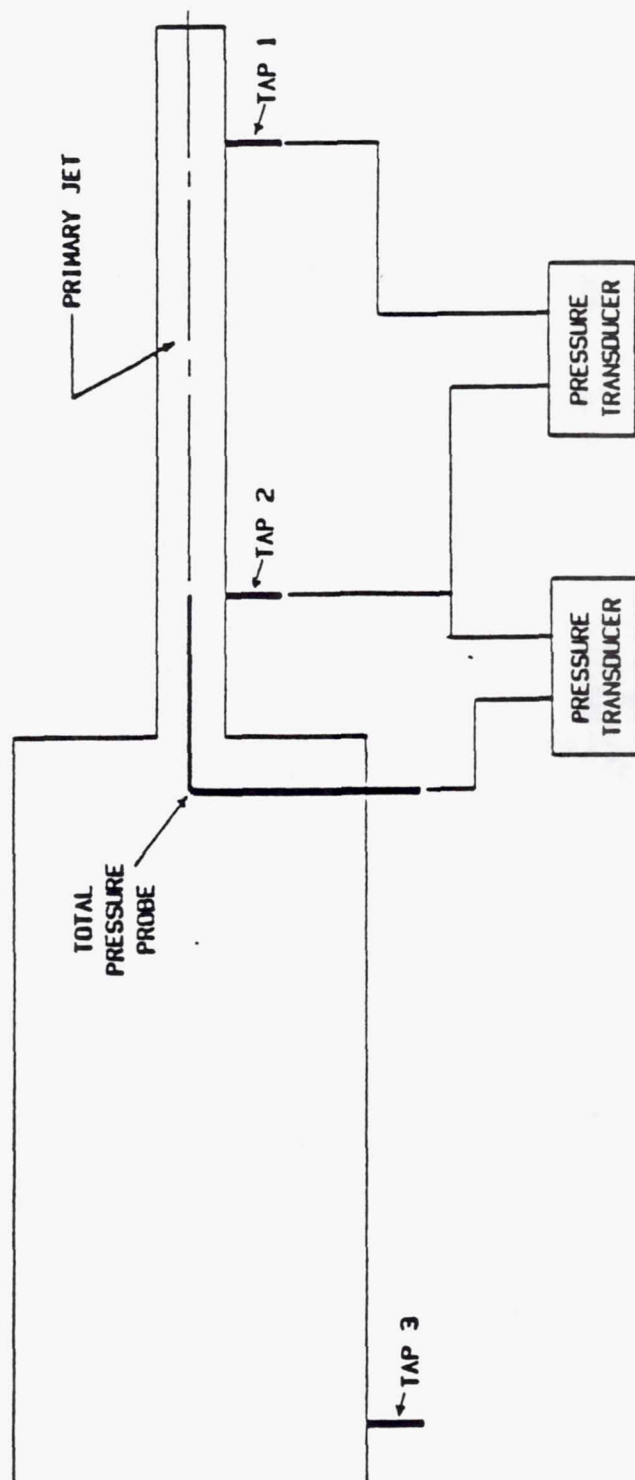


Figure 3.3.2-10. Setup for measurement of flow profile.



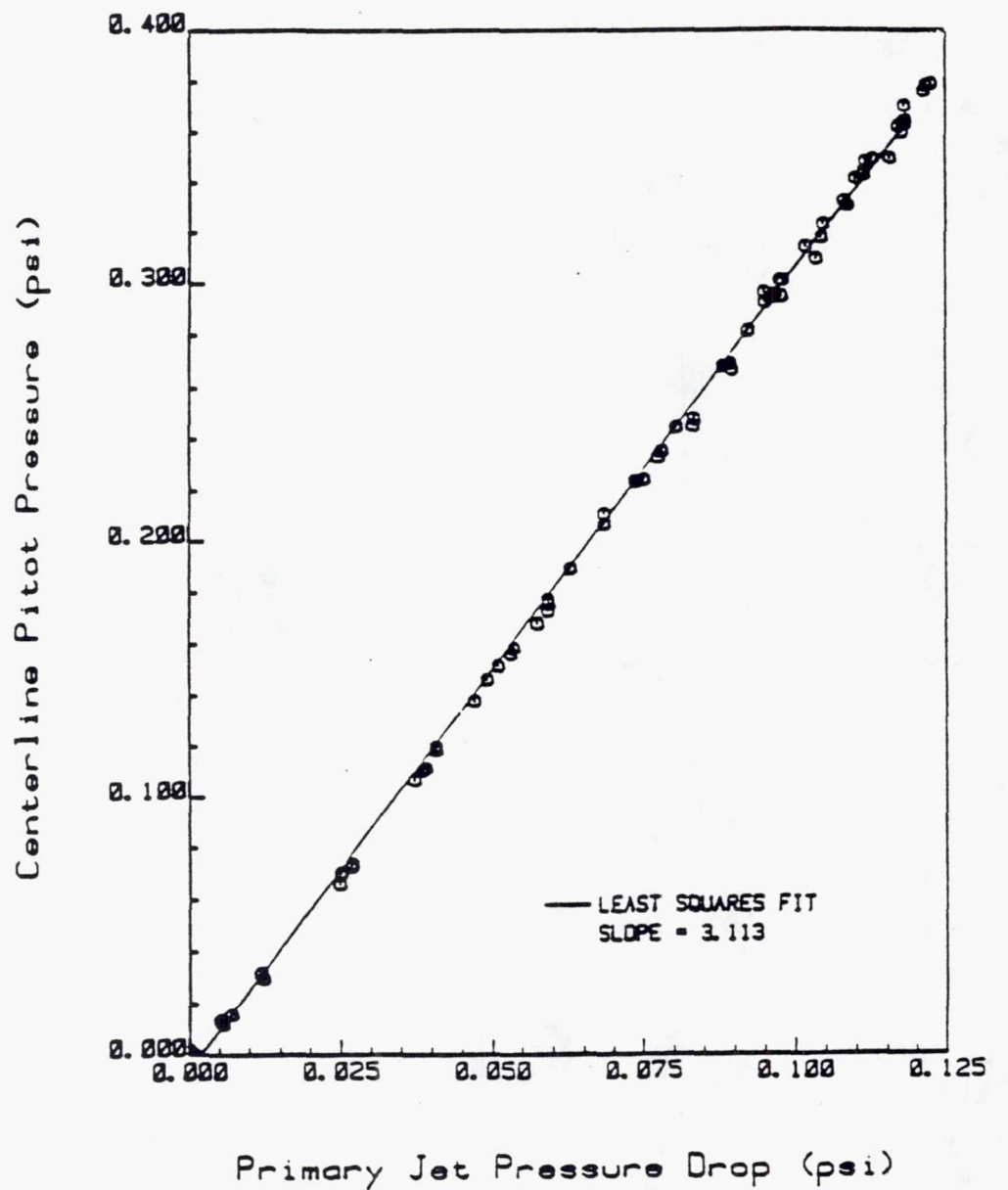
TE92-2423

Figure 3.3.2-11. Primary jet flow profile.



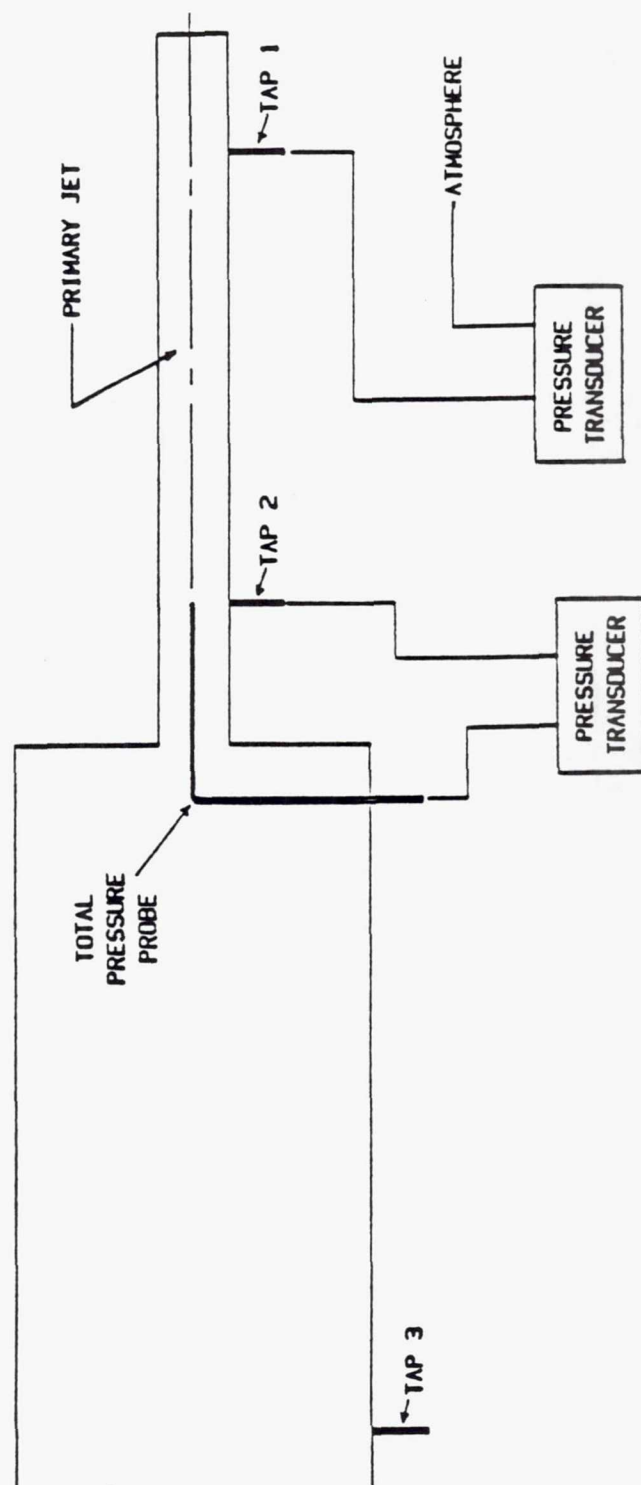
TE92-2424

Figure 3.3.2-12. Pressure transducer arrangement for mass flow calibration of primary jet.



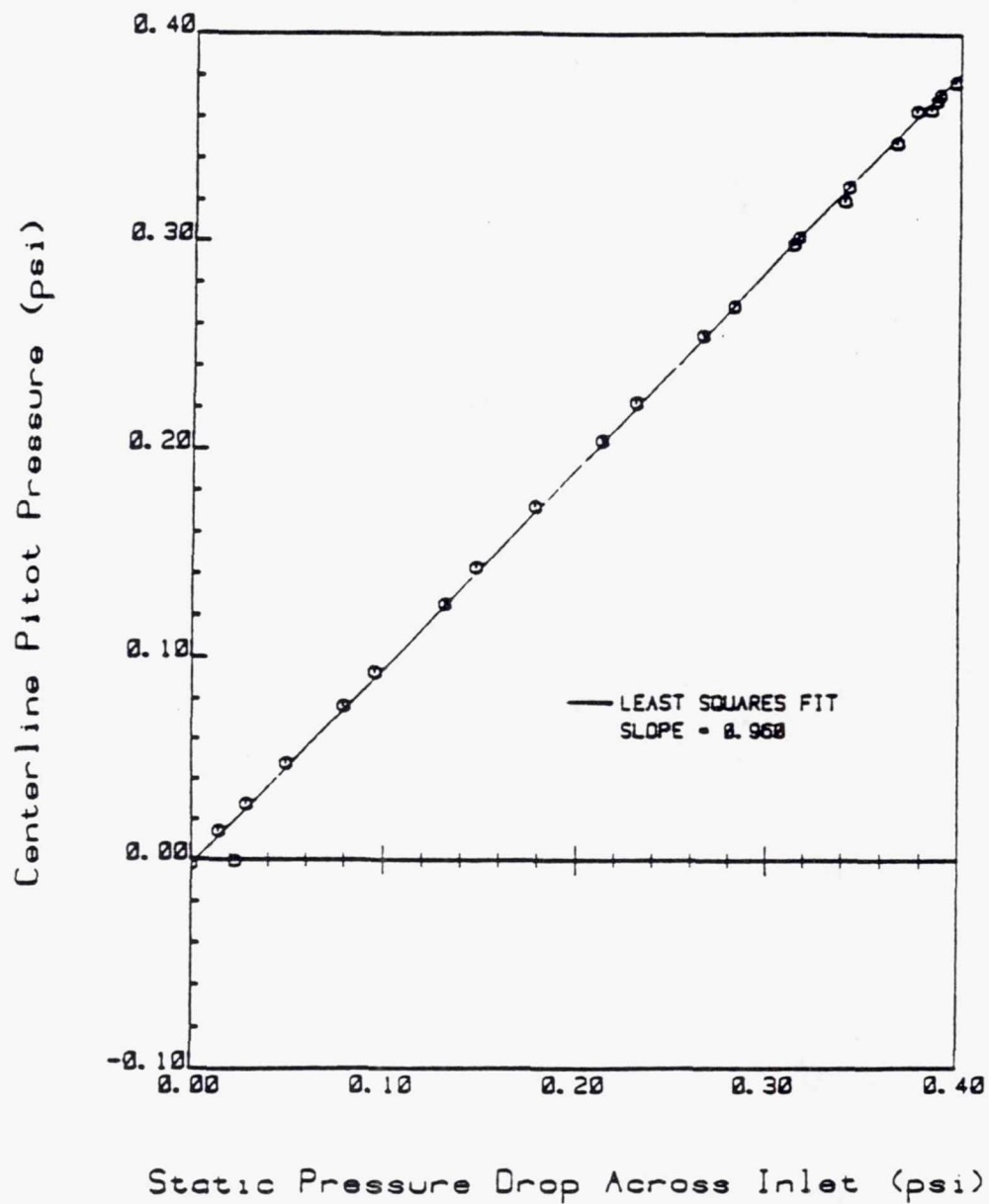
TE92-2425

Figure 3.3.2-13. Mass flow calibration plot for primary jet.



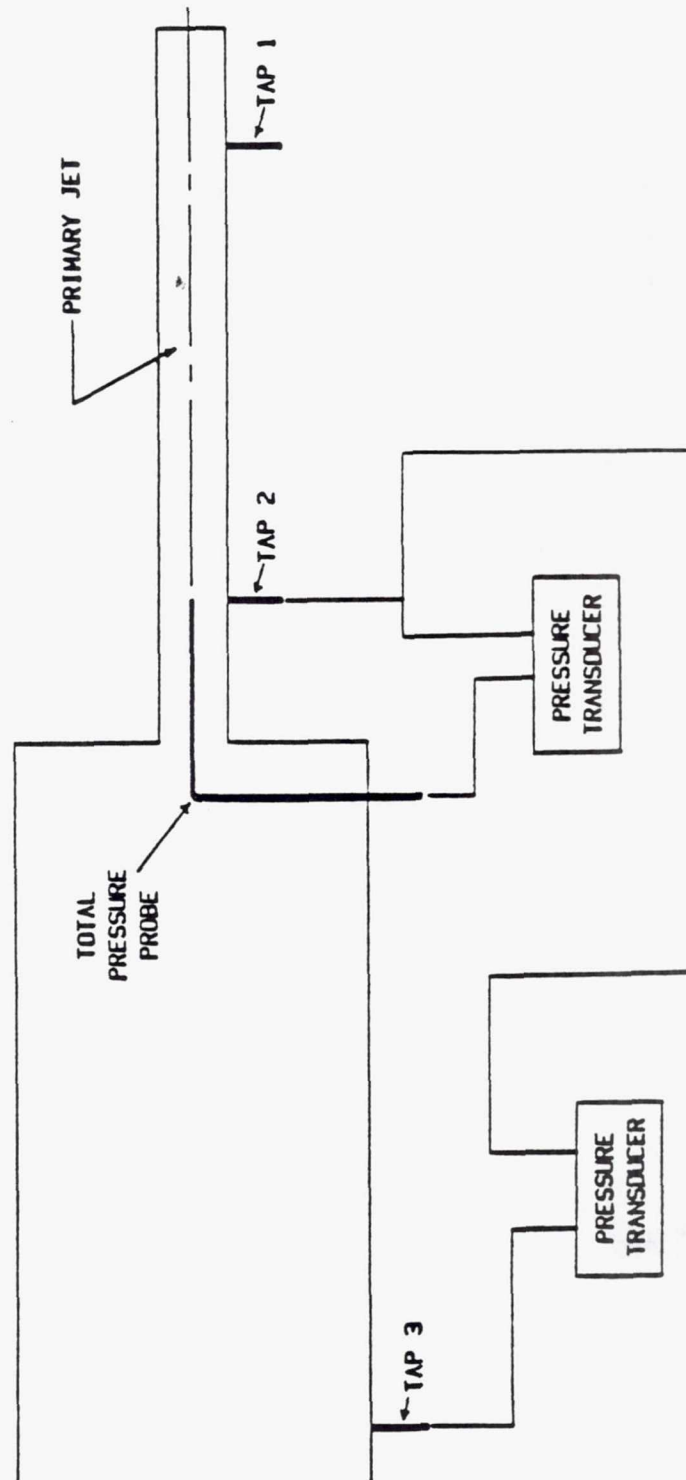
TE92-2426

Figure 3.3.2-14. Pressure transducer arrangement for measurement of primary jet inlet loss.



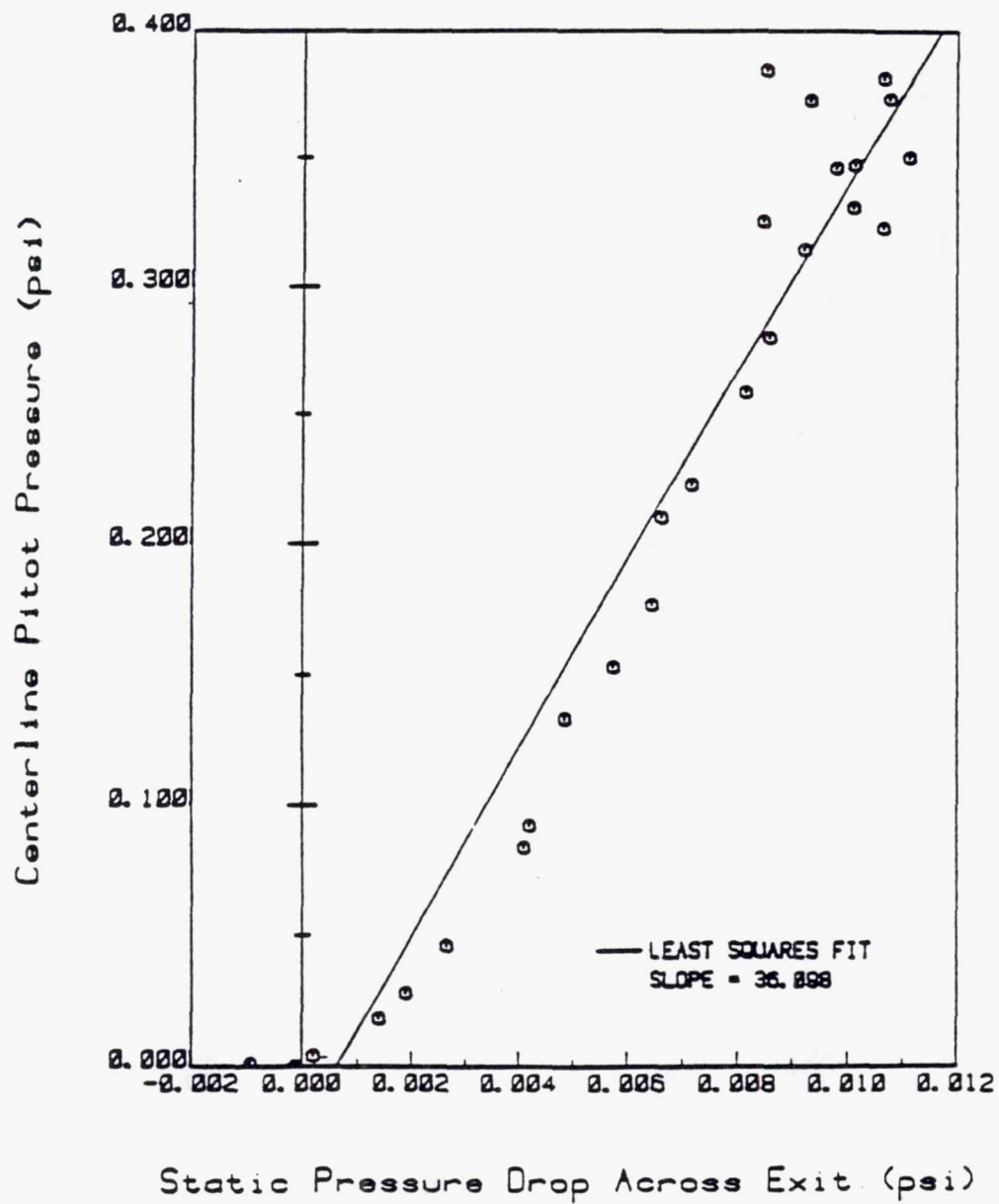
TE92-2427

Figure 3.3.2-15. Pressure transducer arrangement for measurement of primary jet exit loss.



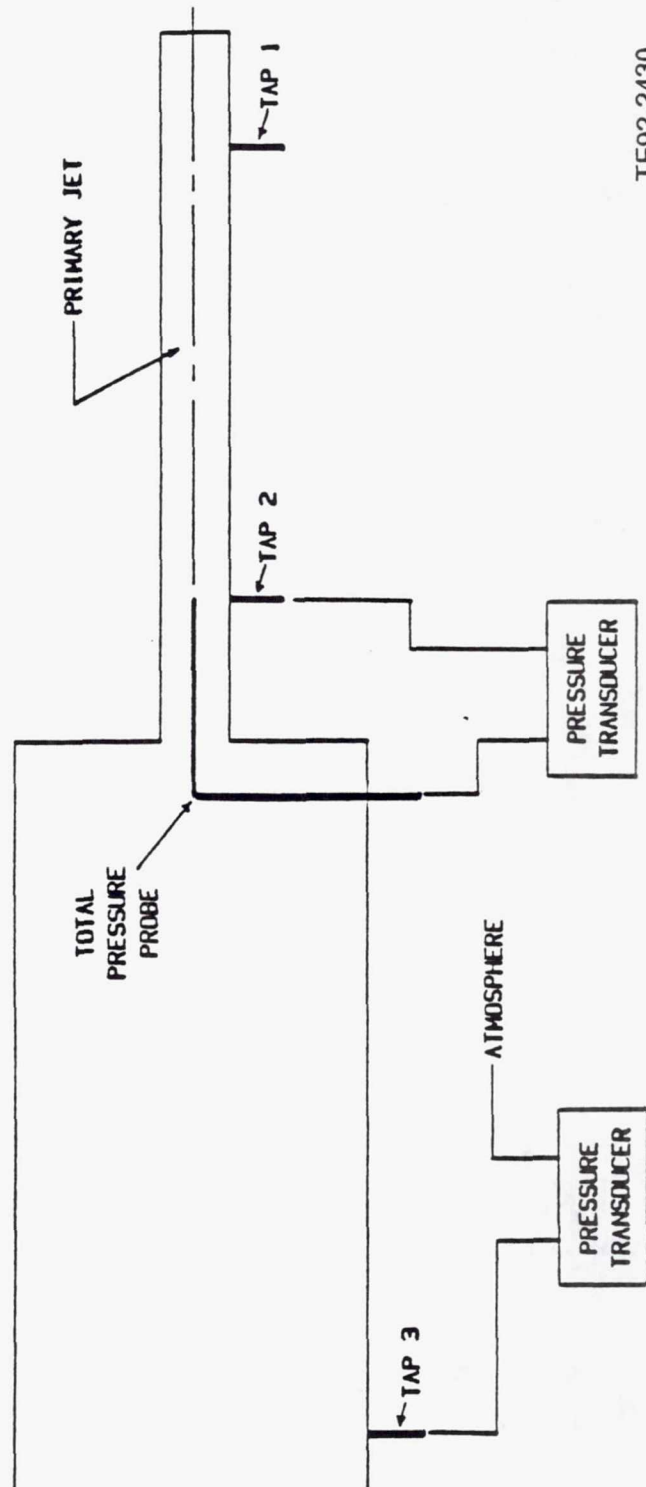
TE92-2428

Figure 3.3.2-16. Pressure transducer arrangement for measurement of primary jet pressure loss.



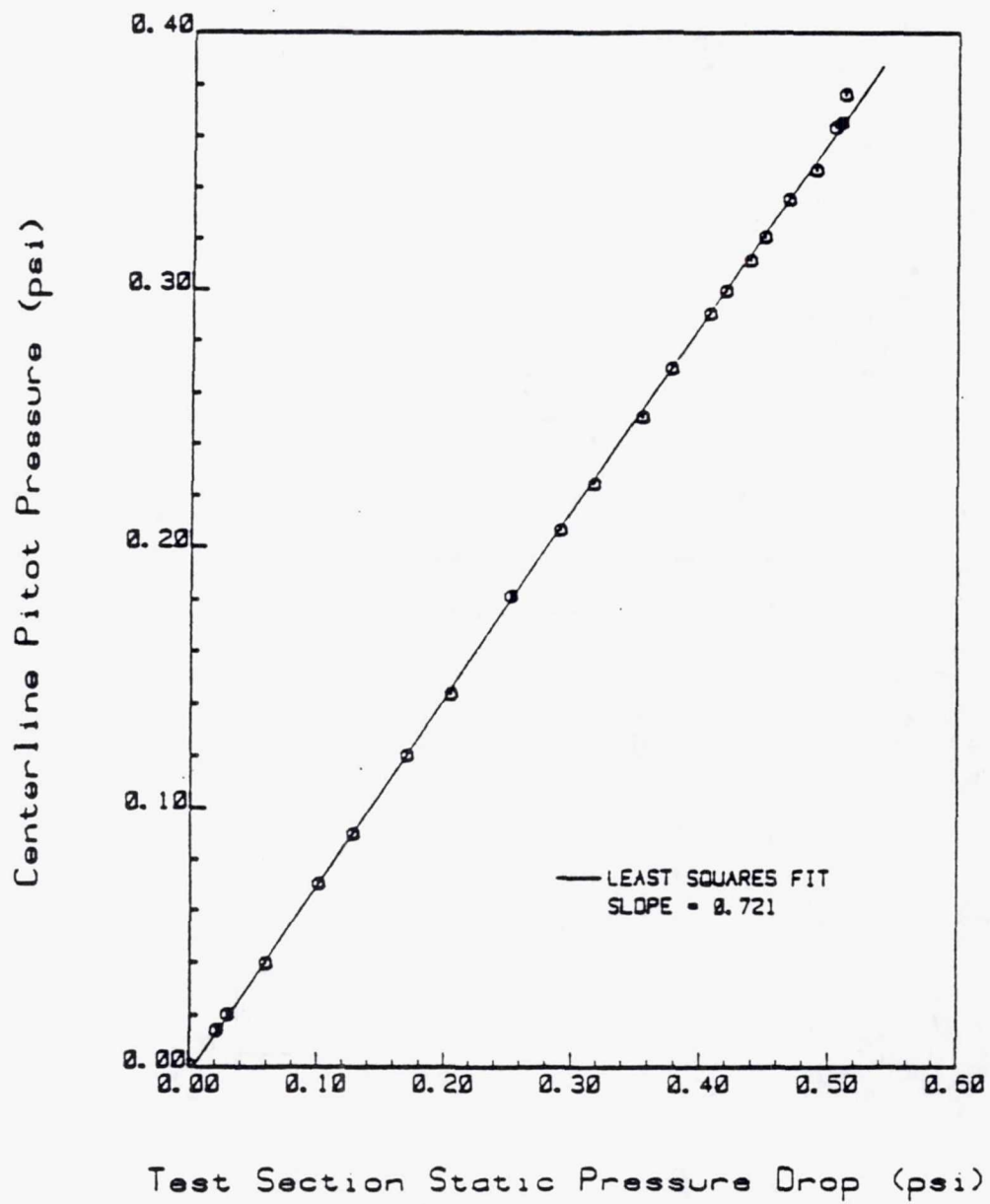
TE92-2429

Figure 3.3.2-17. Plot of primary jet inlet pressure loss.



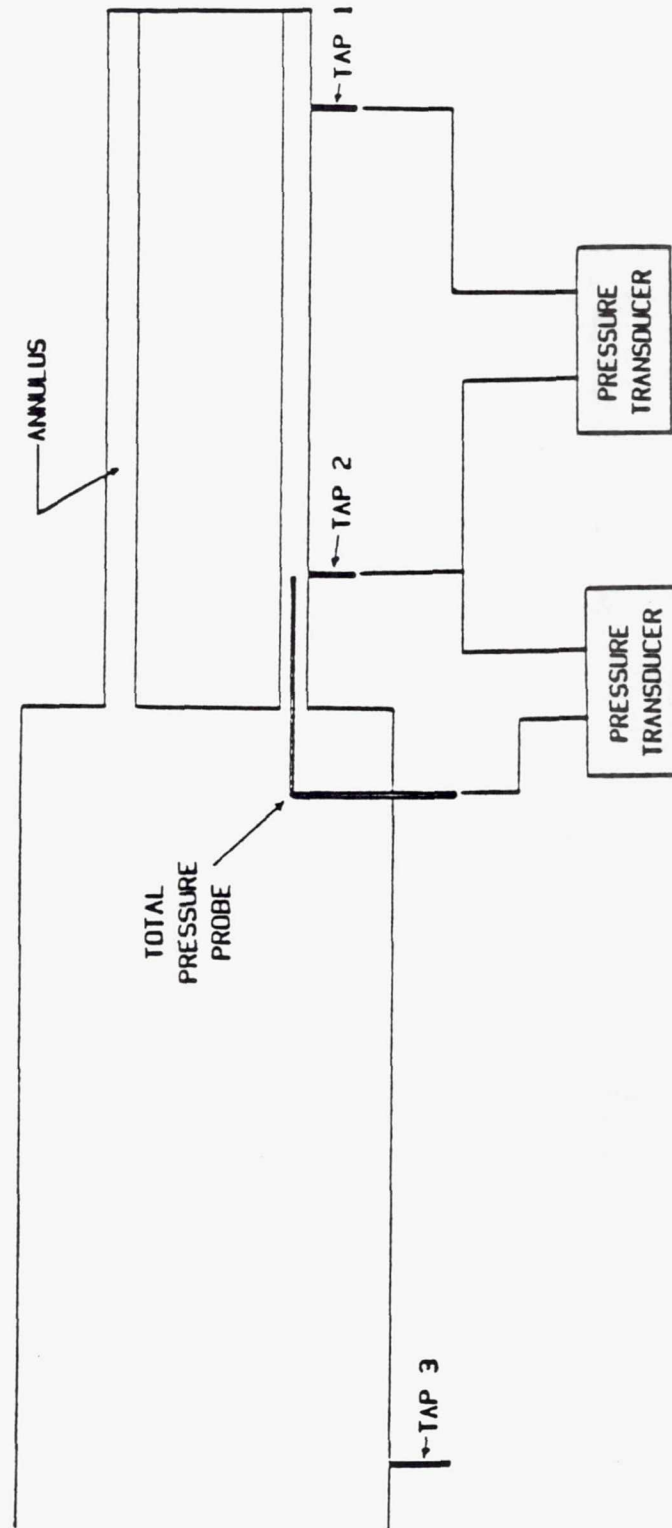
TE92-2430

Figure 3.3.2-18. Plot of primary jet exit pressure loss.



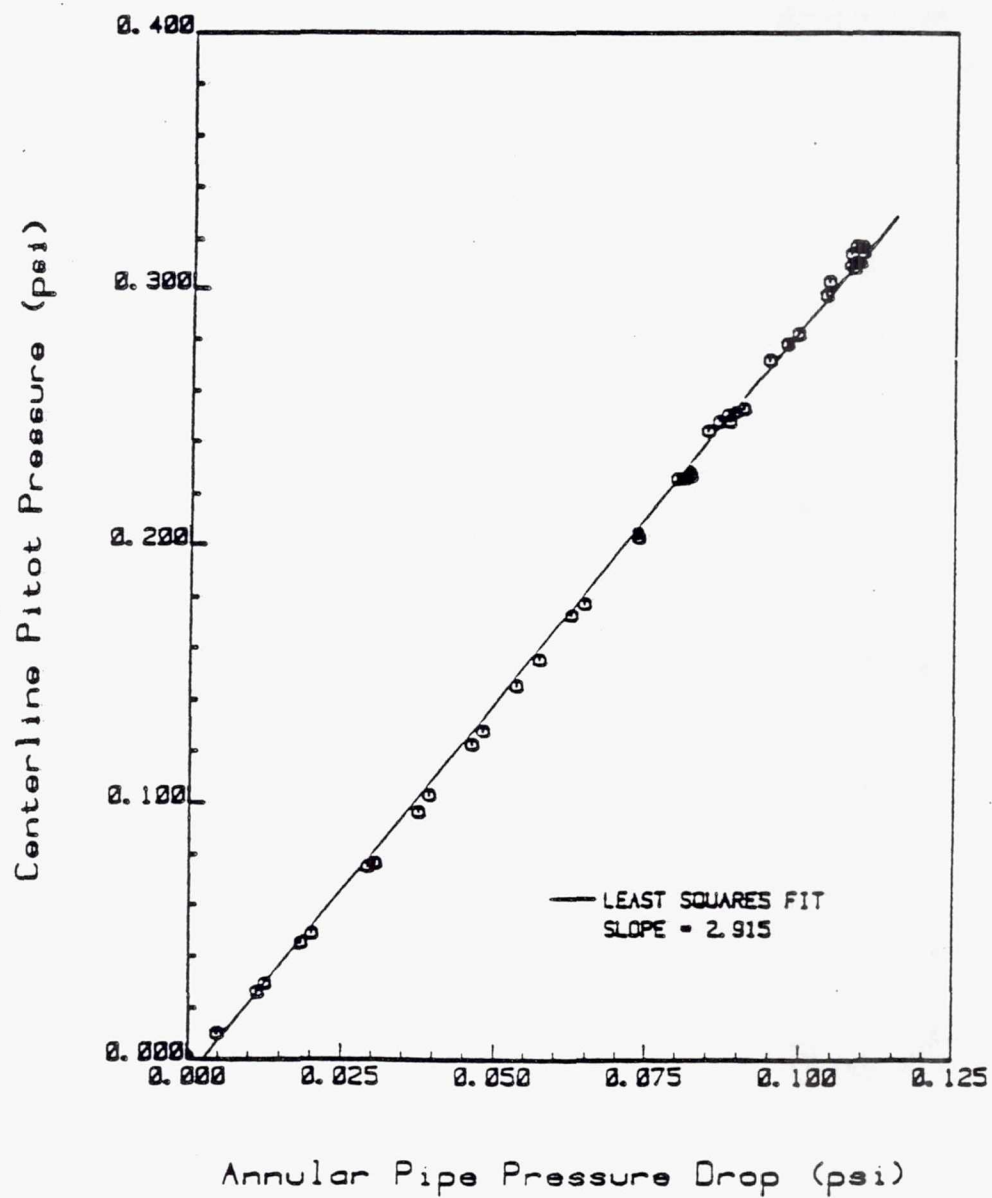
TE92-2431

Figure 3.3.2-19. Plot of primary jet pressure loss.



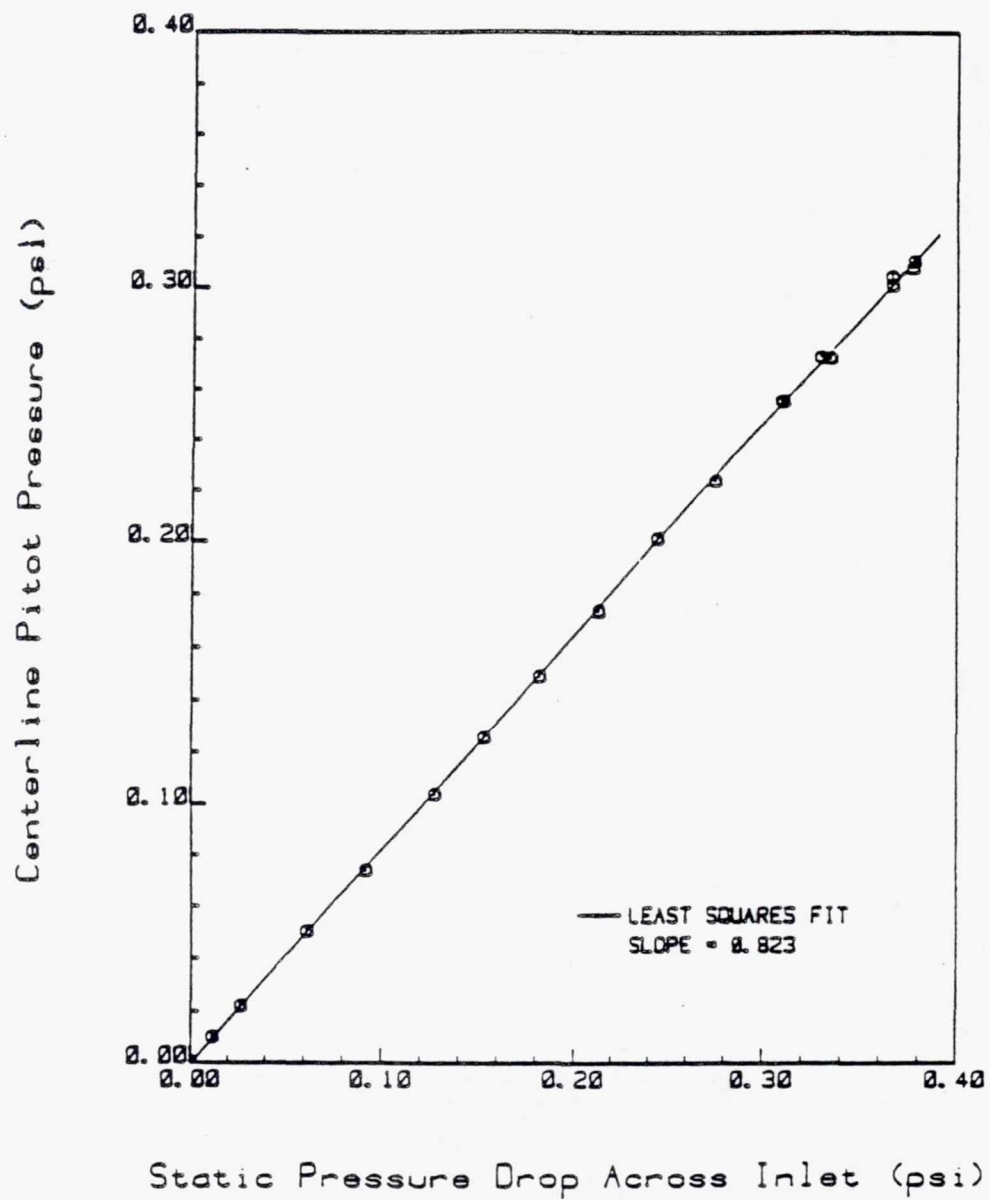
TE92-2432

Figure 3.3.2-20. Pressure transducer arrangement for mass flow calibration of annular pipe.



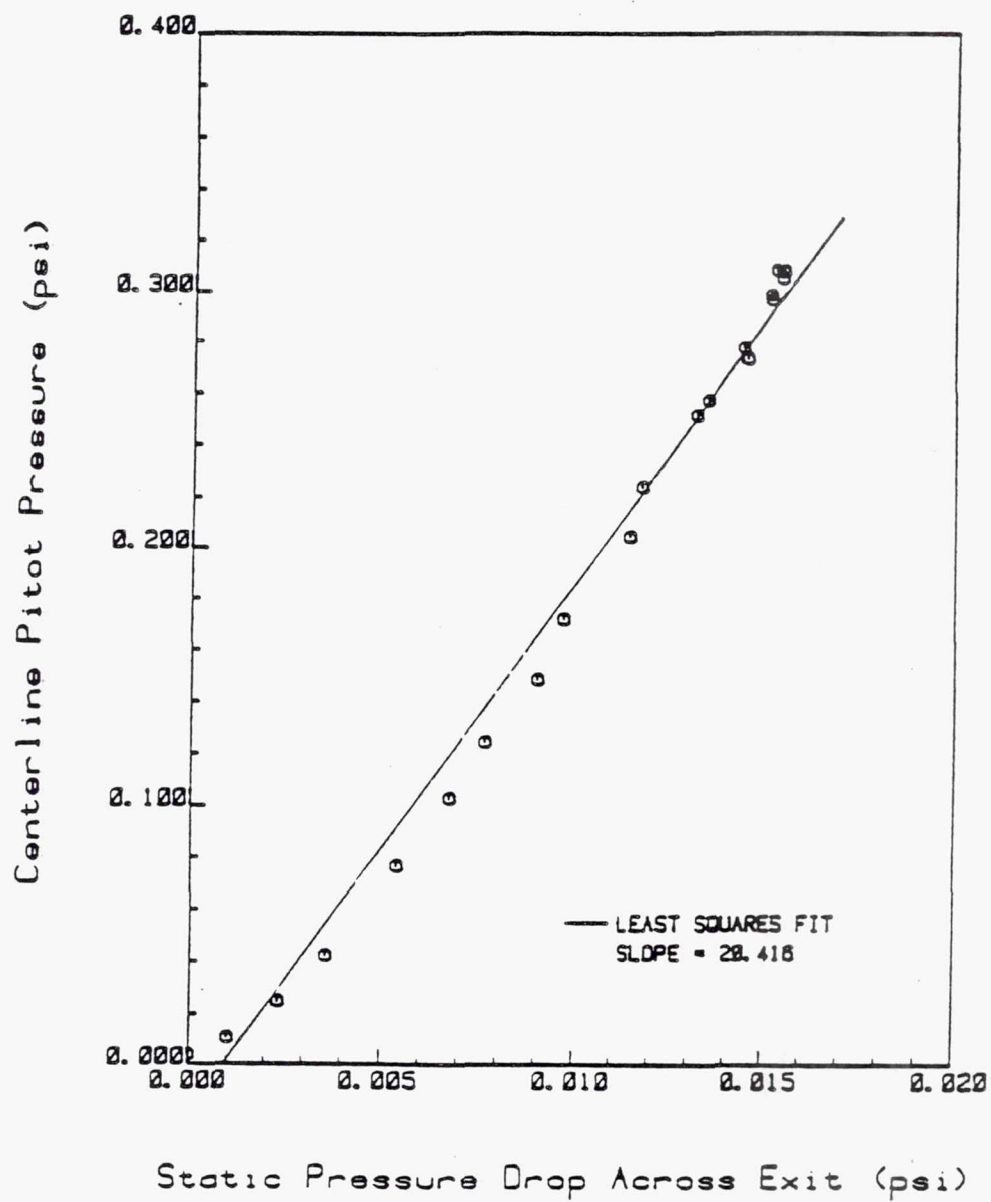
TE92-2433

Figure 3.3.2-21. Mass flow calibration plot for annular pipe.



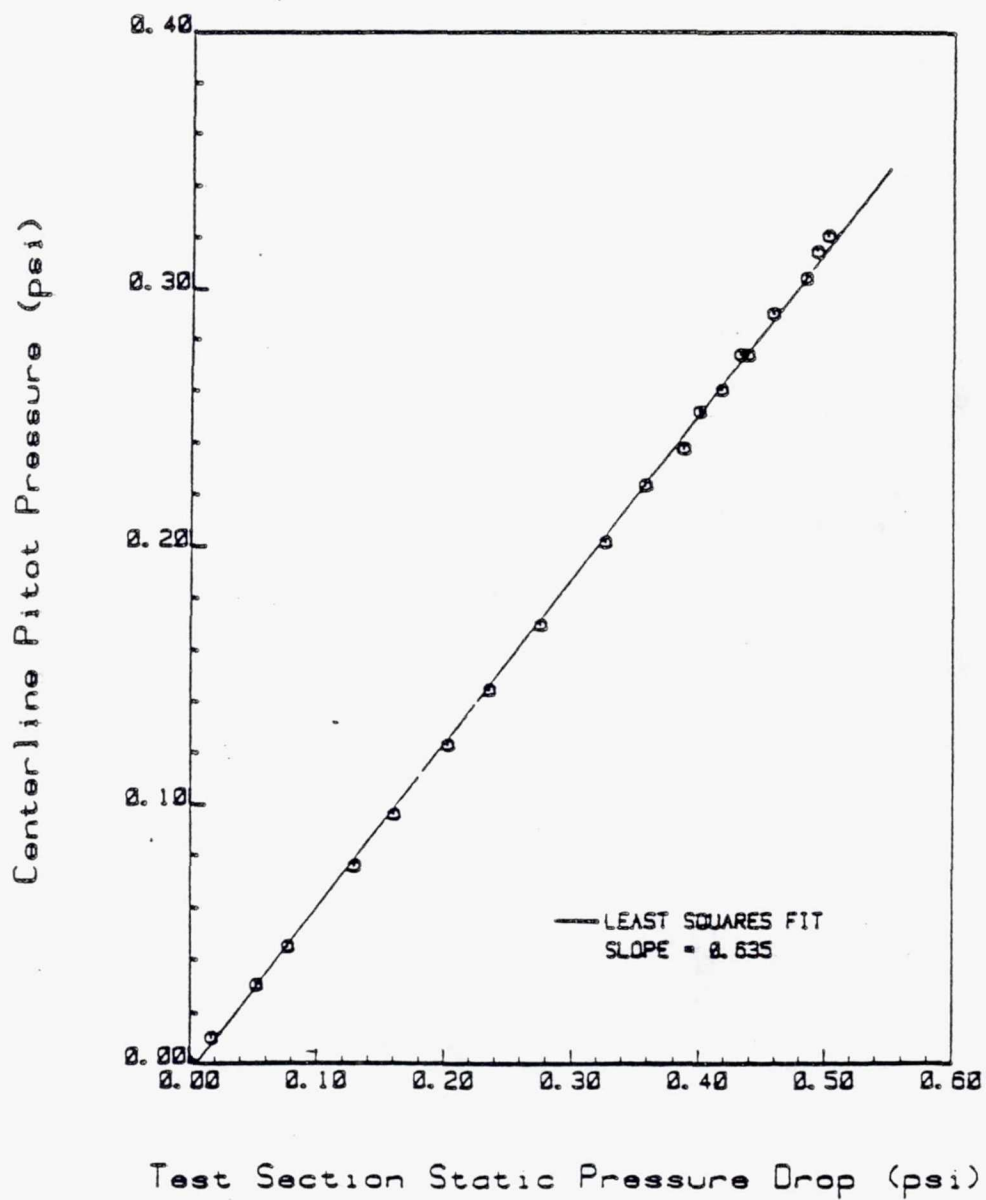
TE92-2434

Figure 3.3.2-22. Plot of annular pipe inlet pressure loss.



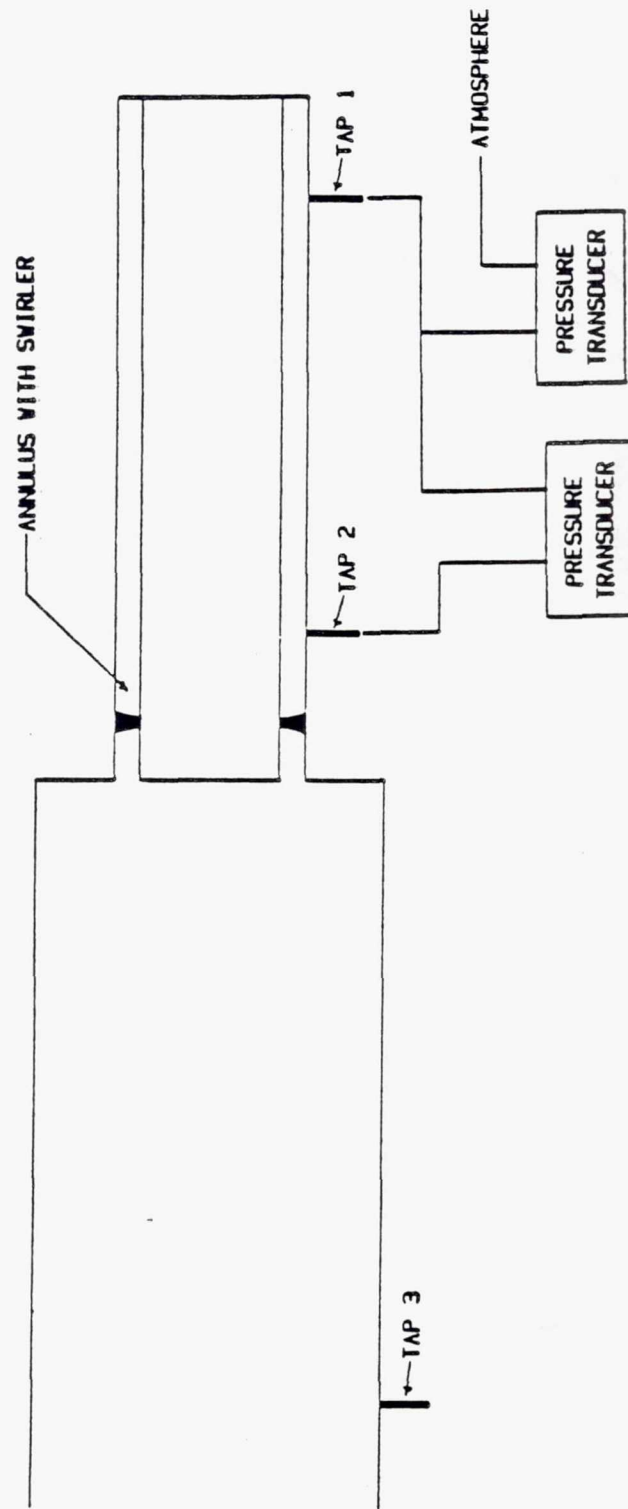
TE92-2435

Figure 3.3.2-23. Plot of annular pipe exit pressure loss.



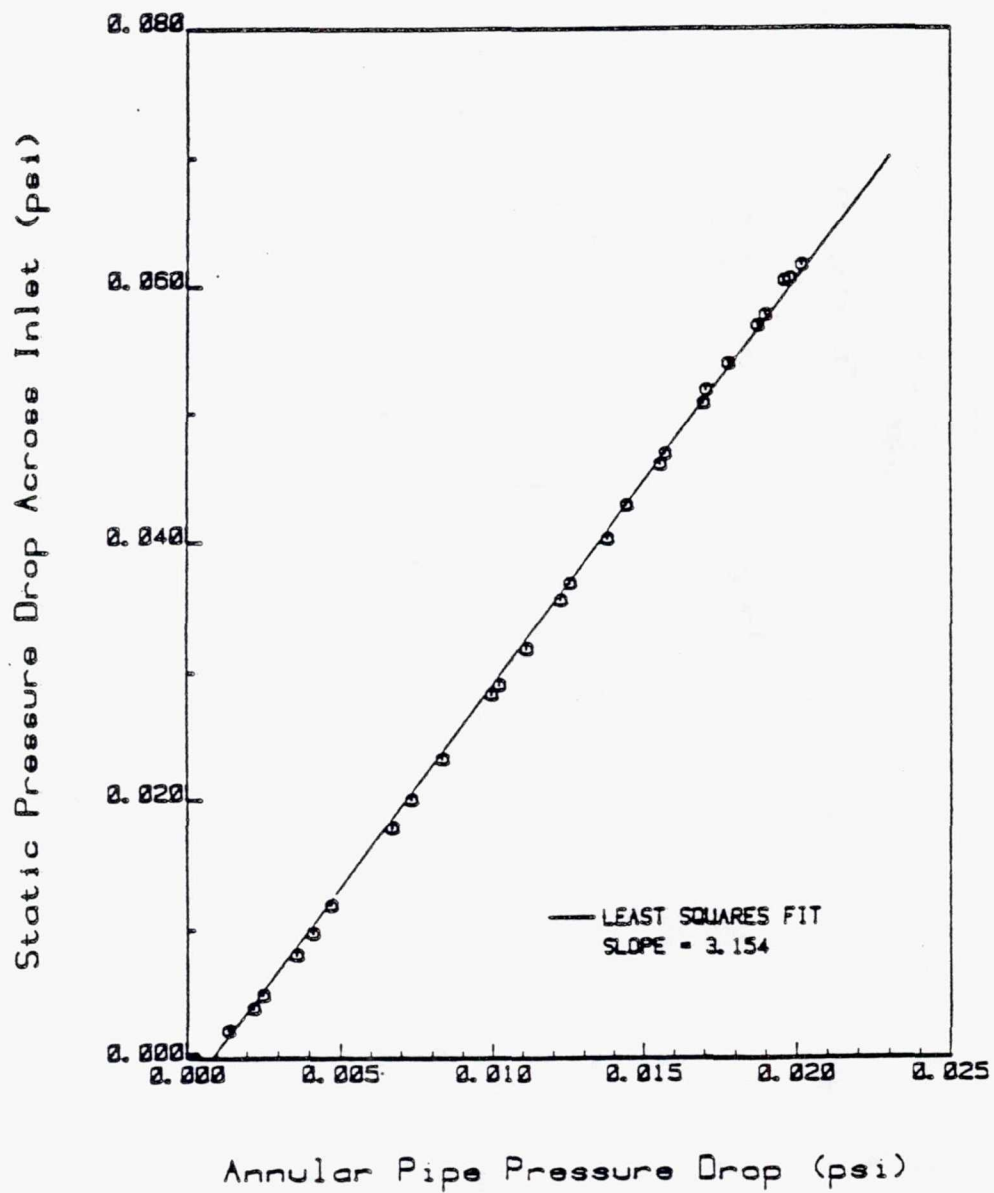
TE92-2436

Figure 3.3.2-24. Plot of annular pipe pressure loss.



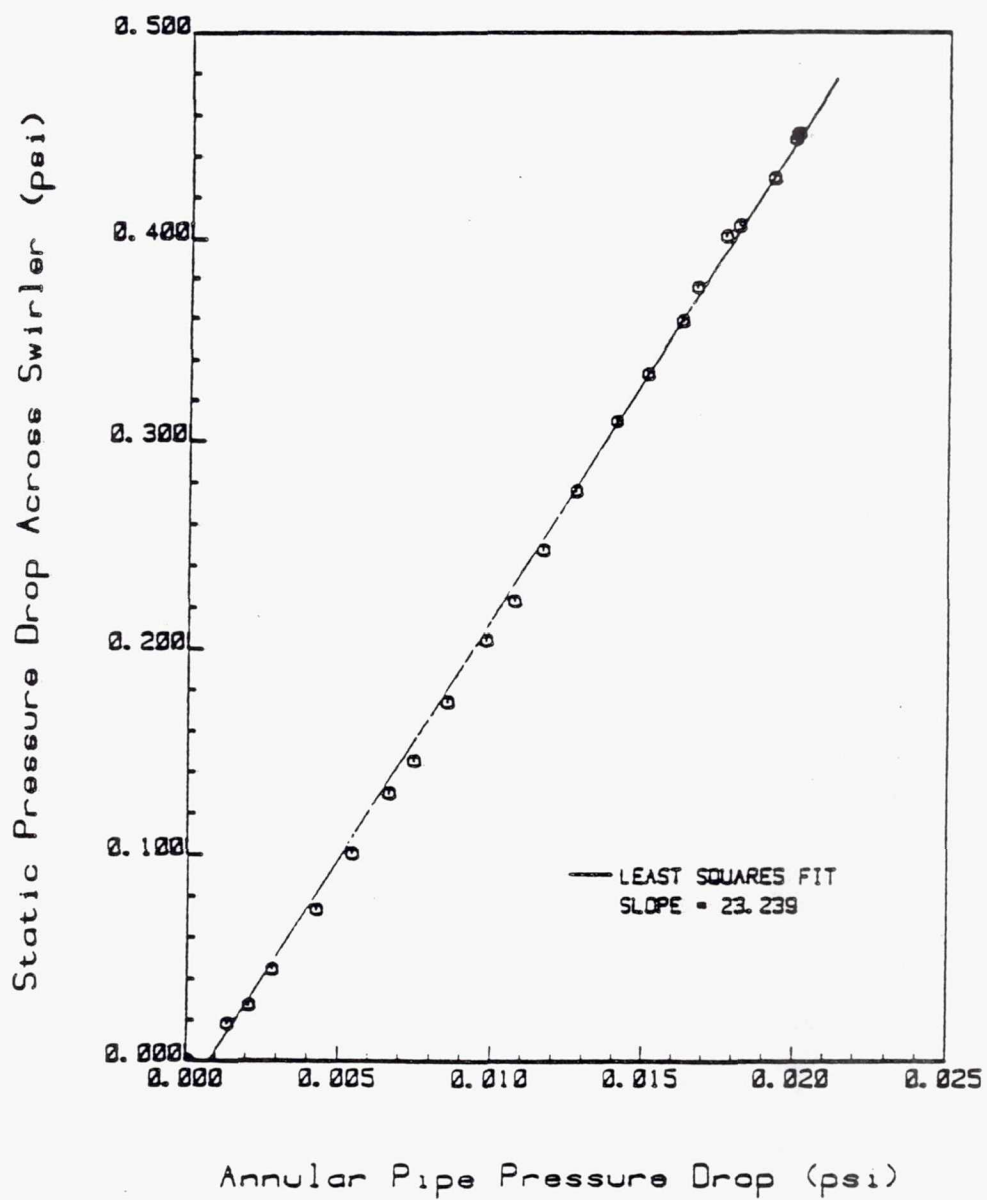
TE92-2437

Figure 3.3.2-25. Pressure transducer arrangement for measurement of swirler inlet loss.



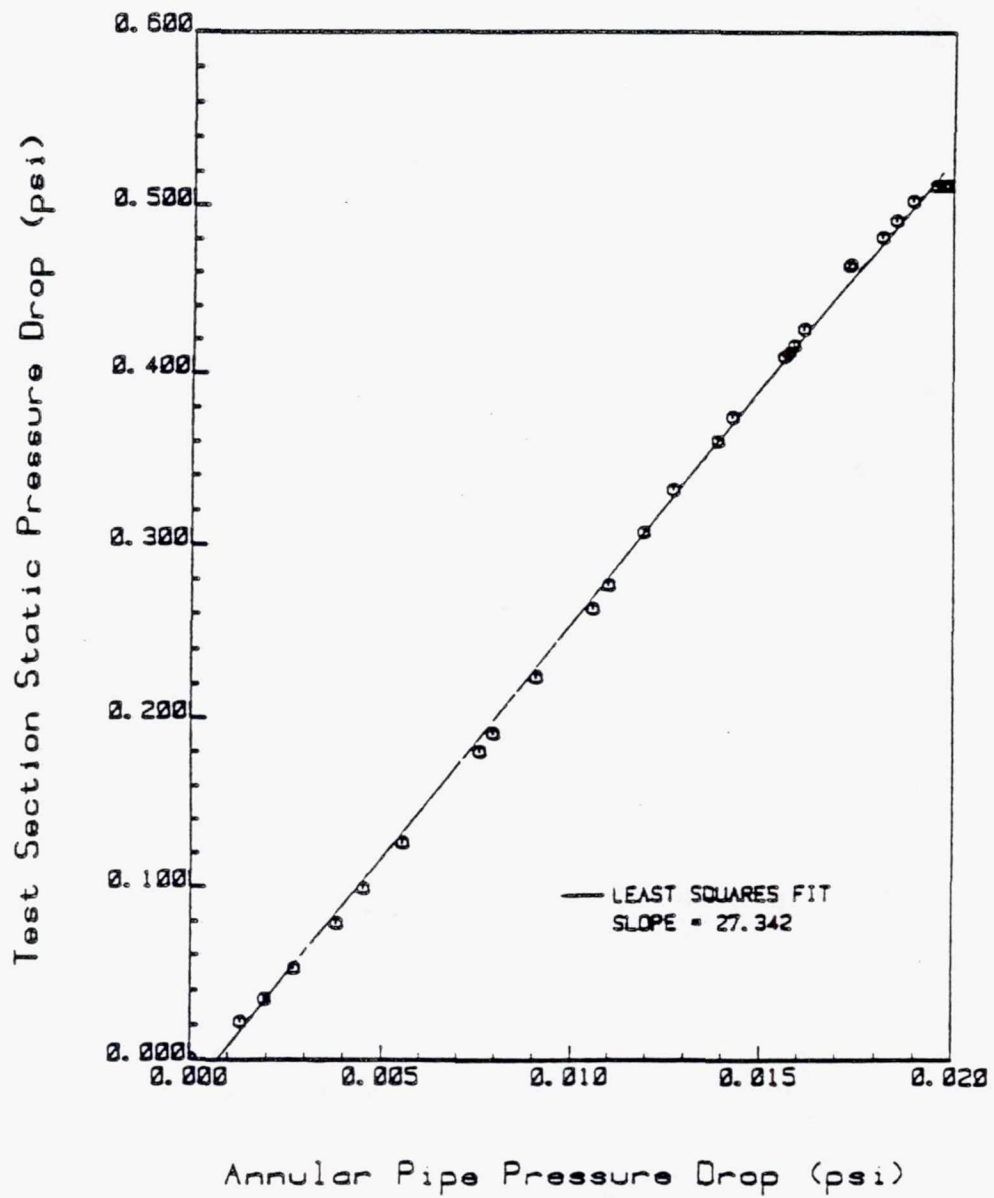
TE92-2438

Figure 3.3.2-26. Plot of swirler inlet pressure loss.



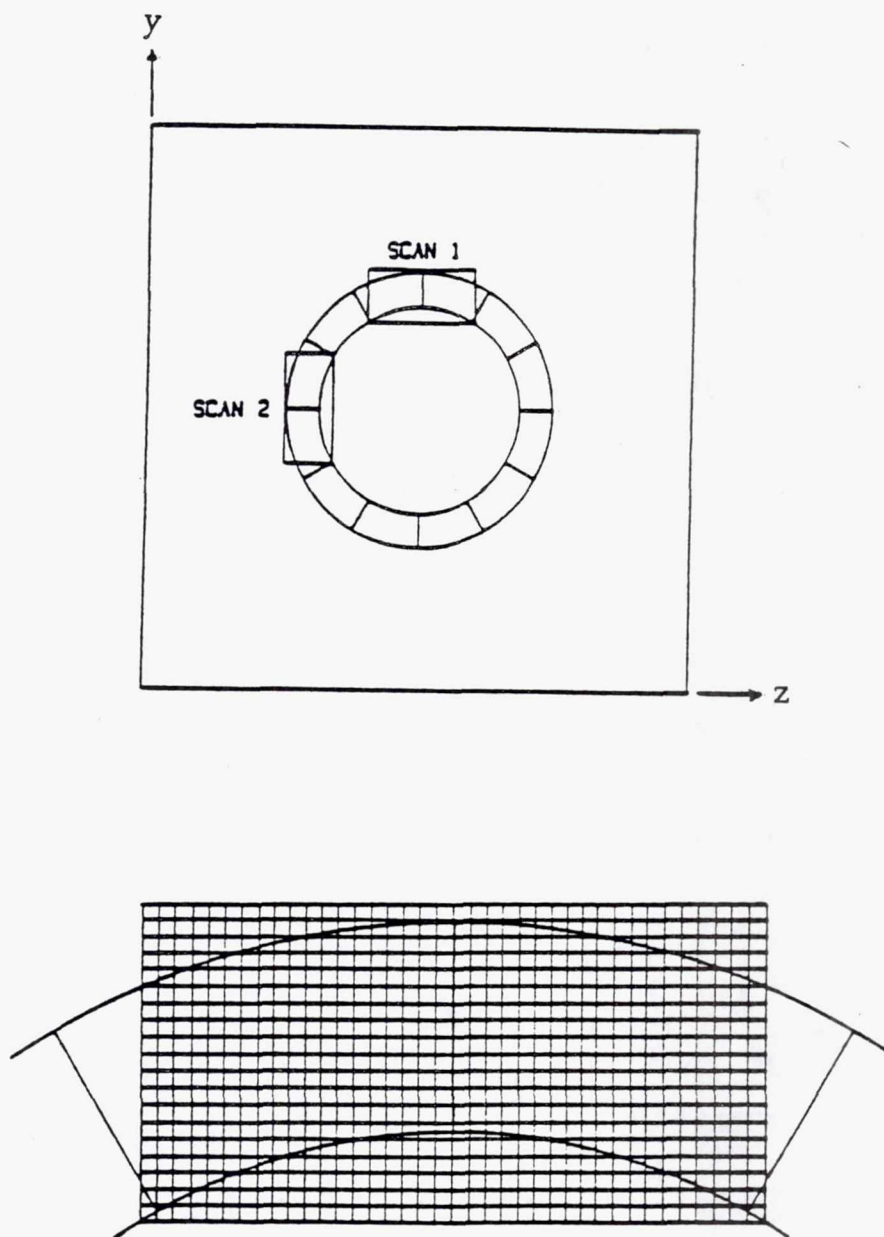
TE92-2439

Figure 3.3.2-27. Plot of pressure loss across swirler.



TE92-2440

Figure 3.3.2-28. Plot of swirler pressure loss.



TE92-2441

Figure 3.3.2-29. Swirler inlet data grid.

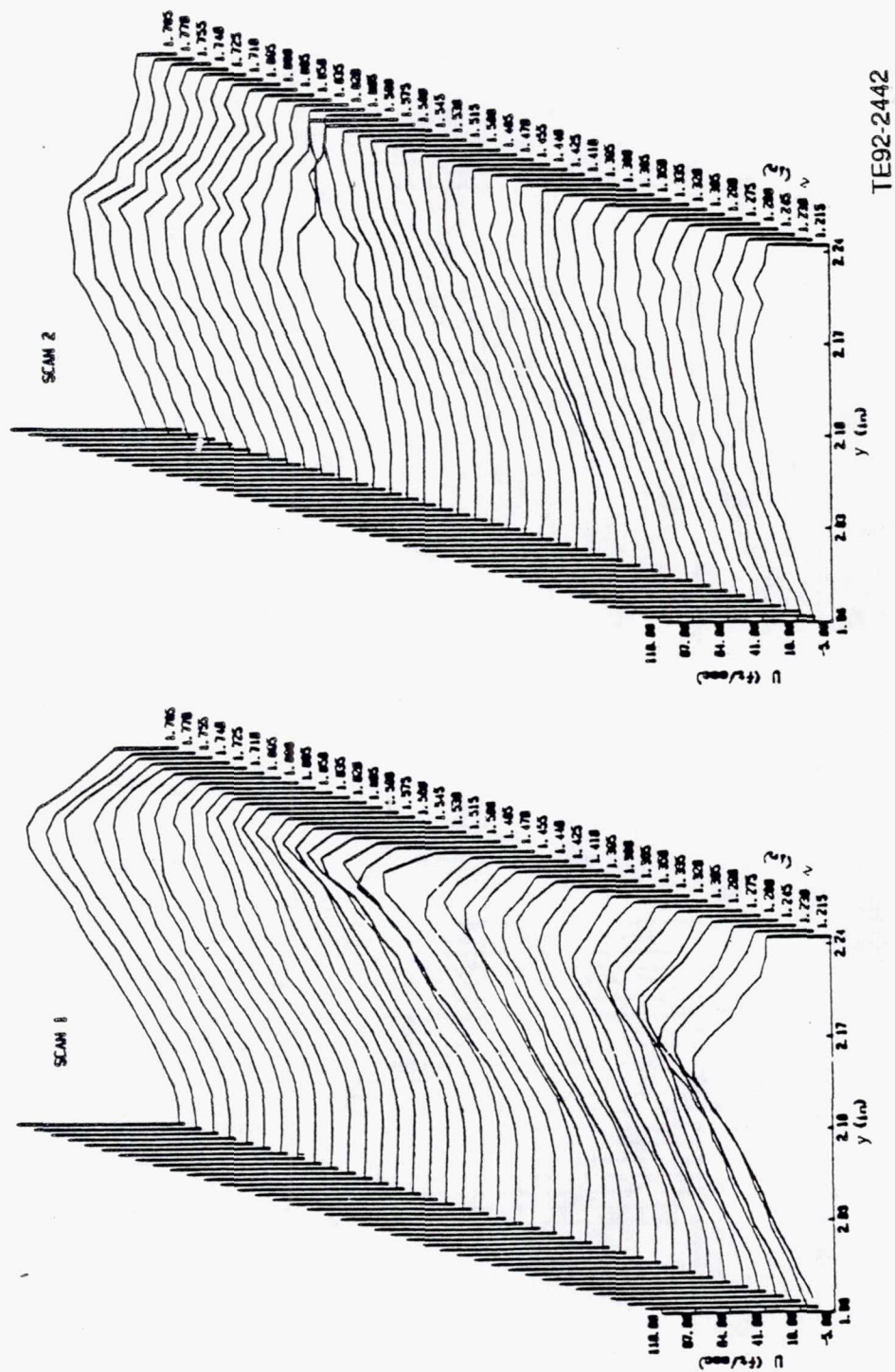
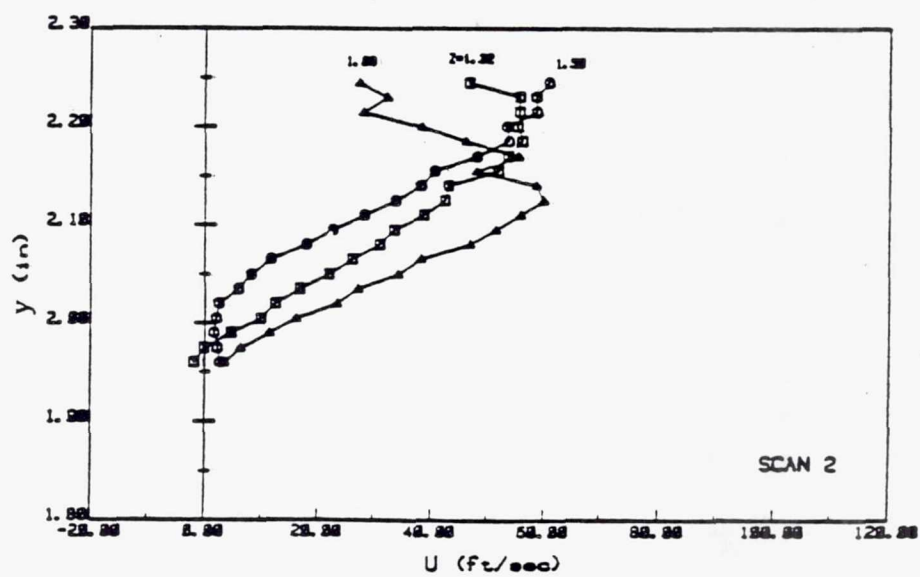
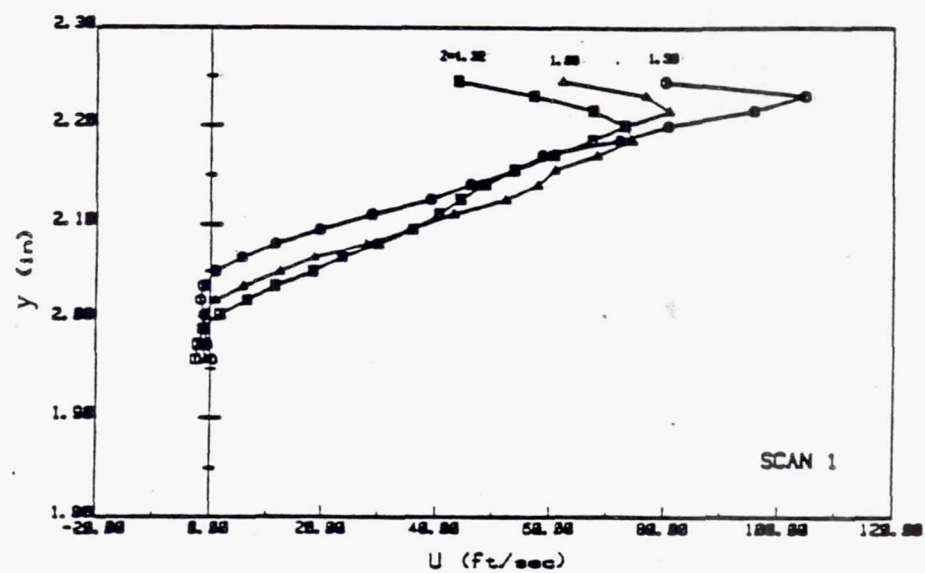
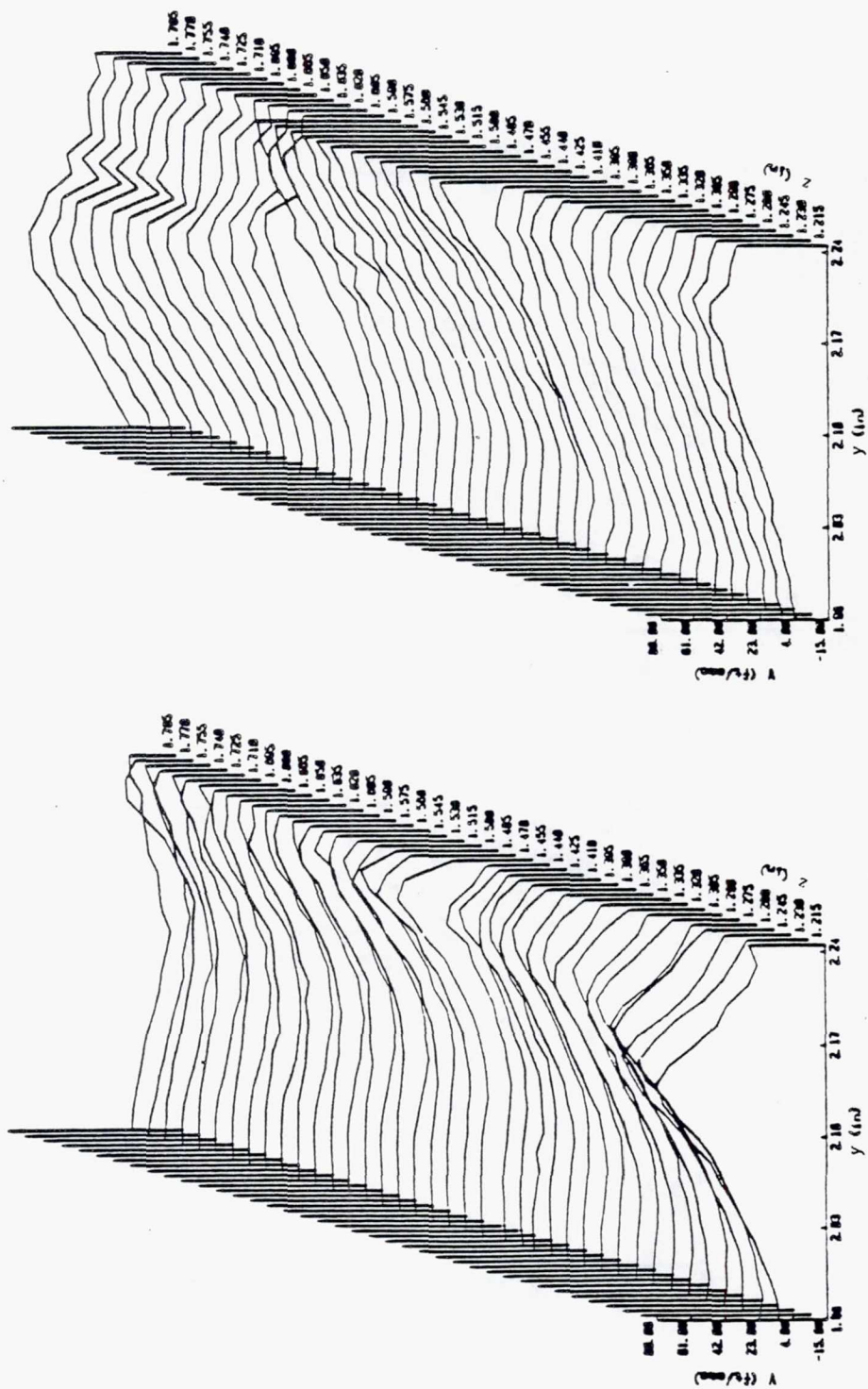


Figure 3.3.2-30. Cascade plots of swirl inlet u velocity (scans 1 and 2).



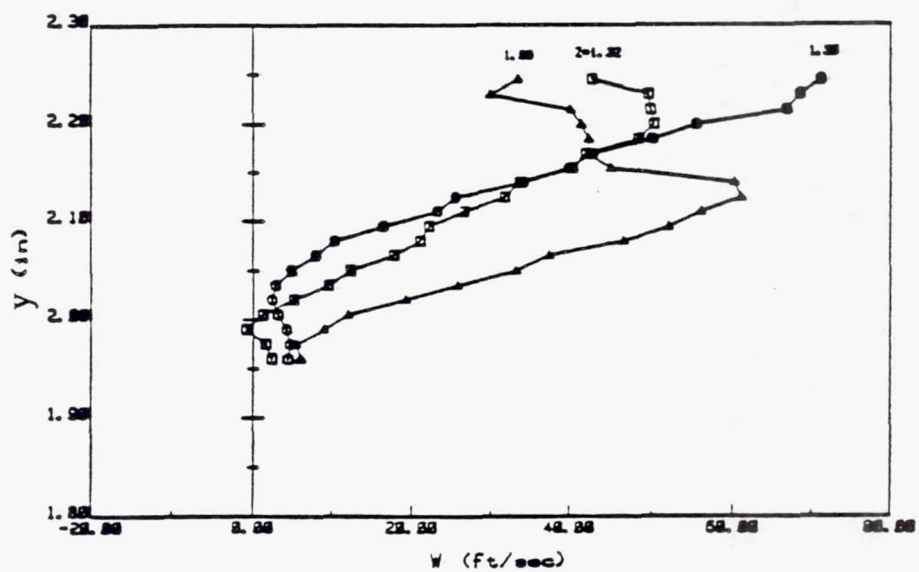
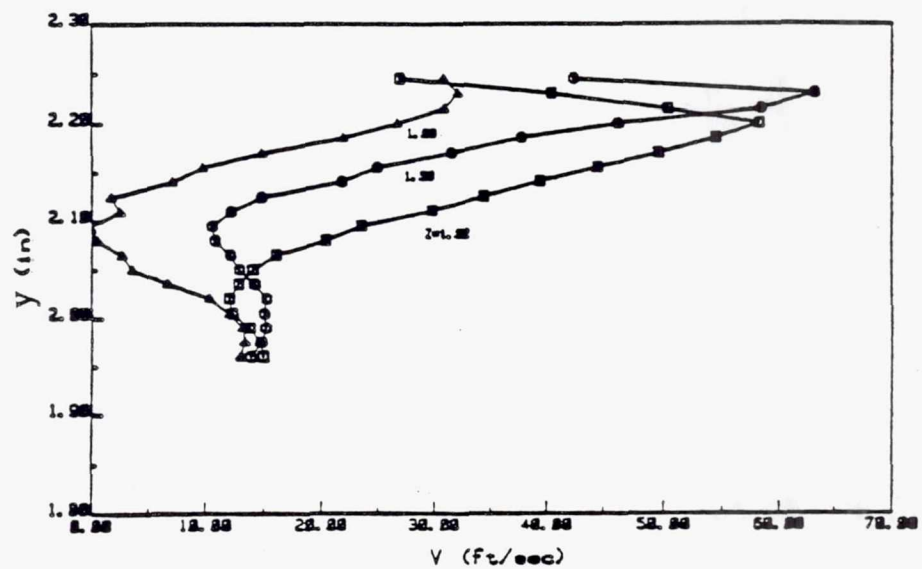
TE92-2443

Figure 3.3.2-31. Swirler inlet plots of u velocity at specific Z locations (scans 1 and 2).



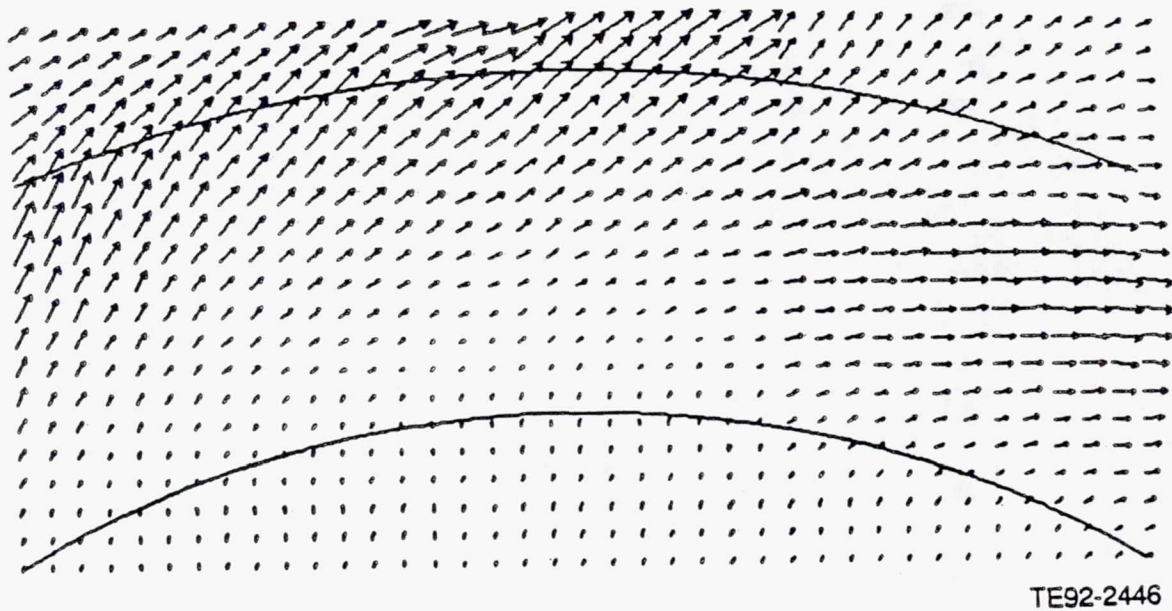
TE92-2444

Figure 3.3.2-32. Cascade plots of swirl inlet v and w velocities.



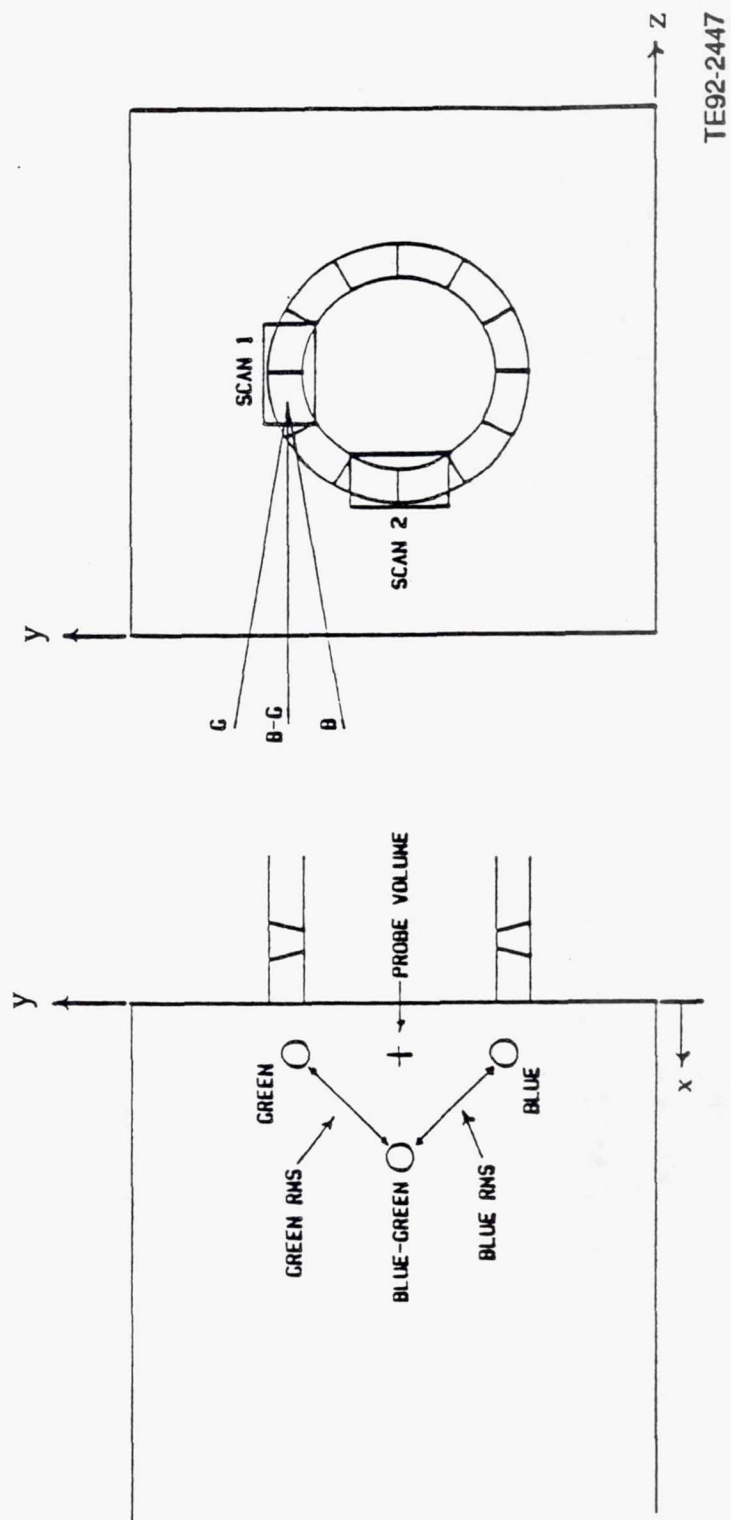
TE92-2445

Figure 3.3.2-33. Swirler inlet plots of v and w velocities at specific z locations.



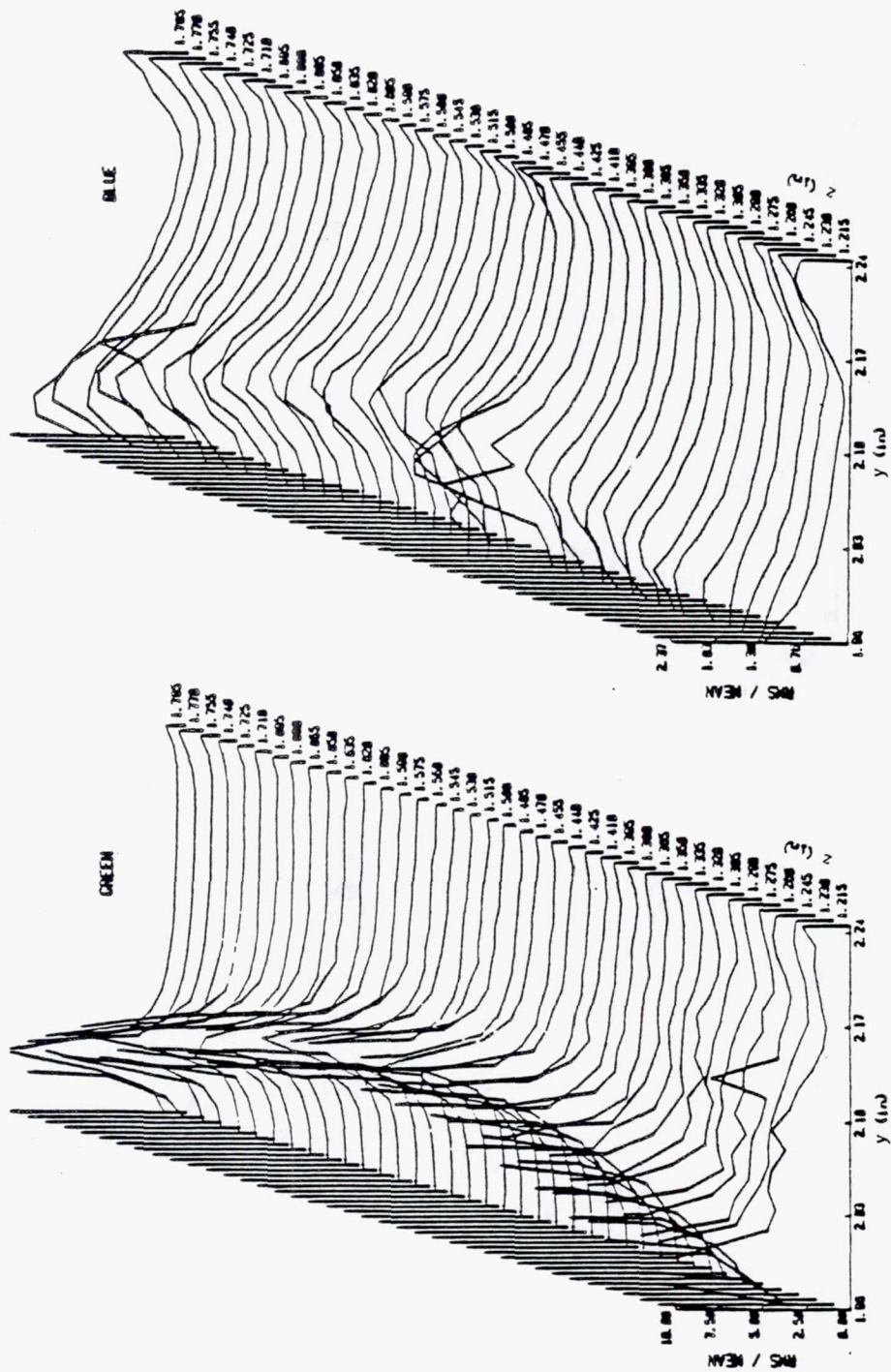
TE92-2446

Figure 3.3.2-34. Vector plot of swirler inlet v and w velocities.



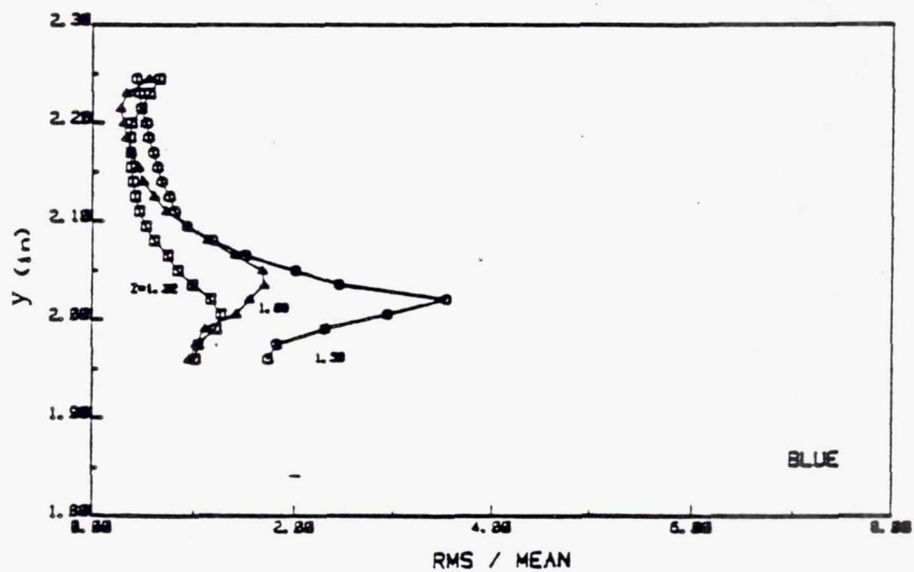
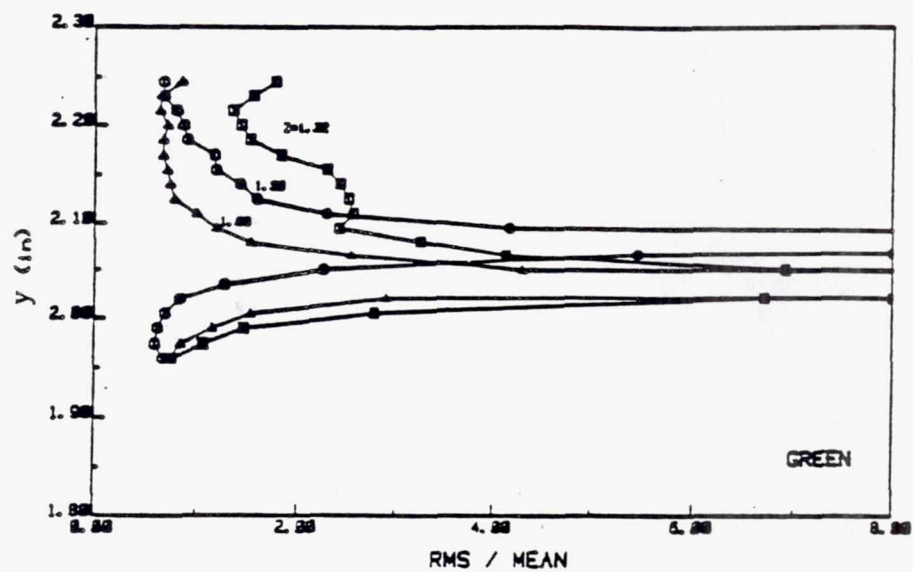
TE92-2447

Figure 3.3.2-35. Swirl inlet laser orientation.



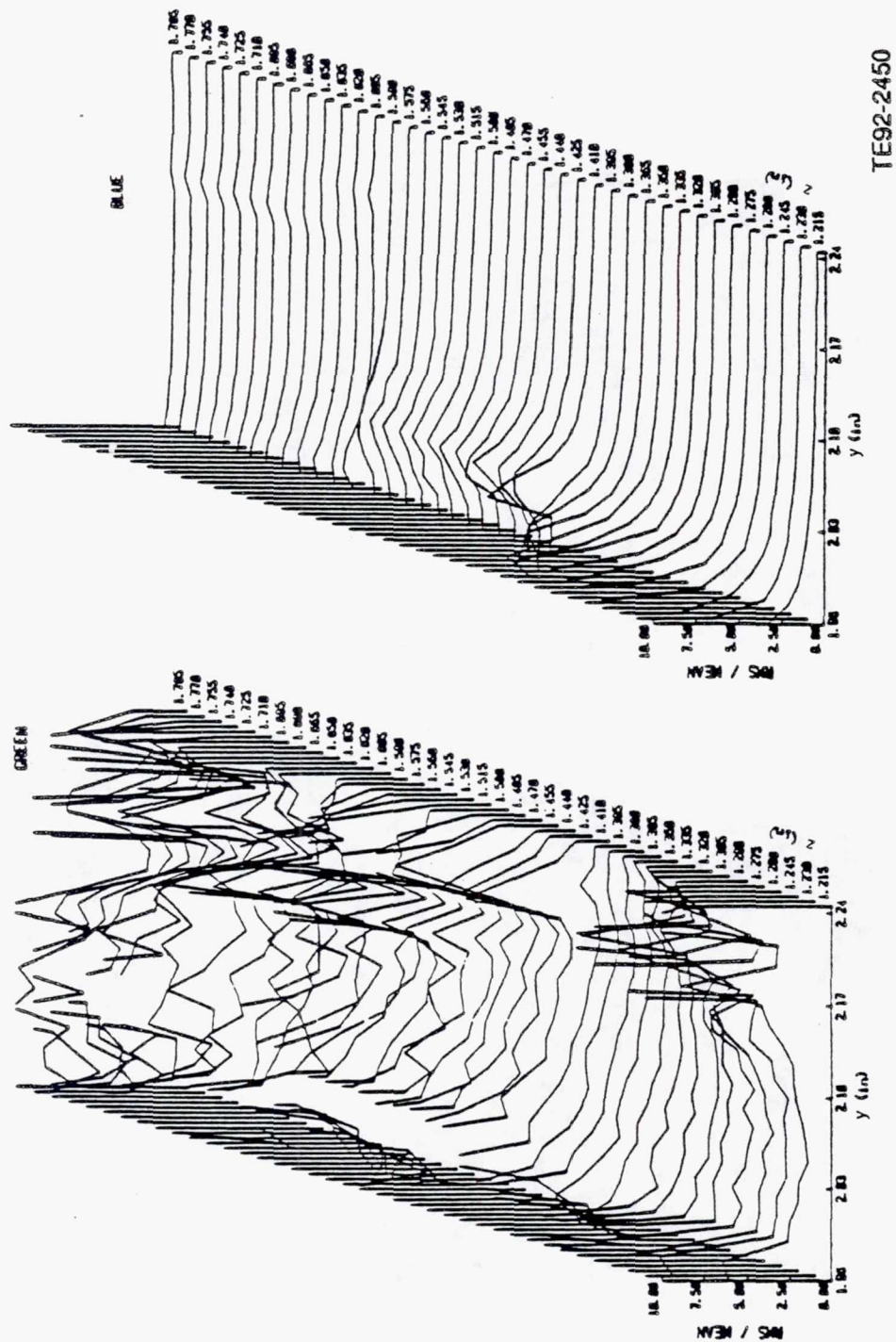
TE92-2448

Figure 3.3.2-36. Cascade plots of turbulence intensity for swirler inlet (scan 1).



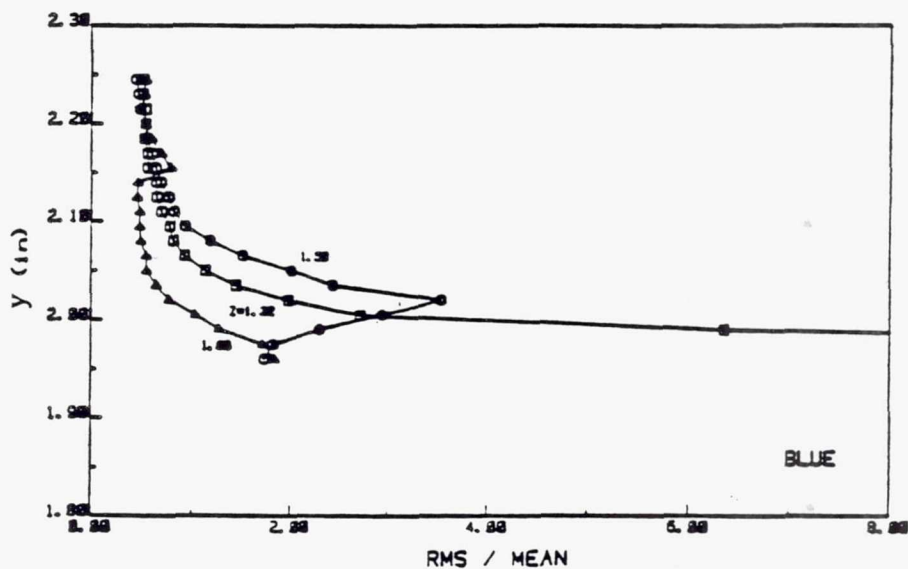
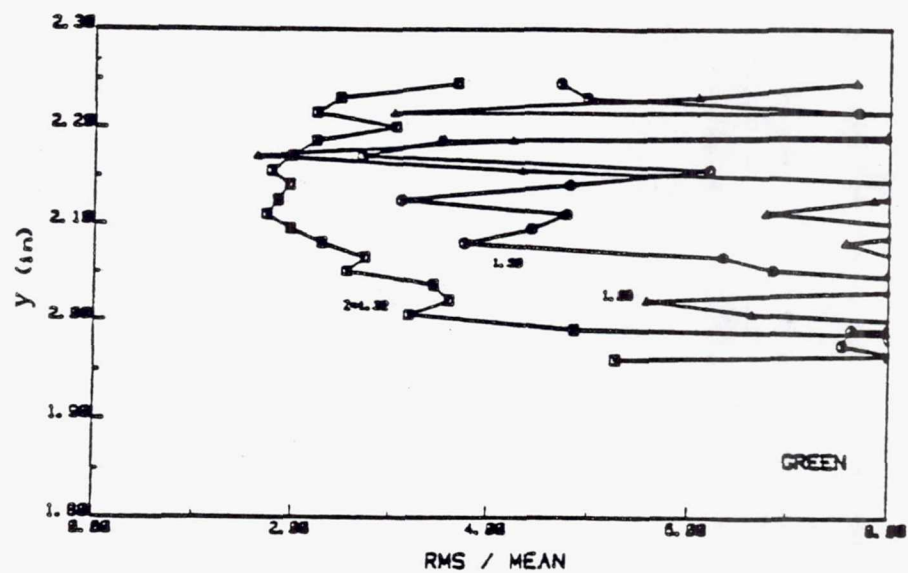
TE92-2449

Figure 3.3.2-37. Swirler inlet plots of turbulence intensity at specific Z locations (scan 1).



TE92-2450

Figure 3.3.2-38. Cascade plots of turbulence intensity for swirler inlet (scan 2).



TE92-2451

Figure 3.3.2-39. Swirler inlet plots of turbulence intensity at specific z locations (scan 2).

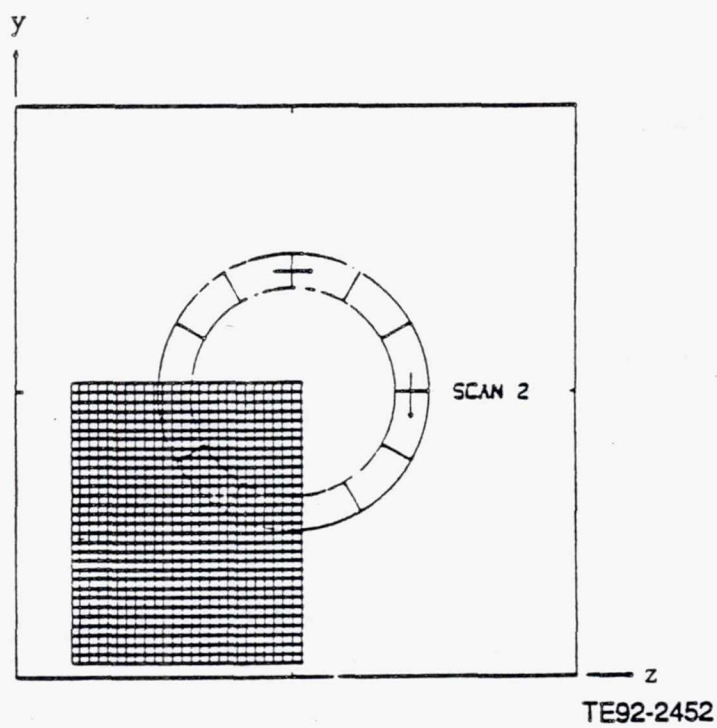
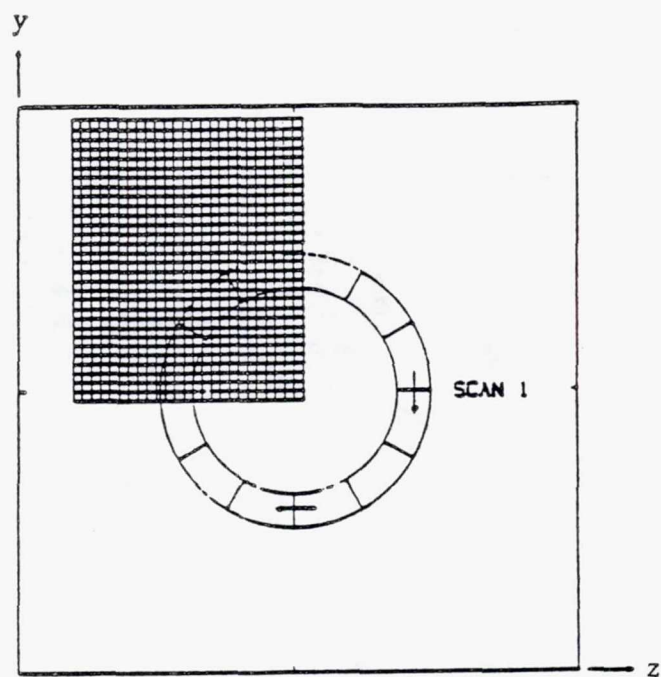
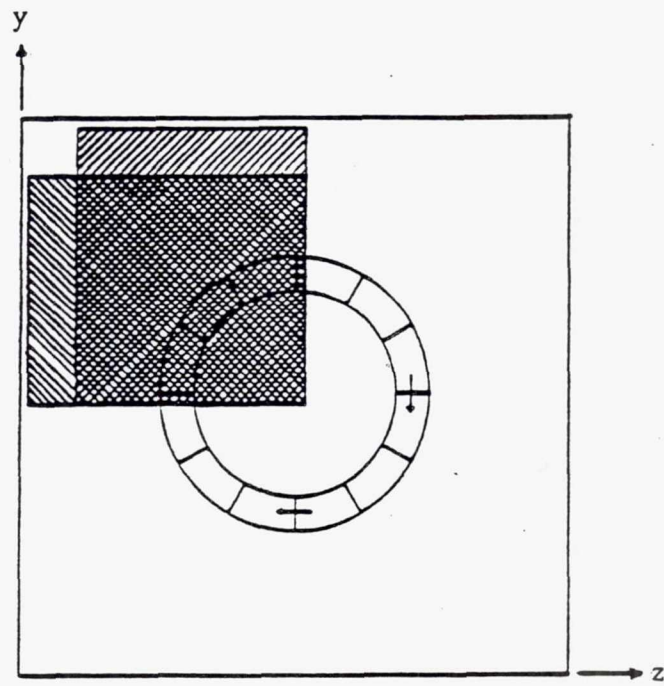
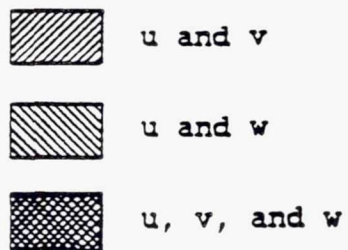


Figure 3.3.2-40. Downstream data grid (scans 1 and 2).

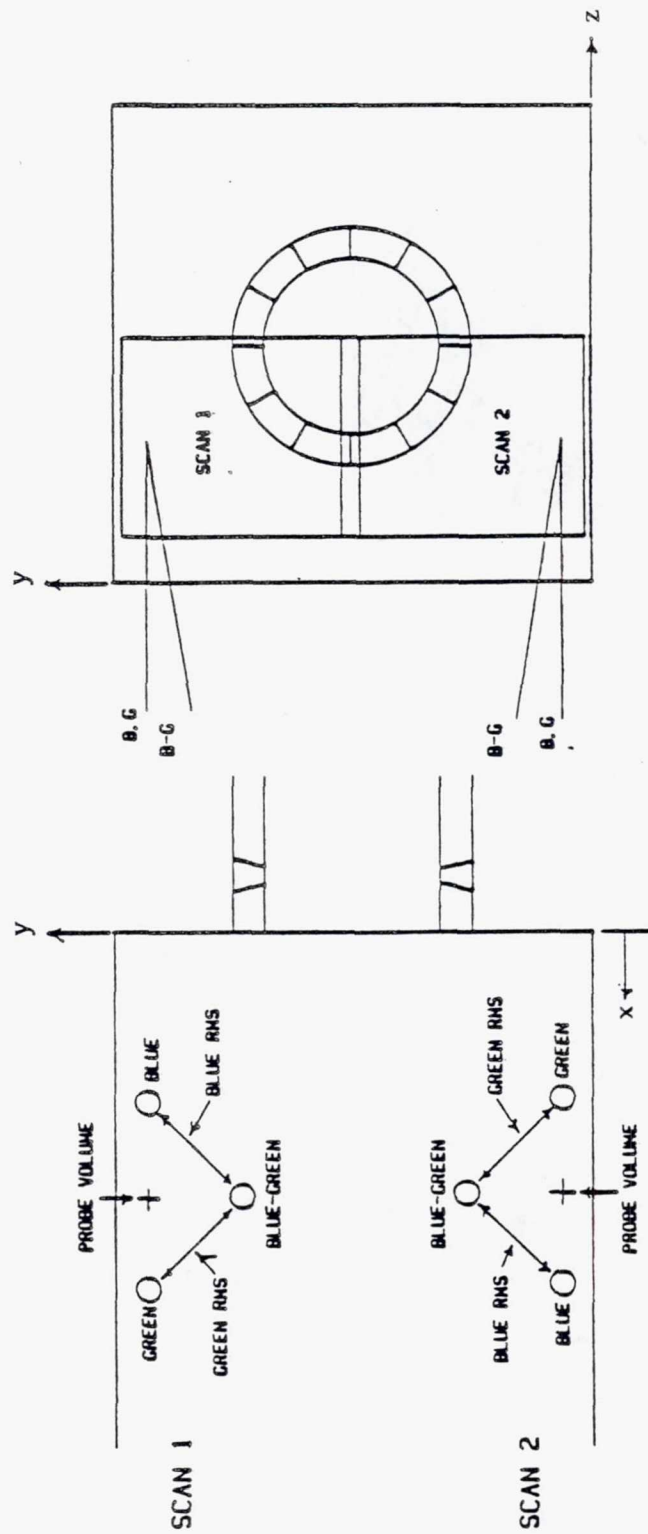


COMPONENTS MEASURED



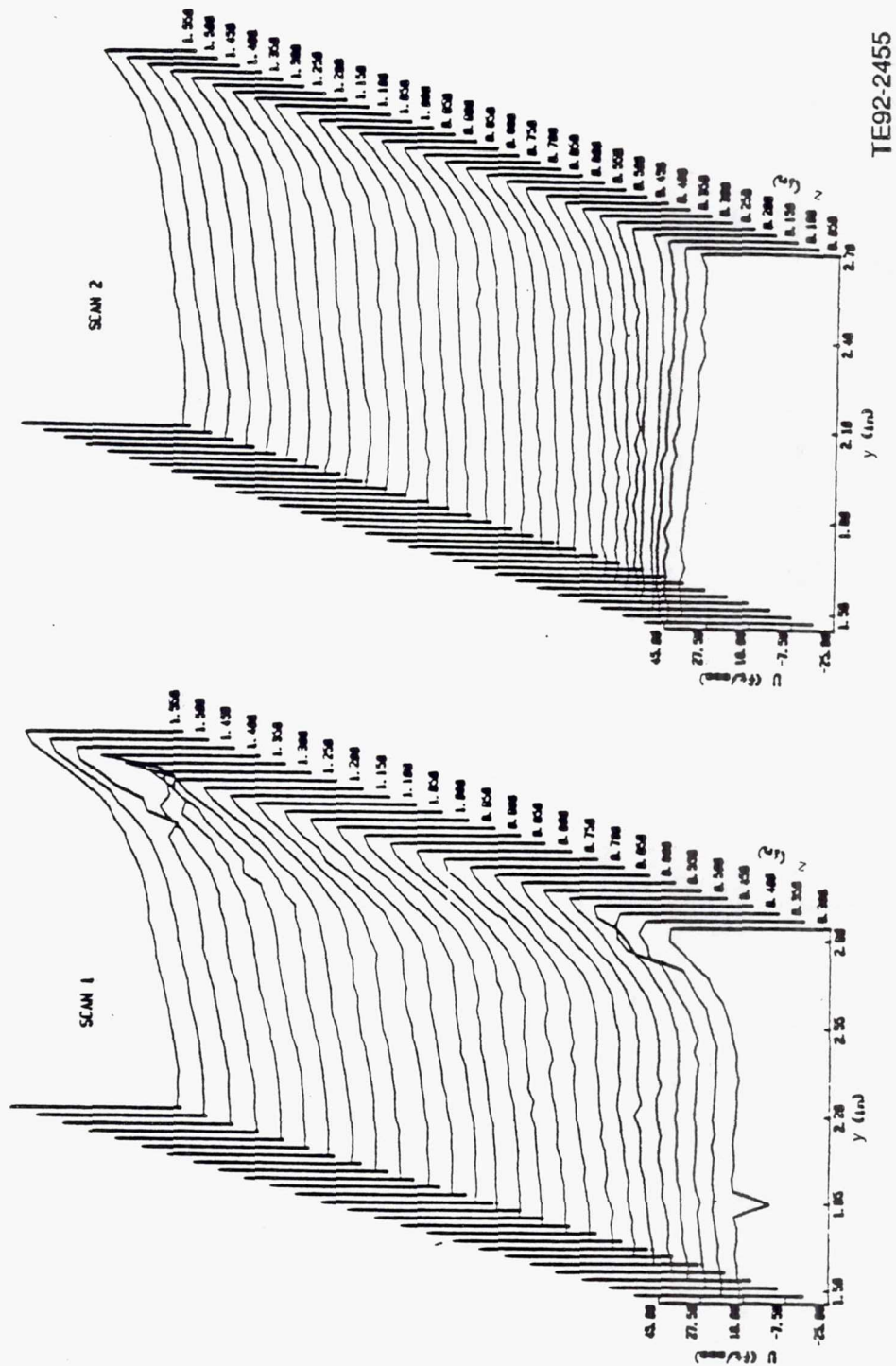
TE92-2453

Figure 3.3.2-41. Combined data grid.



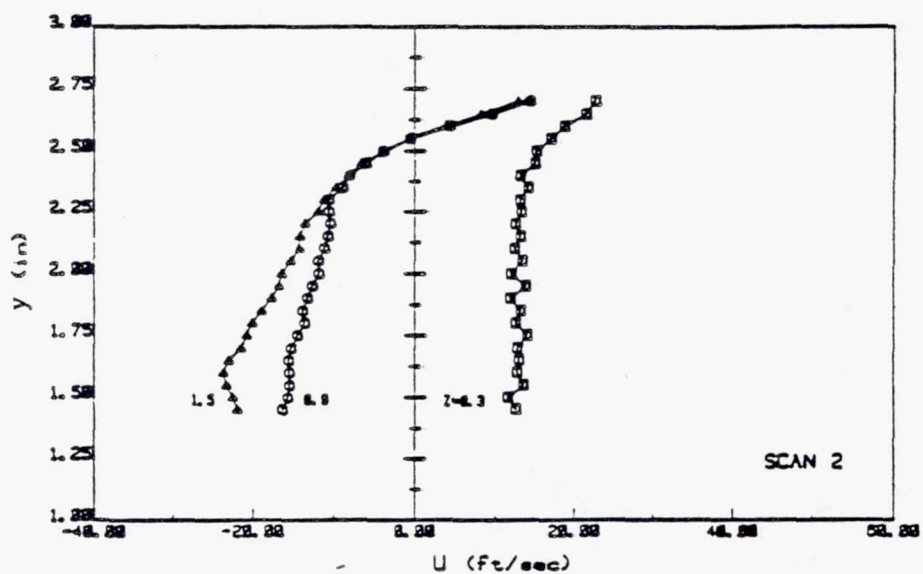
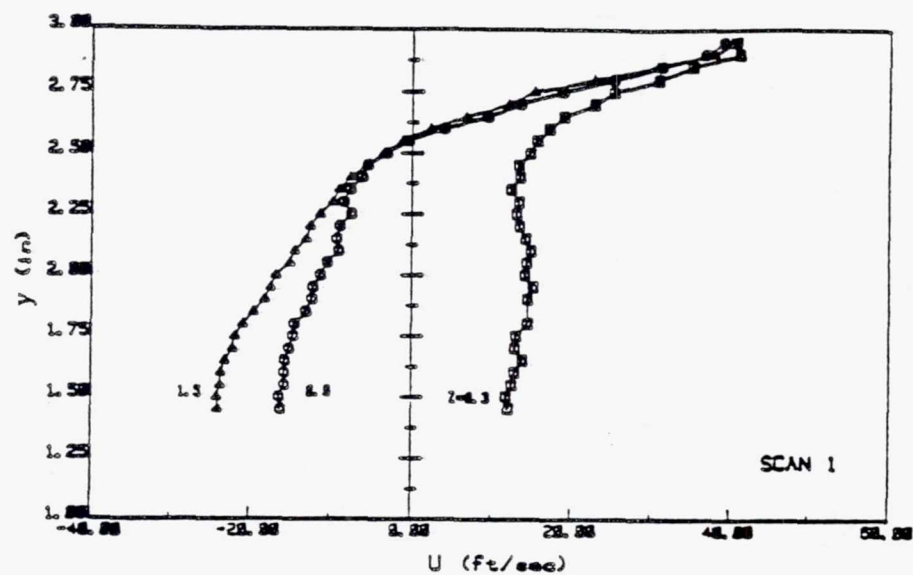
TE92-2454

Figure 3.3.2-42. Laser orientation for downstream data.



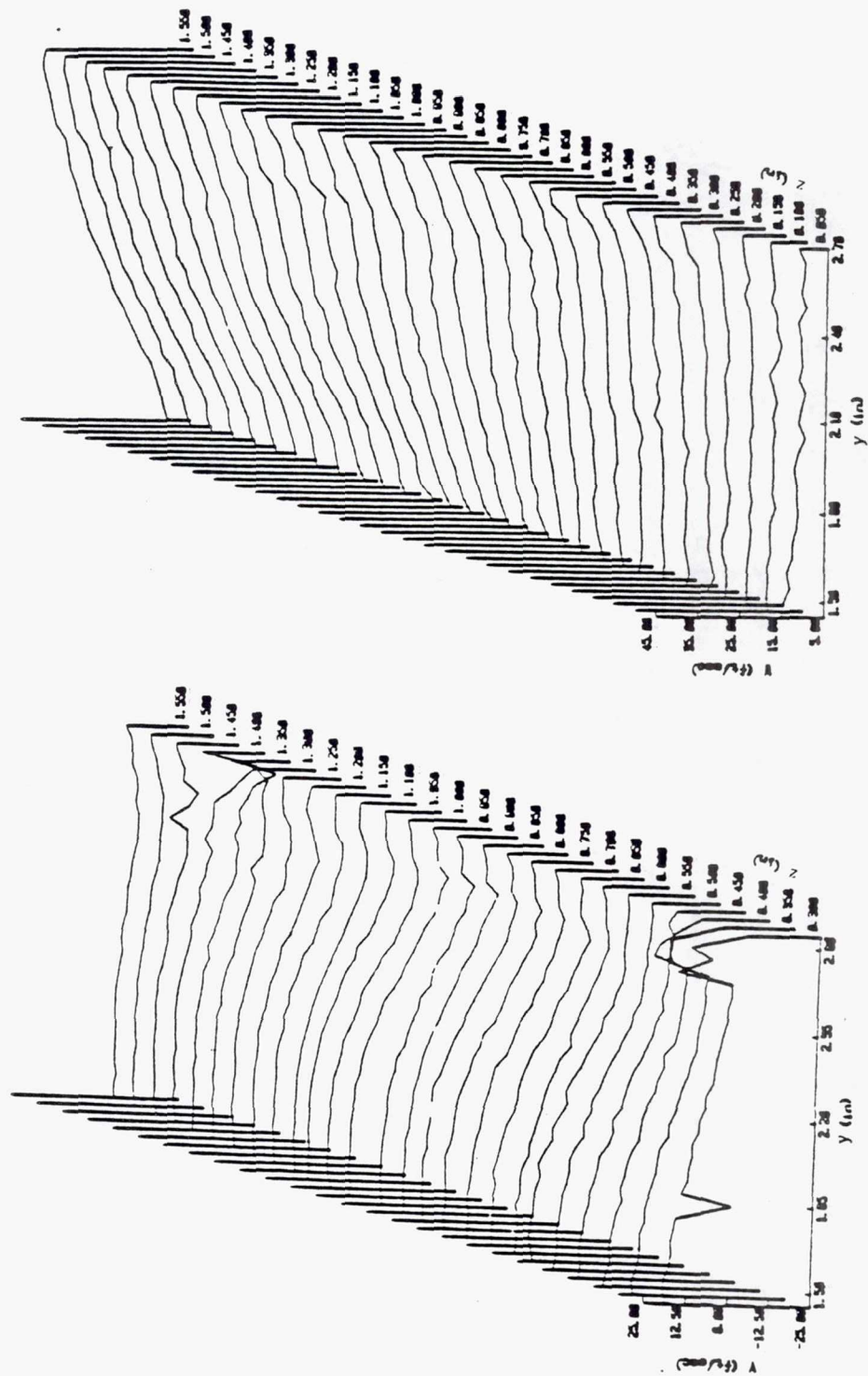
TE92-2455

Figure 3.3.2-43. Cascade plots of u velocity at x=1.5 in. (scans 1 and 2).



TE92-2456

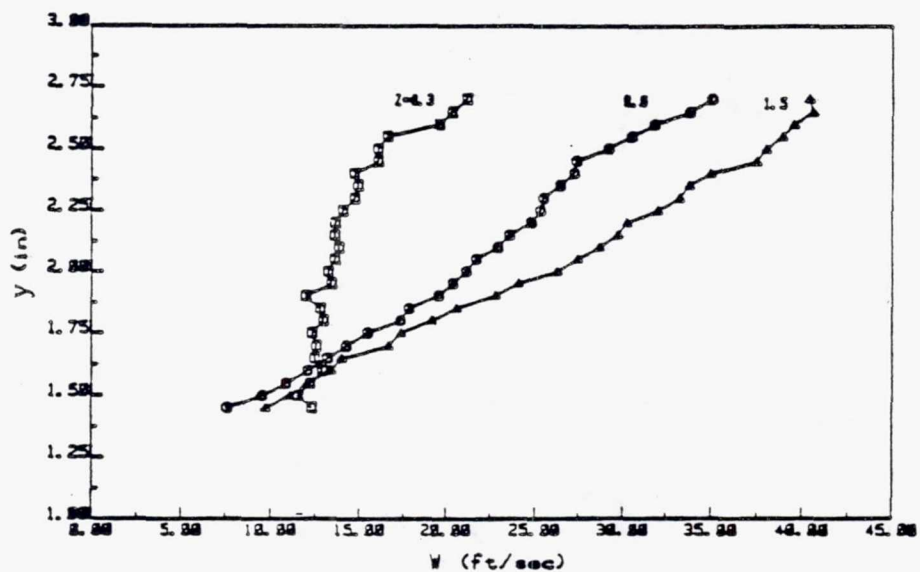
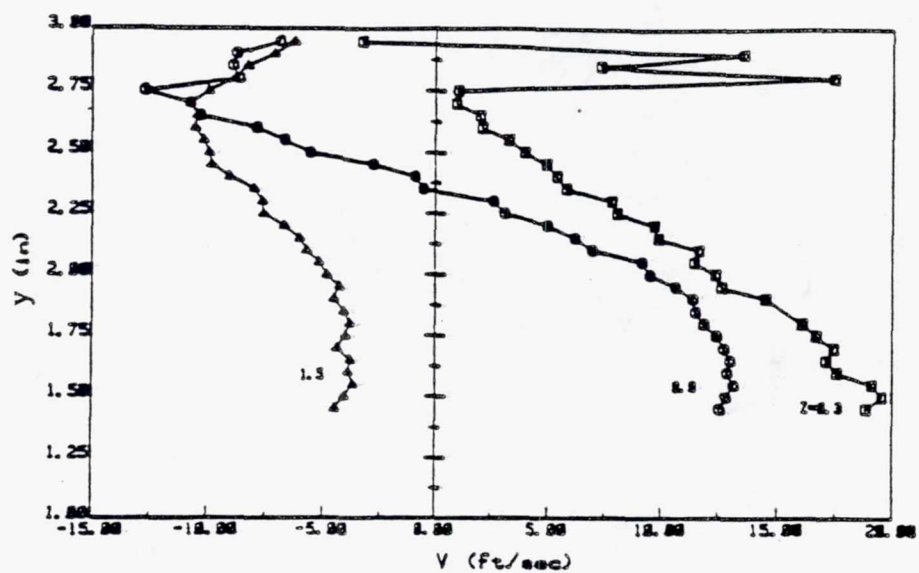
Figure 3.3.2-44. Plots of u velocity at $x = 1.5$ in. (scans 1 and 2).



TE92-2457

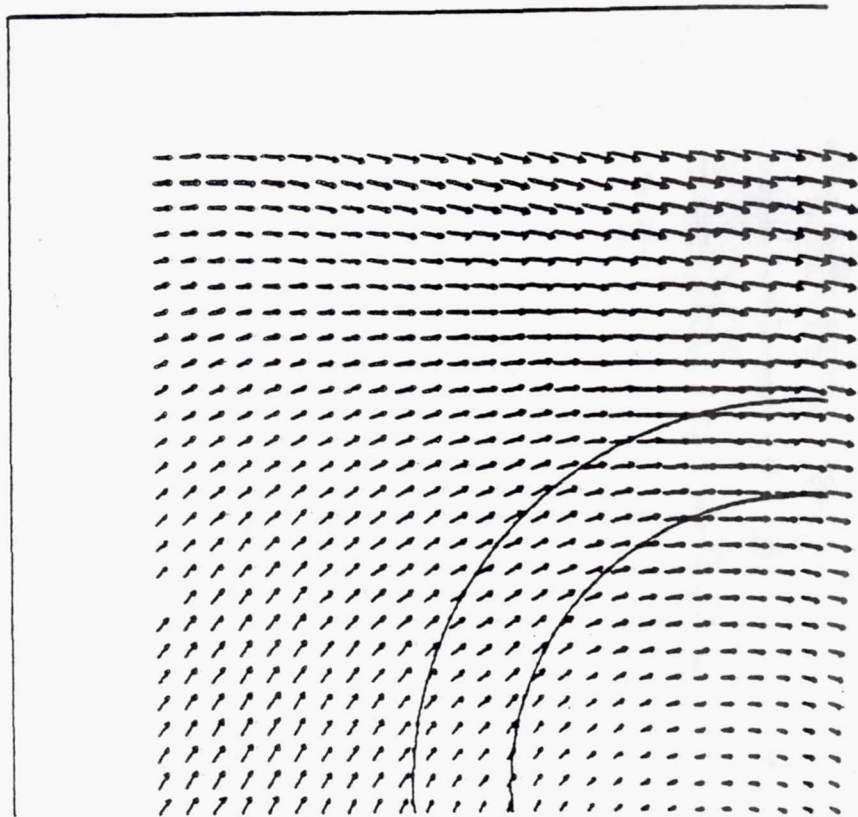
Figure 3.3.2-45. Cascade plots of v and w velocities at $X=1.5$ in.

x



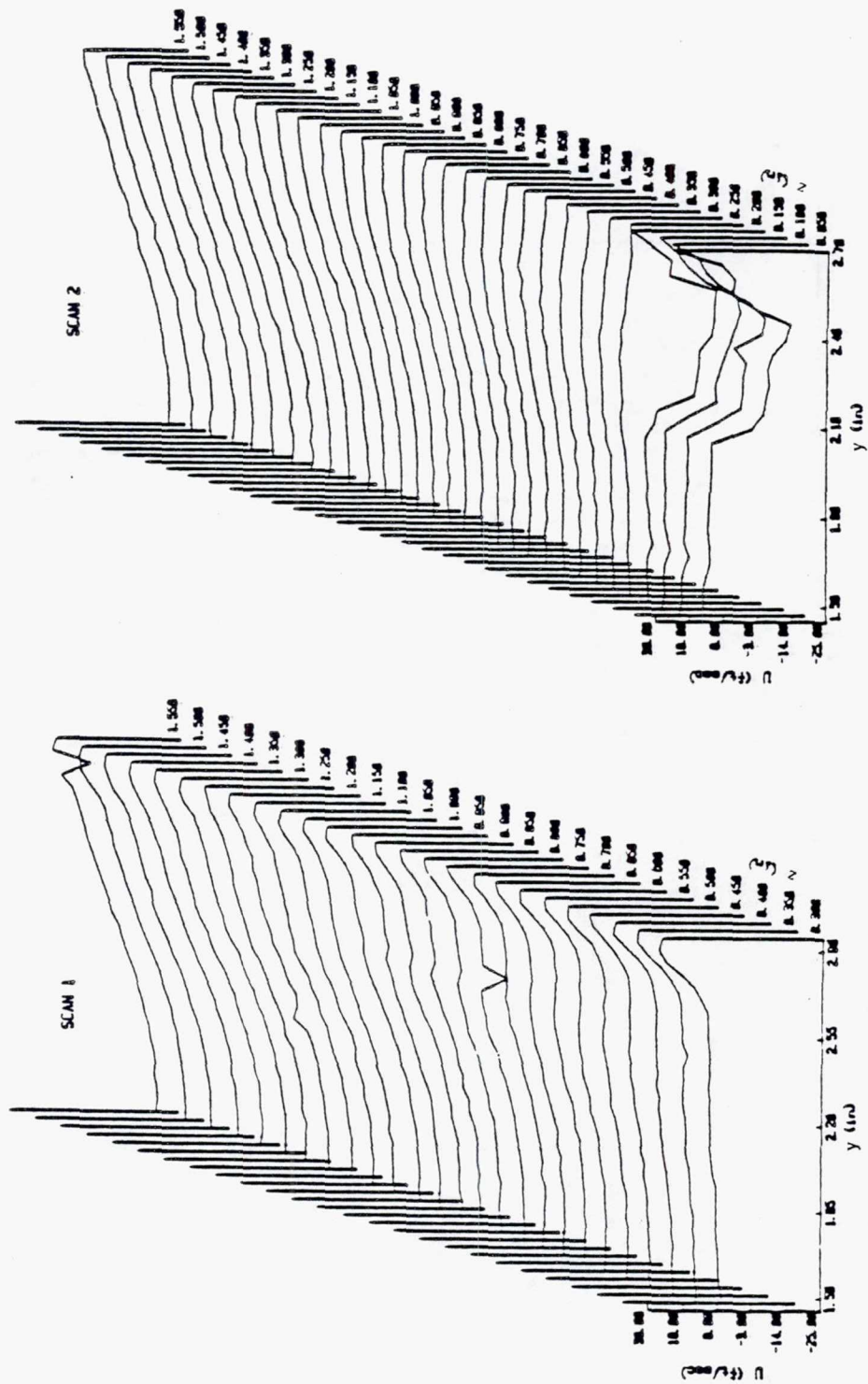
TE92-2458

Figure 3.3.2-46. Plots of v and w velocities at $x=1.5$ in.



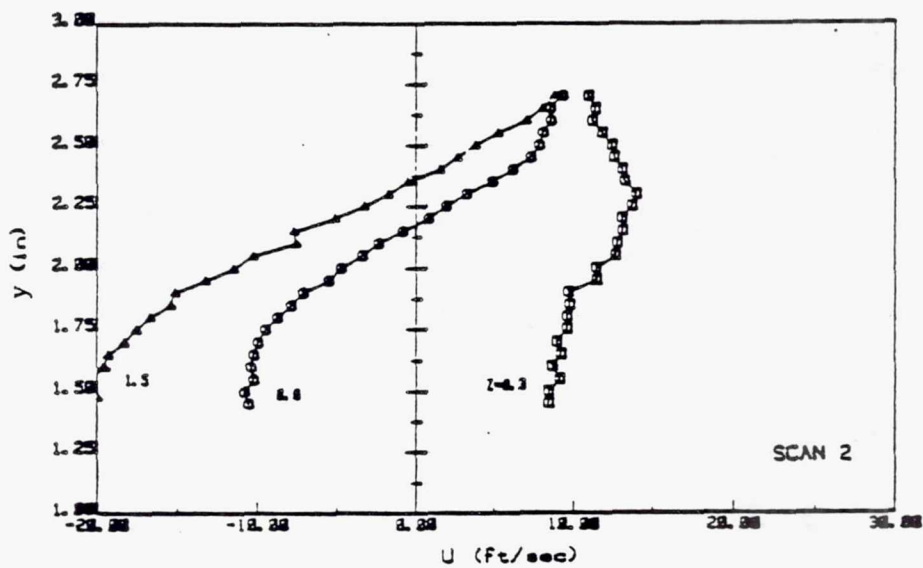
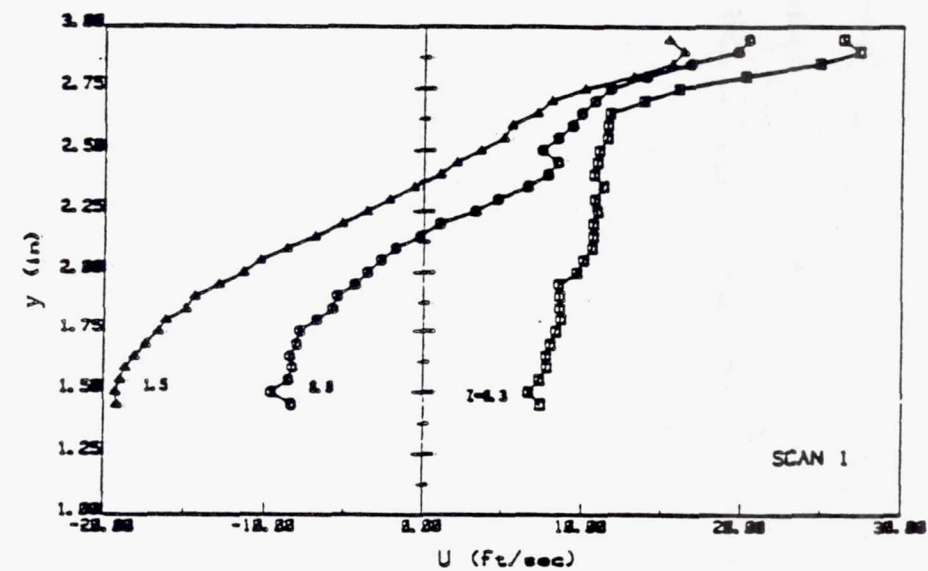
TE92-2459

Figure 3.3.2-47. Vector plot of v and w velocities at $x=1.5$ in.



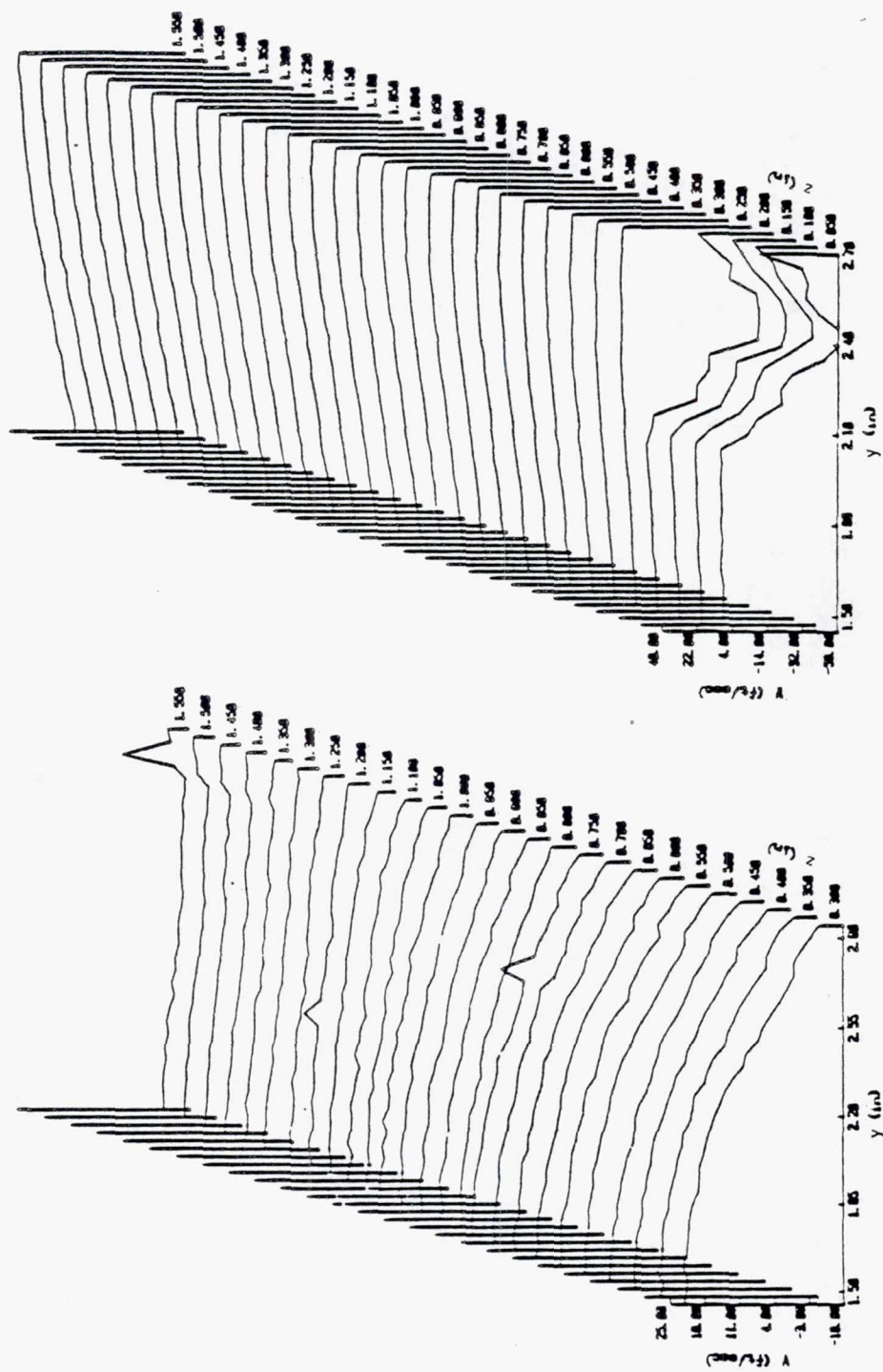
TE92-2460

Figure 3.3.2-48. Cascade plots of u velocity at $x=3.0$ in. (scans 1 and 2).



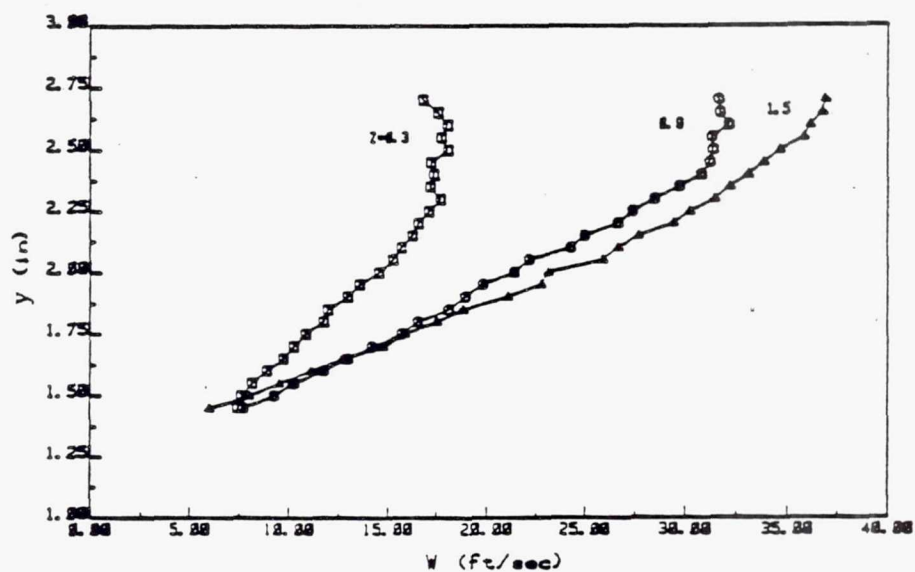
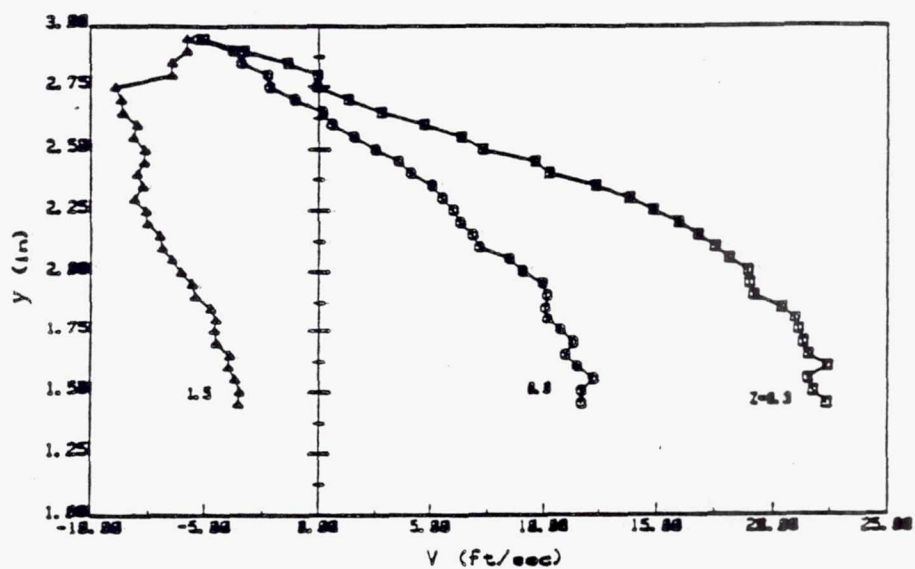
TE92-2461

Figure 3.3.2-49. Plots of u velocity at $x=3.0$ in. (scans 1 and 2).



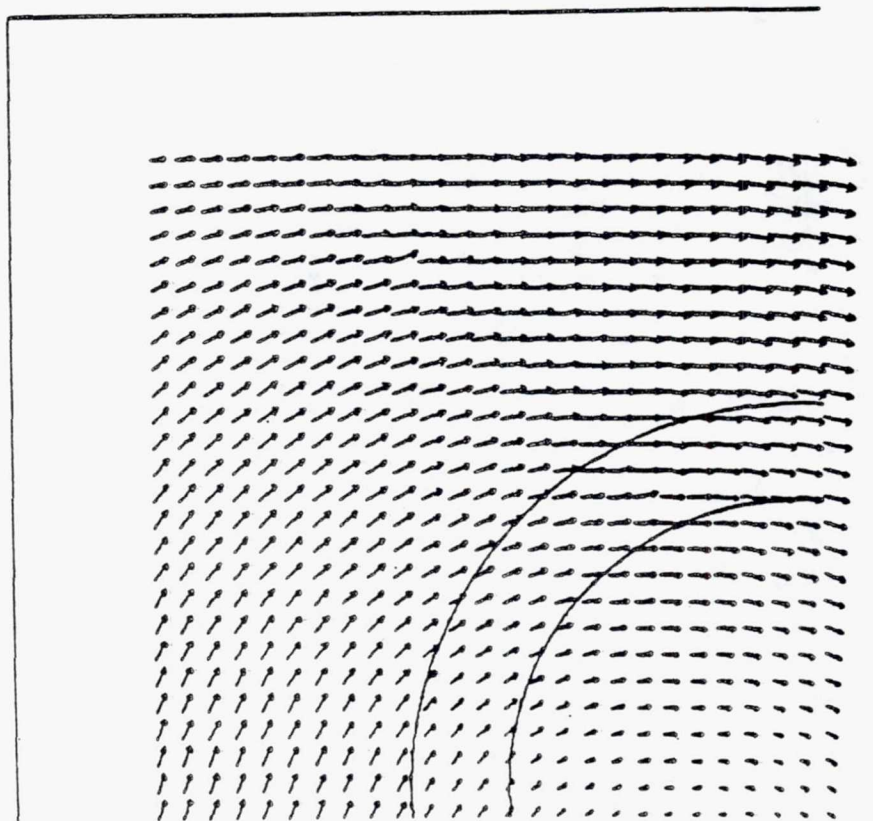
TE92-2462

Figure 3.3.2-50. Cascade plots of v and w velocities at $x=3.0$ in.



TE92-2463

Figure 3.3.2-51. Plots of v and w velocities at $x=3.0$ in.



TE92-2464

Figure 3.3.2-52. Vector plot of v and w velocities at $x=3.0$ in.

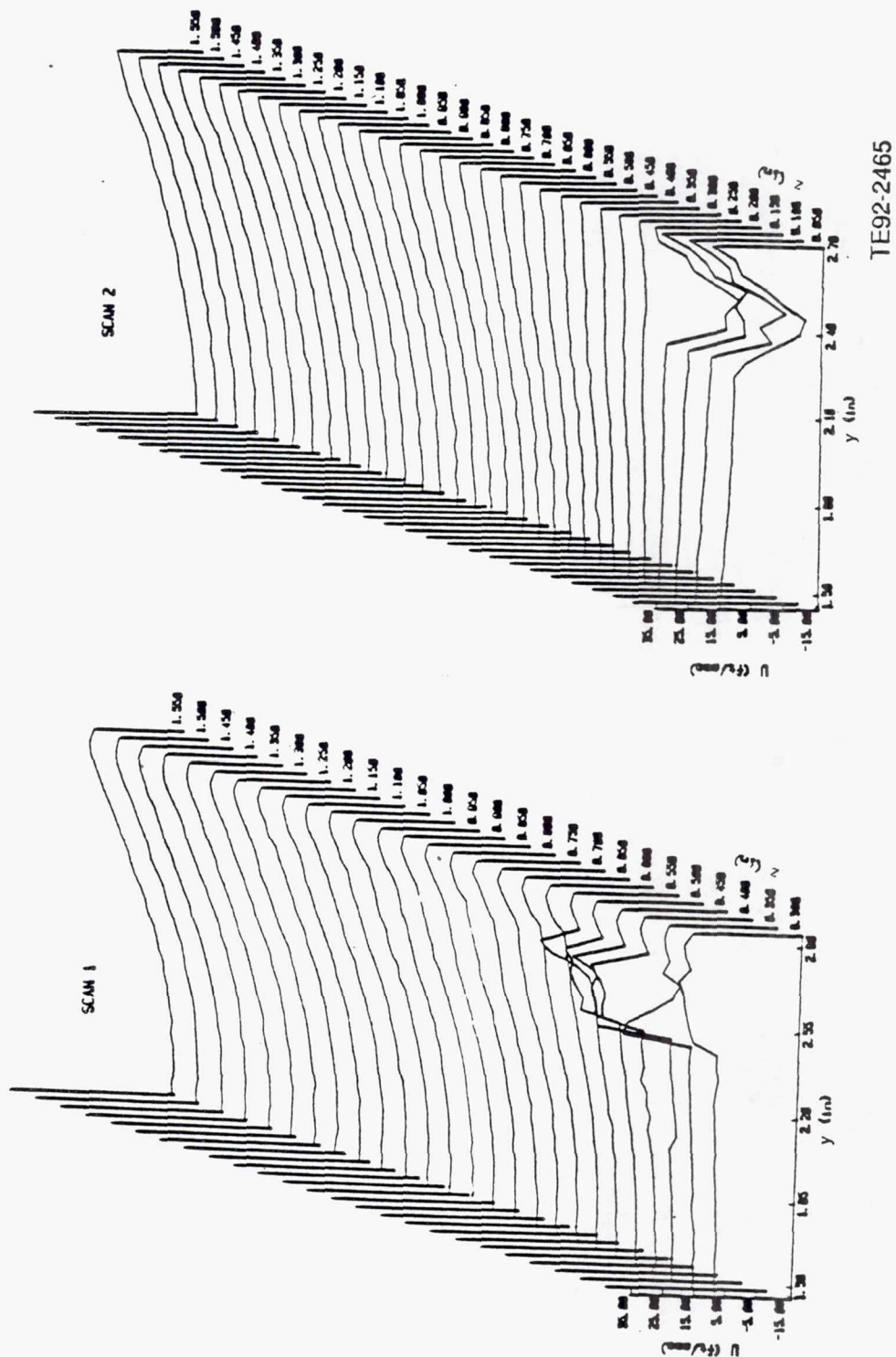
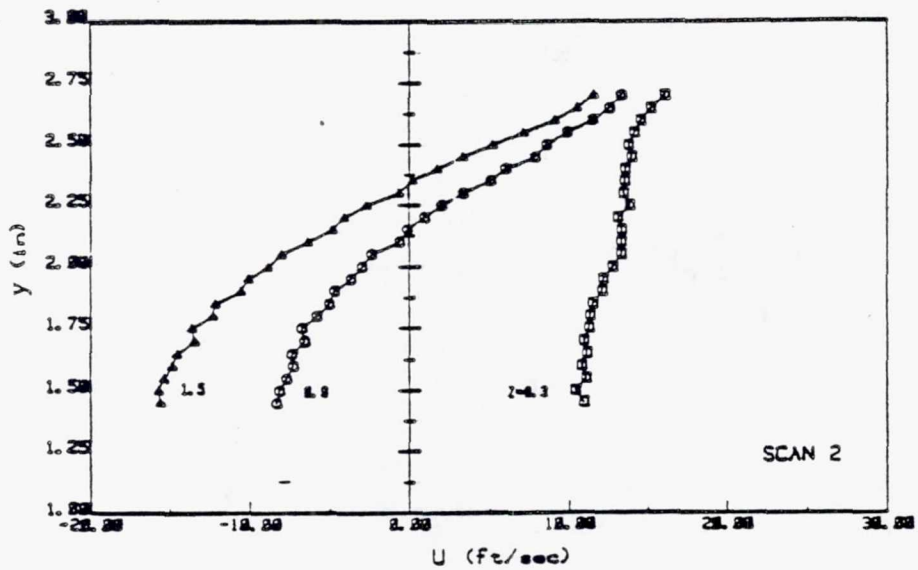
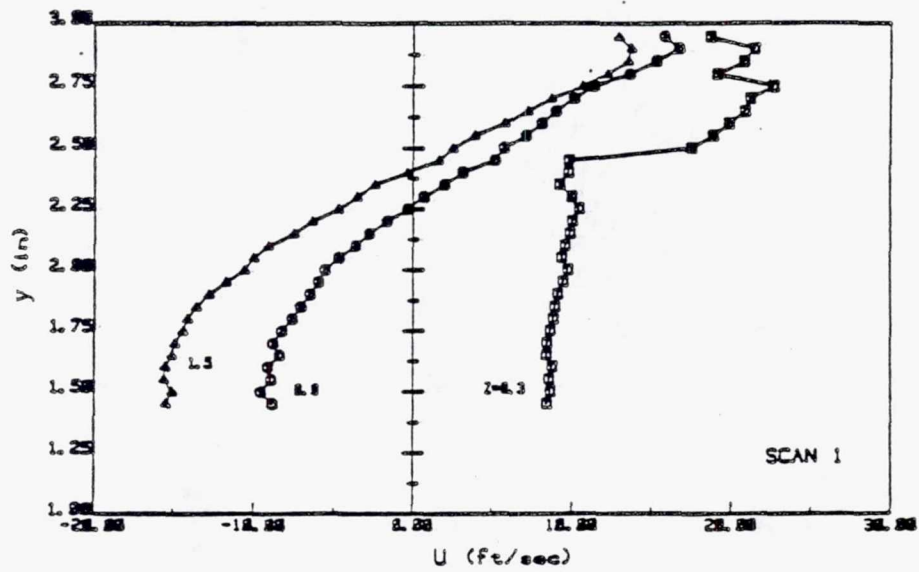
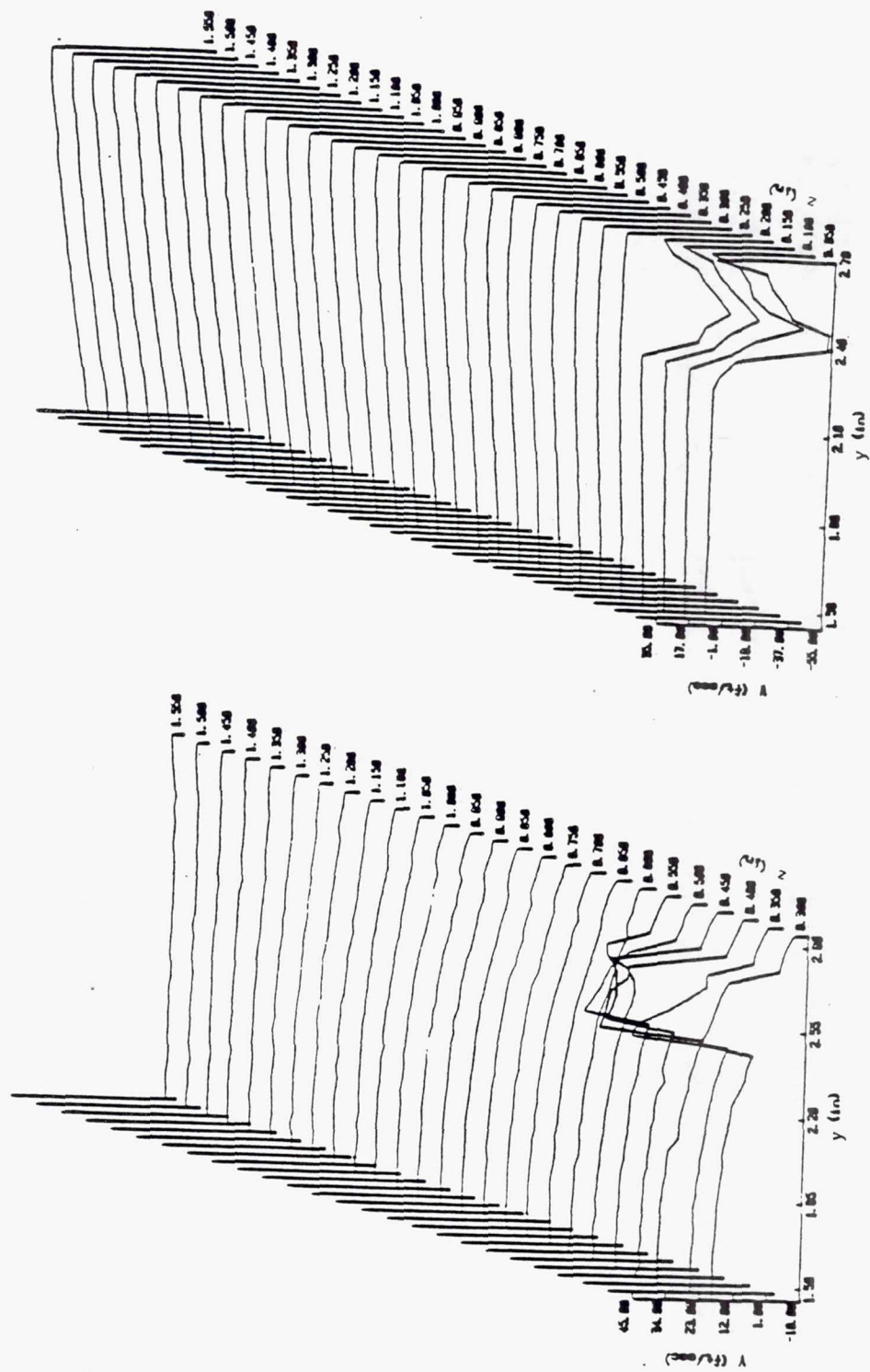


Figure 3.3.2-53. Cascade plots of u velocity at $x=4.5$ in. (scans 1 and 2).



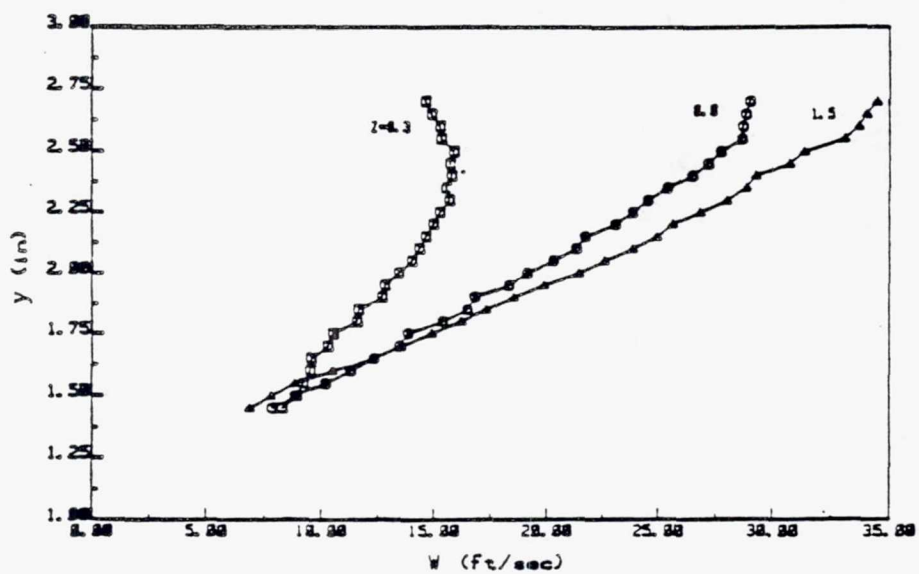
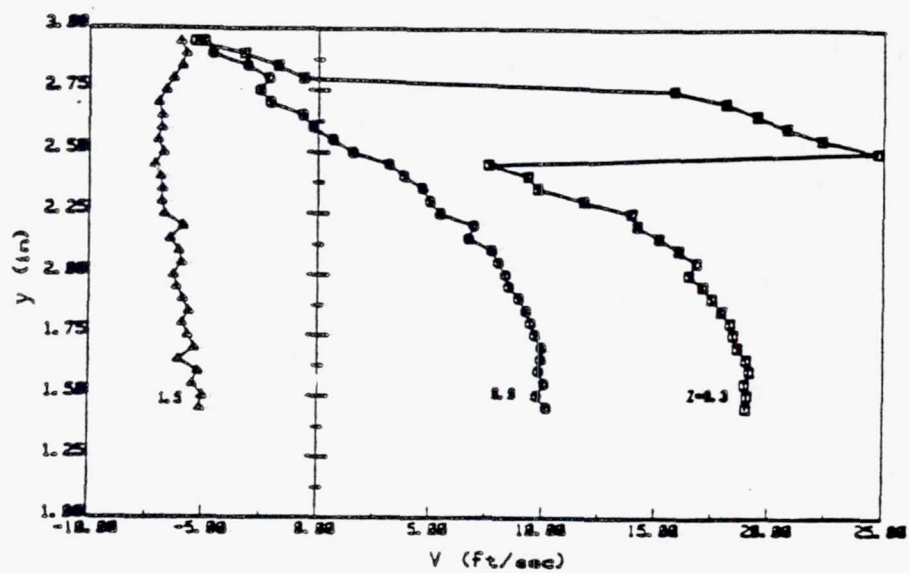
TE92-2466

Figure 3.3.2-54. Plots of u velocity at $x=4.5$ in. (scans 1 and 2).



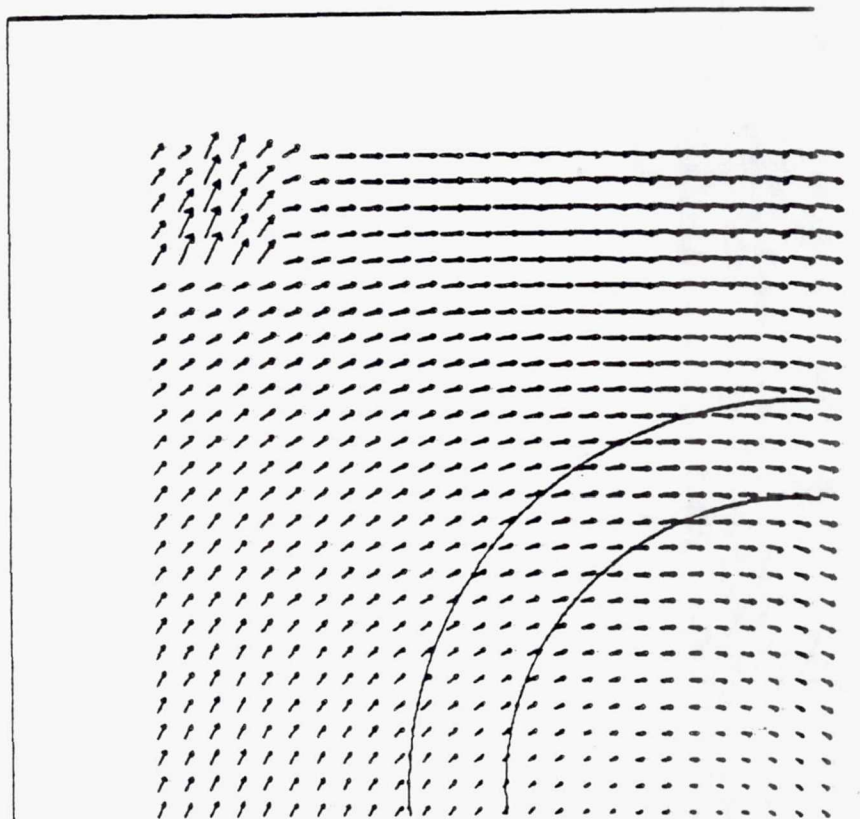
TE92-2467

Figure 3.3.2-55. Cascade plots of v and w velocities at $X=4.5$ in.



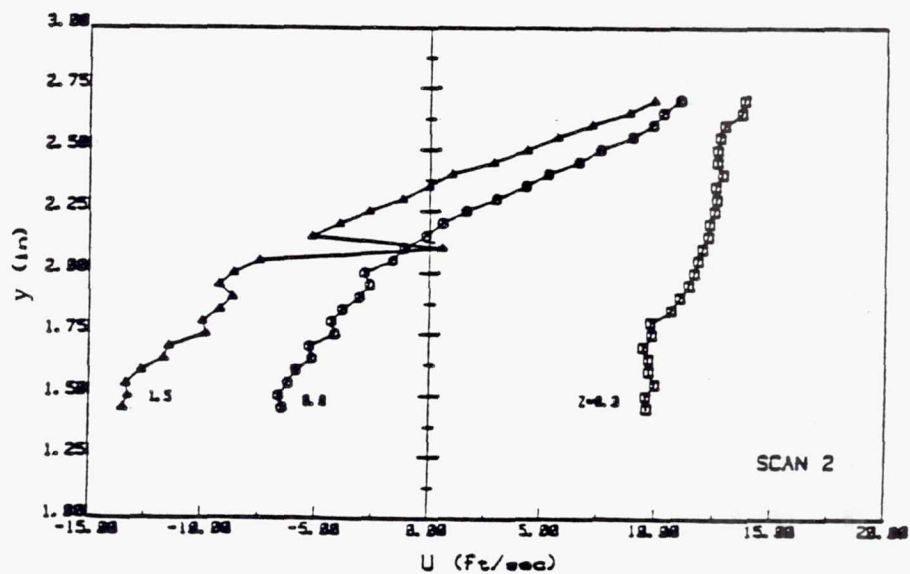
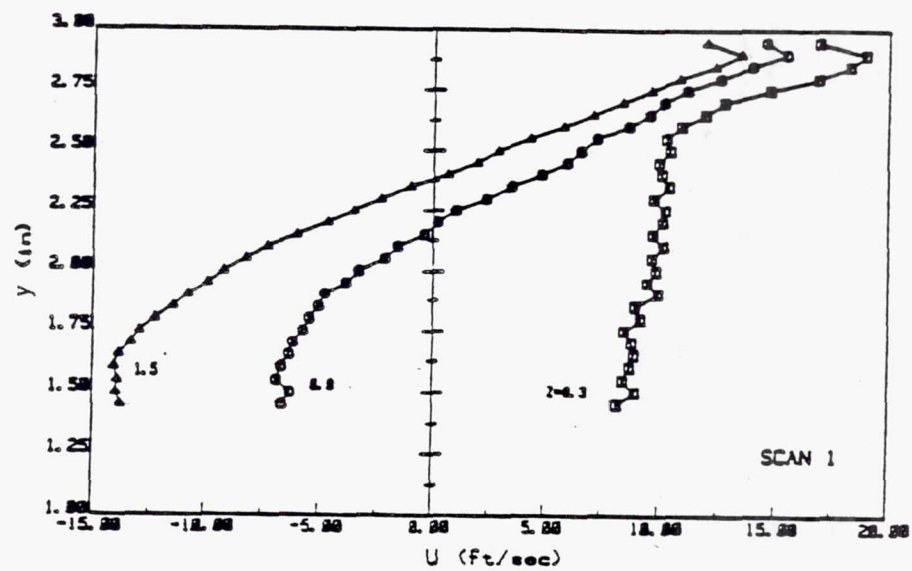
TE92-2468

Figure 3.3.2-56. Plots of v and w velocities at $x=4.5$ in.



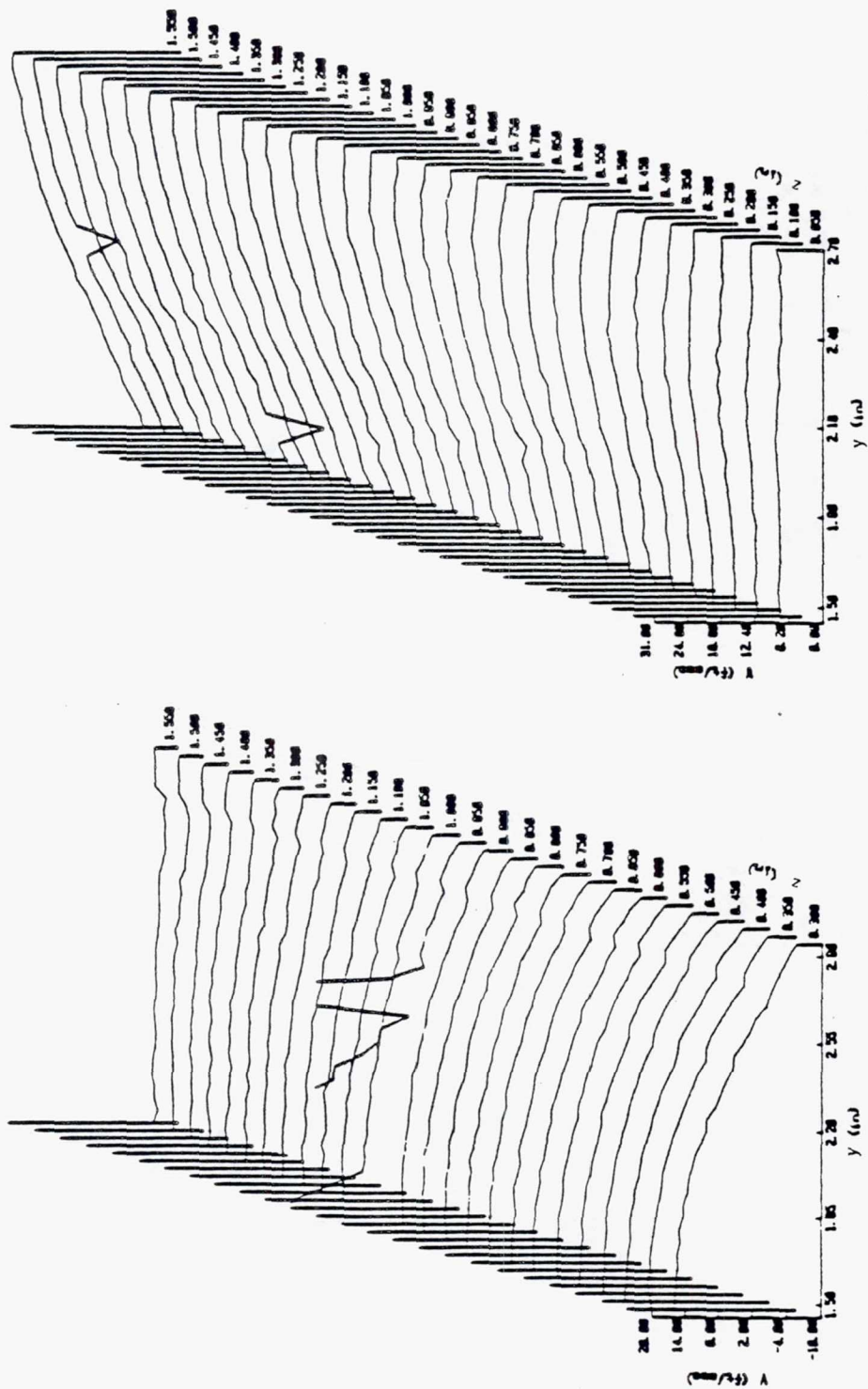
TE92-2469

Figure 3.3.2-57. Vector plot of v and w velocities at $x=4.5$ in.



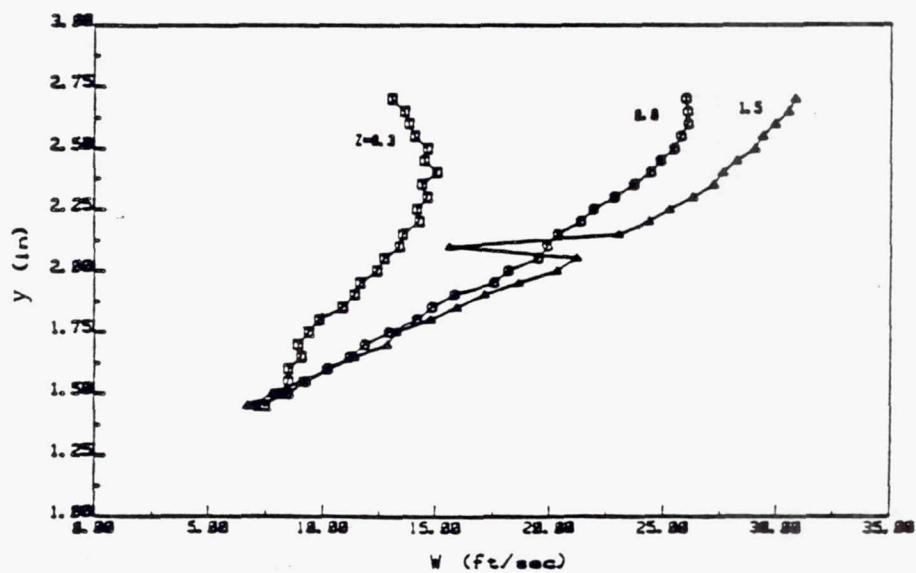
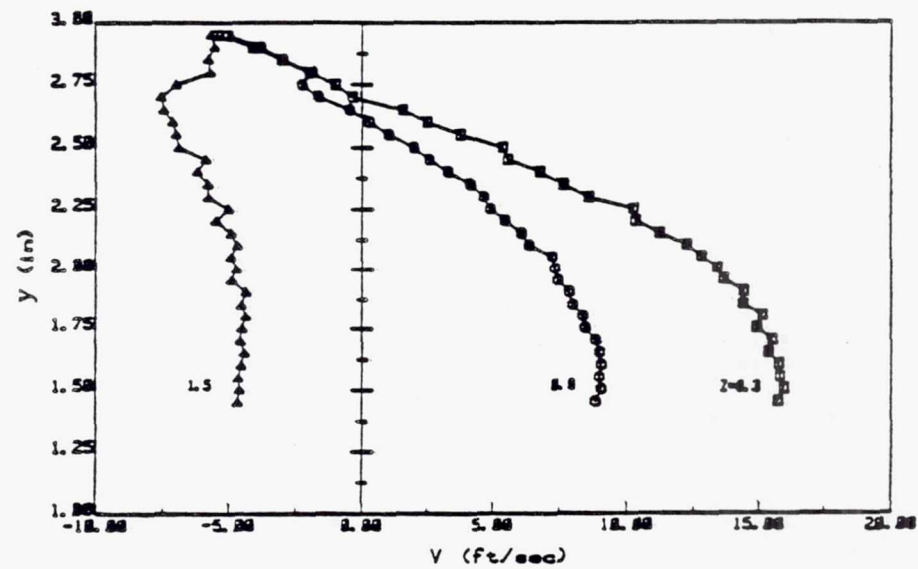
TE92-2471

Figure 3.3.2-59. Plots of u velocity at $x=6.0$ in. (scans 1 and 2).



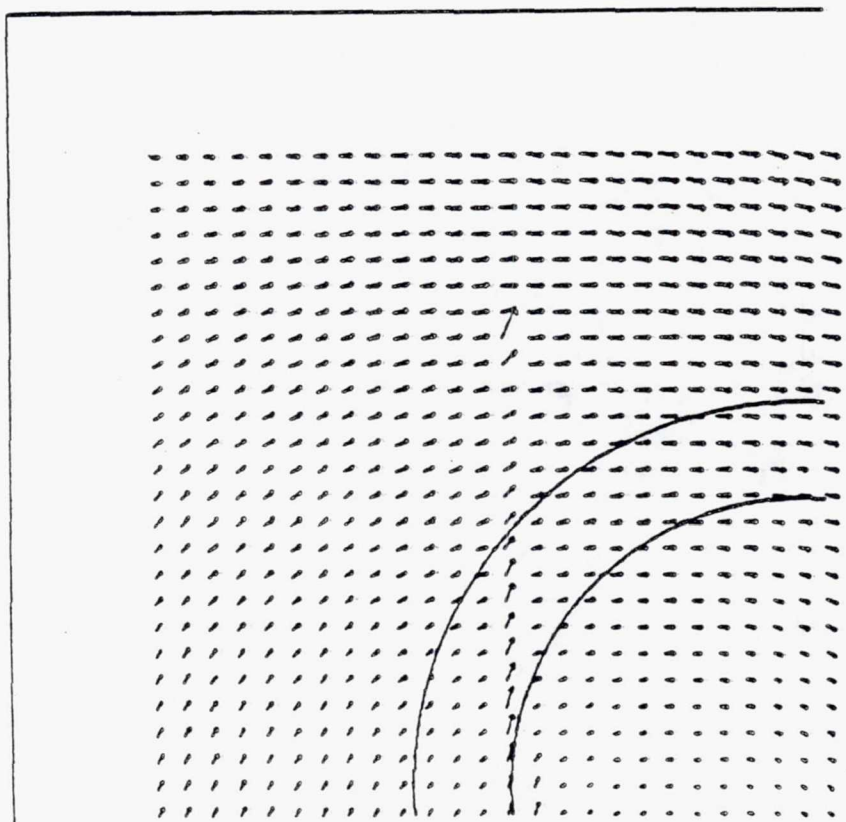
TE92-2472

Figure 3.3.2-60. Cascade plots of v and w velocities at $X=6.0$ in.



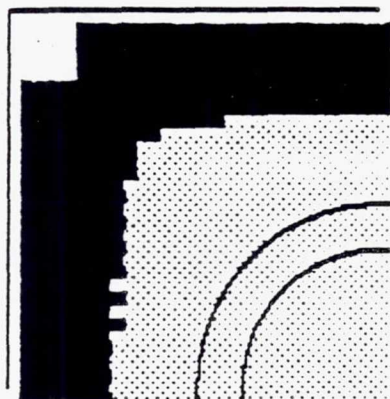
TE92-2473

Figure 3.3.2-61. Plots of v and w velocities at $x=6.0$ in.



TE92-2474

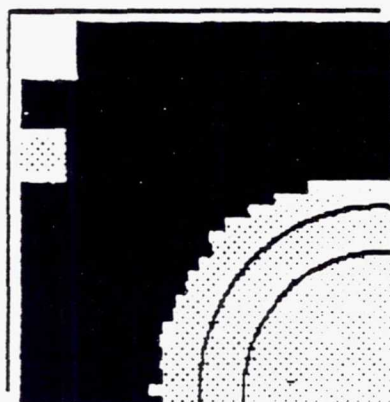
Figure 3.3.2-62. Vector plot of v and w velocities at $x=6.0$ in.



x=1.5"



x=3.0"



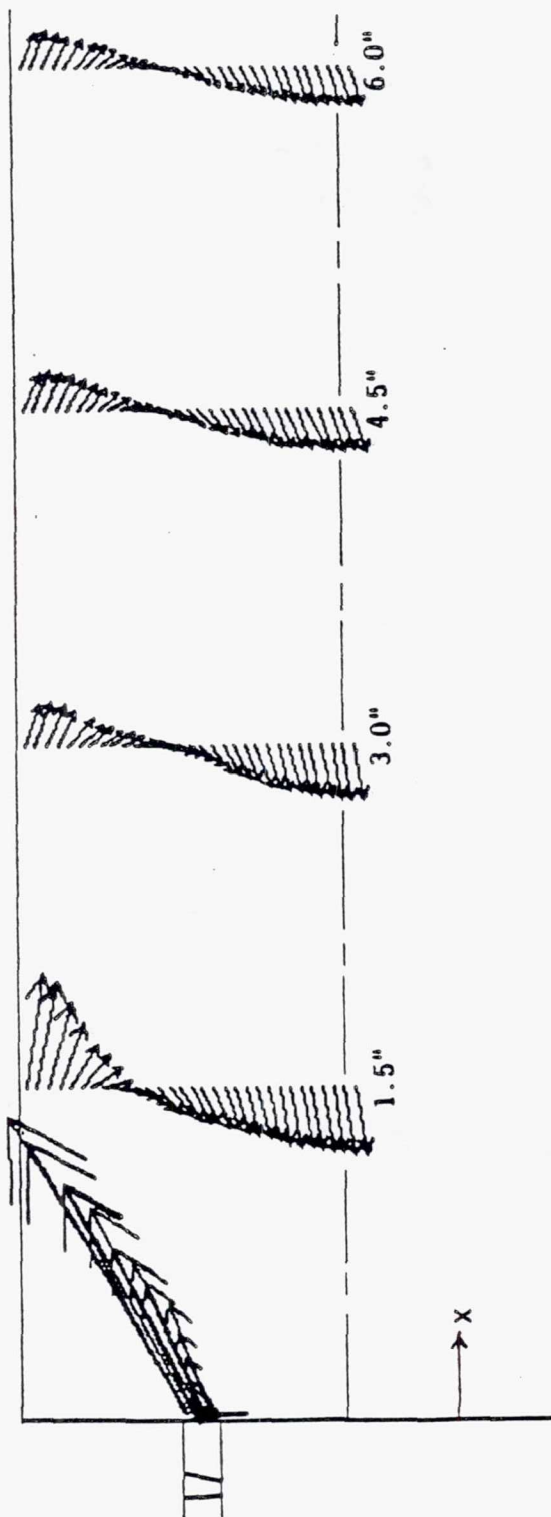
x=4.5"



x=6.0"

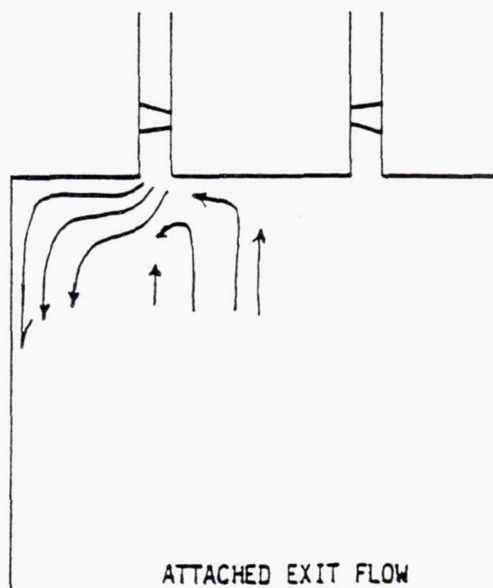
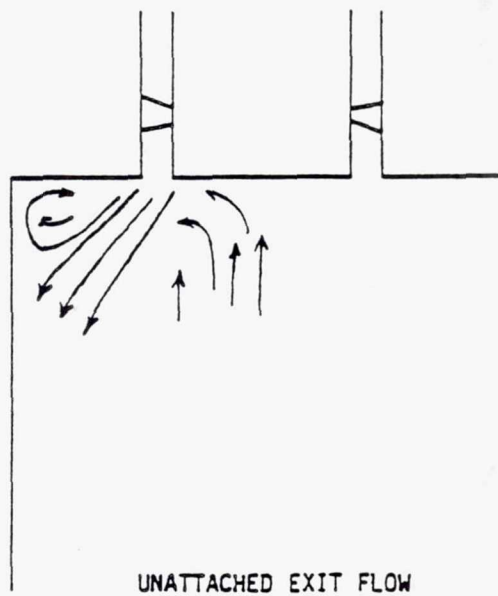
TE92-2475

Figure 3.3.2-63. Contour plots of u velocity indicating regions of reverse flow.



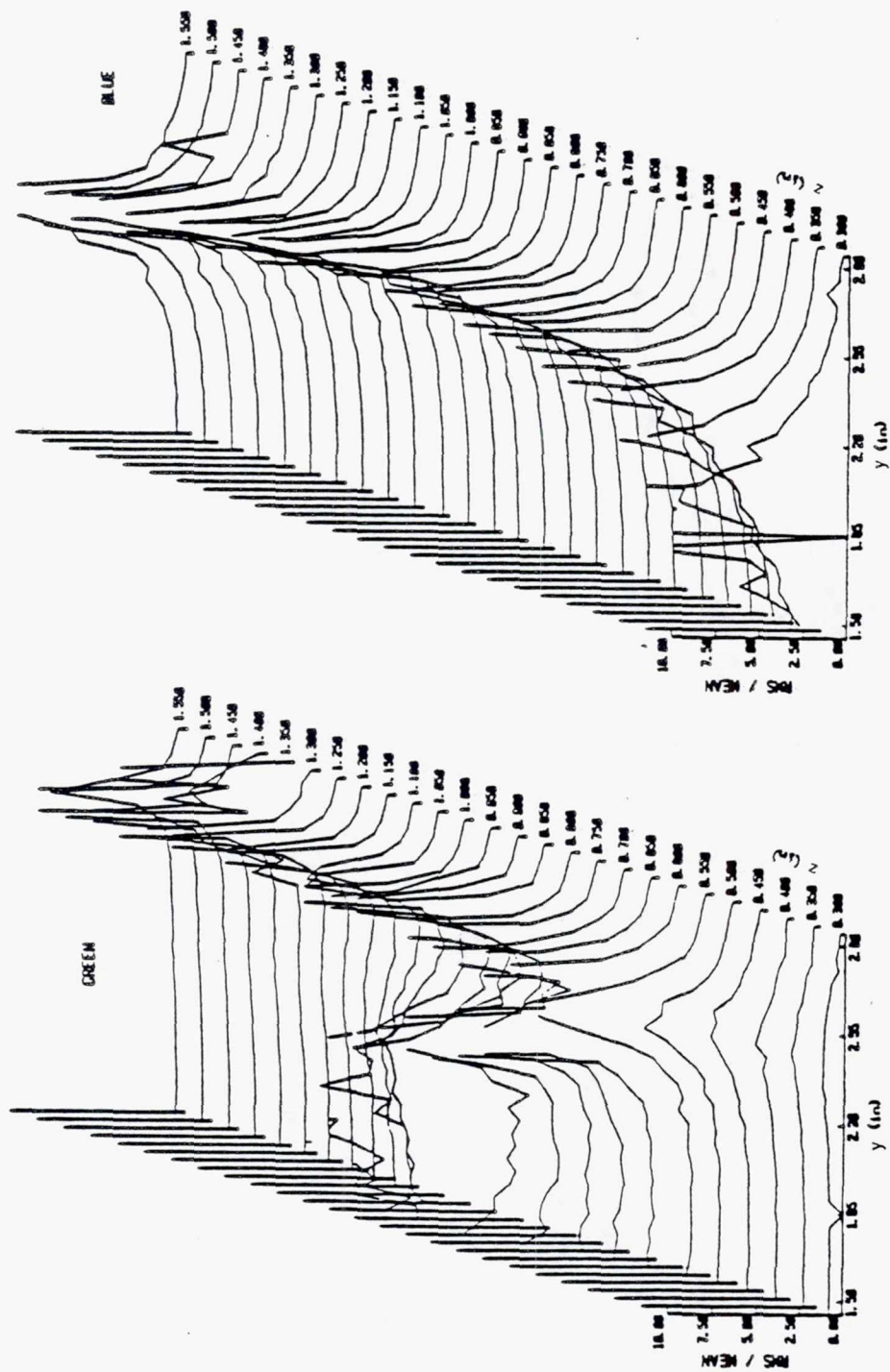
TE92-2476

Figure 3.3.2-64. Vector plot at $Z=1.5$ in.



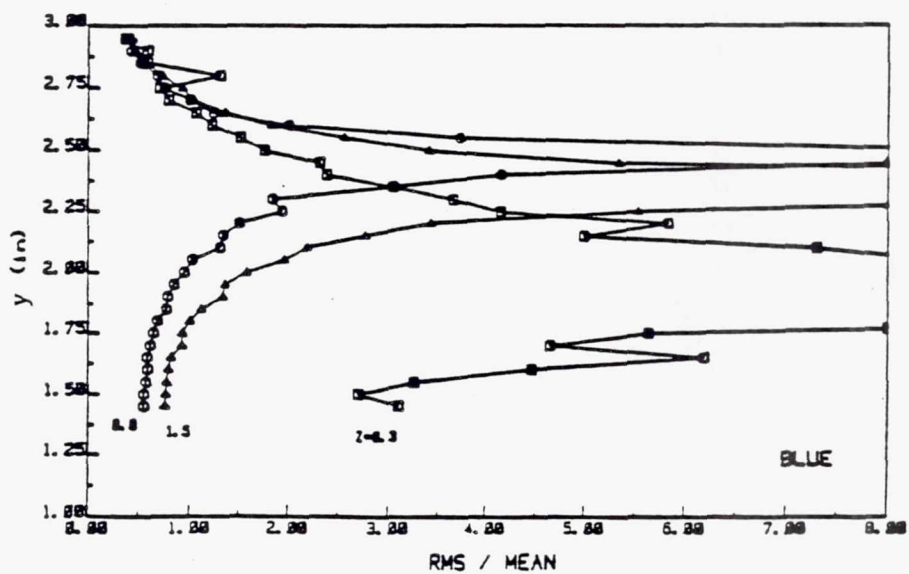
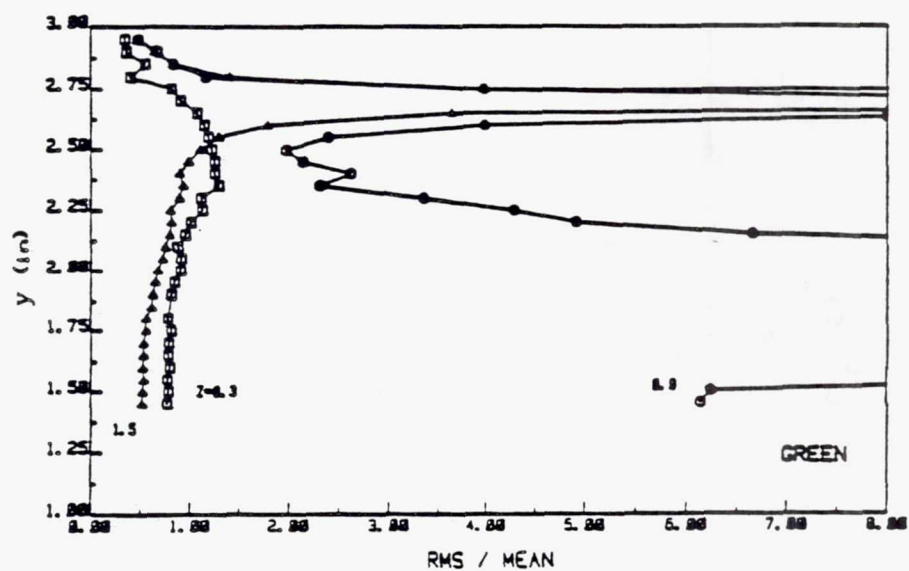
TE92-2477

Figure 3.3.2-65. Sketch of swirler exit flow regimes.



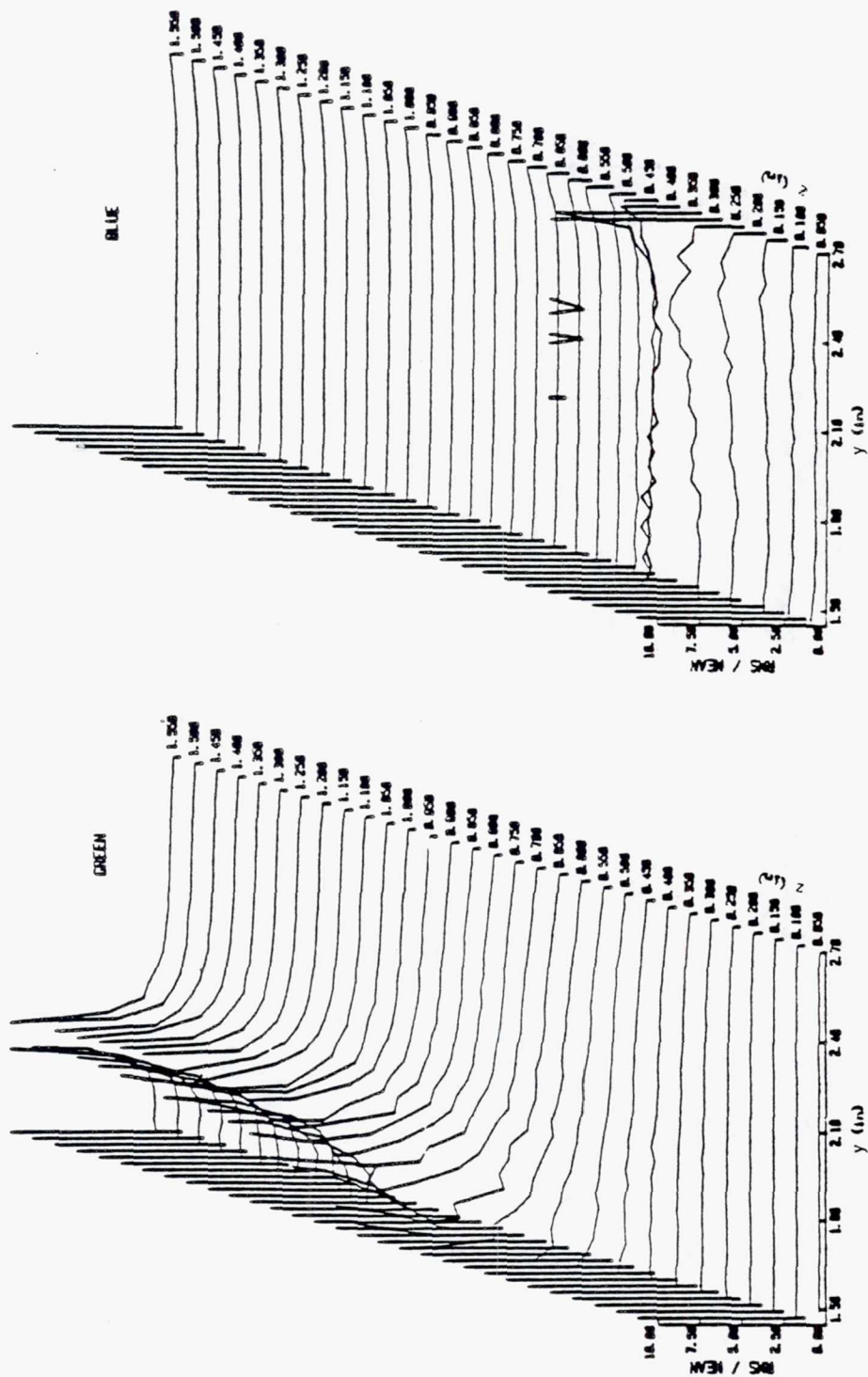
TE92-2478

Figure 3.3.2-66. Cascade plots of turbulence intensity at $x=1.5$ in. (scan 1).



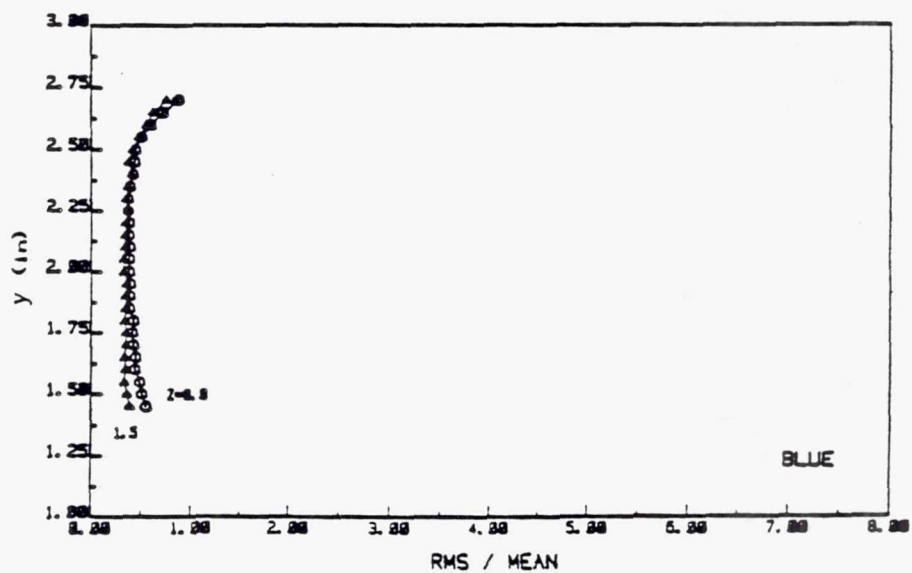
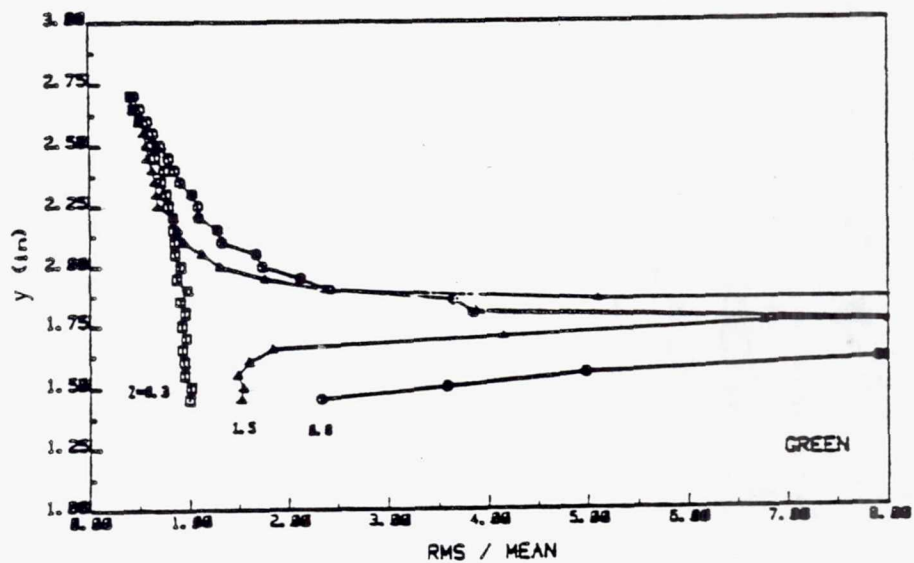
TE92-2479

Figure 3.3.2-67. Plots of turbulence intensity at x=1.5 in. (scan 1).



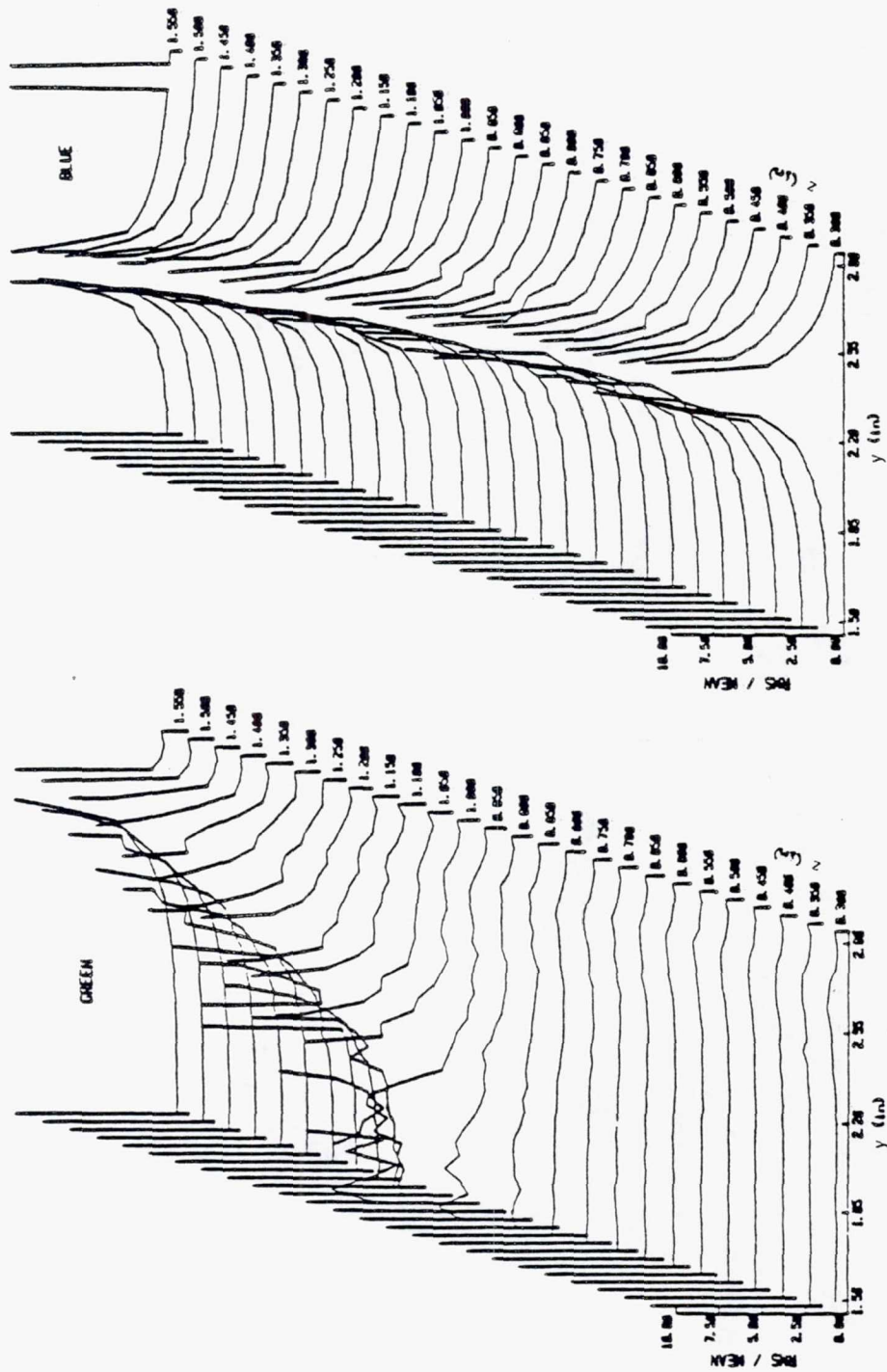
TE92-2480

Figure 3.3.2-68. Cascade plots of turbulence intensity at $x=1.5$ in. (scan 2).



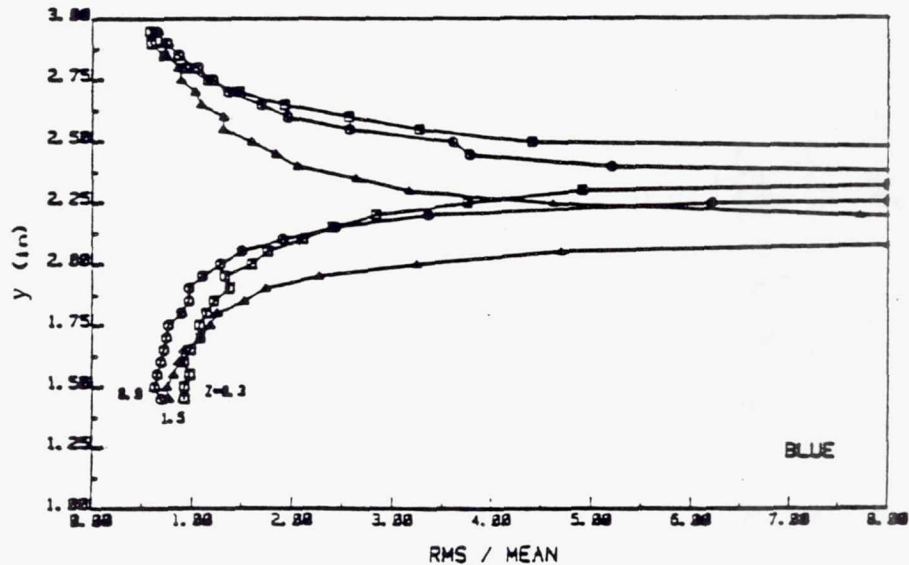
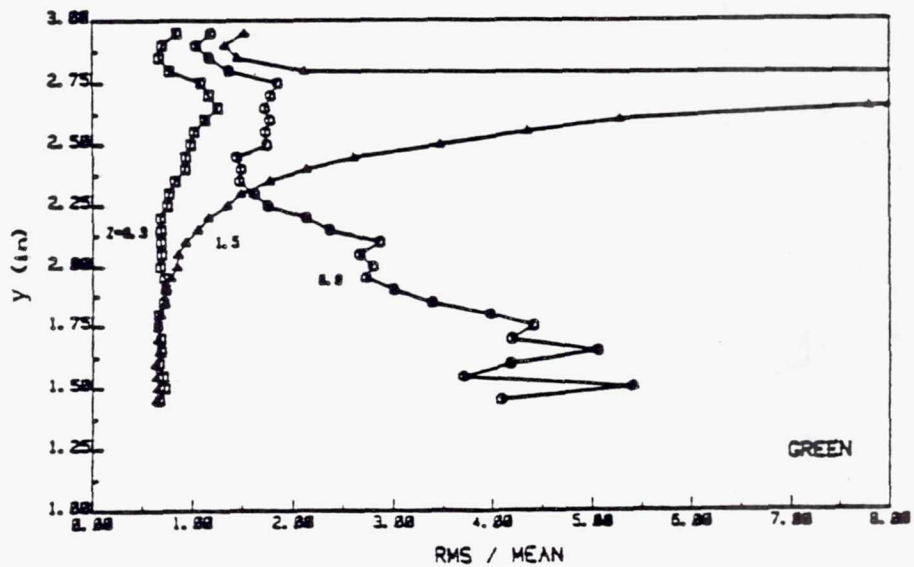
TE92-2481

Figure 3.3.2-69. Plots of turbulence intensity at $x=1.5$ in. (scan 2).



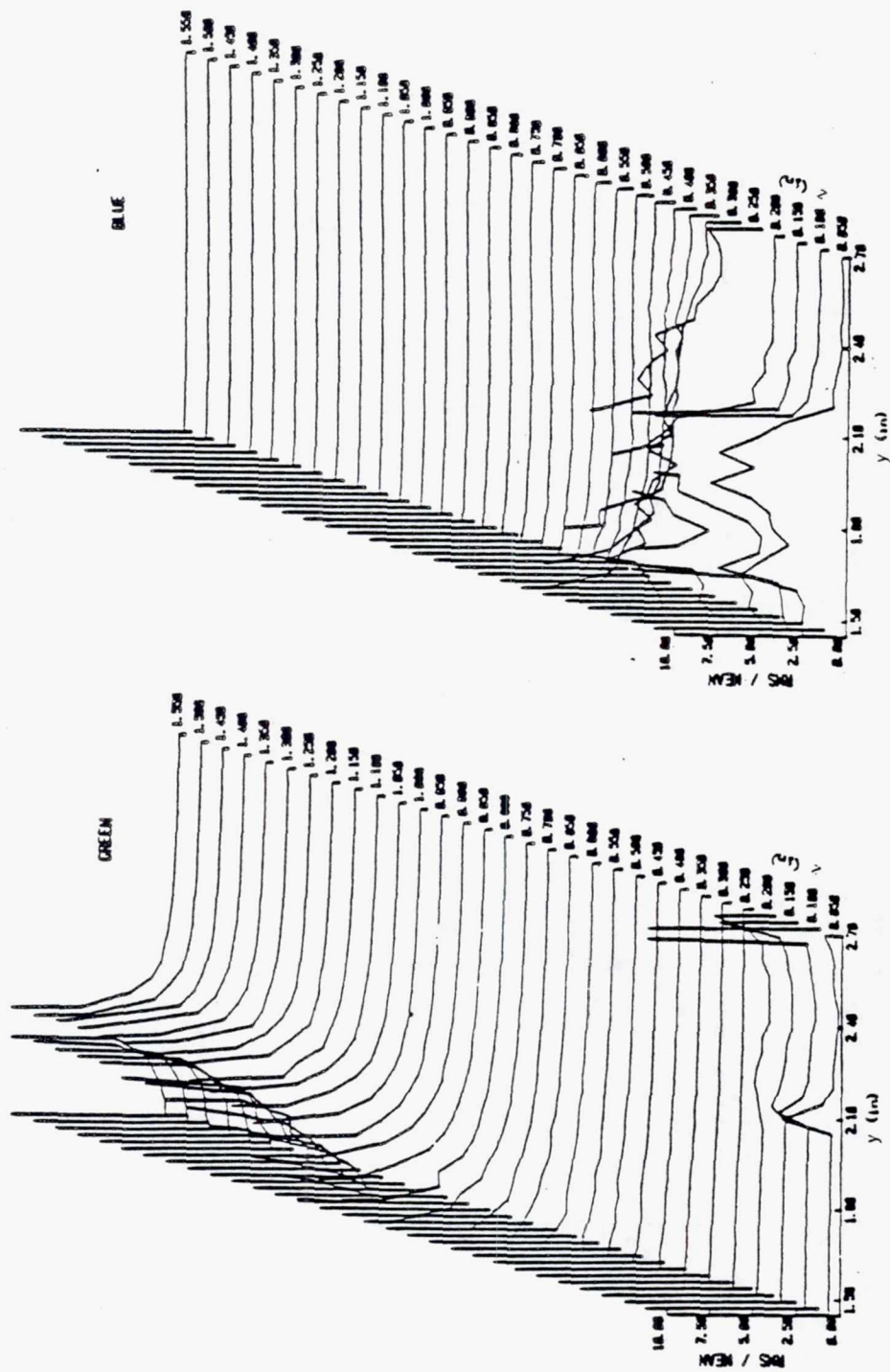
TE92-2482

Figure 3.3.2-70. Cascade plots of turbulence intensity at $x=3.0$ in. (scan 1).



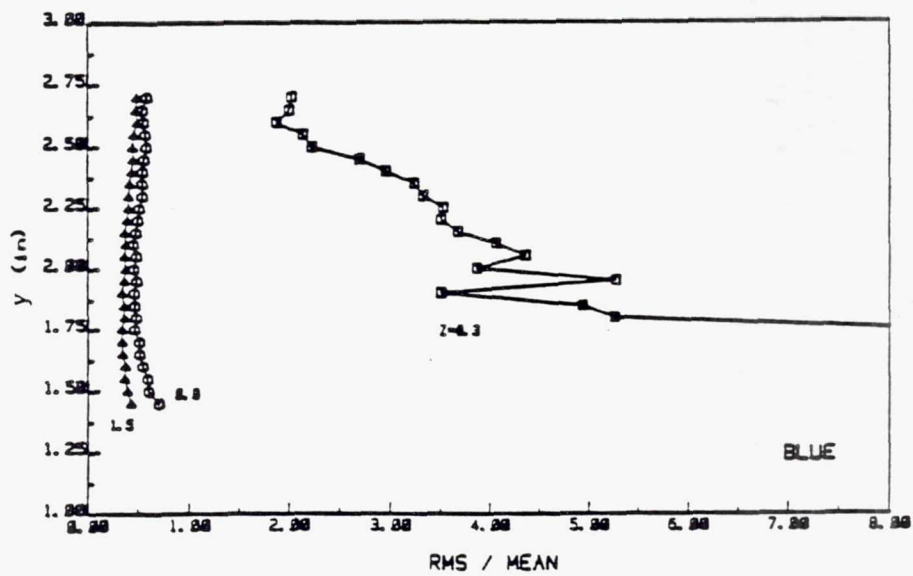
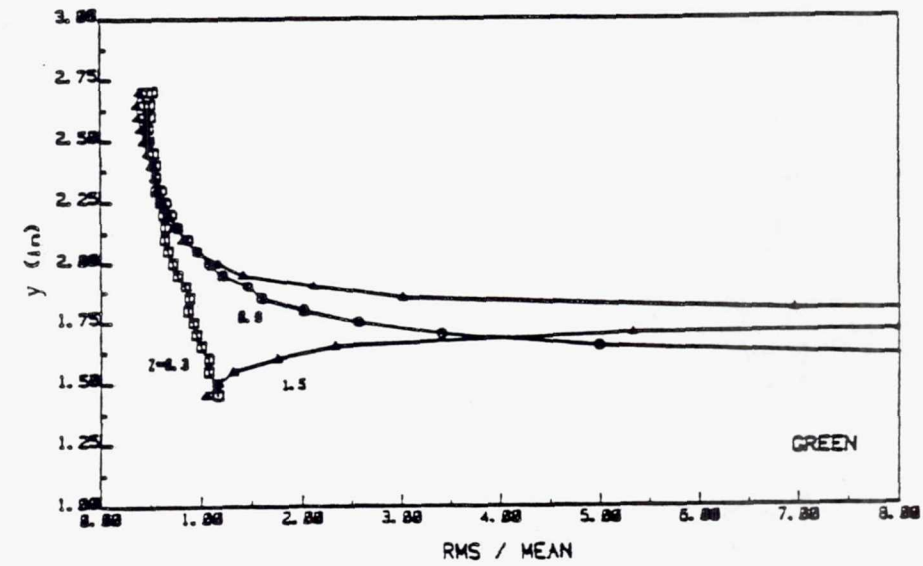
TE92-2483

Figure 3.3.2-71. Plots of turbulence intensity at x=3.0 in. (scan 1).



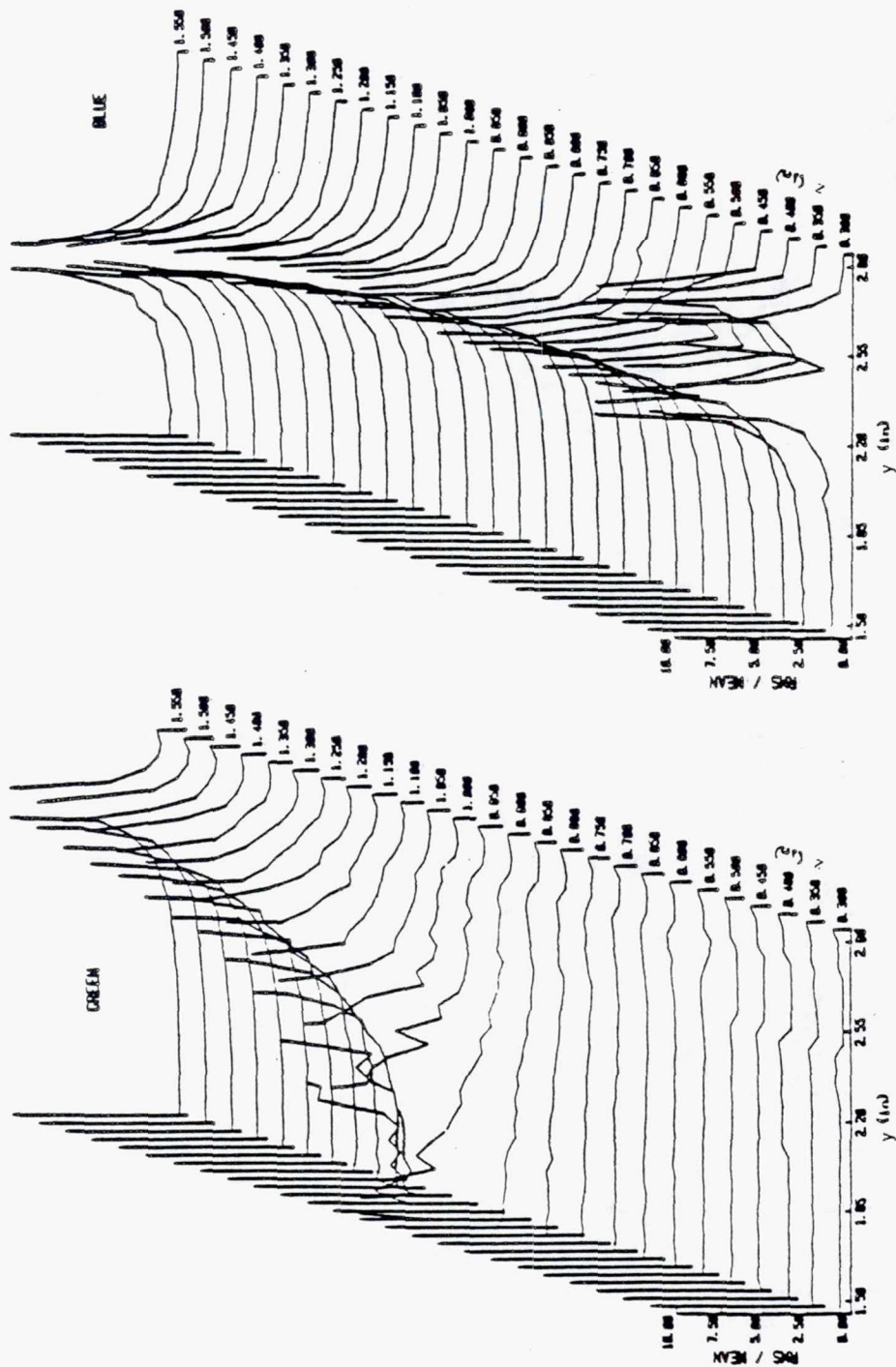
TE92-2484

Figure 3.3.2-72. Cascade plots of turbulence intensity at $x=3.0$ in. (scan 2).



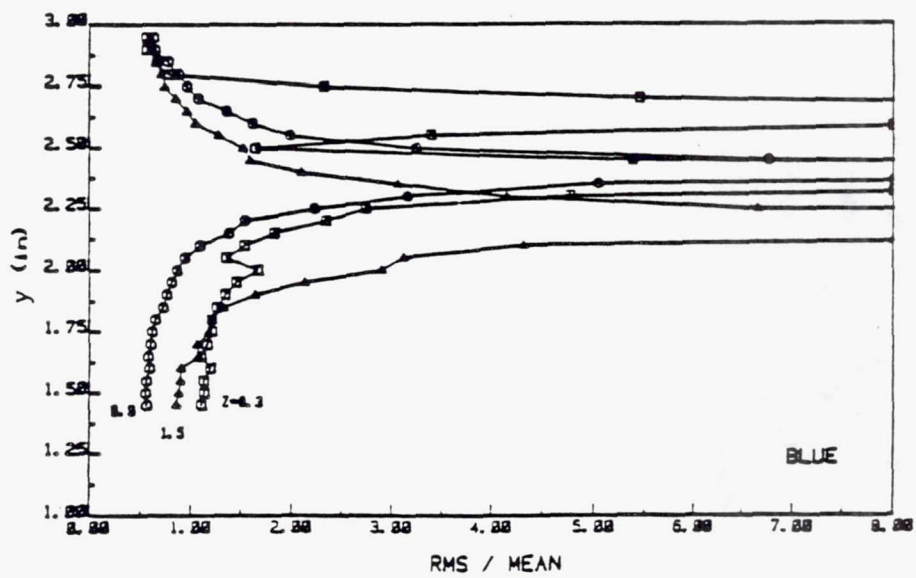
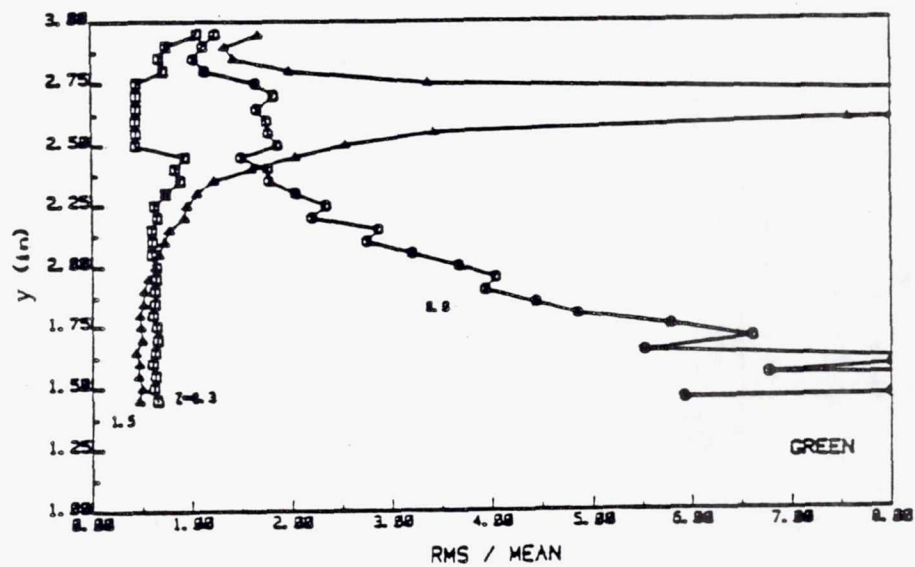
TE92-2485

Figure 3.3.2-73. Plots of turbulence intensity at $x=3.0$ in. (scan 2).



TE92-2486

Figure 3.3.2-74. Cascade plots of turbulence intensity at $x=4.5$ in. (scan 1).



TE92-2487

Figure 3.3.2-75. Plots of turbulence intensity at $x=4.5$ in. (scan 1).

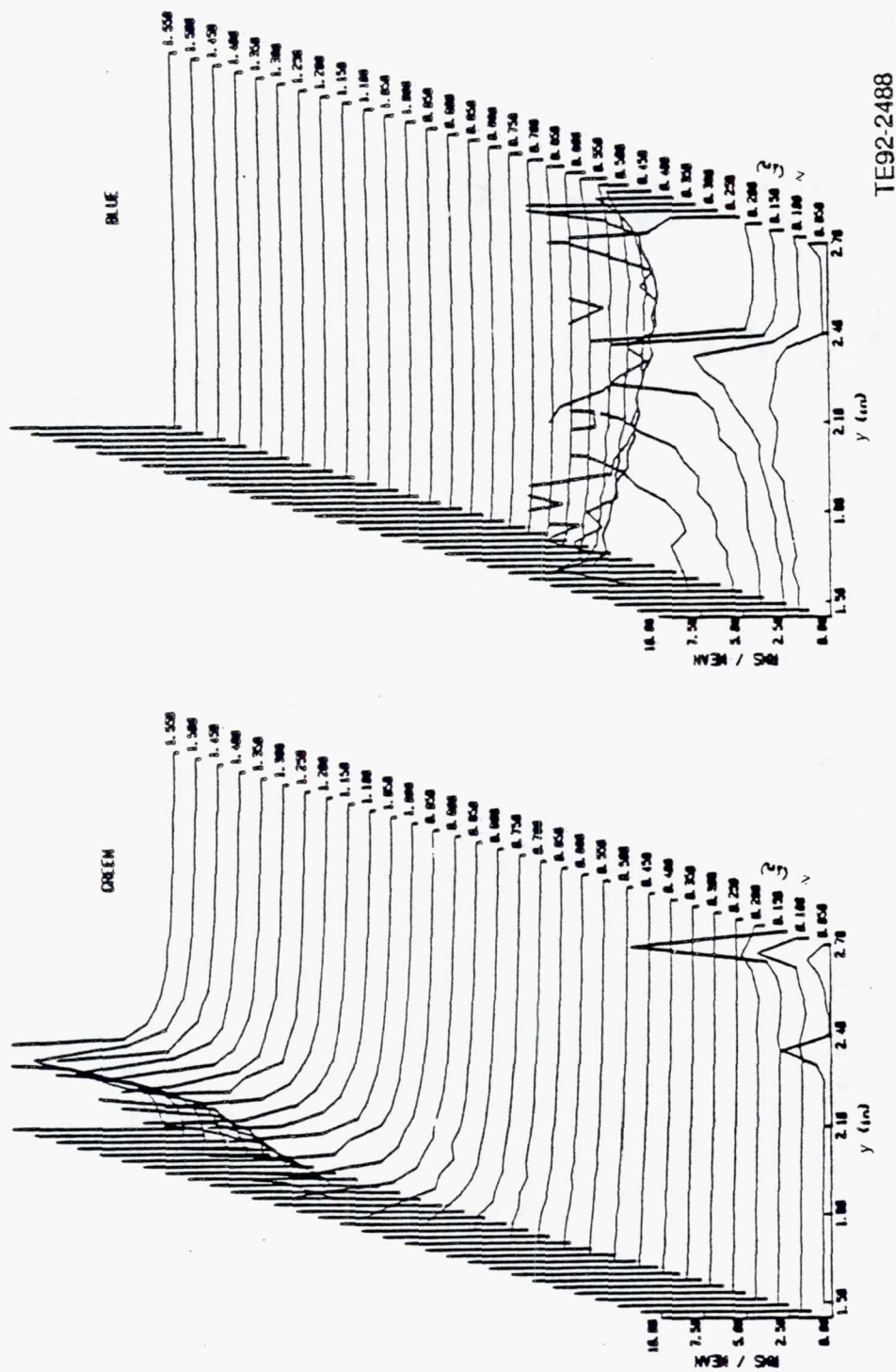
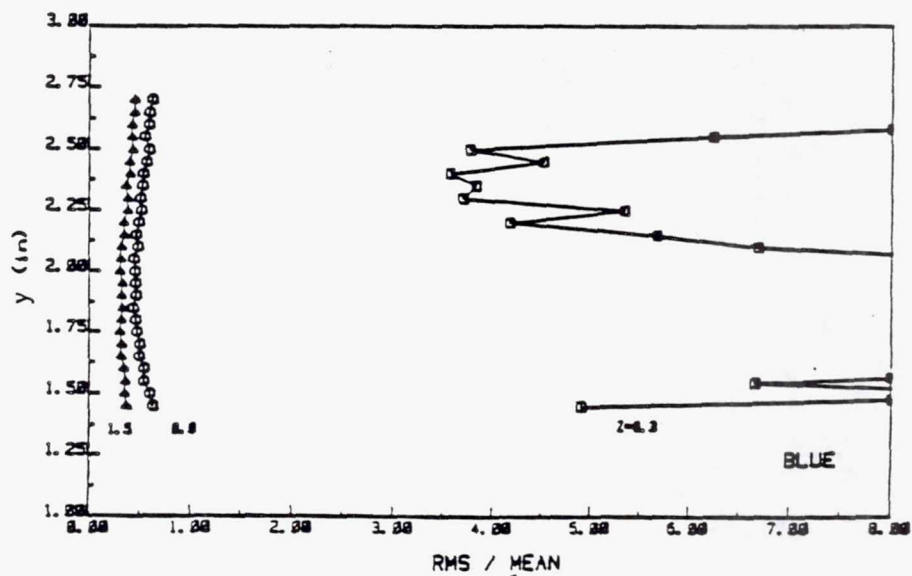
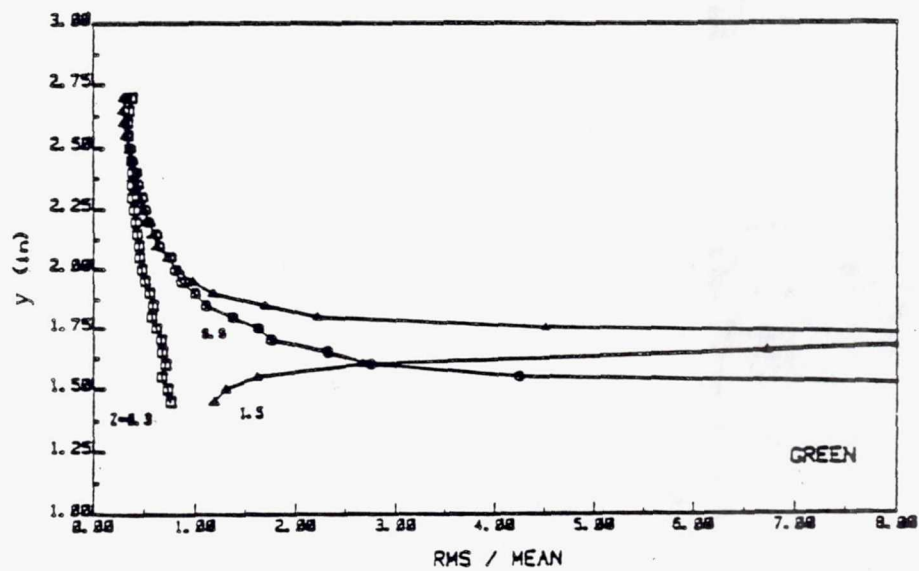
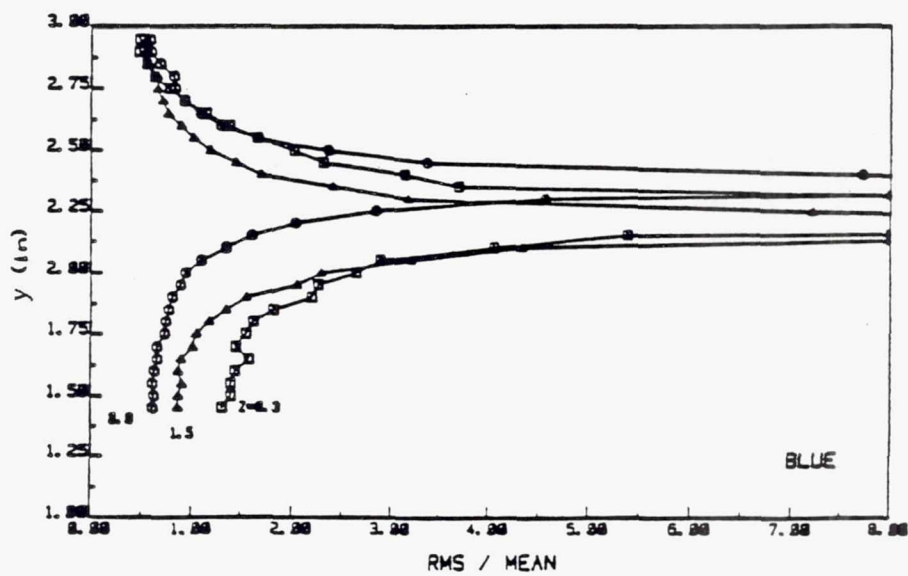
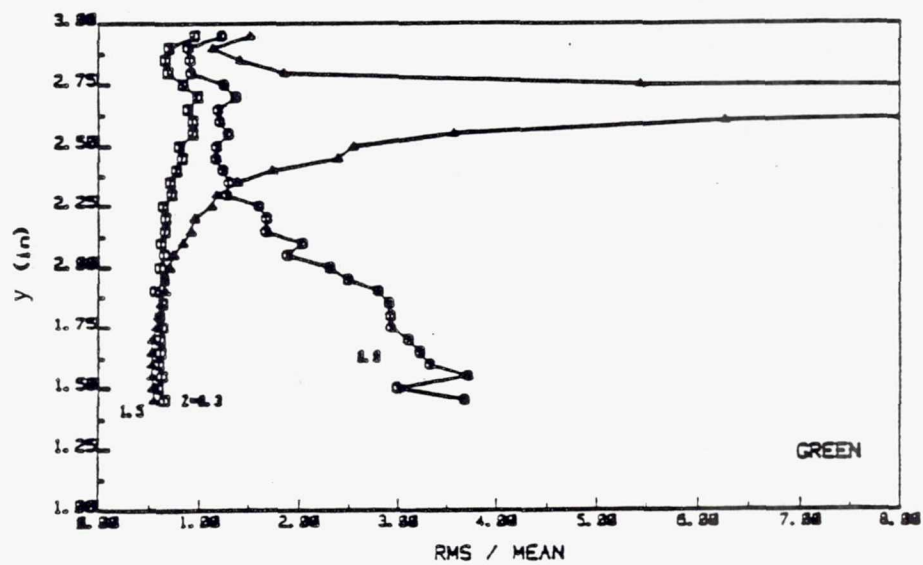


Figure 3.3.2-76. Cascade plots of turbulence intensity at $x=4.5$ in. (scan 2).



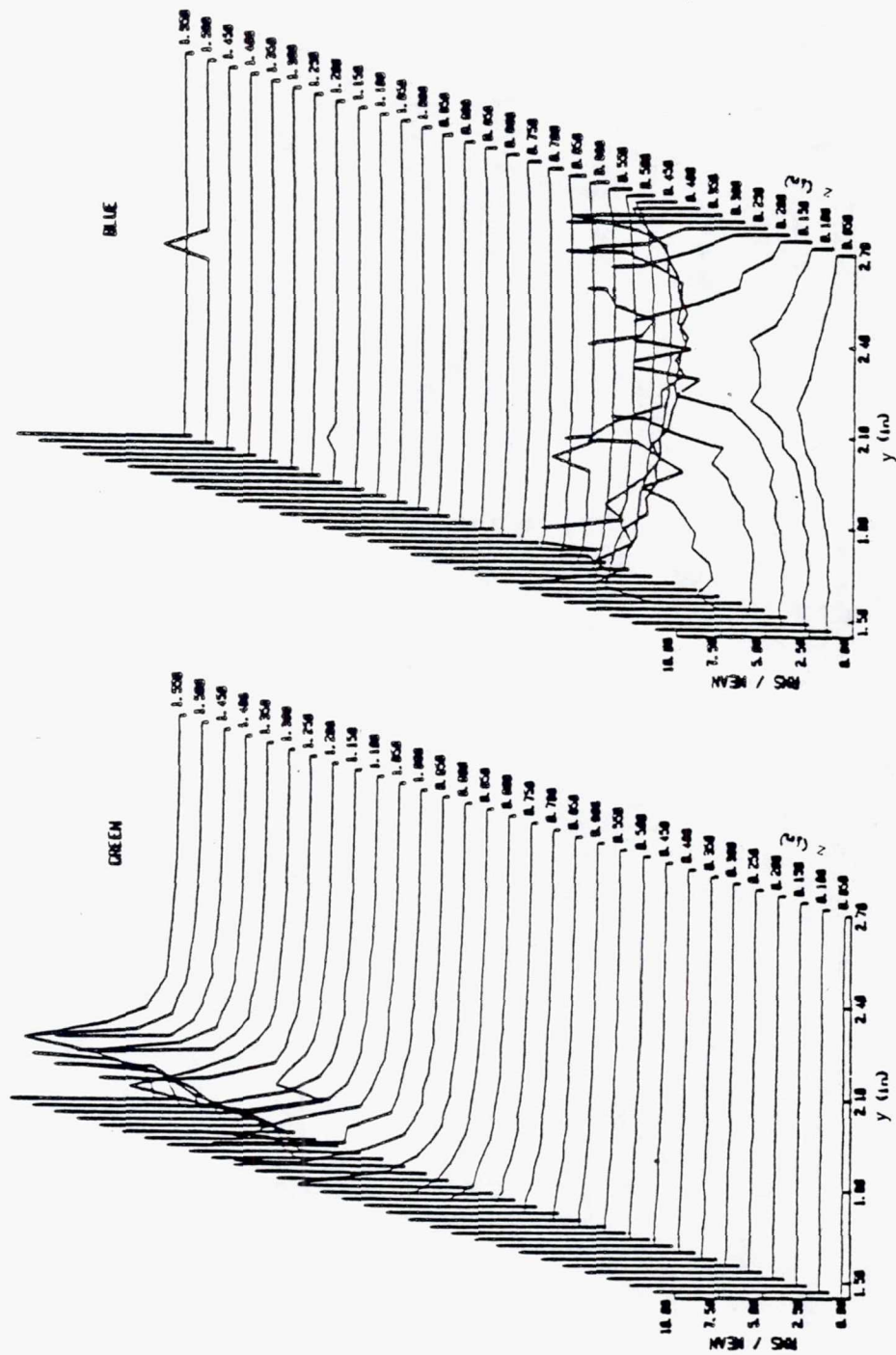
TE92-2489

Figure 3.3.2-77. Plots of turbulence intensity at $x=4.5$ in. (scan 2).



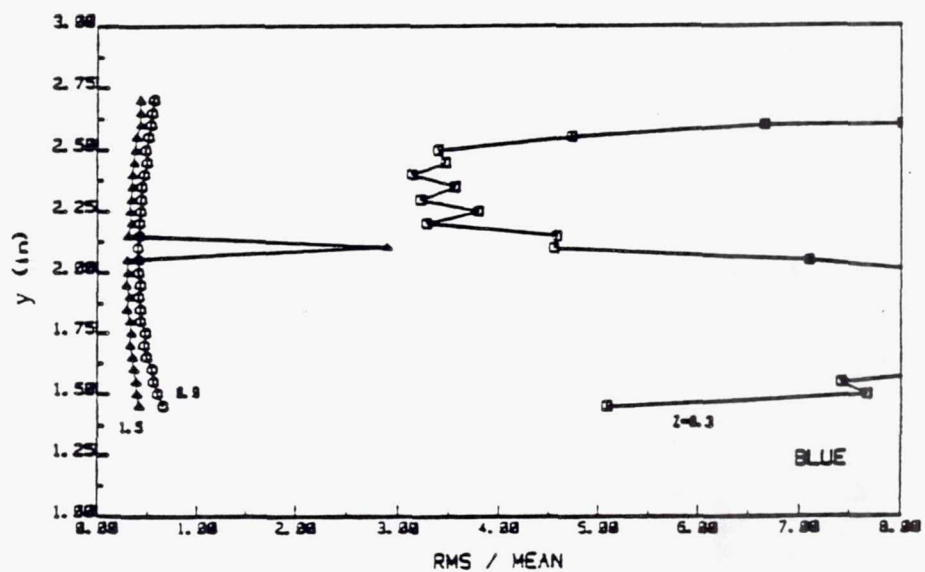
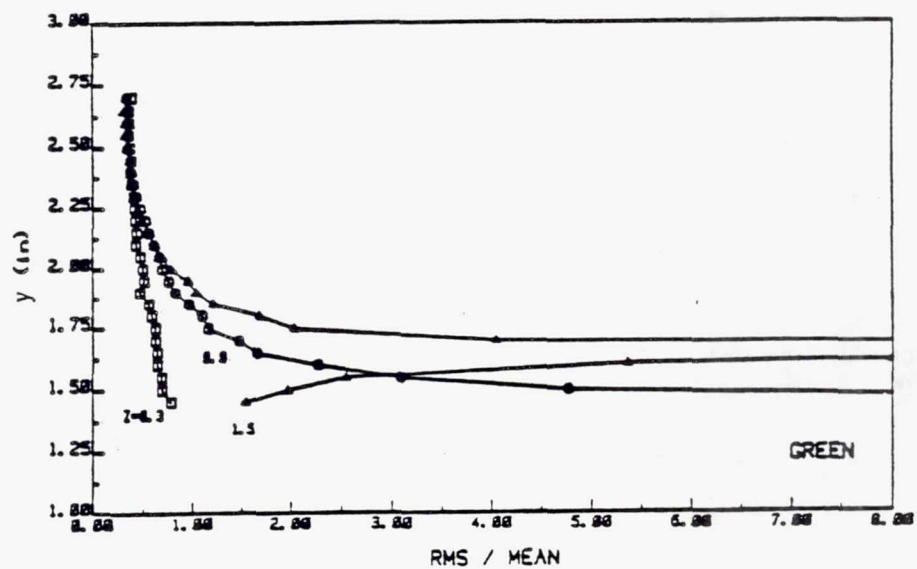
TE92-2491

Figure 3.3.2-79. Plots of turbulence intensity at x=6.0 in. (scan 1).



TE92-2492

Figure 3.3.2-80. Cascade plots of turbulence intensity at $x=6.0$ in. (scan 2).



TE92-2493

Figure 3.3.2-81. Plots of turbulence intensity at x=6.0 in. (scan 2).

3.4 FINAL RIG - INSTRUMENTATION AND DATA REDUCTION

Using the experience gained with the initial rigs, the swirling jet and the single swirler rig, a new air test rig was designed and constructed. The details of the final apparatus are described and the instrumentation, data analysis, and error analysis are presented in the next subsections.

3.4.1 Final Experimental Apparatus

Figures 3.4.1-1, 3.4.1-2, and 3.4.1-3 are three-view drawings of the three configurations of the combustor model. The annular combustor model was designed to simulate the cold flow characteristics of current gas turbine combustors. Five cells were used in its construction in order to allow for any interaction between cells and to remove wall effects. The primary zone of a combustor usually has three flows entering this region. These flows consist of air from the discharge of a compressor through swirlers in a dome wall, fuel injection through the center of the swirler, and primary air jets normal to the mean flow in the combustor. No fuel injection was used in this research.

The cross section was 15 in. wide and 3 in. high. The test section extended downstream a distance of 30 in. Each cell contained one pair of primary jets, located 1.5 in. downstream of the endplate, mounted normal to the flow from the annular jets.

Figure 3.4.1-4 shows a drawing of both annular and primary jets. Both the annular and primary jets were constructed of aluminum, and were designed with a contraction in order to provide a flat velocity profile upon entrance into the test section. The annular jet had an inlet diameter of 2.543 in. and diameter of 1.459 in. at the test section entrance. The center portion of the annular jet had a diameter of 1.084 in. at the test section entrance. This results in an annular gap of 0.1875 in. and entrance area of 0.7489 in². The primary jets were 1.375 in. in length with an inlet diameter of 1.0 in. and diameter of 0.43 in. at the test section entrance. This results in an inlet area of 0.1452 in². for each primary jet.

In order to damp out disturbances and allow uniform mixing of the seed particles before entrance into the test section, tubing was attached to the primary and annular jets. Tubes extending 10.5 in. above the machined jets were connected to all 10 primary jets. Preliminary flow visualization indicated that these tubes helped reduce unsteady displacement of the jet stagnation point. Tubes extending 9.75 in. in front of the annular jets were used mainly to provide adequate length to allow mixing of the smoke. Figure 3.4.1-5 shows a drawing of the model when annular and primary jets are attached to the model.

The exit of the combustor model was connected to a plenum chamber, which was connected to a fan. A centrifugal blower was used to draw air through the test section. Previous work performed on this model indicated that large-scale feedback from the fan existed. To eliminate these large disturbances screens and foam were placed in the last 9.5 in. of the combustor model.

3.4.2 Instrumentation

3.4.2.1 Laser Doppler Velocimeter

The LDV system used in this experiment incorporated a Spectra Physics model 165 Argon ion laser. It was configured to measure a single component of velocity using the wavelength of 4880 Angstroms, blue. Figures 3.4.2-1 and 3.4.2-2 show schematics of the LDV system used.

The transmitting optics used were made up of the DISA 55X components. In the first stage of the transmitting optics, the beams entered a beam waist which was used to adjust the beam diameters to a minimum at the probe volume. This was necessary because when beams have a minimum diameter the wavefronts are planar. The interference pattern produced by the intersection of planar waves produced an evenly spaced interference pattern across the probe volume. If the wave fronts were spherical the

resulting fringe surfaces would be distorted and an evenly spaced interference pattern would not be produced. Particles with the same velocity, but crossing different parts of the probe volume, would produce different Doppler frequencies when spherical wave fronts intersect.

A beam splitter was used next to split the single beam into two equal intensity beams. One beam stayed along the optical axis, while the second beam was translated approximately 30 mm from the optical axis.

The frequency of the beam along the optical axis was acousto-optically shifted by 40 MHz using a Bragg cell. The Bragg cell caused the fringes in the probe volume to move at 40 MHz. With fringe movement in the probe volume, the velocity directions of the particles crossing the probe volume could be detected. A frequency of 40 MHz plus the Doppler frequency resulted when particles were moving in the opposite direction of fringe movement, and a frequency of 40 MHz minus the Doppler frequency resulted for particles moving with the fringe movement. In addition to detection of velocity directions, the Bragg cell helped correct for angle or fringe bias in the velocity measurements.

The final set of optics in the transmitting optics package was the beam translator. The beam translator moved the off axis beam back towards the optical axis. This was necessary in order to allow entrance into the beam expander. Also, adjustments in the beam translator allowed the beams to be focused to a common intersection point.

Upon exit from the beam translator, a beam expander was used to increase the beam diameters by a ratio of 3.75 to 1. The purpose of increasing the beam diameters was to reduce the size of the probe volume. With a smaller probe volume, gradient bias was reduced and greater resolution of the flowfield could be obtained by using smaller grid spacing. The radius and length of the probe volume are given by Equations 17 and 18.

$$b_o = \frac{f \cdot \lambda}{b \cdot \pi} \quad (17)$$

$$l = \frac{2b_o}{\sin\left(\frac{\theta_b}{2}\right)} \quad (18)$$

where:

- b = radius of input beam
- f = focal length of field lens
- λ = wavelength of laser beam
- θ_b = angle between beams

A field lens, made up of two lenses, focused the two incoming beams to a common point. Focal lengths for each lens were $f_1 = 30$ in. and $f_2 = 48$ in. From lens theory, the effective focal length of the two lenses can be expressed by Equation 19.

$$f = \frac{1}{\left[\frac{1}{f_1} + \frac{1}{f_2} \right]} \quad (19)$$

Therefore, the field lens had a focal length of 18.46 in. Table 3.4-I lists parameter settings of the LDV system used for this research.

Table 3.4-I.
LDV parameter settings.

<u>Optical system settings</u>	
wavelength	488 nm = 1.601×10^{-6} ft
focal length of lens	18.46 in.
diameter of input beam	0.175 in.
angle between beams (average)	5 deg
length of probe volume (average)	0.056 in.
diameter of probe volume (average)	0.0027 in.
frequency shift	40 MHz
<u>Data collection settings</u>	
mode of operation	N burst mode
filter settings	20 MHz low pass 2 MHz high pass
number of fringes per signal	16
comparator	1 %
sample size	10,000 samples
data rate	10,000 to 90,000 samples/sec
sample rate	1000 samples/sec
<u>Flow system parameters</u>	
velocity range	$-35 \text{ ft/sec} \leq U \leq 35 \text{ ft/sec}$
seed particles	propylene glycol
seed particle size (average)	2 microns

The receiving optics used consisted of different elements made by DISA. The optics were used in forward scatter, which ensures a stronger signal than in back scatter. Scattered light from the probe volume was focused to a point by a receiving lens. Next, a beam expander working in reverse reduced the diameter of the light from the receiving lens, allowing entrance into a spatial filter.

In order to reduce extra light from reflections, room light, or scattered light not from the probe volume, a spatial filter was used. This filter was the same size as the probe volume. The light passing through the spatial filter entered a photomultiplier. The photomultiplier was used to convert light intensities into electrical signals proportional to the intensity of the light. The output of the photomultiplier was then sent to a signal processing unit.

3.4.2.2 Data Acquisition System

The output signal from the photomultiplier contains a signal that has been shifted by 40 MHz plus or minus the Doppler frequency from a measurement. This signal must first be frequency shifted to allow the processing electronics to handle the signal. A DISA 55N12 frequency mixer was used to mix the signal with a frequency between 31 MHz to 49 MHz. See Figure 3.4.2-3 for a schematic of the data acquisition system.

After frequency mixing, the signal was sent to a TSI model 1980 counter-type signal processor. This signal first entered a model 1984 input conditioner where high and low pass filtering occurred to remove the pedestal or DC component from the signal and to remove any high frequency noise. In addition, gain adjustment and minimum cycles/burst settings were set in the input conditioner. The cycles/burst setting was used to determine the number of fringes a particle must traverse in the probe volume before that signal is accepted by the processing electronics as a valid data point. A setting of 16 cycles/burst was used for all measurements. This eliminated data from particles that passed through the edge of the

probe volume and crossed only a few fringes. The filtered output jack was connected to a Hewlett Packard spectrum analyzer to monitor the Doppler frequency of the signal.

Output of the input conditioner was sent to a model 1985 timer for further analysis. A percent comparison setting is used to make a comparison between the time for N cycles and N/2 cycles. Measurements were made with a 1% setting, which ensured an actual 0.8% comparison between N and N/2 cycles (the time for 16 and 8 cycles must be within 0.8% for the data point to be accepted). Additionally, settings for the exponent and setting manual/auto ranging on the exponent was available. The data ready jack provided a 0.6 microsecond pulse every time a new data point is validated. This was connected to a counter to determine the data rate. A monitor output jack is connected to a Tektronix 215A oscilloscope in order to observe validated data.

Data were output to a PC's Limited microcomputer through digital outputs on the timer unit. In addition to processing the data, the computer controlled the position of the probe volume within the test rig via a Metrobyte Das20 A/D board. Table movement commands were carried out by three stepper motors allowing 3-D movement of the probe volume. A laser table contained two directions of movement, where the third direction of movement was accomplished by movement of the field lens. Probe volume position in the test rig was read into the computer by using an Acu-Rite III digital readout system. A scale attached to each axis of the table provided position information. Each scale had an accuracy of 0.0005 in., which facilitated accurate repositioning of the probe volume for repeated runs.

Velocity bias was caused by the arrival rate of particles in the probe volume being dependent on the flow velocity. A burst mode signal processor was used in this research, which operated on the signals generated by single particles passing through the probe volume. Therefore, particles passed through the probe volume more often when the flow velocity was high and less often when the flow velocity was low. The result of simply averaging these signals would have caused the mean velocity to be biased high and the rms velocity to be biased low.

Many different methods are presently available to correct for velocity bias. Equal time sampling was used to eliminate the velocity bias for this research. Roesler (1980) presents a study done on velocity bias and shows that this velocity bias may be eliminated by using equal time sampling. Data rates of 100 times the sampling rate were recommended to ensure equal time sampling, however it was shown that data rates of 10 times the sampling rate provided equal time sampling. Data rates between 10,000 to 90,000 samples per second were present for this study, with average rates of 45,000 samples per second. A sampling rate of 1,000 Hz was used providing data rates 10 to 90 times the sampling rate. With these data rates, equal time sampling should have existed between samples. A total of 10,000 samples were used to determine mean velocities for each point.

3.4.2.3 Velocity Measurements and Statistics Calculation

Since only a one component LDV system was used to determine U, V, U', V', U'V', and K, measurements in the coordinate directions, only to determine these quantities would be in error. Measurements needed to be taken at +/- 45 deg to the coordinate axes in the plane of each component. By taking measurements at +/- 45 deg both the U' and V' velocity fluctuations contributed to the instantaneous Doppler frequency.

Referring to Figure 3.4.2-1 velocity measurements at +/- 45 deg were

$$\overline{U_{+45}} = \frac{1}{\sqrt{2}} (\overline{U} + \overline{V}) \quad (20)$$

$$\overline{U_{-45}} = \frac{1}{\sqrt{2}} (\overline{U} - \overline{V}) \quad (21)$$

adding Equations 20 and 21, gives

$$\overline{U_{+45}} + \overline{U_{-45}} = \frac{2}{\sqrt{2}} \overline{U} \quad (22)$$

$$\overline{U} = \frac{1}{\sqrt{2}} (\overline{U_{+45}} + \overline{U_{-45}}) \quad (23)$$

Subtracting Equation 21 from 20

$$\overline{U_{+45}} - \overline{U_{-45}} = \frac{2}{\sqrt{2}} \overline{V} \quad (24)$$

$$\overline{V} = \frac{1}{\sqrt{2}} (\overline{U_{+45}} - \overline{U_{-45}}) \quad (25)$$

The instantaneous velocity, U , is made up of a mean term, \overline{U} , and a fluctuation term, U' . The time average of the square of Equation 20 is

$$\overline{(U_{+45} + U'_{+45})^2} = \frac{1}{2} \overline{((\overline{U} + U') + (\overline{V} + V'))^2} \quad (26)$$

expanding Equation 25 results in

$$\begin{aligned} \overline{U_{+45}^2} + \overline{U'_{+45}^2} + 2\overline{U_{+45}U'_{+45}} &= \frac{1}{2} \overline{((\overline{U} + U')(\overline{U} + U') + (\overline{V} + V')(\overline{V} + V') + 2(\overline{U} + U')(\overline{V} + V'))} \\ &= \frac{1}{2} \overline{\{ \overline{U}^2 + \overline{U'^2} + 2\overline{UU'} + \overline{V}^2 + \overline{V'^2} + 2\overline{VV'} + (\overline{UV} + \overline{UV'} + \overline{UV'} + \overline{VV'}) \}} \end{aligned} \quad (27)$$

Since

$$\overline{U_{+45}^2} = \frac{1}{\sqrt{2}} (\overline{U} + \overline{V}) \quad U'_{+45} = \frac{1}{\sqrt{2}} (U' + V') \quad (28)$$

The average of the product of these terms is

$$2\overline{U_{+45}U'_{+45}} = \overline{UU'} + \overline{UV'} + \overline{VU'} + \overline{VV'} \quad (29)$$

Therefore, terms on the right side of Equation 27 cancel resulting in

$$\overline{U_{+45}^2} + \overline{U'_{+45}^2} = \frac{1}{2} (\overline{U^2} + \overline{U'^2} + \overline{V^2} + \overline{V'^2} + 2\overline{UV} + 2\overline{UV'}) \quad (30)$$

Squaring the mean of Equation 20 results in

$$\overline{U_{+45}^2} = \frac{1}{2} (\overline{U^2} + 2\overline{UV} + \overline{V^2}) \quad (31)$$

Subtracting Equation 31 from Equation 30 results in

$$\overline{U'_{+45}^2} = \frac{1}{2}(\overline{U'^2} + 2\overline{UV'} + \overline{V'^2}) \quad (32)$$

A similar result can be achieved by using the -45 deg component.

$$\overline{U'_{-45}^2} = \frac{1}{2}(\overline{U'^2} - 2\overline{UV'} + \overline{V'^2}) \quad (33)$$

By subtracting Equation 33 from Equation 32 a relation for the Reynolds shear stress term in the xy plane results.

$$\overline{UV'} = \frac{1}{2}(\overline{U'_{+45}^2} - \overline{U'_{-45}^2}) \quad (34)$$

By adding Equation 33 to Equation 34 a relation for the rms velocities in the two coordinate directions and the +/- 45 deg directions results.

$$\overline{U'^2} + \overline{V'^2} = \overline{U'_{+45}^2} + \overline{U'_{-45}^2} \quad (35)$$

Since measurements have been made along +/- 45 deg directions and the horizontal coordinate direction, U, an expression for the rms velocity in the vertical coordinate direction can be found.

$$\overline{V'^2} = \overline{U'_{+45}^2} + \overline{U'_{-45}^2} - \overline{U'^2} \quad (36)$$

The 2-D turbulent kinetic energy term can now be calculated by

$$K = \overline{U'^2} + \overline{V'^2} \quad (37)$$

The results of Equations 25, 34, 36, and 37 are used to calculate the quantities of interest.

In order to allow measurements at +/- 45 deg, the transmitting optics had to be rotated about the optical axis. This rotation limited the portion of the rig that could be measured due to beam interference with the edges of the rig resulting in no probe volume formation. Vertical travel of the probe volume was limited between 0.5 in. $\leq y \leq$ 2.5 in.

Orientation of the beams within the rig is seen in Figure 3.4.2-5. The beam located on the optical axis was aligned parallel to the lower wall of the test rig for each measurement. This orientation made the measurements taken not exactly along the axis intended. Figure 3.4.2-6 shows a sketch of measurements taken. Since the beam angle was approximately 5 deg, the cosine of the half angle, 2.5 deg, is 0.999, indicating that negligible amount of error occurs in the measurements.

From the Doppler frequency received from the signal processor computations were done to calculate a mean and rms velocity. For each data point reported an average of 10,000 samples taken at 1,000 Hz sampling frequency was used to determine the statistics. The mean velocity was calculated by using the equation

$$\overline{U} = \frac{\sum_{i=1}^N U_i}{N} \quad (38)$$

where

N = the number of samples taken
 U_i = the instantaneous velocity

The rms velocity was calculated using

$$U_{rms} = \left[\frac{\sum_{i=1}^N U_i^2 - \frac{\sum_{i=1}^N U_i \sum_{i=1}^N U_i}{N}}{N} \right]^{\frac{1}{2}} \quad (39)$$

3.4.2.4 Error Analysis

The use of an LDV for velocity measurements has an advantage of being nonintrusive to the flowfield. One disadvantage is that care must be taken processing data in order to avoid statistical bias problems that exist with the use of an LDV system. This subsection will attempt to identify some possible causes of errors that accompany the use of an LDV system and estimate the uncertainty of measurements reported in this thesis.

3.4.2.4.1 Sources of Statistical Bias

Velocity bias occurs due to the arrival rate of particles in the probe volume being dependent on the flow velocity. A burst mode signal processor was used in this research, which operates on the signals generated by single particles passing through the probe volume. Therefore, particles passed through the probe volume more often when the flow velocity was high and less when the flow velocity was low. The result of simply averaging these signals would have caused the mean velocity to be biased towards high values and the rms velocity to be biased toward low values.

Many different methods were available to correct for velocity bias. This research used equal time sampling to eliminate the velocity bias. Roesler (1980) presents a study done on velocity bias and shows that this velocity bias may be eliminated by using equal time sampling. Data rates for the present study varied from 10,000 to 90,000 samples per second and a sampling rate of 1,000 Hz was used. Data rates remained 10 to 90 times the sampling rate. With these data rates, equal time should have existed between samples.

Filter bias occurs because of the tendency of real systems to have measurement efficiency dependent on the flow velocity. If flow velocities produce a frequency outside of the processor's frequency range the particle will not be processed. A biased average exists if Doppler frequencies are outside the filter settings, since these frequencies are not be processed. For this research, velocity ranges were between +/- 35 ft/sec. The frequencies produced by these particles were well within the frequency response of the processor, and the filter settings were set to have a flat response in these frequencies.

Angle or fringe bias is caused by the inability of processors to measure all velocities at all angles. Counter processors use a preset number of fringes that must be crossed by a particle before a signal is accepted as valid. Therefore, some particle trajectories may not cross the required number of fringes. The flow angle range over which particles will be measured is called the acceptance angle. To correct for this bias it is desired to have the measurement system capable of measuring all flow angles encountered. According to Edwards (1987), by using a Bragg cell with fringe velocity twice the maximum Doppler frequency this error can be corrected. A maximum Doppler frequency of 2 MHz was encountered in the research and a Bragg cell shift of 40 MHz was used. No angle bias should exist.

Gradient bias occurs due to having a finite probe volume size and the possible existence of several different velocities in the probe volume at one time. This error was ignored in this analysis, but with an average probe volume length of 0.06 in. this error is very small compared to others.

3.4.2.5 Uncertainty Errors

Uncertainty of measured values occurs due to finite resolution of measuring devices used to determine constants and settings on equipment used in the data reduction process. Equation 40 shows the relationship between the Doppler frequency, beam angle, and wavelength of laser light used to determine the flow velocity.

$$U = \frac{\lambda}{2 \sin\left(\frac{\theta_B}{2}\right)} f_d \quad (40)$$

Uncertainties existed in the calculated mean velocity due to beam angle calculation and resolution of the processor to provide the Doppler frequency. In addition, a sampling error existed due to a finite number of samples taken and an error due to rotation of the optics at +/- 45 degrees. All contributed to the total uncertainty of the velocities reported. These individual uncertainties were added together to provide a total uncertainty in reported values by the sum of squares technique, Equation 41.

$$\Delta U_{\text{tot}} = \sqrt{(\Delta U_{\theta})^2 + (\Delta U_{f_D})^2 + (\Delta U_{\text{samp}})^2 + (\Delta U_{\text{rot}})^2} \quad (41)$$

3.4.2.5.1 Beam Angle Uncertainty

The uncertainty due to the measurement of the beam angle is calculated by using Equation 42.

$$\frac{\partial U}{\partial \theta} = \frac{-\lambda f_D}{4} \frac{\cos\left(\frac{\theta_B}{2}\right)}{\sin^2\left(\frac{\theta_B}{2}\right)} \Delta \theta \quad (42)$$

For a beam half angle of 2.5 deg and $\Delta \theta = 0.1$ deg (0.001745 radians), an uncertainty was calculated for a representative case at $x=2$ in., $z=7.5$ in. for the annular and primary jets case. Figure 3.4.2-7 shows the results of this calculation on the mean velocity.

3.4.2.5.2 Frequency Uncertainty

The uncertainty due to the processor frequency resolution was determined by Equation 43.

$$\frac{\partial U}{\partial f_D} = \frac{\lambda}{2 \sin\left(\frac{\theta_B}{2}\right)} \Delta f_D \quad (43)$$

The uncertainty in Doppler frequency comes from taking the partial derivative of Equation 44 with respect to the digital mantissa, D_m .

$$f_D = \frac{N \times 10^9}{D_m \times 2^{(n-2)}} \quad (44)$$

where

N = number of cycles per burst
 D_m = digital mantissa
 n = exponent

resulting in

$$\frac{\partial f_D}{\partial D_m} = \frac{N \times 10^9}{D_m^2 \cdot 2^{(n-2)}} \Delta D_m \quad (45)$$

The resolution of the digital mantissa is 1 bit in 4096, $\Delta D_m = 1$. Substituting the result of Equation 45 into Equation 43 and rearranging results in

$$\Delta U_{f_D} = \frac{\lambda}{2 \sin\left(\frac{\Theta_B}{2}\right)} \frac{f_D^2 2^{(n-2)}}{N \times 10^9} \Delta D_m \quad (46)$$

For a beam angle of 2.5 deg, the uncertainties due only to the frequency resolution of the mean velocity are seen in Figure 3.4.2-8.

3.4.2.5.3 Sampling Uncertainty

Since only a finite number of samples were taken to determine the mean velocity, a sampling error will exist. If an infinite number of samples were taken, the true mean would have been reported and, therefore, this error would no longer exist. The 95% confidence interval for the mean velocity is

$$\bar{U} - 1.96 \frac{U_{rms}}{\sqrt{N}} \leq \bar{U}_T \leq \bar{U} + 1.96 \frac{U_{rms}}{\sqrt{N}} \quad (47)$$

where

U_{rms} = root mean square velocity
 \bar{U} = sampled mean velocity
 N = number of samples
 \bar{U}_T = true mean velocity

For the rms velocity, the 95% interval is

$$\frac{\bar{U}_{rms}}{1 + \frac{1.96}{\sqrt{2(N-1)}}} < \bar{U}_{rms_T} < \frac{\bar{U}_{rms}}{1 - \frac{1.96}{\sqrt{2(N-1)}}} \quad (48)$$

where

\bar{U}_{rms_T} = the true root-mean-square velocity

To determine the mean values, 10,000 samples were taken. Figure 3.4.2-9 represents the uncertainty due to this sampling interval for the mean and rms velocities respectively.

3.4.2.5.4 Rotational Uncertainties

In the previous subsection, relations were developed relating velocities measured at ± 45 deg to the coordinate axis and along one coordinate axis to calculate values for V , V' , $U'V'$, and K' . Uncertainties due to accurately rotating the beam to ± 45 deg and 0 deg within the rig will arise in uncertainties in the calculated values (Durst, Melling, and Whitelaw, 1976).

$$U_i = U_1 \cos(a_1) + U_2 \cos(a_2) \quad (49)$$

$$\overline{U_i'^2} = \overline{U_1'^2} \cos^2(a_1) + \overline{U_2'^2} \cos^2(a_2) + 2\overline{U_1'U_2'} \cos(a_1)\cos(a_2) \quad (50)$$

Equation 49 is used to relate the mean velocities measured along lines at angles of ± 45 deg and 0 deg to the axial coordinate (x axis). Equation 50 is the relation between the fluctuating velocity components of the velocities measured at angles to the coordinate axis.

Equations 49 and 50 can be put into matrix form and solved for the calculated quantities \bar{V} , \bar{V}' , and $U'V'$.

$$\begin{bmatrix} \bar{U}_0 \\ \bar{U}_{+45} \\ \bar{U}_{-45} \end{bmatrix} = \begin{bmatrix} \cos(a_{1x}) \sin(a_{1x}) \\ \cos(a_{2x}) \sin(a_{2x}) \\ \cos(a_{3x}) \sin(a_{3x}) \end{bmatrix} \begin{bmatrix} \bar{U} \\ \bar{V} \end{bmatrix} \quad (51)$$

$$\begin{bmatrix} \overline{U_0'^2} \\ \overline{U_{+45}'^2} \\ \overline{U_{-45}'^2} \end{bmatrix} = \begin{bmatrix} \cos^2(a_{1x}) \sin^2(a_{1x}) \cos(a_{1x}) \sin(a_{1x}) \\ \cos^2(a_{2x}) \sin^2(a_{2x}) \cos(a_{2x}) \sin(a_{2x}) \\ \cos^2(a_{3x}) \sin^2(a_{3x}) \cos(a_{3x}) \sin(a_{3x}) \end{bmatrix} \begin{bmatrix} \overline{U'^2} \\ \overline{V'^2} \\ 2\overline{U'V'} \end{bmatrix} \quad (52)$$

Where a_{1x} is the angle of measurement 1 with the x axis. By making the assumption that the measurements along the x axis is correct and no correction is needed, then Equation 51 becomes

$$\begin{bmatrix} \bar{U}_{+45} \\ \bar{U}_{-45} \end{bmatrix} = \begin{bmatrix} \cos(a_{2x}) \sin(a_{2x}) \\ \cos(a_{3x}) \sin(a_{3x}) \end{bmatrix} \begin{bmatrix} \bar{U} \\ \bar{V} \end{bmatrix} \quad (53)$$

To determine uncertainties in V , V' , and $U'V'$, 0 deg is substituted into angle a_{1x} and ± 45 deg ± 0.5 deg is substituted into angles a_{2x} and a_{3x} . These matrices can then be manipulated into equations relating calculated quantities to measured quantities. Relations in the following form result

$$\begin{aligned} \bar{V} &= C_1 \bar{U}_{+45} + C_2 \bar{U}_{-45} \\ \bar{V}' &= C_3 \bar{U}_0 + C_4 \bar{U}_{+45} + C_5 \bar{U}_{-45} \\ \overline{U'V'} &= C_6 \bar{U}_0 + C_7 \bar{U}_{+45} + C_8 \bar{U}_{-45} \end{aligned} \quad (54)$$

These relations were then subtracted from the equations derived previously, resulting in the uncertainty due to rotating the optics. Figures 3.4.2-10, 3.4.2-11, and 3.4.2-12 show the uncertainty due to rotating the optics for V , V' , and $U'V'$ respectively.

3.4.2.6 Total Uncertainty

Total uncertainty due to all previous sources are then calculated by using Equation 41. Figures 3.4.2-13 through 3.4.2-18 represent the total uncertainty for U , U' , V , V' , $U'V'$, and K .

3.4.2.7 Marker Nephelometry

Marker nephelometry is a technique by which concentration fields can be studied by seeding the fluid stream with passive marker particles and detecting the marker particle concentration by a light scattering, optical method. Rosenweig (1966) first developed the theory and basic method and, along with Hottel and Williams (1961), was the first to apply the technique. Becker (1977) gives a very thorough and complete analysis of the technique.

The measured concentration field is relative in nature, not absolute. The actual concentration at a point in the flowfield cannot be directly measured, only the concentration at that point relative to the concentration at another point in the flowfield. This method requires the use of some type of light source (laser, lamp, etc) to illuminate the flowfield of interest, particles to scatter the incident light, and a detection device (photomultiplier tube, SIT, etc) to collect the scattered light. In some flowfields, naturally occurring particles scatter adequate light for the method to be successful but in most cases some type of light scattering seed particle must be added to the flow.

Ideally, the light scattered by marker particles is a linear function of the number of marker particles residing in the measurement volume. This linear behavior depends on two criteria, independent scattering and monodisperse marker particles. The first condition is rather easily satisfied as, from Becker (1977), independent scattering occurs for marker particle density sufficiently small such that the center-to-center distance between particles is greater than 3 radii. This corresponds to a marker particle volume fraction of 30%. For this experiment, this condition was easily satisfied.

The second condition, the need for monodisperse particles, was not as easily met. Monodisperse particles are all of the same size. Since nearly all particle generators created polydisperse particles, the intensity of the scattered light will not be linearly related to the number of particles in the measurement volume but will be a weighted function of the various particle sizes existing there.

From Schaughnessy and Morton (1977) the logical assumption to be made is that the statistical distribution of particle sizes is the same at every point in the flowfield. This assumption will fail when the sample of marker particles is so small (very low concentration) as to not characterize the correct distribution of sizes. This did not create a problem in this experiment since the essential characteristics observed were dictated by the higher levels of concentration.

Both smoke, in the air experiments, and a fluorescent dye, in the water experiments, were used in the course of the investigation. As a test case, a fluorescent dye (Rhodamine 6-G) was injected into the jet flow far upstream (22 jet diameters) of the jet exit to allow thorough mixing. The beam of a Spectra-Physics argon ion laser was passed through a cylindrical lens, producing a thin sheet of light aligned with the jet axis. The sheet of laser light was spread much wider than the measurement region to reduce the effect of the Gaussian intensity variations across the laser sheet. The laser light caused the dye to fluoresce, such that the fluorescent intensity was proportional to the laser power and the local concentration of dye, for laser intensities below the fluorescence saturation level as described by Walker (1987). Koochesfahani and Dimotakis (1984) developed an expression for the dye concentration at a point, i .

$$C(i) = K(i) \frac{V(i) - D(i)}{\beta(i)} \quad (55)$$

where

$C(i)$ = local dye concentration

$K(i)$ = attenuation factor for absorption of the laser intensity by the dye

$V(i)$ = i^{th} pixel output
 $D(i)$ = dark response of i^{th} pixel

The quantity $\beta(i)$ contains the effects of nonuniformity of imaging and pixel sensitivity and laser sheet thickness variations. These effects were experimentally determined to be negligible by observing the measured fluorescent intensity variations across the test section with a uniform dye concentration (see Appendix). The attenuation factor, $K(i)$, was kept very near 1.0 by injecting dye at a very low rate (approximately 20 ppb), thus reducing the amount of dye available to absorb the laser power. The choice of Rhodamine 6-G for the dye also reduced the absorption. Figure 3.4.2-19 shows the mean concentration profile of Fluorescein, another fluorescent dye, in which the laser light entered the jet from the right side of the axis. The apparent variation in concentration across the jet is due to the absorption of the laser intensity by the Fluorescein. This did not occur with the Rhodamine 6-G, which will be demonstrated by the results later in this subsection. To determine absolute concentration levels, the system would have to be calibrated to provide concentration for a given local laser power. However, only relative values of concentration were required for this study. Therefore, the local dye concentration is the difference between the pixel output and the dark response. The dark response was obtained by recording the camera output with no dye in the test section.

Figure 3.4.2-20 shows a schematic diagram of the test equipment setup. The fluorescent intensity was recorded through a Panasonic digital video camera with a pickup element consisting of a 499×574 matrix of charge coupled devices, which will be referred to as segments of the pickup element. The camera was operated in the strobe effect shutter mode, which records each field in $1/1000$ sec instead of the normal $1/60$ sec. This reduces the time averaging across each field. The fields are still $1/60$ sec apart to remain compatible with standard video cassette recorders (VCRs). Two consecutive fields are interlaced to produce a frame. Figure 3.4.2-21 illustrates how the camera acquires the fields and how they are interlaced. The effect of the $1/60$ sec between fields can be seen by plotting the odd and even pixels separately on a vertical scan across the image. This is shown in Figure 3.4.2-22, where the concentration values for a single frame are plotted. The largest changes between fields occur at the jet edges, as expected. This has no effect on the mean and rms calculations.

The camera output was recorded by a GE VCR onto standard $1/2$ in. tape. The recorded images were digitized through an IBM PC/AT equipped with Data Translation's DT-IRIS image processing software and hardware. The digitized image is the result of assigning a value from 0 to 255 (8 bits) to each pixel (480 lines by 512 pixels) based on the recorded intensity. Mean and rms values at selected pixel locations can then be computed from the digitized images. These quantities were calculated from 50 frames, each spaced approximately 1.4 seconds apart. The time between processed frames is due to the computer processing time. Only 50 frames were used because extensive dye recirculation within the test section was encountered after approximately 70 seconds. Mean and rms values were calculated as follows.

$$\bar{C} = \frac{1}{N} \sum_{i=1}^N C_i \quad (56)$$

$$c' = \left[\frac{\sum_{i=1}^N C_i^2 - \frac{1}{N} \left(\sum_{i=1}^N C_i \right)^2}{N-1} \right]^{1/2} \quad (57)$$

where:

\bar{C} = relative mean concentration

c' = rms concentration; $\left(\sqrt{c^2}\right)$

N = number of frames

C_i = i th instantaneous relative concentration ($V(i) - D(i)$)

Visualization images are produced by mapping the intensity levels to colors, which are combinations of red, green, and blue, to provide pseudocolor representations of the concentration field. Pink indicates the highest concentration and dark blue corresponds to the lowest. These color enhanced images allow visualization of the concentration distribution. Figure 3.4.2-23 shows the 127 frame average pseudocolor image of the single jet dark response.

It is desirable to have the concentration measurement system be independent of the flow velocity, especially for this study since no velocity measurements were made. To verify that the measurement system was independent of velocity, the fluorescent light energy incident on a pickup segment was calculated. The fluorescent light intensity received by a single segment of the pickup element is

$$I(t) = [I_0(t) * \varepsilon] \int_{p.v.} C(x, y, z, t) dx dy dz \quad (58)$$

Where several quantities are defined as

$I(t)$ = fluorescent intensity at the pickup segment

$I_0(t)$ = incident laser light intensity

ε = fluorescent efficiency

C = dye concentration in the probe volume

p.v. = probe volume

Let

$$\int_{p.v.} C(x, y, z, t) dx dy dz = \hat{C}(t)$$

Then the total fluorescent light energy incident on the pickup segment during the camera exposure time, t_{exp} is

$$E_{TOT} = A_{ps} \int_0^{t_{exp}} I(t) dt = A_{ps} \int_0^{t_{exp}} [I_0(t) * \varepsilon] \hat{C}(t) dt \quad (59)$$

where

A_{ps} = pickup segment area

Assuming that the incident laser intensity is constant with time, the total fluorescent light energy can then be written as

$$E_{TOT} = (I_0 * \varepsilon) \bar{\hat{C}} t_{exp} A_{ps} \quad (60)$$

where

$$\bar{C} = \hat{C} \text{ time averaged over } t_{\text{exp}}$$

From the above expression, it is apparent that the concentration measurement system is independent of velocity. It is also shown that the concentration measurement is averaged over the exposure time and over the probe volume.

Table 3.4-II shows the sampling time and exposure time requirements for measuring various quantities. There are no sampling time requirements for determination of the mean, and the only requirement for rms determination is that the exposure time should be less than the flow time scale. To maintain the influence of the smallest scale fluctuations, this would require that the exposure time be less than the Kolmogorov time microscale. The spectrum can be determined if the time between samples is also small enough.

3.4.2.8 Test Case - Single Turbulent Jet

The measurement system was tested on a single round turbulent jet because concentration measurements have been made for this configuration by others. This demonstrated the validity of the measurement.

The experimental configuration consisted of a jet of water issuing from a 0.43 in. inside diameter tube, with a length-to-diameter ratio of 25. The water flow was supplied to the tube from a constant head tank. The tank level was maintained constant by a pump which supplied water to the tank and an overflow pipe which discharged to the holding tank. The jet discharged vertically into a clear plexi-glass water reservoir. The apparatus is shown in Figures 3.4.2-24 and 3.4.2-25. Mass flow rate was determined by weighing a sample of water collected over a timed interval. The mass-averaged jet velocity was 1.78 ft/sec, giving a Reynolds number based on jet diameter of 5300. The dye mixture, which was 3.8 ppm dye, was injected at the rate of 0.00058 lb/sec, giving a dye concentration upstream to the jet exit of 20 ppb.

For this test case, the receiving optics were arranged such that the length of the probe volume was 0.006 in. This was determined by counting the pixels in the digitized image corresponding to a known dimension, the jet diameter. As stated previously, the camera was operated in strobe effect shutter mode, which gave an effective exposure time of 0.001 seconds.

The centerline turbulence intensity, u/U , increased through the measurement section, which extended 5.5 jet diameters downstream. From Hinze (1975), the maximum value within the measurement region would occur at 5.5 diameters and be approximately 15%. Borrego and Olivari (1980) show that at 5.5 diameters downstream the centerline velocity would still be equal to the exit velocity. Therefore, the mean velocity U is the exit velocity of 1.78 ft/sec. From the above equations, the Kolmogorov length and time microscales are, respectively, 0.003 in. and 0.0045 sec. This indicates that all but the smallest scale fluctuations are being recorded. As indicated in the previous section, this has no effect on the determination of the mean. The effect on the rms value will be minimal, since only the smallest scale fluctuations are being averaged across the exposure time. Since these scales are smaller than the measurement system can resolve, it is desirable to determine how much of the fluctuation energy is being

Table 3.4-II.
Sampling requirements for determination of various quantities.

<u>Quantity</u>	<u>Sampling time required</u>	<u>Exposure time required</u>
\bar{C}	none	none
c'	none	<flow time scale
spectrum	<flow time scale	<flow time scale

recorded. Becker et al (1967), present a concentration fluctuation spectrum recorded on the jet centerline, plotted against $\Lambda\gamma(K)$, which is the product of the axial integral scale and the wavenumber (Figure 3.4.2-26). They developed a linear relationship for Λ

$$\Lambda\gamma = 0.0445X \quad (61)$$

where:

x = axial distance from the jet exit

Based on the 1/60 sec between image fields, assume that the highest frequency which can be resolved is 20 Hz. This would give a wavenumber of 71 ft^{-1} . The spectrum presented by Becker et al, was measured at 32 diameters downstream, and therefore, the current value of $\Lambda\gamma(K)$ must be multiplied by 32/5.5 to be compatible with their spectrum. This ratioed value for $\Lambda\gamma(K)$ is 3.6, giving a fluctuation energy level which is less than one-tenth of the energy level at low wavenumbers. Therefore, the vast majority of the fluctuation energy is being recorded.

The results of this test case are presented in Figures 3.4.2-27 through 3.4.2-35, with results from other investigators where available. Figures 3.4.2-27 and 3.4.2-28 are visualization images of the jet concentration field. Figure 3.4.2-27 shows a single frame of data, while Figure 3.4.2-28 is the result of averaging 127 frames.

Figure 3.4.2-29 presents the mean and fluctuation intensity c'/C data in a 3-D graphical format. The mean profile can be seen to flatten and spread downstream as expected. The fluctuation intensity increases outside of the peaks at the jet edges. This is due to the nearly zero rms being divided by a decreasing mean value.

Figure 3.4.2-30 presents the concentration profile near the jet exit ($x/D = 0.1$). The shape of the mean concentration profile, flat across the jet and nearly zero outside of the jet, indicates that the dye was thoroughly mixed with the jet flow. The fluctuation intensity has an asymmetric feature, this is due to the mean concentration curve. The value of C on the left side of the jet axis is slightly higher than that on the right side. The jet did spread faster on this side and it was visible in the flow visualization provided by the fluorescent dye. This was apparently due to a manufacturing defect inside the tube near the exit.

Figures 3.4.2-31 and 3.4.2-32 compare results with those obtained by Rosensweig, Hottel, and Williams. They measured concentrations in an air jet marked with smoke particles by recording the scattered light from the particles. Figure 3.4.2-31 presents the mean concentration profile at $x/D = 1.0$. The data from Rosensweig et al, are asymmetric. The authors do not discuss this feature but it may be due in part to the fact that the projected slit width of their receiving optics was 14% of the jet diameter. This would make it difficult to accurately measure the concentration at the jet edges. The present data do agree fairly well on the left side of the jet axis. Figure 3.4.2-32 presents the fluctuation intensity profile at $x/D = 1.5$. As with the jet exit profile, there is a slight asymmetry in the profile at this location due to the defect in the tube. For the present data, a 95% certainty band was calculated by assuming a normal distribution for C , and utilizing Student's t and the χ distributions. The values on the right side of the jet axis show good agreement with those obtained by Rosensweig et al.

Measurements made at downstream locations of 2 and 4 jet diameters are compared with those made by Borrego and Olivari in Figures 3.4.2-33 and 3.4.2-34. They measured oil smoke concentrations, in a round turbulent air jet exhausting into ambient still air, with a light scatter meter. The radial locations are normalized by $\delta_{c_{1/2}}$, the location at which the mean concentration is one-half of the centerline value. This allows direct comparison with Borrego and Olivari's results, finding that the present mean concentration levels outside of the jet are higher than those measured by Borrego and Olivari. This is due to the recirculation of the dye within the reservoir, causing a higher background concentration. Borrego

and Olivari's jet exhausted into a room and therefore did not have this condition. Also included for comparison are concentration profiles from data recorded in air. The configuration was an air jet exhausting into still ambient air, where the light scattered by marker particles was recorded on video tape. The videotaped data were processed for comparison with measurements made in this study. The air data agree quite well with the present results, with the exception that at $x/D = 2.0$, the light intensity saturated the image processing system near the jet centerline. This resulted in a flat mean profile and zero rms. Most of Borrego and Olivari's rms data fall within the 95% certainty band about the current data.

Figure 3.4.2-35 shows the jet half width growth along with air data and Birch et al (1978) and analytical results from Squire and Trouncer (1944), which are taken from Forstall and Shapiro (1950). The current data agree well with the trend from others. As explained above, the current test hardware had a slight flaw, causing the jet to spread slightly faster than would be expected.

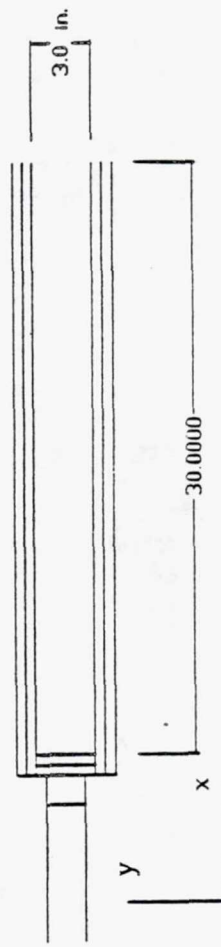
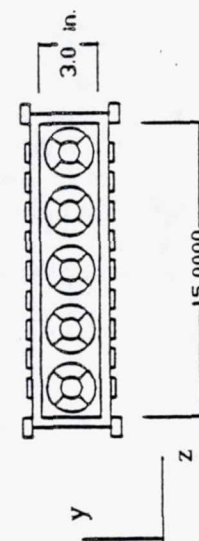
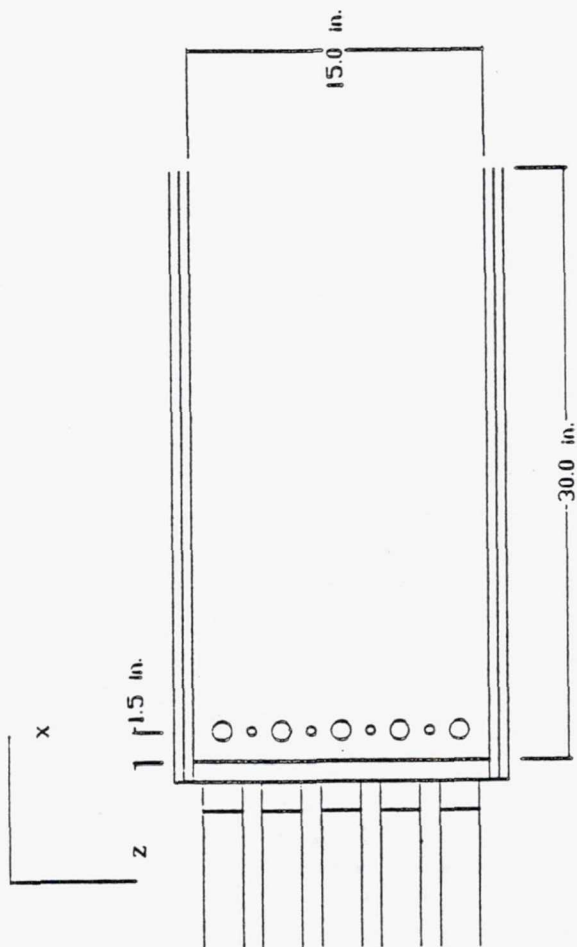
Based on the results of this test case and the comparisons with previous investigators, the measurement system has been found to provide concentration measurements with satisfactory accuracy.

3.4.2.9 Errors

The effect of nonuniformities in the laser sheet and in the camera response were not accounted for in this work. In this section, those effects are investigated. Uniform concentration fields were obtained in the model annular combustor test section by circulating a very dilute dye solution through the test rig. The fluorescent field was recorded for various uniform concentration levels. Dark response data were also recorded with no dye in the rig. These raw data are presented in Figure 3.4.2-36. The values on the vertical axis are the levels assigned by the image digitizer. The increase at the sides of the channel are due to the laser sheet reflecting from the plexiglass sides. This reflection resulted in a higher laser intensity near the wall.

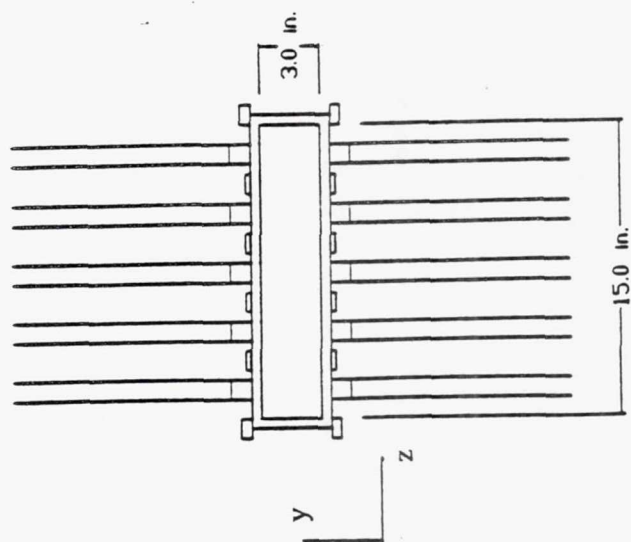
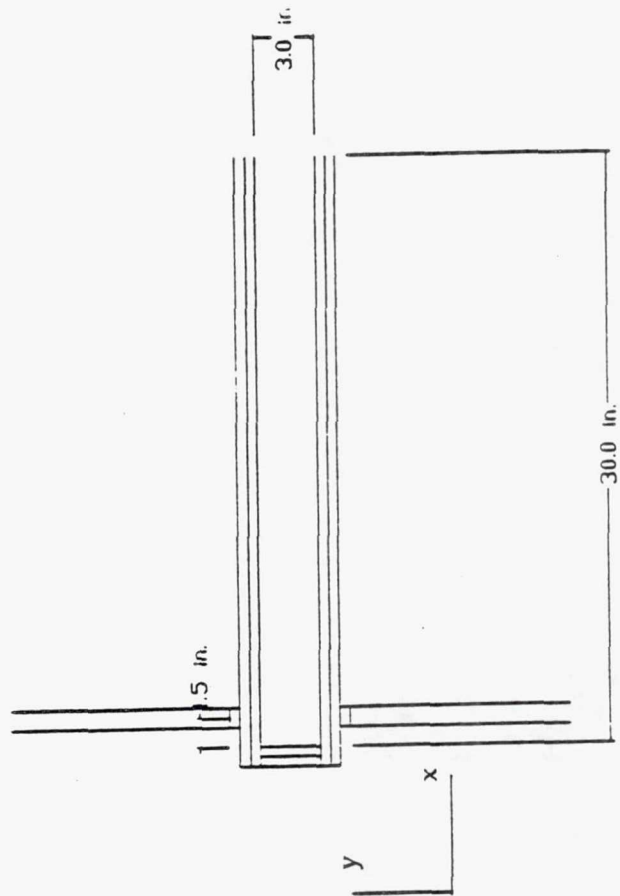
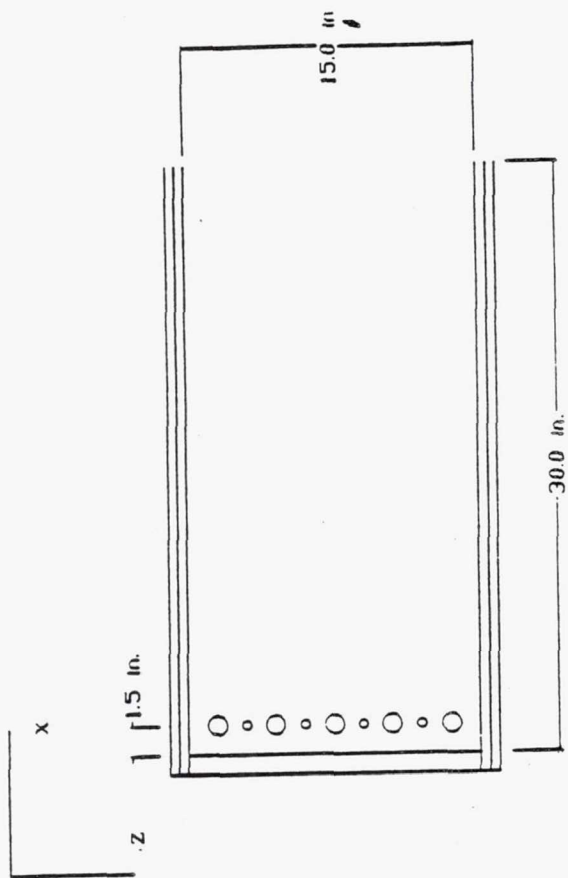
Figure 3.4.2-37 presents the profiles obtained for the different concentration levels by subtracting the dark response from the measured intensity field. This is the method of data correction which was used in this study. As expected, the profiles were fairly flat across the center portion of the channel ($0.5 \text{ in.} < y < 2.0 \text{ in.}$). The response at the sides was apparently nonlinear since the profile drops off at each side. This could be due to a combination of the reflection from the plexiglass walls and nonuniformities in the camera response towards the edge of the image. Long, Chu and Chang (1981) suggest correcting for the camera's nonuniformities by recording an image of a uniform dilute concentration field and dividing the measured image by this dilute response image. This is the second step of a two-step correction which they used. The first step being the subtraction of the dark response mentioned above.

Figure 3.4.2-38 presents the results after performing the two-step correction. The lowest concentration level image was used for the dilute response. The drop at the sides was still apparent and was therefore probably due to the reflection from the plexiglass sides. The profiles over the center portion of the channel were fairly flat, but not significantly improved from those in Figure 3.4.2-37. Therefore, the single step correction used in this study was probably sufficient over the majority of the flow area. The near wall regions could possibly be improved by masking the laser sheet such that the visible sheet width is less than the flow channel width. The sheet must still be maintained much wider than the measurement area to reduce the Gaussian variation effects.



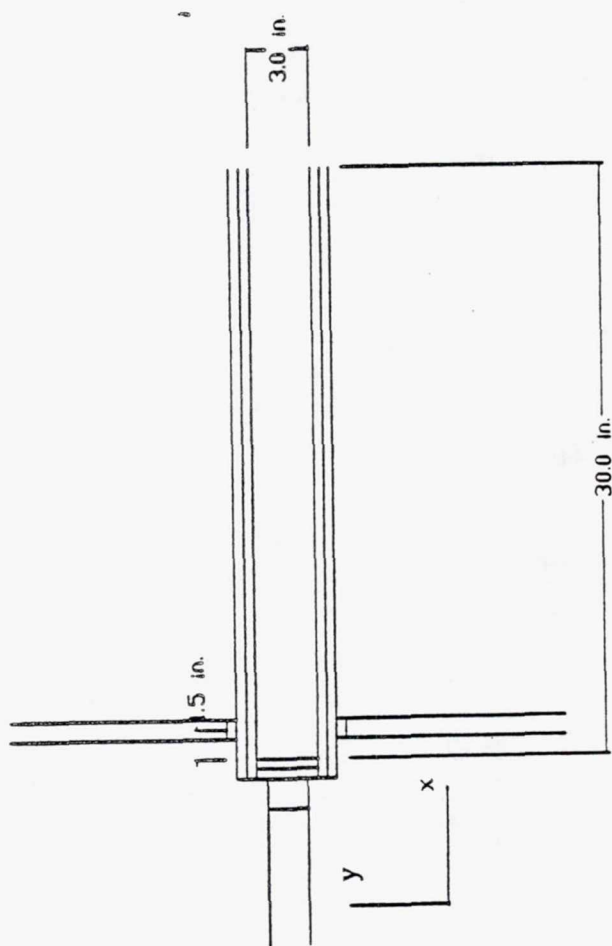
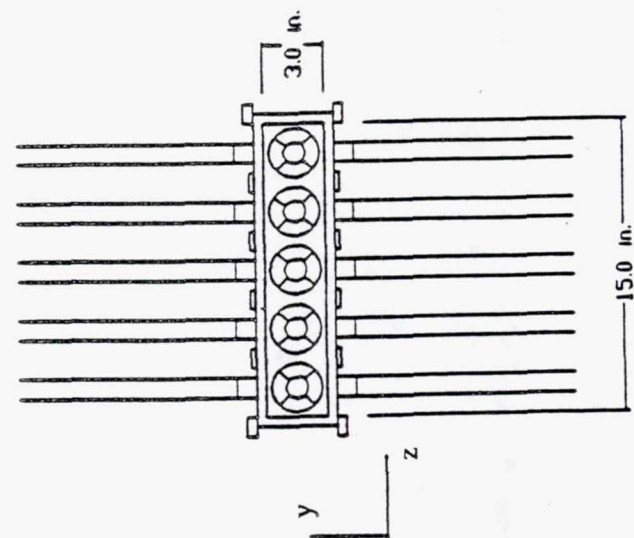
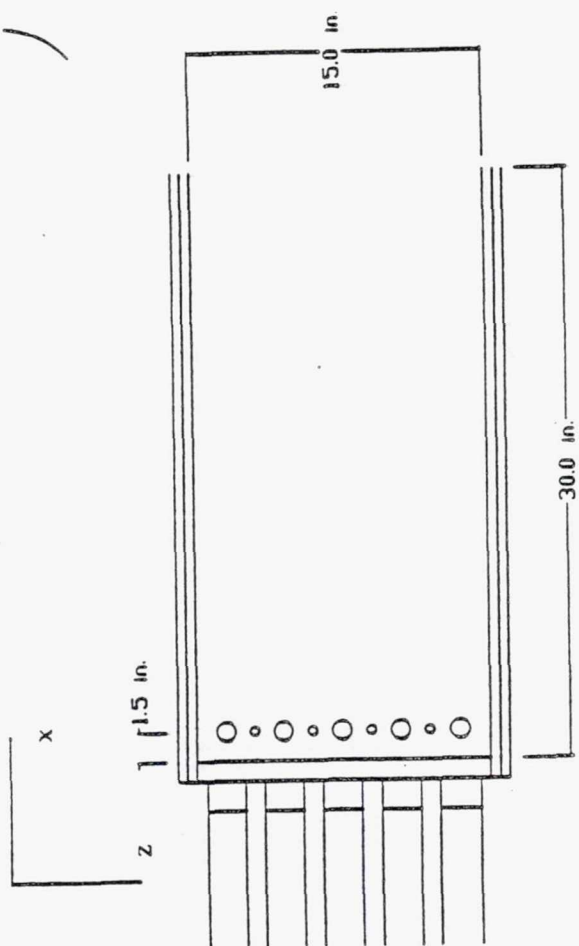
TE92-2494

Figure 3.4.1-1. Annular jets only.



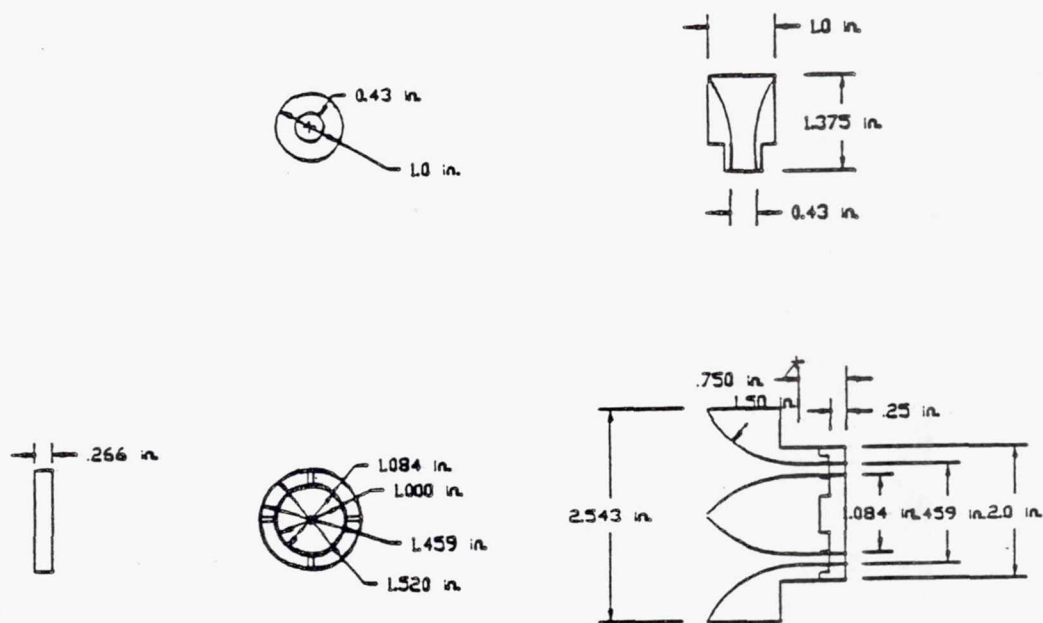
TE92-2495

Figure 3.4.1-2. Primary jets only.



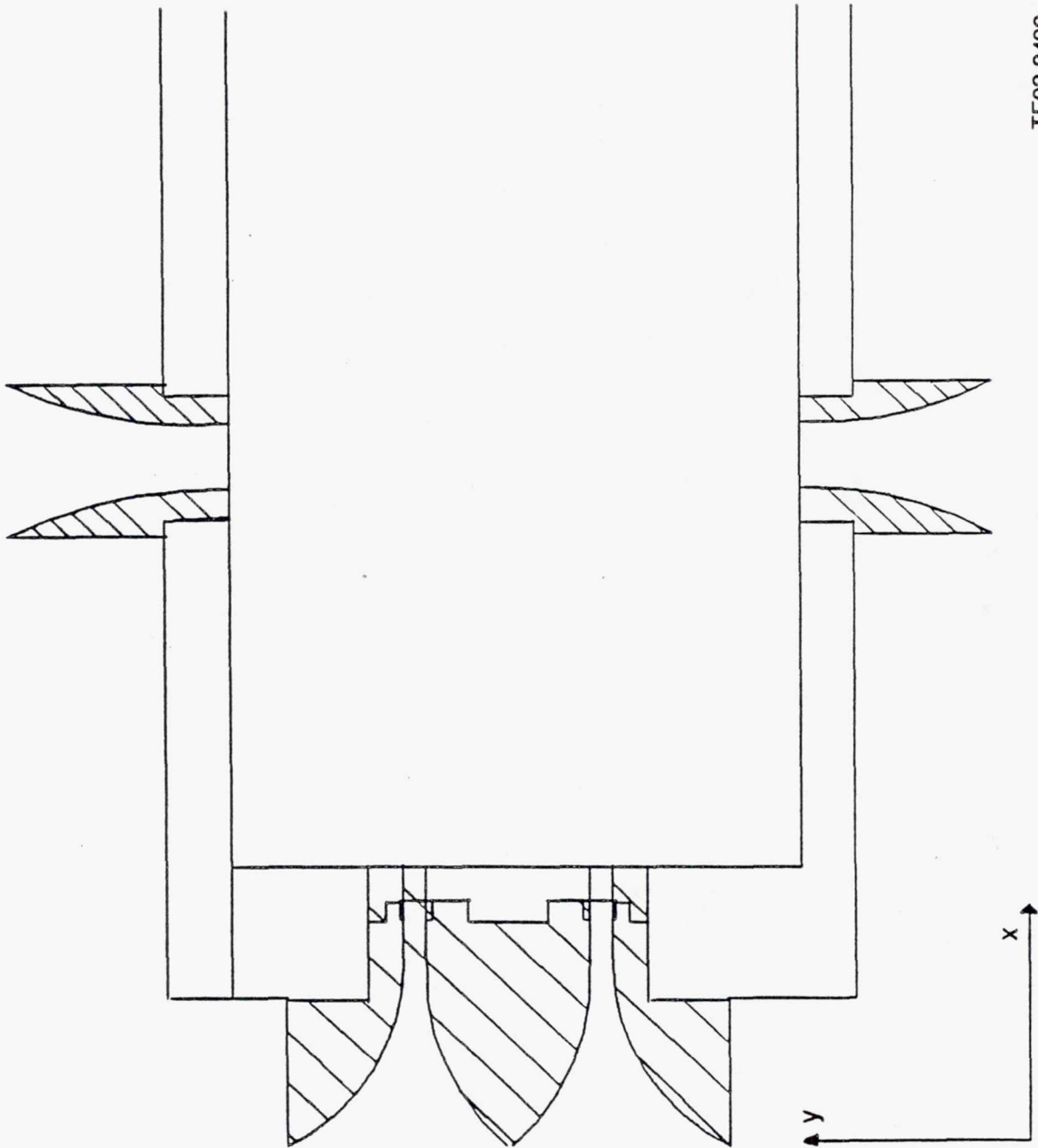
TE92-2496

Figure 3.4.1-3. Annular and primary jets - three-view drawing.



TE92-2497

Figure 3.4.1-4. Primary and annular jet - detail drawing.



TE92-2498

Figure 3.4.1-5. Head assembly - detail drawing.

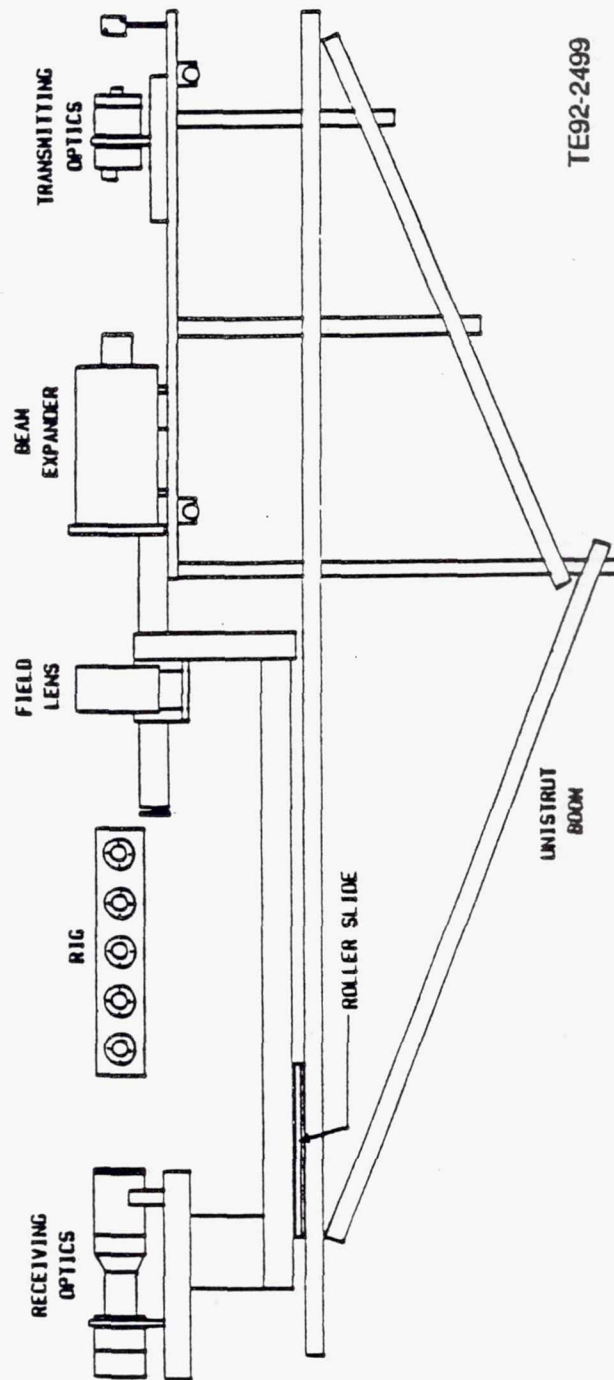
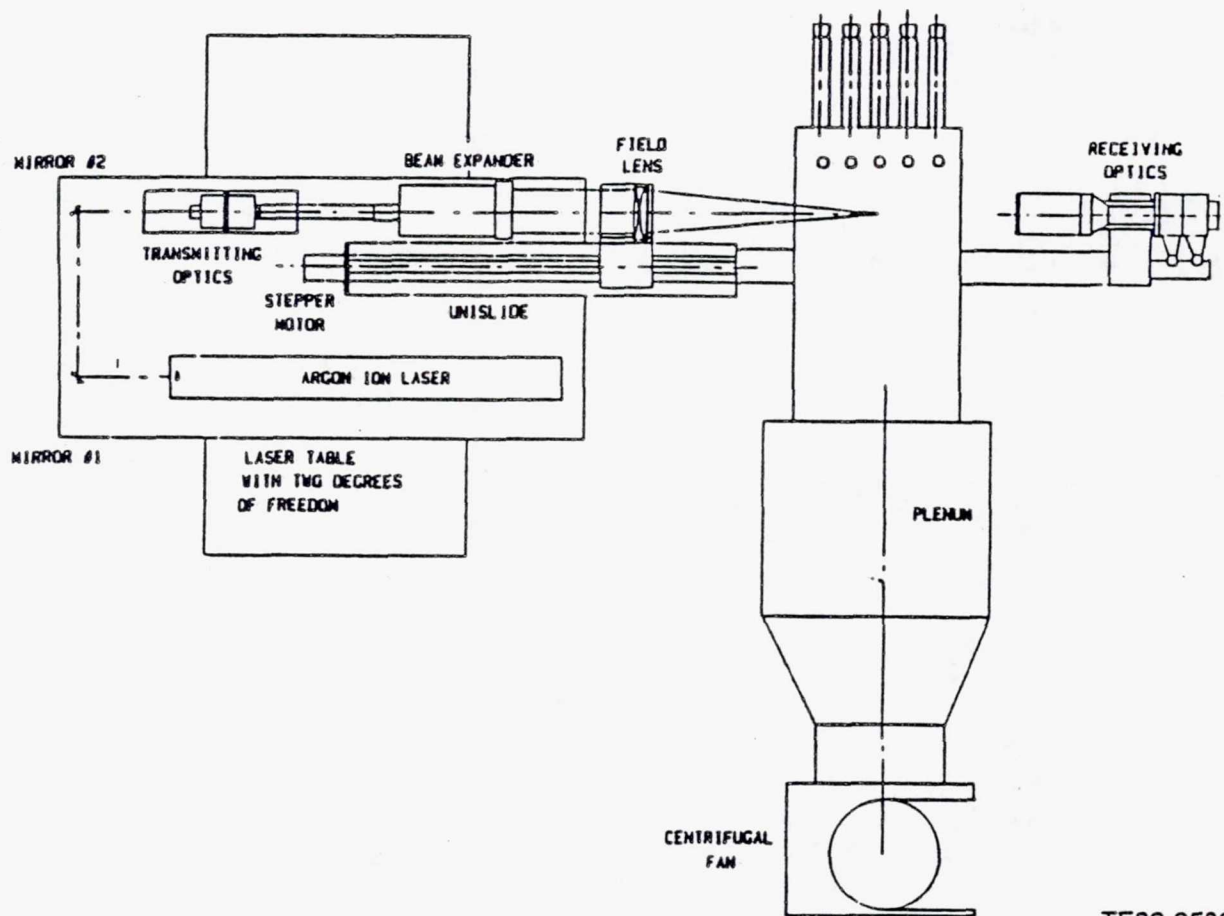
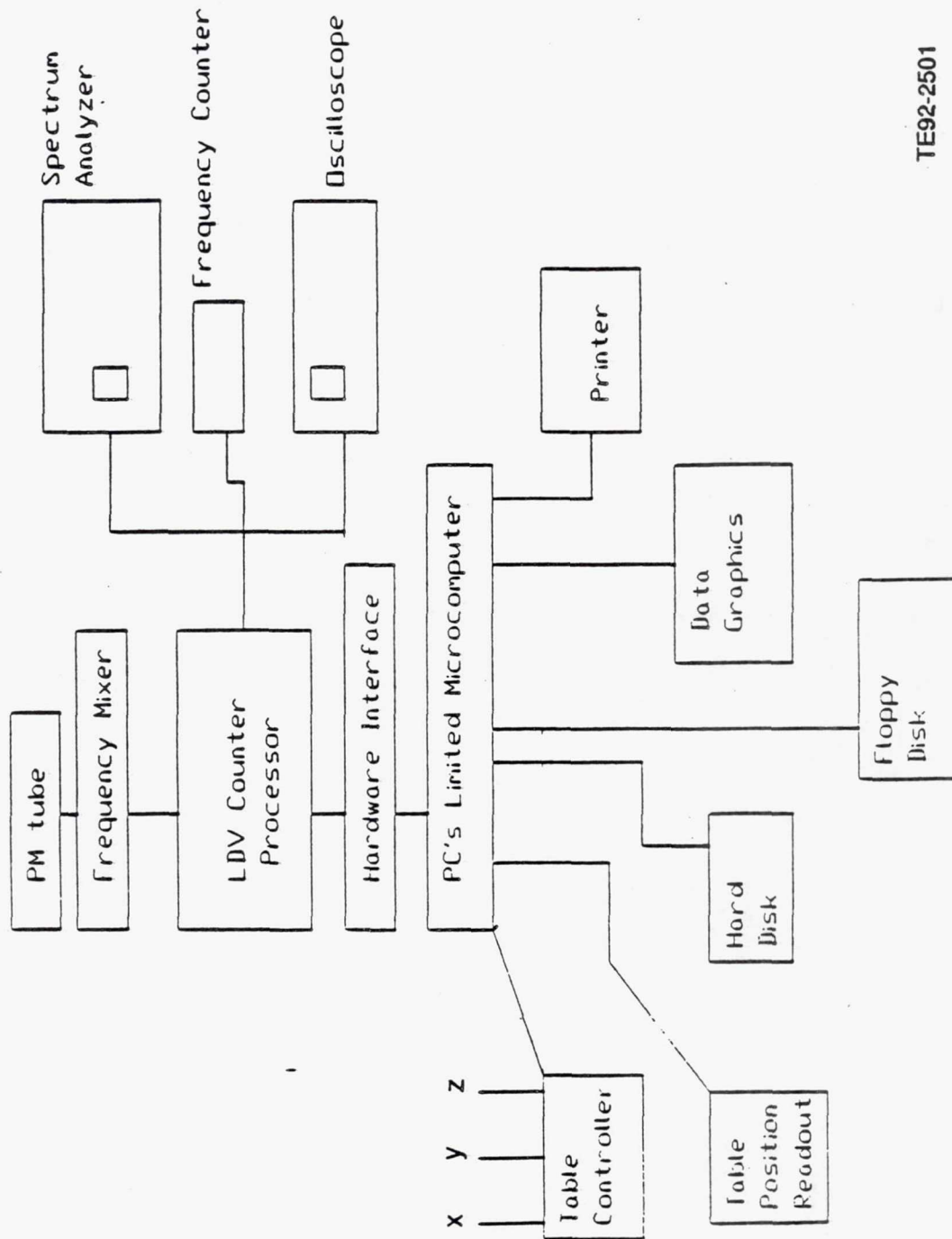


Figure 3.4.2-1. Receiving optics boom support.



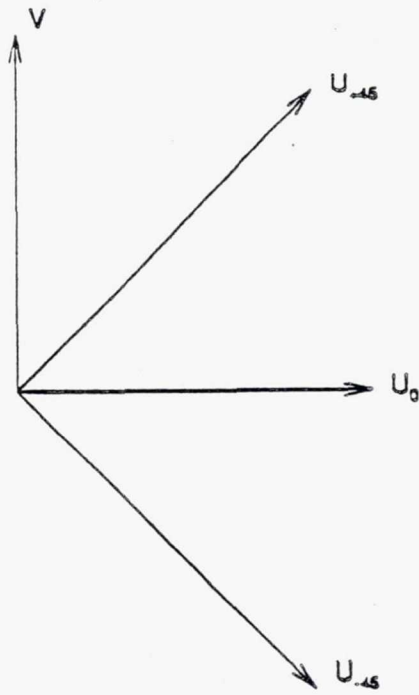
TE92-2500

Figure 3.4.2-2. LDV optics and rig setup.



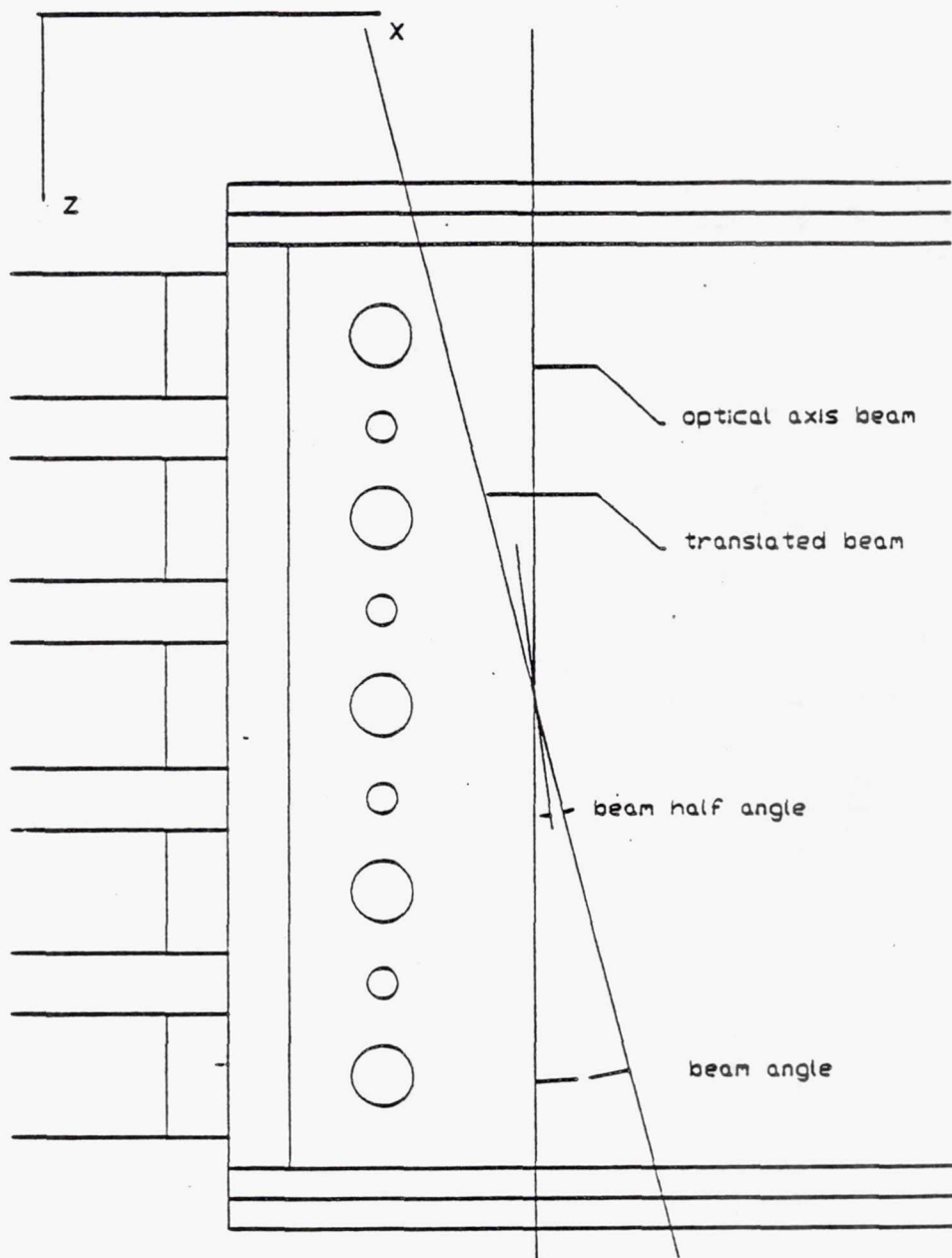
TE92-2501

Figure 3.4.2-3. Schematic of LDV data acquisition system.



TE92-2502

Figure 3.4.2-4. Velocity measurement coordinate relations.



TE92-2503

Figure 3.4.2-5. Orientation of beams for velocity measurements.

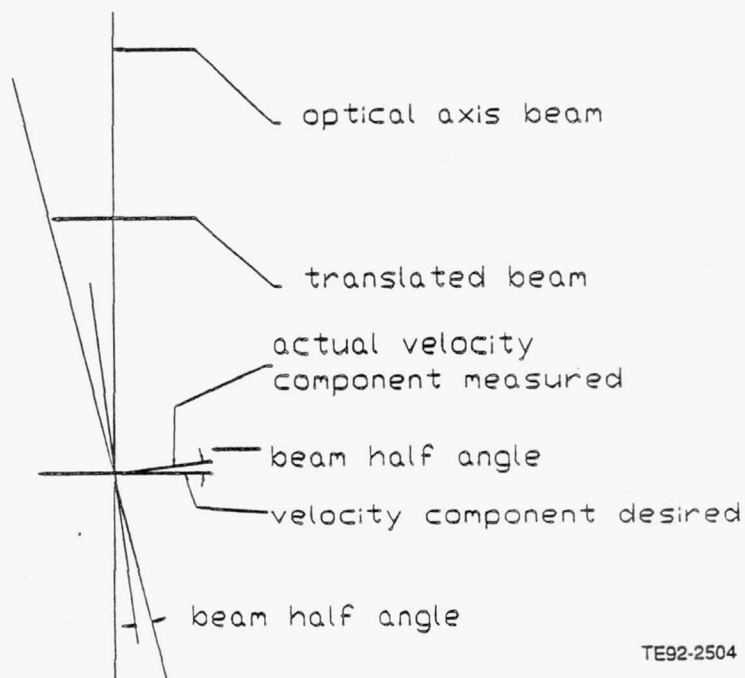


Figure 3.4.2-6. Actual and desired velocity component relations.

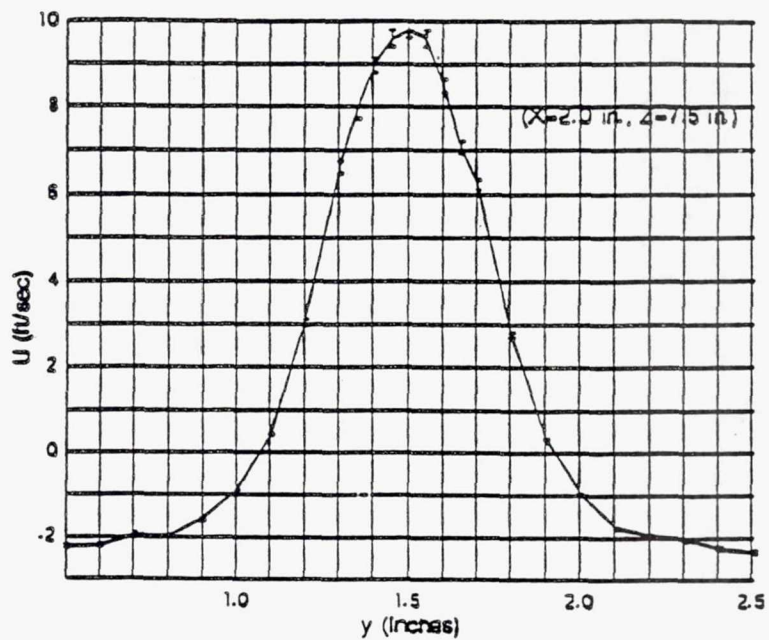
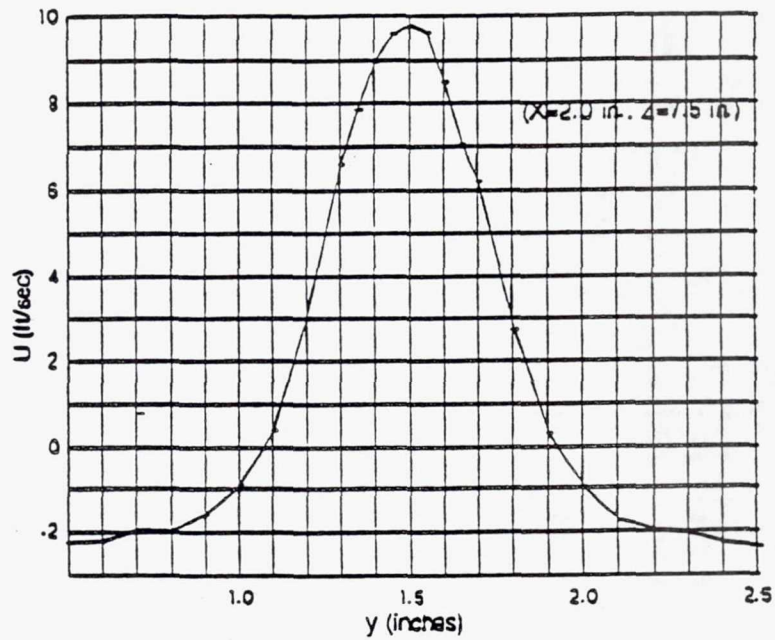
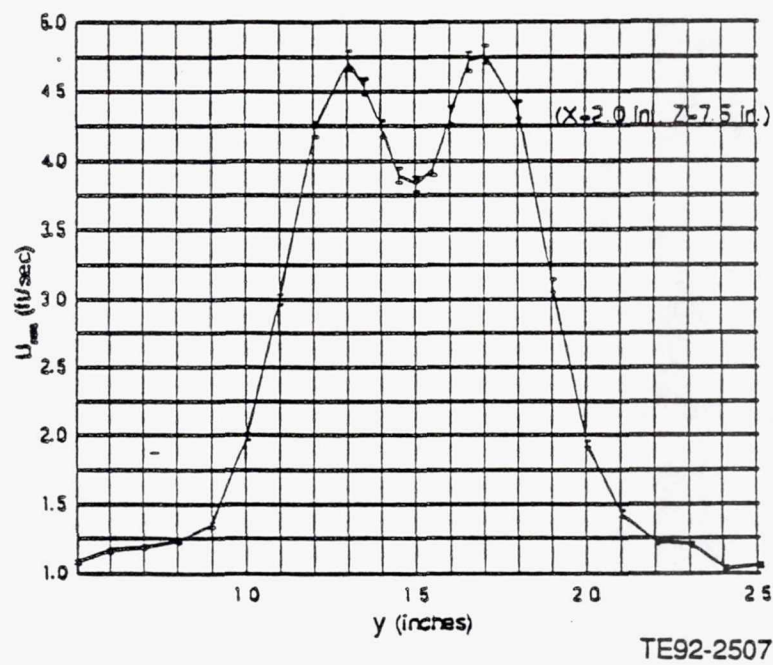
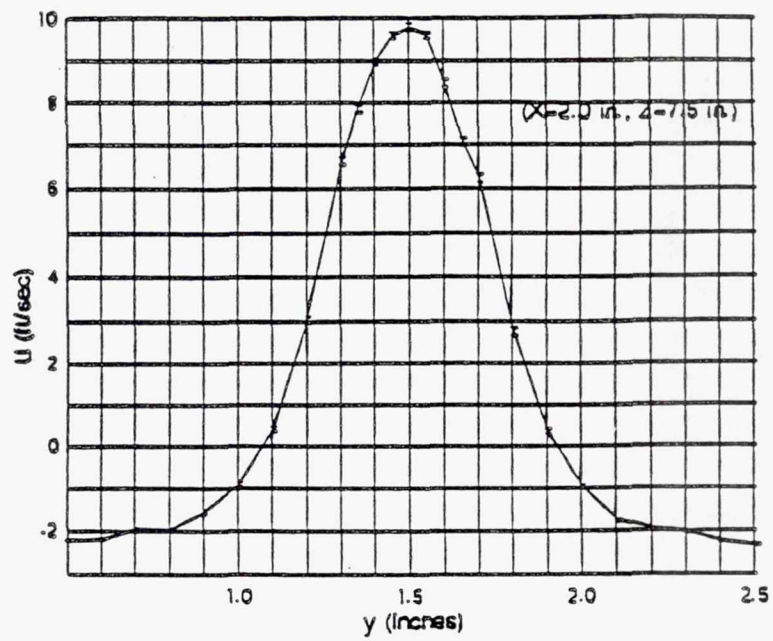


Figure 3.4.2-7. \bar{U} velocity error due to uncertainty in beam angle.



TE92-2506

Figure 3.4.2-8. \bar{U} velocity error due to frequency resolution.



TE92-2507

Figure 3.4.2-9. \bar{U} and U_{rms} velocity error due to sampling uncertainty.

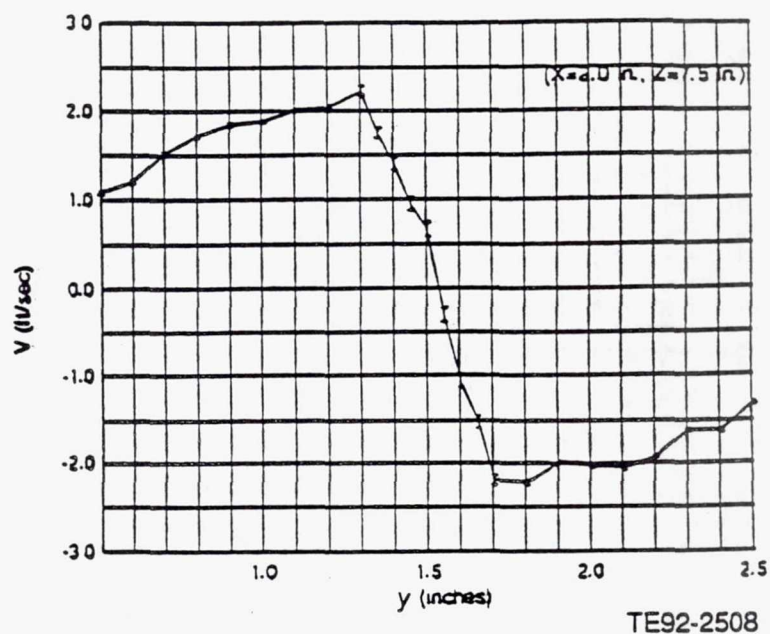


Figure 3.4.2-10. \bar{V} error due to rotation of optics.

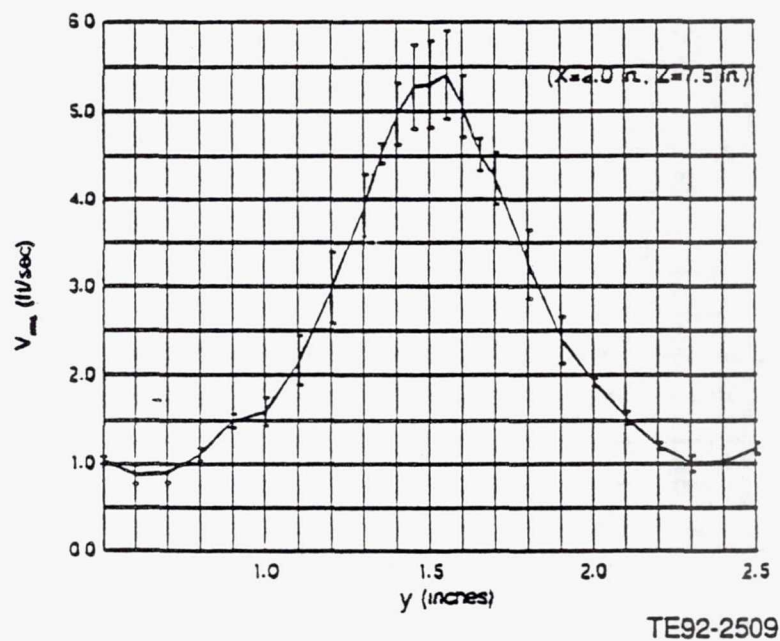


Figure 3.4.2-11. \bar{V}_{rms} velocity error due to rotation of optics.

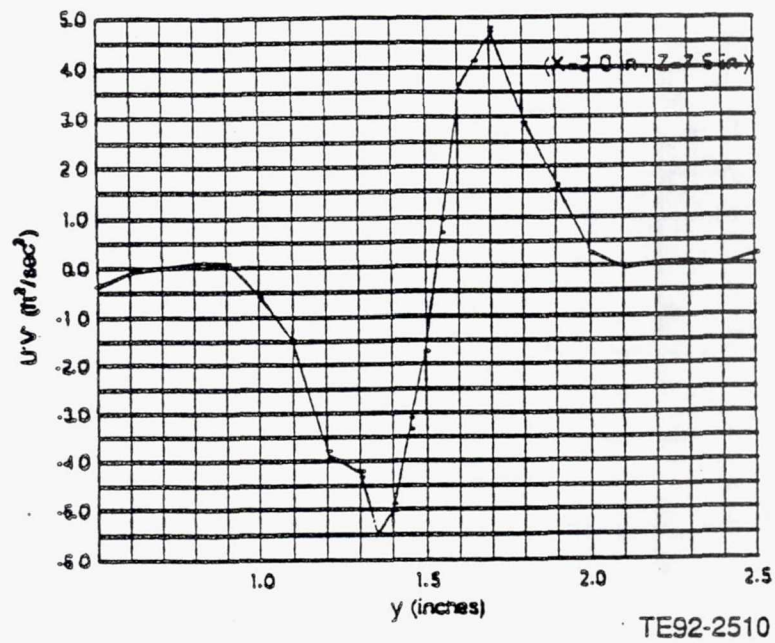


Figure 3.4.2-12. $U'V'$ error due to rotation of optics.

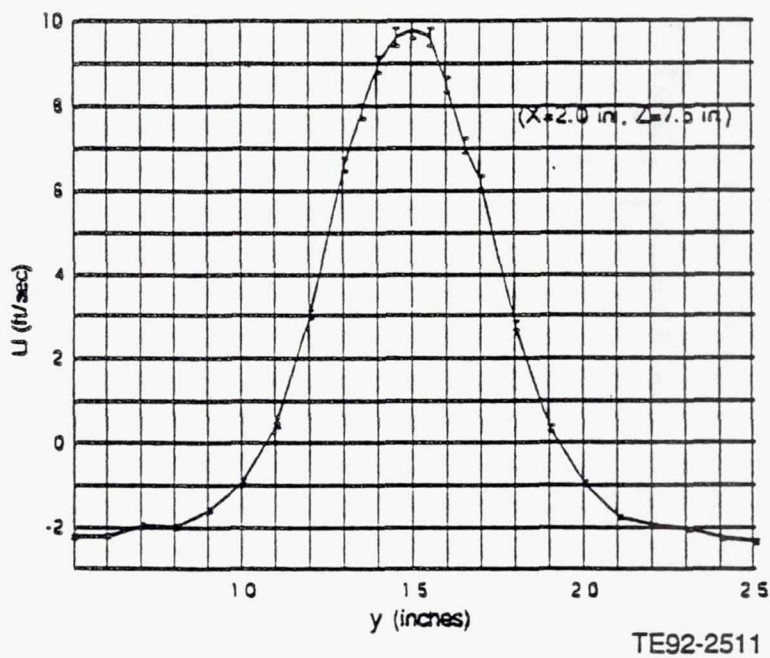


Figure 3.4.2-13. Total \bar{U} velocity error.

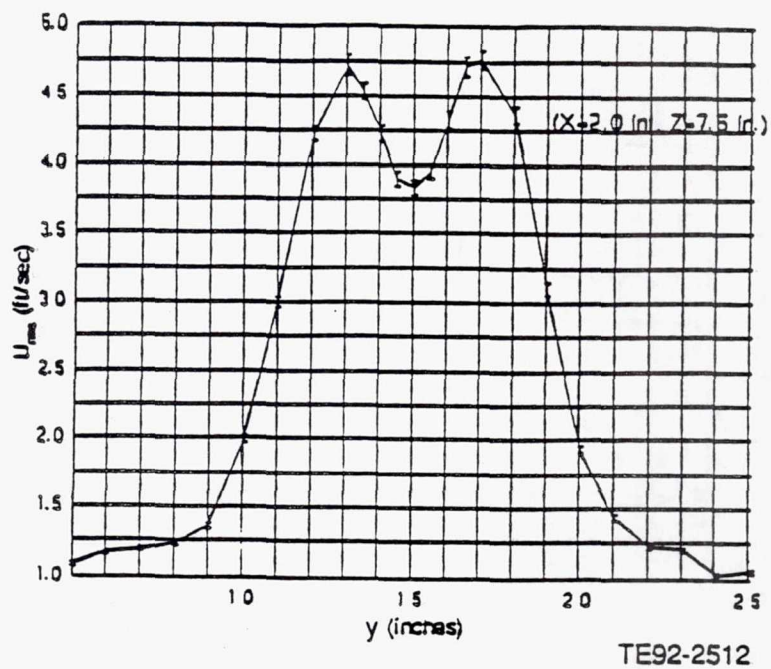


Figure 3.4.2-14. Total U_{rms} velocity error.

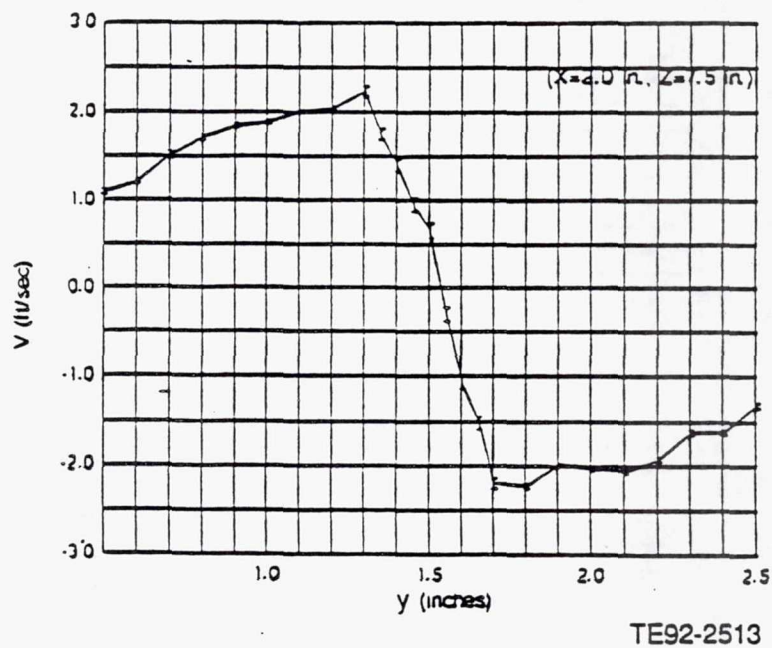


Figure 3.4.2-15. Total \bar{V} velocity error.

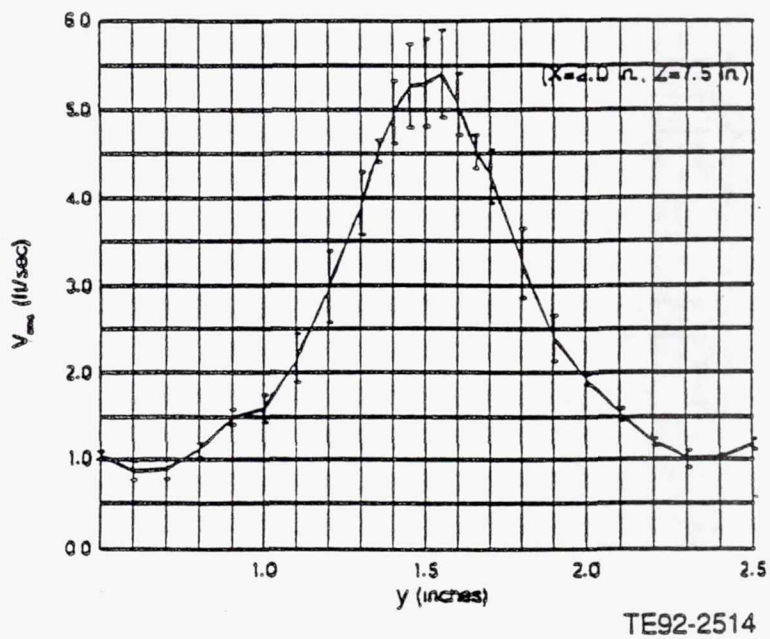


Figure 3.4.2-16. Total V_{rms} velocity error.

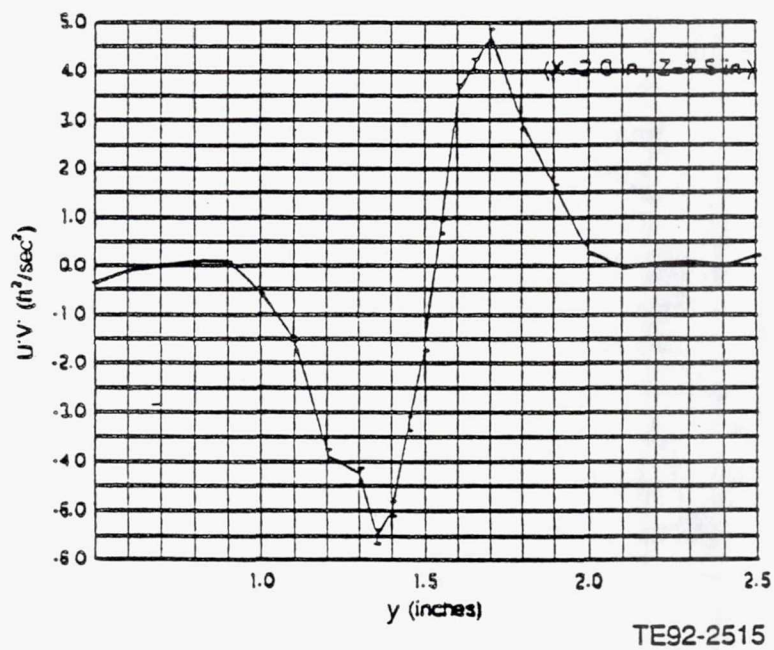


Figure 3.4.2-17. Total $U'V'$ error.

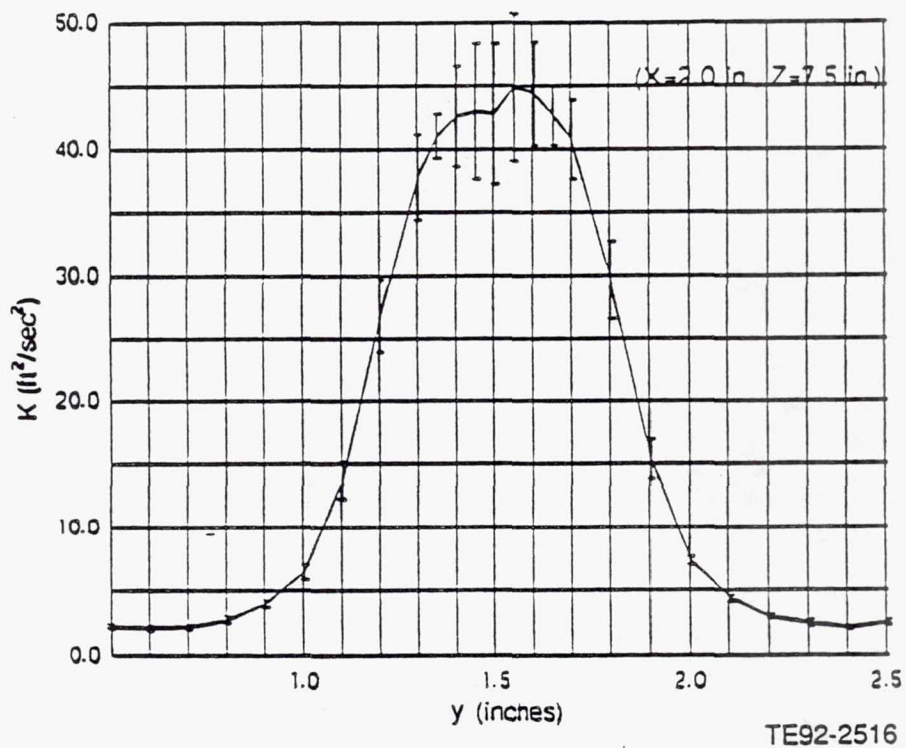


Figure 3.4.2-18. Total turbulent kinetic energy error.

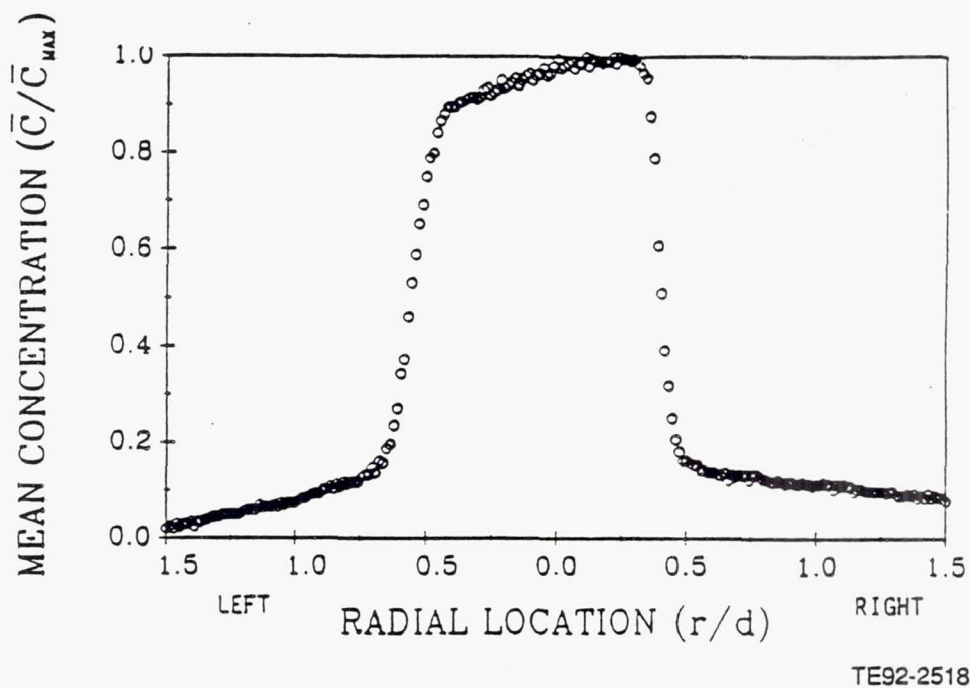
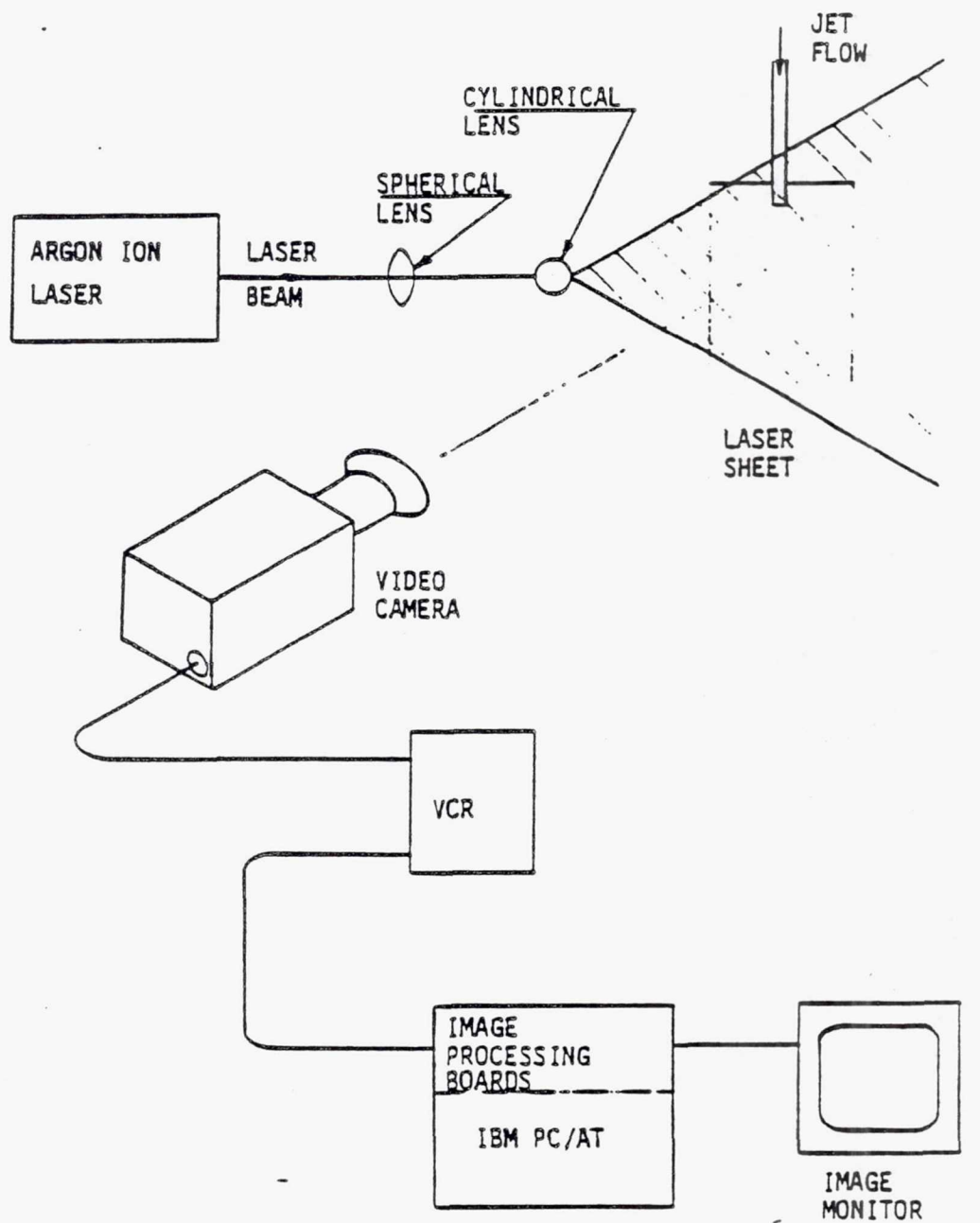


Figure 3.4.2-19. Mean concentration of fluorescent dye in round jet ($x/D=0.5$).



TE92-2519

Figure 3.4.2-20. Test equipment schematic design.

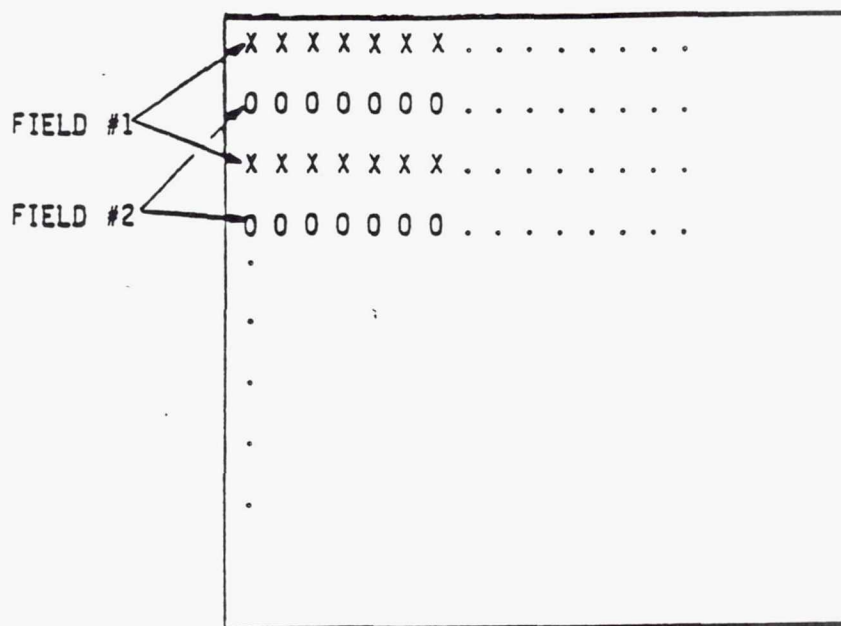
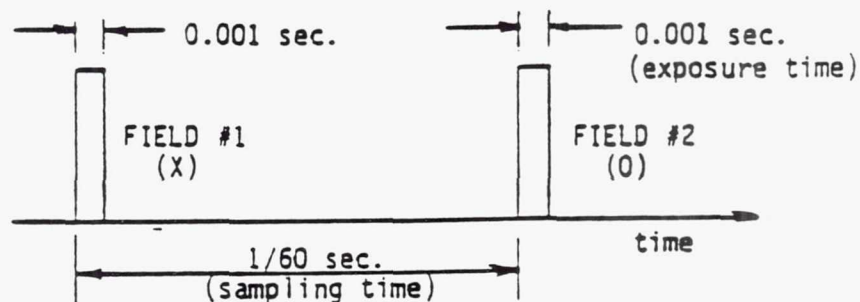
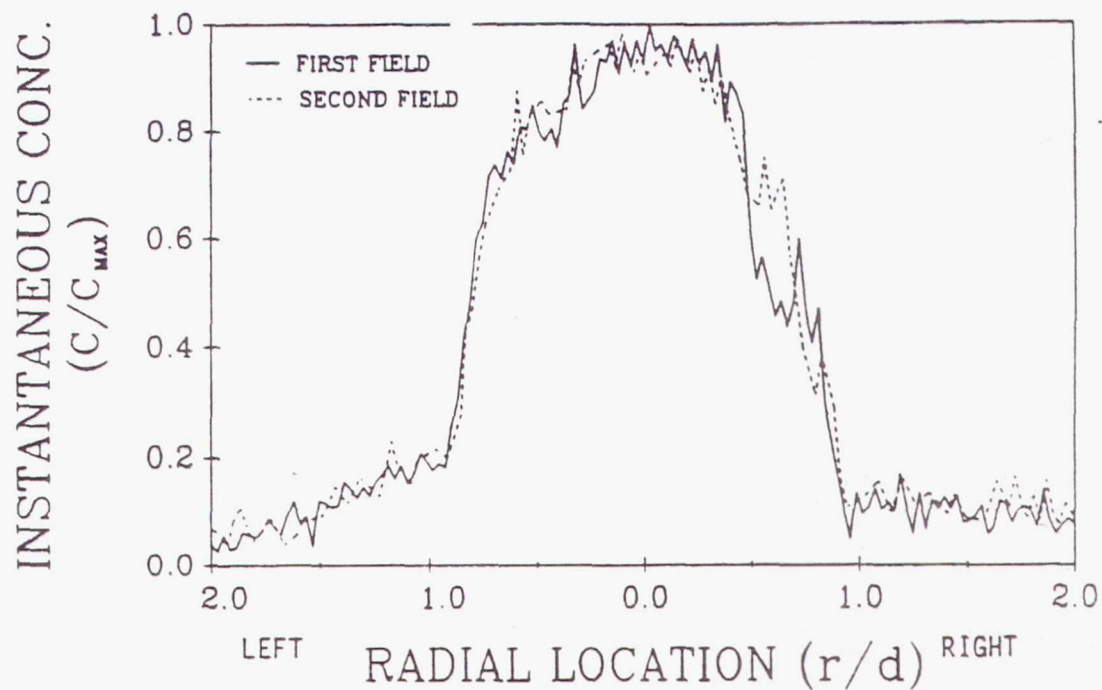


IMAGE PIXEL LOCATIONS



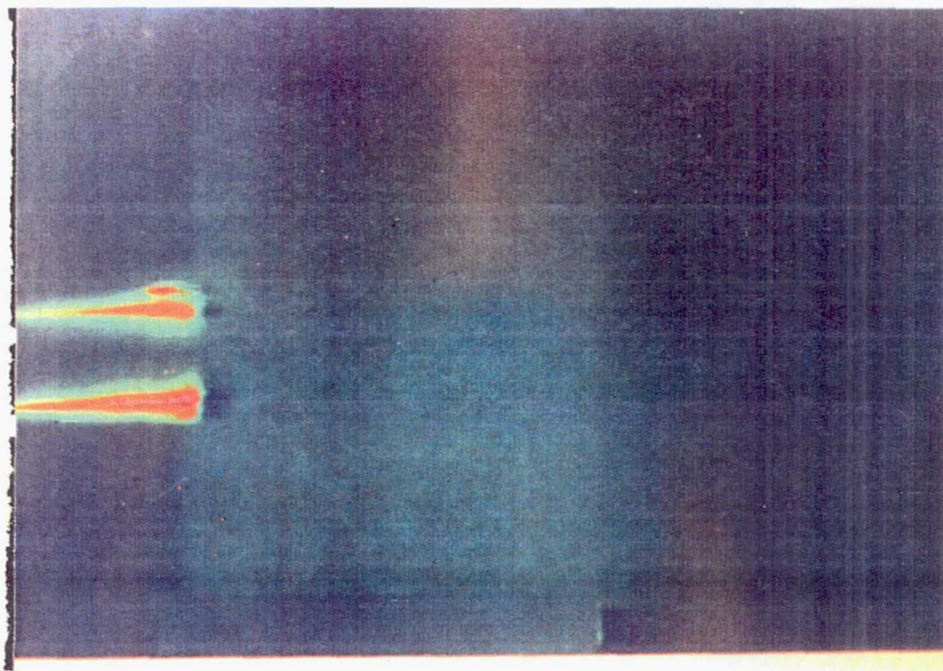
TE92-2520

Figure 3.4.2-21. Temporal and spatial image acquisition scheme.



TE92-2521

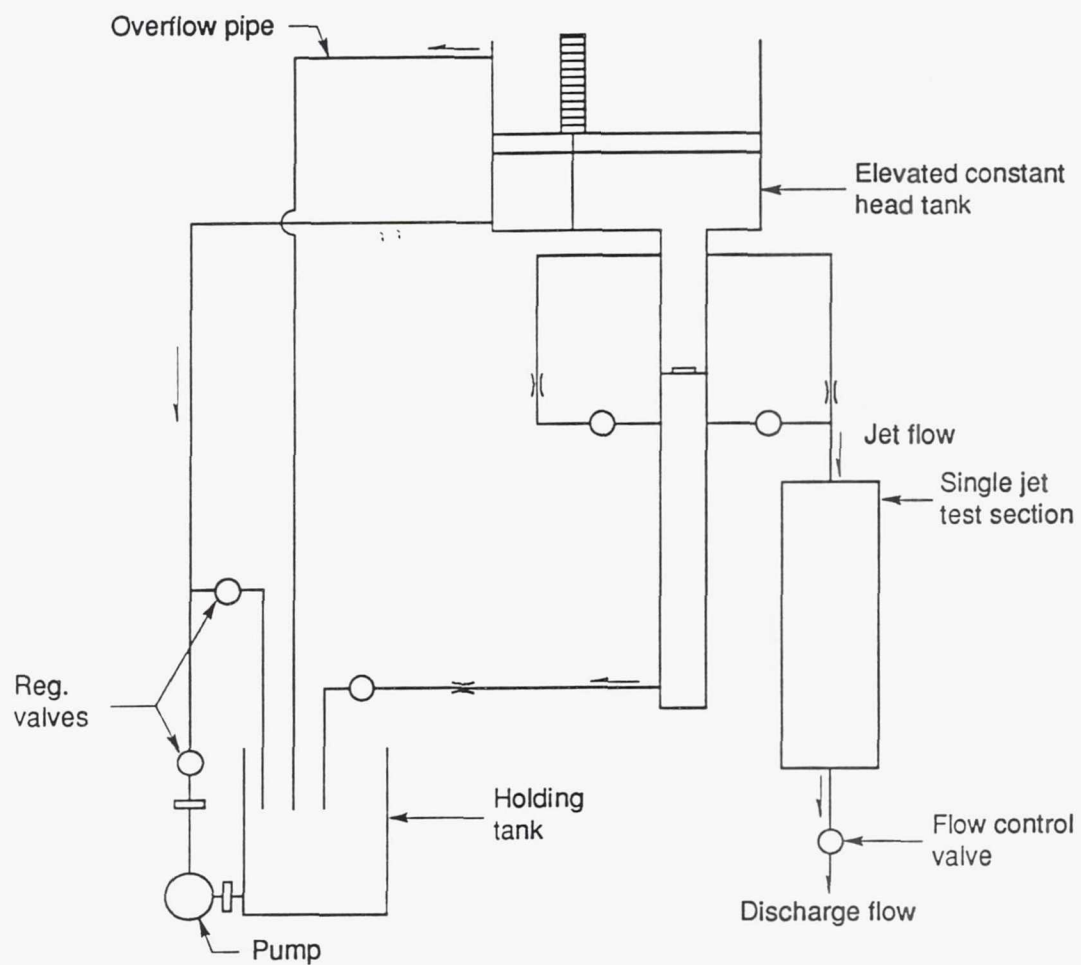
Figure 3.4.2-22. Instantaneous concentration profiles for consecutive image fields ($x/D=1.5$).



TE92-2522

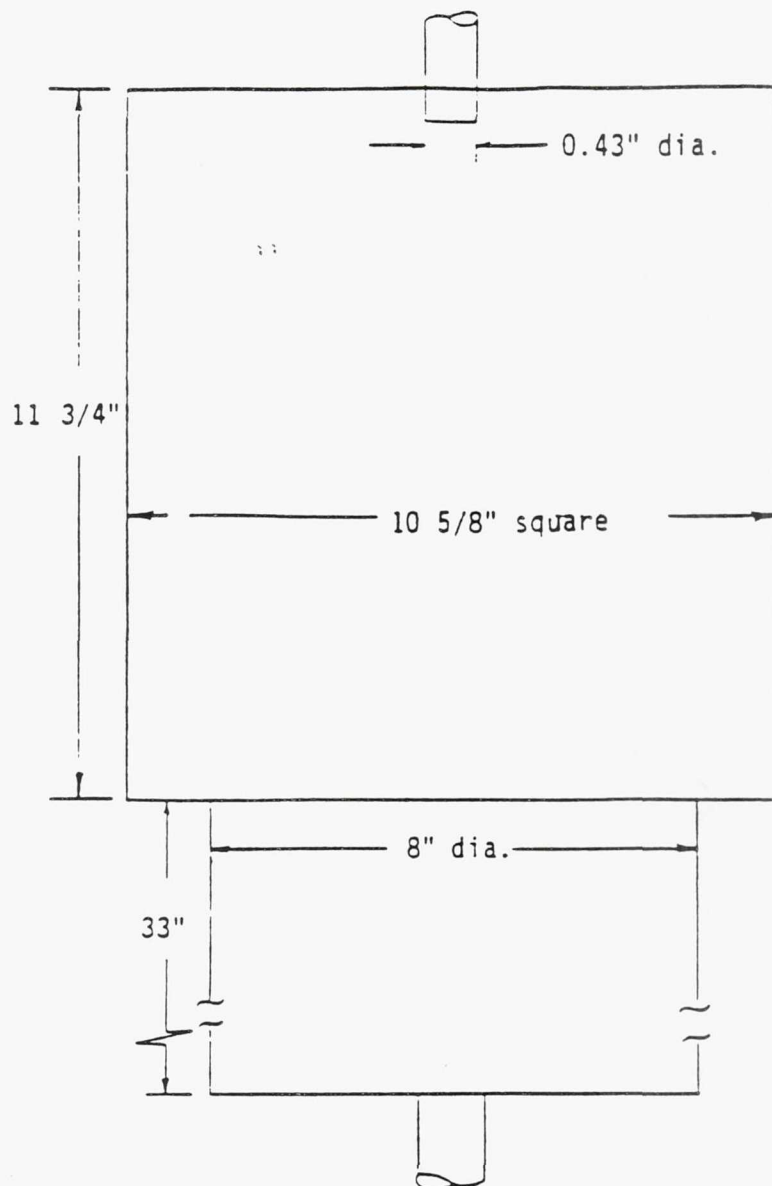
Figure 3.4.2-23. One hundred twenty-seven frame average dark response image of single jet setup.

Page intentionally left blank



TE92-2523-4

Figure 3.4.2-24. General diagram of experimental set-up.



Note: All dimensions are internal dimensions.

TE92-2524

Figure 3.4.2-25. Detail of single jet test section.

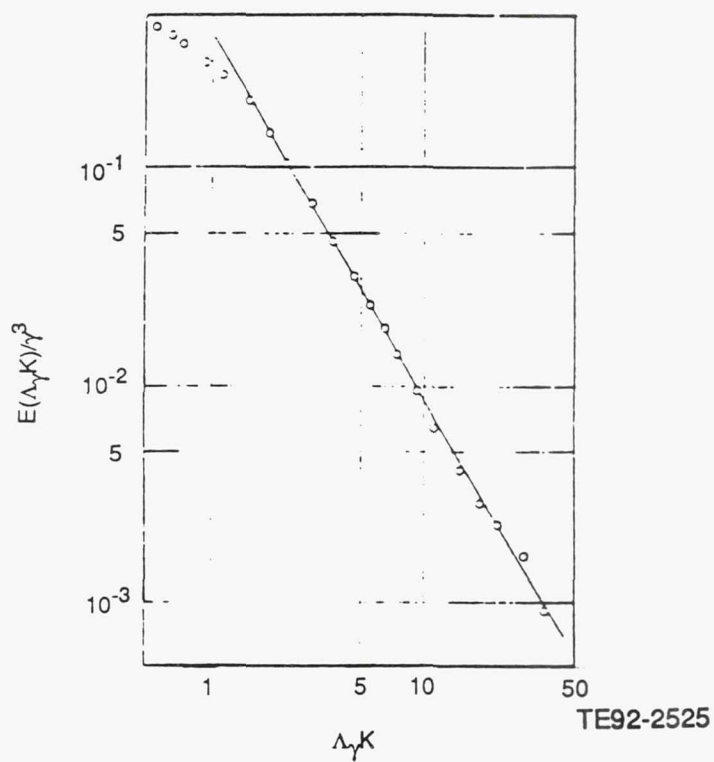
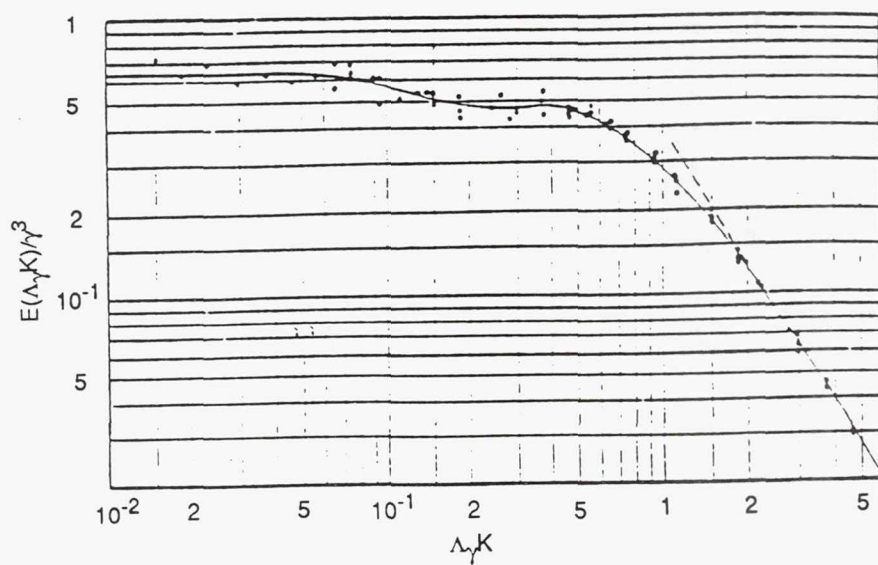
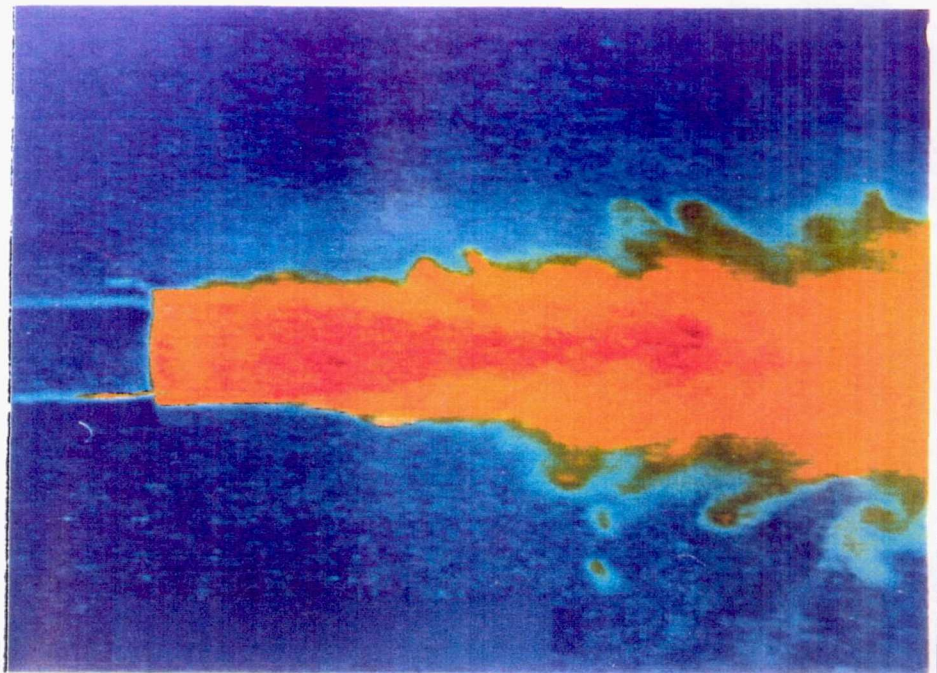


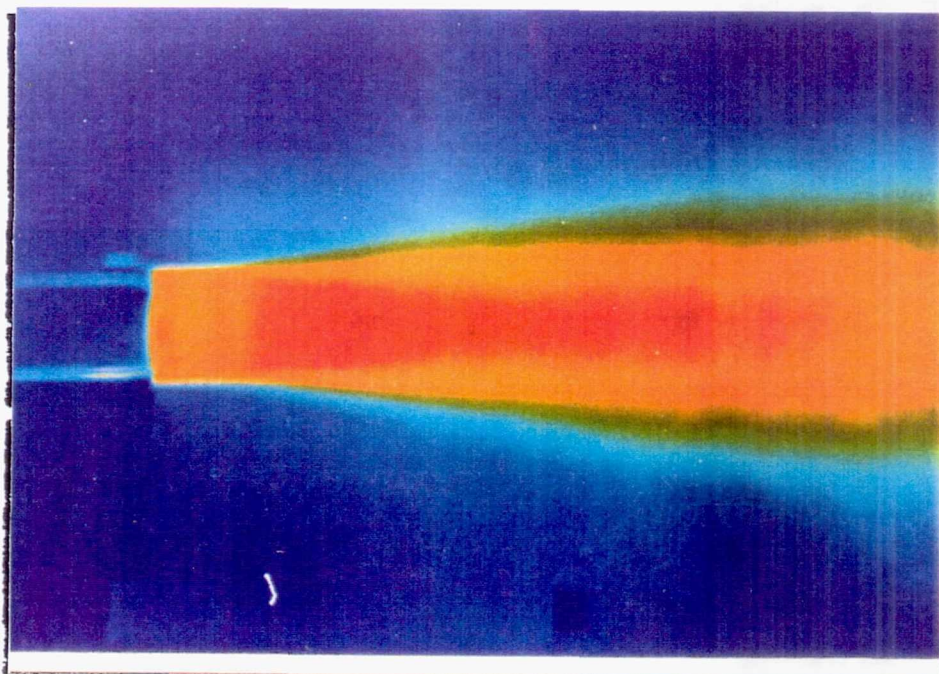
Figure 3.4.2-26. Concentration fluctuation spectrum on jet centerline ($x/D=32$).

Page intentionally left blank



TE92-2526

Figure 3.4.2-27. Single frame concentration field visualization image.

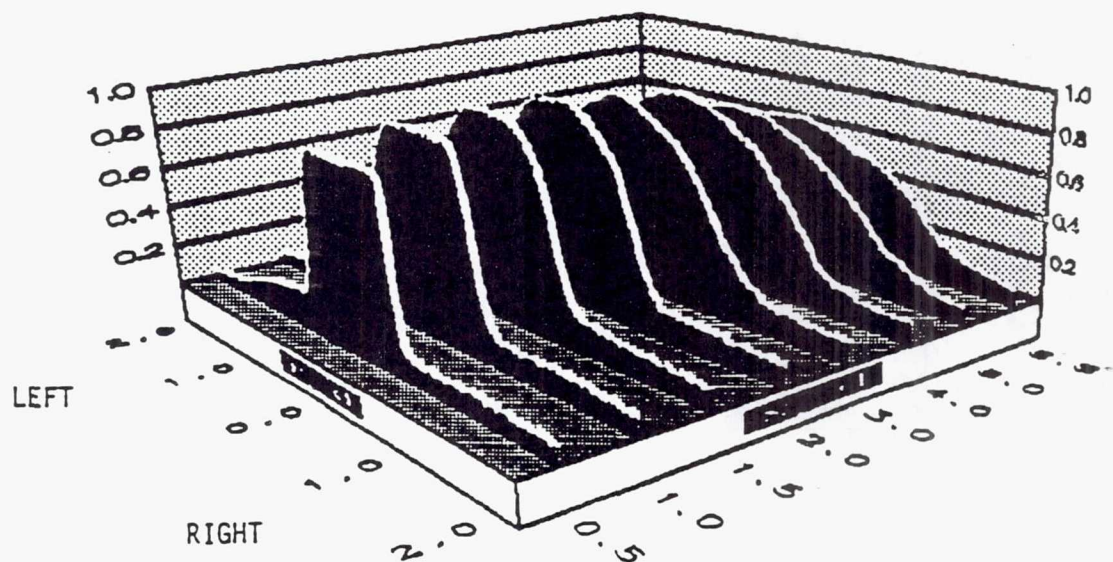


TE92-2527

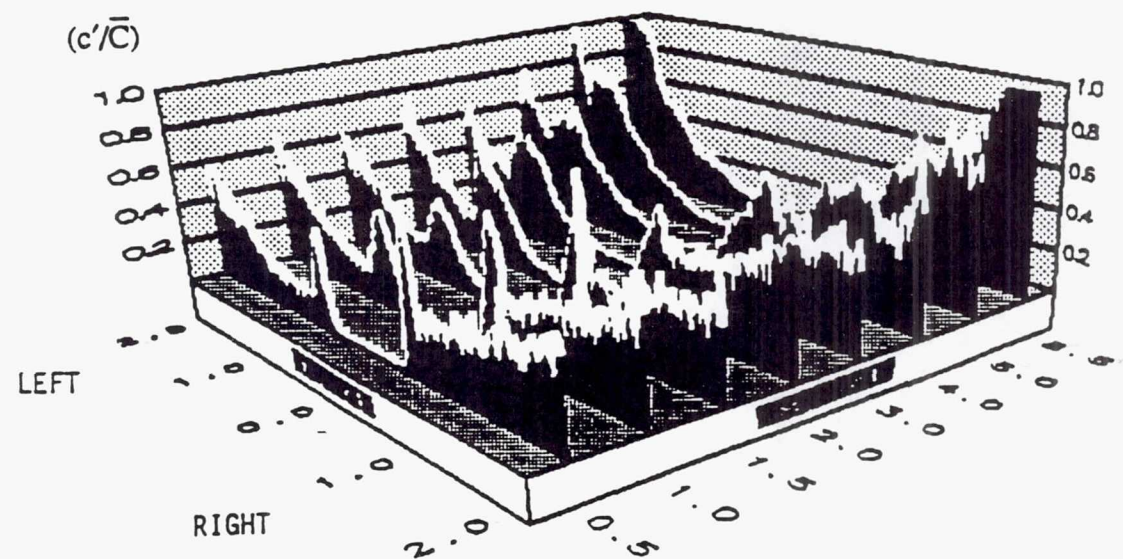
Figure 3.4.2-28. One hundred twenty-seven frames concentration field visualization image.

Page intentionally left blank

MEAN CONCENTRATION



RMS CONCENTRATION



TE92-2528

Figure 3.4.2-29. Three-dimensional representation of mean and rms concentration profiles.

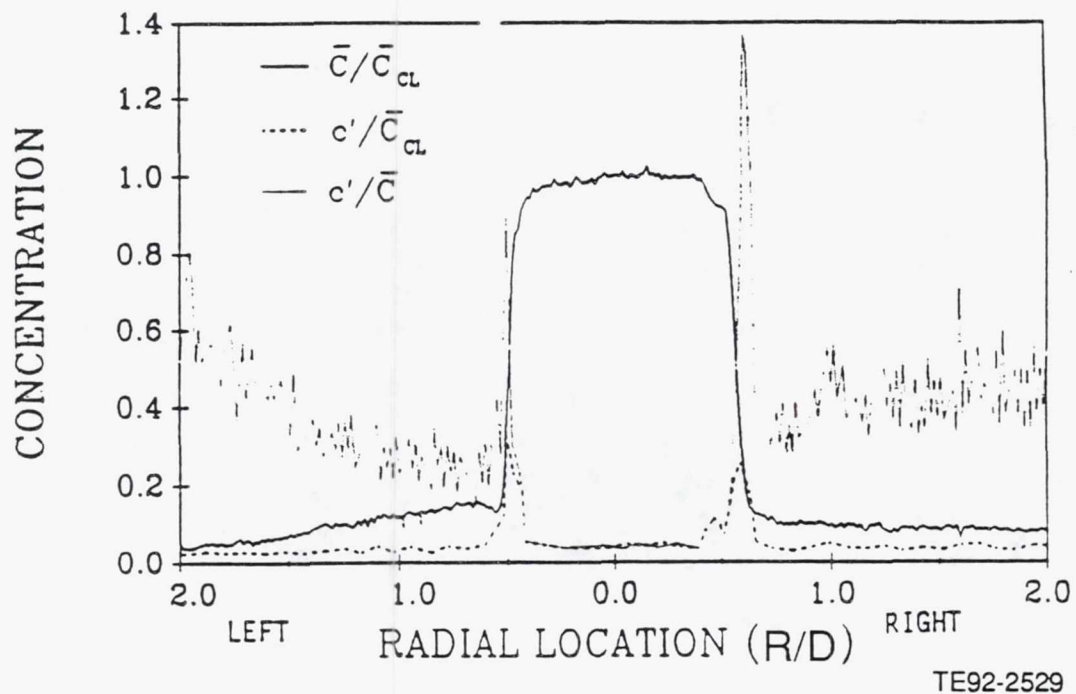


Figure 3.4.2-30. Mean and rms concentration profiles at jet exit ($x/D=0.1$).

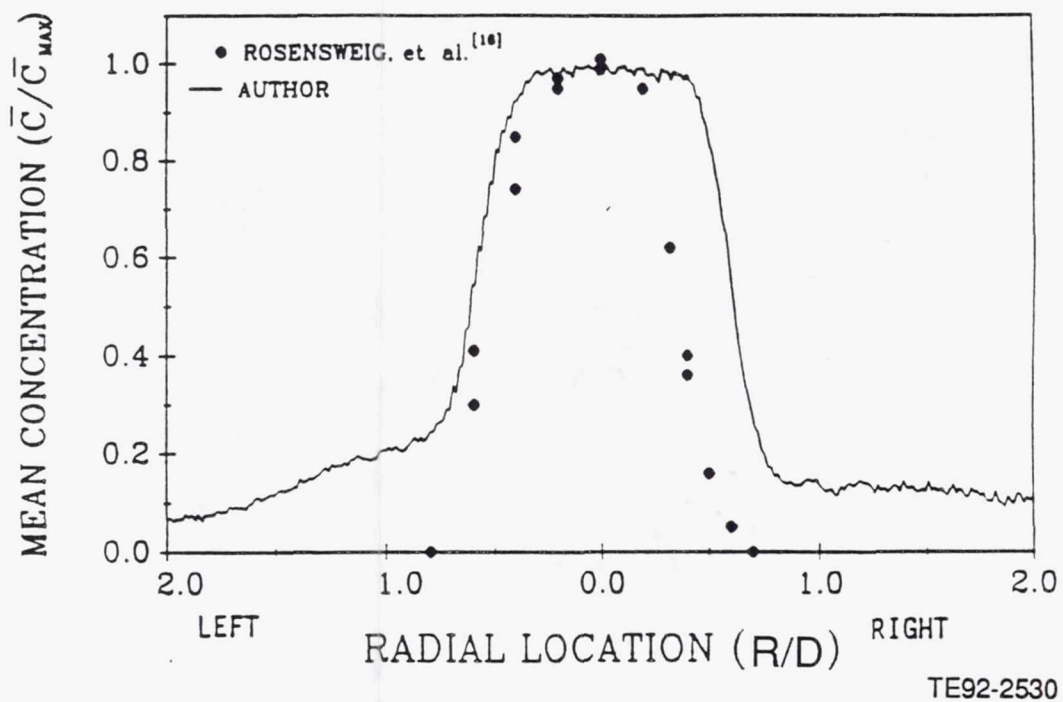
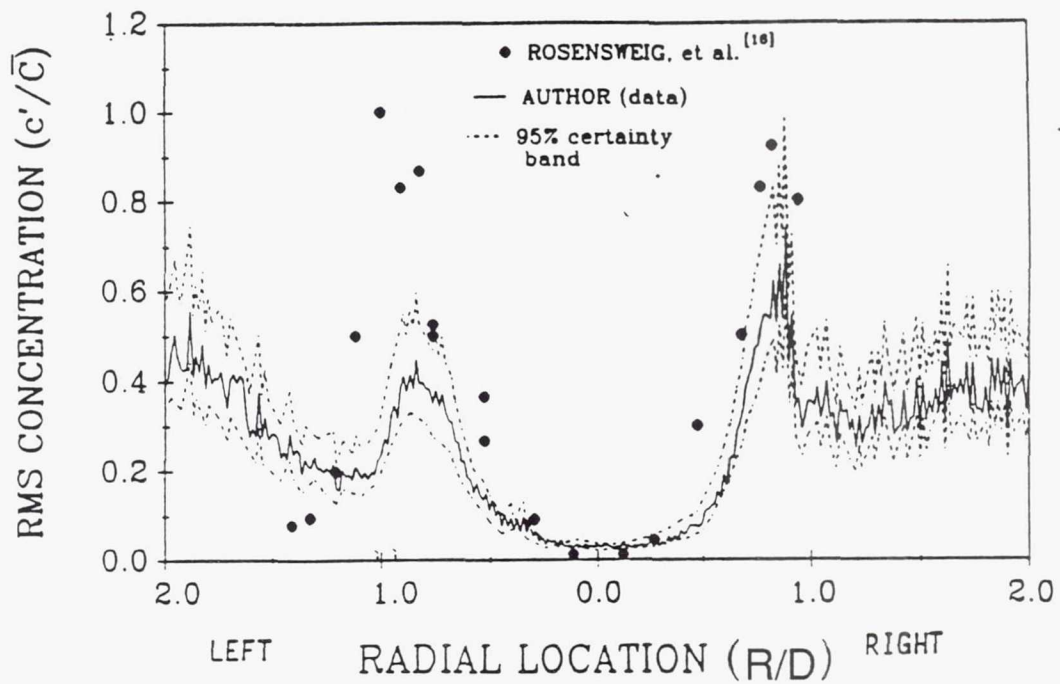
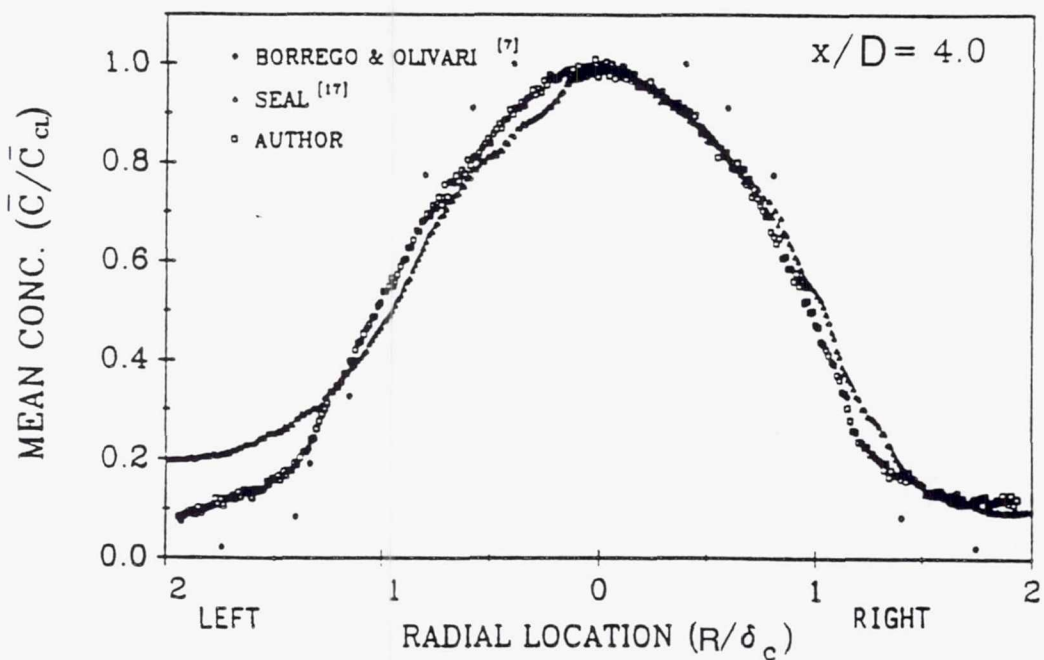
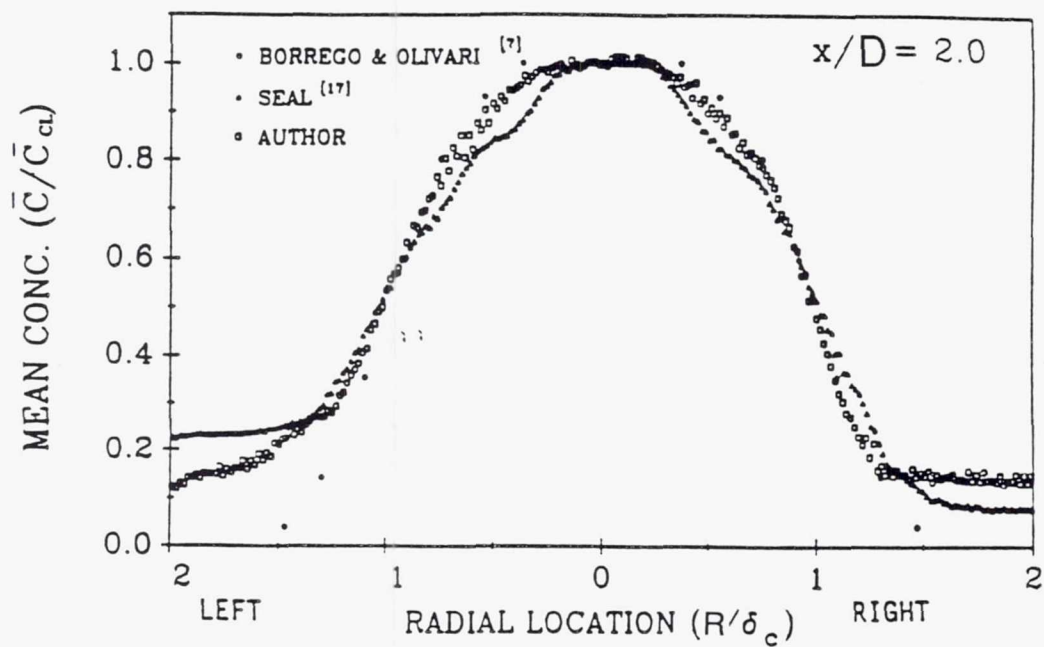


Figure 3.4.2-31. Mean concentration profile at $x/D=1.0$.



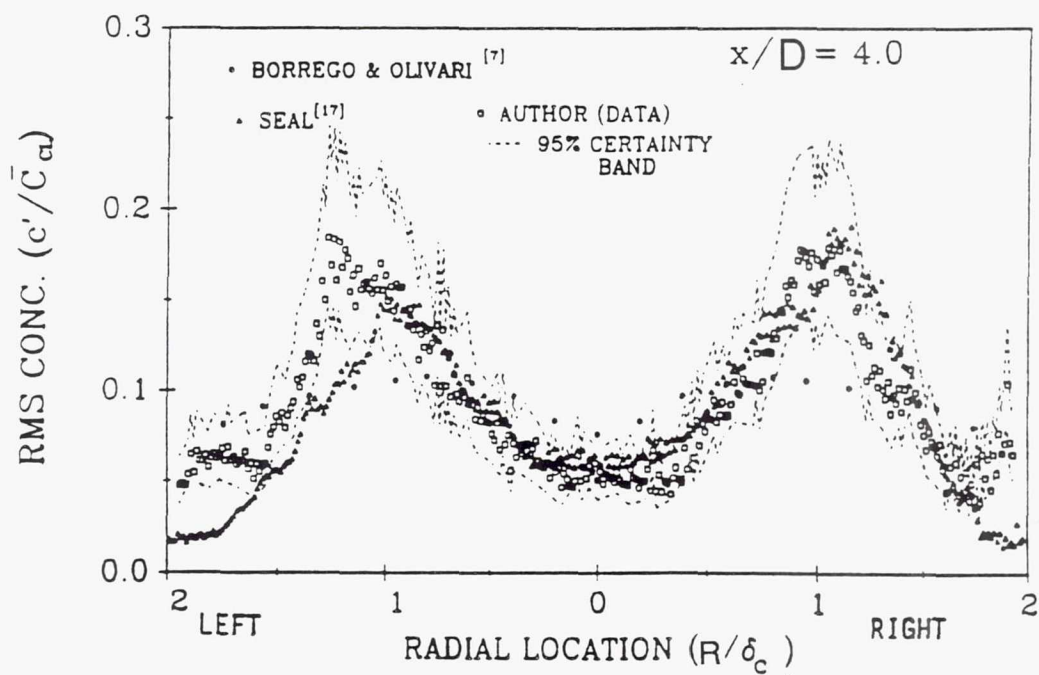
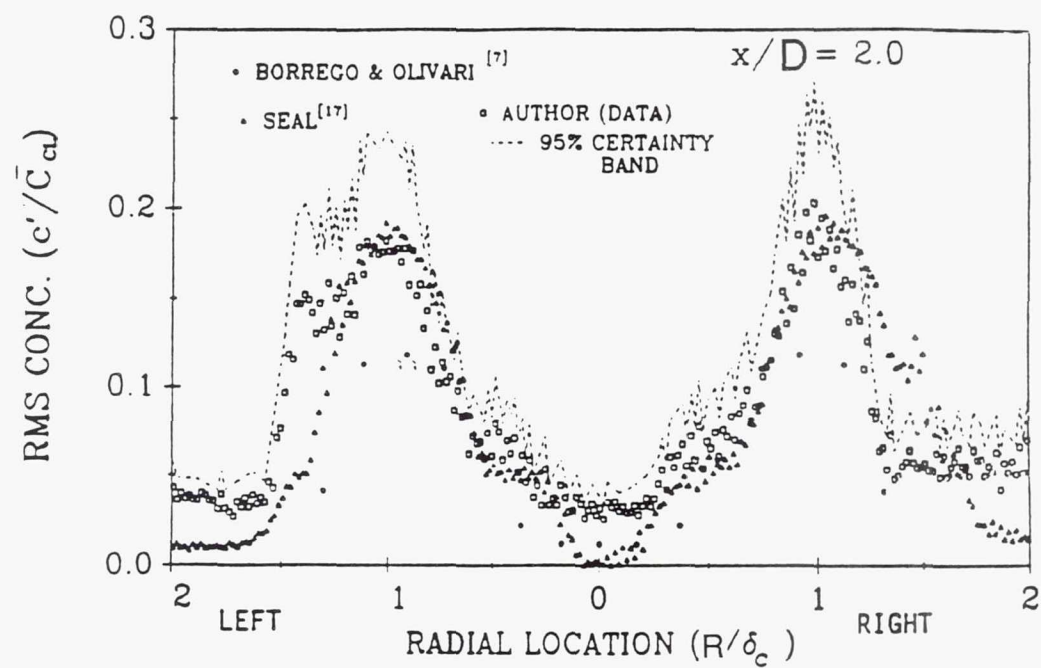
TE92-2531

Figure 3.4.2-32. Concentration profile for rms at $x/D=1.5$.



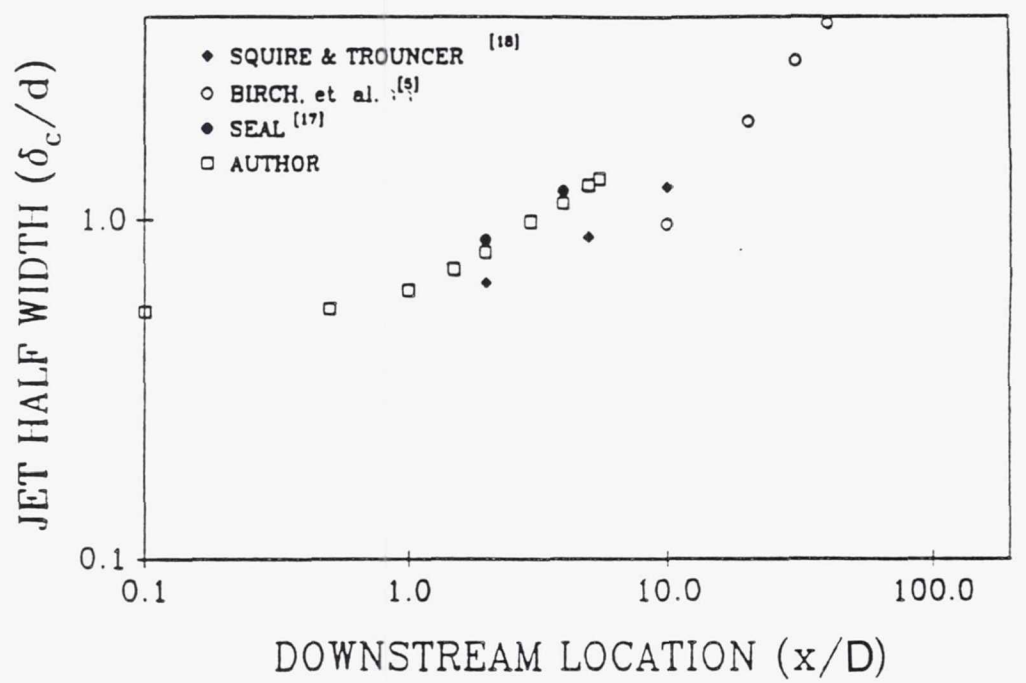
TE92-2532

Figure 3.4.2-33. Mean concentration profiles at $x/D = 2.0$ and 4.0 .



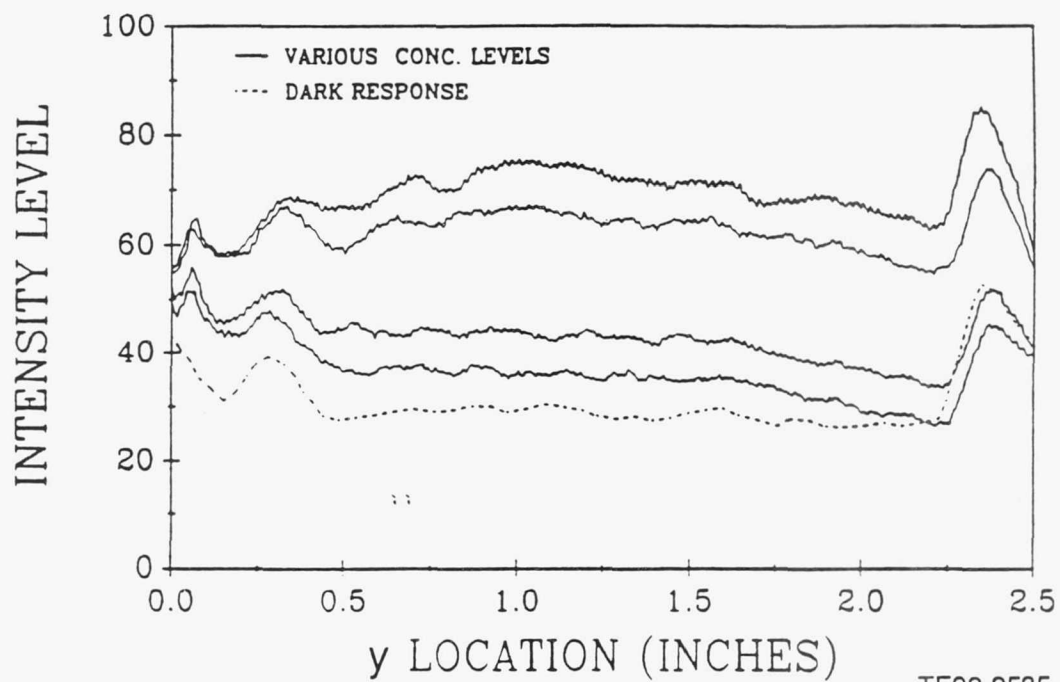
TE92-2533

Figure 3.4.2-34. Concentration profiles for rms at $x/D=2.0$ and 4.0 .



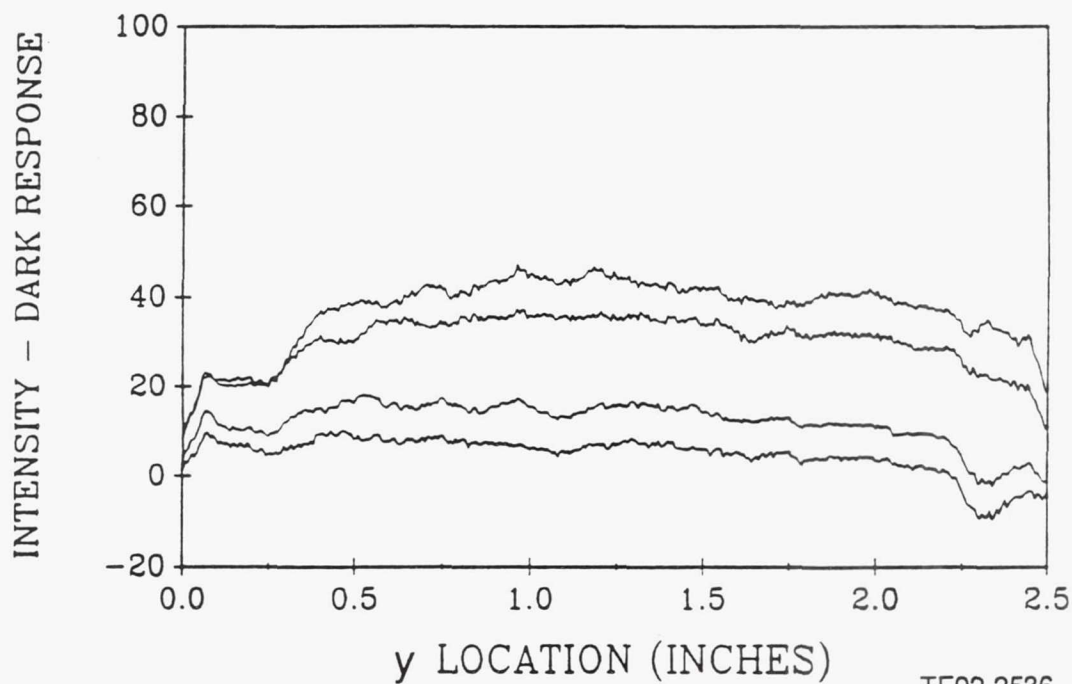
TE92-2534

Figure 3.4.2-35. Jet concentration half width growth.



TE92-2535

Figure 3.4.2-36. Uniform concentration profiles, raw data.



TE92-2536

Figure 3.4.2-37. Uniform concentration profiles, dark response subtracted.

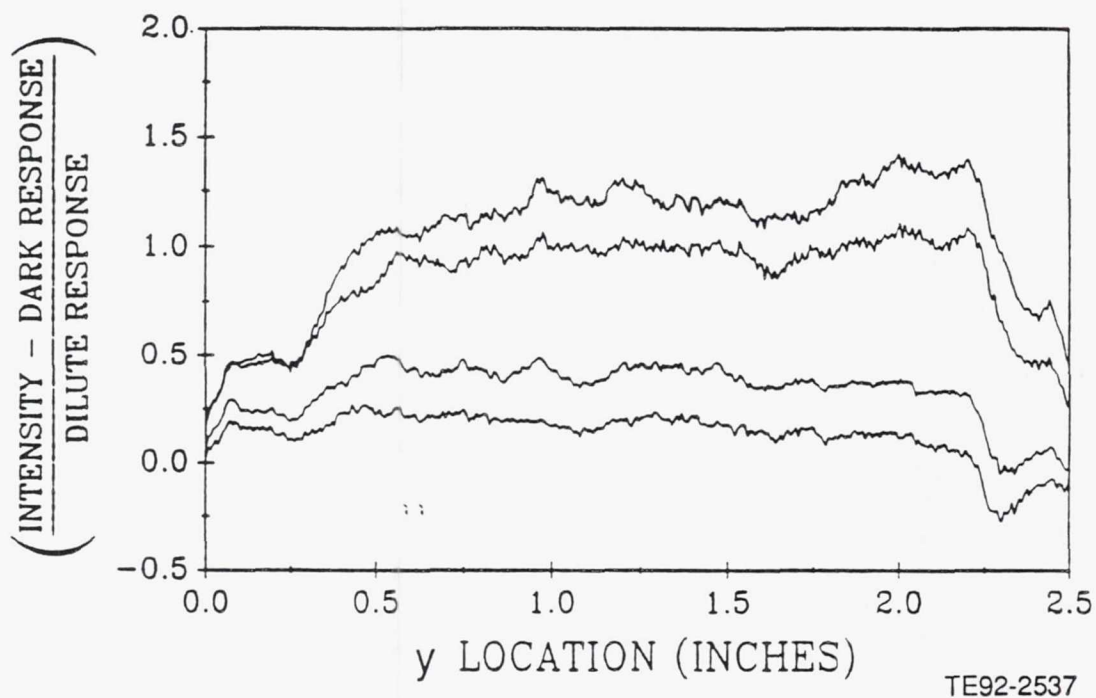


Figure 3.4.2-38. Uniform concentration profiles, two step correction applied.

REFERENCES

- Barron, D. A., 1986, "LDV Measurements in an Annular Combustor Model," M. Sc Thesis, Purdue University.
- Becker, H. A., Hottel, H. C., and Williams, G. C., 1967, "The Nozzle-Fluid Concentration Field of the Round, Turbulent, Free Jet," *Journal of Fluid Mechanics*, Vol 30, Part 2, pp 285-303.
- Becker, H. A., 1977, "Mixing, Concentration Fluctuations, and Marker Nephelometry," *Studies in Convection*, Vol 2, edited by B. E. Launder, Academic Press, New York, pp 45-139.
- Beer, J. M., and Chigier, N. A., 1983, *Combustion Aerodynamics*, Robert E. Krieger Publishing.
- Birch, A. D., Brown, D. R., Dodson, M. G., and Thomas, J. R., 1978, "The Turbulent Concentration Field of a Methane Jet," *Journal of Fluid Mechanics*, Vol 88, Part 3, pp 431-449.
- Borleteau, J. P., 1983, "Concentration Measurement with Digital Image Processing," ICIASF 1983 Record, pp 37-42.
- Borrego, C., and Olivari, D., 1980, "A Method for the Measurements of Mixing Properties in a Flow," AGARD CP-281, *Testing and Measurement Techniques in Heat Transfer and Combustion*, September.
- Brondum, D. C., and Bennett, J. C., 1986, "Numerical and Experimental Investigation of Nonswirling and Swirling Confined Jets," AIAA Paper No. 86-0040, Presented at AIAA 24th Aerospace Sciences meeting, Reno, Nevada, January.
- Brum, R. D., and Samuelson, G. S., 1987, "Two-Component Laser Anemometry Measurements of Non-Reacting and Reacting Complex Flows in a Swirl-Stabilized Model Combustor," *Experiments in Fluids*, Vol 5, pp 95-102.
- Dahm, W. J. A., and Dimotakis, P. E., 1985, "Measurements of Entrainment and Mixing in Turbulent Jets," AIAA Paper No. 85-0056.
- Durst, F., Melling, A., and Whitelaw, J. H., 1976, *Principles and Practice of Laser Doppler Anemometry*, Academic Press.
- Dwenger, R. D., 1990, "Laser Doppler Velocimeter Measurements and Laser Sheet Imaging in an Annular Combustor Model," M. Sc Thesis, Purdue University.
- Edwards, Robert V., 1987, "Report of the Special Panel on Statistical Partial Bias Problems in Laser Anemometry," *Journal of Fluids Engineering*, Vol 109, pp 89-93, June.
- Forstall, W. Jr., and Shapiro, A. H., 1950, "Momentum and Mass Transfer in Coaxial Gas Jets," ASME Transactions, *Journal of Applied Mechanics*, Vol 17, pp 399-408.
- Gore, R. W., and Ranz, W. E., 1964, "Backflows in Rotating Fluids Moving Axially Through Expanding Cross Sections," *AIChE Journal*, Vol 10, pp 83-88, January.
- Gupta, A. K., Lilley, D. G., and Syred, N., 1984, *Swirl Flows*, Abacus Press.
- Hinze, J. O., 1975, *Turbulence*, McGraw-Hill, New York.
- Koochesfahani, M. M. and Dimotakis, P. E., 1984, "Laser Induced Fluorescence Measurements of Concentration in a Plane Mixing Layer," AIAA paper No. 84-0198, AIAA 22nd Aerospace Sciences Meeting, Reno, Nevada, January.
- Laufer, J., 1954, "The Structure of Turbulence in Fully Developed Pipe Flow," NACA Report 1174.
- Long, M. B., Chu, B. T., and Chang, R. K., 1981, "Instantaneous Two-Dimensional Gas Concentration Measurements by Light Scattering," AIAA Journal, Vol 19, No. 9, pp 1151-1157.
- Mathur and MacCallum, 1967, "Swirling Air Jets From Vane Swirlers. Part 1: Free Jets," *Journal of the Institute of Fuel*, May.
- McLaughlin, D. K., and Tiederman, W. G., 1973, "Biasing Correction for Individual Realization of Laser Velocimeter Measurements in Turbulent Flows," *Physics of Fluids*, Vol 16, No. 12, pp 2082-2088, December.
- Morgan, D. C., 1988, "Concentration Measurement in Cold Flow Model Annular Combustor Using Laser-Induced Fluorescent," NASA-CR 182252.
- Roesler, T. C., 1980, "Investigation of Bias Errors in Laser Doppler Velocimeter Measurements," MS Thesis, Purdue University, August.
- Rosenweig, R. N., 1966, Sc.D. dissertation, Massachusetts Institute of Technology, 1966.
- Rosenweig, R. E., Hottel, H. C., and Williams, G. C., 1961, "Smoke Scattered Light Measurements of Turbulent Concentration Fluctuations," *Chemical Engineering Science*, Vol 15, pp 111-129, July.

- Schaughnessy, E. J., and Morton, J. B., 1977, "Light Scattering Measurements of Particle Concentration in a Turbulent Jet," *Journal of Fluid Mechanics*, Vol 80, Part 1, pp 129-148.
- Schlichting, H., 1979, *Boundary-Layer Theory*, McGraw-Hill.
- Seal II, M. D., 1988, "An Experimental Study of Swirling Flows as Applied to Annular Combustors," M. Sc Thesis, Purdue University.
- Squire, H. B., and Trouncer, J., 1944, "Round Jets in a General Stream," ARC Technical Report R&M No. 1974.
- Tennekes, H., and Lumley, J. L., 1973, *A First Course in Turbulence*, MIT Press.
- Vu, B. T., and Gouldin, F. C., 1982, "Flow Measurement in a Model Swirl Combustor," *AIAA Journal*, Vol 20, pp 642-651, May.
- Walker, D. A., 1987, "A Fluorescence Technique for Measurement of Concentration in Mixing Liquids," *Journal of Physics E: Scientific Instruments*, Vol 20, pp 217-224.

REPORT DOCUMENTATION PAGE

Form Approved
OMB No. 0704-0188

Public reporting burden for this collection of information is estimated to average 1 hour per response, including the time for reviewing instructions, searching existing data sources, gathering and maintaining the data needed, and completing and reviewing the collection of information. Send comments regarding this burden estimate or any other aspect of this collection of information, including suggestions for reducing this burden, to Washington Headquarters Services, Directorate for Information Operations and Reports, 1215 Jefferson Davis Highway, Suite 1204, Arlington, VA 22202-4302, and to the Office of Management and Budget, Paperwork Reduction Project (0704-0188), Washington, DC 20503.

1. AGENCY USE ONLY (Leave blank)		2. REPORT DATE November 1993	3. REPORT TYPE AND DATES COVERED Final Contractor Report	
4. TITLE AND SUBTITLE Flow Interaction Experiment Aerothermal Modeling Phase II Final Report--Volume I			5. FUNDING NUMBERS WU-505-62-52 C-NAS3-24350	
6. AUTHOR(S) M. Nikjooy, H.C. Mongia, J.P. Sullivan, and S.N.B. Murthy				
7. PERFORMING ORGANIZATION NAME(S) AND ADDRESS(ES) General Motors Corporation Allison Gas Turbine Division P.O. Box 420 Indianapolis, Indiana 46206-0420			8. PERFORMING ORGANIZATION REPORT NUMBER E-8177 EDR 16026	
9. SPONSORING/MONITORING AGENCY NAME(S) AND ADDRESS(ES) National Aeronautics and Space Administration Lewis Research Center Cleveland, Ohio 44135-3191			10. SPONSORING/MONITORING AGENCY REPORT NUMBER NASA CR-189192	
11. SUPPLEMENTARY NOTES M. Nikjooy and H.C. Mongia, General Motors Corporation; J.P. Sullivan and S.N.B. Murthy, Purdue University, School of Engineering, West Lafayette, Indiana 47907. Project Manager, James D. Holdeman, Internal Fluid Mechanics Division, (216) 433-5868.				
12a. DISTRIBUTION/AVAILABILITY STATEMENT Unclassified - Unlimited Subject Category 07			12b. DISTRIBUTION CODE	
13. ABSTRACT (Maximum 200 words) An experimental and computational study is reported for the flow of a turbulent jet discharging into a rectangular enclosure. The experimental configurations consisting of primary jets only, annular jets only, and a combination of annular and primary jets are investigated to provide a better understanding of the flow field in an annular combustor. A laser Doppler velocimeter is used to measure mean velocity and Reynolds stress components. Major features of the flow field include recirculation, primary and annular jet interaction, and high turbulence. A significant result from this study is the effect the primary jets have on the flow field. The primary jets are seen to create statistically larger recirculation zones and higher turbulence levels. In addition, a technique called marker nephelometry is used to provide mean concentration values in the model combustor. Computations are performed using three levels of turbulence closures, namely k- ϵ model, algebraic second moment (ASM), and differential second moment (DSM) closure. Two different numerical schemes are applied. One is the lower-order power-law differencing scheme (PLDS) and the other is the higher-order flux-spline differencing scheme (FSDS). A comparison is made of the performance of these schemes. The numerical results are compared with experimental data. For the cases considered in this study, the FSDS is more accurate than the PLDS. For a prescribed accuracy, the flux-spline scheme requires a far fewer number of grid points. Thus, it has the potential for providing a numerical error-free solution, especially for three-dimensional flows, without requiring an excessively fine grid. Although qualitatively good comparison with data was obtained, the deficiencies regarding to modeled dissipation rate (ϵ) equation, pressure-strain correlation model, and the inlet ϵ profile and other critical closure issues need to be resolved before one can achieve the degree of accuracy required to analytically design combustion systems.				
14. SUBJECT TERMS Turbulence modeling; Jet-in-cross flow; Three-dimensional flow; Gas turbine combustion; Experimental data; Turbulent flow model validation			15. NUMBER OF PAGES 376	
			16. PRICE CODE A17	
17. SECURITY CLASSIFICATION OF REPORT Unclassified	18. SECURITY CLASSIFICATION OF THIS PAGE Unclassified	19. SECURITY CLASSIFICATION OF ABSTRACT Unclassified	20. LIMITATION OF ABSTRACT	